

Excimer Laser Technology

D. Basting · G. Marowsky (Eds.)

Excimer Laser Technology

With 257 Figures



Editors

Dr. Dirk Basting
2200 South Ocean Lane
Fort Lauderdale, FL 33316-3831
USA

Professor Dr. Gerd Marowsky
Laser-Laboratorium Göttingen e.V.
Hans-Adolf-Krebs-Weg 1
37077 Göttingen, Germany

Copy editor

Dr. Uwe Brinkmann, Göttingen-Bovenden, Germany

Library of Congress Control Number: 2005923161

ISBN-10 3-540-20056-8 Springer Berlin Heidelberg New York
ISBN-13 978-3-540-20056-7 Springer Berlin Heidelberg New York

This work is subject to copyright. All rights are reserved, whether the whole or part of the material is concerned, specifically the rights of translation, reprinting, reuse of illustrations, recitation, broadcasting, reproduction on microfilm or in any other way, and storage in data banks. Duplication of this publication or parts thereof is permitted only under the provisions of the German Copyright Law of September 9, 1965, in its current version, and permission for use must always be obtained from Springer. Violations are liable for prosecution under the German Copyright Law.

Springer is a part of Springer Science+Business Media
springeronline.com

© Springer-Verlag Berlin Heidelberg 2005
Printed in Germany

The use of general descriptive names, registered names, trademarks, etc. in this publication does not imply, even in the absence of a specific statement, that such names are exempt from the relevant protective laws and regulations and therefore free for general use.

Typesetting: by the authors and F. Herweg EDV Beratung using a Springer L^AT_EX macro package
Cover design: E. Kirchner, Springer Heidelberg

Printed on acid-free paper SPIN: 10917886 56/3141/jl 5 4 3 2 1 0

Preface

The aim of this book is to provide a practical guide on the fundamentals, status of present technology and applications of excimer lasers. Theoretical details have been intentionally omitted. The book has emerged from “Excimer laser technology: Laser sources, optics, systems and applications” issued earlier by a manufacturer of excimer lasers. The scope of the book has been considerably enlarged and the knowledge deepened by the participation of several renowned international researchers. Thus, it may form not only the basis for training programs for service and maintenance personnel on excimer lasers, but serves also to address researchers, technologists and newcomers in the field of UV lasers and applications who require a thorough introduction to the field.

The book is divided into two main chapters: Fundamentals and Applications, along with a short introductory chapter, briefly covering a variety of subjects and some historical remarks and a final outlook chapter. The chapter ‘Fundamentals’ provides a short introduction to laser physics and some descriptions of optical components needed for successful operation and application of lasers operating in the UV spectral range. This includes the special demands concerning optical materials, beam shaping optics, and beam diagnostics. The chapter ‘Applications’ opens with an overview of the various fields of actual excimer laser applications, then goes into more detail in important fields like ablative micro-fabrication, nano-structuring with femtosecond excimer laser pulses, material modification including microlithography, deposition of thin films, combustion analysis, and medical applications. At the leading edge of current research, the chapter on ultra-high intensity applications deals with the generation of “hollow atoms”. Micro-fabrication using F₂-laser radiation at 157 nm completes the range of UV-laser applications.

The last chapter focuses on next-generation lithography using 13.5 nm radiation. Radiation sources in the extreme UV (EUV), realized by both laser and discharge pumping, are expected to transform micro-lithography into nano-lithography. The editors and authors hope that this publication will be a valuable source of information for students, engineers, and scientists wishing to work in the field of excimer lasers.

Acknowledgement. The editors wish to thank Jay Jethwa, Charles K. Rhodes and Petra Tregel for critical reading of the manuscripts and many practical hints and fruitful discussions. Valuable coordination and constant technical assistance of Dirk Born, Jutta Steckel, Thomas Müller, Karsten Roetmann, and Sebastian Kranzusch is gratefully acknowledged. Sparkasse Göttingen, represented by Rainer Hald, made the financial backing of this project possible. With the help of the Otto-Hahn-Bibliothek, Bernhard Reuse and Reinhard Harbaum, we have been able to identify additional references from earlier times.

The editors thank R. Srinivasan for various contributions to chapter 1.2, Historical Review of Excimer Laser Development.

We owe particular thanks to our copy editor Uwe Brinkmann, who prepared editable manuscripts from the submitted material and attempted to achieve correct printing together with Thomas Eggers, who coped with the demanding desk-top page making work.

The editors took liberty to make appropriate changes in some of the manuscripts for further improvement of the book.

Göttingen,
December 2004

*Dirk Basting
Gerd Marowsky*

Contents

1	Introduction	1
1.1	Introductory Remarks	1
1.1.1	The Unique Microstructuring Capabilities of Excimer Lasers	1
1.1.2	Commercial Impact of Excimer Lasers	3
1.1.3	Could Excimers Have Been the First Media with Optical Gain?	6
1.1.4	Literature	6
References		7
1.2	Historical Review of Excimer Laser Development	8
References		20
1.3	Trends in Worldwide Excimer Laser Sales	22
1.3.1	The World's Laser Markets at the End of 2004	22
1.3.2	Excimer Laser Markets	23
1.3.3	Excimer Laser Markets: Industrial	25
1.3.4	Excimer Laser Markets: Medical Therapy	27
1.3.5	Excimer Laser Markets: Research	29
References		29

Part I Fundamentals

2	Some Fundamentals of Laser Physics	33
2.1	The Wave-Particle Duality of Light	33
2.2	Electromagnetic Radiation	33
2.3	Spontaneous and Stimulated Emission, Population Inversion	34
2.4	Design Principle of a Laser	37
2.5	Types of Lasers	38
References		40
3	Principles of Excimer Lasers	41
References		45

VIII Contents

4 Design and Technology of Excimer Lasers	47
4.1 Excitation	47
4.2 Preionization	49
4.3 Discharge Electrodes	51
4.4 Discharge Circuits	52
4.5 Power Supplies	58
4.6 Circulation, Laser Gas Cooling, and Cleaning	62
4.7 Safety Standards for Industrial Excimer Lasers	64
4.7.1 CE Mark	65
4.7.2 Electromagnetic Compatibility (EMC) Directive 89/366/ECC	65
4.7.3 Design Rules for Electromagnetic Compatibility	66
4.7.4 Low Voltage Directive 73/23/ECC	68
4.7.5 Pressure Equipment Directive 97/23/EC	68
4.7.6 Machinery Directive 89/392/EEC (Amended 98/37/EEC)	69
4.7.7 Laser Radiation Safety	70
4.7.8 SEMI Standards	71
References	73
5 Specially Designed Excimer Lasers	75
5.1 High-Repetition-Rate and High-Power Lasers	75
References	79
5.2 High-Energy Lasers	81
5.2.1 KrF and ArF Lasers	82
5.2.2 XeCl Lasers	85
References	88
6 Excimer Lasers for Microlithography	89
6.1 Motivation	89
6.2 Wavelengths	92
6.3 Spectral Output	94
6.4 Line Narrowing	94
6.5 Wavelength Control	95
6.6 Laser Power and Energy	98
6.7 Energy Dose Control	98
6.8 Dual-Chamber Lasers	99
6.9 Pulse Length	101
6.10 Outlook	102
References	103
7 Laser Beam Characterization	105
7.1 Introduction	105
7.2 Recording of Spatial Beam Profiles	105
7.3 Evaluation of Beam Parameters	107

7.3.1	Beam Width	107
7.3.2	Beam Divergence	110
7.3.3	Beam Positional and Directional Stability	110
7.3.4	Homogenized Beams	112
7.4	Wavefront Measurement	114
	References	116
8	Optical Coatings for Excimer Laser Applications	119
8.1	Introduction	119
8.2	Basics	119
8.3	Interaction Mechanisms of UV Photons with Coated Optical Elements	120
8.4	Absorption	121
8.5	Coatings	122
8.5.1	Metals	122
8.5.2	Dielectrics	122
8.6	XUV Coatings	124
8.7	Summary	126
	References	126
9	Small Structures with Large Excimer Lasers	127
9.1	Introduction	127
9.2	Nozzle Plates for Ink Jet Printers	127
9.3	Attenuators	128
9.4	Homogenizers	130
9.5	Projection Lenses	132
9.6	Mechanically and Thermally Stable Support System	133
9.7	Beam Diagnostics	133
9.8	Summary and Outlook	135
	References	135

Part II Applications

10	Overview	139
	References	145
11	Ablative Micro-Fabrication	149
11.1	Ablation	149
	References	153
11.2	Micro-Machining	155
11.2.1	Processing Techniques	156
11.2.2	Removal of Thin Layers	160
11.2.3	Drilling	162
11.2.4	Fabrication of Micro Parts	174

11.2.5 Indirect Ablation	179
11.2.6 Micro Optics Fabrication	181
11.2.7 MEMS and Nanofabrication	183
References	184
11.3 Via Drilling	187
11.3.1 Introduction	187
11.3.2 Basics	187
11.3.3 Applications	192
References	199
12 Micro-Processing of Borosilicate Glass and Polymers	201
12.1 Borosilicate Glass	201
12.1.1 Drilling of Holes in Pyrex Glass	203
12.1.2 Generation of Channels in Borosilicate Glass	206
12.1.3 Summary	211
12.2 Polymers	212
12.2.1 Generation of Channels in PMMA Using Scanner	212
12.2.2 Generation of Three Dimensional Structures in PMMA Using Scanner	213
12.2.3 Microstructuring of Polymer Tubes	216
12.2.4 Writing of Mixer Structures in PMMA	217
12.2.5 Acknowledgement	219
References	219
13 F₂-Laser Microfabrication for Photonics and Biophotonics	221
13.1 Introduction	221
13.2 Vacuum-Ultraviolet Optical Tools	222
13.2.1 High-Fluence F ₂ -Laser Optical Tool	222
13.2.2 Optical Resolution	226
13.3 Micromachining of Silica Glasses	228
13.3.1 Ablation Rates and Surface Morphology	229
13.3.2 Heat-Affected Zone	231
13.3.3 Ablation Debris	233
13.4 Micro-Optics Fabrication	234
13.4.1 Microchannels and Holes	235
13.4.2 Fiber and Rib Waveguides	237
13.4.3 Mask Fabrication	238
13.4.4 Gratings	243
13.4.5 Diffractive Optical Elements	245
13.5 Controlling Refractive Index	253
13.5.1 F ₂ -Laser Photosensitivity: Silica Glasses	254
13.5.2 F ₂ -Laser Photosensitivity: Optical Fiber	258
13.5.3 Trimming Planar Lightwave Circuits	261
13.5.4 Writing Buried Optical Waveguides	264

13.6 Biophotonics on a Chip	268
References	272
14 Nano-Structuring	
with Femtosecond Excimer Laser Pulses	279
14.1 Introduction	279
14.2 The Laser System	280
14.3 Mask Projection	281
14.4 Interference Techniques	281
References	283
15 Physical Aspects of Ultra-Fast UV Laser Transfer	285
15.1 Introduction to the Laser Transfer Process	285
15.2 Visualization of the Laser Materials Transfer	287
15.2.1 Time Resolved Schlieren Imaging Method	287
15.2.2 Dynamics of the sub- <i>ps</i> - and <i>ns</i> -Process – A Comparative Study	287
15.2.3 Conclusions	292
References	294
16 Material Modification	295
16.1 Microlithography	295
16.1.1 The Patterning Process	295
16.1.2 Optical Resolution	296
16.1.3 Optical Materials	298
16.1.4 Technology Roadmap	300
References	304
16.2 TFT Annealing	306
16.2.1 Electron Mobility Increases with Grain Size	308
16.2.2 Layer Stratification, Near and Complete Melt-Through	309
16.2.3 Excimer-Laser Based Annealing System	311
16.2.4 Outlook	312
References	312
16.3 Fiber Bragg Gratings	313
16.3.1 Introduction to Fiber Bragg Gratings (FBGs)	313
16.3.2 Manufacturing of Fiber Bragg Gratings	314
16.3.3 Applications for Fiber Bragg Gratings	318
References	320
16.4 Marking	321
References	330
16.5 Activation and Metallization of Dielectrics	331
References	333

17 Excimer-Laser Assisted Deposition of Carbon and Boron	333
Nitride-Based High-Temperature Superconducting Films	335
17.1 Introduction	335
17.2 Characteristics of Excimer Laser Ablation	336
17.3 Deposition Techniques	340
17.4 Deposition and Properties of Tetrahedral Amorphous Carbon (ta-C) Films	341
17.5 Deposition and Properties of Cubic Boron Nitride (c-BN) Films	346
17.6 Summary and Outlook	349
References	350
18 Combustion Analysis	351
18.1 Scattering Methods	352
18.2 Fluorescence Methods	356
References	360
19 Medical Applications of Excimer Lasers	361
19.1 Refractive Laser Surgery	361
19.1.1 Photo Refractive Keratectomy (PRK)	361
19.1.2 Photo Therapeutic Keratectomy (PTK)	363
19.1.3 Laser In-situ Keratomileusis (LASIK)	364
19.1.4 Customized Ablation	365
19.2 Glaucoma Surgery	367
19.3 Laser Angioplasty	369
19.4 XeCl Excimer Laser Treatment of Psoriasis	370
References	370
20 High-Intensity Applications of Excimer Lasers	373
20.1 Introduction	373
20.2 Précis of Experimental Findings	373
20.2.1 Anomalous Nonlinear Coupling to Atoms at 193 nm	373
20.2.2 Direct Multiquantum Inner-Orbital Excitation of N_2 at 248 nm	375
20.2.3 Hollow Atoms and the Cluster Concept	378
20.2.4 Multikilovolt X-ray Amplification with Clusters in Self-Trapped Plasma Channels	380
20.3 Conclusions	381
References	382
21 High-Repetition-Rate Applications of Excimer Lasers	385
21.1 Introduction	385
21.2 Technological Advances	386
21.2.1 Solid-State Pulsed High-Voltage Switch	386
21.2.2 Performance Characteristics	387

21.3 High-Repetition-Rate Applications	390
21.3.1 Flexible Mask Patterning	390
21.3.2 Long-Term Testing of Optical Material and Coatings ..	394
21.3.3 Advanced Medical Excimer Laser Systems	396
References	397
22 New Frontiers: Extreme-Ultraviolet (EUV) Technology at 13.5 nm	399
22.1 Prospects of EUV Lithography Drive the Development of High-Power EUV Sources	399
22.2 Challenges of EUV Lithography	401
22.3 Basic Technology and Requirements for EUV Sources	404
22.4 Gas-Discharge-Produced and Laser-Produced Plasma EUV Sources	406
22.4.1 Gas-Discharge-Produced Plasma EUV Sources	406
22.4.2 Laser-Produced Plasma EUV Sources	408
22.4.3 How to Characterize EUV Sources	409
22.5 GDPP and LPP EUV Sources – State of the Art	412
22.5.1 GDPP EUV Source XTS 13–35 for Integration into EUV Microstepper	412
22.5.2 High-Power Gas-Discharge-Produced Plasma EUV Sources at XTREME Technologies	413
22.5.3 Laser-Produced Plasma EUV Sources at XTREME technologies	417
22.6 Outlook	419
References	421
List of Abbreviations	423
Index	427

List of Contributors

Stephen G. Anderson

Sect. 1.3

Laser Focus World
Associate Publisher, Editor-in-chief
Pennwell
98 Spit Brook Rd.
Nashua, NH 03062
Phone: +1-603-891-9320
Fax: +1-603-891-0574
stevega@pennwell.com

Dr. D. Basting

Sects. 1.1, 1.2

Lambda Physik AG
Now:
2200 South Ocean Lane
Fort Lauderdale
FL 33316-3831 USA
Dirk@Basting.net

Dr. J. Bekesi

Sect. 14

Laser-Laboratorium Göttingen e.V.
Hans-Adolf-Krebs-Weg 1
37077 Göttingen
Phone: +49-551-503528
Fax: +49-551-503599
jbekesi@llg.gwdg.de

Prof. H. von Bergmann

Sects. 3, 4, 5

Laser Research Institute
Dept. Physics
University of Stellenbosch
South Africa

Private Bag X1, Matieland, 7602

Phone: +21-808-3376

Fax: +21-808-3385

hmvb@sun.ac.za

Dr. H. Bernitzki

Sect. 8

Laser-Zentrum Hannover e.V.
Now:
Jenoptik Laser Optik Systeme
GmbH
Göschwitzer Str. 25
07746 Jena
Phone: +49-3641-65 3256
Fax: +49-3641-65 3850
Helmut.Bernitzki@Jenoptik.com

Dr. V. Beushausen

Sect. 18

Laser-Laboratorium Göttingen e.V.
Hans-Adolf-Krebs-Weg 1
37077 Göttingen
Phone: +49-551-503523
Fax: +49-551-503599
vbeushau@llg.gwdg.de

Prof. A. B. Borisov

Sect. 20

University of Illinois at Chicago
Department of Physics
College of Liberal Arts and Sciences
845 West Taylor Street
Chicago, Illinois 60607-7059
USA
Phone: +1-312-996-4868
Fax: +1-312-996-8824
alexbor@uic.edu

Prof. V. M. Borisov

Sect. 5.2

State Research Centre Russian Federation TRINITI
Pushkov Street
142092 Troitsk
Phone: +7-095-334-0666
Fax: +7-095-334-5775
borisov@triniti.ru

Dr. K. Boyer

Sect. 20

250 East Alameda (Apt. 812)
Santa Fe, New Mexico 87501
Keithxb@comcast.net

Dr. I. Bragin

Sect. 5.2

Lambda Physik AG
Hans-Böckler-Str 12
37079 Göttingen
Phone: +49-551-6938204
Fax: +49-551-68691
ibradin@lambdaphysik.com

J. Davis

Sect. 20

davisj@ppdmail.nrl.navy.mil

Prof. N. Djeu

Sect. 1.2

University of South Florida
Tampa FL 33620
ndjeu@chuma.cas.usf.edu

Dr. R.F. Delmdahl

Sect. 21

Lambda Physik AG
Hans-Böckler-Str 12
37079 Göttingen
Phone: +49-551-6938397
Fax: +49-551-68691
rdelmdahl@lambdaphysik.com

Prof. H. Exner

Sect. 12

Laserinstitut Mittelsachsen e.V.
Hochschule Mittweida
University of Applied Sciences
Technikumplatz 17
09648 Mittweida
Phone: +49-3727-580
Fax: +49-3727-58-1379
exner@laserinstitut-mittelsachsen.de

Dr. M. Fiebig

Sect. 16.2

Lambda Physik AG
Now:
Max-Born-Institut Berlin
Max-Born-Str. 2a
12489 Berlin
Phone: +49-30-6392-1404
Fax: +49-30-6392-1404
fiebig@mbi-berlin.de

Prof. C. Fotakis

Sect. 15

Foundation for Research and Technology-Hellas (FORTH)
Institute of Electronic Structure and Laser
P.B. 1527, Vasilika Vouton
Heraklion, GR-711 10
Crete, Hellas
Phone: +30-2810-391273
Fax: +30-2810-391305
fotakis@iesl.forth.gr

Dr. L. Herbst

Sect. 21

Lambda Physik AG
Hans-Böckler-Str 12
37079 Göttingen
Phone: +49-551-6938404
Fax: +49-551-68691
lherbst@lambdaphysik.com

Prof. P.R. Herman*Sect. 13*

Electrical and Computer
Engineering
University of Toronto
10 King's College Road
Toronto, Canada M5S 3G4
Phone: +1-416-978-7722
Fax: +1-416-971-3020
p.herman@utoronto.ca

Dr. M. Hessling*Sect. 11.3*

LINOS Photonics GmbH & Co. KG
BU Bio Photonics
Isartalstr. 43
80469 München
Phone: +49-89-7202-539
Fax: +49-89-7202-141
Martin.hessling@linos.de

Dr. J. Ihlemann*Sects. 11.2, 11.2.5, 14*

Laser-Laboratorium Göttingen e.V.
Hans-Adolf-Krebs-Weg 1
37077 Göttingen
Phone: +49-551-503544
Fax: +49-551-503599
jihle@llg.gwdg.de

Dr. K. Jain*Sect. 1.2*

Anvik Corporation
6 Skyline Dr.
Hawthorne
NY 10532
kjain@anvik.com

Dr. N. Kaiser*Sect. 8*

Fraunhofer Institut Angewandte
Optik und Feinmechanik
Albert-Einstein-Straße 7
07745 Jena
Phone: +49-3641-807-321
Fax: +49-3641-807-601
norbert.kaiser@iof.fraunhofer.de

Dr. B. Keiper*Sect. 12*

3D-Micromac AG
Annaberger Str. 240
09125 Chemnitz
Phone: +49-371-400-4334
Fax: +49-371-400-4340
keiper@3d-micromac.com

J.-H. Klein-Wiele*Sect. 14*

Laser-Laboratorium Göttingen e.V.
Hans-Adolf-Krebs-Weg 1
37077 Göttingen
Phone: +49-551-503529
Fax: +49-551-503599
jhkleinw@llg.gwdg.de

Prof. A. Koch*Sect. 9*

HAWK Fachhochschule
Hildesheim/Holzminden/Göttingen
Von-Ossietzky-Str. 99
37085 Göttingen
Phone: +49-551-3705-100
Fax: +49-551-3705-101
Andrea.koch@pmf.fh-goettingen.de

Dr.-Ing. K. Körber*Sects. 2, 16.3, 16.5*

Oberer Stephansberg 38 E
96049 Bamberg
Phone: +49-951-5098493
klaus koerber@web.de

Dr. C. Kulik*Sects. 2, 16.3*

Laser-Zentrum Hannover e.V.
Hollerithallee 8
30419 Hannover
Phone: +49-511-2788-270
Fax: +49-511-2788-100
kk@lzh.de

XVIII List of Contributors

Dr. H. Lauth

Sect. 8

Jenoptik Laser Optik
Systeme GmbH
Göschwitzer Str. 25
07746 Jena
Phone: +49-3641-65 3188
Fax: +49-3641-65 3764
Hans.Lauth@Jenoptik.com

Dr. H. Lubatschowski

Sect. 19

Laser-Zentrum Hannover e.V.
Hollerithallee 8
30419 Hannover
Phone: +49-511-2788-279
Fax: +49-511-2788-100
h1@lzh.de

Prof. G. Marowsky

Sect. 1.1

Laser-Laboratorium Göttingen e.V.
Hans-Adolf-Krebs-Weg 1
37077 Göttingen
Phone: +49-551-503530
Fax: +49-551-503599
gmarows@gwdg.de

Dr. K. Mann

Sect. 7

Laser-Laboratorium Göttingen e.V.
Hans-Adolf-Krebs-Weg 1
37077 Göttingen
Phone: +49-551-503541
Fax: +49-551-503599
kmann@llg.gwdg.de

Dr. B. Nikolaus

Sect. 21

Lambda Physik AG
Hans-Böckler-Str 12
37079 Göttingen
Phone: +49-551-6938157
Fax: +49-551-68691
bnikolaus@lambdaphysik.com

Dr. P. Oesterlin

Sect. 9

Innovavent GmbH
Bertha-von-Suttner-Str. 5
37085 Göttingen
Phone: +49-551-90047-10
Fax: +49-551-90047-19
oesterlin@innovavent.com

R. Pätzfel

Sect. 6

Lambda Physik AG
Hans-Böckler-Str 12
37079 Göttingen
Phone: +49-551-6938155
Fax: +49-551-68691
rpaetzel@lambdaphysik.com

Dr. D. G. Papazoglou

Sect. 15

Foundation for Research and
Technology-Hellas (FORTH)
Institute of Electronic Structure
and Laser
P.B. 1527, Vasilika Vouton
Heraklion, GR-711 10
Crete, Hellas
Phone: +30-2810-391273
Fax: +30-2810-391305
dpapa@iesl.forth.gr

Dr. T. Petsch

Sect. 12

3D-Micromac AG
Annaberger Str. 240
09125 Chemnitz
Phone: +49-371-400-430
Fax: +49-371-400-4340
petsch@3dmicromac.com

Dr. U. Rebhan

Sect. 4

Lambda Physik AG
Hans-Böckler-Str 12
37079 Göttingen

Phone: +49-551-6938-221
 Fax: +49-551-68691
urebhan@lambdaphysik.com

Prof. G. Reiße

Sect. 17

Hochschule Mittweida
 University of Applied Sciences
 Technikumplatz 17
 09648 Mittweida
 Phone: +49-3727-580
 Fax: +49-3727-58-1379
greisse@htwm.de

Prof. Ch.K. Rhodes

Sect. 20

University of Illinois at Chicago
 Department of Physics
 College of Liberal Arts and Sciences
 845 West Taylor Street
 Chicago, Illinois 60607-7059
 USA
 Phone: +1-312-996-4868
 Fax: +1-312-996-8824
rhodes@uic.edu

Dr. P. Simon

Sect. 14

Laser-Laboratorium Göttingen e.V.
 Hans-Adolf-Krebs-Weg 1
 37077 Göttingen
 Phone: +49-551-503521
 Fax: +49-551-503599
psimon@1lg.gwdg.de

Dr. U. Stamm

Sects. 3, 4, 6, 22

Xtreme technologies GmbH
 Hans-Adolf-Krebs-Weg 1

37077 Göttingen
 Phone: +49-551-82073-101
 Fax: +49-551-82073-110
ustamm@xtremetec.de

Dr. M. Wehner

*Sects. 10, 11.1, 11.2, 11.2.1–11.2.4,
 11.2.6–11.2.7, 16.1, 16.4*
 Fraunhofer-Institut Lasertechnik
 Steinbachstr. 15
 52074 Aachen
 Phone: +49-241-8906-202
 Fax: +49-241-8906-121
wehner@ilt.fhg.de

Dr. S. Weißmantel

Sect. 17

Laserinstitut Mittelsachsen e.V.
 Technikumplatz 17
 09648 Mittweida
 Phone: +49-3727-581396
 Fax: +49-3727-581449
steffen@htwm.de

Dr. I. Zergioti

Sect. 15

Foundation for Research and
 Technology-Hellas (FORTH)
 Now:
 National Technical University
 of Athens
 Physics Department
 Iroon Polytehneiou 9
 15780 Zografou
 Athens, Greece
 Phone: +30-210-772-3345
 Fax: +30-210-772-2928
zergioti@central.ntua.gr

1 Introduction

1.1 Introductory Remarks

D. Basting and G. Marowsky

In 1984, Ch. K. Rhodes stated in the introduction to the world's first-ever book on excimer lasers [1]: "The development of excimer laser systems marked a significant turning point in the development of coherent sources. The progress of the last years has been largely predicated upon the combined knowledge of several disciplines including atomic and molecular physics, optical technology, and pulsed-power technology". This early statement was primarily associated with electron beam excitation of laser transitions of rare gases and rare-gas halogen mixtures. Excimer lasers of today, however, are based upon precisely controlled electrical discharges, and rely on detailed knowledge of material chemistry to provide long lifetimes of the discharge tubes. Hence, cost-effective operation has become possible, a prerequisite for industrial applications. Together with electronic laser beam monitoring and control, the multidisciplinary approach has made excimer lasers important tools for a great variety of industrial and medical applications.

1.1.1 The Unique Microstructuring Capabilities of Excimer Lasers

The properties relevant for microstructural applications of excimer lasers are their short wavelengths in the UV and deep UV, high pulse energy, and high average power. Each feature enables specific applications. Common to all applications: They benefit from (i) the short wavelengths that allow high precision imaging, (ii) the inherent high quantum energy that provides a strong radiation-matter interaction, and (iii) from both simultaneously. With the high peak intensity available, strong non-linear interactions may be achieved and utilized for highly precise material processing, like for example, semiconductor exposure, material microstructuring, and modeling of the refractive power of the human eye to compensate for myopia. An outstanding example of materials processing is the formation of grating structures possessing sub-micrometer dimensions. Figure 1.1 shows the morphology of a periodic structure created by superposition of two plane waves from a KrF excimer

laser at 248 nm wavelength on the surface of a LiNbO_3 crystal, a result taken from Chen et al. [2]. The authors report on a surface modulation of 80 nm and a grating period of 360 nm achieved with a single ablation pulse. The ablation depth could be increased in 10 nm steps upon application of multiple pulses. Figure 1.2 shows for comparison a very recent result of a more complicated nanostructure of similar dimensions obtained by phase-controlled superposition of two pairs of plane waves – details in Ref. [3].

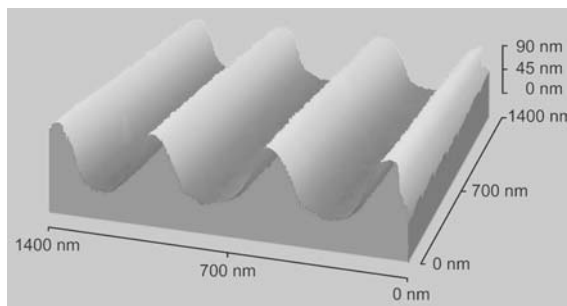


Fig. 1.1. Periodic nanostructure on a LiNbO_3 -crystal obtained by superposition of two plane waves from a KrF excimer laser according to Ref. [2]

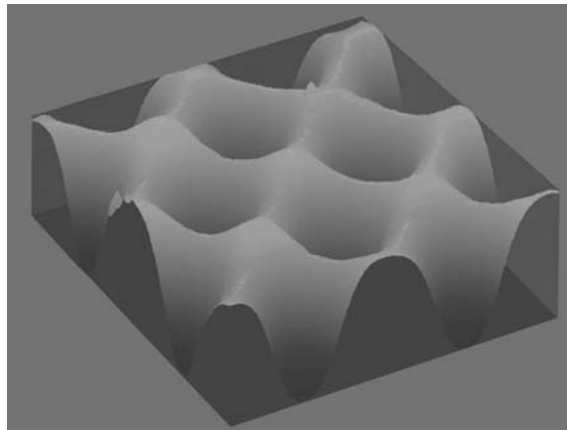


Fig. 1.2. Periodic nanostructure by phase-controlled multiple-beam interference according to Ref. [3]

1.1.2 Commercial Impact of Excimer Lasers

Before getting into the technical and physical details in this book, let us briefly address some aspects of the economics of excimer lasers. Due to their potential for various applications, excimer lasers have gained considerable commercial importance. The position of excimer lasers within the total laser market may be assessed by inspecting two diagrams: Figure 1.3 displays worldwide revenues obtained with all lasers, split into diode lasers and non-diode lasers. The overwhelming part of the diode category shown in the diagram belongs to optical telecommunications and, hence, reflects the well-known uncertainties of this market. In contrast, the non-diode sectors experienced considerably smaller fluctuations because they share many different markets. Compared to the total world laser market with multi-billion dollar revenues, the world-wide excimer laser market (Fig. 1.4) occupies a scale of activity about one order-of-magnitude smaller. A more detailed analysis incorporating the three main application areas namely industrial, medical, and scientific reveals that the industrial and the medical markets were responsible for the ups and downs, whereas the scientific market shows a persistent decline. The latter is not surprising because the above mentioned features of excimer laser radiation are no longer of major importance to scientific applications like spectroscopy or have been replaced by alternative UV sources such as frequency-converted solid state lasers. However, in the earlier years, the scientific segment made up a considerable percentage of the total excimer laser market.

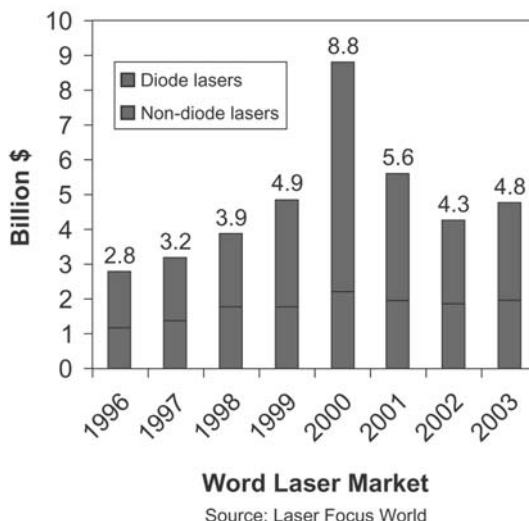


Fig. 1.3. World laser market 1996 to 2003: Diode and non-diode laser sales

Market fluctuations stand out primarily in the industrial sector, which is mainly governed by (a) the semiconductor market, and (b) the medical part which is dominated by fluctuations in the sales of lasers for ophthalmological applications.

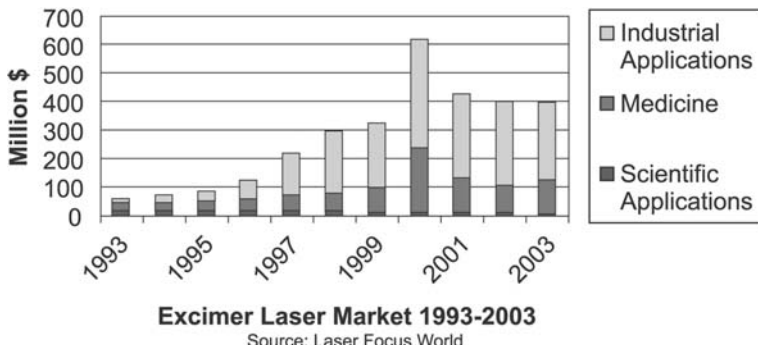


Fig. 1.4. Excimer laser sales between 1993 and 2003 and their distribution according to their main fields of application – industry, medicine, and research

It is interesting to monitor the market position of excimer lasers as compared to all other non-diode lasers, as shown in Fig. 1.5. In 2002, excimer lasers made up 21.7% of all laser sources used in materials processing and 26.5% of all laser sources used for medical therapeutic applications [4]. Materials processing includes all activities with lasers for processing such as welding, cutting, annealing, drilling, semiconductor, and microelectronics manufacturing, and the marking of all sorts of materials.

Medical therapeutics includes all laser applications such as ophthalmology; examples are refractive surgery, where excimer lasers play a major role, and photocoagulation. In addition a strong role is played in general surgery, therapeutics, imaging, and cosmetic applications.

An overview of all laser applications, with the inclusion of these two major applications of excimer lasers, is shown in the following table. Although this table was already presented in the former edition of this book [5], it remains informative because it contains relative numbers only, which are not subject to great changes. This table summarizes laser systems (second column) and the relative laser sources (third column) sales within the various applications which have been collected into two groups. It turns out that Group I, which actually contains materials processing and medical applications, covers only 12% of the worldwide sales activity of laser systems as compared to the majority contribution of 88% for those applications shown in Group II. It should, therefore, be pointed out that materials processing and medical therapeutic applications are actually minor, but very important activities in the large list of worldwide laser applications.

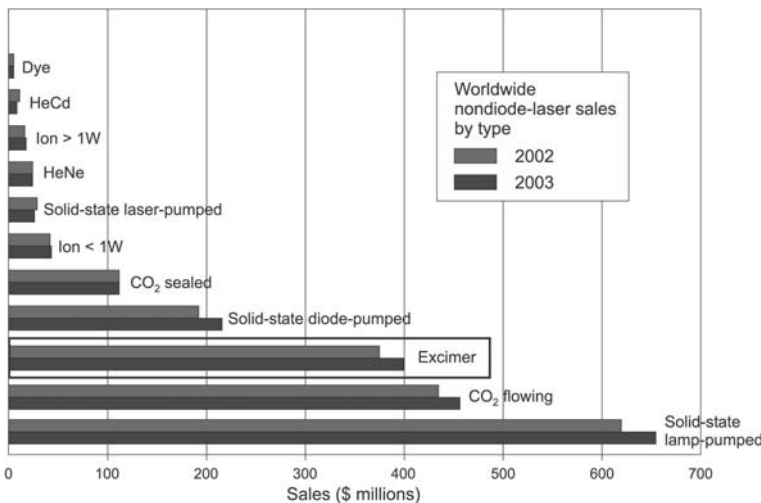


Fig. 1.5. Market position of excimer lasers compared to all other non-diode lasers according to Ref. [4]

The fourth column presents, for completeness, the ratio of the sales prices of the built-in laser source versus total system price for the various applications. The percent values in this column indicate that the laser sources play a much bigger role in Group I than in Group II, so the applications materials processing with 32% and medical therapeutics with 33% are playing the most important role for the light source – and, in fact, this is the part where excimer lasers come in. On average per piece, a laser system is typically a factor 20 more expensive than its source. The two main fields of excimer laser applications (materials processing and medical therapeutics)

Table 1.1. Global distribution (in percent of the actual total sales price) of lasers and laser systems according to applications. The averages in the ratio column refer to weighted averages. Details see text.

Group I	Global Market: Laser Systems	Global Market: Laser Sources	Ratio
Materials Processing	- 42%	- 67%	32%
Medical Therapeutic	- 18%	- 29%	33%
Analytic Applications	- 22%	- 2%	2%
Printing	- 18%	- 2%	3%
Group II			Average 21%
Communication Technology	- 13%	- 53%	10%
Information Technology	- 46%	- 18%	1%
Entertainment	- 40%	- 13%	0.8%
Basic Research	- 0.4%	- 16%	100%
Total	100 %	100 %	Av. 5%

are the exception: Here the price of the laser source is typically nearly one third of the system price. Hence, cost effectiveness of excimer lasers becomes an important issue for applications in industry.

In addition to the use of excimer lasers in materials processing, there exists a large variety of other applications like chemical surface alteration, heating, annealing, vaporization, laser-assisted chemistry, surface cleaning, semiconductor processing, and communications; applications that will be discussed in detail in subsequent chapters of section 3. As to the excimer laser impact on markets: semiconductor processing is considered as the largest-revenue and fastest growing market for excimer laser applications. In optical communications, the excimer laser is of particular importance in the production of optical fiber Bragg gratings, obviously a special case of nondestructive and nonintrusive materials processing.

1.1.3 Could Excimers Have Been the First Media with Optical Gain?

It is tempting to speculate that excimers might have been the first media showing optical gain. As early as 1926, F. G. Houtermans considered in [6, 7] the idea of energy storage and deactivation by photons in experiments with mercury dimers – work done in his thesis with James Franck as advisor in Göttingen, Germany. He considered discharge excitation of mercury and postulated the existence of metastable dimers from spectroscopic studies. Metastable gaseous compounds are in fact excellent candidates for laser operation. In 1960, after the maser had been discovered, Houtermans proposed excimers again as candidates for light amplification, just before the laser was first realized by Maiman in a solid state material – ruby. At that time – i.e. 34 years later – he was still convinced by his early thesis studies and proposed mercury dimers in the famous Helvetica Physica Acta paper [8] as potential candidates. He formulated the idea of avalanche amplification as a result of continuous stimulated emission in a mercury discharge system in this paper. Mercury had no future compared to the reasonable amplification by metastable gaseous compounds. Rare-gas dimers and rare-gas-halide exciplexes were the winners as gaseous laser media.

1.1.4 Literature

The literature on excimer lasers is widespread: Since the 2nd edition of Ch. K. Rhodes' book on this subject [1], no other comprehensive textbook has appeared. Lots of books exist on excimer-laser-related applications such as microstructuring or ablation. We have listed these books in chronological order at the end of this introductory chapter [9, 10, 11, 12, 13, 14, 15, 16, 17]. The relevant references to each sub-chapter are added at the end of each contribution in this book.

References

1. C.K. Rhodes (Ed.): *Excimer Lasers – Topics in Applied Physics*, Vol. 30, 2nd edn. (Springer-Verlag, Berlin, Heidelberg, New York, Tokyo, 1984)
2. K. Chen, J. Ihlemann, P. Simon, I. Baumann, W. Sohler: Appl. Phys. A **65**, 517 (1997)
3. J. Klein-Wiele, P. Simon: Appl. Phys. Lett. **83**, 4707–4709 (2003)
4. S.G. Anderson et al.: Laser Focus World (January issues) (1994–2004)
5. D. Basting (Ed.): *Excimer Laser Technology: Laser Sources, Optics, Systems and Applications* (Lambda Physik AG, Göttingen, 2001)
6. F. Houtermans: Zeitschrift für Physik **41**, 140–154 (1927). Julius Springer-Verlag, Berlin
7. F. Houtermans: Zeitschrift für Physik **41**, 619–635 (1927). Julius Springer-Verlag, Berlin
8. F. Houtermans: Helv. Phys. Acta **33**, 933–940 (1960)
9. H. Stafast, G. Herziger, H. Weber (Eds.): *Angewandte Laserchemie – Verfahren und Anwendungen* (Springer-Verlag, Berlin, Heidelberg, New York, 1993)
10. R. Crafer, P. Oakley (Eds.): *Laser Processing in Manufacturing* (Chapman & Hall, London, Glasgow, New York, Tokyo, Melbourne, Madras, 1993)
11. J. Miller (Ed.): *Laser Ablation – Springer Series in Materials Science*, Vol. 28 (Springer-Verlag, Berlin, Heidelberg, New York, 1994)
12. D. Bäuerle: *Laser Processing and Chemistry*, 2nd edn. (Springer-Verlag, Berlin, Heidelberg, New York, 1995)
13. D. Elliott: *Ultraviolet Laser Technology and Applications* (Academic Press, London, 1995)
14. W. Duley: *UV Lasers - Effects and Applications in Materials Science* (Cambridge University Press, Cambridge, 1996)
15. R. Russo, D. Geohegan, R.H. (Jr.), K. Murakami (Eds.): *Laser Ablation – Proc. of Fourth Int. Conference on Laser Ablation, Monterey 1997* (Elsevier, Amsterdam, 1998)
16. J. Horwitz, H. Krebs, K. Murakami, M. Stuke: “Laser ablation”, in *Proc. of the 5th International Conference on Laser Ablation* (Applied Physics A (1999), Materials, Science & Processing, Göttingen, 1999)
17. U. Stamm: J. Phys. D: Appl. Phys. **37**, 3244–3253 (2004)

1.2 Historical Review of Excimer Laser Development

D. Basting, N. Djeu, and K. Jain

When J. W. Ritter discovered the ultraviolet light in the spectrum of the sun in Jena, Germany in 1801 [1], he could not expect that 200 years later ultraviolet (UV) light has found a wide variety of applications in photochemistry and material processing. The main reason for this development is that at the very short UV wavelengths almost all substances show significant absorption. Historically, this made photochemists ask for powerful UV sources to investigate molecules and compounds under strong UV excitation. Soon after the invention of the laser in 1960, nitrogen lasers were capable to generate laser pulses with megawatts peak power, thus opening new photochemical research areas. In 1970, another revolution in UV photochemistry started with the first experimental demonstration of excimer lasers [2].

The name **excimer** comes from **excited dimer**. The first experimental evidence of excimer lasing was obtained by N. G. Basov et. al in 1970. They used a high-current electron beam to excite liquid Xe [2]. With Xe_2^* emitting around 172 nm excimer lasers were invented as a new class of lasers. It is interesting to note that excimer lasers of today (“exciplex” lasers, **excited complexes**) were discovered basically within the short time frame of one year after the investigation of fluorescence spectra of their active molecules, the rare-gas monohalides. Having actively taken part in the further development, we present here our view of the rapid growth of excimer laser technology.

Fluorescence spectra of rare-gas halides were investigated almost at the same time, i.e. in 1974, by several groups at University of Cambridge, Cambridge, UK [3], at Kansas State University, Kansas, USA [4], and at the Avco Everett Research Laboratory, Everett, Massachusetts, USA [5]. The first laser action of exciplexes was then reported in 1975, again almost simultaneously by several research teams at Naval Research Laboratory, Washington, USA [6], Northrop Research and Technology Center, Hawthorne, USA [7], at Avco Everett Research Laboratory, Everett, Massachusetts, USA [8, 9, 10], and at Sandia Laboratories, Albuquerque, USA [11]. At the end of 1975, excimer lasers with all important UV wavelengths had been experimentally demonstrated.

One of the authors of this chapter, N. Djeu, at U.S. Naval Research Laboratory in Washington D.C., was among the first scientists to work in the field since the mid's 70's. The Navy had an interest in developing efficient, powerful blue-green lasers for a variety of underwater applications. When the rare-gas halide (RGH) lasers were discovered, it appeared they would fit the bill, since they were both efficient and energetic, and it was suspected that down-conversion from the UV to the blue-green would not be a serious challenge. However, those early RGH excimer lasers were pumped by electron beams. These machines were bulky and had excruciatingly slow pulse repetition rates. Worse yet, the foil that separated the laser gas from the e-beam

generator ruptured with great regularity. At that time, the transverse-electric-discharge-pumped atmospheric (TEA) CO₂ laser was already an established technology, suggesting discharge excitation also for excimer lasers. However, halogen-containing gases, with their tendency for electron attachment, appeared to be a stumbling block at that time. Djeu enlisted the help of Ralph Burnham (an NRL contractor) and decided to attempt discharge pumping of RGH excimers. For the initial try they used a pair of band saw blades as electrodes. To the great delight of the researchers, lasing in XeF was obtained without much effort. Although the discharge was erratic, on the best shots an overall efficiency of 0.1% was realized [12].

Encouraged by those results, they went on to build a more elaborate (though still primitive) device. This second laser made use of polished nickel-plated electrodes, and, more importantly, incorporated an UV preionization source to initialize the electric discharge. The resulting improvements in the laser's performance were dramatic. An output of 100 mJ with an overall efficiency of 1% was obtained for XeF. Also, discharge pumping of the KrF laser was demonstrated for the first time [13].

Their work on excimer lasers might have ended, if Charlie Chase from Tachisto had not visited them shortly afterwards. Sensing his interest in developing a commercial excimer laser, Djeu persuaded him to provide them with a Tachisto CO₂ laser to see how it would work with the excimers. Realizing the importance of preionization, they modified the Tachisto laser to have a variable delay between the preionizer and the main discharge. With this device, efficiencies of better than 1% were achieved in XeF and KrF as well as ArF [14]. Within a short time, Tachisto introduced the excimer version of its TEA laser. However, as is often the case, being the first to market did not guarantee long-term success. Tachisto eventually went out of business as more agile companies came on the scene.

The main difficulty in developing commercial excimer lasers arose from the lack of combined technologies, for example the handling of the strongly aggressive gas in the laser. Pretty fast, the German start-up company Lambda Physik developed and manufactured its first commercial excimer laser – the EMG 500, the first commercial multigas laser – which was introduced into the market in 1977. Figure 1.6 shows a photograph of the EMG 500. That laser could be operated at wavelengths 193 nm, 222 nm, 248 nm, 282 nm, 308 nm, 337 nm (as nitrogen laser), 351 nm, 427 nm (as nitrogen laser), and 713 nm, with repetition rates selectable between 0.05 Hz (i.e. 1 pulse in 20 seconds) and 20 Hz. The laser allowed applications in basic research, with an until that time unachievable peak power up to 10 MW (!). Its pulse energy at 248 nm exceeded 220 mJ, almost two orders of magnitude higher than the energy obtained from the UV nitrogen laser. In 1977 about 5 lasers were shipped to the first customers, some of them still being in use today.



Fig. 1.6. The first commercial multigas excimer laser EMG 500. Pulse energy of 220 mJ @ 248 nm , repetition rate between 0.05 Hz and 20 Hz .

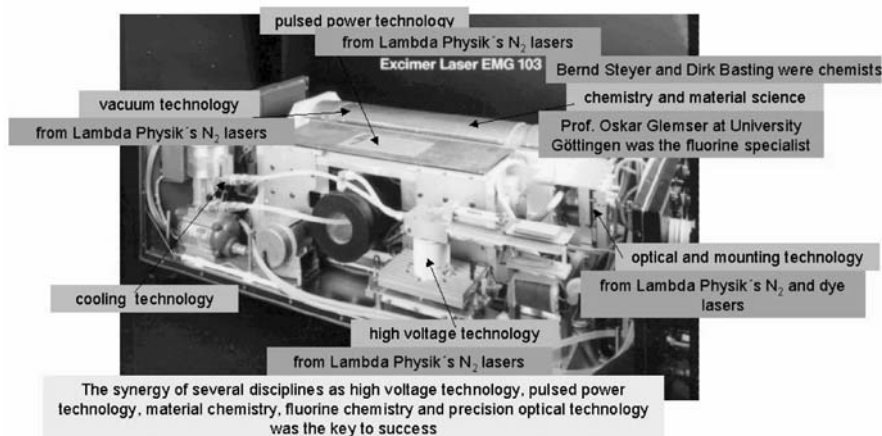


Fig. 1.7. Excimer laser EMG 103 MSC without cover showing the main components including high-voltage circuit, pulsed power modules with thyatron, laser chamber, and cooling circuit

To illustrate the main modules and technologies involved in excimer lasers, Fig. 1.7 shows the basic components of the model EMG 103 MSC, introduced in 1983. The following technologies and components were necessary:

- i as the heart of the laser, a fast high-voltage and pulsed-power technology including thyratron switching, main gas discharge, and pre-ionization,
- ii fluorine and/or chlorine resistive materials and their mounting technology for the vacuum tight and high pressure resistant excimer laser chamber,
- iii optical components like sealing UV transparent windows or resonator mirrors used in contact with the corrosive laser gases,
- iv cooling technology for the powerful high-voltage excitation module and excimer laser tube,
- v gas fill circuit technology for the fluorine/chlorine gases and the preparation and handling of high purity laser gases.

At Lambda Physik, pulsed transverse-excitation nitrogen lasers had been developed earlier for UV generation. This technology was adapted to the requirements of excimer lasers. In addition pre-ionization was developed to ensure a uniform large-volume discharge. Since both company founders, Dirk Basting and Bernd Steyer, were chemists they were used to work also with aggressive chemicals. Located in Göttingen, Germany, they had close contact to scientists both at the Max-Planck-Institutes and the University of Göttingen. For example, fluorine was not available on the market with the required purity and in sufficient quantities. So the support by Prof. Oskar Glemser from University of Göttingen, one of the worldwide experts in fluorine chemistry, did accelerate the development of excimer lasers significantly. Lambda Physik had started its business with nitrogen lasers for dye laser pumping as spin-off from Prof. Fritz Schäfer's laboratory at the Max-Planck Institute for Biophysical Chemistry. Thus, the multi-disciplinary know-how available at Lambda Physik and in the area of Göttingen facilitated the fast development of the excimer laser, providing an advantage over the Tachisto approach based on CO₂ laser technology.

With respect to possible applications, there were different requirements for the ideal ultraviolet laser source. Some applications need high pulse energy or variable pulse energy, and good pulse-to-pulse energy stability. Other applications demand for high repetition rate and/or high average power. Homogeneous near field and/or far field beam profile and beam profile stability are always necessary. Other applications require high brightness, i.e. low-divergence short laser pulses of nanosecond duration or less, down to the femtosecond time scale. Some applications need narrow spectral bandwidths. Common to all applications, the lasers should ideally be maintenance free with a long lifetime of all components. Also, buying cost and cost of operation should be low and installation requirements simple – for example water cooling should be avoided.

Soon after the introduction of the EMG 500 fast progress improved excimer laser performance. The automatic synchronization of pre-ionization and main gas discharge led to better output energy stability. The development of gas processors that purified the laser gas resulted in increased laser gas lifetime. This resulted in reduced operating cost and increased mainte-

nance intervals. The incorporation of *magnetic assist* (Questek trademark) and *switch control* (Lambda Physik trademark) increased the thyratron lifetime, discharge electrode lifetime, and gas lifetime by an order of magnitude. With the *magnetic switch control* technique (MSC) the excimer lasers EMG 100/200 MSC could be run under typical operation conditions in research environment for several years without change of thyratrons or the laser chamber. For the first time, the available UV laser power exceeded the 100 W level. The gas lifetime was increased by more than an order of magnitude; on September 16, 1983, scientists switched off an *EMG 103 MSC* after 110 million shots of continuous operation with a single gas fill of XeCl - a world record of gas lifetime (a gas lifetime of 100 million shots is comparable to the gas lifetime requirements for today's lithography lasers in semiconductor chip manufacturing).

In addition to the direct use of the excimer lasers in photochemistry, material research, and micromachining of materials, a large application of excimer laser arose in pumping dye lasers. Early work by F. P. Schäfer, first at University of Marburg and then at Max-Planck Institute of Biophysical Chemistry in Göttingen [15, 16, 17, 18], and P. P. Sorokin at IBM [19, 20, 21] had demonstrated lasing of organic dyes. Until 1976, using nitrogen laser excitation, hundreds of organic dyes had been investigated and demonstrated lasing at almost any wavelength across the visible and near UV spectrum [22, 23, 24]. With orders-of-magnitude higher power and energy, XeCl excimer lasers at 308 nm wavelength were the ideal excitation sources for dye lasers. In 1978 the first excimer-pumped tunable narrow-bandwidth dye laser – the “Farbstoff-Laser” FL 1000 was developed at Lambda Physik. With the excimer-laser-pumped dye laser FL 2000 (Fig. 1.8) and frequency doubling crystals any laser wavelength between 200 nm and 1000 nm was available for high-resolution spectroscopy [25, 26], for photochemists a dream of experimental equipment. Thus dye laser pumping became one of the driving forces for the development of the excimer laser market.

In 1984 an oscillator-amplifier configuration of excimer lasers with unstable resonator was commercialized. The principle of the EMG 150 was adapted from solid-state lasers, which had been operated with amplifiers over many years. The resonator of the excimer laser oscillator contained apertures that reduced the beam divergence from several $mrad$ to about $100 \mu rad$. The beam from the oscillator was injected into the excimer amplifier equipped with an unstable resonator. The injection seeding of the high-power amplifier by the low divergence beam from the oscillator resulted in orders-of-magnitude higher brightness, lowest beam divergence, and extremely good focusability of the laser pulses at energy levels in the several 100 mJ range. In a special oscillator configuration with bandwidth-narrowing resonator, the EMG 150 delivered high-power UV pulses with less than 3 pm spectral bandwidth – later used to investigate the ozone hole [27, 28], and an early predecessor of the lasers for deep-UV photolithography.

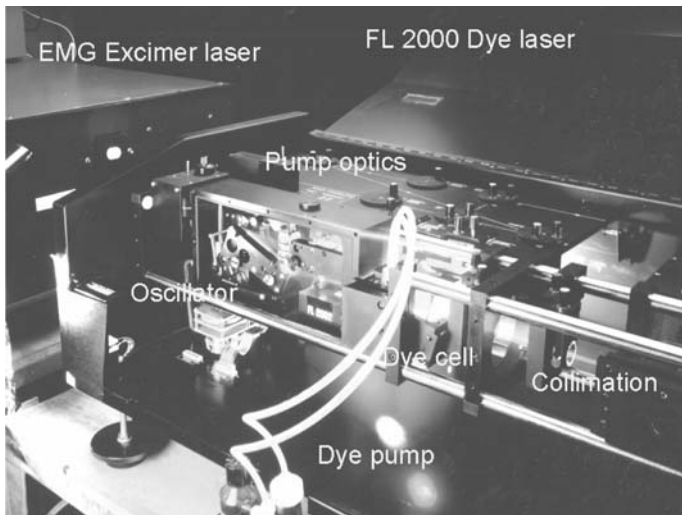


Fig. 1.8. Excimer-laser-pumped dye laser FL 2000 from Lambda Physik in 1981

The availability of oscillator-amplifier excimer laser systems led to the successful demonstration of ultraviolet laser systems operating in the picosecond and femtosecond time scale. In 1982, by amplification of ps light pulses from a synchronously pumped cavity-dumped dye laser and their frequency conversion into the ultraviolet, seed pulses for excimer amplifiers became available. After amplification in XeCl excimer modules [29] and ArF excimer modules [30], ultraviolet pulses with 40 mJ energy and several picoseconds pulse duration could be generated. For the first time intense ultraviolet pulses with peak powers reaching above 10 GW could be used for fundamental studies of the interaction with matter. While these new UV ps light sources were extremely complicated and very expensive laser systems, in 1983 Szatmári and Schäfer succeeded in a considerably simplified approach based on the combination of an EMG 150 oscillator-amplifier with quenched and distributed feedback dye lasers as well as dye amplifiers [31]. A few years later the continued research efforts resulted in the availability of 150 fs laser pulses with 45 mJ , yielding 300 GW peak power [32] and new ideas for the experimental approach to develop X-ray laser sources with pulse durations in the attosecond range [33].

During the 80's, in order to achieve highest energies from excimer lasers, various approaches for pre-ionizing and exciting the laser gas mixtures were investigated as X-ray pre-ionization [34, 35], creeping discharge pre-ionization [36] and electron beam pumping [37]. With those methods pulse energies of several 10 J up to kJ could be obtained. The intense UV pulses have been applied in fusion research, plasma generation, and material processing. However, while SOPRA and Lambda Physik were trying to commercialize

excimer lasers using these technologies they could not find their way into excimer lasers manufactured in mentionable quantities until today. Another way of possible extension of excimer laser applications was the development of high-repetition-rate lasers. In 1986 the first high-repetition-rate excimer laser was commercialized (EMG 105i) operating at 1 kHz pulse repetition frequency. Developed on request of a customer having a specific application in mind, that laser delivered 20 W average power at 1 kHz at 248 nm – more than 10 years before the first 248 nm , 1 kHz lithography laser was installed. However, the development was too early. The application was not successful and other markets did not arise at that time. Lambda Physik built about 20 EMG 105i lasers and then discontinued the product as no significant sales could be seen.

In the early and mid 80's the progress in excimer laser parameters and technology as well as extensive results about innovative applications of excimer lasers from research laboratories fueled the first industrial applications of excimer lasers. As early as 1980 Kanti Jain at IBM Almaden Research Center developed the concept of excimer laser lithography, and demonstrated the first results. Due to the importance of the technology to the company in as critical a business as IC chip manufacturing, its public disclosure did not come about until March 1982, when he published the first paper on excimer laser lithography [38] in IEEE Electron Device Letters. Simultaneously, the new development was presented at the 1982 SPIE Microlithography Conference [39] and protected by a core patent on excimer laser lithography [40], which was issued in 1984 and covered the basic lithography process using excimer lasers as well as a variety of lithography system configurations incorporating an excimer laser as a light source.

Jain had recognized that excimer lasers uniquely combine all the desirable attributes required in a light source for high-volume lithography, namely: they emit at deep-UV and shorter wavelengths, enabling high-resolution imaging; they deliver high average powers, enabling high-throughput exposure; they have high conversion efficiency, enabling low effective cost; they emit no unwanted IR or visible radiation, enabling better lithography system design; and their emission has very low spatial coherence, enabling speckle-free image definition. For experimental demonstration of the basic concept of excimer laser lithography and its key benefits, he drew upon a number of resources in different IBM departments. His immediate goal was to show patterning of features down to $0.5\text{ }\mu\text{m}$ in conventional photoresists with short exposure times and absence of speckle. (Recall that commercial ICs with $0.5\text{ }\mu\text{m}$ geometries did not arrive until 1989.) In the fall of 1980, he carried out lithographic exposure experiments using XeCl , KrF , and KrCl excimer lasers operating at 308 nm , 248 nm , and 222 nm , respectively. The lasers were a Lambda Physik Model EMG 102, and Lumonics Models TE-861-T and TE-290. Conventional mid-UV and deep-UV photoresists were patterned in contact mode using standard chrome-on-quartz masks. In these experiments, he was fortunate to obtain

the assistance of several of his IBM colleagues, including C.G. Willson in photoresist materials, B.J. Lin in processing, and P.P. Sorokin in excimer lasers. In the very first set of exposures, high-quality images down to $0.5\text{ }\mu\text{m}$ resolution were achieved (Fig. 1.9) with which all of the expected benefits of excimer laser lithography were clearly demonstrated, including high resolution, fast exposure, and speckle-free features.

For the demonstration of excimer laser projection lithography, in the fall of 1981 Jain's group modified a Perkin-Elmer Micralign 111 scanning projection lithography tool by replacing its Hg-Xe arc lamp source with a Lambda Physik Model EMG 102 excimer laser and adding a novel anamorphic illumination optics subsystem. Since the Micralign tool uses a ring-field imaging system, it was necessary, for efficient coupling of the laser radiation into the tool, to transform the laser output into an arc-shaped beam so as to match the Micralign condenser slit. Several illumination systems to achieve such anamorphic optical transformation were invented, demonstrated and patented. With the modified Micralign system, excimer laser projection lithography was experimentally demonstrated on a commercial tool with resolution down to $1.5\text{ }\mu\text{m}$ [41] (see also [42] and [43]). This success was immediately followed in the summer and fall of 1982 by modification of a Perkin-Elmer Micralign 500 system, then the state-of-the-art production lithography tool for high-volume IC manufacturing. The laser used in this implementation was a Lumonics Model TE-860. High-quality excimer laser projection lithography results were achieved with a Micralign-500 system resulting in $1\text{ }\mu\text{m}$ resolution with conventional photoresists on 125 mm silicon wafers [43].

The successful demonstration of high-resolution, high-throughput projection lithography on the modified Perkin-Elmer Micralign tools coupled with excimer laser sources prompted IBM to enter into a joint development agreement with Perkin-Elmer to further develop and optimize the design of excimer-laser-scanning projection lithography systems and to build several of them for installation at an IBM chip manufacturing division. This joint development program with Perkin-Elmer, led from the IBM research division by Jain, resulted in the first commercial excimer-laser-scanning projection lithography system prototype, called the 'Alpha' tool, which subsequently evolved into the 'step-and-scan' production tools called 'Gamma' when the management of the tool development effort on the IBM side had transferred from its research division to its chip manufacturing division and by which time the Perkin-Elmer lithography equipment business had been acquired by SVGL (which subsequently was acquired by ASML) [44].

In 1985 the German company Karl Süss introduced an industrial lithography mask aligner system with a Lambda Physik EMG laser. Shortly after GCA – the leading manufacturer of lithography equipment at this time – introduced the world's first excimer laser DUV stepper using a Lambda 248 L excimer laser, of which several were sold. At another IBM laboratory, the T.J. Watson Research Center in Yorktown Heights, NY a group under R. Srinivasan

vasan undertook from 1977 to 1982 a systematic study of the action of far-UV light at 185 nm from a mercury resonance lamp on small organic molecules in solution [45]. This investigation followed their studies from 1961 to 1977 of photochemistry in the near- and mid-UV regions. Around 1980, an excimer laser (Lambda EMG 500) became available to this group. Although this laser had an intense, monochromatic pulse at 193 nm , the total output of photons per unit time was small since it had a repetition rate of only 1 Hz and a gas lifetime of only a few hours. It was therefore decided to look at the chemical modifications of polymer surfaces using this beam rather than study the photochemistry of small molecules. To the intense surprise of Srinivasan and V. Mayne-Banton who conducted the first experiments, the laser beam was found to etch the surface of the polymer, a sample of polyethylene terephthalate or Mylar, without the need for any subsequent chemical development [46, 47, 48, 49]. With the further assistance of S.E. Blum and K.H. Brown, it was recognized that a Riston film, a commercial negative photoresist of general use could be patterned to $5\text{ }\mu\text{m}$ resolution, once again without any subsequent wet development [50] (see Fig. 1.9). Note that the laser effect makes Riston a positive photoresist and the exposure to the beam can be conducted in room light.

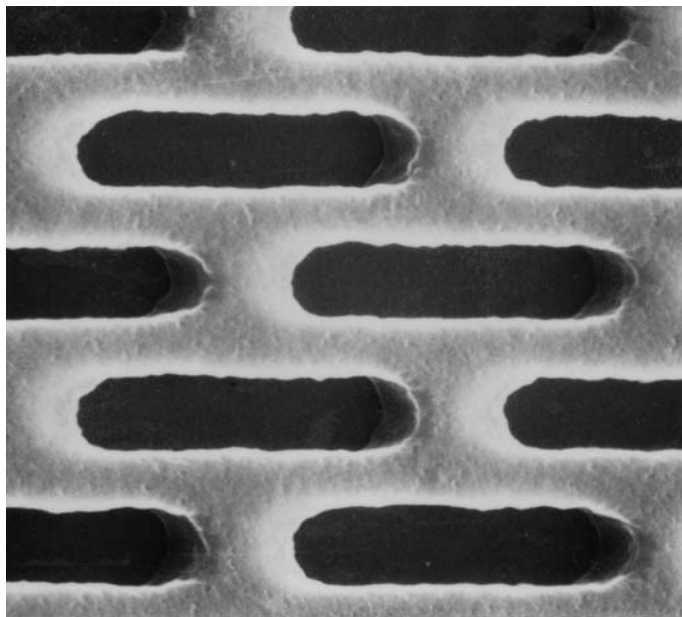


Fig. 1.9. Features with 0.5 micron resolution patterned by excimer laser lithography in AZ 2400 photoresist with a XeCl laser with an exposure dose of 100 mJ/cm^2 (K. Jain et al. [38])

There was some initial confusion about the underlying mechanism of the etching process. This happened because the experiments were conducted in an open system in which the surface that was being irradiated was exposed to atmospheric oxygen. Also there was no information about the products into which the polymer had been broken up since these were not trapped and analyzed. Leigh and Srinivasan conducted the first studies of the action of 193 nm laser pulses on Mylar in an evacuated container. When the products were analyzed, it was observed that benzene was a major product and that its yield rose in a non-linear fashion with the intensity of the pulse. This was a crucial study since it showed that (1) pulsed, 193 nm laser radiation decomposed and blew away the products in a single pulse, (2) more than one photon was attacking a single absorbing center in order to produce benzene, and (3) the process was non-linear in that an energy threshold had to be exceeded before the process was observed. When this work was published [51] the etching process was characterized as an “ablation” and the name, “Ablative Photodecomposition (APD)” was given to it. *It cannot be emphasized enough that APD was suggested to occur at this wavelength because the 193 nm photon (as shown already from studies at 185 nm) broke chemical bonds with a high (0.1–1.0) quantum yield and the non-linear nature of the process was inferred from the analysis of the products.*

This discovery of the ablation process was the key for excimer laser material processing. Over the last decades the excimer laser has obtained a leading position among lasers as a manufacturing tool. Mainly because of two reasons: (i) The short wavelength of the excimer laser offers sub-micron spatial and depth resolution due to the short absorption length and the connected small heat-affected zone in most materials resulting in excellent quality of machining, (ii) the progress in basic excimer laser technology has made the excimer laser a reliable, cost-effective tool suitable for the industrial environment.

The mid 80's was the time when the idea of taking the next challenge in excimer laser development was born – making excimer laser machines for use in an industrial manufacturing environment. The largest industrial installation of excimer lasers in the world at that time was built up at Siemens Nixdorf Informationssysteme in Augsburg, Germany, finally using 20 lasers (see Fig. 1.10). The underlying process of via hole drilling in printed circuit boards had been developed under leadership of F. Bachmann at Siemens AG Munich [52]. Independently and simultaneously IBM-researchers around J.R. Lankard at the Yorktown Heights developed a machine to manufacture multi-chip modules (MCM) for mainframe computers using a 100 W excimer laser and a specially developed high-resolution optical imaging systems [53].

At the end of the 80's several companies had been established worldwide who did manufacture excimer lasers, as Cymer (USA), Komatsu (Japan), Lambda Physik (Germany), Lumonics (Canada), and Questek (USA), acquired by Lambda Physik in 1993, in order to mention only some of them. Together with companies specialized in developing excimer laser work sta-



Fig. 1.10. Large industrial excimer installation at Siemens Nixdorf Informationssysteme, Augsburg, Germany, containing 9 EMG 1003i excimer lasers in 1988

tions and application job shop companies such as Exitech (Great Britain) they significantly contributed to the development of excimer laser technology as well as the increase in excimer laser applications. It should be emphasized that in Europe both the excimer laser technology and the applications received a considerable push by the Eureka program, which started as a European research initiative in 1985 and began to bear first results for excimer laser technology in the late 80ies.

It may be interesting to know, how the original work of Srinivasan aiming at industrial processes found its application in the medical field. In November of 1981, on Thanksgiving Day, he was inspired by the turkey on his plate to extend the study of APD to tissue. He had a background in protein chemistry, which he had studied for his Ph.D. thesis at the University of Southern California (1956) and in his post-doctoral work at the California Institute of Technology (1955–56). On the day after Thanksgiving, he conducted the first experiments on the etching of the soft meat on a turkey leg using 193 nm laser pulses. He was gratified to note that the etched surface showed no trace of burning or scarring of the underlying material. In short order, S.E. Blum and J.J. Wynne in Srinivasan's group conducted further experiments on the turkey meat as well as on other animal tissue to show that this process was generally applicable to all soft tissue. Their first publication [54] appeared in 1983 and a patent [55] was issued in 1988. Srinivasan produced many photos

of biological materials that had been cut or etched by the APD process at 193 nm in order to convince the viewers of the precision and the lack of heat damage in this technology. Figure 1.11 shows one of the most successful of these photos.

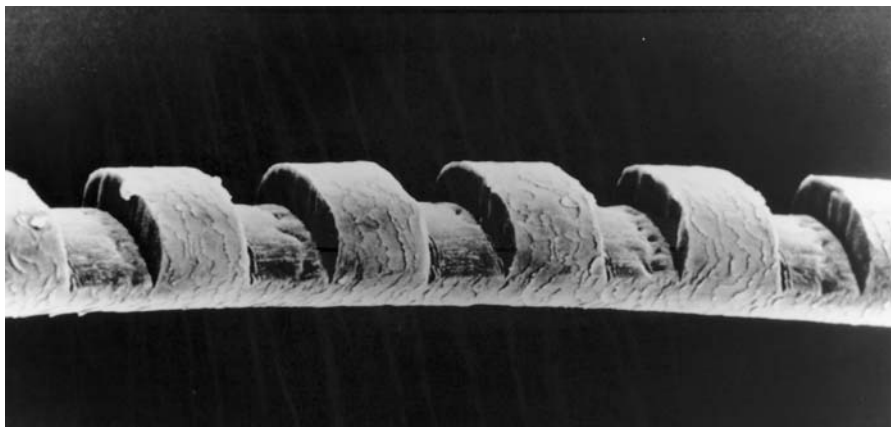


Fig. 1.11. $50\text{ }\mu\text{m}$ notches etched in a human hair with an excimer laser operating at 193 nm

In late 1982 and early 1983, Srinivasan and his group published their findings about APD on polymers and tissue at 193 nm . In mid-1983, Dyer and his group at the University of Hull, U.K. showed [56] that similar results could also be obtained on polymers at the other strong excimer laser wavelengths at 248 nm and 308 nm . IBM released an announcement to the general public in June 1983 on the discovery of APD and its potential in semi-conductor processing as well as surgery. This resulted in a flood of enquiries to Srinivasan, many of it from surgeons who were interested in using this technology in their specialty. One of the first to collaborate actively with Srinivasan was Dr. Stephen Trokel, Associate Professor of Ophthalmology at the Columbia Presbyterian Medical Center in New York City. Srinivasan and Trokel with the assistance of B. Braren showed [57] that APD was a highly efficient method for the precise etching and cutting of the cornea in the eye. The excimer wavelength of 193 nm has been found to be particularly suitable, since the morphology of the cut is superior to those obtained when the radiation of another wavelength in the UV or IR is used. Furthermore the high absorption cross-section for this wavelength limits the depth of the damage of the bottom and sides of the cut, and mutagenesis seems also to be non-existent. The possibility of not only creating grooves but of reshaping an entire surface to generate a controlled refractive path in the cornea has led to one of the largest medical laser applications, the refractive laser surgery (PRK, PTK, and LASIK).

A little over 20 years later, not only has APD of both polymers and the cornea become accepted technologies, but also the fundamental study of the phenomenon has continued to interest the scientific workers. In February 2003, the journal Chemical Reviews published an entire issue of over 300 pages that was devoted to the interaction of ultraviolet laser pulses with organic solids. Co-incidentally, the journal Applied Physics A in its July 2003 issue devoted about half of the total pages to current trends in the study of the interactions of UV laser beams with matter. Dyer [58], who wrote the first article in this issue, reviewed the field. Some of his words are worth quoting here:

It is now twenty years since the publications first appeared on using UV excimer lasers to process polymers in the form of conventional resists and as ‘self-developing’ resists... Since that time a veritable wealth of papers on polymer ablation has appeared, pointing to the enduring character of a topic that combines practical utility with scientific interest.

At the end of that article, he expresses the opinion:

Though, 20 years on, UV laser polymer ablation must be viewed as a mature field, it is far from extinct and still continues to attract scientific interest and find new applications.

References

1. J.W. Ritter: Annalen der Physik **7**, 527 (1801)
2. N.G. Basov, V.A. Danilychev, Y.M. Popov, D.D. Khodkevich: Zhourn. Eksperim. Fisika i Tekhnika Pis. Red. **12**, 473 (1970)
3. M.F. Golde, B.A. Trush: Chem. Phys. Lett. **29**, 486 (1974)
4. J.E. Velazco, D.W. Setser: J. Chem. **62**, 1990 (1975)
5. J.J. Ewing, C.A. Brau: Phys. Rev. Lett. A **12**, 129 (1975)
6. S.K. Searles, G.A. Hart: Appl. Phys. Lett. **27**, 243 (1975)
7. E.R. Ault, R.S. Bradford, M.L. Bhaumik: Appl. Phys. Lett. **27**, 413 (1975)
8. J.J. Ewing, C.A. Brau: Appl. Phys. Lett. **27**, 350 (1975)
9. C.A. Brau, J.J. Ewing: Appl. Phys. Lett. **27**, 435 (1975)
10. J.A. Mangano, J.H. Jacob: Appl. Phys. Lett **27**, 495 (1975)
11. G.C. Tisone, J.M.H. A. K. Hays: Opt. Commun. **15**, 188 (1975)
12. R. Burnham, N. W. Harris and N. Djeu: Appl. Phys. Lett. **28**, 86 (1976)
13. R. Burnham, F. X. Powell and N. Djeu: Appl. Phys. Lett. **29**, 30 (1976)
14. R. Burnham and N. Djeu: Appl. Phys. Lett. **29**, 707 (1976)
15. F.P. Schäfer, W. Schmidt, K. Marth: Phys. Letters **24A**, 280 (1967)
16. F.P. Schäfer, W. Schmidt, J. Volze: Appl. Phys. Letters **9**, 306 (1966)
17. F.P. Schäfer, W. Schmidt, J. Volze, K. Marth: Ber. Bunsenges. phys. Chemie **72**, 328 (1968)
18. F.P. Schäfer: *Principles of dye laser operation*, Vol. 1, 3rd edn. (Springer Verlag, Berlin, Heidelberg, 1990)

19. P.P. Sorokin, J.R. Lankard: IBM J. Res. Develop. **10**, 162 (1966)
20. P.P. Sorokin, J.R. Lankard: IBM J. Res. Develop. **11**, 148 (1967)
21. P.P. Sorokin, J.R. Lankard: Phys. Rev. **186**, 342 (1969)
22. D. Basting, F.P. Schäfer, B. Steyer: Appl. Phys. **3**, 81 (1974)
23. F.P. Schäfer, B. Steyer: Appl. Phys. **7**, 113 (1975)
24. F.P.S. D. Basting D. Ouw: Opt. Commun. **18**, 260 (1976)
25. L.P. dye laser: (1981), "FL 2000 brochure"
26. Lambda Physik HIGHLIGHTS **5**, 4 (1987)
27. Lambda Physik HIGHLIGHTS **2**, 2 (1986)
28. Lambda Physik HIGHLIGHTS **5**, 1 (1987)
29. P.B. Corkum, R.S. Taylor: IEEE J. Quant. Electron. **18**, 1962 (1982)
30. H. Egger, T.S. Luk, K. Boyer, D.F. Muller, H. Pummer, T. Srinivasan, C.K. Rhodes: Appl. Phys. Lett. **41**, 1032 (1982)
31. S. Szatmári, F.P. Schäfer: Opt. Commun. **48**, 279 (1983)
32. S. Szatmári, G. Kühnle, J. Jasny, F.P. Schäfer: Appl. Phys. B **49**, 239 (1989)
33. F.P. Schäfer: Phys. Bl. **42**, 283 (1986)
34. M. Trentelman, P.J.M. Peters, Q.C. Mei, W.J. Wittemann: J. Opt. Soc. Am. B **12**, 2494 (1995)
35. M. Steyer, K.A. Stankov, H. Mizoguchi, B. Ouyang, F.P. Schäfer: Appl. Phys. B **49**, 331 (1989)
36. V.Y. Baranov, V.M. Borisov, D.N. Molchanov, V.P. Novikov, O.B. Khristoforov: Sov. J. Quantum Electron. **17**, 978 (1987)
37. M.J. Shaw, F. O'Neill, C.B. Edwards, D.J. Nicolas, D. Craddock: Appl. Phys. B **28**, 127 (1982)
38. K. Jain et al.: IEEE Electron Device Lett. **EDL-3**, 53 (1982)
39. K. Jain et al.: Proc. SPIE **334**, 259 (1982)
40. K. Jain, C.G. Wilson: "High resolution optical lithography method and apparatus having excimer laser light source", U.S. Patent 4,458,994, July 10, 1984
41. K. Jain: Appl. Optics **23**, 648 (1984)
42. K. Jain, R. Kerth: Proc. Microcir. Engg., Cambridge p. 181 (1983)
43. K. Jain, R. Kerth: IEEE Electron Device Lett **EDL-7**, 299 (1986)
44. K. Jain: SPIE Press (1990)
45. W.J. Leigh, R. Srinivasan: Acct. Chem. Res. **20**, 107 (1987)
46. R. Srinivasan, V. Mayne-Banton: Appl. Phys. Lett. **41**, 576 (1982)
47. R. Srinivasan: *Laser processing and diagnostics* (Springer Verlag, 1984)
48. R. Srinivasan, B. Braren, D. Seeger, R.W. Dreyfus: Macromol. **19**, 916 (1986)
49. R. Srinivasan: Science **234**, 559 (1986)
50. S.E. Blum, K. Brown, R. Srinivasan: U.S. Patent 4,451,503
51. R. Srinivasan, W.J. Leigh: J. Amer. Chem. Soc. **104**, 6784 (1982)
52. F. Bachmann: Chem. Tronics **4**, 149 (1989)
53. J.R. Lankard, G. Wolbold: Appl. Phys. A **54**, 355 (1992)
54. R. Srinivasan, J.J. Wynne, S.E. Blum: Laser Focus p. 62 (1983)
55. R.S. S. E. Blum, J.J. Wynne: U.S. Patent 4,784,135
56. J.E. Andrew, P.E. Dyer, D. Forster, P. Keys: Appl. Phys. Lett. **43**, 717 (1983)
57. S.L. Trokel, R. Srinivasan, B. Braren: Am. J. Ophthalmology **96**, 710 (1983)
58. P.E. Dyer: Appl. Phys. A **77**(2) (2003)

1.3 Trends in Worldwide Excimer Laser Sales

Stephen G. Anderson

1.3.1 The World's Laser Markets at the End of 2004

As we move into 2005, worldwide sales of all types of lasers for all applications reached about US \$ 5.4 billion, a 10% increase over 2003 [1]. Although this number is still well below the peak of US \$ 8.8 billion during the so-called telecommunications “bubble” of 2000, it does continue an upward trend that started in 2002 after the effects of the telecommunication market collapse had worked their way through the system (see Fig. 1.12). One interesting aspect of the overall laser market numbers in 2004 was the degree of price erosion that occurred. While pricing trends were mixed – as is typical for nondiode lasers – in the diode laser sector across-the-board price decreases were much more prevalent than in previous years and many were significant. The reasons were varied and sometimes specific to a laser type, but competitive pressures and customer expectations played a major role. The net result was that overall laser unit sales volumes actually increased 20% during 2004; this despite the Japanese Yen’s appreciation against the US dollar during 2004, a factor that usually “increases” revenues expressed in US dollars because of the number of lasers made in Japan for optical storage applications. For 2005, some degree of recovery is expected in average selling prices, with the market overall gaining about 9% in revenues and 5% in units to reach US \$ 5.9 billion.

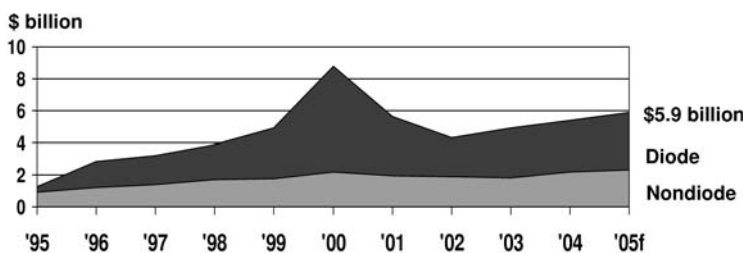


Fig. 1.12. The ten-year history of global laser revenues clearly shows the “bubble” that occurred during the 1999–2000 timeframe. Although sales of excimer lasers benefited somewhat from the telecommunications ramp up (because of fiber Bragg grating manufacture), the bubble was driven almost entirely by semiconductor lasers sold for telecommunications. After the bubble burst, laser sales reached a low point in 2002 and have trended upwards ever since. Image Courtesy of *Laser Focus World*

Another major market trend worth noting is the increasing importance of consumer applications to revenue growth of almost all types of lasers, even in-

cluding excimers. Fred Welsh, former executive director of the Optoelectronics Industry Development Association (www.oida.org), noted in November 2004 that consumer electronics is now the fastest growing segment of optoelectronics component sales. He pegged the global optoelectronics component market at US \$ 63 billion in 2003 and although he was not specifically talking about lasers, they were included in his analysis. Even outside the consumer electronics arena, large segments of laser sales are consumer driven, most notably right now for use in medicine. So-called “elective” procedures such as hair removal, skin resurfacing, and vision correction (with excimer lasers) have driven significant market growth over the past few years and continue to do so, even though medical insurance companies typically do not pay for these procedures.

1.3.2 Excimer Laser Markets

Global sales of excimer lasers for all applications reached the second highest revenue number in their history in calendar year 2004 (see Fig. 1.13). Revenues from sales of excimer laser sources were US \$ 421 million – about 8% of all lasers sold and putting the excimer at number three in terms of global sales revenues of non-diode lasers, after solid-state lamp-pumped systems (US \$ 645 million) and flowing-gas carbon dioxide lasers (US \$ 521 million; see Fig. 1.14). The only year when excimer sales revenues were higher than in 2004 was in 2000 during the telecommunications bubble, when global revenues reached US \$ 576 million. It is deceptively simple, however, to think in terms of a single homogeneous “excimer laser market.” There are in fact significant variations in both the lasers themselves and in the distribution channels through which they reach the end-users.

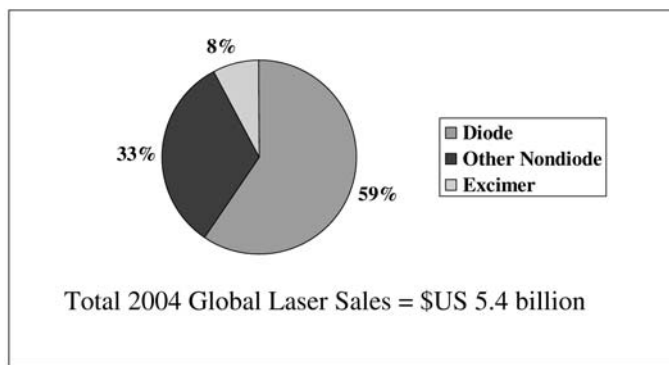


Fig. 1.13. Excimer laser sales represented about 8% of all lasers sold in 2004.
Image Courtesy of *Laser Focus World*

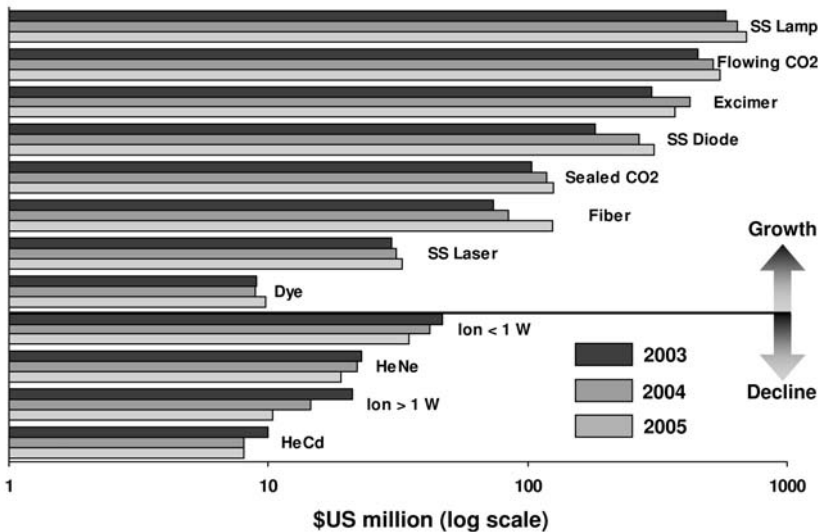


Fig. 1.14. Global revenues from sales of excimer laser sources were US \$ 421 million in 2004, which put excimers at number three in terms of global sales revenues of non-diode lasers. A 12% revenue decline is forecast for 2005, with unit sales dropping about 6%. Image Courtesy of *Laser Focus World*

Depending on how one actually defines the laser (that is, how much value is added to the light source itself), and depending on the laser's intended application, the average selling price of excimer lasers can range from a few tens of thousands of U.S. dollars for a low-end spectroscopy system to a million U.S. dollars for a system to be used, for example, in photolithography. Furthermore, while many excimers are manufactured and sold as a standalone component or subsystem to an OEM customer, many others are made and "sold" internally – at a medical laser systems manufacturer, for instance, who then sells an entire system to the end-user, such as a doctor or hospital. These variations in the distribution channels must be taken into account when assessing the overall market, and are particularly important to keep in mind when looking at the average selling prices.

If a laser is simply being transferred from one department to another within the same company there is no real "sale" of the device involved, so the selling prices used in assessing the global market revenues assume these lasers are actually transferred at the going market price for a similar laser. It is also worth noting here that the number of lasers sold at the higher selling prices in the semiconductor processing market do tend to overwhelm the numbers of those sold at lower prices, so the gross trends reflected in global totals can be misleading in terms of what's happening in the smaller market niches. While this problem exists for all global market averages, it

is particularly problematic in the excimer laser business because of the huge differences in average pricing concerned.

As discussed already in some detail in the previous chapter 1.2, excimer lasers are currently being sold into three primary market areas. These are, materials processing or industrial, medical therapy, and basic research (see Fig. 1.15). Within each of these general market areas are multiple smaller niches, and it is generally useful to examine the trends within each of these underlying segments.

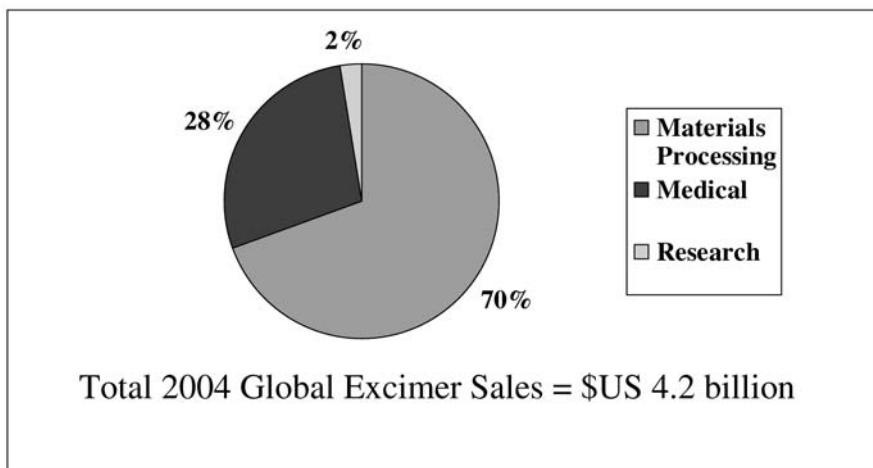


Fig. 1.15. The three primary market segments for excimer lasers are materials processing (US \$ 292 million), medical therapy (US \$ 119 million), and research (US \$ 10 million). Image Courtesy of *Laser Focus World*

1.3.3 Excimer Laser Markets: Industrial

The largest segment by far (70%), materials processing includes the use of excimer lasers for micromachining, metrology, telecommunications, and semiconductor and microelectronic processing. Examples of micromachining applications would be ink-jet nozzle drilling, marking, and micro-structuring among others. While hopes were high for some of these market niches when first developed, they either matured quickly or non-excimer alternatives offered strong competition. So the number of excimer lasers involved here has remained relatively flat. In the case of telecommunications, writing of fiber Bragg gratings was considered a major growth opportunity in the early days of the telecommunications bubble, but soon evaporated like many other related laser applications. Today, this grating market is all but dead as far as excimers are concerned.

The reason materials processing represents such a large revenue segment for excimer lasers is the semiconductor and microelectronic processing arena. Among the many niches here are annealing of thin film transistors, mask writing, and wafer inspection, but the largest part of this segment is microlithography. Of the 480 excimer lasers sold in this segment in 2004, roughly 360 (about 75% in units; 90% in revenues) of them were for microlithography.

Production of microchips requires exposing the wafers to ultraviolet (UV) light in a system called a wafer stepper. Non-laser mercury arc lamp ultraviolet sources (at 365 nm , called i-line) currently account for about 42% of stepper sales, with excimer lasers taking the remaining 58% (see Fig. 1.16). In this application the ultraviolet output of the excimer laser has become crucial to the production of integrated circuits with the highest circuit densities – because of its short wavelength, the excimer laser can be used to create very small circuit features. As the circuit densities required by the chipmakers increase, the resolution of the imaging systems that create the circuits also must increase. Progressively shorter wavelengths are part of the route to higher resolution imaging, which has been a driving force behind development of high-end short wavelength “deep UV” excimer systems at 193 nm (ArF) and these excimer lasers will certainly gain more overall market share over the next few years.

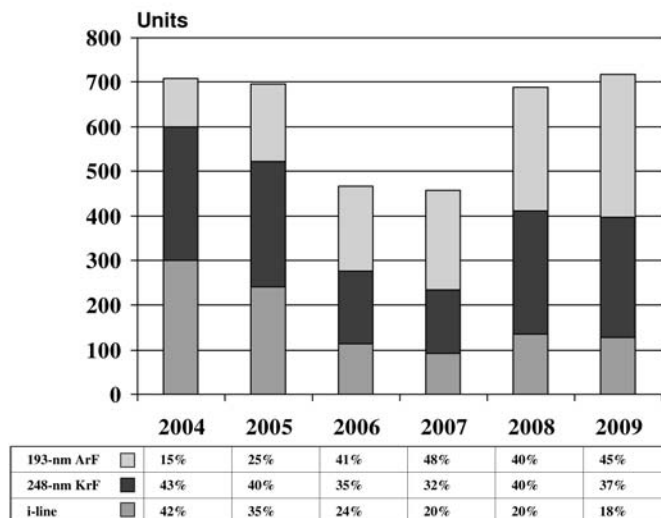


Fig. 1.16. It is still early days for 193 nm ArF excimer lasers in photolithography, which hold about a 15% market share in 2004. By 2008, the 193 nm and 248 nm systems are expected to hold equal share as the number of I-line systems diminishes. Source: Gartner Dataquest

Even so, other techniques such as immersion lenses have also been developed to address the need for higher resolution. Immersion lenses improve resolution by raising the numerical aperture (NA) value of the stepper's objective lens: a higher NA equates to better resolution. In fact even with immersion lenses and the adoption of deep UV excimer lasers, the imaging resolution is already falling behind the projected needs of the chip making industry and one of the big open questions is, what comes next.

For the time being, it seems likely that, given an increasing number of options to enhance resolution, 248 nm lithography will continue with the largest market share through the current chip making technology cycle and that 193 nm lithography will extend the dominance of excimers further on – at least through 2010. Beyond then, while excimer lasers can emit at 157 nm (fluorine), the shorter wavelength 157 nm lithography presents a significant new set of problems and many observers believe it will never happen in a full-fledged manufacturing situation. A variety of other options exist for the long term, all of which are at different stages of evaluation. None of them is based on the use of excimer lasers [2].

As for the immediate market outlook, the organization that represents semiconductor equipment manufacturers (SEMI; www.semi.org) released its year-end edition of the SEMI Capital Equipment Consensus Forecast in November 2004. According to the forecast, the leading manufacturers expected 2004 sales of their new chip manufacturing, testing and assembly equipment to grow by 59% to US\$ 35.31 billion – which would represent the second largest annual level ever recorded. Based on discussions with companies representing a majority of the total sales volumes for the global semiconductor equipment industry and conducted in October and November 2004, the SEMI forecast also concluded that 2005 would bring a moderate cyclic decline of about 5% to revenues of US\$ 33.49 billion before rising again in 2006.

Sales of equipment for the manufacture and testing of semiconductor and microelectronic devices represent one of the largest global markets for lasers of all types so such forecasts are of particular interest to the laser industry. For 2004, laser sales in this market sector are expected to reach a total of US\$ 356 billion – up 41% from 2003. The vast majority of these sales are excimer lasers (US\$ 292 billion or 82%). Given the size of the excimer business relative to the other lasers, it should come as no surprise that the overall segment outlook for 2005 reflects that of SEMI's forecast. Sales of all lasers for semiconductor and microelectronic processing are expected to fall about 12% in 2005, driven almost entirely by a 16% drop in sales of excimers for photolithography.

1.3.4 Excimer Laser Markets: Medical Therapy

The medical therapy market for excimers consists primarily of lasers sold for ophthalmology (eyes), cardiology (heart), dermatology (skin), and dentistry

(teeth). Excimer lasers are probably best known in the medical markets for their use in refractive surgery or vision correction. Here the short (UV) wavelength of the laser means it can be used as a precision surgical tool, while exhibiting low water absorption, so the laser output does not heat surrounding tissue and dehydrate the cornea. The laser is used to modify the cornea of the patient's eye and induce a permanent improvement in the eye's vision characteristics.

This ophthalmic application is currently dominated by VISX, a company based in Silicon Valley, California, which makes its own lasers and controls about 50% of the U.S. laser vision correction market. Although VISX's penetration outside of the U.S. is lower, the situation will likely change because VISX was acquired in late 2004 by Advanced Medical Optics of Santa Ana, California. Advanced Medical Optics is a global supplier of ophthalmic surgical device and eye care products with a worldwide presence and with no product overlap with VISX. The combined company could bring a major boost to VISX's global vision correction market share.

For all the companies operating in this field the ongoing revenues produced by the vision correction procedures done using the lasers are actually much more important than those revenues resulting from sales of the laser systems themselves. In 2004, for instance, VISX revenues for the nine-month period ended September 30, 2004 totaled US\$ 125 million, but only US\$ 20 million (16%) resulted from laser system sales – 72% were procedure related, with the remaining 12% related to service.

Nonetheless, because it's a very competitive field refractive surgeons are always looking for new ways to compete. Offering the latest technology is one way for them to attract patients and maintain premium pricing. So process improvements are rapidly incorporated into new systems and adopted as quickly as possible, thereby producing new system sales. The latest systems are starting to incorporate wavefront analysis capability that can significantly improve the overall quality of vision correction obtained from refractive surgery. This technique is probably the most popular current trend in refractive surgery and pushed excimer unit sales up by 13% in 2004 (over 2003). For 2005, the extremely competitive nature of the business will hold down continuing system growth, even while the growth in the number of procedures performed is likely to remain very strong for the foreseeable future.

In cardiology, excimers have been FDA approved for removing arterial blockages and problematic pacemaker and implantable cardiac defibrillator (ICD) leads. They have also been investigated for use in transmyocardial revascularization (TMR), which involves drilling a series of holes from the outside of the heart into the heart's pumping chamber in order to relieve severe angina or chest pain. In many of the cardiology applications, alternative procedures exist that have been proven over time and so present a real competitive challenge to the lasers – a particular problem in the US, where insurance reimbursement for new procedures is often not easy to obtain. Sim-

ilar problems have stalled the growth of an excimer laser based procedure for dealing with psoriasis, a disfiguring condition of the skin. Only a few years ago, this was expected to provide a major boost to excimer laser sales but has not materialized. And in the field of dentistry, excimers are currently being researched for precise surgery of both hard and soft tissue but this is not expected to grow into a major market. Notwithstanding these challenges the market for non-ophthalmological excimers has grown at a steady rate over the past few years and will reach about US\$ 9 million in 2004 (+20%) and is expected to continue its upward trend into 2005, gaining another 22% to reach US\$ 11 million.

1.3.5 Excimer Laser Markets: Research

Scientific applications of excimer lasers can be divided into three niches. These are, laser pumping – such as for pumping dye lasers for spectroscopic applications – which includes such techniques as laser-induced fluorescence, laser-induced breakdown spectroscopy, and others; and laser ablation for thin film and pulsed laser deposition. As a UV source, the excimer laser certainly has some unique attributes of significant interest to researchers, but the advent of alternative UV sources, especially solid-state diode-pumped systems, has eroded the overall importance of excimers for basic science, so their sales into this market have remained essentially constant for the past several years. In 2004, excimer lasers sales for research applications accounted for only 2% of the total or US\$ 10 million (105 units) with a flat outlook for 2005.

Despite the emergence of alternative UV sources, opportunities do still exist for small, economical excimer lasers in science. Researchers in fields such as environmental monitoring, surface science, and the study of reaction dynamics, for instance, are using compact excimers in the field for fluorescence spectroscopy, flash photolysis, and laser-ionization mass spectrometry [3]. While this will never be a blockbuster market segment it will likely remain at its current level for the foreseeable future.

References

1. K. Kincade: *Laser Focus World* **41**(1), 83 (2005)
2. K. Kincade: *Laser Focus World* **39**(2), 55 (2003)
3. J. Grondin: *Laser Focus World* **40**(11), 112 (2004)

Part I

Fundamentals

2 Some Fundamentals of Laser Physics

K. Körber, C. Kulik

2.1 The Wave-Particle Duality of Light

To understand the extraordinary characteristics of laser radiation, let us briefly recall the physics of light. At the end of the 16th century, the Dutch mathematician and physicist Christian Huygens formulated a theory on the nature of light in which he compared light to wave motion (*wave theory*). Although many properties of light can thus be correctly explained, light sometimes behaves like moving particles (*wave-particle duality*). This was the basis for a second theory which was published in 1704 by Sir Isaac Newton (*corpuscular theory*). The particle theory of light dominated scientific thought for over a century, completely overshadowing Huygens' contributions. On the basis of studies on the phenomenon of interference, which could only be explained if light was to consist of waves, T. Young and A. J. Fresnel resurrected the wave theory of light during the early 1800s. However, neither the wave nor the corpuscular theory offered a generally applicable model that explained all the characteristics of light. The groundwork for the present view of light was the introduction of the Quantum Theory proposed by Max Planck in 1900, which explained that radiant energy is emitted in discrete units, or quanta. Coupled with the findings that light can be regarded as an electromagnetic wave, the theory of ‘quantum electrodynamics’ was developed to describe all phenomena of light very precisely [1].

2.2 Electromagnetic Radiation

What is commonly known as ‘light’ is only a very small section of the electromagnetic radiation spectrum, which ranges from 380 nm to 780 nm and is visible to the human eye. In vacuum, the electromagnetic radiation propagates with velocity $c_0 = 299\,792\,458\text{ m/s}$. The electric and magnetic field vectors are orthogonal to each other and to the direction of propagation, as shown in Fig. 2.1.

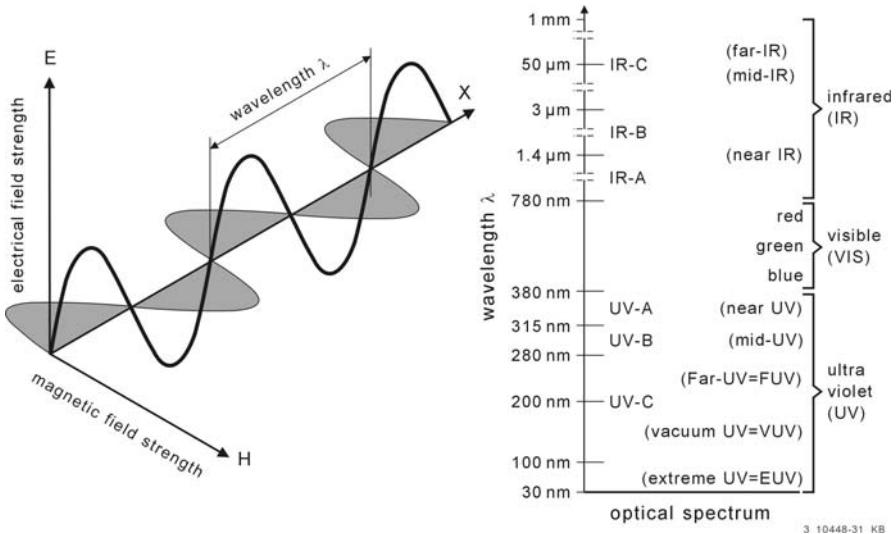


Fig. 2.1. Electromagnetic wave propagation and optical spectrum. Notice that the spectral section shown here extends both to shorter and longer wavelengths.

Wavelength and frequency are reciprocal parameters being connected by the equation:

$$c_0 = \lambda \nu \quad (2.1)$$

If the electromagnetic radiation interacts with atoms, ions or molecules, transfer of energy can take place. Albert Einstein discovered in 1905 that the minimal energy amount ΔE that can be transferred is connected to the frequency of the radiation according to the equation

$$\Delta E = h \nu \quad (2.2)$$

where h is the Planck's constant ($h = 6.6260755 \cdot 10^{-34} \text{ Js}$). Thus electromagnetic radiation of some frequency ν can be regarded as a stream of these minimal energy portions called 'photons'. By defining these photons as 'energy particles', the above mentioned wave-particle duality of light becomes plausible.

2.3 Spontaneous and Stimulated Emission, Population Inversion

As discovered in the early 20th century, atoms, molecules, crystals and any other solid-state matter are quantized systems characterized by electron shells. In order to visualize the different energetic states, an energy-level

diagram is used (Fig. 2.2), for atoms as well as any other physical system like molecules. If such a system receives energy by a collision/interaction with other electrons, atoms or photons, the system is transferred into an excited state. For photons, this mechanism is called ‘absorption’. A prerequisite for this kind of interaction is that the transferred energy is large enough to overcome the energy gap between the ground state and one of the excited states.

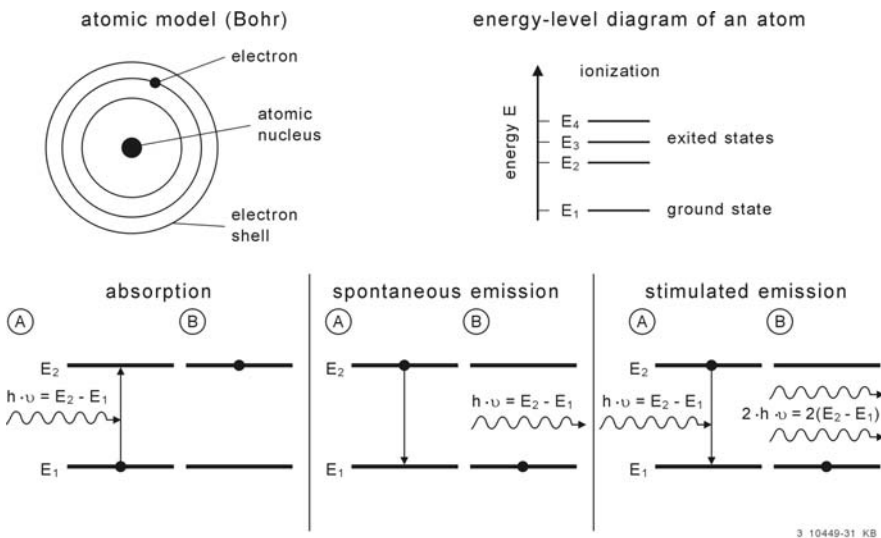


Fig. 2.2. Absorption and emission of radiation

If a physical system has been raised to a higher energetic state E_2 , it will normally remain there for a very short period of time (roughly 10^{-8} s).

It will then return to a lower energetic state e.g. E_1 . By this transition, the energy difference ΔE is emitted as a photon of frequency ν_{12} :

$$\Delta E = E_2 - E_1 = h \nu_{12} \quad (2.3)$$

Since this transition takes place statistically in time and space, this kind of energy emission is called ‘spontaneous emission’. The processes of absorption and spontaneous emission are completely reversible.

Another interaction process also shown in Fig. 2.2 is called ‘stimulated emission’, which is essential for the laser process. This effect was already predicted by Albert Einstein in 1917, but it took until 1960 before Theodore H. Maiman designed a system that actually realized stimulated emission. Stimulated emission can occur when photons interact with a physical system in an excited state E_2 if their frequency matches the excitation energy of the system according Eq. 2.3. This photon stimulates the emission process. The key for any laser operation is that the emitted photon is moving in the

same direction as the initial one and that its wave is in phase (coherent) with the stimulating radiation so that light amplification becomes possible. However, for laser action, the aspect of ‘population inversion’ within the active laser medium has to be considered. Under normal condition, known as the thermodynamic equilibrium, quantized systems tend to drop to their lowest available energy level, i.e. the system’s ground state. Considering a two-level system with N_1 atoms in the ground state and N_2 atoms in the excited state, the distribution of the atoms among the two levels can be mathematically expressed in terms of a ‘Boltzmann distribution’:

$$\frac{N_2}{N_1} = e^{-\frac{\Delta E}{kT}} = e^{-\frac{h\nu}{kT}} \quad (2.4)$$

where k is the Boltzmann constant ($k = 1.380658 \cdot 10^{-23} J/K$) and T the temperature in Kelvin (K). Due to the fact that no negative temperatures (in Kelvin) can be achieved, the ratio of N_2/N_1 will always be < 1 , so that an initial photon is far more likely to be absorbed by the system than used to stimulate emission from an excited state. Under these conditions, spontaneous emission dominates and no light amplification can be achieved.

Population inversion (i.e. $N_2 > N_1$) is needed to create a situation where stimulated emission is more likely to occur than absorption and subsequent spontaneous emission. The result is light amplification, the precondition for a LASER – ‘Light Amplification by Stimulated Emission of Radiation’. Light amplification arises from the difference between stimulated emission and absorption. The subsequent equations describe the probability of absorption, spontaneous and stimulated emission during interaction with radiation of spectral density $\rho(\nu)$. The number of transitions dN in the time dt can be described by:

$$dN_{12} = B_{12} \rho(\nu) N_1 dt \quad (\text{absorption}) \quad (2.5)$$

$$dN_{21, \text{spon}} = A_{21} N_2 dt \quad (\text{spontaneous emission}) \quad (2.6)$$

$$dN_{21, \text{stim}} = B_{21} \rho(\nu) N_2 dt \quad (\text{stimulated emission}) \quad (2.7)$$

where A and B are the ‘Einstein coefficients’ representing the transition probability of spontaneous emission (A) and stimulated emission (B). With some mathematical effort (see in detail in [2] or [3]) the following equation 2.8 can be derived:

$$\frac{A_{21}}{B_{21}} = \frac{8\pi h \nu^3}{c_0^3} \quad (2.8)$$

Thus the probability of spontaneous emission increases proportional to ν^3 compared to the probability of stimulated emission. This physical dependence defines the problem to design a light amplifying system that emits short wavelength radiation.

2.4 Design Principle of a Laser

In order to generate a coherent, highly directionally orientated beam, it is essential that the light amplification takes place in an optical feedback system. Such a feedback system is generally provided by mirrors which are arranged on opposite sides of the laser medium to force the radiation to oscillate within the ‘laser resonator’ or ‘laser cavity’. A simple design of a laser resonator is shown in Fig. 2.3. One of the mirrors is totally reflective ($R = 100\%$), while the other lets a part of the light escape from the cavity through a partially transmitting section, thereby forming the laser beam.

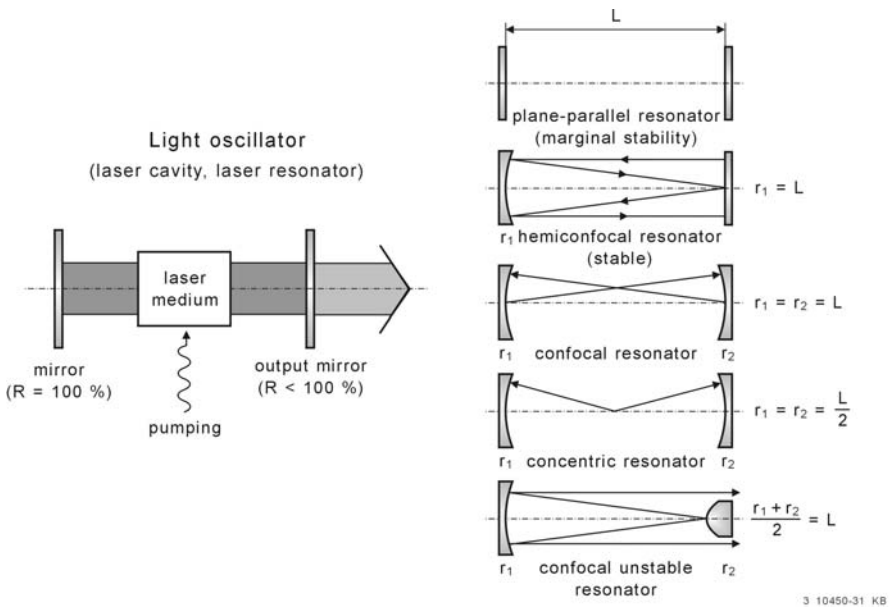


Fig. 2.3. Principle set-up of various mirror configurations for a laser resonator

To achieve population inversion, the laser medium can be excited, also called ‘pumped’, in many different ways. The efficiency of these pumping mechanisms is dependent on the kind of the laser medium:

- discharge excitation (an electrical current flows through the laser medium),
- electrical or ion beam excitation (pulses of electrons/ions are deposited in the laser medium from an accelerator),
- radio-frequency or microwave excitation (energy transfer by these kinds of electromagnetic waves),
- chemical excitation (energy from an exothermic chemical reaction is used for the excitation),
- gas-dynamic excitation (applicable only for gas lasers; population inversion is realized by the expansion of a high-pressure gas),
- optical excitation (the energy transfer is achieved by photons)
- nuclear excitation (laboratory method; energy transfer from products of a nuclear reaction to the laser medium).

Depending on the mirror configuration, different types of resonators can be distinguished which are defined by the distance L between the mirrors and the radii r_1 and r_2 of the mirrors in Fig. 2.3. The conceptual simplicity of a plane-parallel resonator is offset by the practical difficulty of aligning the mirrors precisely enough for stable operation of the laser. Nevertheless, for most excimer lasers, this configuration is the state of the art.

If the energy of the radiation is limited by the design in a volume close to the resonator axis, the resonator is called ‘stable’. In contrast, the diffraction losses in an ‘unstable’ resonator are fairly high (see also confocal unstable resonator, Fig. 2.3). But the radiation that is escaping from the resonator cannot directly be regarded as a loss because it is essentially the outcoupled “useful” laser radiation. The advantage of unstable resonators is the uniform intensity distribution of the available laser radiation.

2.5 Types of Lasers

The classification of lasers can be made by considering different aspects. Commonly the ‘laser medium’ is used as the basis for this classification. We therefore have:

- gas lasers,
- solid-state lasers,
- semiconductor lasers,
- liquid lasers,
- and some laboratory developments like free-electron lasers or X-ray lasers.

Only the first three types, which have the highest relevance for industrial processes next to the excimer lasers, will be briefly discussed below.

Gas lasers dominate any list of commercially available laser types and can emit radiation with the widest variety of wavelengths compared to lasers

using other active media. The group of gas lasers includes helium-neon (He-Ne) lasers, noble (rare) gas ion lasers (e.g. Ar⁺ lasers), helium-cadmium (He-Cd) lasers and carbon dioxide (CO₂) lasers. The latter ones, which emit at a wavelength of $\lambda = 10.64 \mu m$, have a high relevance for industrial applications like cutting and joining of metallic materials.

Solid-state lasers: Although in electronics the word ‘solid-state’ includes semiconductor materials, in the laser world a slightly different situation exists. There, the laser medium of a solid-state laser is a nonconductive solid with either a crystalline or an amorphous (glass-like) composition that is doped with laser-active ions. These ions will be excited by optical pumping (e.g. by flashlights or laser diodes). Thus, the host material has to be transparent at the absorption and emission wavelength of the laser-active elements. It should be mentioned that the first laser was the ruby laser, a solid-state laser, invented in 1960 by Theodore H. Maiman. The laser medium consists of an aluminum oxide crystal (sapphire) doped with chromium atoms. Nowadays the Nd:YAG laser is the most important solid-state laser. It can generate continuous output powers up to the kilowatt range and it is one of the most important lasers for material processing. The matrix consists of yttrium-aluminum-garnet (YAG), a synthetic crystal with a garnet-like structure and the chemical formula Y₃Al₅O₁₂. The crystal is doped with a few percent neodymium (Nd) that is responsible for the laser transition. Typically the laser operation can be described in terms of a simplified 4-level scheme. Starting from the ground state, pumping occurs via optical excitation to various pump bands (closely lying energy levels). The most effective pump bands are situated between 500 nm and 900 nm. The lower laser level is still above the ground state, under normal conditions it is not populated. The strongest laser line is in the region of 1.06 μm , but laser emission can also be obtained at 1.32 μm .

Semiconductor lasers are widespread in the field of low-power applications like communication transmission or data storage. In order to achieve high output powers – up to several kilowatts – many single emitters have to be combined to get one incoherent diode laser. Usually GaAs ($\lambda = 808 nm$) and InGaAs ($\lambda = 910 nm$ –980 nm) are used to build commercial systems with up to 5 kW output power. Compared to the other lasers mentioned above, these systems have a much higher efficiency (~ up to 50%) and compactness. Unfortunately, the divergence of the emitted radiation is relatively high and therefore the beam quality is fairly low. In order to improve the beam quality, several optical elements have to be incorporated in such a laser system. Enormous improvements have been made in this field during the last few years and can be expected to continue in future.

References

1. H. Weber: *Laser: Eine revolutionäre Erfindung und ihre Anwendungen* (München: Beck, C. H., 1998. ISBN 3-406-43290-5)
2. F.K. Kneubühl, M.W. Sigrist: *Laser* (Stuttgart: Teubner, B. G., 1999. ISBN 3-519-43032-0)
3. O. Svelto, D.C. Hanna: *Principles of Lasers* (New York: Plenum Press, 1982. ISBN 0-306-40862-7)

3 Principles of Excimer Lasers

H. von Bergmann, U. Stamm

Excimer lasers are the most powerful lasers existing in the UV. A number of different pumping or excitation mechanisms have been applied to deposit the required energy into the active lasing medium. The most important pumping techniques are electron beam pumping, pumping by an electrical high-pressure gas discharge and by microwave discharges. These are described in detail in chapter 4.

Many different excimer laser transitions have been used to generate laser output at various wavelengths between 126 nm in the vacuum UV and about 660 nm in the red. An overview of excimer lasers with their respective emission wavelengths is shown in Fig. 3.1. Among those the most commonly

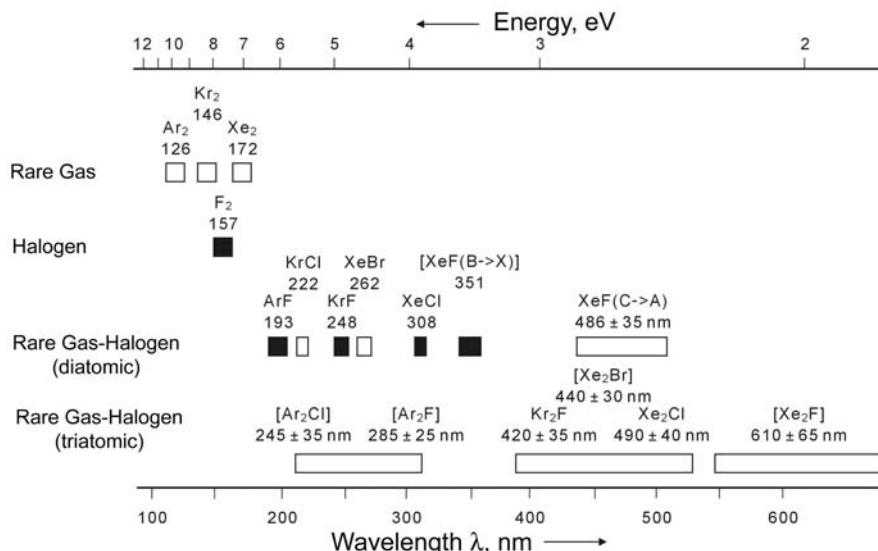


Fig. 3.1. Lasing wavelengths (lower scale) and corresponding photon energy (upper scale) of the different excimer lasers. The solid blocks indicate commercially important wavelengths.

employed excimer laser media are krypton fluoride (KrF , 248 nm), argon fluoride (ArF , 193 nm) and xenon chloride (XeCl , 308 nm). Recently also the fluorine laser (F_2 , 157 nm) with its very short wavelength receives increasing interest and applications, c.f. chapter 13 of this book.

The name **excimer** comes from **excited dimer**, a class of molecules formed by the combination of two identical constituents in the excited state.

For the most common excimer lasers of today the name “excimer” laser is used only by convention since here excited complexes (exciplexes) of rare-gas monohalides rather than excited dimers form the active laser medium. In addition, exciplexes exist with some stability only in the excited state. The rare-gas halide exciplexes are formed between the rare gasses Ar, Kr, or Xe and the halides F or Cl. The most important lasing species are ArF , KrF , XeCl and XeF .

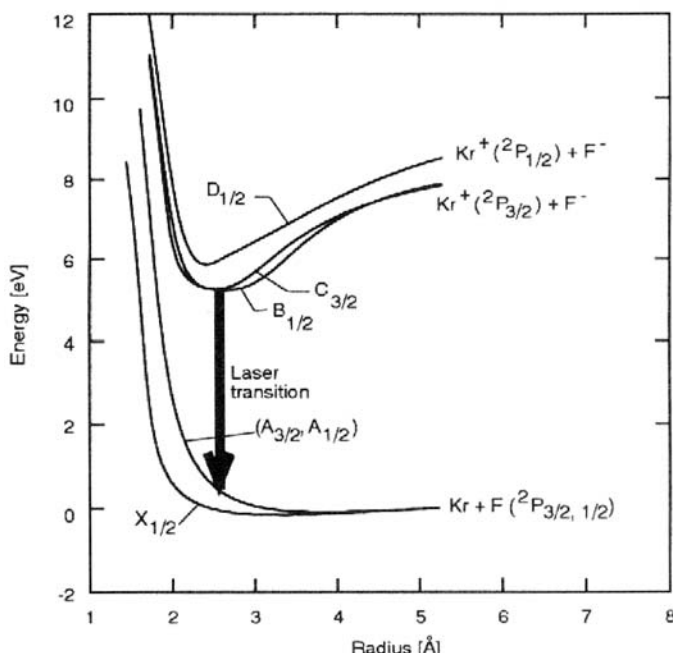


Fig. 3.2. Schematic potential energy diagram for the KrF rare-gas monohalide

The general principle of the excimer laser transitions is shown for the example of KrF in Fig. 3.2. The upper laser level is an ionically bound charge transfer state of the ${}^2\text{P}$ rare-gas positive ion (Kr^+) and the ${}^1\text{S}$ halogen negative ion (F^-). The production of the excited excimer molecules in an electrical discharge relies on complex plasma reaction processes. As an example, a simplified reaction scheme for KrF is shown in Fig. 3.3. The formation of

the rare-gas halogen molecule is dominated by two reaction channels: the ion channel, where ion pair recombination of a positive rare-gas ion and a negative halide ion takes place in the presence of a third body (buffer gas, for example Ne or He), and by the neutral channel, where an excited-state rare-gas atom reacts with a halogen molecule in the so-called “harpooning” reaction. These reactions take place on the nanosecond time scale and can be very efficient, with upper laser level production efficiencies of several tens of percent. While there is a minimum in the potential energy curve in the upper state, it is still rather unstable and the excited KrF^* molecule decays after several nanoseconds via emission of a photon into Kr and F. These form the ground state that has covalent character and consists of separate Kr and F atoms for large inter-nuclear separations. The components Kr and F are then available for another excitation cycle. Because of this unstable ground state, excimer lasers belong to the class of four-level lasers, which do not suffer from ‘bottle-necking’ and have therefore an inherently high efficiency. The short spontaneous lifetime of the laser transition and its large bandwidth and short wavelength lead to a small stimulated emission cross-section. The excitation rate has to compete with fast loss processes, collisions and spontaneous decay, which lead to the deactivation of $(\text{KrF})^*$ with a combined time constant of a few ns. As a result pump power densities exceeding 1 MW/cm^3 are required for the excitation of excimer lasers, which can only be reached

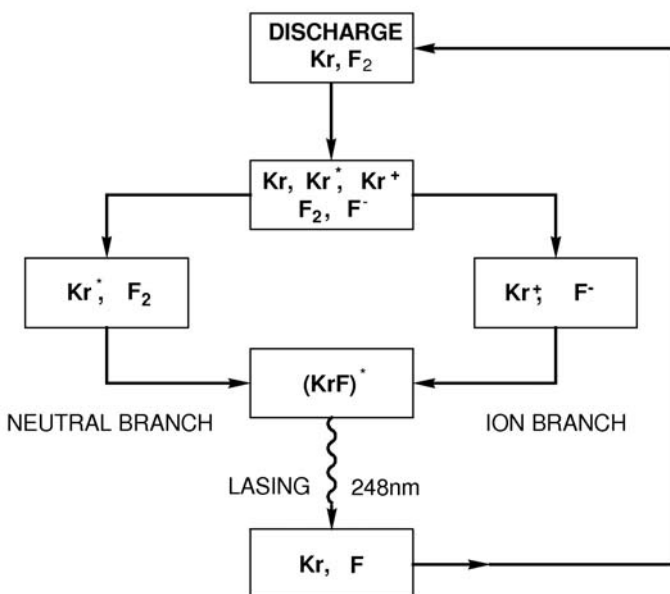
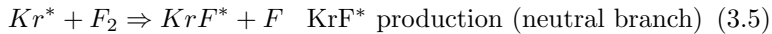
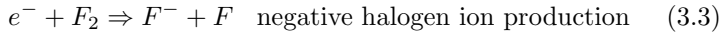
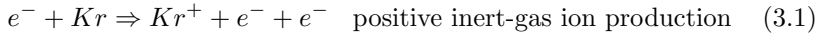


Fig. 3.3. Dominant formation kinetics of the $(\text{KrF})^*$ excimer

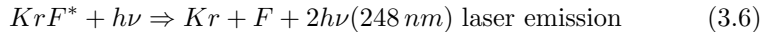
in pulsed systems. Excimer lasers are therefore intrinsically limited to the pulsed mode of operation.

In more detail the most important expressions describing the inherent chemical reactions, the pumping, stimulated emission and loss processes are shown below for the example of a KrF excimer laser:

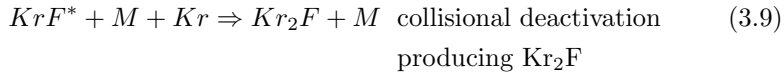
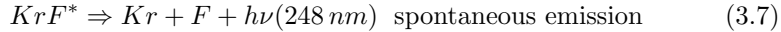
Pumping:



Stimulated emission:



Losses:



* indicates the excited state of an atom or molecule, M is a third body collision partner and X represents impurities of the laser gas.

Similar reactions are responsible for the excitation and lasing processes in the other excimer diatomic [1] and triatomic [2] gases. The spectral properties of the major rare-gas mono-halide excimer lasers ArF, KrF and XeCl are shown in Fig. 3.4.

The comparatively large bandwidth of the fluorescence emission of 1–4 nm is reduced significantly to 0.05–0.5 nm by the lasing process and can be narrowed down even further by incorporating frequency selective resonators similar to those found in dye lasers. Due to the relatively wide fluorescence bandwidth, the laser wavelength can be tuned over a range of 0.3–1 nm.

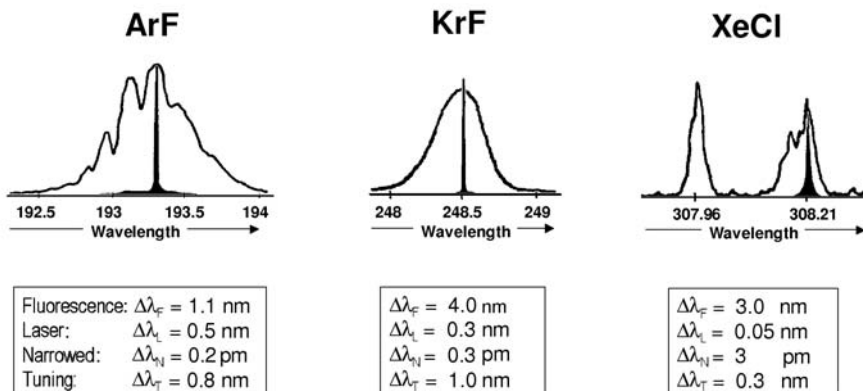


Fig. 3.4. Spectral properties of the rare-gas mono-halide excimer lasers ArF, KrF and XeCl showing fluorescence spectrum and lasing spectrum (narrow black line)

References

1. C.A. Brau: *Excimer Lasers. Topics in Applied Physics*, Vol. 30, 2nd edn. (Springer-Verlag, Berlin, 1983)
2. D. Huestis, G. Marowsky, F. Tittel: *Excimer Lasers, Topics in Applied Physics*, Vol. 30, 2nd edn. (Springer-Verlag, Berlin, 1983)

4 Design and Technology of Excimer Lasers

H. von Bergmann, U. Rebhan, U. Stamm

Although the chemical reaction processes responsible for the excitation of excimer lasers seem to offer ideal operational conditions, the technical realization of reliable laser systems for scientific and industrial use is a demanding task. The design of excimer lasers is complicated by several factors. The gas mixtures used in the laser contain the halogens fluorine or chlorine, which are highly corrosive. The laser systems are operated at gas pressures of up to $6 \times 10^5 \text{ Pa}$ and can contain relatively large gas volumes, making high-strength mechanical construction necessary. Voltages of more than 40 kV are used for the excitation, requiring efficient high-dielectric-strength insulators. These factors severely limit the choice of materials that can be employed for the construction of the laser. The design of lasers to be employed in the industrial environment is more demanding than that for scientific and laboratory use. In contrast to scientific applications, where performance is the most important question, in industry issues such as low operating cost, long-term reliability, ease of operation and safety are of overriding importance. As a consequence, designs prefer simple and proven technology, being cautious of possibly more efficient, but more complex and therefore higher risk approaches.

4.1 Excitation

The design of the laser system mainly depends on the method of excitation, which can be performed either by electron beam, microwaves or gas discharge. In the first case, the excitation energy is transmitted by a pulsed electron beam, which laterally penetrates the gas-filled laser tube through a thin foil. While electron-beam-excited systems have the advantage of very high pulse energies, up to several kJ , and large beam cross sections, they employ complex and inefficient high voltage technology and are intrinsically limited to repetition rates of only a few Hz . For industrial applications this laser design is not appropriate because of high operational costs as well as short tube lifetimes. Microwave excitation can be realized by applying a microwave signal to electrodes attached to a laser-gas-filled capillary tube. Even

though experimental designs have reached pulse frequencies of up to 8 kHz , the microwave excitation method is of no industrial relevance due to the low achievable energy per pulse of about $100\text{ }\mu\text{J}$ [1] and associated average powers of fractions of a *watt*. The technology, almost exclusively employed by reliable, high-power industrial excimer lasers, is high-pressure gas discharge excitation, which can provide outputs of up to several *joule* and repetition rates in the kHz range. Figure 4.1 shows the gas discharge section of a typical transversely excited excimer laser tube schematically.

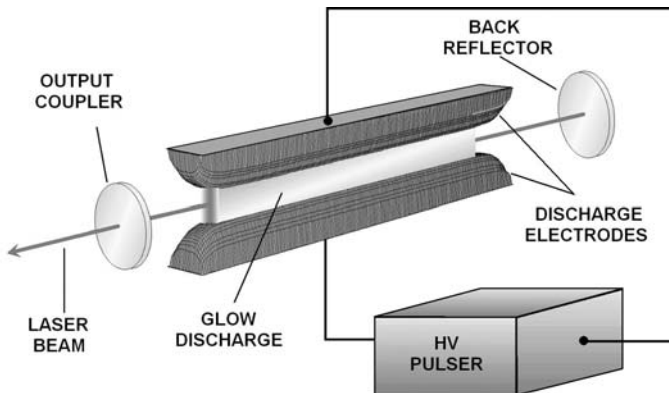


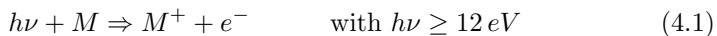
Fig. 4.1. Schematic diagram of excimer laser

The discharge unit is integrated into the laser tube, which is designed as a high-pressure gas vessel. The laser gas mixture consists of a 0.05% to 0.5% halogen component for halogen excimer lasers, 3% to 10% inert gas component, and the buffer gas (helium or neon) at a pressure of $1.5 \times 10^5\text{ Pa}$ to $6 \times 10^5\text{ Pa}$. This high pressure makes a continuous gas discharge virtually impossible. After some ten nanoseconds streamers start to develop and the initial glow discharge degrades into an arc or spark discharge, which is not suitable for the excitation process and will damage the electrodes. Therefore, most industrial excimer lasers utilize short excitation pulses, which terminates the discharge prior to the onset of streamer and arc formation. This leads to the typical short laser pulses of 10 ns to 30 ns . The technique to produce and control a homogeneous gas discharge is crucial for the performance of an excimer laser. The most critical parts of this technique are the preionization of the laser gas, the discharge electrodes, the gas flow system, and the high-power discharge circuit.

4.2 Preionization

Preionization means the seeding of the discharge volume uniformly with electrons prior to the initiation of the main discharge. It is necessary in order to prepare a uniform glow discharge and avoid arcing. Parameters that affect the preionization, such as threshold value, seed electron density and uniformity, are heavily dependent on the design of the discharge system such as type of electrode and profile, gas pressure, duration of preionization, electron loss processes, time delay between preionization and main discharge, rise time of electrode voltage, as well as on the overall discharge system geometry. Electron densities of 10^7 to 10^9 cm^{-3} are required to produce a uniform arc-free discharge. However, even if an arc-free discharge is obtained the output energy and the discharge stability are improved with increased electron densities. At low preionization densities the discharge consists of a large number of filaments, which lead to increased electrode erosion, and unsatisfactory utilization of the gas medium. Also the timing of the preionization with respect to the main discharge and the spatial uniformity are of extreme importance.

There are several electrode structures and preionization techniques that can be employed for the excitation of the laser. These determine the discharge cross-section and quality and with it the laser energy output and efficiency, which in turn have a strong impact on the design of the laser and power conditioning system. The electrode systems commonly used for the excitation of high-repetition-rate excimer lasers fall into two categories: solid electrodes with side preionization, spark arrays or corona bars, and combinations of solid and screen electrodes with the preionization source located behind the screen. Preionization relies on photo ionisation of background trace impurities M of the gas and proceeds according to the following reaction:



Preionization can either be effected by UV radiation [2] or by X-rays. X-rays allow to preionize large discharge cross-sections and to achieve pulse energies of up to several joule, but they considerably increase system cost and complexity. In addition, the high X-ray fluxes required at high repetition rates necessitate elaborate X-ray shielding and are therefore generally not desirable in systems for industrial use. Finally suitable X-ray sources have not yet demonstrated reliable long-life operation at high repetition rates. Industrial excimer lasers therefore generally rely on UV preionization by either spark discharges or surface corona discharges. Schematic arrangements used for UV preionization are shown in Fig. 4.2.

The typical set-ups employed for spark preionization are shown in Figs. 4.2a and 4.2b. Preionization pins arranged in a row adjacent to the discharge electrodes or behind a screen electrode generate a spark discharge some 10 ns before the main discharge. The UV radiation produced by the sparks is sufficient to preionize the laser gas between the electrodes with a homogeneous

initial seed density of at least $10^8 \text{ electrons/cm}^3$. While sparks provide high electron densities, the uniformity tends to be relatively poor and spark electrode burn-off causes system pollution, which limits gas and electrode life. In recent industrial excimer laser designs the spark preionization could be significantly improved by placing a dielectric material like alumina between the preionization pins as shown in Fig. 4.2c [3]. The resulting surface-guided discharge spreads over several millimeters instead of forming a very thin discharge channel and the erosion rate of the preionization pins is reduced by an order of magnitude or more. This design enables longer gas lifetime and electrode life of 10 billion pulses. Most of the high-average-power industrial excimer lasers benefit from this preionization design.

For high-repetition-rate lasers the surface corona preionization (SCP) has been introduced (see Fig. 4.2d) [4]. SCP proved to be superior to conventional preionization sources at $k\text{Hz}$ repetition rate because of the ability to generate sufficient electron density levels for a narrow high-repetition-rate discharge volume using a significantly lower amount of energy and with a much higher spatial uniformity. This results in improved output stability and increased discharge electrode life.

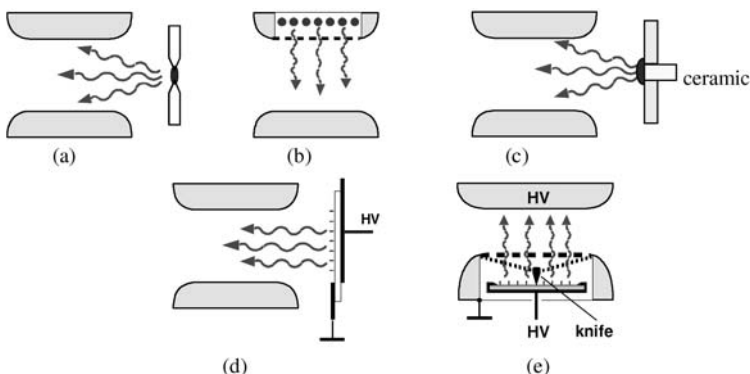


Fig. 4.2. Preionization arrangements used for excimer lasers: (a) spark preionization from the side, (b) spark preionization through screen electrode, (c) dielectric surface-guided spark preionization, (d) surface corona preionization from the side and (e) surface-guided preionization through screen electrode (creeping discharge).

Another surface-guided preionization arrangement has been developed for large-aperture excimer lasers. The surface-guided discharges (sometimes also called creeping discharges [5]) are generated on a dielectric surface backed by a ground electrode by applying a fast high voltage pulse to a knife edge electrode placed on the surface as shown in Fig. 4.2e. Discharges distributed over large surface areas can be produced using this technique. The advantage of using surface-guided discharges compared to the low-current corona

discharge SCP of Fig. 4.2d is the possibility to relatively easily optimize the intensity of the preionization.

4.3 Discharge Electrodes

Electrode systems employed in excimer lasers are either screen electrodes with behind-the-screen preionization or solid discharge electrodes using side preionization. Screen electrodes can provide superior homogeneity of preionization, especially in large cross section systems, but are intrinsically fragile and can easily be destroyed by discharge arcing at high repetition rates. Solid discharge electrodes utilizing side preionization are therefore commonly used for the excitation of high power and of high-repetition-rate industrial excimer lasers.

In high-pressure gas discharge lasers the discharge electrodes have to be carefully profiled in order to provide a highly uniform electric field distribution in the discharge region and to avoid field concentrations near the electrode edges. A field uniformity of the order of $\Delta E/E \leq 10^{-3}$ is generally required to avoid premature discharge instabilities and arcing. This requirement results in mechanical tolerances of the electrode of better than $50 \mu\text{m}$. The electrode profile does not only determine the maximum arc-free energy loading of the discharge but also the discharge width and profile, which in turn controls the profile of the laser beam. Uniform field electrode profiles can be derived empirically, calculated analytically [6, 7] or by numerical methods [8], and are manufactured to the required tolerance of a few μm using numerically controlled milling machines. Design criteria include field uniformity, edge-enhancement of field, compactness of the electrode (i.e. ratio of discharge and electrode width) and generated discharge profile. While analytical techniques provide useful results, they do not include second order effects such as field distortions caused by nearby current returns and insulating structures. Numerical techniques are therefore superior for the electrode design [8].

Material and surface finish of the electrode have a strong influence on the discharge characteristics and electrode service life. The electrodes have to withstand the erosion caused by the high-current discharge and have to be chemically resistant to the fluorine or chlorine component used in the gas mixture. Materials employed include stainless steel, pure nickel, aluminum nickel alloys and brass as well as combinations such as nickel-plating on a copper or aluminum base.

Commercial excimer lasers running with fluorine as halogen component are normally equipped with brass electrodes, which proved to be superior above all other electrode materials. The benefits of brass electrodes are a long lifetime and a lower window contamination rate compared to nickel or stainless steel electrodes. Intensive material studies have been done to determine the optimum brass alloy for cathode and anode. A lead content of 3 to

4% is preferable for the anode material [9]. A relatively uniform and homogeneous 100 to 200 μm thick fluoride layer develops by proper treatment like high temperature annealing and fluorine passivation [10] and covers the entire active discharge surface. This forces the discharge current to flow through tiny fluoride layer holes, which typically tend to have a diameter of 20 to 150 μm . The surface covered by the fluoride layer does not suffer from substantial further erosion. Essential for a long lifetime is a homogeneous fluoride layer on the anode. For the cathode a lead-free brass alloy is preferable because it has a two times lower erosion rate [11]. Again high temperature annealing can reduce the electrode wear substantially. Typical brass electrode lifetime is several billion pulses for high-energy lasers and 10 to 20 billion for high-repetition-rate lasers.

For XeCl excimer lasers tungsten-based alloys proved to be the most suitable electrode materials. Sintered tungsten filled with either copper or rhodium [12] provides an outstanding low erosion rate and enables therefore electrode lifetime of 3 to 10 billion pulses for high-power industrial excimer lasers.

The beam profile of industrial excimer lasers must be constant over the entire laser tube lifetime. One approach to achieve a constant discharge width is the use of a compound electrode made from two alloys with different erosion rates [13]. The central part of the electrode is made from an alloy with low erosion rate while the outer parts or shoulders of the electrode are made from a material with a higher erosion rate. Compound electrodes for lasers with fluorine containing gas mixtures are made either from two different brass alloys or brass for the central part and nickel for the outer ones. The faster erosion rate of the outer electrode parts avoids any widening of the discharge area over the laser tube lifetime. Another approach is the use of an electrode with a low erosion central parts and dielectric outer parts. The so-called dielectric shoulders effectively prevent downstream arcing at multi-kilohertz operation and they strongly limit the discharge width. This results in a very stable beam profile width over the tube lifetime.

4.4 Discharge Circuits

The threshold values for population inversion in excimer lasers are high due to the short wavelength and the considerable line width of the relevant transitions. A typical value for the concentration of the active species (upper laser level) is 10^{14} cm^{-3} to 10^{15} cm^{-3} . Such concentrations can only be obtained by very high pump energy densities (10^{-2} J/cm^3) supplied in a short time interval (10^{-8} s to 10^{-7} s) usually achieved, as explained above, by a high-power discharge pulse. Excimer lasers are therefore invariably pumped using a discharge circuit (pulser) that discharges the stored electrical energy directly into the active medium. The pumping schemes involve efficient switching of this stored electrical energy into the discharge system in a very short time

and with a well defined spatial and temporal profile as this determines the discharge uniformity and – in turn – influences the spatial uniformity of the extracted laser beam. These requirements impose severe requirements on the pumping scheme in terms of peak currents and voltage rise times. Besides the charging section, the pumping scheme of excimer lasers usually consists of a network of inductors and capacitors (discharge circuit), which is designed to closely match the dynamic behavior of the gas discharge, where the resistance is rapidly changing with time. The discharge circuit conventionally used for the excitation of medium-power excimer lasers is the basic capacitor transfer (C-C transfer) circuit as shown in Fig. 4.3. The C-C transfer circuit employs simple matched energy transfer from a storage capacitor C_1 , which is initially charged to the required high voltage, to the discharge peaking capacitor C_2 . Once the voltage on C_2 and with it the electrode voltage rises to the level necessary for discharge initiation the energy is then switched into the discharge. The loop inductance L_2 consists of the stray inductance of the electrode system and can be kept at a few nH , resulting in a fast current pulse and extreme power deposition levels.

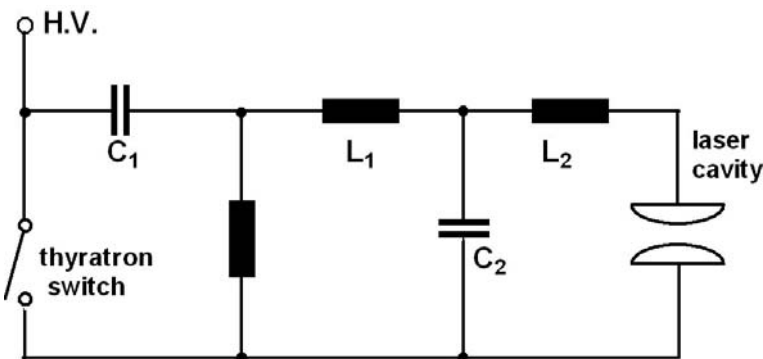


Fig. 4.3. Excimer laser discharge circuit with thyatron switch

The limiting component in this type of circuit is the high-voltage switching element, which has to withstand the high voltage and current during the discharge cycle (peak voltage up to 40 kV , peak current at about 10 to 100 kA , current rise times of 30 to 100 ns) [14, 15]. In the first excimer lasers, spark gaps were used as high-voltage switches. These were quickly replaced by thyatrons due to their better reliability and lifetime characteristics. The design of a basic three-electrode thyatron and an improved multi-grid thyatron for laser applications are shown in Fig. 4.4.

A thyatron tube is filled with hydrogen at a low gas pressure, provided by heating of an internal hydrogen-metal reservoir (palladium). Thyatrons operate on the left side (vacuum side) of the Paschen curve and the hydrogen pressure determines the hold-off voltage of the tube. In the non-conductive

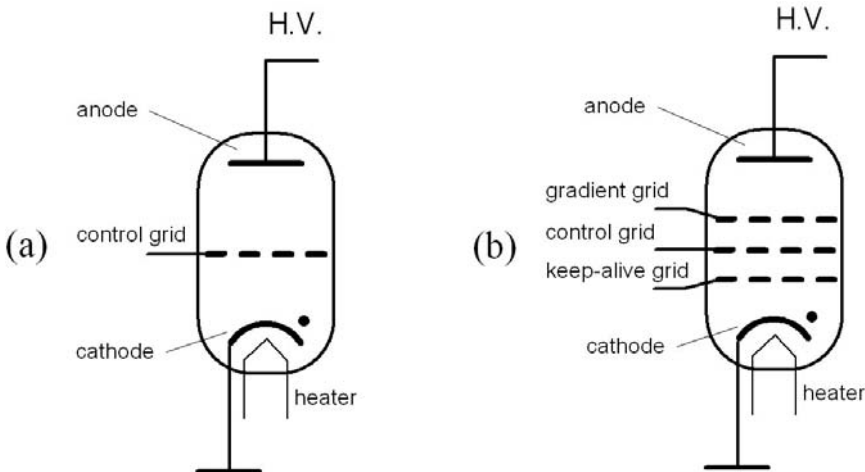


Fig. 4.4. Basic three-electrode thyratron (a) and improved multi-grid thyratron for low-jitter laser applications (b)

state, the control grid between the electrodes is negatively biased in order to restrict the free electrons, released from the thermionic cathode, to the cathode region. By applying a positive trigger pulse to the grid, the electrons can pass the grid into the anode region switching the thyratron to the conductive mode. A thyratron behaves like a diode, which means that it will remain conducting as long as a positive voltage is applied and normal thyratrons cannot conduct reverse currents. Recovery (opening) of the thyratron is affected by diffusion of the ions to the inner walls and electrodes of the tube. Negative transient electrode voltages at the end of the conduction pulse can lead to reverse arcing, which is detrimental to thyratron life. The maximum allowable forward current scales with the tube diameter and size of the cathode.

The use of deuterium instead of hydrogen as well as additional grids employed in multi-grid thyratrons help to achieve a higher hold-off voltage, more reliable triggering, and a more homogeneous discharge. Special thyratron designs allow for higher achievable (forward) currents by employing special larger-area cathodes, and hollow-anode designs tolerate conduction in the reverse direction, making the thyratron less vulnerable to reverse currents. In spite of the improvements in thyratron design, the lifetime of this component is limited in the C-C transfer circuit to several 100 million pulses. Consequently, particularly in excimer lasers that operate at high pulse repetition rates, discharge circuits involving magnetic pulse compression [16, 17] are used to reduce thyratron stress (see Fig. 4.5).

In magnetic pulse compression circuits the electrical energy is not delivered to the laser cavity in a single step, as e.g. in the case of the C-C transfer circuit, but it is initially transferred on a slow time scale by the thyratron

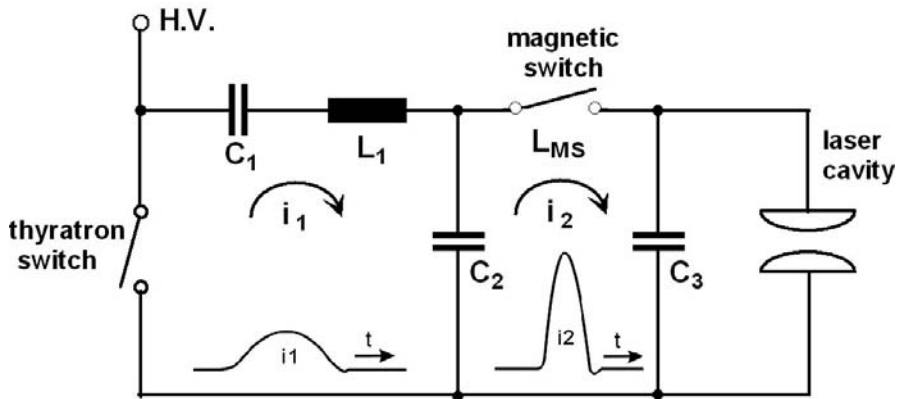


Fig. 4.5. Single stage magnetic switch circuit

from the primary energy store C_1 to an intermediate energy store C_2 , from where it is then transferred rapidly to C_3 and the laser cavity by the magnetic switch (L_{MS}). Because of the slow initial transfer rate, peak currents carried by the thyratron can be reduced, allowing it to operate well below its rise time and peak current limits and thereby leading to extended thyratron life of up to 2 billion pulses.

The magnetic switch is realised by a saturable inductor employing ferrite or amorphous metal as core material. The non-saturated, high inductance of the inductor does not permit significant current flow and does therefore constitute the open position of the switch. Switch closure is affected by driving the inductor into saturation, which reduces the inductance to close the equivalent air core value. Total energy transfer between successive loops is achieved if the energy transfer time from C_1 to C_2 is matched to the time required for inductor L_{MS} to be driven into saturation (hold-off time). The pulse compression ratio δ between the loops is defined as

$$\delta = \frac{t_1}{t_2} = \sqrt{\frac{L_1}{L_{MS}^{sat}}} \quad (4.2)$$

where t_1 and t_2 are the transfer times of loops 1 and 2, respectively, and L_{MS}^{sat} is the saturated inductance of L_{MS} . Typically achieved compression ratios for a single stage range from 2 to 5 and several stages can be cascaded to achieve overall pulse compression ratios of several orders of magnitude [18]. Since saturable inductors are passive switching elements they can be designed for very high peak currents and hold-off voltages and have a virtually unlimited lifetime.

Various types of excitation circuits employing magnetic pulse compression have been used. Figure 4.6a shows a L-C inversion circuit employing a single stage of pulse compression [18]. The L-C inversion circuit has the advantage of voltage doubling and therefore halves the operating voltage for the switch.

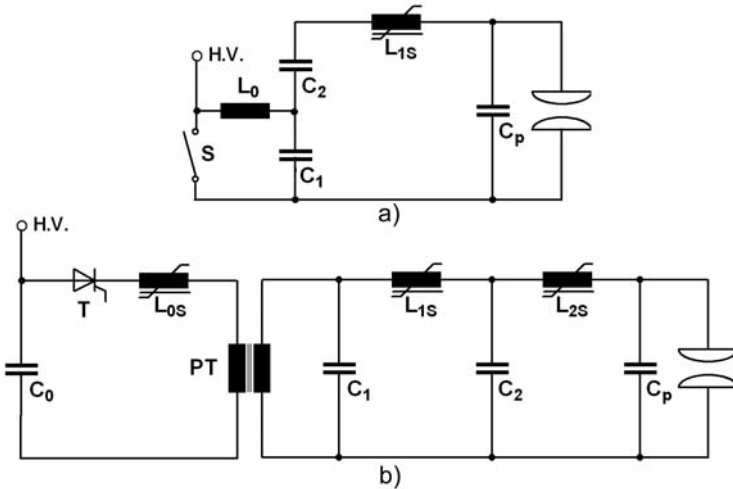


Fig. 4.6. Excitation circuits employing magnetic pulse compression: (a) L-C inversion circuit with single-stage pulse compression and (b) thyristor-switched circuit using double-stage pulse compression.

The associated disadvantage of increased switching currents at the lower voltage can be removed by the addition of one or more pulse compression stages.

Thyatron can be eliminated entirely by the use of multi-stage pulse compression techniques and all-solid-state switching by modern semiconductor switches such as thyristors, GTOs (gate turn-off) or IGBTs (insulated gate bipolar transistor) [14]. Solid-state switches have important advantages compared to thyatron, which include longer service lifetime, low cost and better availability. Solid-state switches are limited to comparatively low voltages and long switching times and they are in general sensitive to over-voltages and over-currents. Special excitation circuits including voltage step-up techniques such as pulse transformers as well as multi-stage magnetic pulse compression and protection against voltage and current surges have therefore to be employed. The thyristor-switched compressor shown schematically in Fig. 4.6b employs a pulse step-up transformer and two stages of magnetic pulse compression to bring the pulse voltage and switching times into the regime of commercially available thyristors. All-solid-state switching technology constitutes a major advancement towards highly reliable industrial excimer laser systems, since solid-state switches are maintenance free and have demonstrated a practically unlimited lifetime. Today all high-power industrial excimer lasers and high-repetition-rate lasers for microlithography applications are utilizing solid-state switching technology and achieve maintenance free operating times of several 1000 hours on routine base. Even low energy medical excimer laser systems benefit from solid-state switching be-

cause the solid-state switch does not require any warm-up time and makes laser radiation immediately available.

The all-solid-state switching technology allows recovering the energy, which is reflected by the discharge due to impedance mismatch. Either diodes or active circuits can achieve this. In both cases the reflected energy is flowing back to the main storage capacitor instead of ringing through the stages of the excitation circuit and returning to the laser electrodes after several 100 ns to some microseconds. This late pulse creates a poor discharge and results in excessive electrode wear. Therefore all solid-state switching technology allows to extend the electrode life, reduces the halogen consumption and the contamination generation.

The electrical switching technology as described above, although reliable and effective at high repetition rates, suffers from one principle problem. The fast high voltage pulse, required for the formation of a homogeneous discharge, is not consistent with the efficient impedance matching of pulser and discharge. For single pulse discharge circuits the pulser-to-plasma energy transfer efficiency is therefore limited to 40 to 60%, resulting in overall wall plug efficiencies for the laser of 1 to 3%. Higher efficiencies can only be achieved by double pulse excitation circuits (spiker-sustainer circuits) [15] as shown schematically in Fig. 4.7, where the functions of gas breakdown and discharge formation are separated from the process of energy feeding during the quasi steady state of the discharge. A fast, low-energy, high-voltage pre-pulse circuit is employed for discharge initiation and a separate low-impedance pulse forming line (PFL) as a sustainer. The impedance-matched PFL is charged at a slow rate to the matched voltage of twice the self sustained plasma voltage, and can achieve transfer efficiencies approaching 100%. Magnetic switches are generally employed for the main switch, to isolate the PFL during discharge initiation. In addition to generating higher efficiencies, this technique also allows for the extraction of long optical pulses. Efficiencies and pulse durations that have been produced with this technique are about 5% [19] and $1.5\text{ }\mu\text{s}$ [20] respectively for low-repetition-rate XeCl lasers. An additional benefit of this technique is the lowering of the demands for the high-voltage switch, since only the low-energy spiker circuit has to be switched at a fast rate, while the PFL can be charged at a slow rate, compatible with thyristor switching. An example of such a system is shown in Section 5.1. Although the double pulse excitation circuit has some inherent advantage it is not used in commercial excimer lasers because of the added complexity of the electrical circuit and the reduced pulse energy stability achieved at high repetition rate operation.

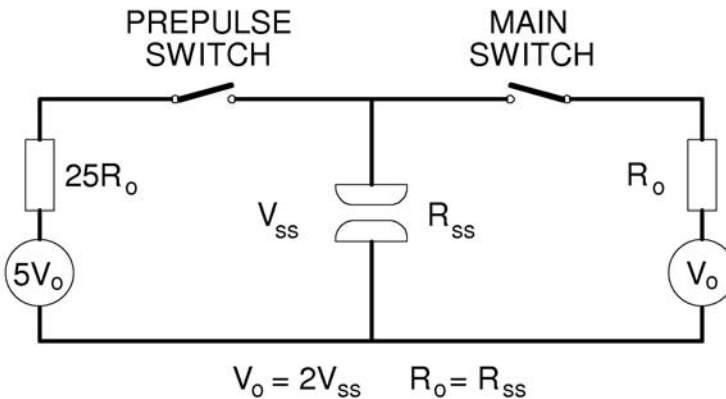


Fig. 4.7. Double pulse spiker-sustainer excitation circuit

A homogeneous glow discharge can also be initiated by photo switching, where the pre-pulse circuit is replaced by a strong UV [21] or X-ray [22] preionization pulse, which directly generates the electron density required for gas breakdown. The PFL can be connected directly to the discharge electrodes, eliminating the need for an isolating switch. A problem of this technique is that, in order to achieve a sufficiently fast gas breakdown, the PFL voltage has to be close to the self-breakdown voltage of the gap, reducing the transfer efficiency of the circuit and causing premature breakdown problems at higher repetition rates. The PFL therefore has to be pulse charged in times of less than $1\ \mu s$ for high repetition rate applications to avoid premature breakdown, re-introducing the need for fast high-voltage switching. Average output powers in excess of $1\ kW$ at a repetition rate of $450\ Hz$ have been reported from a UV photo switched XeCl laser with a discharge efficiency of 4% [23].

4.5 Power Supplies

For pulsed operation of gas discharge lasers the primary storage capacitor of the laser pulser has to be charged to the desired high voltage level prior to energy transfer to the discharge. At single-shot and low-repetition-rate operation resistive charging can be employed, however, due to its inherently low efficiency (about 50%) this technique is not suitable for high-average-power applications. Resonant charging schemes are widely used in high-repetition-rate high-power systems [24] because of the high efficiency of dc resonant charging ($> 90\%$). More control and better reproducibility can be obtained using command resonant charging schemes, however, at increased complexity. More recently, with the advancement of switched-mode power supply (SMPS) technology commercial excimer lasers mainly employ switched-mode power

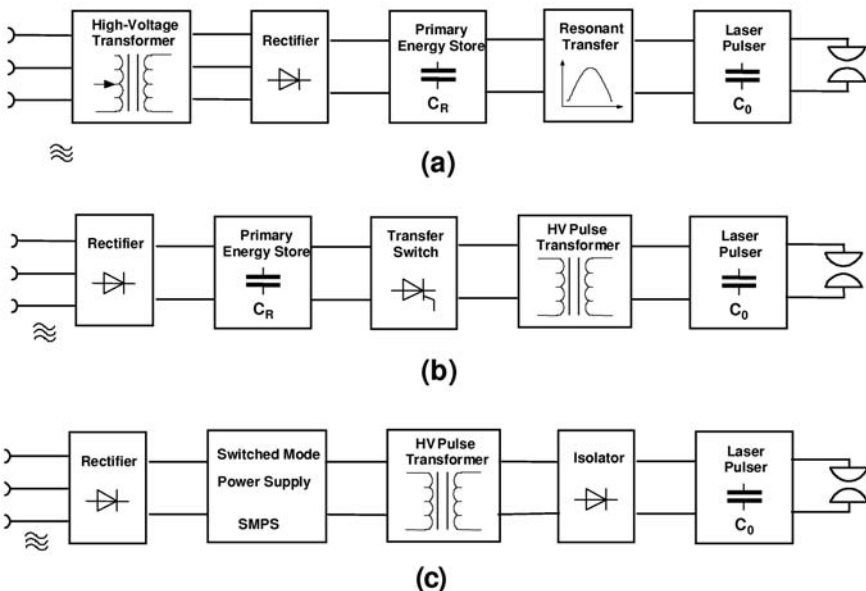


Fig. 4.8. Power supply topologies for capacitor charging in high-power excimer lasers: (a) DC resonant charging, (b) DC resonant command charging and (c) switched-mode power supply

supplies. Figure 4.8 shows the most important power supply topologies employed for high power excimer lasers.

The dc resonant charging power supply of Fig. 4.8a uses a high-voltage transformer and rectification to charge a large reservoir capacitor from which the energy is transferred resonantly to the laser pulser. A technical implementation of the principle, widely employed in early commercial excimer lasers (e.g. EMG series of Lambda Physik) is depicted in the simplified circuit diagram of Fig. 4.9. The reservoir capacitor C_R is charged through a variable transformer T_1 (Variac), high-voltage transformer T_2 and the input rectifier D_{in} to the desired high voltage level. The energy is then transferred resonantly to the primary storage capacitor C_0 of the laser pulser through the charging choke L_T and reverse blocking diode D_T . The voltage on C_0 reaches twice the charging voltage of C_R if $C_R \gg C_0$. This circuit has proven to be very robust and efficient, giving favorable pulser switch recovery conditions in low-repetition-rate applications. A principle drawback of the circuit is given by the fact that for the first charging cycle, there is no voltage doubling on C_0 . In addition, at high repetition rates and duty cycles the scheme suffers from switch recovery problems which can lead to massive short circuit currents carried by isolating diodes and switch with the associated danger of catastrophic failure. Technical refinements of the power supply include electronic regula-

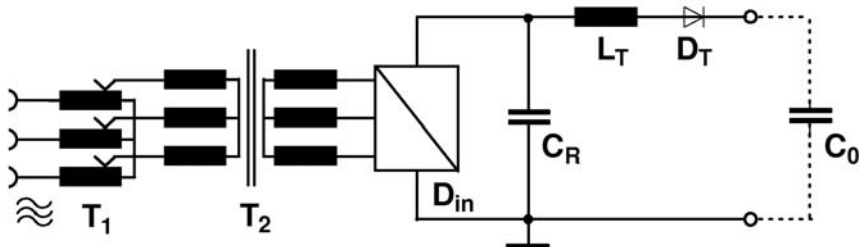
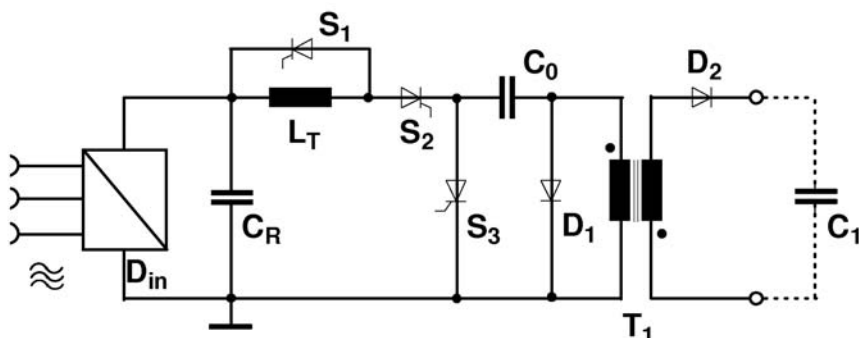


Fig. 4.9. DC resonant power supply

tion of the charging voltage, replacing mechanical Variac control, and the addition of an auxiliary power supply to circumvent the “first shot” problem.

Command resonant charging power supplies (Fig. 4.8b) utilize an additional switch, which isolates the power supply from the laser switch until it has fully recovered after the discharge. The reservoir capacitor C_R is charged directly from the rectified mains voltage and the laser pulser is charged through a high-voltage pulse transformer to the required voltage. The resonant regulating pulsed power supply (R^2P^2) of Fig. 4.10 employs switch S_2 to resonantly charge the intermediate storage capacitor C_0 to the desired voltage [25]. Diode D_1 serves to bypass the transformer primary during the charging of C_0 . Accurate voltage regulation on C_0 is achieved by the regulating thyristor S_1 , which serves to divert the transfer charging current, once triggered, thereby effectively stopping energy transfer to C_0 . Matched energy transfer between C_0 and the primary storage capacitor of the laser pulser C_1 through high voltage pulse transformer T_1 is initiated by switching thyristor S_3 . Average power levels of up to 50 kW have been demonstrated using multiple time-multiplexed R^2P^2 power supply modules [26].

Fig. 4.10. Resonant regulating pulsed power supply (R^2P^2)

In contrast to the resonant charging supplies discussed above, the switched-mode power supply (SMPS) does not transfer the required energy in a single transfer cycle but in a large number of successive small charge quantities (buckets), which are delivered at high frequency until the desired charging voltage has been reached. High-power switched-mode power supplies became commercially available in the early 1970's, however, were only used for high-voltage laser power supplies from the mid 1980's. Initially power supplies suffered from sensitivity to the high levels of EMI, generated by the laser, and comparatively low efficiency. The development was driven by new efficient semiconductor switches reaching the market, increasing switching frequency and efficiency. A block diagram of a modern regulated SMPS is shown in Fig. 4.11.

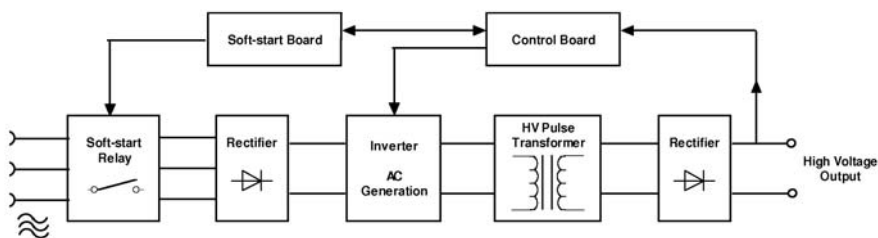


Fig. 4.11. Block diagram of high-power switched-mode power supply

The AC line voltage is rectified, smoothed, and supplied to the electronic inverter (chopper), which operates at high frequency (50 to 150 kHz). A HV transformer then steps up the chopped DC voltage and the secondary voltage rectified and smoothed to provide the required HV output. The output voltage is sensed by a control circuit that adjusts the duty cycle of the switching transistor to provide voltage regulation. The soft start feature gradually increases the transistor duty cycle after switch-on, preventing excessive inrush currents.

The typical charging voltage wave shape at the laser storage capacitor is shown in Fig. 4.12. After the laser has fired, the power supply has to be inhibited for a period t_d to allow for pulser switch recovery. The power supply is then enabled, charging the capacitor in a time t_c which is determined by the peak charging rate of the power supply and the size of the storage capacitor. Once the charging voltage level is reached a short settling time t_s is required for the voltage to reach its pre-programmed level. The combined time then limits the maximum repetition rate f_{max} of the laser to

$$f_{max} = \frac{1}{t_d + t_c + t_s} \quad (4.3)$$

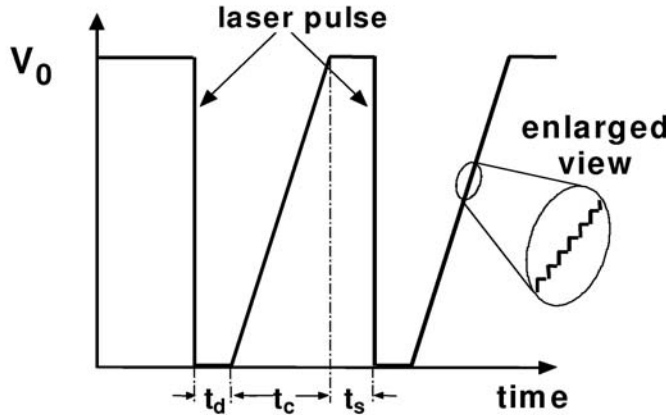


Fig. 4.12. Switched-mode power supply charging of laser storage capacitor

A principle problem of switched-mode power supplies is that the load capacitor is charged by a succession of small voltage steps caused by the finite size of individual charge buckets (see enlarged view in Fig. 4.12). The resulting size of the individual voltage steps determines the accuracy of voltage regulation achievable from the power supply. The step size ΔV can be calculated from [27]:

$$\Delta V = I_{out} / (C_L \times f_{PS}) \quad (4.4)$$

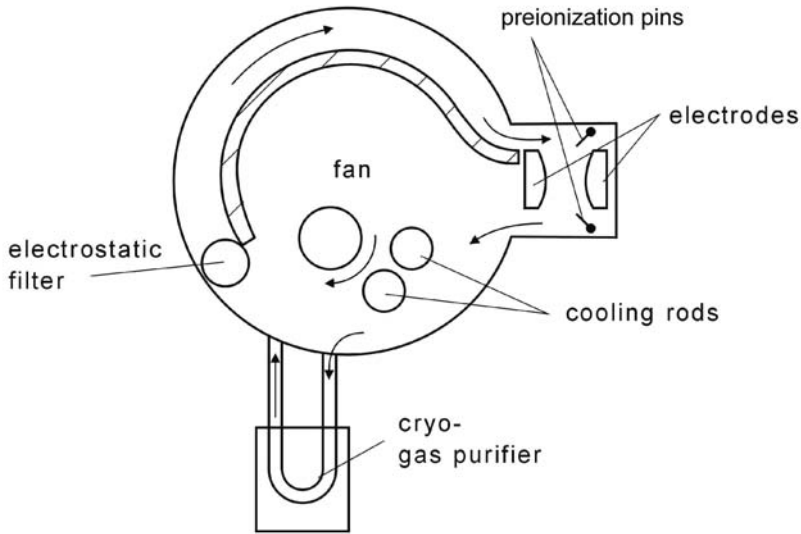
where I_{out} is the rated charging current of the power supply, C_L the load capacitor and f_{PS} the switching frequency of the power supply. In order to increase voltage regulation accuracy for a given load it is clearly desirable to run the SMPS at high switching frequencies. Modern SMPS operate with switching frequencies of about 40 kHz resulting in a typical voltage accuracy of 1%. For certain applications of excimer lasers, such as photolithography, this voltage accuracy and repeatability is not sufficient. Voltage repeatability as low as 0.05% can be achieved using advanced frequency and phase shifting techniques [28]. Capacitor charging power supplies are today commercially available that provide peak charging rates of up to 37 kJ/s and average DC powers of up to 50 kW with overall efficiencies of better than 85%.

4.6 Circulation, Laser Gas Cooling, and Cleaning

In excimer lasers, operating at typically 2% conversion efficiency between electrical input power and optical output power, the surplus energy has to be removed efficiently as excess heat. Usually the active medium is contained in an aluminum or stainless steel pressure vessel of sufficient volume. An internal fan causes a forced circulation of the laser gas in order to keep the

active medium well mixed and renewed in the lasing region and to obtain a high flow rate through the gas filter and the heat exchanger. Gas circulation is achieved by cross flow fans that provide a homogeneous gas flow rate over the entire electrode length. Typical gas circulation speed is about 25 m/s for high energy and about 50 m/s for high-repetition-rate industrial excimer lasers.

As with all gas laser cooling systems, the efficient heat transfer between the laser gas and the heat exchanger is a challenge. The heat exchanger, which in most designs uses water as cooling medium in a closed or open loop system, needs a sufficient contact area to allow good temperature stability, especially at high pulse repetition rates. On the other hand the gas flow pressure drop across the heat exchanger must be small in order to be compatible with the cross flow fan characteristic. Nickel-plated copper heat exchanger tubes with small to medium-sized fins are today standard in excimer lasers. A schematic sketch of an excimer laser tube cross section is shown in Fig. 4.13.



3 10454-31 MR

Fig. 4.13. Cross-section of an excimer laser gas flow system

The laser tube windows are very sensitive to all kinds of contamination. The outside of a tube window is frequently purged by dry pure nitrogen to remove all gaseous contaminations and impurities present in the environmental air. Sophisticated purge systems are today standard on all high-power and high-repetition-rate excimer lasers, even at 308 nm . Active and passive contamination control is necessary to keep the inside of the tube windows clean. A window service time of up to 10 billion pulses can be achieved with

an optimized contamination control system and is a precondition for long uninterrupted operating times of excimer lasers.

Passive contamination control starts with the selection of a low-erosion-rate electrode material and suitable materials for the pressure vessel and its internal components. All parts of the pressure vessel must be carefully cleaned because even traces of grease, oil and other lubricant in the *ppm* range strongly affect the laser performance. Wet chemical cleaning followed by plasma cleaning and clean room assembly are today the standard procedure. A highly sophisticated passivation procedure is applied to build up a halide layer on all internal parts of the laser tube and avoid any contamination build-up by reaction of the halogen component of the gas mixture with the pressure vessel.

Active contamination control is achieved by electrostatic dust filtration and in some cases by cryogenic gas purification. The electrode burn-off – unavoidable even with the best electrode material – causes solid and gaseous impurities. Electrostatic dust precipitators can remove most of the solid reaction products. A fraction of the main gas flow is directed through the dust precipitator device. The pressure difference between intake and exit port of the precipitator drives the gas through the device without any additional active fan or gas pump. Corona wires are used to charge dust particles of the incoming dust-loaded laser gas. The gas flow speed within the precipitator is normally reduced to below 1 m/s to allow settling of the charged dust particles on the grounded precipitator walls. The cleaned dust-free gas is returned to the laser tube near the windows via so-called baffle boxes, which prevent shock waves from transporting dust up to the windows. A window lifetime of 10 billion pulses and more is today standard in high repetition rate industrial excimer lasers with a well-designed dust precipitation system.

The unavoidable halogen gas loss due to the electrode erosion is compensated by halogen injections. Sophisticated self-learning replenishment algorithms add very small portions of halogen gas to the laser gas mixture without affecting energy stability of the laser during the injection phase. The replenishment rate depends on laser operating time, laser input energy and laser performance parameters like high voltage level or temporal pulse width. The algorithms allow keeping the high voltage level and therefore all essential beam parameters stable over up to one billion pulses with a single gas fill.

4.7 Safety Standards for Industrial Excimer Lasers

Today industrial laser systems have to fulfill the requirements of numerous standards and regulations like other machinery. Among these regulations is the European CE (Conformité Européenne) mark, which appears on products that meet safety standards that apply to all countries of the European Union (EU). The CE mark was introduced to facilitate the free movement of goods within the European Union.

The compliance with laser radiation safety standards is also mandatory for industrial excimer laser equipment. Additionally, users in the semiconductor industry frequently ask for compliance of laser equipment with the applicable standards of SEMI organization.

4.7.1 CE Mark

Industrial excimer laser systems have to carry the European CE mark and must comply with four applicable European directives:

- Electromagnetic Compatibility (EMC) Directive 89/366/ECC
- Low Voltage Directive 73/23/ECC
- Pressure Equipment Directive 97/23/EC
- Machinery Directive 89/392/EEC (Amended 98/37/EEC)

4.7.2 Electromagnetic Compatibility (EMC) Directive 89/366/ECC

The EMC directive came into force on 1st January 1992, and replaced all existing legislation for electrical and electronic equipment concerned from 1st January 1996. EMC stands for Electromagnetic Compatibility and describes the way an electric or electronic apparatus behaves (regarding EM aspects) in the presence of other equipment. This discipline investigates the unwanted emissions and unwanted susceptibility of electronics against electromagnetic fields and a number of associated phenomena, known to interfere with electronics in a similar way. The technical goal of this directive is two-way:

- Protect the radio spectrum against interfering equipment
- Protect equipment from common interference

In essence the requirements of the directive are very simple – it basically states that a laser system must not emit unwanted electromagnetic pollution (interference). Because there is a certain amount of electromagnetic pollution in the environment, the directive also states that a laser system must be immune to a reasonable amount of interference. The directive itself gives no figures or guidelines on what the required levels of emissions or immunity are, nor does it state the frequency band limits. This interpretation of the directive's requirements is left to the standards that are used to demonstrate compliance with the directive.

All EMC standards are today summarized in the European standard series EN61000. This series include four generic standards for EMC. Two generic standards are specifying the levels for residential, commercial and light-industrial environments; the other two generic standards set the levels for industrial environments. An environment is regarded as industrial if a separate mains substation supplies it.

Table 4.1.

Standard	Year	Title
EN61000-6-1	2001	Electromagnetic compatibility (EMC) — Part 6-1: Generic standards — Immunity for residential, commercial and light-industrial environments
EN61000-6-2	2001	Electromagnetic compatibility (EMC) — Part 6-2: Generic standards — Immunity for industrial environments
EN61000-6-3	2001	Electromagnetic compatibility (EMC) — Part 6-3: Generic standards — Emission standard for residential, commercial and light-industrial environments
EN61000-6-4	2001	Electromagnetic compatibility (EMC) — Part 6-4: Generic standards — Emission standard for industrial environments

For the purposes of being able to test whether or not a laser system complies with the directive, tests are divided into five classes:

Radiated emissions Checks to ensure that the product does not emit unwanted radio signals

Conducted emissions Checks to ensure the product does not send out unwanted signals along its supply connections and connections to any other apparatus

Radiated susceptibility Checks that the product can withstand a typical level of electromagnetic pollution

Conducted susceptibility Checks that the product can withstand a typical level of noise on the power and other connections

Electrostatic discharge Checks that the product is immune to a reasonable amount of static electricity

The test conditions and test limits for the susceptibility and the electrostatic discharge are defined by European standards of the EN61000 series. The applicable standards for industrial excimer lasers are:

4.7.3 Design Rules for Electromagnetic Compatibility

The fast high-voltage high-peak-current gas discharge of an excimer laser is a powerful broadband source for radiated and conducted electromagnetic emission. The emission level of the gas discharge itself exceeds the applicable maximum threshold value by far. Therefore, the laser design has to focus on the source design, consequent radiation shielding and filtering of the conducted noise.

The electromagnetic noise level generated by the fast electrical discharge can be reduced effectively by a good design of the fast high-voltage circuit itself. The electrical connections must have a low resistivity and inductivity. Therefore all connectors should have a long-term stable and corrosion-free surface finish. The discharge has to be completely encapsulated by a

Table 4.2.

Standard	Year	Title
EN61000-4-2	2001	Electromagnetic compatibility (EMC) – Part 4-2: Testing and measurement techniques – Electrostatic discharge immunity test
EN61000-4-3	2004	Electromagnetic compatibility (EMC) – Part 4-3: Testing and measurement techniques – Radiated, radio-frequency, electromagnetic field immunity test
EN61000-4-4	2004	Electromagnetic compatibility (EMC) – Part 4-4: Testing and measurement techniques – Electrical fast transient / burst immunity test
EN61000-4-5	2004	Electromagnetic compatibility (EMC) – Part 4-5: Testing and measurement techniques – Surge immunity test
EN61000-4-6	2001	Electromagnetic compatibility (EMC) – Part 4-6: Testing and measurement techniques – Immunity to conducted disturbances, induced by radio-frequency fields
EN61000-4-11	2001	Electromagnetic compatibility (EMC) – Part 4-11: Testing and measurement techniques – Voltage dips, short interruptions and voltage variations immunity tests

grounded return current path. The introduction of high-voltage excitation circuits driven by all-solid-state switches further reduced the electromagnetic noise level of the fast excitation circuit significantly in comparison to a thyratron-driven circuit.

A field-proven housing design concept for an excimer laser meeting the EMC standards starts with effective radiation shielding by a Faraday laser housing made of magnetic steel. The fast gas discharge and the high voltage power supply have to be located within one shielded compartment. Electrical gaskets must seal all panels or doors of the housing. Cooling air entries and exists must be protected by honeycomb EMC filters. The number of electrical lines into and out of the Faraday cage should be reduced to the minimum number because an appropriate line filter, which should be located in the wall of the Faraday cage, must filter each electrical connection to and from the Faraday cage against conducted noise. Fiber optical data lines can replace electrical wire connections; this technique is of special interest for fast data signals because it is difficult to filter those lines to avoid transfer of electromagnetic noise from the shielded cabinet into the environment. These design rules result in a clear layout, avoid cumbersome electromagnetic emission leaks and minimize the filtering costs.

A well-shielded excimer laser will pass many of the required immunity tests without special effort. Only the surge immunity and the voltage dip tests bring in additional demands to the design. The surge tests normally require the installation of a varistor-based mains-in module that can absorb the high-energy pulses and protect the electronic units. The voltage dip tests add special demands to the control electronics that must keep the laser system

in a controlled status during and after a voltage dip. A battery-buffered main controller is a proven approach, which enables compliance with the voltage dip standard.

Consequent EMC design of an industrial excimer laser will result in an emission level well below the low limit values for residential, commercial and light-industrial environments. On the other hand the same laser will fulfill the demanding immunity standards for harsh industrial environments. An independent EMC test laboratory normally proves compliance with the EMC standards.

4.7.4 Low Voltage Directive 73/23/ECC

The Low Voltage Directive (LVD) 73/23/EEC is one of the oldest European directives. It was originally published in 1973 and has only one modification, 93/68/EEC, published 22nd July 1993. The scope of this directive is electrical equipment designed for use within the input voltage rating 50 to 1000 VAC or 75 to 1500 VDC. This directive defines the essential electrical safety and protection requirements. This means the equipment must be safe and constructed in accordance with the principles generally accepted as constituting good engineering practice in relation to safety matters.

There are numerous standards within the framework of the Low Voltage Directive. The application field of an electrical device ‘laser’ defines which standards out of the large group are applicable and have to be followed. There are 2 important electrical safety standards for industrial lasers:

Table 4.3.

Standard	Year	Title
EN 60204-1 IEC 60204-1	1997	Safety of machinery — Electrical equipment of machines — Part 1: General requirements
EN 61010-1 IEC 61010-1	2001	Safety requirements for electrical equipment for measurement, control, and laboratory use — Part 1: General requirements

The standards give specifications for the man-machine interface, circuit breaker selection, wiring design rules and safety circuitry layout. Conformity with the Low Voltage Directive and the related applicable standards can be either checked by the manufacturer itself or by an independent test house, which provides a detailed evaluation report, frequently requested by the laser users.

4.7.5 Pressure Equipment Directive 97/23/EC

The European Pressure Equipment Directive (PED) 97/23/EC came into force on 29th November 1999. All items of pressure equipment placed on the

market in the European Economic Area after May 2002 must comply with the directive and have evidence of compliance by carrying the CE marking as applicable. The directive provides an adequate legislative framework on European level for equipment subjected to a pressure hazard.

The directive concerns manufacturers of items such as vessels, pressurized storage containers, heat exchangers, steam generators, boilers, industrial piping, safety devices and pressure accessories. Under the community regime of the directive, pressure equipment and assemblies above specified pressure and/or volume thresholds must:

- be safe;
- meet essential safety requirements covering design, manufacture and testing;
- satisfy appropriate conformity assessment procedures; and
- carry the CE marking and other information.

Excimer lasers are high-pressure gas lasers and must be compliant with this directive. The entire gas system must be designed in accordance with this directive and the related standards. Compliance can be achieved without the effort of regular pressure vessel safety inspections at customer site as long as the maximum operating temperature of the pressure system does not exceed 50°C and the stored energy of the compressed gas does not exceed 20 kJ. A gas tank of 40 l filled with 5 bar or 71 psi overpressure is just reaching this limit.

The gas system of an excimer laser consists of the laser tube, a valve manifold, a halogen scrubber unit, a vacuum pump and connecting tubing. The corrosive properties of the excimer laser gas mixture set strong limitation to the usable materials and alloys for the gas system. Flanges, valve manifold and gas lines are normally made from stainless steel. The laser tube as pressure vessel is typically made from a low-silicon aluminum alloy, which may be nickel-plated for improved resistance to halogen gas attack. The laser tube is a complex pressure vessel because some structural parts of the vessel are made from alumina and the tube has two windows typically made from a crystalline material like calcium fluoride. Calculation of the overpressure strength of such a vessel is extremely complicated. Therefore compliance with the standards is normally proven by an overpressure type test at 2.25 times of the maximum nominal operating pressure.

4.7.6 Machinery Directive 89/392/EEC (Amended 98/37/EEC)

On 14th June 1989 the Council of the European Communities adopted a Directive (89/392/EEC) requiring the approximation of the laws of the member states relating to machinery. The Machinery Directive came into force on 1st January 1993. The Second Amending Directive (93/44/EEC) was incorporated into the regulations and a third Amending Directive (98/37/EC) is still pending.

This directive defines essential general protection requirements. This means the equipment must be safe and constructed in accordance with the principles generally accepted as constituting good engineering practice in relation to safety matters. Other directives such as the Low Voltage Directive overlap with the Machinery Directive regarding all electrical safety aspects. The European Committee for Standardization (CEN) is working to produce a complex of European standards at three levels in support of the Machinery Directive. The first (A) level comprises general principles for the design of all types of machinery (e.g. EN 292 Mechanical Design, or EN 1050 for risk assessment). The second (B) level covers specific safety devices and ergonomic aspects of ranges of machinery types (e.g. EN 418 Emergency Stop Equipment). Finally, the third (C) level covers specific classes of machinery by calling up the appropriate standards from the first two levels and addressing requirements specific to class. To date, most of the Level A and B standards have been published. A specific Level C standard for excimer lasers does not exist and is not under preparation. Meanwhile, conformity with the essential requirements of the regulations can be demonstrated by using Level A and B standards. Here is a list of the harmonized key standards under the Machinery Directive:

EN 292-1, -2: Safety of machinery – Basic concepts, general principles for design

EN 1050: Safety of machinery – Principles for risk assessment

EN 60204-1: Safety of machinery – Electrical equipment of machines

EN 954-1: Safety of machinery – Safety-related parts of control systems

EN 1088: Safety of machinery – Interlocking devices

Excimer lasers as stand-alone units do not come under the Machinery Directive but industrial excimer lasers must be compliant with the Machinery Directive because they will be integrated into a system that must comply with this directive. Compliance with the machinery directive requires a risk analysis, and in most cases an independent test house evaluates the laser.

4.7.7 Laser Radiation Safety

Of course every laser product must fulfill the laser radiation safety requirements. An excimer laser is by its wavelength and power always a class-IV laser which is the highest risk class. The laser must meet the requirements of the standard EN / IEC 60825-1:1994; Safety of laser products – Part 1: Equipment classification, requirements and user's guide.

Compliance with laser radiation safety does not only specify design rules for a laser manufacturer. The EN / IEC 60825-1 standard also specifies responsibility guidelines for users and operators of a laser system in order to achieve safe working conditions and laser radiation protection.

4.7.8 SEMI Standards

Industrial excimer lasers are frequently used in production processes of the microelectronic and lithography industry. This industry created the Semiconductor Equipment and Materials Institute known as SEMI. It developed its own standards applicable to semiconductor industry equipment. The SEMI standards partially overlay with the CE safety standards and North American safety standards like NFPA 79 Electrical Standard for Industrial Machinery.

The SEMI S2 standard (**SEMI S2-0703a Environmental, Health, and Safety Guideline for Semiconductor Manufacturing Equipment**) is the most important SEMI standard for industrial excimer laser systems. This standard has a very broad scope and covers environmental aspects, general safety, and health guidelines. An industrial excimer laser has to be evaluated for SEMI S2 compliance regarding the following issues:

- Documents provided to user:
The requirements are specified by the standard **SEMI S13-0298 Safety Guidelines for Operation and Maintenance Manuals used with Semiconductor Manufacturing Equipment**.
- Hazard warning labels:
The standard **SEMI S1-0701 Safety Guideline for Equipment Safety Labels** defines three safety label levels, which are distinguishable by the key words Danger, Warning, or Caution. The labels have a common layout and the usage of pictographs is strongly recommended.
- Safety interlock systems:
This chapter specifies the requirements for the laser beam shutter and other interlocks. In general the interlocks must be of fail-safe type and clear operator information is required in case of any activation.
- Emergency shutdown:
This chapter defines design rules for emergency off circuitries.
- Electrical design:
The electrical design of the entire laser has to be in accordance with electrical safety standards like EN 60204-1 or NFPA79.
- Fire protection:
The latest revision of the SEMI S2 standard included new requirements regarding fire protection. A fire risk assessment of a laser system according to the standard **SEMI S14-0200E Safety Guidelines for Fire Risk Assessment and Mitigation for Semiconductor Manufacturing Equipment** must be carried out. This can only be done by an especially certified test house.
- Ergonomics and human factors:
Detailed specifications are given in the standard **SEMI S8-1103 Safety Guidelines for Ergonomics Engineering of Semiconductor Manufacturing Equipment**. The focus of this standard is ergonomics and human factors for operators, for example accessibility of control elements

for operators, and maintenance and service personnel, for example design of laser housing panels and component access.

- Hazardous energy isolation:

This chapter gives design rules for laser operation, maintenance and service. In each case access to dangerous mechanical or electrical energy must be prohibited by the housing design.

- Mechanical design:

The mechanical design of the laser housing must prevent access to dangerous parts like rotating shafts or hot surfaces. All structural elements must be designed with sufficient strength for the intended usage. Corrosion resistance and pressure safety must be considered for all pressurized systems.

- Seismic protection:

The laser system must have provisions for anchorage the housing to the building. The strength of the anchorage must be proven by a stability calculation.

- Environmental considerations:

This chapter gives guidelines for resource conservation, chemical selection and prevention and control of unintended chemical release.

- Exhaust ventilation:

Excimer lasers are supplied with toxic gases and have a toxic gas inventory. Therefore, the laser housing has to be properly ventilated for safety reasons. A small under-pressure within all laser compartments containing parts of the laser gas system achieves this. The design of the laser housing and proper ventilation of all critical parts is tested according to the standard **SEMI F15-93 Test Method for Enclosures Using Sulfur Hexafluoride Tracer Gas and Gas Chromatography**.

- Chemicals:

The manufacturer has to list the chemical inventory and to provide a risk analysis. Engineering controls and administrative controls have to be taken to minimize any risk.

- Non-ionizing radiation and fields:

This chapter covers electromagnetic compatibility as discussed for the CE mark.

- Lasers:

This chapter covers laser safety.

- Sound pressure level:

This chapter specifies the acceptable sound pressure level for operation, maintenance and service.

Compliance with the SEMI S2 and related standards is mandatory for equipment acceptance by major companies of the semiconductor industry. Compliance is normally proven by a third-party evaluation report.

References

1. S. Altmeyer: RWTH Aachen (1993)
2. R.S. Taylor: Appl. Phys. B **41**, 1–24 (1986)
3. G. Gallant, E.S. Williams, R.W. Weeks: (1992), “Excimer laser”, US patent 5,081,638
4. V. Hasson, H.M. von Bergmann: J. Phys E: Scientific Instruments **9**, 73–76 (1976)
5. V.M. Borisov, O.B. Khristoforov, Yu.B. Kiryukhin, et al.: Proc. SPIE **3574**, 56–66 (1998)
6. W. Rogowski: Arch. Elektrotech. **12**, 1 (1923)
7. E.A. Stappaerts: Appl. Phys. Lett. **40**, 1018 (1982)
8. F. Ciocci, T.W.P.M. Hermsen: ENEA Report RT/TIB/89/32 (1989)
9. R.G. Morton: (2004), “Discharge laser with porous insulating layer covering anode discharge surface”, US-Patent 6,711,202
10. R.G. Morton, T.S. Dyer, T.D. Steiger, R.C. Ujazdowski, T.A. Watson, B. Moosman, A.P. Ivaschenko: (2004), “High rep-rate laser with improved electrodes”, US-Patent 6,690,706
11. R.G. Morton, T.S. Dyer, T.D. Steiger, R.C. Ujazdowski, T.A. Watson, B. Moosman, A.P. Ivaschenko, W. Gillespie, C. Rettig: (2004), “High rep-rate laser with improved electrodes”, US-Patent Application 20040022292
12. J. Bäumler, M. Zeh: (1989), “Electrode for pulsed gas laser”, US-Patent 4,860,300
13. T.S. Dyer, R.G. Morton, W.D. Gillespie, T.D. Steiger: (2004), “Anodes for fluorine gas discharge lasers”, US-Patent Application 20040071178
14. H.M. von Bergmann, P.H. Swart: IEE Proc. B **139**, 123 (1992)
15. W.H. Long, M.J. Plummer, E.A. Stappaerts: Appl. Phys. Lett. **43**, 735 (1983)
16. W.S. Melville: Proc of the IEE 98 **185** (1951)
17. P.H. Swart, H.M. von Bergmann: “Comparative evaluation of pulsing circuits for kHz excimer laser systems”, in *Proc. 7th IEEE Pulsed Power Conf.*, Monterey, California (1989), pp. 293–296
18. D. Basting, K. Hohla, E. Albers, H.M. von Bergmann: Laser und Optoelektronik **16**, 128 (1984)
19. J.W. Gerritsen, A.L. Keet, G.J. Ernst, W.J. Wittemann: J. Appl. Phys. **67**, 3517 (1990)
20. R.S. Taylor, K.E. Leopold: J. Appl. Phys. **65**, 22 (1989)
21. B. Lacour, C. Vannier: J. Appl. Phys. **62**, 754 (1987)
22. S. Bollanti, P. DiLazzaro, F. Flora, G. Giordano, T. Hermsen, T. Letardi, C.E. Zheng: Appl. Phys. B **50**, 415 (1990)
23. B. Lacour, H. Besaucèle, H. Brunet, C. Gagnol, B. Vincent: Proc. SPIE **3092**, 362–365 (1996)
24. G.N. Glasoe, J.V. Lebacqz: *Pulse Generators* (Dover, New York, 1965)
25. P. Swart, G. Bredenkamp, H.M. von Bergmann: “A resonant pulsed power supply with pulse-energy regulation”, in *Proc. 6th IEEE Pulsed Power Conf.* Arlington, Virginia (1987), pp. 723–726
26. P.H. Swart, H.M. von Bergmann: Proc. SPIE **1397**(2), 559–562 (1990)
27. Lambda EMI Corp.: (2002), “Regulations and Repeatability, Application Note 402”
28. G.L. Bees, A. Tydeman: “Capacitor charging power supply design for high pulse-to-pulse repeatability applications”, in *IEEE Pulsed Power Conference* (1999)

5 Specially Designed Excimer Lasers

5.1 High-Repetition-Rate and High-Power Lasers

H. von Bergmann

Over the years outputs of excimer lasers have increased steadily, and today lasers of a few hundred *watts* average power are commercially available and outputs of more than 1 *kW* have already been demonstrated in the laboratory.

Basically there are two design options for the power scaling of excimer lasers into the *kW* regime: they can either be operated at relatively low repetition rates with associated increased pulse energies of more than 1 *J*, or they can be run at increased repetition rates of several *kHz* where the pulse energies then can be kept low. While the electrical power conditioning system generally favours small pulse energies at high repetition rates, the gas circulation unit becomes increasingly bulky and costly at high repetition rates. These two conflicting requirements have to be carefully weighed and traded off against each other in order to arrive at an optimized system.

The key technological problems associated with high-repetition-rate high-average-power operation of excimer lasers are related to the discharge stabilization, the gas circulation system and the pulsed power conditioning system.

Repetitive operation of excimer lasers requires gas exchange in the discharge volume between successive excitations of the laser. This is necessary to remove waste heat and discharge products, which otherwise would lead to a degradation of the discharge quality and arcing for subsequent excitation pulses. A flow-clearing ratio C can be defined by (see Fig. 5.1)

$$C = \frac{s}{w} = \frac{v}{w \times f} \quad (5.1)$$

where w is the discharge width, v the gas flow velocity and f the repetition rate of the laser. The clearing is complicated by auxiliary discharges used for preionization, which can extend beyond the main discharge region, effectively increasing the discharge width, and by insufficient flow clearing of boundary layers in the vicinity of the electrodes, which can cause arcing to down-stream structures. Clearing ratios of 2 to 3 are needed in high-power excimer lasers [1], necessitating gas flow velocities of 50–100 *m/s* at repetition rates of 1 to 2 *kHz*.

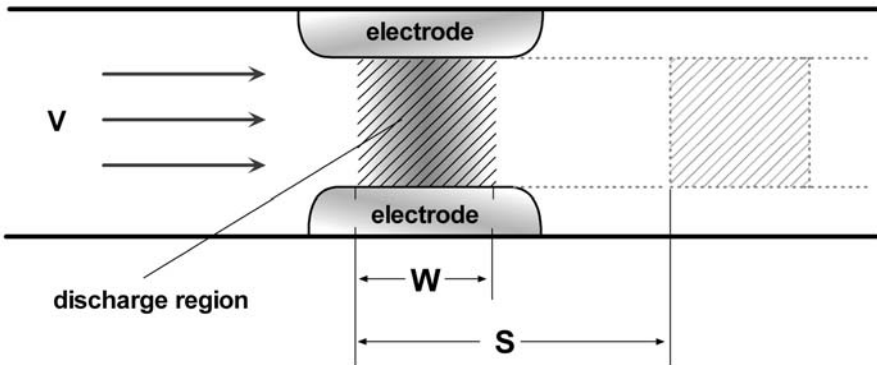


Fig. 5.1. Flow clearing of discharge region

High-repetition-rate operation is further complicated by the disturbance of the discharge medium by acoustic waves and shock waves, caused by the rapid energy deposition into the discharge volume [2]. Acoustic and shock waves lead to gas density perturbations, which are detrimental to the discharge quality and adversely affect the far-field beam quality of the laser output. The density non-uniformity has to be maintained below a level of 1% to avoid discharge instabilities and below 0.1 to 0.01% to ensure adequate beam quality.

Three main pressure waves, differentiated by their direction of propagation, are generated in closed cycle pulsed lasers [3]: Shock waves traveling in the direction of the optical axis, waves traveling up- and down-stream in the direction of the flow, and waves reflected between the electrode surfaces. Shock waves traveling in the direction of the optical axis can affect the discharge stability at high repetition rates. Pressure waves travelling in the direction of the gas flow or between the electrodes can be reflected back into the discharge region where they cause a deterioration of the discharge quality. Main sources of reflections are obstacles in the flow loop, such as current feed-throughs, flow loop corners, preionization devices and cross section discontinuities. These waves can be dissipated and damped to acceptable levels by flow grids, sidewall dampers, mufflers and a suitable electrode contour. The temporal development of the shockwaves in the electrode region can be visualized using “Schlieren” imaging techniques. This is demonstrated by the set of Schlieren images in Fig. 5.2, which were recorded in a 1 kHz ArF laser at various time delays after discharge initiation [4]. The development and propagation of up-stream and down-stream waves and waves initiated at the electrode surfaces are clearly visible.

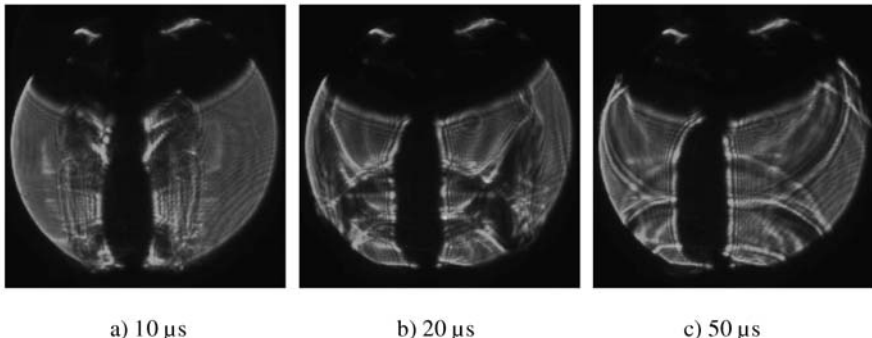


Fig. 5.2. Schlieren images of discharge region recorded at various time delays after discharge initiation (gas flow direction from right to left)

In addition to these waves, duct oscillations, building up resonantly with the laser frequency, cause standing and slowly moving pressure distributions in the discharge region, which – through feedback with the energy deposition distribution in the discharge region – lead to discharge instabilities and ultimately limit the maximum repetition rate of the laser [5]. The effect of duct oscillation can be reduced by pressure dampening structures placed in close vicinity to the discharge region.

Two types of flow loop configurations are employed to furnish the required flow velocities of up to 100 m/s (see Fig. 5.3). External flow loop systems, similar in design to conventional wind tunnels, can be assembled from conventional components, utilizing centrifugal and axial fans. However, they tend to be bulky and incorporate large gas volumes. Because of their design flexibility and accessibility to measurements they are mainly employed in the laboratory. The internal flow loop configuration integrates specially designed flow loop components in a single compact pressure vessel. Because of the high aspect ratio of the cavity geometry, internal flow loop systems are most easily adapted to cross flow fans. Most industrial laser systems employ this type of flow system. The discharge system is designed to closely resemble a flow nozzle in order to optimize the flow pattern in the discharge region and avoid flow separation on the electrode surfaces and downstream of the electrodes.

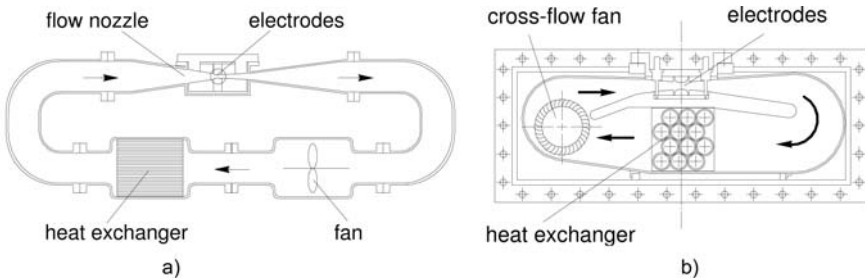


Fig. 5.3. Cross-section of gas flow system: (a) external flow-loop and (b) internal flow-loop

The flow loop design is complicated by mechanical distortions of the system at the high operating pressures of up to 5 bar. Distortions can effect the alignment of discharge electrodes and can therefore not be tolerated. These requirements can lead to bulky and expensive flow systems.

Pulsing circuits used for the excitation of high-power high-repetition-rate excimer lasers with average powers in the *kilowatt* range have to be capable of delivering excitation energy at a level of 30 to 50 kW. This requires high-voltage switching devices not only capable to provide pulses of high peak current but also average currents of several *ampere* and *rms* currents in excess of 100 A. These are very demanding parameters and can only be provided by expensive large-diameter metal-envelope thyratrons utilizing dispenser-cathode technology or by complex circuits connecting multiple thyratrons in parallel. The industrial-proven alternative to this expensive and complex technology are all-solid-state switched pulsers employing solid-state switches in combination with multiple-stage pulse compressors. These circuits have to be carefully designed using specially selected magnetic materials and circulating oil cooling for thermal management (for more details see section 4.4).

Commercial excimer lasers are available today with repetition rates of more than 4 kHz and average powers of tens of *watts* at wavelengths ranging from 157 nm to 248 nm [6]. High-average-power lasers for industrial applications exist with average powers of 270 W at 248 nm (KrF) and 315 W at 308 nm (XeCl) operating at repetition rate 300 Hz [7]. In the laboratory a number of excimer lasers have been demonstrated with outputs in the *kW* range. Average powers of up to 500 W have been achieved for KrF lasers at a repetition rate of more than 1.5 kHz [8] and up to 2 kW and repetition rates of 1000 Hz for XeCl lasers [9, 10, 11]. Cross-sectional views of a 500 W KrF and a 1 kW XeCl laser are shown in Figs. 5.4a and 5.4b, respectively.

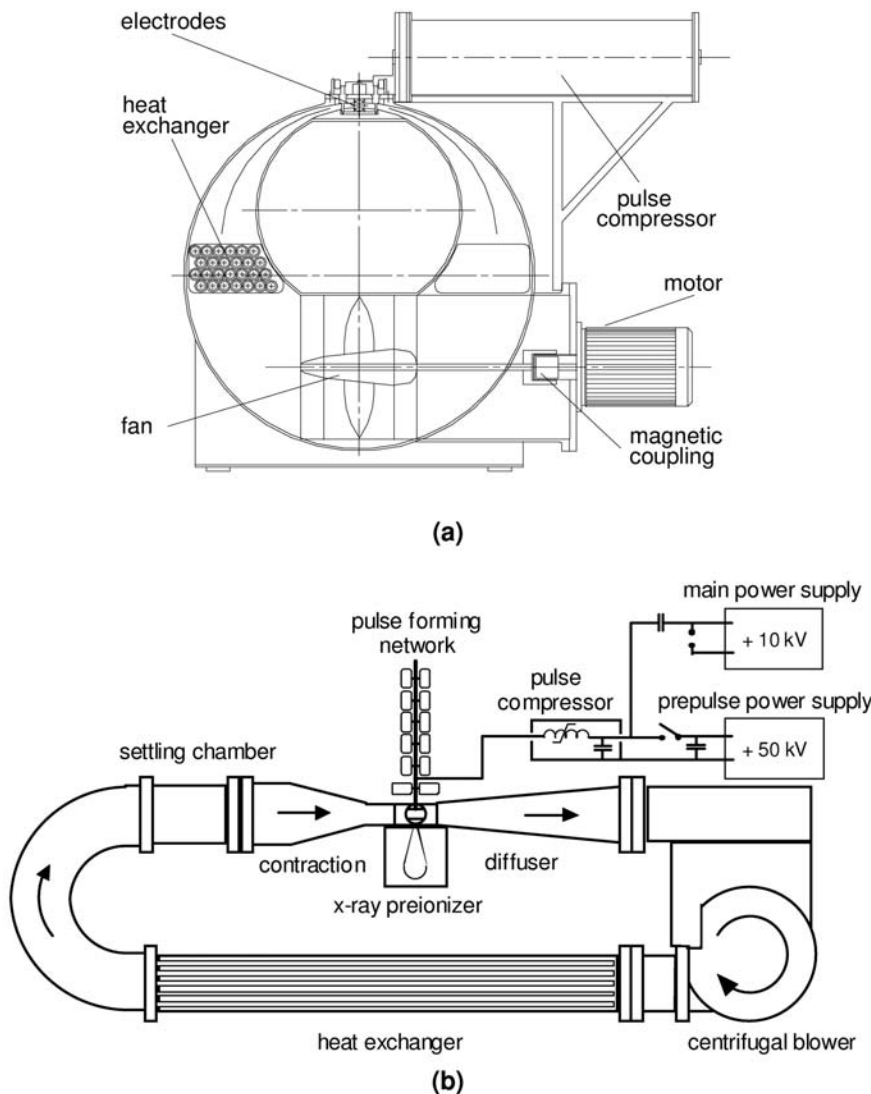


Fig. 5.4. High-repetition-rate, high-average-power excimer lasers: (a) 500 W KrF laser [8] and (b) 1 kW XeCl laser [10]

References

1. H.M. von Bergmann, P.H. Swart: Proc. SPIE **1397**, 63 (1990)
2. P.E. Cassady: AIAA Paper **83**, 1682 (1983)
3. M.L. Sentis, J.P. Truong, O. Uteza, B.M. Forestier, B.L. Fontaine, P.C. Delaporte: Proc. Int. Conf. on Lasers'91 p. 748 (1992). STS Press, McLean

4. N. Niemöller, I. Bragin: *Measurement of gas-flow and acoustic-waves, Internal Report* (Lambda Physik GmbH, Göttingen, 2002), unpublished
5. O. Uteza, P. Delaporte, B. Fontaine, B. Forrestier, M. Sentis, I. Tassy, J.P. Truong: *Appl. Phys. B* **64**, 531–537 (1997)
6. Lambda Physik: *Lambda STEEL series of excimer lasers* (Lambda Physik, Göttingen, 2004)
7. Lambda Physik: *Steel series of excimer lasers* (Lambda Physik, Göttingen, 2004)
8. P.H.S. H. M. von Bergmann, G.L. Bredenkamp: *Proc. Int. Conf. on Lasers '89* pp. 80–87 (1990). STS Press, McLean
9. P. Oesterlin, D. Basting: *Physics World* **3**, 43–46 (1990)
10. J.C.M. Timmermans: *Proc. SPIE* **3343**, 687–691 (1998)
11. K. Haruta, Y. Saito, M. Inoue, A.S. Y. Sato S. Fujikawa, H. Nagai: *Appl. Phys. B* **68**, 663–669 (1999)

5.2 High-Energy Lasers

V. Borisov and I. Bragin

Excimer laser output energy of about 10 kJ is obtained today with electron-beam-pumped systems (see for example [1]). In that case excitation of the active laser gas medium is performed using one or several high-current high-energy electron beams. Each electron beam is formed by an electron gun vacuum diode. To provide the necessary uniformity of the electron beam and high efficiency of the laser, a high-voltage pulse of an amplitude $> 250\text{ kV}$, duration $> 500\text{ ns}$ with a rise speed above 10^{12} V/sec should be applied to the cathode of the vacuum diode. Such voltage pulses are delivered by high-voltage generators based on a pulse forming network. The electron beams are transferred into the active volume via a thin metal foil, separating the vacuum region of the electron gun from the laser gas vessel. Such a foil should withstand significant mechanical (due to the difference of pressure about several Bar) and thermal load. An external magnetic field provides efficient and uniform delivery of the electron beam into the laser chamber with current density about 10 to 20 A/cm^2 . A cross section of an e-beam-excited laser including gas flow vessel for repetitive operation is presented in Fig. 5.5.

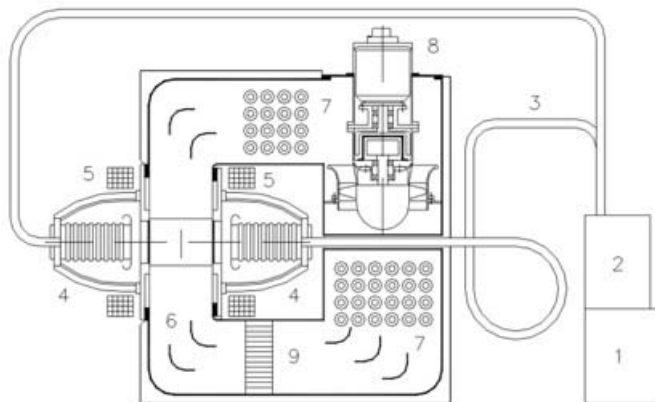


Fig. 5.5. Schematic of the compact e-beam-excited repetitively operating KrF laser with expected output power of about 8 kW (100 J , 80 Hz). Here are: 1 high voltage power supply, 2 high voltage pulse generator, 3 high voltage cables transmitting line, 4 e-beam sources, 5 magnetic coils, 6 gas flow vessel ($1.2\text{ m} \times 1.3\text{ m} \times 1.5\text{ m}$), 7 heat exchanger, 8 blower assembly, 9 gas flow spoilers.

A similar high-power KrF laser with 112 J pulse output energy and 20 Hz repetition rate (active medium volume $15\text{ cm} \times 15\text{ cm} \times 100\text{ cm} = 22.5\text{ l}$) was created in TRINITI in 1990 [2].

Electron-beam-pumped excimer lasers are proven means to reach multi-kilo *Joule* and multi-kilo *Watt* excimer laser operation. However, such systems are not widely used for high-power lasers due to the significant technological problems, among them:

- Introduction of the electron beam into the laser chamber
- Difficulty to arrange the uniform electron-beam-pumping of the laser medium from opposite directions and sufficient gas exchange in the active volume
- The use of a high-power electron beam demands to protect the personnel against the X-ray radiation
- Complexity of the electron-beam-pumped lasers makes them not competitive with electrical-discharge-excited lasers in the power range below 1 kW

The main problem arising in high-energy and power excimer lasers excited by a self-sustained gas discharge is the creation of a uniform gas discharge during the energy deposition at higher repetition rate. The results of many investigations of the conditions, necessary for the uniform energy depositions shows that the quality of the energy input depends on several parameters and their relations. Those parameters are:

- Pre-ionization conditions
- Regime of the energy deposition
- Geometry of the active volume
- Type of the electrodes

Pulse energies in the *kJ* range are also achievable with discharge-pumped excimer lasers. This type of laser is the commercially most important one because its realization is relatively simple, the overall efficiency can be high and the reliability is good. A main task is the efficient deposition of the electrical power into the discharge during a short time. Usually, for ArF and KrF lasers the energy must be deposited in the gas within 30 to 100 ns. For XeCl lasers the deposition time can be several times longer, strongly depending on the total electrical power, which should be close to optimum. This fact is the main reason for the differences in the creation of powerful ArF and KrF lasers compared to XeCl lasers.

5.2.1 KrF and ArF Lasers

The technical features of powerful KrF and ArF lasers depend on the gas discharge uniformity and the dynamics of its development as well as on the kinetics of the excimer molecules in plasmas. Extensive theoretical and experimental investigations show the dependency of the gas discharge stability on the initial electrons density n_{eo} and the reduced electrical field E/N (here E is the electrical field strength, N the gas density). Relatively small variations

of the initial electron density or E/N produce with time strong changes of the energy dissipation in different discharge areas. Fluctuations of the reduced electrical field produce stronger changes than the variations of the initial electron density. Relatively small variations of E/N can change the electron density in the discharge by an order of magnitude. Non-uniformity of the electrical field E in the discharge can be caused not only by electrode roughness or by features of the electrode profile but also by the positioning of constructive elements of the laser chamber located close to the discharge area. Variations of the reduced electrical field E/N can also occur due to acoustic disturbances at high-repetition-rate operation. As a result, the disturbances of the discharge uniformity appear due to the non-linear amplification of the initial electron density that develops at the variations of n_{eo} or E/N . Criterion of the discharge stability is the spatial uniformity during the whole period of the electrical power deposition. The dominant mechanism of the glow discharge instability is the contraction into small (about $100 \mu\text{m}$) filaments in the areas with increased E/N . The characteristic time of the discharge instability development at the optimal excitation power density (about 2.5 MW/cm^3 for typical KrF laser) is about 60 ns . The instability of the discharge increases with higher halogen concentration in the laser gas.

As mentioned above, the time of the electrical excitation (which depends on the square root of discharge loop inductivity) should be possibly less than the time of the instability development, setting limits on the cross section of the discharge area. The increase of the discharge width and electrode distance leads to a rise of the inductance and as the result an increase of the electrical excitation time. Experimental dependency of the laser efficiency on the discharge inductivity is shown in Fig. 5.6.

As follows from the presented data the efficiency of the laser strongly decreases with rising inductance. The highest efficiency for ArF and KrF lasers were achieved at $L < 3.8 \text{ nH}$. This limits the cross section of the discharge to $25 \text{ mm} \times 8 \text{ mm}$ at 75 cm length. Possibilities to increase the laser output energy by the discharge length are restricted due to saturation of the laser-medium amplification coefficient while the losses generally do not saturate. Due to that fact the optimal length of the electrodes for KrF and ArF lasers does normally not exceed 80 cm .

Enhancement of the output energy by increasing the electrical excitation intensity W_{in} is efficient only up to the optimal value W_{in} depending on the kinetics of excimer molecules formation. The rise of W_{in} above the optimal value leads to a drop of the efficiency. The dependency of the laser efficiency on the average level of W_{in} for KrF, ArF and XeCl lasers having the same cross section of typically $25 \times 8 \text{ mm}^2$ is presented in Fig. 5.7 [3].

The decrease of the KrF laser efficiency with the rise of W_{in} above 2.5 MW/cm^3 is attributed to quenching of KrF* excimer molecules and excited atoms Kr* by electrons and due to the collisions with each other. The optimal values of W_{in} for KrF and ArF lasers are $2-2.5 \text{ MW/cm}^3$, however

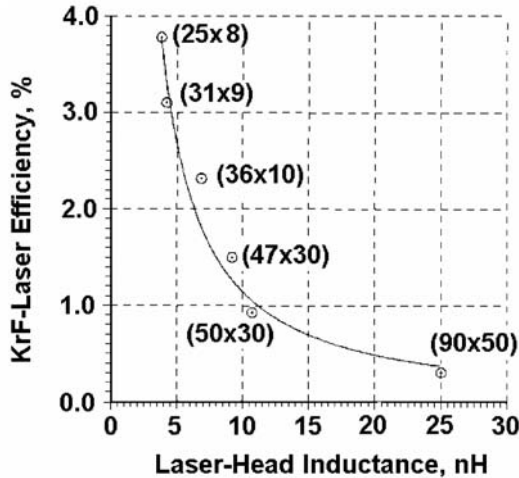


Fig. 5.6. Dependency of laser efficiency on discharge inductivity [2]. Separate points in the plot correspond to measurements at different KrF lasers. Appropriate discharge cross-sections (electrode gap by discharge width in mm) are indicated near the points.

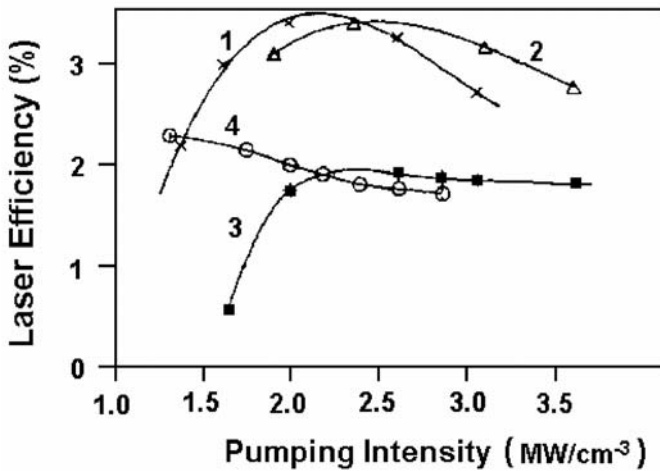


Fig. 5.7. Dependency of laser efficiency on discharge pumping intensity for KrF (curve 1,2), ArF (curve 3) and XeCl (curve 4) lasers

for the XeCl laser W_{in} is significantly lower – about $1 \text{ MW}/\text{cm}^3$. The threshold excitation intensity for ArF and KrF lasers is also higher than for the XeCl laser. Following from that consideration: the possibilities to increase the output energy of KrF and ArF lasers with acceptable efficiency are limited. Such lasers will have relatively low aperture and moderate pulse energy ($< 1 \text{ J}$ for KrF).

As maximum power for KrF lasers of such type, 620 W and an output pulse energy of 1 J were achieved with the system schematically shown in Fig. 5.8. The same laser tube operating with ArF laser gas provided a maximum output power up to 300 W [4].

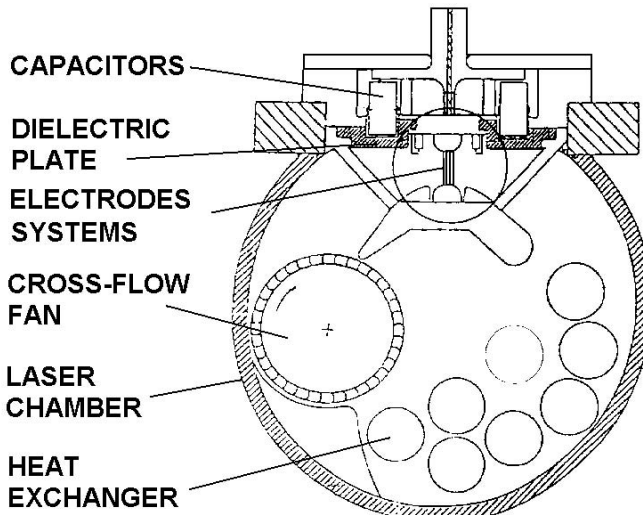


Fig. 5.8. Cross-section of the KrF laser tube with output power 620 W. The laser tube had a cylindrical shape with 42 cm inner diameter. The relatively low size of the discharge area ($3.6 \times 1 \times 88 \text{ cm}^3$) provided a moderate discharge inductance of less than 6.5 nH . This allowed an output energy of up to 1 J with a reasonable efficiency of 2.6%.

Lambda Physik currently manufactures commercially available KrF and ArF lasers with the highest output energy. Output energy reaches 1200 mJ for KrF and 900 mJ for ArF lasers. High pulse-to-pulse energy stability (<1.5%) is reliably provided during the extended gas (>100 million pulses) and windows lifetime.

5.2.2 XeCl Lasers

The optimal pumping intensity for XeCl laser is about 1 MW/cm^3 , which is significantly less than with ArF and KrF lasers, and the duration of the uniform glow discharge phase is longer than that for KrF and ArF lasers. That makes the demand of the low inductivity of the electrical discharge not so severe for XeCl lasers and allows to significantly enlarge the discharge cross section and the duration of the gas discharge excitation. Correspondingly the laser pulse energy can also be increased. A significant increase of the discharge aperture results in additional demands on the preionization system.

The traditional UV preionization by two rows of spark gaps located along the gas discharge electrodes is not optimal any more due the necessarily higher distance to the discharge. Nevertheless, a sufficiently uniform gas discharge could be obtained in a spark-preionized laser with a relatively large aperture (6.5 cm electrode gap, 4.5 cm discharge width). The best efficiency of the laser (3.6%) with 3.63 J pulse energy and 210 ns light pulse duration was demonstrated in a system with reduced discharge cross section of $5 \times 3.3\text{ cm}^2$ [5].

Preionization by an external X-ray X-ray source is traditionally used in very large active volume XeCl lasers. An output energy 66 J was demonstrated in 1985 at NRL (USA) operating an electrical-discharge-pumped XeCl laser with 22 cm electrode gap [6]. However, the arrangement of the electrode system did not allow a gas flow necessary for a repetitive operation. The X-ray pre-ionization was also utilized in high-power lasers developed by ENEA, SOPRA, LASERDOT, and NRCL.

Another approach to the preionization of large volumes is the use of UV light from an auxiliary gas discharge stabilized by a dielectric surface (Fig. 5.9). This type of creeping discharge preionization was developed in TRINITI [2, 7].

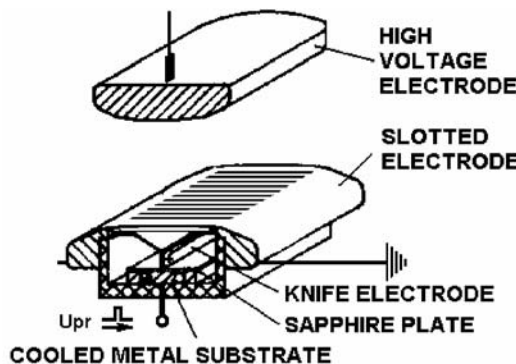


Fig. 5.9. Creeping discharge pre-ionizer arrangement

A creeping discharge develops across the surface of the dielectric (sapphire) plate after applying the high-voltage pulse between the knife electrode and the cooled substrate. Such a preionizer is located behind the slotted grounded electrode of the main gas discharge, and the knife electrode of the preionizer is connected directly to that slotted electrode. The advantage of such a system with respect to also used low-current corona or barrier discharge is the possibility to optimize relatively easily the intensity of the preionization.

A creeping discharge preionizer was used in the first XeCl laser of 1 kW average output [7]. The gas discharge with the dimensions $9 \times 6 \times 74\text{ cm}^3$ was excited via compact pulse forming lines with liquid insulation. The inductance

of the gas discharge electrical circuit was 25 nH . The laser pulse duration was about 80 ns (FWHM) and the peak power reached 1.1 kW . The design of that laser is presented schematically in Fig. 5.10.

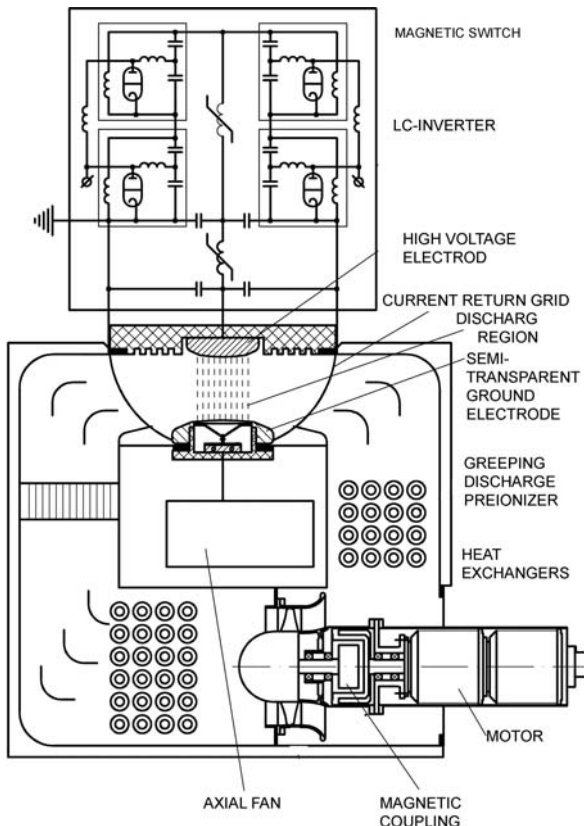


Fig. 5.10. Cross-section of 10 J and 100 Hz XeCl laser with UV pre-ionization

Another XeCl laser called VEL (Very large Excimer Laser) with X-ray pre-ionization and similar output parameters ($1\text{ kW} = 10\text{ J} \times 100\text{ Hz}$) was built by SOPRA company [8]. The laser was able to operate continuously only for 10 seconds . A laser system for amorphous silicon annealing was built by combining three modules. The first module operated as master oscillator, two others as power amplifiers. The laser system reached a maximum energy of 60 J at a repetition rate of 0.16 Hz .

With a multi module XeCl gas discharge system, Mitsubishi Electric Corp. demonstrated the operation with high pulse energy (up to 2.6 J) and high average power (2.1 kW) [9]. The system comprised three modules with gas discharge cross-section $4 \times 2.5\text{ cm}^2$ and total active length of about 3 m . The ac-

tive volume was pre-ionized by the separate barrier discharge occurring near the perforated main-discharge grounded electrode. Electrical excitation circuits with high-voltage prepulses provided long optical pulses (up to 300 ns) at high efficiency of about 3%. The modular structure of the system allowed an optimization of conditions for the energy extraction of the active medium. Best performance was achieved using a stable resonator and additional delay introduced between the modules.

The high-energy XeCl laser systems excited by electrical gas discharge were created mainly as laboratory prototypes. Currently, the commercially available XeCl laser with the highest output energy is the Lambda STEEL 2000 produced by Lambda Physik. The laser is able to deliver up to 1.4 J pulse energy with repetition rate up to 300 Hz . Stabilized output power of 315 W is provided over the whole gas lifetime (typically above 100 million pulses).

A consideration of the current progress and main limitations in high-power high-energy excimer laser systems performed above shows principal possibilities to create machines with an average maximum power up to several kilowatts and energies up to several kilojoules per pulse. While there is nearly no physical limitation for the scaling of power, the concrete features of such lasers are strongly dependent on the target application. However, the complexity of the resulting devices increases very rapidly and the reliability drops with the output laser power and energy. Really there are no known applications that would motivate the creation of very high power and energy industrial lasers now. In fact the maximum power level, which is proven by the industrial use in the moment, is about 400 W from a Lambda STEEL 2000 laser.

References

1. L.A. Rosocha, J.A. Hanlon, J.M. et al: Fusion Technology **11**, 497–531 (1987)
2. V.M. Borisov, O.B. Khristoforov, Y.B.K. et al.: Proc. SPIE Int. Soc. Opt. Eng. **3574**, 56–66 (1998)
3. V.M. Borisov, I.E. Bragin, A.Y. Vinokhodov, V.A. Vodchits: Quantum Electronics **25**(6), 507–510 (1995)
4. V. Borisov, O. Khristoforov, Y.K. et al.: Proc. SPIE Int. Soc. Opt. Eng. **4184**, 348–352 (2000)
5. V.M. Borisov, A.V. Demyanov, Y.B. Kiryukhin: Quantum Electronics **27**, 23–28 (1997)
6. L.F. Champagne, A.J. Dudas: J. Appl. Phys. **62**, 1576–1584 (1987)
7. V.M. Borisov, O.B. Khristoforov, Y.B.K. et. al.: Proc. SPIE Int. Soc. Opt. Ing. **1503**, 40–47 (1991)
8. B. Godard, P.M. et al.: “First 1-kW XeCl laser”, in *Proc. CLEO 93*, Baltimore, Maryland (1993), paper CThll
9. Y. Sato, M. Inoue, S.F. et al.: IEEE J. of Selected Topics in Quantum Electronics **1**(811–824) (1995)

6 Excimer Lasers for Microlithography

R. Pätzelt, U. Stamm

Microlithography is a term describing a particular branch of lithography that is applied to manufacturing of integrated circuits. It has been introduced shortly after the invention of the integrated circuit in 1958. For an overview on microlithography, see for example [1]. Microlithography started as optical lithography, using lamps for generating the image of a mask pattern in the photoresist on a wafer. The use of excimer lasers with wavelengths shorter than that of mercury lamps for optical microlithography was proposed already in 1980 in order to keep up with the demand for advanced semiconductor chips. Since then optical lithography has been one of the main drivers for the development of excimer laser technology (c.f. section 1.3). The demands on excimer laser technology are unique for this application and will be discussed in detail in this article. Driven by the efforts for the lithography application new optical specifications and a mature, economic performance has become available and has led to the spin-off of new applications.

6.1 Motivation

Optical lithography presents an extremely successful example in which conventional optical technology has been replaced by excimer laser technology that meets the technical as well as the economic requirements in large-scale production. The paradigm of the semiconductor industry is the increase of functionality and a simultaneous shrink in geometry of advanced integrated circuits such as DRAM memory chips, or microprocessors. Gordon Moore [2] formulated his observation, now famous as “Moore’s Law”, already in 1965, just seven years after the integrated circuit had been invented. Moore observed an exponential growth in the number of transistors per integrated circuit and predicted that this trend would continue. Through relentless technology advances, Moore’s Law, the doubling of transistors every couple of years, has been maintained with some modifications regarding the rate of doubling between 1 and 2 years and still holds today. The shrink of the geometries is defined by the so-called technology nodes, which are characterized by the

size of the printed feature. Industry wide the process requirements and control parameter are getting tracked and defined by the ITRS (International Technology Roadmap for Semiconductor) [3], which gives recommendation for preferred technical solutions.

The wavelength of the exposure light for feature sizes shrinking over the years is shown in Fig. 6.1 [4]. To keep up with the demand, the wavelength of the exposure light has been reduced and with the switch to 248 nm the era of DUV (deep ultra violet) lithography started by replacing conventional mercury lamps by excimer lasers. In the following table the main requirements of the semiconductor industry, the technology demand for the optical scanner and the requirements on laser specification are listed.

Table 6.1. Industry requirements, technology demand and laser specifications

Industry Requirement	Technology Demand	Laser Specification
Higher resolution	shorter wavelength	248nm – 193nm – 157nm
	higher NA	spectral bandwidth
		wavelength control
Higher throughput	faster scan speed	repetition rate
		laser power
		energy dose control
High yield	tight process control	stability of laser parameter
		on-board metrology
		<ul style="list-style-type: none"> o spectral performance o energy dose o beam pointing
Reduced running cost	maintenance	maintainability
	uptime	reliability
		<ul style="list-style-type: none"> o (remote) diagnostics o serviceability
	lifetime	<ul style="list-style-type: none"> module lifetime o laser discharge unit o line narrowing optics
		pulse length, repetition rate

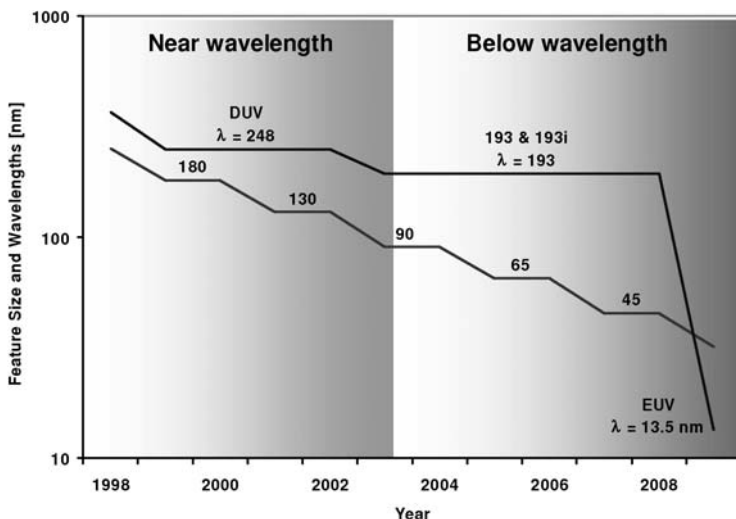


Fig. 6.1. Feature size and wavelength in IC fabrication

Until today the excimer laser technology has been the enabling technology for the advances in optical lithography by providing mature performance and meeting economic goals. In the following, the progress, status and outlook of excimer laser technology are discussed in more detail.

In 2002, most companies considered 157 nm lithography the successor for 193 nm lithography, and there was a sense that extreme UV (EUV) was the solution to the demand for shorter wavelengths and finer resolution. During SPIE Microlithography Conference in 2002 immersion was proposed for full-field microlithography. Soon after, an industry-wide initiative started to investigate the opportunity of immersion to extend the performance of optical microlithography. Although the use of an index-matching fluid – instead of air – is well established in microscopy, there arise many questions when an immersion fluid is to be used in a full-field microlithography tool scanning at 500 mm/sec. The appeal of using an immersion fluid is that for a given wavelength the system performance can be improved so that the market chances for excimer lasers are increased [5]. The opportunity to expand the application of 193 nm lithography by means of immersion made the 157 nm wavelength unattractive. At present 157 nm lithography is not considered as a mainstream technology for microlithography.

Immersion may be utilized in two ways. First the use of immersion leads to an increased depth of focus (DOF) if the numerical aperture (NA) of the lens remains unchanged, thus smaller features may be printed with acceptable process window at high yield.

$$DOF \sim n \times k \times \lambda/NA^2 \quad (6.1)$$

n – refractive index

k – process factor

λ – wavelength

NA – numerical aperture of the
projection lens

Secondly, as a long-term perspective, the use of the high-index immersion fluid will allow further increase of the numerical aperture. Using water, which shows high transparency at 193 nm and a refractive index of 1.44, an NA of up to 1.35 will be possible. Using this technology, 193 nm excimer laser lithography has the potential to extend to the 45 nm node.

6.2 Wavelengths

Optical microlithography utilizes light to transfer the feature pattern from the mask to the wafer. For this, mainstream optical microlithography utilizes the reduction stepper or nowadays scanner that transfers the pattern with a reduction ratio of 1 : 4 to the wafer. The goal is to project a high-contrast image of the mask onto the resist of the wafer at the targeted small structure size. In a stepper the mask and wafer are stationery during exposure whereas in the scanner mask and wafer are both synchronously scanned at high speed to achieve a large exposure field. With the semiconductor industry looking at smaller and smaller feature size to be imaged, shorter wavelengths come into play. According to the Raleigh equation the minimum feature size (MFS) that may be resolved is limited by the wavelength of the used light:

$$MFS \sim k1 \lambda/NA \quad (6.2)$$

$k1$ – process factor

λ – wavelength

NA – numerical aperture of the
projection lens

In order to reach the smaller feature size the semiconductor industry has extensively worked on all those parameters, which have different trade-offs.

The first parameter which may support a reduction of the feature size is the wavelength of the illuminating light. The wavelength of the commonly used mercury lamps is limited to the use of the g-line at 436 nm and finally the i-line at 365 nm wavelength. To enable higher resolution by the use of even shorter wavelengths the excimer laser source emitting at 248 nm , 193 nm , or 157 nm , respectively, is expected to support optical microlithography down to the 45 nm node with some potential for the 32 nm node (c.f. Tab. 6.2).

The second parameter is $k1$, the process factor, which explains the overall lithographic process including the exposure, the resist development and the etching. Tighter process control and add-on features to enhance the imaging contrast have lead to a decrease of the $k1$ factor. Using off-axis illumination such as annular, dipole or quadrupole illumination and employing phase shift masks and enhancement structures on the mask, the $k1$ factor has been reduced and will be less than 0.4 for the 65 nm node. Imaging at such low $k1$ factor makes high demands on the control of all process parameters including the laser light source. On the other hand, it enables the generation of features on the chip much shorter than the wavelength in use, like the 90 nm feature size that is produced by an imaging lens with numerical aperture of 0.85 and 193 nm laser light.

The third parameter – the numerical aperture NA of the projection lens – has been driven by the demand to resolve smaller feature size. The first production-worthy 248 nm stepper on the market was aiming to produce features at the $0.35\text{ }\mu\text{m}$ node for which an NA of 0.45 with a $k1$ factor of 0.8 had been employed.

Table 6.2. Technology nodes and lithography wavelengths [3]

Node (half pitch)	Wavelength	Remark
250 nm	365 nm i-line, 248 nm	
180 nm	248 nm, 365 nm i-line	
130 nm	248 nm	
110 nm	248 nm, 193 nm	
90 nm	193 nm	dry, immersion
65 nm	193 nm	dry, immersion
45 nm	193 nm, 13.5 nm EUV	immersion, extreme ultra violet
32 nm	13.5 nm EUV 193 nm, 157 nm	extreme ultra violet high-index immersion
22 nm	13.5 nm EUV, 157 nm or 193 nm	extreme ultra violet, innovative immersion

6.3 Spectral Output

High-precision projection lenses are utilized to transfer the mask pattern to the wafer. Whereas operation at 365 nm (i-line) is still achieved with high-quality glass, the use of the 248 nm wavelength requires the use of high-quality fused silica for the lens elements. This reduction to a single material limits the option for chromatic aberration correction in the lens and requires the use of monochromatic light. At the advent of DUV lithography using a NA of 0.45 to resolve 0.35 mm features a laser spectral bandwidth of 3 pm was required. To produce DRAM or logic chips with 110 nm feature size the bandwidth of the KrF laser must be limited to 0.5 pm in order to reach an optimum contrast with a numerical aperture of 0.85. Achieving a narrower spectral bandwidth and higher power has been an ongoing task of the development of excimer laser technology.

6.4 Line Narrowing

To reach a laser bandwidth of 0.5 pm , the natural emission spectrum of the laser of about 600 pm must be narrowed by introducing dispersive elements into the laser resonator (Fig. 6.2).

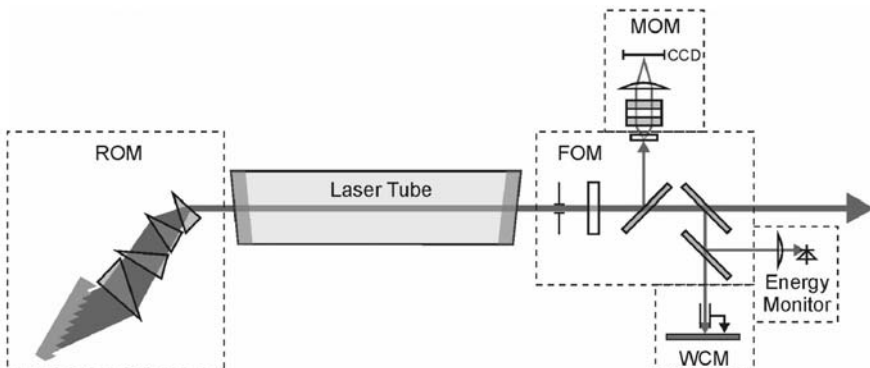


Fig. 6.2. Optical scheme of line narrowing resonator

In a typical setup the laser beam is expanded using a prism by a magnification factor of 20 to 40. The expanded and collimated beam is directed to an echelle grating used in Littrow configuration. Using the 193 nm wavelength the typical prism material is CaF_2 to reach a high transparency and little degradation. At all excimer laser wavelengths a completely purged beam path is mandatory to avoid optics contamination, absorption, ozone production, and to enable a long module and component lifetime. A typical purge

gas for the beam path is high-purity nitrogen. The scheme described here is applied in several excimer lasers used in lithography [6, 7]. A bandwidth of 0.30 pm is achieved at 4 kHz repetition rate, allowing 20 W laser output power (Fig. 6.3). To support optimum imaging contrast, the laser spectrum must not only show small FWHM bandwidth but must present a narrow spectral interval in which 95% of the output energy is contained.

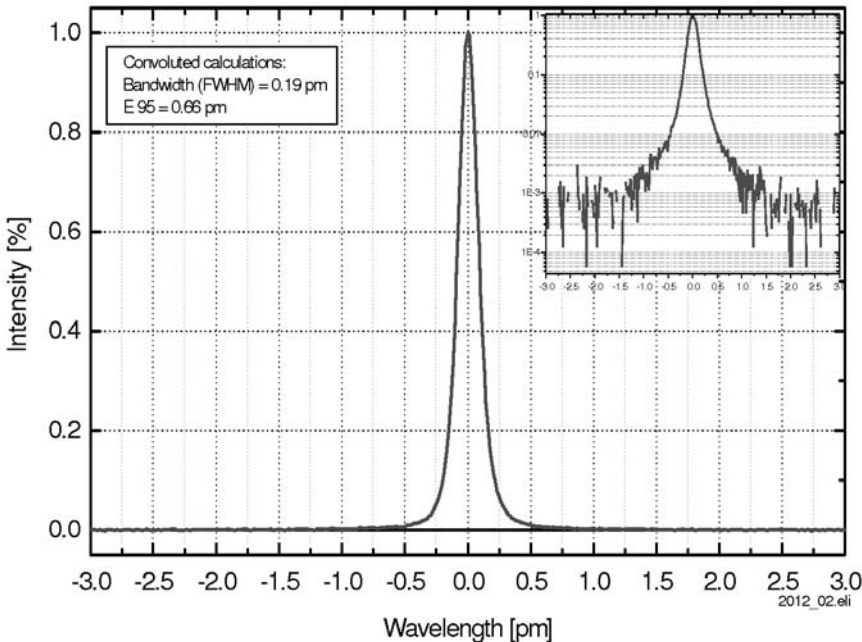


Fig. 6.3. Spectral output of Lambda Physik NovaLine A4003 – 193 nm lithography laser measured using a high-resolution grating spectrometer

This value, named E95%, must be below 0.75 pm . With this data, projection lenses with numerical apertures of up to 0.85 are supported and 193 nm lithography is performed for the 90 nm node. The output spectrum of a typical 20 W 193 nm microlithography laser is shown in Fig. 6.3. The spectrum was measured using a high-resolution grating spectrometer with a system spectral function of $< 0.05\text{ pm}$ at FWHM. Deconvolution of the measured data leads to the bandwidth of 0.19 pm .

6.5 Wavelength Control

To optimize the performance of the projection lens, to minimize aberrations and enable precise focus control, the wavelength of the excimer laser must be

controlled in absolute and relative terms. For this purpose on-board metrology has been developed that measures the relative wavelength with an accuracy amounting to only a small fraction of the bandwidth. Pulse-to-pulse wavelength jitter or short-term drifts lead to a similar effect as a broadening of the bandwidth, lower the contrast of the image and complicate the control of focusing. The wavelength stability for an exposure pulse window requires 1/15 of the bandwidth; practical specification for the 0.2-*pm* laser is a wavelength stability of only $\pm 12 \text{ fm}$, measured over a pulse window of 50 pulses. Such relative-wavelength monitoring is preferably realized by an array of etalons. The principle of the relative-wavelength monitoring system using etalons is shown in Fig. 6.4.

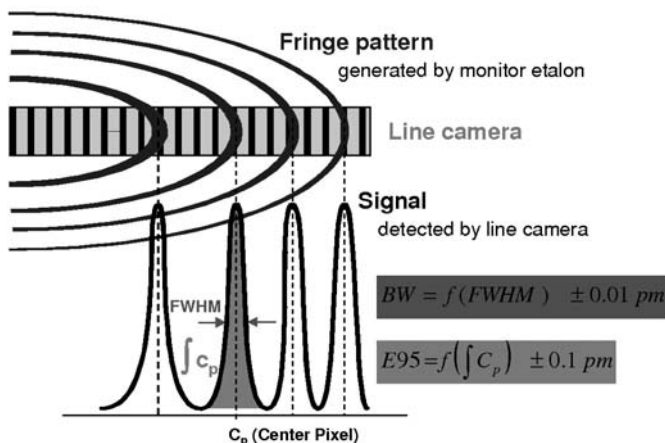


Fig. 6.4. Scheme of relative wavelength monitor

A small portion of the laser light is fed via a diffuser or diffractive element to the monitor etalon. To measure a bandwidth of 0.20 pm , a monitor etalon with free spectral range (FSR) of 1 pm to 2 pm and finesse of 30 may be used. Such a system offers a resolution of about 0.01 pm (FWHM) and for the E95% value a resolution of 0.1 pm . The etalon generates a fringe pattern that is recorded by a linear camera array. The position of the fringes on the camera pixels represents the wavelength whereas the width of the fringe represents the laser bandwidth. The camera system is able to pick-up a wavelength and bandwidth reading with each single laser shot up to the 4 kHz operation rate. Using specific algorithms for averaging of the signal, the wavelength deviation and bandwidth are detected and then used to control the wavelength setting of the laser. Unwanted changes in wavelength, which may be constituted by either wavelength jitter, drifts or chirping, may be thermally compensated by any of the resonator optics or by direct index changes in the gas medium. All drifts and chirps must be eliminated by the fast wavelength control. Fast

actuators have been developed to achieve the required wavelength stability of the laser. In a preferred embodiment a piezo stack or a voice coil motor is employed to perform the angle change of either the prism or the grating.

Another parameter that must be controlled is the absolute wavelength. Monitor systems that utilize the opto-galvanic effect have been developed for this purpose. A portion of the laser beam is split off and guided through a hollow-cathode lamp. That lamp may be filled with a species showing resonant absorption in the wavelength range of the particular excimer laser in use. For the 248 nm KrF excimer laser commonly iron is used, which shows resonant absorption at 248.3271 nm . That reference wavelength is then applied to calibrate the monitoring etalon system. For the calibration, an automated software procedure may tune the laser until resonant absorption is detected.

To achieve a narrow output at 157 nm special effort is necessary. The natural spectrum of the 157 nm fluorine molecule laser consists of two lines with the main line at 157.6309 nm . The main line has a bandwidth of 1 pm only, at 300 kPa operating pressure [8]. This narrow “natural” linewidth and the relative low output of the 157 nm laser compared to ArF or KrF made the industry look for projection optics designs that can tolerate a 1 pm laser bandwidth. Using a catadioptic design, with main optical power in a mirror rather than a refractive lens, such projection optics was developed. Line narrowing of the 157 nm is limited to the suppression of the 2^{nd} unwanted line, which has been developed with high efficiency (Fig. 6.5).

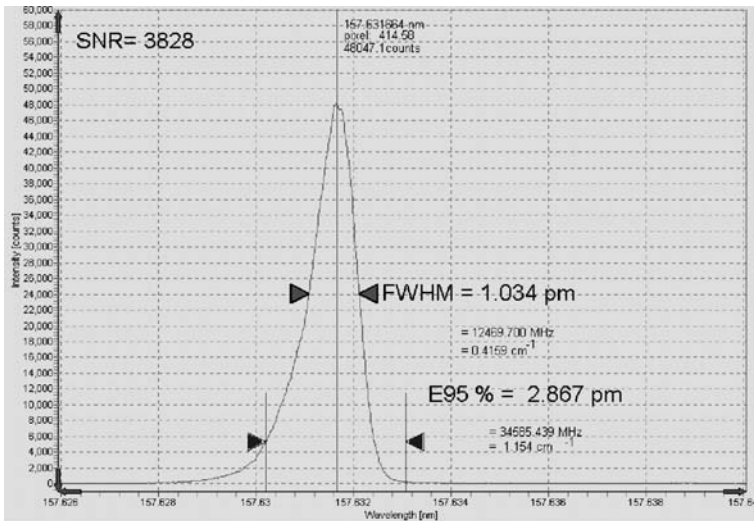


Fig. 6.5. Emission spectrum of a “line selected” 157 nm laser

6.6 Laser Power and Energy

The economic operation of the lithography tool is tightly connected to high throughput and, hence, to laser power and repetition rate. Wafers with 200 mm diameter were used during setting-up of 248 nm DUV microlithography. Starting about year 2000, the wafer size is shifting to the more economic processing of 300 mm diameter wafers, which drives up both repetition rate and laser power. Faster scan speeds of 500 mm/sec have become available in the scanner system and call for repetition rates of the excimer laser up to 4 kHz . Scanning at 500 mm/sec with a scan-slit width of 5 mm leads to a pulse window of only 40 pulses to expose the resist. Still a large number of pulses in the slit are desired to minimize speckle problems, avoid dose quantization errors and allow for tight energy dose control. All these aspects are driving excimer laser technologists to look for even higher repetition rates. With a typical field size of $26 \times 33\text{ mm}$, an optical transmission of about 15% leads to a resist dosage of: $5\text{ mJ} \times 12\% \times 40\text{ pulse}/0.5\text{ cm} \times 2.6\text{ cm} \sim 18\text{ mJ/cm}^2$.

The industry trend is to use resists that require higher dosage but, in return, give better resolution and process capabilities. In response to this trend dual-chamber 193 nm lithography lasers have been developed that operate at 10 up to 15 mJ energy per pulse and can support higher resist dosage at 4 kHz repetition rate.

6.7 Energy Dose Control

In lithography applications, an exact predictable dose has to be applied to the resist to reach a high uniformity of the critical dimension. Any instability of the dose will translate, by the transfer slope of the resist, to a change in the critical dimension. In a stepper the dose comprises many pulses (~ 200), and the exact control of the total dose to approach the target value can be very accurate by monitoring and controlling each single pulse. With the advent of scanners the dose control has become a main driver for improved laser energy stability and more feedback loops between the scanner and the laser. In a scanning system the dose in the scan slit comprises only a small pulse window (~ 25 to 100) depending on scan speed and repetition rate. To stabilize the dose at the target some sort of energy feedback from the scanner to the laser has become the standard. Using this feedback signal the laser will stabilize the energy dose for each pulse window, which is represented by the moving average integrated over the pulse window. With this approach the dose may be controlled with an accuracy of $\pm 0.2\%$ (Fig. 6.6).

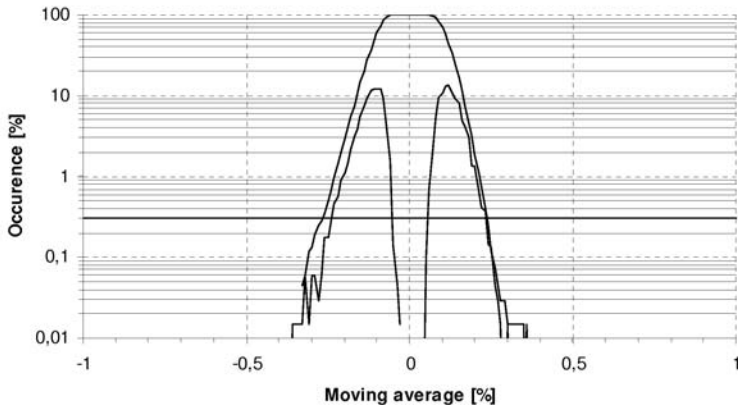


Fig. 6.6. Dose energy stability of a 193 nm lithography laser triggered at 4 kHz repetition rate in burst mode at different duty cycle

6.8 Dual-Chamber Lasers

Driven by economic aspects and technology requirements the required laser power has increased continuously. First KrF lithography lasers delivered 2 W laser power using 200 Hz repetition rate, now a laser power of up to 80 W at 193 nm wavelength is projected, using i.e. 6 kHz repetition rate. Moreover, this trend to higher and higher power goes inline with a steady reduction in bandwidth to support higher numerical apertures. In response to this industry trend, oscillator-amplifier excimer laser systems have been proposed [9, 10, 11] for 193 nm and 157 nm . In such a system the tasks are split; the oscillator is configured and optimized to produce the narrow output spectrum at reduced energy level whereas the amplifier boosts this low energy to a value of 10 to 20 mJ to reach 40 up to 80 W output power. To reach high functionality of such dual-chamber lasers an inherent stable chassis structure of the laser system is required, which provides the rigid thermo-mechanically stable base for all the optical modules. For example, the LithoTEX laser of Lambda Physik features two frames; primary tasks of the two frames are the support of the laser discharge units and supply modules, and for the separated second frame the support of the optical resonator structure. A typical setup for an excimer laser in oscillator-amplifier setup is shown in the Fig. 6.7.

The laser requires minimized footprint and all service and maintenance actions require single-side access. The oscillator in such a system shows no major difference to the configuration of a commonly used single-stage lithography laser as described in Fig.6.2. Only low energy, such as 1 mJ , is targeted for the oscillator and with that a narrower output spectrum of $< 0.2\text{ pm}$ and improved component lifetime is achieved. For the optical set-up used in the amplifier several approaches such as MOPA (master oscillator – power ampli-

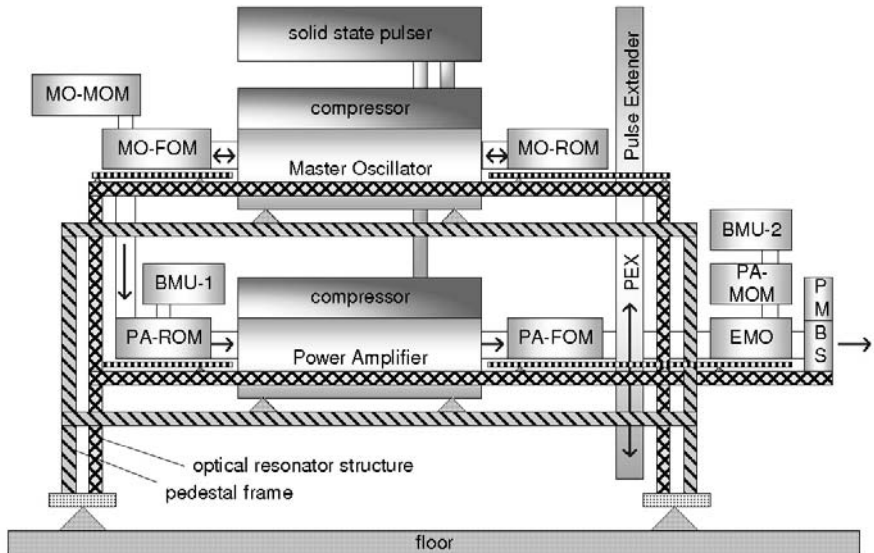


Fig. 6.7. System layout of a dual-chamber lithography excimer laser

fier) or MOPO (master oscillator – power oscillator) are realized in commercial systems. Yet another setup is realized by the MORRA (master oscillator – regenerative ring amplifier) concept (Fig. 6.8).

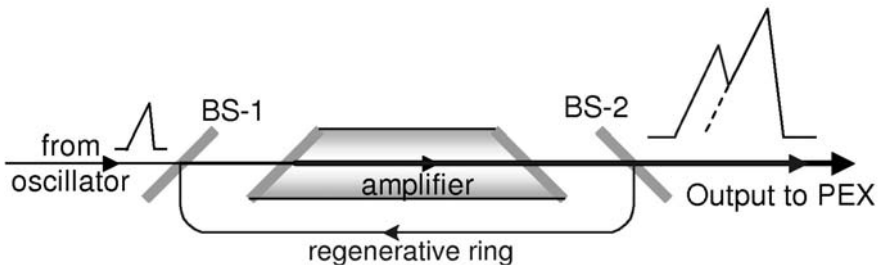


Fig. 6.8. Optical set-up of the regenerative ring amplifier

The regenerative ring structure avoids any coupling between oscillator and amplifier. In addition, the ring acts as a spatial filter and fully suppresses the coupling of amplified spontaneous emission (ASE) into the amplifier. The output consists of 2–3 “roundtrips”, each delivering moderate peak power and therefore a long pulse length. This intrinsic long pulse turns out a big advantage for the following pulse extender, which then efficiently stretches the

laser pulse in one single stretcher. The compaction effect, which is prominent for future 193 nm scanner lenses, is greatly reduced by this longer pulse.

6.9 Pulse Length

In particular, oscillator-amplifier lasers are suitable to reach a high energy per pulse and with that high output power. Such higher energy per pulse is not desired since it also increases the peak power of the beam, which introduces degradation of the optical material. Of specific interest is the compaction mechanism that is observed in fused silica constituting the majority of the material in the scanner's projection lens. The compaction that leads to a densification of the material introduces index changes that may not be tolerable for the imaging properties of the lens [10]. The change of the refractive index scales with the time integral pulse length (peak power) of the laser light according to

$$\delta n = k(NI^2/T_{is})^{0.5}$$

N – number of pulses

I – flux/pulse, mJ/cm^2 (6.3)

In this equation T_{is} is the integral-square pulse duration defined as:

$$\text{pulse length (integral square)} T_{is} = \frac{\left(\int_0^\infty T(t)dt\right)^2}{\int_0^\infty T^2(t)dt} \quad (6.4)$$

T describes the dependency of the intensity on time, “k” is a material-dependant constant. Optical pulse stretching concepts have been developed for the 193 nm lithography laser. Using a partial beam splitter and an optical delay line that matches the input pulse length (T_{is}) such optical pulse stretcher yields temporal extension of the laser pulse by about factor 3. The output of the pulse stretcher consists of the superposition of the original and the delayed beam portions. Figure 6.9 shows the resulting laser pulse with 83.5 ns pulse length (T_{is}) and the input pulse to the pulse stretcher.

With such pulse length a lifetime of about 5 years corresponding to 100 billion pulses for the scanner lens is expected.

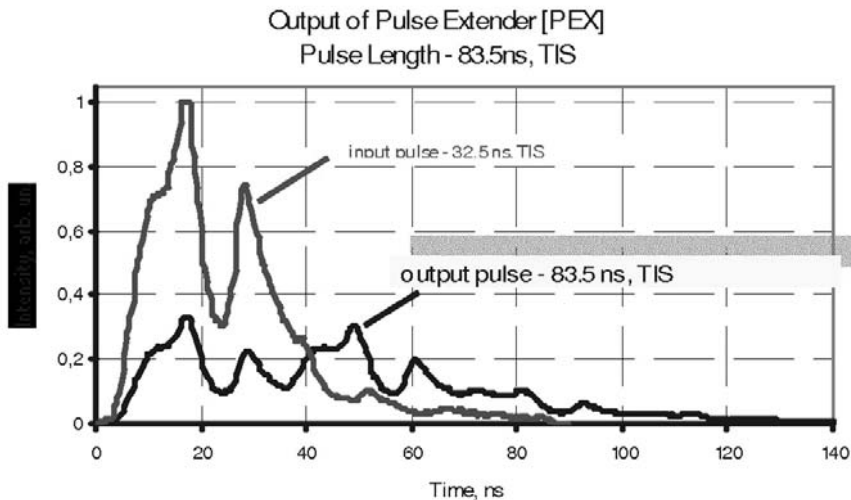


Fig. 6.9. Input and output of the pulse stretcher

6.10 Outlook

Excimer lasers have become the workhorse for optical microlithography. The progress in laser technology has been impressive over the years and has lead to mature laser light sources that meet the industry demand (Fig. 6.10).

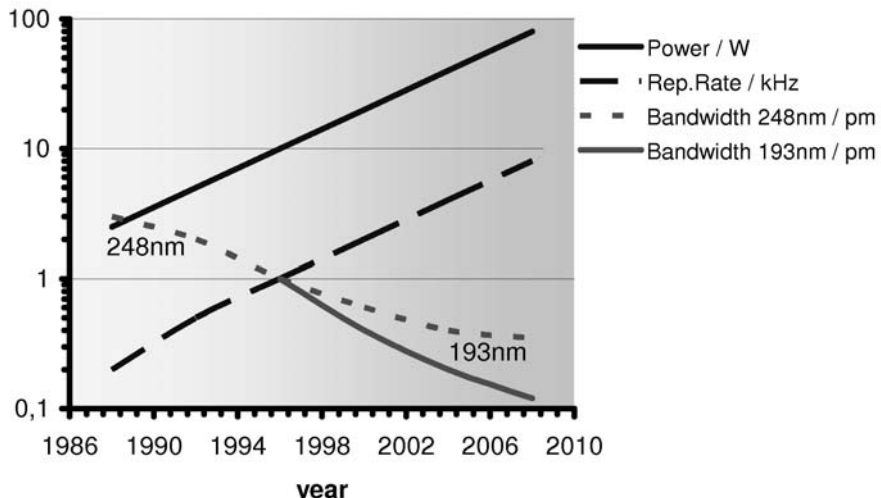


Fig. 6.10. Evolution of excimer laser in microlithography

In only 20 years the power has increased 20-fold while the spectral bandwidth has reduced about 10-fold. In addition, the excimer laser has proven to be cost-effective for the microlithography application. Continuous engineering efforts and innovative new technologies increased the lifetime of the main consumables such as the laser discharge tube and the line-narrowing optics to more than 10 billion laser pulses. Numerous excimer laser applications in microelectronics or automotive industry take advantage of this technology development. Further developments for lithography will target at even higher power of up to 80 W at 193 nm with condensed spectral output and improved energy dose control.

References

1. P. Rai-Choudhury (Ed.): *Handbook of Microlithography, Micromachining and Microfabrication* (co-published by SPIE and The Institution of Electrical Engineers, 1997)
2. G.E. Moore: Electronics **38**(8) (1965)
3. <http://public.itrs.net/>
4. D. Tennenhouse: "Nano-scale technologie: Getting from science to engineering", in *Proceedings of Nanotech*, Intel, Boston, MA, USA (08 March 2004)
5. B.J. Lin: Journal of Microlithography, Microfabrication and Microsystems **3**, 377 (2004)
6. W. Zschocke, H.S. Albrecht, T. Schroeder, I. Bragin, P. Lokai, F. Seddighi, C. Reusch, A. Cortona, K. Schmidt, R. Paetzel, K. Vogler: Proceedings of SPIE **4691**, 1722–1733 (2002)
7. C. Oh, V.B. Fleurov, T. Hofmann, T.P. Duffey, F. Trintchouk, P. O'Keeffe, P.C. Newman, G.M. Blumenstock: Proceedings of SPIE **4691**, 1753–1760 (2002)
8. K. Vogler, I. Klaft, F. Voss, I. Bragin, E. Bergmann, T. Nagy, N. Niemoeller, S. Spratte, R. Paetzel: Proceedings of SPIE **4691**, 660–670 (2002)
9. S.V. Govorkov, A.O. Wiessner, G. Hua, T.V. Misuryaev, A.N. Knysh, S. Spratte, P. Lokai, T. Nagy, I. Bragin, A. Targsdorf, T. Schroeder, H. Albrecht, R. Desor, T. Schmidt, R. Paetzel: Proceedings of SPIE **5377**, 1787–1796 (2004)
10. K. Kakizaki, J. Fujimoto, T. Yamazaki, T. Suzuki, T. Matsunaga, Y. Kawasuji, Y. Watanabe, M. Kaminiishi, T. Inoue, H. Mizoguchi, T. Kumazaki, T. Ariga, T. Watanabe, T. Yabu, K. Sasano, T. Hori, O. Wakabayashi, A. Sumitani: Proceedings of SPIE **5377**, 1805–1814 (2004)
11. T. Ishihara, H. Besaucele, C.A. Maley, V.B. Fleurov, P. O'Keeffe, M.E. Haviland, R.G. Morton, W.D. Gillespie, T.S. Dyer, B. Moosman, R. Poole: Proceedings of SPIE **5377**, 1858–1865 (2004)

7 Laser Beam Characterization

K. Mann

7.1 Introduction

Many industrial applications of excimer lasers, like for example photolithography or material processing, strongly rely on the stability and the precise control of the characteristics of the emitted radiation, such as pulse energy, beam width, divergence, pointing stability etc. Therefore reliable standardized methods for the evaluation of beam parameters as well as accurate diagnostic tools for UV laser beam characterization are mandatory. Whereas the output energy and power of excimer lasers can be monitored with standard calorimetric or piezoelectric measuring tools used also for other high power lasers, recording of spatial beam profiles, or more exactly the energy density distributions, requires specific instrumentation adapted to the output characteristics of excimer lasers.

Beam profiling, both in the near-field and the far-field of the radiation, is of special importance for excimer laser technology. In addition to a rapid assessment of the overall shape of a typically relatively large beam, it allows evaluation of the most important parameters and propagation characteristics. Table 7.1 gives an overview of the relevant quantities to be evaluated from the acquired energy density profiles, addressing also the respective ISO standards [1, 2, 3, 4, 5]. Thanks to the substantial improvements achieved in recent years within the EUREKA project CHOCLAB [6], these standards can in their current version be applied successfully to excimer laser beams. This has been checked also in Round-Robin experiments by testing different measuring tools at the same laser source [7].

7.2 Recording of Spatial Beam Profiles

Besides the sensitivity for various emission wavelengths in the UV/VUV spectral range, a beam diagnostics system for excimer lasers must also exhibit high spatial resolution, have a large detector aperture adapted to the near-field beam cross-section and, most importantly, guarantee long-term stability of

Table 7.1. Relevant beam parameters of excimer lasers and evaluation procedures according to ISO standards. $H_{NF}(x,y)$ and $H_{FF}(x,y)$ denote the near-field and far-field energy density distributions, respectively.

Beam parameter	Evaluation	ISO standard
Near-field profile:		
<i>centroid</i>	(x_c, y_c)	1^{st} moment of $H_{NF}(x,y)$
<i>beam positional stability (x,y)</i>	$\Delta_x = 2 s_x$	standard dev. of centroid distribution of consecutive pulses
<i>beam width (x,y)</i>	$d_{sx} = 4 \sigma_x$ $d_{sy} = x_2^{1/2} - x_1^{1/2}$	2^{nd} moment of $H_{NF}(x,y)$ or: moving slit evaluation
<i>eff. irradiation area</i>	$A_{\text{eff}}(\eta)$	integration over beam areas with energy density $H_{NF}(x,y)$ above threshold η
<i>edge steepness</i>	$s = (A_{10\%} - A_{90\%}) / A_{10\%}$	normalized difference of eff. integration areas
<i>plateau uniformity</i>	$U_p = \Delta H_{NF} / H_{\max}$	peak width of histogram curve
Far-field profile:		
<i>divergence (x,y)</i>	$\Theta = d / f$	beam width in far-field
<i>beam directional stability (x,y)</i>	$\delta\alpha_x = 2 s_x / f$	standard dev. of centroid distribution of far-field profiles
<i>Wavefront</i>	$w(x,y)$	Hartmann-Shack measurement
<i>Spatial coherence</i>	I_c	Young's double slit experiment

the employed optics and sensors under pulsed UV irradiation. Such requirements can be fulfilled by camera-based devices, provided that the employed materials have been thoroughly tested.

A corresponding beam profiling system was developed and tested at Laser-Laboratorium Göttingen and optimized in cooperation with Lambda Physik and ASML/Veldhoven. This device allows simultaneous monitoring of both the near-field and the far-field profiles at the excimer laser wavelengths of 248 nm , 193 nm and 157 nm , as described below [8] (cf. Fig. 7.1). For operation at 157 nm , the entire optical set-up is mounted in a purgeable vacuum chamber. With the help of two wedged CaF_2 plates, the excimer laser beam is oriented collinear to the optical axis of the measuring apparatus and simultaneously attenuated. A beam splitter divides the beam into a near-field and a far-field path, both folded using mirrors for compactness. While the near-field profile is imaged with a CaF_2 lens onto the detector, the far-field beam is focused using a CaF_2 lens of long focal length (930 mm) to minimize errors caused by spherical aberration. After further attenuation by a set of neutral density filters, the near-field and far-field distributions are

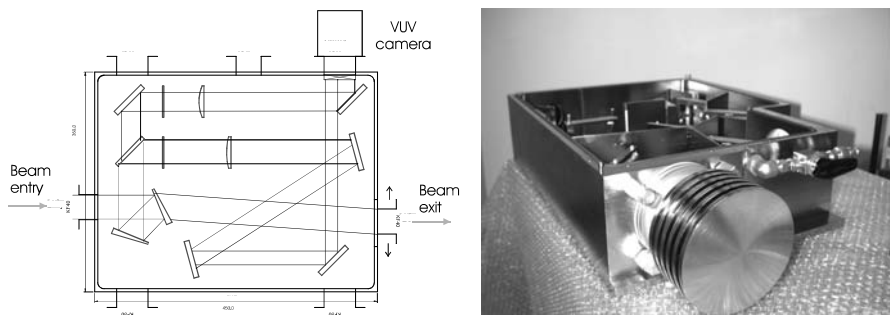


Fig. 7.1. Schematic set-up and photograph of near-field / far-field beam profiling system for 248 nm, 193 nm and 157 nm (courtesy of ASML / Netherlands)

recorded simultaneously and side by side by a UV camera of large active area ($70\text{ mm} \times 50\text{ mm}$).

The UV sensitivity of this camera is obtained by the use of a suitable quantum converter: The incident UV radiation is converted into visible, followed by a (demagnifying) projection of the fluorescence onto a CCD chip. Highly linear, uniform and UV-radiation-resistant converter materials are commercially available. A personal computer equipped with a frame grabber is used for the profile acquisition, real-time display and evaluation of the characteristic beam parameters.

As an example, Fig. 7.2 shows the near-field (NF) and the far-field (FF) beam profiles recorded for a lithographic F₂ laser (Novaline F1030, Lambda Physik), indicating rather smooth and symmetric profiles. From these two-dimensional energy density distributions ($H_{NF}(x,y)$ and $H_{FF}(x,y)$) beam parameters can be evaluated according to the ISO standards (cf. Table 7.1), as described in the following.

7.3 Evaluation of Beam Parameters

7.3.1 Beam Width

From the recorded energy density distribution $H_{NF}(x,y)$ in the near-field, the beam dimensions can be determined. For excimer lasers, two different evaluation methods have been successfully applied, i.e. the ‘2nd moment’ and the ‘moving slit’ method that are both described in ISO 11146 [1]. The ‘2nd moment’ method first requires a determination of the centroid (x_c, y_c), i.e. the 1st moment of the distribution H_{NF} . The beam width is defined as the four-fold standard deviation of the profile data with respect to the centroid position [1]:

$$d_{\sigma,x}(z) = 4\sigma_x(z), \dots d_{\sigma,y}(z) = 4\sigma_y(z) \quad (7.1)$$

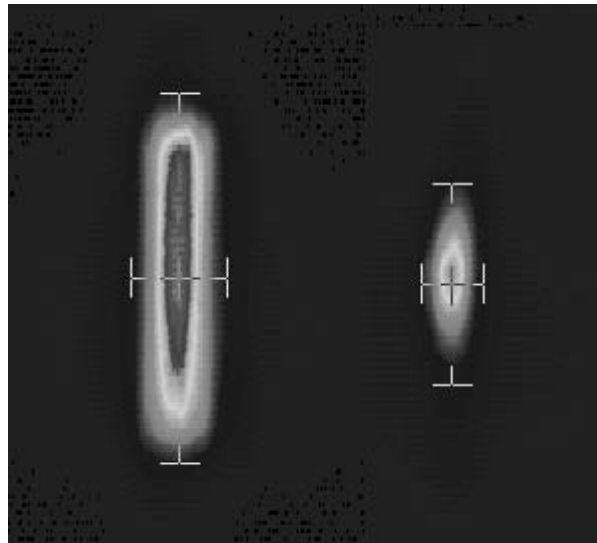


Fig. 7.2. Near-field (left) and far-field profile (right) of F₂ laser (157 nm, Novaline F1030, Lambda Physik) recorded simultaneously with the system shown in Fig. 7.1. The near-field represents a demagnifying projection of a plane close to the laser exit aperture onto the detector, while the far-field profile is acquired in the focal plane of a lens. The evaluated 2nd moment beam widths in horizontal and vertical direction are indicated.

with the 2nd moments

$$\begin{aligned}\sigma_x^2(z) &= \iint (x - x_c)^2 \cdot H_{NF}(x, y) dx dy / \iint H_{NF}(x, y) dx dy \\ \sigma_y^2(z) &= \iint (y - y_c)^2 \cdot H_{NF}(x, y) dx dy / \iint H_{NF}(x, y) dx dy\end{aligned}\quad (7.2)$$

Alternatively, the computational ‘moving slit’ method can be employed, which does not mean measurement with a physically translated slit in front of an integrating detector, but rather a mathematical evaluation of the distribution $H_{NF}(x, y)$ acquired for a single laser pulse. For a determination of the beam width $d_{\sigma,x}$ in x -direction, $H_{NF}(x, y)$ is integrated over y , resulting in a function with a maximum in the vicinity of the beam centroid. The distance between the two $1/e^2$ (= 13.5%) points on either side of the maximum is defined as the ‘moving slit’ beam width [1].

Both methods for beam width determination were tested for their applicability to excimer laser beams [8]. While the computed ‘moving slit’ beam widths are extremely stable, it has turned out that the 2nd moments are rather sensitive to inaccurately determined zero levels and background variations, especially in the outer regions of the profile, which contribute to a

higher extent due to the quadratic weighting (7.1). Thus a proper background treatment is mandatory.

The stability of the 2nd moment is significantly improved by the subtraction of a background map acquired immediately before recording the laser beam profile. In addition, background noise must not be clipped, since positive and negative noise peaks compensate each other. A further improvement is obtained by self-consistent iterative methods [8], e.g. by checking the stability of the calculated beam widths against variations of the integration area. In combination with these accurate background subtraction techniques, both ‘moving slit’ and ‘2nd moment’ methods can be applied safely for standardized evaluation of excimer laser beam widths. The accuracy achieved is on the order of 1%. For the highest precision, however, the ‘moving slit’ method is superior.

As an example, Fig. 7.3 shows the near-field profile of a standard KrF laser with stable resonator (ComPex 205, Lambda Physik, pulse energy 540 mJ). The beam widths in horizontal and vertical direction were computed using both the ‘2nd moment’ and ‘moving slit’ evaluation method, indicating a deviation of less than 1%.

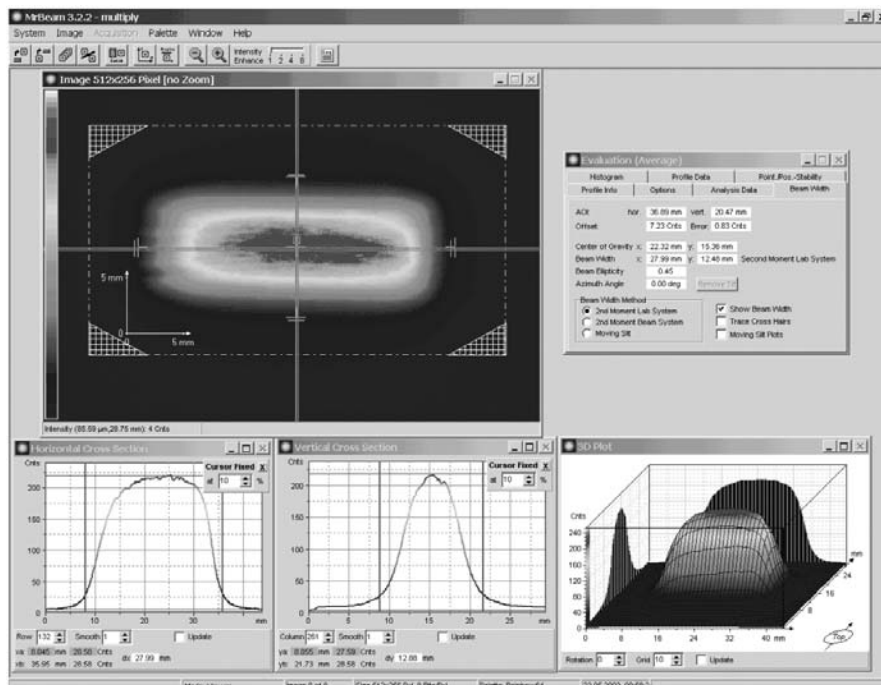


Fig. 7.3. Near-field profile of excimer laser (COMPex 205, Lambda Physik) measured at 248 nm. ‘2nd moment’ beam widths ($d_{\sigma,x} = 27.5 \text{ mm}$, $d_{\sigma,y} = 11.8 \text{ mm}$) are indicated (beam diagnostics software ‘MrBeam’, Laser-Laboratorium Göttingen).

7.3.2 Beam Divergence

The beam divergence is obtained from the far-field recorded in the focal plane of the focusing lens (focal length f), by determining the widths d_x and d_y of the distribution $H_{FF}(x, y)$ in the same way as described above for the near-field profile. The divergences in x and y directions are given by [1]:

$$\Theta_x = d_x/f \quad \Theta_y = d_y/f \quad (7.3)$$

Provided that the focal length is known from the geometrical radius of curvature and the index of refraction of the lens material, an accurate determination of the far-field divergence is possible. An example was already shown in Fig. 7.2 (right) for a fluorine laser (NovaLine, 157 nm). The divergences computed from the beam widths are $\Theta_x = 2 \text{ mrad}$ and $\Theta_y = 6 \text{ mrad}$ for the short and long axis, respectively.

Alternatively, the divergence can also be evaluated from a caustic measurement, i.e. by recording the beam widths at various positions along the beam waist produced by the focusing lens. From a hyperbolic fit to the caustic distribution, both the divergence and the (invariant) beam propagation ratio M^2 , determining the focusability of a beam, can be computed, as described in detail in ISO 11146 [1]. However, for excimer lasers, the M^2 factor is of minor importance since most applications are based on projection imaging rather than focusing. Moreover, caustic measurements turn out to be problematic due to the strong astigmatism and anisotropic divergence of excimer laser beams. Thus, for standard applications, the simple method according to (7.3), which does not require any movable parts, is recommended.

7.3.3 Beam Positional and Directional Stability

To characterize the extent of lateral pulse-to-pulse fluctuations, the beam positional stability can be evaluated in accordance with the ISO standard 11670 [2].

Following this standard, the eventual lateral movement of the beam centroid (x_c, y_c) , i.e. the 1st moment of the recorded near-field profile $H_{NF}(x, y)$, is monitored for 1000 consecutive pulses. The beam positional stability Δ at a location z of the detector is expressed as the two-fold standard deviation s of the centroid distribution in x - and y -direction (perpendicular to the beam axis), respectively:

$$\Delta_x(z) = 2s_x(z), \quad \Delta_y(z) = 2s_y(z) \quad (7.4)$$

According to the standard, a recording time of 1 *second* for short term, 1 *minute* for medium term, and 1 *hour* for long term stabilities has to be chosen.

If the measurement is carried out in the far field behind a focusing lens (focal length f), the directional or pointing stability of a laser can be determined [2], which is defined by a possible angular movement $\delta\alpha$ of the centroids:

$$\delta\alpha_x(z) = 2s_x/f, \quad \delta\alpha_y(z) = 2s_y/f \quad (7.5)$$

In contrast to the beam positional stability, the directional stability of the beam is independent of the distance z from the laser exit aperture.

Using the near-field camera of the diagnostic system, the beam positional stability of a KrF excimer laser was determined. A direct plot of the calculated centroid coordinates reveals an uncorrelated cloud of data points (Fig. 7.4, left), but after applying a moving average over 20 successive centroid positions, a lateral movement in horizontal direction within the first ten pulses (warm-up phase) is obvious (Fig. 7.4, right). However, the beam positional variations evaluated from these data ($\Delta_x = 93 \mu\text{m}$ parallel and $\Delta_y = 79 \mu\text{m}$ perpendicular to the electrodes) are rather small (much less than 1% of the beam widths).

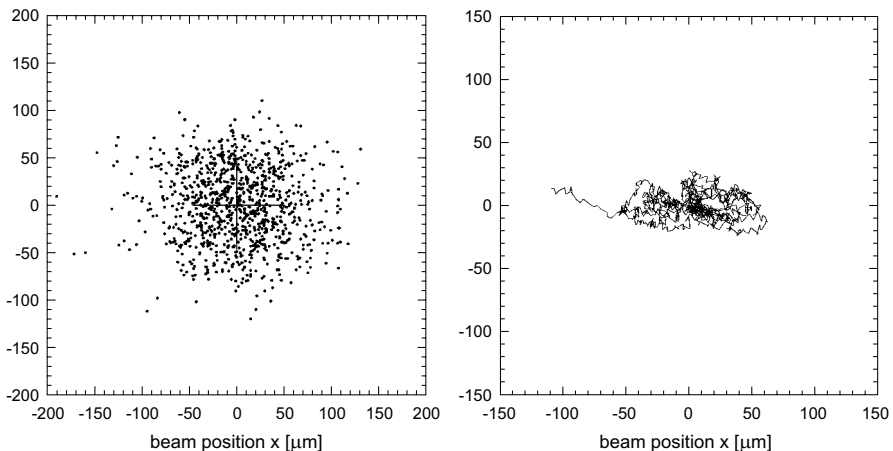


Fig. 7.4. Left: positional stability of KrF laser; the centroid positions of 1000 consecutive pulses measured at 70 cm distance away from the exit aperture at a repetition rate of 12.5 Hz are shown. The positional stability evaluated in accordance with ISO 11670 is displayed for the x - and y -direction as a black cross ($\Delta_x = 93 \mu\text{m}$, $\Delta_y = 79 \mu\text{m}$). Right: moving average of 20 data points of left-hand figure, revealing movement of the beam in x -direction within the first few pulses.

Thus the ISO 11670 standard can be successfully applied for the determination of beam positional and directional stabilities of excimer lasers. It should be noted, however, that the procedure cannot distinguish between a movement of the entire beam and fluctuations in an otherwise spatially stable

profile. Therefore an additional evaluation of the shape of the beam profile has to be performed.

7.3.4 Homogenized Beams

A variety of excimer laser applications, especially in the semiconductor industry and in the production of TFT flat panel displays, strongly depend on the use of homogenized beam profiles of high quality, i.e. top-hat distributions with steep edges and high uniformity in the plateau region. Examples can also be found in laser-based material processing in microelectronics, or medical applications such as corneal reshaping. In all these cases only a narrow process window with respect to the laser energy density is tolerable. Therefore different techniques for homogenization of the excimer laser radiation are employed, which all mix fractions of the original beam to smooth out the intensity spikes [9, 10, 11, 12, 13]. In Fig. 7.5 the principle of a simple fly's eye homogenizer is illustrated, which enables an effective planarization of excimer laser beam profiles [12].

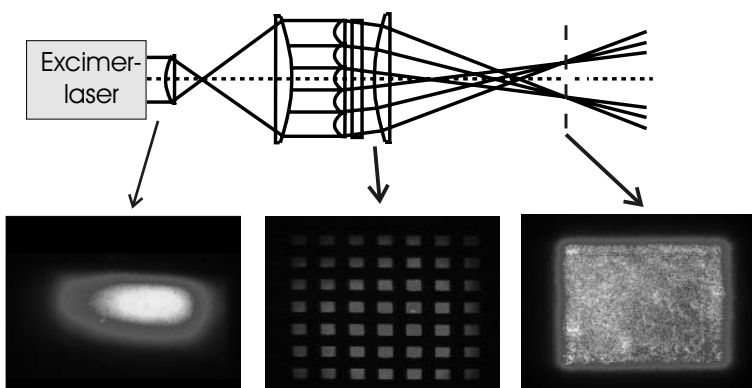


Fig. 7.5. Homogenization of KrF excimer laser beam by use of crossed arrays of cylindrical lenslets. The optical paths of boundary rays forming the edge of the homogenized field are displayed.

The optics consist of two crossed arrays of cylindrical lenslets that split the incident laser beam into partial rays. A spherical lens provides an effective integration of the beam into a flat-topped beam profile.

The respective profiles have to be characterized unambiguously, using definitions which take into account the entire 2D distribution rather than the arbitrarily chosen cross-sections. The following definitions have been implemented into the ISO standard 13694 [3] for characterization of power/energy density distributions:

The ‘edge steepness’ s of a distribution can be characterized by a comparison of the effective irradiation areas A_n at two different energy density levels close to the bottom (e.g. 10% of maximum H_{max}) and close to the top (e.g. 90% of maximum H_{max}) of the profile (Fig. 7.6):

$$s_{10\%,90\%} = \frac{A_{10\%} - A_{90\%}}{A_{10\%}} \quad (7.6)$$

In case of very steep edges, s approaches 0; for homogenized profiles values of $s_{10\%,90\%} < 0.2$ are achieved, for Gaussian-like distributions $s_{10\%,90\%} \leq 1$.

For a description of the remaining inhomogeneity in the plateau area, a ‘plateau uniformity’ U_p can be defined. This quantity is derived from a plot of the energy density histogram curve $N(H_i)$, i.e. the number of data points corresponding to a certain energy density H_i . For nearly flat-top distributions, this function exhibits a peak slightly below the maximum H_{max} . The plateau uniformity is given by

$$U_p = \Delta H / H_{max} \quad (7.7)$$

where ΔH denotes the full-width at half-maximum (FWHM) of the peak, approaching 0 for ideally flat distributions.

These definitions are independent of the background effects and may be applied to flat-top profiles of arbitrarily shaped footprints. As an example, respective values were determined for a homogenized XeCl laser beam profile with an extreme aspect ratio ($60\text{ mm} \times 0.8\text{ mm}$, Fig. 7.6).

The evaluation of the edge steepness yields a value $s_{10\%,90\%} = 0.1$, the plateau uniformity has been computed to be $U_p = 2.5\%$.

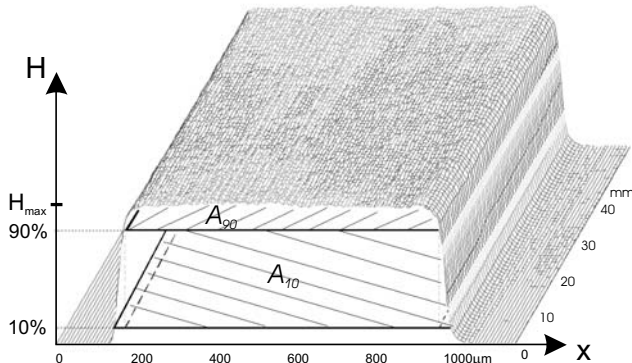


Fig. 7.6. For definition of edge steepness: homogenized XeCl laser profile with extreme aspect ratio (length 60 mm , width $850\text{ }\mu\text{m}$). Line beam profiles formed by optics of MicroLas GmbH/Göttingen are used in the production of flat panel displays. The displayed distribution was acquired by rastering a high resolution beam profiling camera.

7.4 Wavefront Measurement

In addition to the diagnostics described for standardized near- and far-field beam parameters, the designer or operator of optical systems for excimer lasers most frequently needs also information about the directional distribution of sub-rays within the beam, i.e. the laser beam wavefront. The wavefront carries detailed information about the beam aberrations, both its intrinsic as well as those introduced by optical components. Hence, it allows to study the influence of optical elements on beam quality and propagation behaviour.

According to the newly released standard ISO 15367-1 [4], the wavefront of a laser beam at a position z_0 along the beam path is defined as the surface $w(x, y)$ that is normal to the local direction of energy propagation (i.e. the local Poynting-vector $S(x, y, z_0)$) of the electromagnetic field. For coherent sources, this is simultaneously a surface of constant phase. The knowledge of both wavefront and energy density distribution permits a complete beam propagation for coherent lasers, whereas for partially coherent sources like excimer lasers, a simple ray-tracing is feasible after all.

The measurement of laser beam wavefronts can be performed by Hartmann or Hartmann-Shack wavefront sensors, as described in ISO 15367-II [5]. The technique is based upon a segmentation of the incoming beam into a large number of sub-rays, which can be accomplished either with a pinhole array (Hartmann) or a micro-lens array (Hartmann-Shack principle) [14]. The intensity and position of the individual spots are monitored with a position sensitive detector, e.g. a camera, placed at a distance f behind the segmenting screen (cf. Fig. 7.7). The centroid positions of the partial rays are then evaluated within each sub-aperture according to ISO 11146 [1]. The displacements of the centroids compared to their reference positions, determined for example by illumination with a plane wave, represent the local wavefront gradients, allowing the reconstruction of the entire wavefront. This can be achieved either via polynomial expansion (modal approximation) or by direct numerical integration with the help of a suitable difference scheme for neighbouring sub-apertures (zonal method) [5, 15].

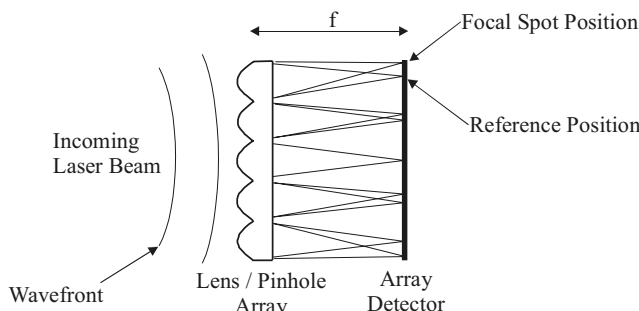


Fig. 7.7. Principle of a Hartmann-Shack wavefront sensor

An example for a wavefront and propagation analysis of excimer lasers is shown in Fig. 7.8 for an F₂ laser (LPX 140i /Lambda Physik, operated at 157 nm). Due to the lack of transmissive micro-lenses in the VUV spectral range, an orthogonal array of pinholes was employed for segmentation of the incoming beam (Hartmann principle). Intensity and position of the individual rays were recorded with a UV sensitive camera calibrated with the help of a collimated He-Ne laser, yielding plane wave reference positions within each sub-aperture. The resulting spot distribution of the F₂ laser obtained with this Hartmann camera is displayed in the upper left of Fig. 7.8. Obviously, there is a strong resemblance with the respective near-field profile measured without the pinhole array (lower left), which can also be obtained from the spot distribution by integrating the pixel counts within the individual sub-apertures. Thus the calculation of standardized near-field parameters like beam widths, uniformity, edge steepness etc. is possible from the Hartmann measurement.

On the other hand, evaluation of the experimental gradient data (Fig. 7.8, upper right) yields the directional distribution of the laser beam, from which the wavefront $w(x, y)$ was reconstructed employing a modal approach (Fig. 7.8, lower right). The displayed wavefront $w(x, y)$ clearly indicates a relatively large and anisotropic divergence which is known for broadband excimer lasers (peak-to-valley wavefront amplitude $\sim 200\lambda$) [15]. Quantitative information on these and other aberrations (astigmatism, coma, higher order

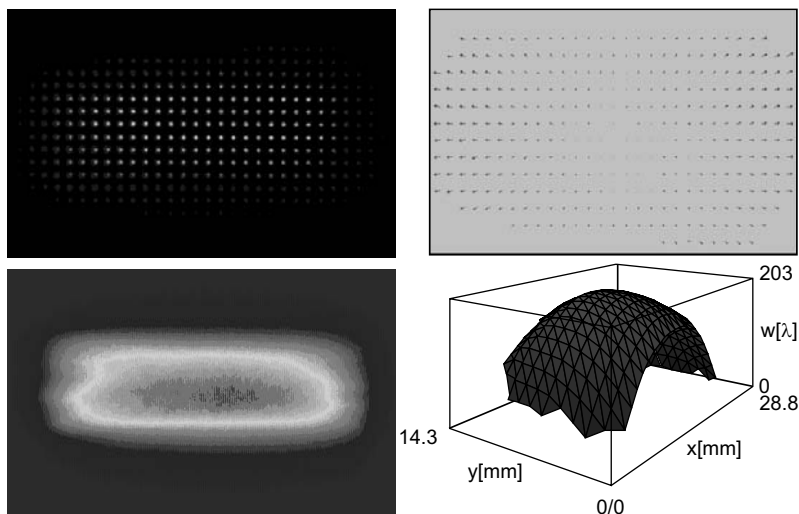


Fig. 7.8. Wavefront measurement of F₂ laser radiation (157 nm) using a Hartmann camera (40 × 30 pinholes, dia. 100 μm , pitch 1 mm). Measurements were performed in a vacuum chamber after attenuating the beam with dielectric mirrors.

terms) can be obtained from a Zernike analysis of the measured wavefront distribution [5].

Moreover, the data can be used as input for ray-tracing calculations on beam steering optics, since at each point the normal of the surface $w(x, y)$ represents the local beam direction. The Hartmann-Shack technique has already been applied successfully for compensation of wavefront aberrations in excimer laser beams with the help of diffractive optical elements (DOE) or in combination with adaptive optics [16].

In conclusion, since both near- and far-field of the beam are registered simultaneously, the Hartmann technique provides comprehensive beam characterization and propagation analysis of excimer lasers by a single measurement [6], enabling for example on-line optimization of the resonator adjustment. An extended version of the Hartmann-Shack sensor with an additional independent far-field measurement on the same detector allows even evaluation of the spatial coherence properties of partially coherent beams [17].

References

1. ISO/DIS 11146-I: (2003), "Test methods for laser beam widths, divergence angles and beam propagation ratios – part 1: Stigmatic and simple astigmatic beams"
2. ISO/DIS 11670: (2002), "Test methods for laser beam parameters: Beam positional stability"
3. ISO/DIS 13694: (1999), "Test methods for laser beam parameters: Power (energy) density distribution"
4. ISO/DIS 15367-I: (2003), "Test methods for determination of the shape of a laser beam wavefront – part 1: Terminology and fundamental aspects"
5. ISO/DIS 15367-II: (2003), "Test methods for determination of the shape of a laser beam wavefront – part 2: Hartmann-shack sensors"
6. D. Nickel (Ed.): *Instruments and Standard Test Procedures for Laser Beam and Optics Characterization* (VDI-Technology Center, Düsseldorf, Germany, 2003), brochure to the final presentation of EUREKA project CHOCLAB II (EU-2359)
7. B. Schäfer, K. Mann, D. Neal, B. Eppich, B. Neubert, W. Scharfe, T. Stark, C. Roundy: "Round-robin test on laser beam characterisation / ISO 15367 and ISO 11146", to be published
8. K. Mann, J. Ohlenbusch, V. Westphal: "Characterization of excimer laser beam parameters", in *Proc. of 3rd Int. Workshop on Laser Beam and Optics Characterization (LBOC), Quebec/Kanada, Juli 1996, SPIE Vol. 2870* (1996), p. 367
9. M.R. Latta, K. Jain: *Optics Comm.* **49**, 435 (1984)
10. K. Jain: "Excimer laser lithography" (SPIE Optical Eng. Press, Bellingham, USA, 1990)
11. Y. Ozaki, K. Takamoto: *Appl. Optics* **28**(1), 106 (1989)
12. K. Mann, A. Hopfmüller: "Characterization and shaping of excimer laser radiation", in *Proc. of 2nd Workshop on Laser Beam Characterization Berlin* (1994), p. 347

13. W. Singer, H.P. Herzig, M. Kuittinen, E. Piper, J. Wangler: Opt. Eng. **35**(10), 2779 (1996)
14. D.R. Neal, W.J. Alford, J. Gruetzner, M. Warren: "Amplitude and phase beam characterization using a two-dimensional wavefront sensor", in *SPIE Vol. 2870* (1996), p. 72
15. B. Schäfer, K. Mann: "Investigation of the propagation characteristics of excimer lasers using a hartmann-shack sensor", Rev. Sci. Instrum. **71**, 2663 (2000)
16. D. Schäfer, J. Ihlemann, K. Mann, G. Marowsky: Appl. Phys. A **69**(319), 1999
17. B. Schäfer, K. Mann: Appl. Optics **41**(15), 2809–2817 (2002)

8 Optical Coatings for Excimer Laser Applications

N. Kaiser, H. Lauth, H. Bernitzki

8.1 Introduction

The high quantum energy and the corresponding short wavelength give ultraviolet radiation a prominent role in optics to provide high resolution. Mainly excimer lasers show potentials for future applications like ultra-precision machining and measurement, minimal invasive brain-, vascular-, and eye surgery, components for data communication, and large-scale integrated (LSI) electronic devices. For the engineer, the main challenge is to provide efficiency. In order to take advantage of the expensively generated UV photons, efficient optical components are required with extreme technical demands. Efficient UV optics can only be realized by dielectric coatings, hence stable coatings belong to the most important issues to improve efficiency.

Optical lithography is the technology driver in the development of optical components and coatings for shorter and shorter wavelengths. Investigations have been concentrated on the excimer laser wavelengths 248 nm , 193 nm , and 157 nm . Now, considerably shorter wavelengths of about 13.5 nm are becoming important for the so-called Next Generation Lithography.

In this short overview, first of all the basic interaction mechanisms of UV photons with dielectrics are reviewed. Then, results achieved at coatings for deep ultraviolet (DUV, 248 nm and 193 nm) and vacuum ultraviolet (VUV, 157 nm – 50 nm) are presented. Finally, a preview for applications in the extreme ultraviolet (XUV: 50 nm – 1 nm) will be given.

The primary repositories of information in the UV-coating field are the annual proceedings of the “Boulder Conference on Laser-Induced Damage in Optical Materials”, the SPIE and OSA conferences, and the SEMATECH Meetings. Recently published review articles which include detailed references can be found in [1].

8.2 Basics

When irradiated with an intensity I , the surface element dA of a coating receives, at normal incidence, the radiation power $dP = I dA$. Over a time

interval dt , this area accumulates the fluence $F = \int I dt$. If damage to the coatings occurs, the corresponding fluence is called damage fluence or damage threshold or Laser-Induced Damage Threshold (LIDT). When irradiating a coating over a time t with pulsed laser radiation of repetition rate f_p the irradiation dose amounts to $D = F t f_p$.

Transmitting optical elements consist of dielectric material. In the ideal case of no absorption the basic relations between pulsed laser beam of intensity $I [Wcm^{-2}]$, single pulse energy $E_p [J]$, fluence $F [Jcm^{-2}]$, pulse length τ , irradiated area A , and the induced electric field $E [Vcm^{-1}]$ inside the dielectric with refractive index n are:

$$I = \frac{E_p}{A\tau} \quad (8.1)$$

$$F = I\tau \quad (8.2)$$

$$E^2 = \frac{I}{n\sqrt{\epsilon_0\mu_0}} \quad (8.3)$$

ϵ_0 being the absolute permittivity of free space and μ_0 the absolute magnetic permeability of free space. $\sqrt{\epsilon_0/\mu_0}$ is the vacuum admittance ($2,65 \times 10^{-3} A/V = 1/377 S$).

The function of a dielectric thin film coating depends on interference effects and the interference results in standing waves. The variation of the electric field amplitude accompanying these standing waves can be considerably. Losses like absorption are highest where the electric field is strongest; so the distribution of the electric field is an important parameter in the design of coatings where losses should be minimized. Dielectric coatings applied to UV-optical elements are mostly either anti-reflective (AR) or highly reflective (HR) for the corresponding laser wavelength. When a surface is made anti-reflective, the electric field amplitudes both at the air-coating-interface and at the coating-substrate-interface are nearly the same. On the other hand, when applying a multilayer dielectric mirror on a substrate for high reflectivity, the electric field is very high in the outermost layers of the mirror and nearly zero at the coating-substrate-interface. Consequently, absorptive properties of the mirror substrate have low influence on the total absorption.

8.3 Interaction Mechanisms of UV Photons with Coated Optical Elements

Excimer lasers are powerful commercial UV sources. Lithography with the 248 nm (5 eV) KrF laser is well established. 193 nm (6.3 eV) ArF lithography has entered production since 2002 and will extend resolution below the 65 nm

node. These lasers have output powers of up to 60 W , pulse lengths between 10 ns and 40 ns and repetition rates up to 4 kHz . To increase the throughput, the fluence on optics continues to approach 100 mJcm^{-2} and repetition rates 8 kHz . The Next Generation Lithography will probably work with extreme-UV (EUV) radiation of about 13.5 nm and will reach a resolution down to the 22 nm node. The 45 nm node will be fulfilled by 193 nm immersion lithography and 193 nm immersion, 157 nm immersion and EUV are candidates for the 32 nm node.

The interaction of high-energy UV-photons with coated optics is rather complex. Electromagnetic energy is converted to electronic, thermal, chemical, and mechanical energy. The primary interaction produces electron-hole pairs, heats the free electrons and may generate local heating around optically absorbing centres. According to our experience most of UV optics show limited lifetime as a result of defects and atomic contamination having its source in the optics technology (polishing, cleaning, coating, packaging, mounting etc.) or in the surroundings of the optics under working conditions. But even under these conditions, degradation starts with the above described interaction procedures, too.

8.4 Absorption

The electronic band edge (short wavelength transmission cut-off) of the substrate and coating-building materials should be as far away from the laser wavelength as possible. However, there is no choice in the UV where only oxides and fluorides can be used. 157 nm : low refractive materials such as MgF_2 , AlF_3 , Na_3AlF_6 and $\text{Na}_5\text{Al}_3\text{F}_{14}$; high refractive materials such as LaF_3 , NdF_3 , GdF_3 , and DyF_3 . 193 nm : additional low refractive as SiO_2 ; high refractive Al_2O_3 . 248 nm : additional high refractive materials such as HfO_2 , Y_2O_3 , Sc_2O_3 and ZrO_2 . In general, fluorides are more robust and resistant to laser damage than oxides. On the other hand, oxides are mechanically resistant and can be deposited by modern coating technologies with higher packaging densities as fluorides.

In some cases metal mirrors are required. In the UV only aluminum can be used. Aluminum reflects in a broad spectral region, but a few percent of absorption and scatter losses can never be prevented.

Early investigations on oxide and fluoride coatings have been performed in the wavelength region between 260 nm and $1.06\text{ }\mu\text{m}$ (5 ns – 15 ns), and at 248 nm (25 ns – 200 ns). It was shown that the damage fluence F_D scales with the square root of the pulse length τ :

$$F_D \propto \tau^{0.5}. \quad (8.4)$$

This is the basic scaling law for thermally induced damage. Damage to coatings and surfaces in excimer lasers is generally associated with localized

defects and contaminants that act as centres of high absorption and poor thermal and mechanical contact to the host.

Ideal transmitting optical elements show zero absorption between the short wavelength transmission cut-off and the infrared transmission cut-off. Real materials absorption is caused by defects which may be intrinsic or extrinsic. Absorption can be strongly influenced by external conditions. These are temperature, pressure, electrical and magnetic fields, and irradiation with energetic particles or XUV rays. Dynamic effects may occur during energy deposition when optical constants and defect concentrations change due to the rise of temperature. This is typical for phase transitions (melting or recrystallization). Here, the relation of the characteristic time constants of the processes to the laser pulse length plays a major role. However, in the case of single-photon coating-defect-induced absorption, which takes place at relative moderate intensities and temperatures, these effects can be neglected.

8.5 Coatings

8.5.1 Metals

In cases where high reflectance is needed in an extended wavelength range, aluminum layers offer the best solution, even though its reflectance is only about 90%. Thin films of MgF_2 , evaporated at low substrate temperature immediately in the same vacuum cycle on top of a freshly deposited Al mirror, protect aluminum from extensive oxidation, and hence from a drop of reflectance at short wavelengths. Typically, for a protected aluminium mirror deposited under high vacuum conditions and with a high evaporation rate of about 30 nm/s a reflectance of 88–90% at 193 nm and 84–86% at 157 nm is achievable.

8.5.2 Dielectrics

Anti-reflective coatings (AR) are required to get single-wavelength antireflection. At least one high-refractive and one low-refractive layer (each of non-quarterwave thickness) and in some cases (193 nm) 3 layers are necessary. Better resolution for lithography requires also larger numeric apertures and larger and curved substrates. In these cases AR coatings consisting of more than two layers are necessary. For high-reflective coatings (HR) many alternating high-refractive and low-refractive quarterwave layers are necessary. Lithography tools require both mirrors for normal and for 45° angle of incidence. Due to their large layer number, problems with mechanical stress have to be taken into consideration. Partial reflectors or beamsplitters and variable attenuators are also made using large-number multilayers.

The demand is an efficient use of the UV photons since cost of ownership may determine whether lithography remains in the optical domain. Today

wafer stepper producers push their optics suppliers to the limits. Coated 193 nm optics should be stable over 1.5×10^{12} pulses at fluences of some mJ/cm^2 or 5×10^9 pulses at fluences of more than 100 mJ/cm^2 at repetition rates of 4 kHz . The transmission of AR coatings has to exceed 99% for both sides coated, reflection of HR coatings at normal incidence has to exceed 99% and at 45° 97%. 157 nm optics should be stable over 10^{11} pulses at fluences of 0.5 mJ/cm^2 and repetition rates of 1 kHz . Transmission of AR coatings has to exceed 98.8% per surface, reflection of HR coatings at oblique incidence should be greater than 95%. The key to meet these requirements is the design of the coating's real microstructure.

Coatings for $\geq 248\text{ nm}$. These wavelength regions have been investigated very intensely. The rule-of-thumb which can be summarized for coatings technology is simply to prevent absorbing defects whenever possible and to tailor the microstructure.

Coatings for 193 nm . The step to 193 nm has been connected with intensive investigations on fluorides, SiO_2 , and Al_2O_3 to further reduce optical losses due to scattering and absorption. AR coatings require minimum extinction coefficients. For HR coatings also mechanical stress has to be minimized. Special care has to be taken on the complex connections between substrate material, surface finishing and coating. Nonlinear absorption was shown to become more important for coatings stability. Coating technologies are now under optimization. The following performances are reached: AR 193 nm , normal incidence: both-side-coated substrates show a transmission higher than 99%. The coatings are still working after 10^{10} pulses at 15 mJcm^{-2} . HR 193 nm , normal incidence: reflection 99%, $LIDT = 5\text{ J/cm}^2$, without changes after 5×10^9 pulses at $> 100\text{ mJcm}^{-2}$. HR 193 nm , 45° incidence: reflection 97%, $LIDT = 1.5\text{ Jcm}^{-2}$ without changes after 1.5×10^{10} pulses at 20 mJcm^{-2} .

Coatings for 157 nm . The transition from DUV to VUV is characterized by strongly increasing absorption and scattering losses. The primary substrate material is CaF_2 and coating materials can also be fluorides only. Reliable optical constants for VUV coatings are not available. The measurement of optical constants and losses is much more difficult than in the DUV. During 157 nm laser irradiation nonlinear processes like multiphoton absorption and fluorescence exist in analogy to 193 nm . But again, as proposed by theory, current investigations address single photon interactions and chemical reactions as the main limiting factor for 157 nm optics performance. The main difference to DUV optics is by contamination processes, which play a dominant role at 157 nm . Apart from the increasing single photon absorption of coating materials, not the materials intrinsic properties but extrinsic chemical factors govern currently optics lifetime. The high laser photon energy of 7.9 eV is capable of breaking chemical bonds of environmental residues like hydrocarbons, silicon compounds and water (which remained nearly unaffected at longer wavelength). Therefore, with 157 nm laser radiation, secondary reactions grow up on standard optics. Water is strongly absorbing in the VUV

and provides potential for secondary chemical reactions due to hydrolysis of water in OH and H at 157 nm (not at 193 nm). Solutions are sophisticated cleaning, handling and manufacturing procedures, which limit the amount of extrinsic degradation factors on optics to a minimum level.

Current performance data have been achieved by several international tests of VUV components using enhanced cleaning and handling procedures. AR 157 nm , normal incidence: both-side-coated substrates show a transmission of about 99%. HR 157 nm , normal incidence: reflection 98%, HR 157 nm , 45° incidence 96%. The coatings are still working after 2.4×10^9 pulses at 2.5 mJ cm^{-2} . 157 nm laser exposure for 10^9 pulses at 2 mJ/cm^2 to AR both-sides-coated on CaF_2 results in a stable transmission of about 98%. Also broadband (from normal incidence to 50°) AR coatings have reached superior performance, due to precise measurement of optical constants. Internal stress of fluoride films play also an important role. Much work has to be done to further improve ultraviolet dielectric coatings performance.

Coatings for non-lithography applications. Interference coatings for the VUV find several classical non-lithography applications in astronomy, synchrotron radiation optics, materials processing and medicine. Research on optical interference coatings, as the key element for resonant light amplification and laser optics, has currently gained vital interest at VUV wavelengths. Up to the present day, absorption of optical crystals prevents generation of laser harmonics below 180 nm in solids, while the use of gas Raman cells is limited so far by efficiency restrictions. Classical optical resonator designs, available from microwave down to UV wavelengths, meet with strong material limitation at wavelengths shorter than 200 nm . Strong challenges have to be faced with free-electron lasers (FELs) which represent a next generation of accelerator-based light sources, capable in principle of operating at any wavelength from the far infrared to the X-ray region. In the VUV region, FEL oscillators represent excellent light sources for scientific research, as soon as high quality mirrors are developed. Durability for this application requires resonator coatings to survive in a harsh environment caused by the combination of high energy synchrotron radiation and residual gases from the cavity vacuum. In 2001, 330 mW power at 250 nm was measured at the European FEL project at Elettra with customized transmission mirrors, and lasing at 189.7 nm was obtained with high-reflection oxide mirrors, the shortest wavelength obtained so far with FEL oscillators.

8.6 XUV Coatings

Since it is impossible to use refractive optics at these short wavelengths because of strong absorption, optical systems have to be made up entirely of reflective multilayer coatings. The optical performance of EUV multilayer coatings for a specific wavelength is optimized by selection of the available

materials and the proper design. The most perspective material combination found today for $\lambda = 13.5\text{ nm}$ ($R_{theor} \cong 76\%$) is Mo/Si. Because short-wavelength radiation is used to carry out the imaging, the surfaces of the mirrors are required to exhibit unprecedented perfection ($rms < 1\text{ nm}$). EUV coatings call for minimum residual mechanical stresses.

Current designs for future EUV projection lithography tools include nine Mo/Si mirrors, i.e. the overall reflectivity of the system is given by R^9 . Therefore, the task of optimizing the throughput in future EUV lithography systems has resulted in big efforts to maximize the reflectivity of Mo/Si mirrors to $> 70\%$. However, because of structural imperfections of the multilayer mirrors the EUV reflectivity of pure Mo/Si layers is typically limited to 69.5%. When using an industrial magnetron sputtering system, the reflectivity of Mo/Si multilayer mirrors was $R = 68.4\%$. Further improvement in reflectivity up to 70% was provided on Mo/B₄C/Si/B₄C and Mo/Si/C multilayer systems due to particular suppression of interdiffusion processes on the interfaces. The Mo₂C/Si perspective material combination excels in its thermal stability and is therefore particularly suited to be used in applications with high thermal load, e.g. in the vicinity of a plasma source. At the same time, the reflectivity of Mo₂C/Si multilayer mirrors has been improved to $R = 66.8\%$.

A serious drawback of multilayer coatings for application in EUV optics is their limited range of reflectivity in the spectral and angular range. Firstly, the spectral halfwidth of typically $0.01\text{ nm} - 1\text{ nm}$ covers only a small part of the output of an EUV plasma source, and, secondly, the fact that the reflectivity decreases significantly at angles of incidence exceeding 9° , a few degrees from Bragg condition, causes serious problems when using multilayer coatings on curved substrates. One solution for this problem is the fabrication of laterally graded multilayer mirrors, i.e. coatings with a well-defined lateral thickness distribution. However, such graded multilayer mirrors can be fabricated only in highly specialized and expensive coating machines, and are actually limited to axially symmetric optics. Apart from this, broadband multilayer mirrors have been designed on the basis of a specific depth variation of the multilayer period. In all cases where maximum peak reflectivity is not required, e.g. in EUV metrology, astronomy and microscopy, broadband mirrors provide a useful alternative which is easier to deposit than graded multilayers. The lower reflectivity of broadband mirrors may be compensated by the use of large apertures which are possible due to the broad angular range of reflectivity.

The discovery of optical harmonics generation marked the birth of nonlinear optics. It was demonstrated that atoms could absorb simultaneously two optical photons and emit a photon of doubled energy. Due to the symmetry of the interaction only odd harmonics are generated in atomic gases. This discovery opened wide perspectives for extension of coherent light sources to shorter wavelength. The XUV multilayer coatings are the preferable monochroma-

tors for separation of concrete harmonics and application of monochromatized radiation for different applications. It should be noted that the reflectivity bandpass of XUV coating can be decreased in an effective way by using higher reflectance orders.

The development of a high-power discharge-pumped Ne-like Ar soft-X-ray laser working at 47 nm is an outstanding achievement of laser physics of the recent decade. At present, this laser is the brightest source of short-wavelength radiation and is used for different applications. Therefore, development of high-reflective and stable Sc/Si multilayer coatings for the wavelength range of $35\text{--}50\text{ nm}$ is very actual and has direct interconnection with the rapid development of XUV lasers.

8.7 Summary

A trend towards use of shorter wavelengths can be observed in many applications, including vacuum ultraviolet and extreme UV up to soft X-rays. Optical lithography is one of the most significant applications for short wavelengths in the field of optics. Thus, the semiconductor industry has enormous interest in the continuous development of this technology. KrF lasers with a wavelength of 248 nm are already in use. The next developmental milestones will include utilization of the ArF wavelength at 193 nm , 193 nm immersion and 157 nm immersion. Furthermore, in several research laboratories work is already being conducted on Next Generation EUV Lithography techniques for the future. This presupposes the maintenance of extremely tight accuracy tolerances as regards the thickness of the individual layers, as well as minimum roughness at the interfaces. The fact that the thickness of the layers amounts to only a few atoms represents a great challenge for coating technology and for layer analysis methods.

The use of thin-film technologies for extremely short wavelengths is not restricted to the field of photolithography. Optics for extremely short wavelengths are also required for X-ray astronomy, for research with the help of synchrotron radiation and for the development of X-ray microscopes. Multi-layer mirrors with individual layers of less than 1 nm thickness are already feasible.

References

1. N. Kaiser, H.K. Pulker (Eds.): *Optical Interference Coatings*, Vol. 88 of Springer Series in Optical Sciences (Springer, 2003)

9 Small Structures with Large Excimer Lasers

P. Oesterlin, A. Koch

9.1 Introduction

Excimer lasers found their place in industrial manufacturing processes during the last years. The most prominent of these applications is microlithography where features smaller than $0.1 \mu m$ are created. Besides this, a large variety of manufacturing processes with structure sizes between 10 and $100 \mu m$ and sub- μm accuracy exist. Such an application is the manufacturing of nozzle plates for ink jet printers. The short wavelength of excimer lasers, mainly $248 nm$ and $308 nm$, combined with the short pulse duration of $10\text{--}30 ns$, leads to a clean removal of material (“cold ablation”), with only very limited thermal damage to the surrounding material.

The beam of an excimer laser, however, has properties which seem to make these lasers unfit for this type of high precision material removal at a first glance. The beam is rectangular in shape, it has a non-uniform intensity distribution, and the divergence is large and is different in the two dimensions of the beam. Such a laser beam is impossible to focus to a small and well defined spot.

9.2 Nozzle Plates for Ink Jet Printers

Color ink jet printers are used virtually in every office and every household in industrialized countries. Most of these printers use exchangeable print heads, which are replaced with each new ink cartridge. This is the only way to secure high print quality over long usage periods.

The nozzle plate of a typical ink jet printer has the following data:

- 2 rows, with approximately 150 nozzles in each row
- length of the rows $1/2$ inch
- nozzle diameter: between 20 and $40 \mu m$ at the entrance, and between 10 and $20 \mu m$ at the exit
- acceptable tolerance of the diameter: $\pm 0.25 \mu m$
- acceptable ovality: smaller than $0.5 \mu m$

Of course these figures vary with the different ink jet products, but they are typical for the type of product and help to understand the requirements for mass production. Figure 9.1 shows schematically the principle of an ink jet print head.

Typical HP Thermal InkJet Print Element and ejected ink drop

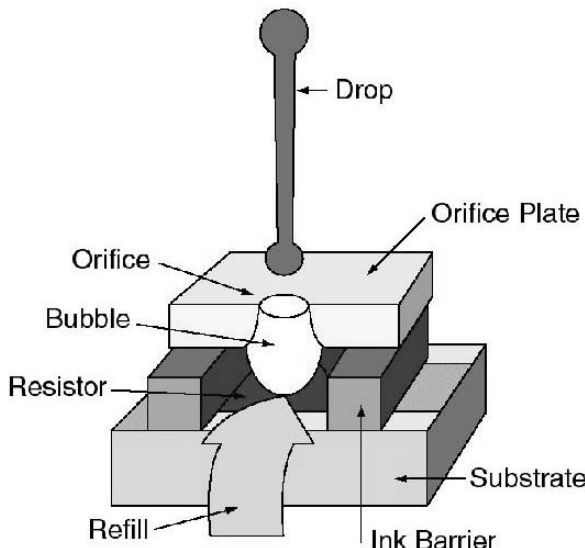


Fig. 9.1. Principle of an ink jet print head (courtesy Hewlett Packard USA)

The nozzles are drilled into the plastic material (mostly polyimide) by mask projection. A high precision mask contains the geometry of the holes and their locations, typically 5 times enlarged. This mask is illuminated by a highly homogeneous excimer laser beam, and is imaged onto the work piece by a projection lens with suitable parameters, as resolution and image field size.

9.3 Attenuators

The results of micromachining processes like the drilling of nozzles depends strongly on the energy density of the laser light impinging on the work piece. It is not only the quality of the holes, like the edge sharpness, but also the hole diameter and the taper angle of the walls which depend on the energy

density or fluence. It is therefore necessary to have a precise control over the fluence of the beam on the work piece.

Excimer lasers change their beam characteristics slightly over the life time of the discharge tube. Thus even if the total pulse energy of the beam remains constant over time, the fluence of the light arriving on the work piece will change. Additionally, optical elements used in excimer beams with very high peak powers degrade over time as well. This degradation manifests itself mainly in a slowly decreasing transmission of the optical system. Both effects lead to a decreasing energy density on the work piece over time, if not compensated for.

Variable attenuators control and fine-tune the energy density on the part to be processed, and thus control the outcome of the laser process. Figure 9.2 shows such an attenuator. The main element is a substrate made from fused silica, which is coated with a special attenuator coating. The transmission of this substrate depends on the angle between the incident light and the substrate. By tilting the substrate, the transmission of the laser light can be varied continuously, for instance between 10% and 90%, with the device shown in Fig. 9.2. A second substrate, coated with an anti-reflex coating, does not contribute to the attenuation process, but compensates the beam displacement which is introduced by the attenuator substrate.

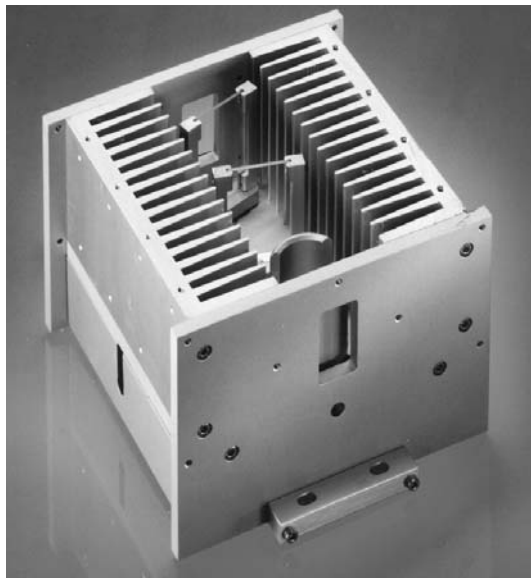


Fig. 9.2. Variable attenuator module, used in industrial manufacturing optical systems

The portion of the laser light which is not allowed to follow the beam path through the optical system onto the work piece, is reflected out of the beam onto the inner walls of the attenuator housing. Cooling fins absorb the light and transport the heat towards the outer walls of the housing. When used with high-power excimer lasers emitting up to 300 W of average power, water cooling is required to dissipate the power. In general these attenuators are computer-controlled. They can be combined with an on-line energy detector which constantly measures the energy density at a suitable location in the optical system, e.g. in the mask plane, and compares the measured fluence with a preset value. The attenuator module, together with this control system, keeps the energy density on the mask constant over very long periods, even if the laser and the optics slowly degrade.

9.4 Homogenizers

The diameters of holes which are machined into the typically 25 or 50 μm thick polyimide foil with a UV laser by ablation depend on the energy density of the laser light. In order to “drill” many holes at a time with the same dimensions, it is thus a requirement to homogenize the otherwise inhomogeneous excimer laser beam so that a mask can be illuminated with high uniformity. The literature knows different types of homogenizers [1, 2, 3, 4]. They all use the principle of dividing the laser beam into many small beamlets, and then overlap or combine them at the location of the mask.

The best results have been achieved with fly eyes homogenizers which are composed of individually polished cylindrical lenses. Figure 9.3 explains the principle of such a homogenizer. The incoming laser beam is divided by an array of cylindrical lenses f_1 into several beamlets with size d . These beamlets match with the cylindrical lenses of a second array f_2 . This second array and a condenser lens f_3 overlap all these beamlets in the focal plane of f_3 .

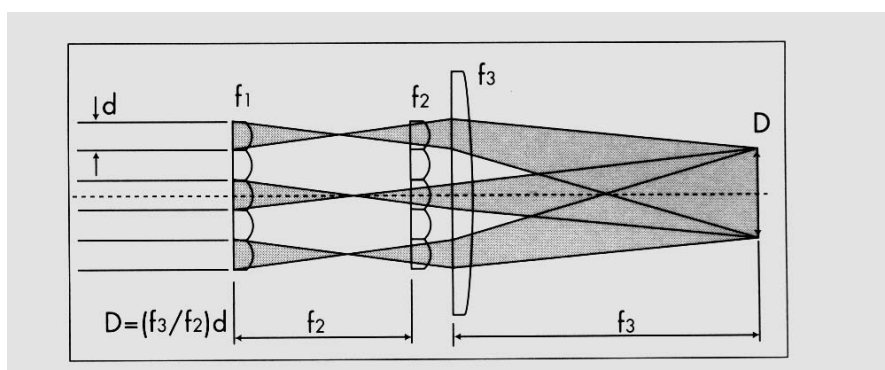


Fig. 9.3. Principle of a cylindrical lens array homogenizer

Ink jet printers often use 2 rows of nozzle plates in a single print head. Thus, 2 lines of features must be illuminated on the mask, with dark space in between. For this special application, MicroLas developed a “dual-line” homogenizer. It creates 2 illumination fields at the same time, with the same size and a fixed distance to each other. The special design assures that the 2 lines have the same intensity and homogeneity. This homogenizer thus eliminates beam dividers which often create unequal intensity in the two fields resulting in unequal nozzle diameters in the two rows.

Figure 9.4 shows the measured intensity distribution of such a dual-line mask field. The measurement was performed with the beam profiler system “MrBeam” from Metrolux, Göttingen. The two homogeneous fields, which can be seen in the figure, have a statistical deviation from perfect homogeneity of only 1.3%. This degree of homogeneity can only be achieved with high performance homogenizer modules and a stringent quality control in production.

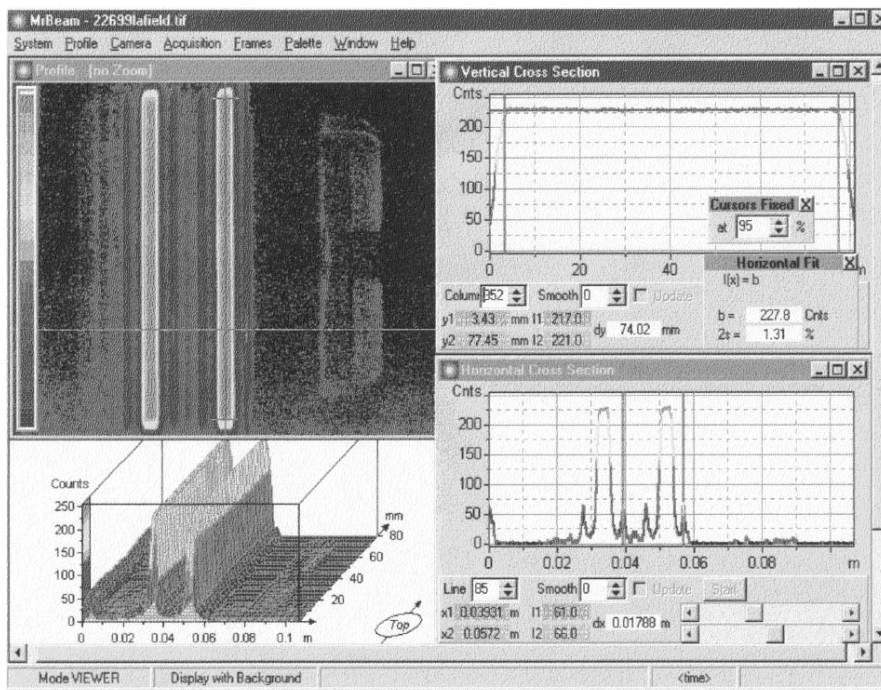


Fig. 9.4. Beam profile measurement of a dual-line mask illumination field. Both lines are created simultaneously with a special dual-line homogenizer. Upper right: Intensity distribution along the long dimension of one of the fields. Lower right: Intensity distribution across the 2 lines. The size of each of the lines is 74 mm × 1.8 mm.

9.5 Projection Lenses

The projection lens has to image the mask features onto the work piece with high resolution. Besides this, a constant resolution over the entire image field is required, and the homogeneous illumination of the mask features have to be maintained in the imaging process.

MicroLas has developed a set of different projection lenses for excimer laser micromachining applications. For processing of polymers, the so-called “5x/18-248” projection lens is often used. It is diffraction limited, meaning that it achieves the optical resolution which is determined by its numerical aperture. Its key specifications are:

- demagnification: $5\times$
- numerical aperture: 0.13
- image field 18 mm diameter
- resolution: $2\mu m$
- wavelength: corrected for 248 nm and 546 nm
- depth of focus: approximately $20\mu m$
- optical materials: fused silica and CaF₂

This projection lens has excellent optical quality not only in the UV but also in the visible spectral range (546 nm). This is important for observation of alignment fiducials, which are machined on the work piece prior to laser processing for alignment purposes.

Figure 9.5 shows a photograph of such a projection lens. It is mounted in a stainless steel body with a high precision mounting flange and consists of 11 optical lens elements. The high quality performance can only be assured by individual testing and aligning of the projection lenses.



Fig. 9.5. High-resolution projection lens 5x/18-248, which is one of the key components in ink jet nozzle plate production systems

9.6 Mechanically and Thermally Stable Support System

High-resolution optical micromachining systems require a stable mechanical basis. Especially the small depth of focus is very demanding for the position stability of the mask, the projection lens, and the work piece. This requires thermal stability, damping of vibrations which are often introduced by movements of the work piece, and precise adjustment. Of course, if the system is once adjusted, it has to remain adjusted for long periods if it is to be used in mass production.

MicroLas has developed different optical mounts which fulfill these requirements. They have large openings since excimer laser beams have large cross-sections, and they have the required degrees of freedom for the alignment, together with excellent long-term stability.

The materials of choice for very stable production systems are aluminum and natural stone, namely granite. Aluminum extrusion profiles are used throughout the system where the requirements on mechanical stability are not extremely high, as for the mask illumination section with the homogenizer. Tolerances of 0.1 mm are acceptable in this part of the system. The extrusion profiles allow the placement of optical elements or components everywhere in the beam path. They thus give the amount of freedom for the alignment of distances of optical elements, as it is necessary to fine-tune, for example, a beam expanding telescope or a homogenizer.

The imaging part of the system has much higher demands on stability. The depth of focus of the projection lens is only $20\text{ }\mu\text{m}$. Hence the distance of the work piece to the projection lens must be stable within this range, if long-term trouble-free operation is mandatory. Aluminum structures cannot fulfill this requirement because of their high thermal coefficient and the low damping of vibrations. Therefore a platform of granite is used to hold the mask, the projection lens, and the work piece in place.

9.7 Beam Diagnostics

Although not directly necessary for the operation of the nozzle plate machining tool, a set of optical diagnostics is often built into the systems. These diagnostics serve to locate problems fast and easily, and to assist in aligning the optical system. Typical diagnostics are:

- Laser beam profiler to measure the intensity distribution of the beam exiting the laser. Although the homogenizer removes many inhomogeneities from the beam, it can function satisfactorily only if the incoming beam has a symmetric intensity distribution. This beam profiler therefore serves to check the laser beam profile, and is a criterion for the alignment of the laser resonator.

- Laser beam power meter. A mirror which can be driven into the beam path directly at the exit port of the laser allows to deflect the beam onto an external power or energy meter. The purpose is to have a standard to which the internal laser energy detector can be calibrated from time to time.
- Mask beam profiler. The uniformity of the illumination field on the mask determines to a high degree the quality of the laser process. Process windows for typical laser processes often require that inhomogeneities are smaller than $\pm 2.5\%$ (2σ). The mask beam profiler allows a quick measurement of this parameter, and it also aids in aligning the homogenizer to achieve this goal.
- Mask observation system. It allows to check the integrity of the mask while installed in the system, as well as to check the alignment of the mask features relative to the laser beam. It normally consists of an illumination light source and a CCD camera with a suitable camera lens.
- On-line energy detector. It continuously measures the energy density on the mask, using a beam splitter and a small energy detector. Its signal is fed back into the controller of the attenuator module, in order to stabilize the energy density on the mask over long periods of operation.
- Substrate energy detector. A pneumatically or electrically driven energy detector is moved into the beam path at the location of the work piece. In this way the energy impinging on the work piece can be measured, taking into account all losses which can occur along the beam path. This measurement is performed from time to time and is used to calibrate the on-line energy detector.

The nozzles are drilled into the plastic material (mostly polyimide) by mask projection. A high-precision mask contains the geometry of the holes and their locations, typically 5 times enlarged. This mask is illuminated by a highly homogeneous excimer laser beam, and is imaged onto the work piece by a projection lens with suitable parameters, as resolution and image field size.

Figure 9.6 is a REM photograph of an ink jet nozzle and the ink channel, micromachined with a 248 nm excimer laser system as described in this article. Both the nozzle and the channel are made by laser ablation in the same system. The high precision of the edges of the features is clearly visible.

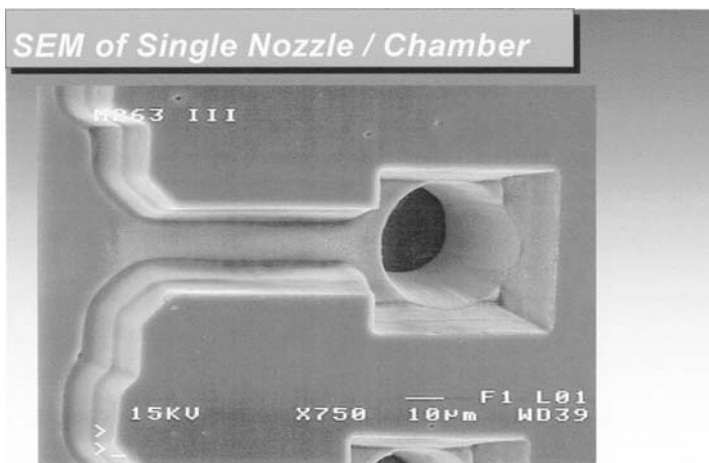


Fig. 9.6. REM photo of nozzle and ink channel of a printer cartridge (courtesy Lexmark, USA)

9.8 Summary and Outlook

The use of homogenizers and projection lenses, developed for highly demanding micromachining applications, allows to make structures with sizes of a few μm and sub- μm precision with excimer lasers in mass production. Due to a continuing feedback from the users of these systems, a constant improvement has led to a stability and performance of these systems which was unthinkable 5 years ago.

Of course the development does not stop at this point. Not only the resolution, the feature size and special hole geometries are in the focal point of development, but the creation of very special illumination beam profiles on the mask is a “hot topic” in the R&D labs as well.

Standard cylindrical lens array homogenizers can only create rectangular illumination fields. If other shapes are advantageous, then so-called diffractive elements are employed. These are holographic elements which require an extensive computer algorithm for their design. They can form any shape out of the excimer laser beam, while they simultaneously homogenize the beam as good as the cylindrical lens array homogenizers do [5]. The design and testing of these elements in industrial applications is presently employed. Preliminary results are very encouraging, and it does not seem to be long before these elements will be used in mass production tools as well.

References

1. K. Mann, A. Hopfmueller, P. Gorzellik, R. Schild, W. Stoeffler, H. Wagner, G. Wolbold: Proc. SPIE **1834**, 184 (1993)

2. K. Jasper, S. Scheede, B. Burghardt, R. Senczuk, P. Berger, H.J. Kahlert, H. Hügel: *Appl. Phys.* **A69**, 315 (1999)
3. C. Lewis, I. Weaver, L. Doyle, G. Martin, T. Morrow, D. Pepler, C. Danson, I. Ross: *Rev. Scientific Instr.* **70**(4), 2116 (1999)
4. Y. Kato, K. Mima, N. Miyanaga, S. Aringa, Y. Kitagawa, M. Nakatsuka, C. Yamanaka: *Phys. Lett.* **53**(11), 1057 (1984)
5. K. Christophe, R. Lionel, P. Meyrueis: *J.Optics A: Pure and Applied Optics* **1**, 398 (1999)

Part II

Applications

10 Overview

M. Wehner

The realization of discharge-pumped rare-gas halide (RGH) excimer lasers [1, 2] formed the basis for the development of commercial laser sources. Soon after, researchers began to exploit the potential of high-power UV light in different technical areas. As one of the first researchers, R. Srinivasan recognized that excimer lasers are excellent tools for the precise ablation of organic material and biological tissue [3] without any melting of material or scar. To illustrate this, Fig. 10.1 shows a human hair which was “scribed” by an excimer laser. From his findings Srinivasan introduced the term of “ablative photo decomposition” for the unique processing capability of polymers by excimer laser radiation. This led to the slogan of “cold ablation”, which means that the heat-affected zone is of minimum dimension and can be neglected in the borderline case of ablative photo decomposition.

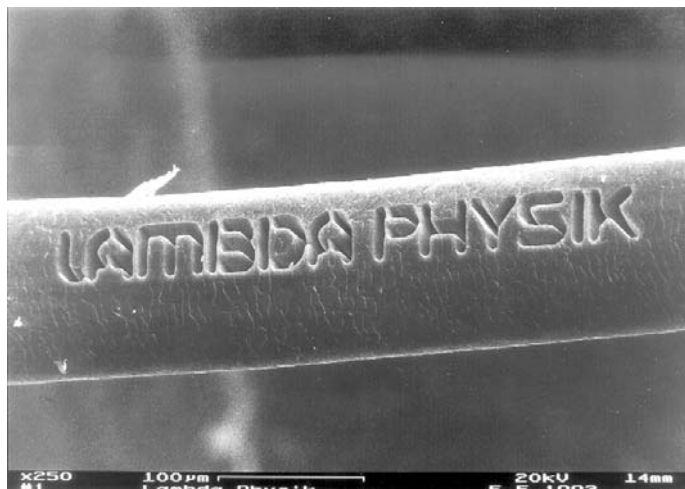


Fig. 10.1. Writing on a human hair with excimer laser radiation

The first industrial applications were developed for microelectronics manufacturing. This also led to the term “etching” for the ablation process which suggests that precise layer control is given and clean structures can be obtained where thermal effects are neglectable. Today, most of the excimer lasers in an industrial environment are employed in microelectronics manufacturing (lithography, thin film transistor (TFT) annealing, and ink jet nozzle drilling). Writing of fiber Bragg gratings is potentially one of the strongly growing applications.

Laser-induced chemical vapor deposition (LCVD) applying excimer lasers has been investigated since the early 1980's. The first applications focussed on fabrication of microelectronic devices. For example, work was done on the deposition of thin metallic films [4], titanium silicide [5], InP [6], Si₃N₄ [7], poly-silicon films [8] and diamond-like films on silicon wafers [9]. Further, very effective reflecting coatings for X-ray mirrors [10] were formed by super-lattices of tungsten and carbon which are needed as optical elements in X-ray microscopes or lithography exposure tools.

Laser sputtering or pulsed laser deposition (PLD) emanated as a novel coating technique. The laser beam evaporates material from a solid target, which condenses on a substrate. Both the target and the substrate are mounted inside a processing chamber where the pressure is typically in the range of 1 Pa. Feeding of a processing gas, e.g. oxygen, can cause specific gas phase reactions. Furthermore, control of substrate temperature has an influence on surface kinetics and can alter structural parameters of the deposited films. The most prominent feature of the PLD technique is the nearly congruent evaporation of multi-element materials where the vapor pressure of the single elements plays a minor role so that transfer of films in stoichiometric composition is possible. By that technique, the first thin films of high-temperature superconductors were prepared [11]. Many other groups worked on PLD of various materials like deposition of LinBO₃ films for waveguides on chips [12] and diamond-like carbon films on silicon [13] using ultrahigh vacuum PLD. The subsequent irradiation of different target materials allows for graded layer fabrication (the concentration of elements changes along a spatial coordinate) or deposition of multilayer systems which are suitable as X-ray mirrors [14]. A survey of investigated materials and prospective applications of PLD can be found in [15] which gives a comprehensive overview of the formation of thin films by PLD.

After more than a decade of steadily increasing basic research and development pulsed laser deposition is now entering industrial applications and will share the market with the existing PVD technologies (pulsed vapor deposition) like thermal evaporation and the sputtering processes. Due to relatively costly equipment, PLD will not rule out conventional physical vapor deposition techniques. First applications arise in the formation of films that are difficult to deposit using conventional technologies like multi-component ceramics (e.g. YBa₂Cu₃O₇ for SQUIDs, SrBi₂Ta₂O₉ or PbZr_{0,52}Ti_{0,48}O₃ for memory

and sensor applications) or thin film deposition with restrictive boundary conditions such as the need for low deposition temperatures (e.g. back end processing on CMOS structures or hard diamond like coatings on polymer surfaces). Further, pulsed laser deposition will be increasingly used for rapid synthesis of new materials as thin films due to the inherent flexibility regarding varying stoichiometry and fabrication of graded layers [16]. For research and small-scale manufacturing, commercial PLD-systems are now available from different manufacturers (e.g. [17, 18, 19]). However, the interest for LCVD and PLD has slowed down because these techniques are hindered by economic barriers since process monitoring techniques are required which deteriorate cost competitiveness [20].

In microelectronics, there is an ongoing transition from aluminum to copper interconnects [21]. Laser dry etching (LDE) has the potential for resistless direct patterning of copper interconnects [22, 23], but many questions concerning the lowest achievable resolution and process compatibility still have to be answered. Moreover, etching of silicon is of great interest for the fabrication of micro-mechanical devices where electronic and mechanical functions have to be integrated on a wafer. LDE of silicon in chlorine atmosphere [24] has been investigated with the intention to obtain reduced process temperatures and preferentially to induce anisotropic etching. Etch rates of about $1 \mu\text{m}/\text{min}$ compared to $0.1 \mu\text{m}/\text{min}$ typical for plasma etching have been reported by a novel method termed microwave-assisted LDE (MALDE) [25]. Despite the conceptual advantages of the photon-assisted technologies, it seems that there is a long way to go before implementation in a production environment.

Surface cleaning by UV laser radiation is a field of research where reports on many promising applications in the electronics industry [26] are available. Cleaning of silicon stencils (masks used for e-beam lithography), magnetic head sliders, optical glasses and mirrors were investigated. Small particles of a few micrometer size, grease, organic contaminations, finger prints and dust have been removed without any damage to the surfaces. Particles are preferably removed with the assistance of thin liquid films [27]. Then, relatively low energy densities are sufficient for an explosive evaporation of liquid films of water or ethanol, which blows away the particles while the surface temperature is kept considerably lower. A large area application is the cleaning of rotogravure cylinders (see chapter 11.2), where residues from the printing process have to be stripped off. This contamination results from paint adhering in the grooves of the chromium-copper-plated rotocylinders. Due to the distinct ablation thresholds of the organic film and the chromium layer, the laser process is capable of cleaning the structured surface very reliably. Wet chemical cleaning and solvent waste can be avoided in this way. Excimer laser cleaning is regarded as an environmentally friendly process which has the potential to replace chlorofluorocarbon (CFC) cleaning when fragile parts are to be treated and small quantities of material have to be removed.

Spectacular results were achieved in the restoration of 17th century paintings which were previously treated unsuccessfully by conventional mechanical and chemical methods [28] (see Fig. 10.2 and Fig. 10.3). Particles, fungi and various organic and inorganic contamination adhering to the paint-protecting varnish film were removed, allowing conservation through mild chemical cleaning. Both paint and varnish have a typical thickness of about 50 µm which is several times higher than the typical ablation depth per pulse of about 1 µm. Careful investigations on model glasses revealed that the ablation threshold and the alteration threshold (inducing cracks) of the corrosion crust turned out to be lower than for the gel layer and the bulk glass [29, 30]. Therefore the excimer laser process is capable of removing crusts without damaging the corroded glass surface. Applying process monitoring, e.g. by laser-induced breakdown spectroscopy (LIBS) [31], allows for precise control of the ablation depth and the identification of different layers. With the joint effort of companies and research institutes [32] this technique has been exploited for the cleaning of paintings, where a LIBS detection system is used for on-line process control [33].



Fig. 10.2. Laser cleaning workstation consisting of Lambda Physik COMPEX 205, LIBS detection system and beam steering and suction device for the restoration of works of art; by courtesy of Art-Innovation b.v., Hengelo, The Netherlands



Fig. 10.3. Partially laser-cleaned (left) and fully cleaned (right) fine arts painting; by courtesy of Dr. V. Zafiropulos (F.O.R.T.H., Greece), M. Doulgeridis (National Gallery of Athens) and Art-Innovation b.v., Hengelo, The Netherlands

Table 10.1 gives an overview of the most relevant excimer laser applications, including industrially realized processes [34] and laser vision correction. The most prominent applications are dealt with in detail later. In addition to the diversified applications of excimer lasers in production, sophisticated measurement techniques have become available. Recently, research concentrated on fluorine laser applications where the high photon energy of the 157 nm radiation leads to efficient bond breaking. Now materials critically to treat like quartz glass, fluorinated polymers (Teflon), and thin diamond films are under the scope of 157 nm laser ablation.

Market watch [35] reports an increase in world-wide sales of excimer laser units in the years 1998 to 2000, followed by a strong drop till the year 2002 (see Figs. 10.4, 10.5). Most of the units are employed in materials processing and in medical therapeutics, a minor market share covers basic research applications. The research market comprises lasers used in universities, research centers and industrial laboratories. In materials processing, the units are used for TFT annealing for flat panel displays, inkjet nozzle drilling, writing of fiber Bragg gratings and in microlithography. Laser vision correction has become a huge consumer market where excimer lasers are needed for photorefractive keratectomy (PRK) and for laser in-situ keratomileusis (LASIK). In year 2000

a phase shift occurred between materials processing and medical applications. Looking only at the number of units, the medical market has overtaken the materials processing market, but the market volume in dollars is nearly 3-times higher for industrial lasers yet. For more data on the excimer laser market see Sects. 1.1 and 1.3.

Table 10.1. Industrial relevant applications of excimer lasers

Application	Approved Laser Source	Comments
Microlithography	NovaLine K2010, K2020 (KrF)	In production
	NovaLine A2010, A2020 (ArF)	β-site testing (demonstration lines)
	NovaLine F1020, F2020 (F ₂)	
Annealing of TFTs	LAMBDA 4308B (XeCl) LAMBDA STEEL 670 (XeCl) LAMBDA STEEL 1000 (XeCl)	In production
Drilling of ink jet nozzles	LAMBDA 4308 (XeCl) NovaLine 100 (KrF)	World-wide approx. 95% of print heads are laser drilled
Marking:		
Material removal	ArF, KrF, XeCl	Identification codes, glass marking
Photochemical marking (change in color)	KrF, XeCl, XeF	SMD's, airplane cables, medical and consumer products
Writing fiber Bragg gratings	LAMBDA L1-FBG (KrF)	High spatial coherence > 1 mm
Micro fabrication:		
Via drilling	LAMBDA 4308B (XeCl) LAMBDA STEEL 670 (XeCl) LAMBDA STEEL 1000 (XeCl)	MCM's, BGA's, FPCB, typically 30 µm vias
Wire stripping	NovaLine 50/100 (KrF)	Wiring of hard disk drives
LCVD and PLD	LAMBDA 4308 (XeCl)/4248 (KrF) LAMBDA STEEL 670 (XeCl) LAMBDA STEEL 1000 (XeCl)	Super conducting films, diamond films
Micro structuring	NovaLine 100 (ArF, KrF)	Shaping & drilling of catheters, structuring of solar cells, micro systems technology
Laser vision correction	OPTex, COMPex (ArF)	PRK and LASIK
Measurement techniques	COMPex (KrF)	Laser induced fluorescence

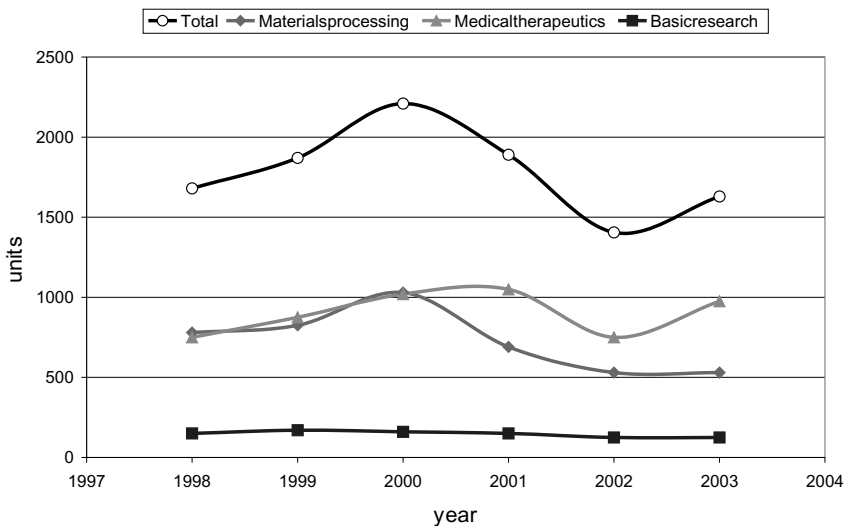


Fig. 10.4. Excimer laser sales in units per year (after [35])

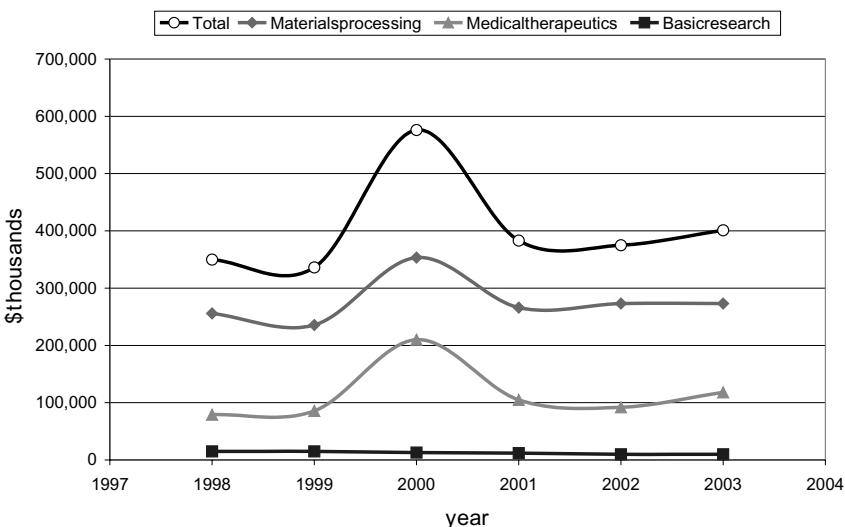


Fig. 10.5. Excimer laser sales in \$ thousands per year (after [35])

References

1. R. Burnham, N. Harris, N. Dieu: Appl. Phys. Lett. **28**, 86 (1976)
2. C. Wang, H. Mirels, D. Sutton, S. Suchard: Appl. Phys. Lett. **28**, 326 (1976)
3. R. Srinivasan: Science **234**, 559–565 (1986)

4. D. Ehrlich, R. Osgood, T. Deutsch: *J. Vac. Sci. Technol.* **21**(1), 23 (1982)
5. A. Gupta, G. West, K. Beeson: *J. Appl. Phys.* **58**(9), 3573 (1985)
6. V. Donnelly, D. Brasen, A. Appelbaum, M. Geva: *J. Appl. Phys.* **58**(5), 2020 (1985)
7. D. Lowndes, D. Geohegan, D. Eres, Pennycook, D. Mashburn, G.J. Jellison: *Appl. Phys. Lett.* **52**, 1868 B 1870 (1988)
8. A. Yamada, A. Satoh, M. Konagai, K. Takahashi: *J. Appl. Phys.* **65**, 4268–4272 (1989)
9. J. Goto, T. Yagi, H. Nagai: “Synthesis of diamond films by laser-induced chemical vapor deposition”, in *Mat. Res. Soc. Symp. Proc.* (1989), no. 129, pp. 213–217
10. M. Katsuhiko, Y. Yamady, T. Iwabuchi, T. Miyata: *J. Appl. Phys.* **68**, 1361–1363 (1990)
11. D. Dijkkamp, T. Venkatesan, et al.: *Appl. Phys. Lett.* **51**, 619 (1987)
12. D. Ghica, M. Gartner, F. Ciobanu, V. Nelea, C. Martin, I.N. Mihailescu: “High optical quality LiNbO₃ thin films obtained by pulsed laser deposition”, in *OPTIKA '98: 5th Congress on Modern Optics / SPIE; Int. Comm. Opt.; Hungarian Nat. Committee for Tech. Dev. Found. Ind.; et al. - 14–17 Sept. 1998. Proc. SPIE - Int. Soc. Opt. Eng. (USA). - Budapest, Hungary* Vol. 3573 (1998), pp. 130–3
13. Y. Yamagata, A. Sharma, J. Narayan, R. Mayo, J. Newman, K. Ebihara: *J. Appl. Phys.* **86**, 4154 (1999)
14. R. Dietsch, T. Holz, H. Mai, C.F. Meyer, R. Scholz, B. Wehner: “High precision large area pld of x-ray optical multilayers”, in *4th International Conference on Laser Ablation / COLA '97, 20.–25.7.97, Monterey, CA* (Applied Surface Science, 1998), no. 127–129, pp. 451–456
15. D.B. Chrisey, G.K. Huber (Eds.): *Pulsed Laser Deposition of Thin Films* (Wiley-Interscience, New York, 1994)
16. I. Takeuchi, H. Chang, C. Gao, P. Schultz, X.D. Xiang, R.P. Sharma, M.J. Downes, T. Venkatesan: *Appl. Phys. Lett.* **73**, 894 (1998)
17. Epion corporation, Boston, USA,
<http://www.epion.com/PLD%20Products.htm>
18. Surface, Hueckelhoven, Germany,
<http://www.surface-tec.com/>
19. Neocera, Beltsville, USA,
<http://www.neocera.com /html-files/pld/systems.htm>
20. E. Lerner: *Laser Focus World* **12**(35) (1999)
21. P. Burggraaf: *Solid State Technology* p. 31 (2000)
22. W. Sesselmann, E.E. Marinero, T.J. Chuang: *Appl. Phys. A* **41**, 209–221 (1986)
23. S. Küper, K. Brannon, J. Brannon: *Laser Ablation of Electronic Materials* (Elsevier Science Publisher B.V., 1992), 213–220
24. W. Sesselmann, E. Hudeczek, F. Bachmann: *J. Vac. Sci. Technol. B* **7**, 1284–1294 (1989)
25. W. Pfleging, D.A. Wesner, E.W. Kreutz: “CCl₄-assisted CF₄ etching of silicon in a microwave-assisted LDE (laser dry etching)-process”, in *Laser Ablation. Symposium F: Third International Symposium on Laser Ablation (COLA'95) 1995 E-MRS Spring Conference / Council of Eur.; Comm. Eur. Communities. - 22–26 May 1995. In: Appl. Surf. Sci. (Netherlands). Vol. 96–98, April 1996* (Strasbourg, France, Netherlands: Elsevier, 1996), pp. 496–500

26. Lambda Highlights No. 47, May 1995, Publication by Lambda Physik
27. A.C. Tam, et al.: *J. Appl. Phys.* **71**(7) (1992)
28. E. Hontzopoulos, C. Fotakis, M. Doulgeridis: in *Proc. SPIE* Vol. 1810 (1992), p. 749
29. C. Troll, H. Römich, K. Dickmann, J. Hildenhaben: “Cleaning of corrosion crusts on stained glass windows with excimer lasers”, in *Proc. of 12th Triennial Meeting of the ICOM COMMITTEE FOR CONSERVATION, Lyon, France, 29. August – 3. September 1999*, Vol. 2 (1999), pp. 816–820
30. K. Dickmann, F. Fekrsanati, S. Klein, H. Römrich, C. Troll, U. Drewello: *Laser Magazin* **2**, 9–13 (1999)
31. S. Klein, T. Stratoudaki, V. Zafiroopoulos, J. Hildenhaben, K. Dickmann, T. Lehmkuhl: *Appl. Phys. A* **69**, 441–444 (1999)
32. European research project (CRAFT) “Advanced workstation for controlled laser cleaning of artwork” (ENV4-CT98-0787)
33. <http://www.art-innovation.nl/>
34. H. Endert, M. Kauf, R. Pätzelt: *Laser Opto* **31**(4), 46–53 (1999)
35. K. Kincade, S.G. Anderson: *Laser Focus World* **35** (2000)–**39** (2003).
see also Pennwell’s archive: <http://lfw.pennnet.com/Articles/>

11 Ablative Micro-Fabrication

11.1 Ablation

M. Wehner

Due to their high photon energy between 3.5 eV (351 nm) and 7.9 eV (157 nm), the excimer laser radiation is strongly absorbed by molecules via electronic transitions into an excited state. Examples are C=C double bonds or the carbonyl group C=O. Table 11.1 shows the excitation energies of some important groups in polymers. The absorption is correlated to transitions between certain electronic states. The molecules acting as absorption centers are often called “chromophores”. When these chromophores are part of a conjugated chain, the transition energies are broadened and shift to lower values. The wavelengths mentioned in [1] should, therefore, be considered as the typical center wavelength for absorption. Materials containing these groups are expected to strongly absorb UV laser radiation. That confirms the observation that, for example, polyimide containing benzene rings and carbonyl groups show a very strong absorption whereas PTFE (polytetrafluoroethylene) lacking these groups is very hard to attack. The excited molecules can reach an unstable state when the excitation energy equals the binding energy of electrons forcing the molecules to fragment (model of bond breaking). If the molecule is part of an ensemble (or solid), rapid thermal degradation is more likely, the excess energy is then converted into vibration, rotation and translation of surrounding molecules. The absorbed laser energy leads to rapid heating of the bulk material, and when the energy density (or temperature) is sufficiently high, fragmentation occurs where small volatile molecules may be formed. The high vapor pressure then results in explosive evaporation and the formation of a blast wave.

Table 11.1. Wavelength, photon energy and transition energies of chromophores

Group	Photon Energy [eV]	Peak Wavelength [nm]	Related Excimers
C = C	6.9 - 7.75	160 – 180	ArF, F ₂
C = O	6.7 , 4.2	185, 295	ArF, KrF, XeCl
- NO ₂	4.4, 5.9	280, 210	ArF, KrF, XeCl
- N = N	3.5, > 4.8	350, < 260	XeF, ArF, KrF
Benzene Ring	4.9, 6.2, 7.75	180, 200, 255	ArF, KrF, F ₂

E = hc/λ, that means 1 eV binding energy = 1.24*10⁻⁶ m photon wavelength

When the laser beam irradiates the surface of a material, a fraction corresponding to R is reflected; the penetrating radiation is absorbed inside the bulk material where the intensity decreases for linear absorption corresponding to Beer's law:

$$I(x) = (1 - R) I_0 e^{(-\alpha x)}$$

I_0 : intensity at surface $x = 0$
 α : absorption coefficient
 R : reflectance

(11.1)

The inverse of the absorption coefficient can be regarded as the optical penetration depth after which the intensity has fallen to $1/e$ of the incoming value. In the model of ablative photo decomposition proposed by R. Srinivasan [2], the radiation is absorbed by the chromophores. When the density of the excited chromophores exceeds a certain threshold, the large molecules are fragmented in small volatile species which escape from the bulk with high velocity taking away most of the absorbed laser energy. As the laser intensity inside the bulk decreases corresponding to Beer's law, the density of the excited chromophores decreases as well, until the threshold ϵ_τ for decomposition is approached in a certain depth h . Re-arranging Beer's law and introducing the expression $\epsilon = I * \tau$ (τ : laser pulse length), the ablation depth can be described as a function of two material parameters α and ϵ_0 , and laser fluence ϵ :

$$h = \alpha^{-1} \ln \left(\frac{\epsilon}{\epsilon_0} \right) \quad \epsilon_0: \text{threshold fluence}$$
(11.2)

For practical reasons, the term $(1 - R)$ is omitted, since the reflectance R is typically 0.05 for polymers at normal incidence. A typical etch plot is depicted in Fig. 11.1 where ablation of polyimide is shown for different wavelengths.

The ablation rate is well below $1 \mu\text{m}/pulse$, which means it is possible to remove layers as thin as some 100 nm by a single pulse. The equation 11.2 fits to a straight line in the semi-logarithmic plot of the data; numerical evaluation of the data points allows the derivation of α and ϵ_0 . This simple model is in reasonable agreement with the experimental results for many polymers at low fluences ($\approx 10 \epsilon_0$), however deviations can occur at higher fluence which lead to a steeper (cf. data points 308 nm Fig. 11.1) or flatter (cf. data points 193 nm Fig. 11.1) slope. The reasons for this can be found in photochemical processes influencing absorption properties and degradation kinetics, which will not be discussed here in detail. In general, the ablation rates depend on the material, the wavelength, the ambient atmosphere and the geometry of the beam. Examples will be given in the following chapter.

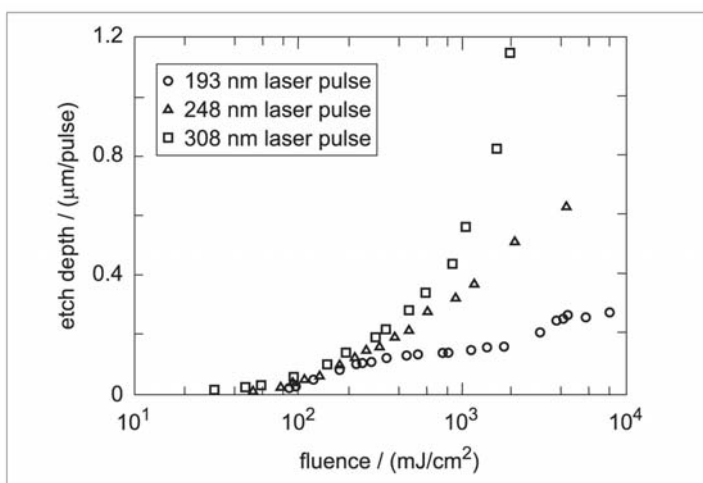


Fig. 11.1. Ablation of PI (polyimide = Kapton) by radiation of different wavelengths [3]

A remarkable feature observed is the formation of an ablation plume in front of the irradiated surface. When the laser beam hits the surface, soon after expulsion of material in the form of gases, clusters and particles appear. High-speed frames show that some ns after the leading edge of the laser pulse, vaporization starts and a shock wave expands. During the pulse duration of an excimer laser of typically $10 \text{ ns} - 30 \text{ ns}$ FWHM, there is an interaction between the laser radiation and the hot material.

At high fluences, the shock front partly absorbs the incoming radiation thereby shielding the sample material. Then the efficiency of the ablation process declines which was confirmed in case of the ablation of metals [4]. After some 100 ns , emission of larger particles forming a dense cloud oc-

curls [5]. Depending on the beam parameters and the ambient atmosphere, a re-circulation fan can be formed which transports the particles back to the surface. This is a highly unwanted effect because the re-deposition of material (“debris”) leads to a contamination of the surface near the ablation site. Under certain circumstances, the formation of conical structures may be introduced by high threshold residues (particle contamination) spreading over the ablation area. The particles sitting at the top of the cones protect the underlying material from radiation.

To understand the influence of the thermal and optical properties of materials, a simple model will be discussed assuming the coefficient of thermal diffusivity as constant, being unaffected by temperature effects and phase transitions. If the absorption takes place in an infinitesimal thin layer (surface absorber), the temperature rise in the bulk can be described by a simple expression:

$$T(x, t) = T_0 \operatorname{erf} \left(\frac{x}{\sqrt{2\kappa t}} \right)$$

T_0 : surface temperature
 κ : coefficient of temperature diffusion
 erf : error function

(11.3)

The term $2\kappa t$ can be designated to a thermal diffusion length which is defined by the coefficient of thermal diffusivity κ , which is a physical property of the material, and the time span t , since the surface has reached temperature T_0 .

The energy transport inside the material is effected by two processes: the energy transport by photon diffusion and heat conduction. The depth which is affected by the laser beam depends on the material’s properties and the laser pulse duration. In Table 11.2 estimations of the optical penetration depth and the heat diffusion length are given. The transition from metallic behavior to the transparent region passes the region of strong absorbers, when both the optical penetration depth and the heat diffusion length are in the sub-micrometer range. Ablation of materials belonging to that group results in clean structures with minimal thermal degradation.

As the absorption coefficient α is strongly wavelength dependent in the UV, ablation can be very different at the various excimer wavelengths.

For example, fused silica can hardly be ablated by 248 nm radiation while 193 nm ablation is possible and 157 nm ablation gives excellent quality [6].

Table 11.2. Optical penetration depth α^{-1} and heat diffusion length $l_{30\text{ ns}}$ for different materials, examples for ablation with 248 nm radiation and 30 ns pulse duration [7], [8]. Abbreviations: PI = polyimide, PET = polyethylene-terephthalate, PC = polycarbonate, PE = polyethylene, PMMA = polymethyl methacrylate

Material	$\alpha^{-1} [\mu\text{m}]$	$L_{30} = 2\sqrt{k\tau} [\mu\text{m}]$ ($\tau = 30\text{ ns}$)	Ratio $k_E = \alpha^{-1}/L_{30}$	Material Characteristics
Aluminum	0.007	3.3	0.002	Metallic behavior $k_E < 0.01$
Silicon nitride	0.06	1.0	0.06	Strong absorber
Alumina	0.08	0.8	0.1	$0.01 < k_E < 10$
PI	0.07	0.16	0.4	
PET	0.1	0.14	0.7	
PC	0.2	0.13	1.5	
PE	6	0.16	38	Weak absorber
PMMA	16	0.11	145	$10 < k_E < 1000$
Quartz glass	$> 10^8$	0.32	$> 10^8$	Transparent region $1000 < k_E$

The nature of ablative photo decomposition is discussed controversially in the literature, models describing a purely photochemical model [2] are proposed or evidence for a thermal nature [9] is given. Regardless of the exact mechanism of the ablation process, the technique to evaluate the absorption coefficient from etch plots gives a phenomenological characterization of the ablation process and has proved to be very useful in comparing results obtained under different experimental conditions. From the correlation of surface quality and absorption coefficient, it can be concluded that the term “strong absorber” coincides with the ability to obtain high quality microstructures with precise definition of the edges and a smooth surface profile, where thermal side effects can be ignored. That is the case when

- i The absorption coefficient is sufficiently high $> 10^4\text{ cm}^{-1}$
- ii The heat diffusion length does not exceed the optical penetration depth α^{-1}

From the rules above it is very easy to conclude whether a material is suited for micro-structuring by excimer lasers. Condition 1 can be tested in a simple “etchplot experiment” or derived from literature. Condition 2 is fulfilled for polymers and roughly valid in case of ceramics.

References

1. P.W. Atkins: *Physical Chemistry* (Oxford University Press, data taken from J.G. Calvert and J.N. Pitts, Photochemistry, Wiley, New York, 1966)

2. R. Srinivasan: *J. Vac. Sci. Technol.*, B(4), Oct–Dec. 1983 pp. 923
3. R. Srinivasan: “UV laser ablation of polymers and biological tissue”, Lambda Highlights No. 1, October 1986, Publication by Lambda Physik
4. R. Poprawe: “Materialbearbeitung und Plasmaformation im Strahlungsfeld von UV-Lasern”, Thesis D17 Darmstadt 1984, Fachbereich Physik der Technischen Hochschule Darmstadt
5. R. Srinivasan, B. Braren, K.G. Casey, M. Yeh: Applied Physics Letters (1990)
6. U. Stamm, M. Fiebig, S. Govorkov, E. Mayer, R. Osmanov, M. Scaggs, E. Slobodchikov, A. Wiesner, D. Basting: “Novel results of laser precision microfabrication with excimer lasers and solid-state lasers”, in *Proceedings, 1st International Symposium on Laser Precision Microfabrication*, SPIE, Omiya, Saitama, Japan (2000)
7. M. Wehner: “Werkstoffbearbeitung mit Excimerlaser-Strahlung”, Thesis, Aachen: Verlag der Augustinus-Buchhandlung, 1991. – ISBN 3-86073-002-9
8. M. Aden, D. Wesner: “Strömungsmechanik des Plasmamaterialtransfers bei der Ablation mit UV-Laserstrahlung”, research report Fkz 13 N 6843/4, German Ministry for Education and Science
9. J.E. Andrews, P.E. Dyer, D. Forster, P.H. Key: Applied Physics Letters **43**(8), pp. 717 (1983)

11.2 Micro-Machining

M. Wehner, J. Ihlemann

This chapter discusses techniques by which parts – or features on parts – are fabricated by removal of material. In general, the energy of the laser beam is absorbed in a thin layer or small volume and the ablation process takes place through rapid fragmentation. Depending on the wavelength and the material, this can have the characteristics of ablative photo decomposition (e.g. ablation of polyimide) or rapid heating and vaporization associated with melt expulsion (e.g. drilling of metals or oxide ceramics).

Depending on the material, particular wavelengths and fluences are recommended to achieve best results. In Table 11.3 typical fluences are listed which result in high ablation rates and assure good quality. As discussed before, the efficiency of the ablation process rises when fluence is increased reaching a more or less pronounced maximum. At high fluences, the emerging hot material in the expanding plume could have detrimental side effects on fine structures because edges are getting smoothed. This can be a reason for keeping the “optimum” fluence below the fluence with the highest efficiency for ablation. As in case of polymers, the ablation depth is correlated to the optical penetration depth, the highest ablation rates are achieved with long wavelengths. Therefore, longer wavelengths are preferred if they assure a reasonable quality. The differences in surface quality vanish in the ablation of ceramics, but the ablation rates are higher for 308 nm than in the case of 248 nm or 193 nm radiation. For practical reasons, 248 nm is a good choice for processing ceramics. Materials which are transparent or weakly absorb-

Table 11.3. Typical ablation depths and fluences for polymers and ceramics [1, 2]

Material	Wavelength [nm]	Fluence [J/cm ²]	Ablation Depth / Pulse [μm]
Polycarbonate (PC)	248	4.0	0.40
Polyester (PES)	248	4.0	0.80
Polyethylene (PE)	248	3.7	1.0
	193	6.0	0.4
Polyimide (PI)	308	0.3	0.10
	248	0.7	0.30
Alumina	193	45	0.06
	248	45	0.19
	308	25	0.17
Zirkonia	248	10	0.12
Boron nitride	193	20	0.15
Silicon nitride	248	10	0.18
Silicon carbide	248	10	0.13
Piezoelectric ceramics (PZT)	248	5.0	0.05
	308	5.4	0.20

ing at 248 nm and 308 nm wavelength may require 193 nm or 157 nm laser radiation for ablation, as for example fused silica or PTFE.

11.2.1 Processing Techniques

M. Wehner

In excimer laser technology, usually a mask projection scheme is applied to illuminate the sample. For low fluence applications, metal masks can be placed directly on the sample to shape the beam (contact mask technique). This set-up is very simple and requires just a few optical elements, but the fluence is limited to the ablation threshold of the mask material, typically to $\epsilon < 0.8\text{ J/cm}^2$. The conformal mask mode is a specific arrangement where the mask is created by a metal layer on top of the sample. The top layer is structured, for example, by a lithographic technique and defines the areas where the insulation has to be removed. This process has been employed industrially to manufacture the contact holes between subsequent metal layers (blind vias) in multilayer boards for computers [3]. A principle drawback of using contact masks is the direct contact between the mask and the sample. In a non-touching variation, the mask is positioned in close proximity to the sample (proximity mask technique) such that there exists a small gap. The resulting sharpness of the edges depends on the span of the gap and the divergence of the illuminating beam. A resolution in the $100\text{ }\mu\text{m}$ range is easily obtained and, therefore, it is a convenient method for marking products and for the shielding of particular areas in large area processing.

Higher fluences or better spatial resolutions are feasible using imaging optics. A carefully designed system allows for a working field of several millimeters in diameter and a resolution better than two microns. The layout considerations of the optical system rely on the energy and the required fluences (see Chap. 9). The necessary precision of the masks depends on the

Table 11.4. Comparison of various mask fabrication techniques; (SS: Stainless Steel; RIE: Reactive Ion Etching); by courtesy of ILT

Technique	Single Pulse Threshold [J/cm^2]	Average Power Limit [W/cm^2]	Resolution [μm]	Costs
Laser cutting ($200\text{ }\mu\text{m}$ SS foil)	> 1	> 10	< 10	low
Lithography & wet chemical etching ($100\text{ }\mu\text{m}$ SS foil)	> 0.8	> 5	< 20	low
Chrome on quartz	> 0.5	< 5	< 2	moderate
Dielectric masks	> 1	> 50	< 2	high

required resolution and the demagnification ratio of the set-up. Masks can be produced by laser cutting, etching or lithographic techniques; Table 11.4 lists the features of the different fabrication techniques. Dielectric masks are distinguished from others by outstanding load capacity and excellent edge definition, but the costs are high compared to other techniques. A mask projector can be operated in two different processing modes (cf. Fig. 11.2):

step-and-repeat mode

- The size of the mask is smaller than or equals the beam size.
- The workpiece is at rest.
- The laser fires a sequence of pulses to engrave a structure.
- The workpiece is offset and then the laser fires again.
- The whole area is covered consecutively by imprints.

conformal scanning

- The size of the mask is much larger than the laser beam.
- The workpiece and the mask are moved simultaneously while the laser beam is fixed.
- The laser fires permanently while mask and workpiece are scanned.
- The velocity of the workpiece is smaller than the velocity of the mask corresponding to the demagnification ratio.

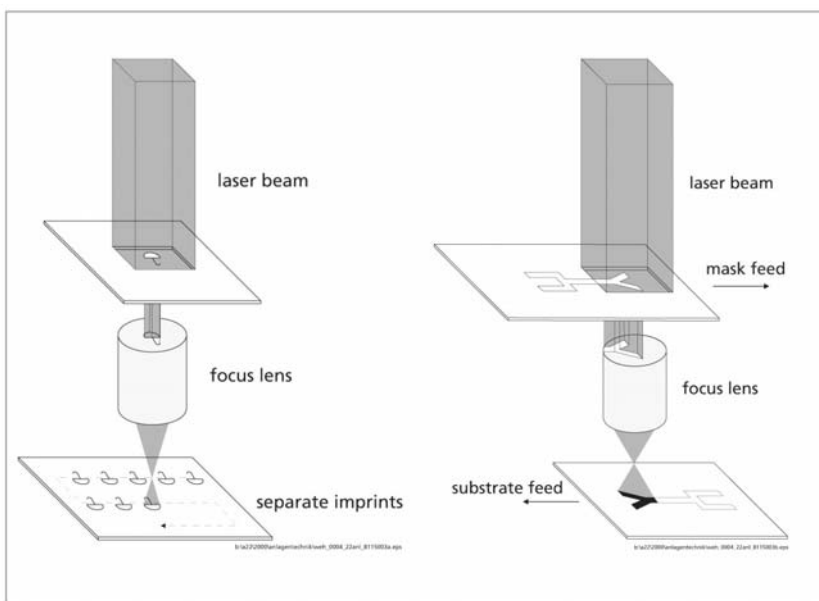


Fig. 11.2. Principle of subsequent processing in step-and-repeat mode (left) and conformal scanning (right); by courtesy of ILT

For step mode operation a stable positioning system is required with an accuracy depending on the desired position accuracy of structures. The overall dimension of an arbitrary pattern is restricted to the size of the working field. Larger patterns have to be combined from subsequent imprints. The adjustment of the offset between different imprints is critical because edge effects lead to inhomogeneous transitions in the form of ripples. In the conformal mode, that restriction does not exist; extended structures can be reproduced without any disturbances or edge effects. In practice, the working field is only limited by the travel range of the translation stages. However, the demands on the positioning system are more severe because precise speed control and laser synchronization are required to ensure homogeneous processing. Technical solutions are available using advanced control techniques, but the investment costs are higher than for simple point-to-point positioning systems.

A disadvantage of mask techniques is caused by the fact that, in most cases, the ratio of open to opaque areas is relatively small. That results in a low overall efficiency when comparing the energy at the workpiece to the totally delivered laser energy. To circumvent this drawback, sophisticated mirror designs have been evaluated, where the beam is reflected from the opaque sites of the mask and directed back by a special optical arrangement (cf. Fig. 11.3). In the case of micro-hole arrays, just a small portion of the beam is "lost" by the openings and the laser energy ping-pongs inside the illuminator. An increase of efficiency by more than a factor of 6 was achieved for nine roundtrips compared to standard single pass illumination [4]. The

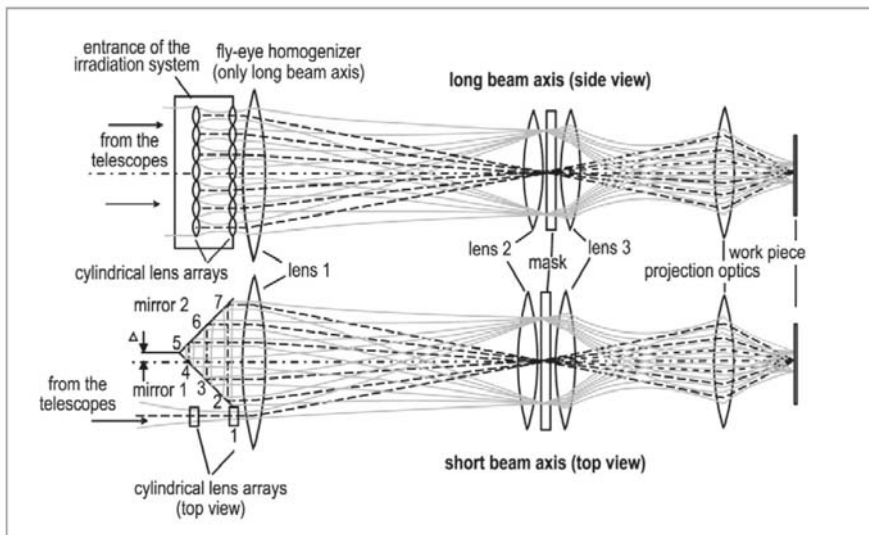


Fig. 11.3. Operational diagram of the multipass-illuminator [4]

time delayed addition of the subsequent beam passes forms a resulting pulse with approximately four times the peak fluence and temporal broadening from about 30 ns FWHM (full width half maximum) to 80 ns FWHM. The achieved ablation rates and the hole quality are not distinct from single pass drilling using the same total fluence.

For small field applications (drilling single holes) a more simple set-up can be used (cf. Fig. 11.4). The beam is expanded by a factor of 2 to 3 in the short axis and illuminates an aperture which is imaged by a demagnification ratio of typically 5:1 (polymers) to 30:1 (ceramics). Fine tuning of the optical elements allows the precision to drill through-holes without the need for a homogenizer. A small workstation can be realized by feeding the beam into a microscope by an additional dichroic mirror similar to the illumination source and using the objective for beam focussing. Here a specially designed UV objective lens or reflecting Schwarzschild optics can be applied. Simply, the translation stage is manually moved in position which is watched by the operator through a binocular viewing head, and then the laser is fired. Also, the procedure can be automated using an electrically actuated translation stage and a video camera in conjunction with image analysis software. This type of set-up, for example, allows biologists to perform in-vitro experiments on living cells where the laser beam perforates the outer sheath (zone drilling) to permit DNA transfer directly into the cell. Small openings of micron (μm) size can also introduce fusion of cells. Further, laser micro-dissection permits preparation of microscopic amounts of tissue material for biopsy, cut out by the laser beam under visual control [5]. Laser micro techniques have improved new techniques in replication medicine where sperms unable to penetrate could be fed into the oocytes through laser-drilled openings.

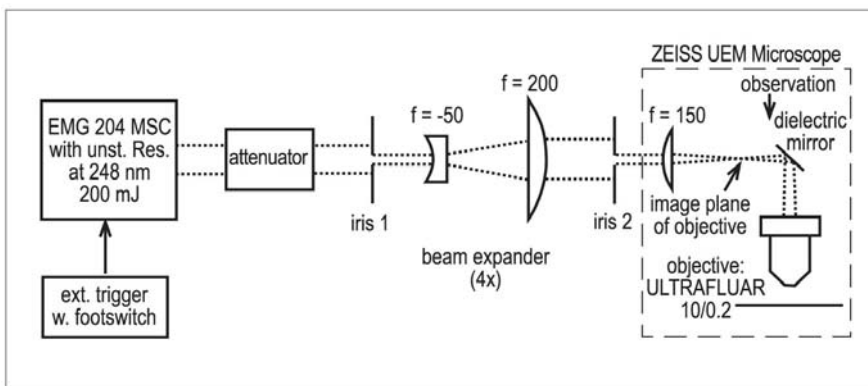


Fig. 11.4. Simple set-up for drilling of single holes [6]

11.2.2 Removal of Thin Layers

M. Wehner

In many technical areas polymer films on metal substrates are used for insulation or as a protective coating. Here processes are concerned where a layer in a predefined thickness is to be removed and the laser beam illuminates a small area or is scanned across a large area. For example, thin wires of down to $50\text{ }\mu\text{m}$ diameter are used to contact read heads in magnetic disk drives or ultrasonic transducers in medical ultrasonic systems. Mechanical stripping is an impossible task and chemical stripping has drawbacks due to corrosion problems when it has to be integrated into a production line. A 248 nm ablation process has turned out to be the winning solution [7]. The distinct difference in ablation thresholds offers the possibility for selective material removal, because the threshold for ablation of polyurethane with 248 nm radiation is around 0.1 J/cm^2 and the threshold for copper near to 0.8 J/cm^2 . Working between these two levels allows for selective removal of only the polymer which leads to a self-limiting process. Here only a simple set-up is needed where the tip of the wire is irradiated by two or three beams impinging from different directions. The length of the stripped part can then be defined by a proximity mask attaining a good edge definition and clean removal of the insulation (cf. Fig. 11.5).

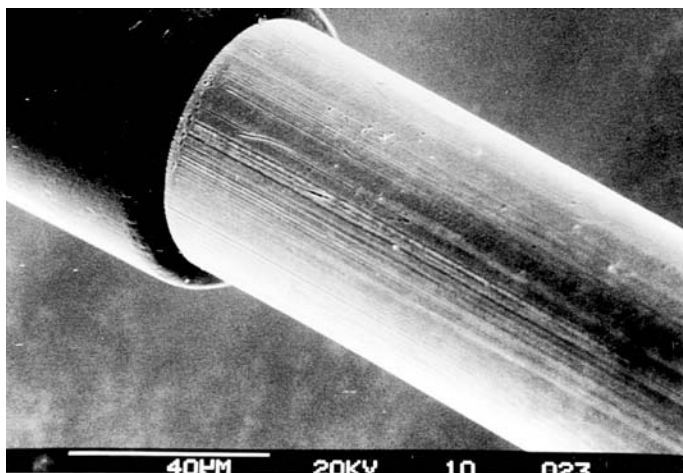


Fig. 11.5. A $50\text{ }\mu\text{m}$ copper wire with the insulation stripped off by 248 nm radiation [2]

Cleaning of rotogravure cylinders is a newly evolved large area application for excimer lasers. Traditionally, the cylinders are cleaned from paint residues by chemical solvents. Here laser technology can offer a more environmentally

friendly procedure. A prototype installation (Fig. 11.6) has been successfully tested for effective removal of the paint without destroying the underlying chromium layer. The beam of a KrF laser is expanded by an anamorphotic telescope and fed by beam steering mirrors through a homogenizer to a zoom lens (see Fig. 11.7). The zoom lens is used to correct the beam size when the path length between the laser and the homogenizer is shifted during processing of long cylinders. Further the beam size and the fluences can be adjusted to different requirements. The cleaning is performed as the rotogravure cylinder rotates while the focussing optics are slowly moved along their axis. Then the whole surface of the cylinder is covered following a spiral trajectory. An



Fig. 11.6. Prototype installation for the cleaning of rotogravure cylinders; by courtesy of ILT

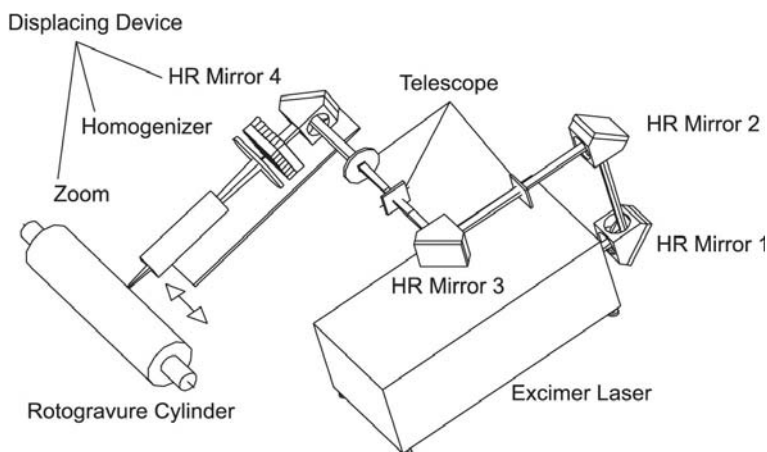


Fig. 11.7. Principal diagram of the optical set-up; by courtesy of ILT

integrated distance sensor automatically matches the position of the optics to the diameter of the cylinders and the surface is continuously monitored to calculate the required pulse number per site which helps to speed up the process. Depending on the type and thickness of residues, a processing speed of $2\text{ m}^2/\text{h}$ to $8\text{ m}^2/\text{h}$ has been obtained using an excimer laser of 150 W average power [8].

One further application with the base of removing thin layers with excimer lasers is manufacturing of finest electrical paths for various technical fields. For example, electrodes for capacitive sensor components are manufactured by scribing techniques. Therefore the excimer laser beam is limited by a rectangular mask. That geometry is imaged onto the workpiece. By moving the bulk material under the stationary laser beam, the wished electrode is structured. In the shown example (Fig. 11.8) a glass substrate is covered with a micrometer thin, conductive layer. Ablating material with the laser produces the insulating areas between fine electrodes. In a post-processing step copper electrodes are manufactured for contacting the sensor while use.

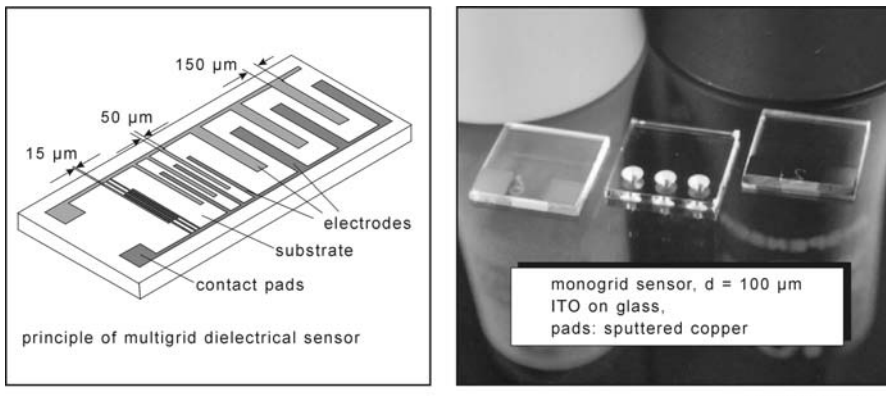


Fig. 11.8. Dielectrical sensor, ITO on glass removed with 248 nm

Those dielectrical sensors are used for capacitive measurement of fluid states. For example curing polymers within moulds change their dielectrical behaviour during their hardening. Using sensors, the curing during the production of polymer parts can be controlled for faster production and quality control for safety relevant products.

11.2.3 Drilling

M. Wehner

When the depth of an ablation site becomes comparable to or exceeds the diameter of the beam, the process is usually referred as drilling. As a measure

for the geometrical shape, the ratio of the length to the diameter of the channels (aspect ratio) can be taken. Depending on the application, the channels can perforate the material (through hole) or stop after a certain depth (blind hole). In most cases the holes have a circular cross-section similar to that obtained when they are drilled mechanically. As a mask is usually employed for excimer laser machining, the cross-section can be any pattern defined by the mask, for example rectangular (see Fig. 11.9).

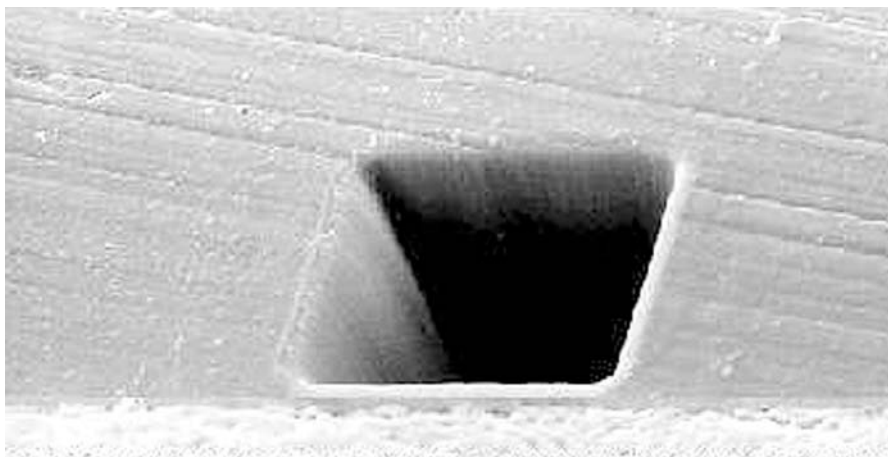


Fig. 11.9. Nozzle with $40\ \mu m$ square - cross-section drilled in Vacrel[®] by KrF laser radiation; by courtesy of ILT

The shape and the maximum depth of holes depend on the fluence applied and the optical set-up. The numerical aperture (NA) of the imaging lens is related to the depth of focus (DoF), where the DoF scales inversely with NA^2 . This could limit the length of a channel when the beam has a high divergence. For example, a wavelength of $248\ nm$ and an imaging lens of $0.1\ NA$, which is quite low compared to lithography lenses, provides a DoF of approx. $25\ \mu m$. In practice, the restriction is not so severe as it seems at first glance. In contrast to lithography, sub- μm resolution are usually not required, which enlarges the useful range. Further, the beams are reflected by the side walls of the hole because they strike at under nearly grazing incidence. This provides the possibility of drilling deep holes with aspect ratios of up to 40, but also it adds a certain tolerance to the geometry and the need to carefully adjust the laser beam parameters. When the beam travels along the channel, small changes in surface roughness or deviations of the wall angle influence the direction and the intensity of the reflections. The beam is guided inside the channel like in an optical waveguide, but fluctuations of the inner surface cause small changes in direction which could affect the straightness of the bore. The length of the channels is limited by the fact that the vaporized

hot material has to be driven out. The kinetic energy of the vapor and the particles has to be sufficiently high to escape from the bore, otherwise the ablated material re-condenses at the side walls and the drilling process stops.

The geometry of the upper part of the bore can be described by a simple model, where the wall angle is defined by the incidence of rays, the resolution of the optical system, the laser fluence and the threshold for ablation [9]. When starting drilling, the beam hits the surface and the angle of incidence is roughly normal to the surface with deviations corresponding to the *NA* of the optics. Regarding the entrance funnel of a hole, the incoming radiation is reflected from the side walls near the edge (depth $z = 0$) to hit the opposite side wall in depth $z = h_1$ (cf. Fig. 11.10):

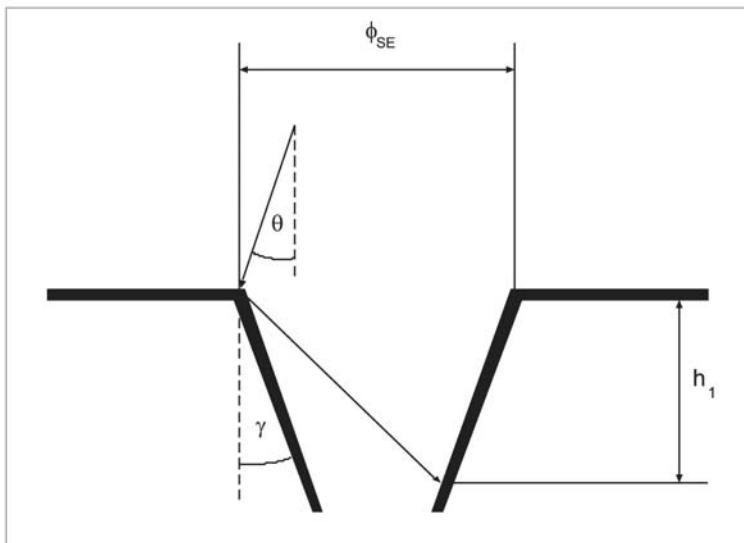


Fig. 11.10. Reflection of the laser beam from the edge of a hole impinging in depth h_1

In the deeper part of the hole, the reflections from side walls have to be taken into account. The depth h_1 , up to which the shape is unaffected by reflected beams can be calculated as follows:

$$h_1 = \frac{\Phi_{SE}}{2} \cot \gamma \left[\frac{\cot \gamma - \cot(2\gamma + \theta)}{\cot \gamma + \cot(2\gamma + \theta)} - 1 \right]$$

with: γ : wall angle

θ : angle corresponding to NA of optics

Φ_{SE} : hole diameter at entrance

(11.4)

When the depth of a hole increases by applying subsequent pulses, the side walls approach an angle where the effective fluence matches the ablation threshold. Under that presumption, the wall angle γ is given by:

$$\sin \gamma = \frac{\epsilon_0}{\epsilon}$$

with: ϵ : fluence
 ϵ_0 : threshold fluence

(11.5)

Combining equations 11.4 and 11.5, the wall angle and the depth h_1 can be calculated depending on the ablation threshold, which relies on material and wavelength, and the hole diameter. To illustrate this model, the results for the drilling of diamond are given in Fig. 11.11 where the wall angle and the aspect ratio are depicted. The calculation has been carried out for the wavelengths 193 nm (ArF), and 355 nm (third harmonic generation of solid state lasers, THG) where experimental results for the threshold fluence ϵ_0 were used. With high fluences, wall angles of less than 2° can be obtained, where a shorter wavelength results in a smaller angle due to the lower ablation thresholds. The aspect ratio is calculated to be in the range from 10 to 25, describing the entrance funnel before entering the “waveguide” region. Using that model, one has to consider that arbitrary high fluences are often not applicable, because the interaction of the laser beam with the hot material can lead to the formation of detonation waves, which deteriorates edge definition. Designing a workstation could pose other restrictions due to de-magnification factor, beam forming and field size. For practical reasons, a fluence of 100 J/cm² should be regarded as an upper limit.

The hole geometry in the transition regime depends strongly on the laser fluence and the material properties. If the upper part of the channel remains stationary, that means $\epsilon \sin \gamma_0 < \epsilon_0$, the angle of incidence may change after the first reflection such that the fluence impinging at the opposite wall will exceed the ablation threshold $\epsilon_{R1} \sin \gamma_1 > \epsilon_0$. Then ablation takes place from the side walls, forming an inverse funnel which corresponds to a widening of the bore (negative wall angle). This effect is most striking in the case of polymers (cf. Fig. 11.12), but has also been observed for the drilling of diamonds. When blind holes are drilled, the first reflection often leads to the formation of a small groove at the bottom of the hole near to the wall. Cross-sections of holes then exhibit a slight “W”-shape in depth.

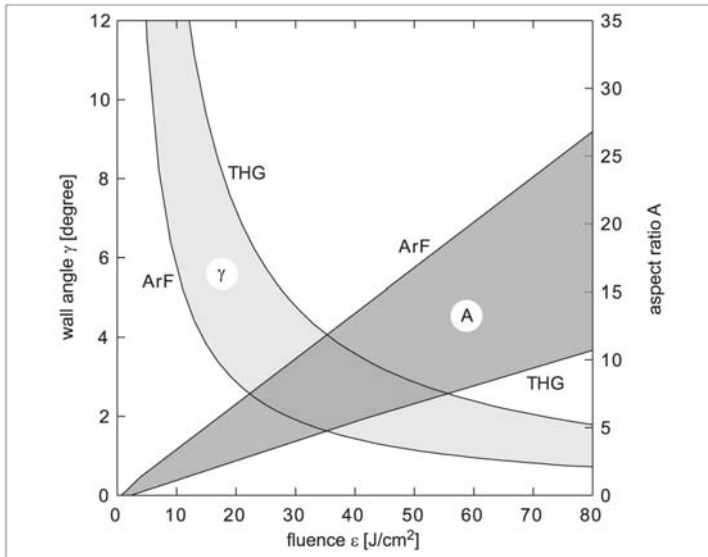


Fig. 11.11. Diagram describing the wall angle and maximum aspect ratio of the entrance funnel of a laser-drilled hole (Example: Drilling of natural diamond by ArF (193 nm) and THG (355 nm) radiation); by courtesy of ILT

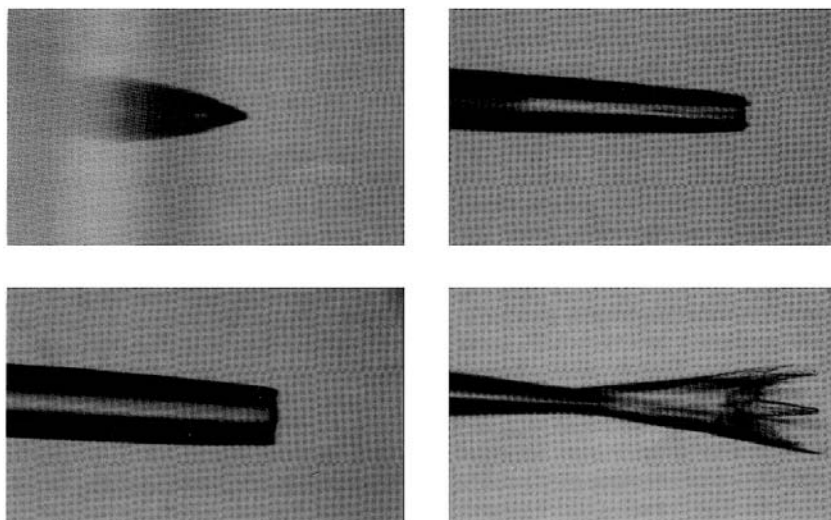


Fig. 11.12. Variations of the hole shape when drilling PMMA (polymethyl-methacrylate) by an ArF laser: upper left: 0.3 J/cm² depth is limited; upper right: 0.8 J/cm² deep hole drilling; lower left: high-energy density 2.2–3 J/cm²; lower right: 0.6 J/cm² transition regime with inverse funnel [10]

In summary, the shape of deep laser-drilled holes can be divided into three distinct sections:

- i A funnel-shaped upper part (beam entrance), where the wall angle is primarily defined by the beam parameters
 - robust processing with high reproducibility.
- ii A transition regime, where large geometrical deviations can occur induced by reflections from side walls
 - wide variation of geometry, obligates careful control of process parameters.
- iii The trail into the bulk, where the beam is guided by multiple reflections and the energy of the beam and material properties become important
 - drilling of holes with high aspect ratio, higher tolerances in geometry.

Polymers. Precise drilling and ablation of polymers has evolved into a prime task for excimer lasers. As mentioned before, the ablative photo decomposition of polymers by UV radiation is a unique feature enabling precise structuring. Although frequency-converted solid state lasers have became available, wavelengths of 355 nm (THG, third harmonic generation) and 266 nm (FHG, forth harmonic generation) are for many polymers not appropriate. The shorter wavelengths of excimer lasers are more strongly absorbed and, therefore, better suited for precision machining. Ultimate edge definition and surface quality is only guaranteed when working in the “strong absorber” regime (see chap. 11.1) that cannot be reached for most materials when working with wavelengths of 266 nm and above. In the following chapters, some of the industrially relevant processes like drilling vias in printed circuit boards or drilling of ink jet nozzles for office printers will be treated in detail.

For medical devices and non-permanent use inside the body, various polymer materials have been approved by FDA (U.S. Food and Drug Administration) and European regulations. Catheter tubings are often made from polyethylene (PE), polypropylene (PP), polyamide (PA) and polyurethane (PU). Small openings for the delivery of drugs are usually cut, but holes in multi-lumen catheters made by cutting or punching suffer from poor accuracy due to the movement of the flexible material under the applied forces. In a comparative study [11], a laser drilling process was investigated as an alternative. Irradiation by ArF laser radiation results in ablation rates of typically $0.5\text{ }\mu\text{m}$ per pulse, whereby PU is in the lower range ($0.3\text{ }\mu\text{m}$ to $0.5\text{ }\mu\text{m/pulse}$) and PP is in the upper range ($0.5\text{ }\mu\text{m}$ to $0.8\text{ }\mu\text{m/pulse}$). The ablation thresholds are well below 0.1 J/cm^2 , except for the PE approaching $\epsilon_0 \sim 0.5\text{ J/cm}^2$. In case of KrF laser radiation, the ablation rates and the threshold fluences are substantially higher and the differences between the materials are more pronounced.

For comparison with conventionally cut or punched holes, relatively large holes of approximately 0.5 mm in width and 3 mm in length were laser drilled into two-lumen catheters (see Fig. 11.13) which show an excellent edge definition in contrast to punched openings. Functional testing revealed that the

mean value of the flow rate was in both cases the same, but the laser drilled samples showed lower variations from sample to sample. Apart from the desired geometry, requirements of biocompatibility have to be fulfilled. In-vitro tests of cytotoxicity and haemocompatibility were performed and successfully passed [11]. From these results, the biocompatibility of the laser-drilled holes can be considered as sufficiently good.

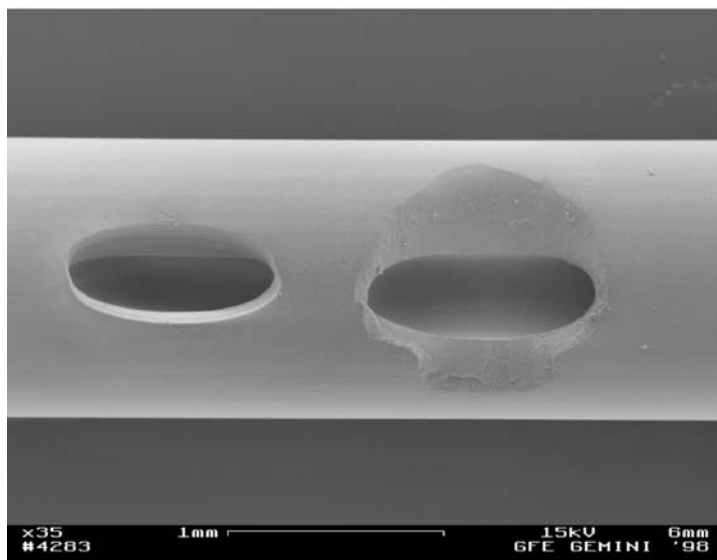


Fig. 11.13. Comparison of laser-drilled hole (left) and punched hole (right) in a multi-lumen catheter; by courtesy of ILT

Since the processing speed is correlated to the pulse rate, it is desirable to work with high pulse rates in order to achieve short drilling times. Following the simple ablation model, a layer of the material accepting an energy density above the ablation threshold is ablated and the absorbed energy is carried away by the emerging fragments. The energy absorbed in the layer below ablation threshold is converted to heat, which is spread in the bulk material by heat conduction. That amount of heat is typically very low, but the accumulation in a series of pulses could lead to substantial heating of the bulk material up to the melting point. The fraction of energy which heats up the bulk is determined by material properties (absorption coefficient, heat conductivity, phase transitions) and by laser parameters such as wavelength, fluence and pulse rate. As a characteristic, the extension of the heat-affected zone (HAZ) can be measured by optical microscopy. Typical features of HAZ are melting and burr visible at the edge of the hole. When irradiated by the ArF laser, the HAZ extends to less than $20 \mu\text{m}$ in case of PA, PE, PP and

pulse rates up to 100 *pps*, where even in case of PU no HAZ was detectable. In general, the weaker absorption of KrF radiation leads to stronger thermal effects. For example, the high precision of the 193 nm process also has been applied to fabricate the invasive probe of a multiparameter blood-gas monitor system [12]. The probe consists of an acrylic fibre of 175 μm diameter in which small rectangular slots are drilled. When the probe is inserted into the body and the small cavities are filled with blood the probe acts like an array of micro-cuvettes. The absorbance spectrum is used to calculate oxygen and CO₂ concentrations as well as the pH-value of blood. It is essential for the proper function of the probe to keep the size and shape of the slots within tight tolerances.

When very soft and flexible implant materials are needed, silicones are preferably used to fabricate flexible catheters, patches to cover lesions in cardio-vascular surgery and oesophagoplasty or for scaffolds serving as a supporting structure for artificial skin transplants in burn surgery. Because silicones can be applied as a resin, they can be easily used for the encapsulation of electronic devices, leadthroughs or for the insulation of stimulating electrodes. As an example for such an active implantable device, the requirements of a retina implant will be discussed. Retinitis pigmentosa (RP) is an ophthalmic disease which causes degeneration of photoreceptor cells and leads to blindness. Patients suffering from RP are able to perceive light sensations when the nerves on the retinal surface are stimulated by electrical pulses which are applied by an electronic chip. An electrode array will be placed on top of the retina and has to be fixed there permanently. One promising approach is the formation of a biomimetic matrix between the tissue and the coating layer of the electronic chip (see Fig. 11.14 left side). The fixation will be achieved by proliferation of retinal glia cells into the micro-pores of the implant to induce anchoring of the implant. The coating layer is made from cross-linked silicone (PDMS) where many pores of 50 μm to 100 μm diameter have to be drilled (cf. Fig. 11.14 right side). Comparing the results obtained with 193 nm and 248 nm radiation show again that ArF laser radiation assures best quality. The definition of the hole shape is more precise than in case of KrF radiation and the wall angles are steeper (typically 5° vs. 20°). Thermal effects are minimized and drilling can be performed even at repetition rates of 100 *pps*. The indispensable biocompatibility tests on laser-drilled medical devices were passed successfully and animal tests confirmed the migration of cells into the pores [13]. Regarding the typical polymers which are used for medical devices, such as PA, PE, PP, PU and silicones, it turned out that it is obligatory to use 193 nm radiation to attain the best surface quality.

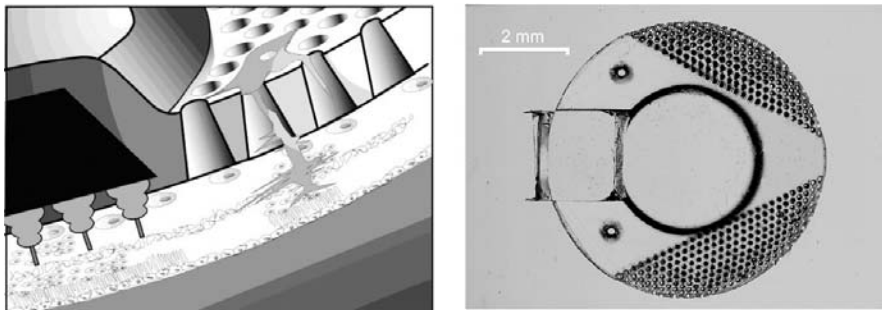


Fig. 11.14. Left: Schematic drawing of the device with glia cells migrating through the laser-drilled holes. Right: Micro-perforated retina stimulator coating (without electronics); by courtesy of ILT

Ceramics and Glass. Ceramic materials are used when rigorous requirements on hardness, service temperature, wear and corrosion resistance have to be fulfilled. The same attributes that are highly appreciated in their usage makes the machining of small ceramic components difficult. Due to the high hardness and brittleness, mechanical techniques are usually restricted to grinding and lapping where high precision and surface quality can be obtained, but the accessible geometries are limited. Milling of small pockets or similar shaped geometries into the bulk can be performed by ultrasonic machining, which is associated with high tool wear, or electro discharge machining (EDM), which can only be applied to electrically conducting materials like SiC.

For example, many of the electronic circuits intended for use at higher temperatures are fabricated on a large alumina (aluminum oxide) substrate simultaneously. After completing the processing, the individual boards have to be separated from another. As an alternative to mechanical slicing, a laser process can be applied, where the beam of a CO₂ laser “scribes” the surface of the substrate along the proposed dissection line. By the thermal gradients, stresses are induced, which exceed the fracture strength of the material and lead to the formation of micro-cracks near the surface. Applying forces by bending against a wedge, the micro-cracks grow until the substrate breaks.

Since the structural integrity of a surface layer greatly influences the fracture toughness of a component, the crack-free machining of surfaces is a demanding task for high-performance components. Mechanical finishing can induce small defect sites and sub-surface cracks can result. On the basis of that understanding, surface finishing of ceramic components by laser radiation has been considered. The beam of an excimer laser, with a typical penetration depth of a less than a μm , can rapidly heat up a thin layer such that material melts and vaporizes. If by application of subsequent pulses surface layers can be removed without the formation of cracks, the fracture toughness of a sample should approach its intrinsic value. Since the process parameters influence the morphology of a surface layer and therefore the

fracture strength of the components, 4-point-bending tests are carried out to specify the process window. The results on silicon nitride samples revealed that low fluences ($\sim 10 \text{ J/cm}^2$ for XeCl laser) and a large beam size $> 1 \text{ mm}$ preserved the original strength of the samples [14]. Laser glazing of grinded ceramic parts has been studied as well. When oxide ceramics like alumina are irradiated, a thin surface layer ($\sim 1 \mu\text{m}$) melts. After solidification, the density of open pores and the roughness can be reduced significantly [15] through compaction and sealing of the surface.

Laser drilling of small holes in temperature sensitive materials like SrTiO_3 -substrates for high-TC-superconductors (Fig. 11.15) allows for the construction of very sensitive magnetic probes (superconducting quantum interference device: SQUID). Thin tungsten wires are fed through a hole in the substrate where the superconducting loop senses the magnetic field. The wire concentrates the magnetic field lines inside the loop and acts as a small sensor tip. The hole is located just a few $10 \mu\text{m}$ next to the current path and the Josephson-contact [16]. Heating of the superconductor has to be prevented since a structural degradation results in reduced performance of the sensor. Also laser-induced thermal stresses have to be minimized because structural changes in the substrate could affect the performance of the superconducting layer. Careful processing, starting with relatively low fluences at the beginning and increasing the fluence when the hole becomes deeper, avoid these problems.

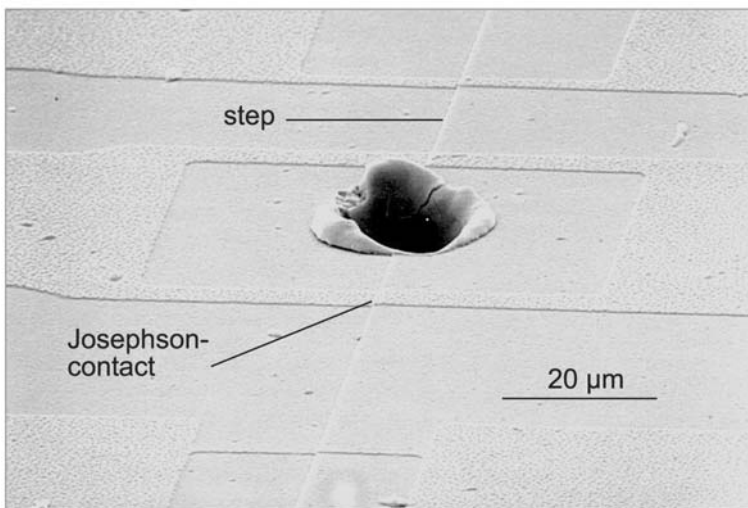


Fig. 11.15. Laser-drilled through-hole in the current loop of a SQUID on a 1 mm thick SrTiO_3 substrate; by courtesy of ILT

When drilling small holes of about $100\ \mu m$ size the diameter of the beam has a noticeable influence on the drilling rate. Investigations on alumina showed that between a beam size of approximately $20\ \mu m$ and $100\ \mu m$, the average ablation rate changes dramatically by a factor of more than two (see Fig. 11.16). These deviations are most striking at fluences of $20\ J/cm^2$ to $40\ J/cm^2$ which have to be considered when holes are to be drilled in a mask projection scheme. A qualitative explanation for this effect can be found in the expansion characteristics of the hot material, the plasma plume. When material is vaporized by an intense laser pulse, a laser-supported combustion wave (LSC wave) emerges, where vaporized material and the ambient gas are partly ionized by the laser radiation. The velocity of the wave front has been measured in the range of $10^5\ cm/s$ to $10^6\ cm/s$ in the case of steel [17]. Comparing the expansion length of the plume during the laser pulse

$$l_P \sim 10^5 \dots 10^6\ cm/s * 30ns = 30\mu m \dots 300\mu m$$

with the beam diameter shows that the shape of the plume can change drastically. In case of small beams, the shape is nearly a half-sphere, and for large beams, the flow is nearly 1-dimensional. Thus the particle density becomes higher in the case of extended beams, which results in a larger fraction of the incoming radiation being absorbed in the vapor cloud above the substrate. Experimental observations [17, 18] confirm that explanation, but the details are yet not fully understood. Further, reflection of the beam inside the hole as described earlier may have an effect on the ablation rates.

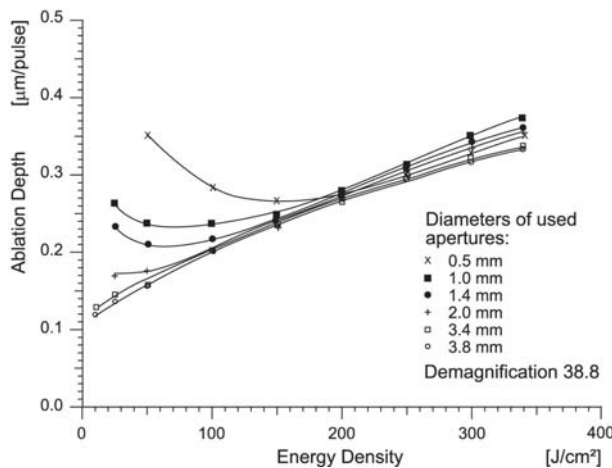


Fig. 11.16. Variation of ablation rate with beam diameter (KrF laser, beam size corresponds to 38.8-fold reduction of aperture) (Lambda Highlights No 34, Fig. 3 p. 3, 1992)

The fabrication of high-precision ceramic components by excimer laser ablation has been demonstrated on precision orifices and micromechanical components. For example, spinnerets are used to draw textile fibers and are needed in various shapes. When applying a mask projection technique, the shape of a hole could be very different from a circular cross-section (see Fig. 11.17 [19]). Furthermore, the creation of small 2-dimensional objects like micro gears (see Fig. 11.18) is feasible. Production of these components takes a few seconds using a high-repetition-rate excimer laser.

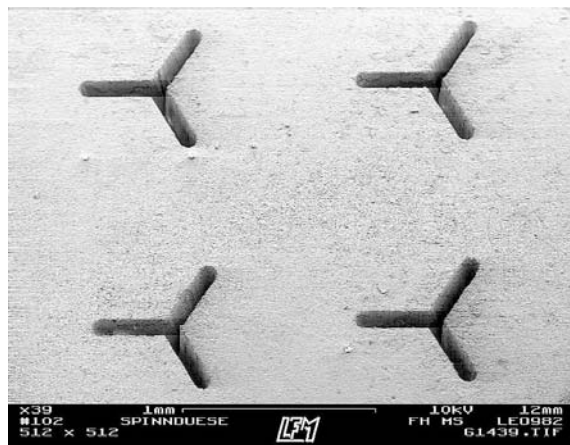


Fig. 11.17. Machining of trilobal ceramic spinnerets in alumina by KrF laser radiation; by courtesy of LFM

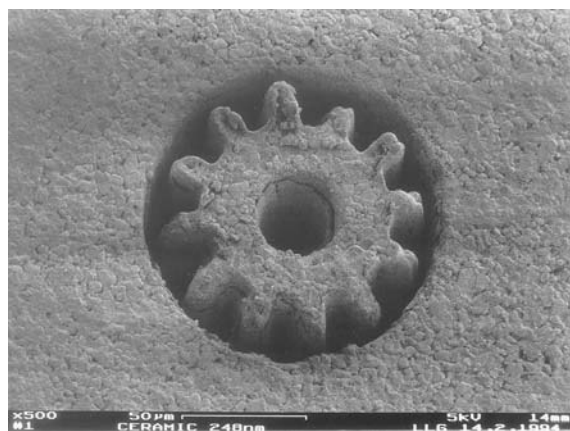


Fig. 11.18. Gear of about $120\mu\text{m}$ diameter produced by 248nm ablation in alumina; by courtesy of MicroLas

Metals. The energy transport in metals is governed by heat conduction, where the thermal diffusion length for 30 ns pulses is in the micrometer-range (see chap. 11.1). The laser beam induces melting and vaporizing of the material, by which liquid metal is driven out of the bore under the force of the vapor pressure. The expulsion of liquid material is clearly visible by the “frozen” melt at the edge of the hole as is evident by the micrograph shown in Fig. 11.19. Also the beam diameter is of $10\text{ }\mu\text{m}$ size and the melt structures have a typical size of some micrometers at the beam entrance side: it is possible to drill through-holes in thin metal foils with less than $1\text{ }\mu\text{m}$ in diameter (see Fig. 11.19) at the beam exit. Such small holes can serve as micro nozzles, for gas flow calibration or as test leaks in leak detectors. A reduction of the HAZ and avoidance of melt structures is expected using shorter pulse durations. Experiments with a femtosecond KrF excimer laser confirmed this assumption; gratings with a periodicity of 364 nm were written on copper and silicon surfaces by laser ablation [20].

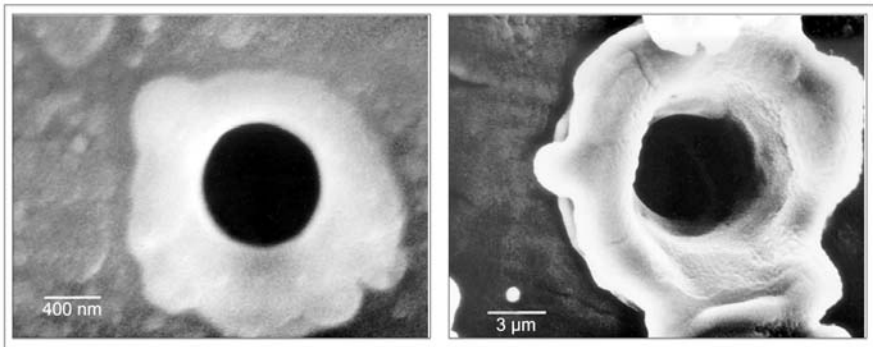


Fig. 11.19. Sub- μm hole drilled in molybdenum foil with KrF laser radiation; left: beam entrance side; right: beam exit side [6]

11.2.4 Fabrication of Micro Parts

M. Wehner

One advantage of the excimer laser mask projection scheme is the simultaneous structuring (“printing”) of extended patterns. This technique could be useful for the fabrication of microfluidic devices which are employed in biotechnology research as cell containers (well plates), in analytical techniques for the identification of proteins by electrophoresis, or in combinatory chemistry for producing minute amounts of chemicals. The concept of a “lab-on-chip” pursue the idea that a high number of specific antibody reactions will be performed simultaneously and detected by an automated system. This may help to speed up medical diagnosis or the tracing of substances in the environment. Principal functions of such devices comprise delivery of test substances, mixing with agents, incubation, exposing to a sensing area and

disposal of reactants. These devices are intended for high volume production where mass fabrication methods like injection molding or hot embossing will be employed. In the development phase of such devices, excimer laser machining of polymer materials can deliver prototype devices for design tests in a short time and at reasonable cost. The mask projection technique in conformal mode (see chap. 11.2.1) is perfectly suited to machining semi-3-dimensional structures. Extended patterns consisting of tapered channels or junctions of separate channels can be machined in a constant depth with high surface quality (see Fig. 11.20, 11.21).

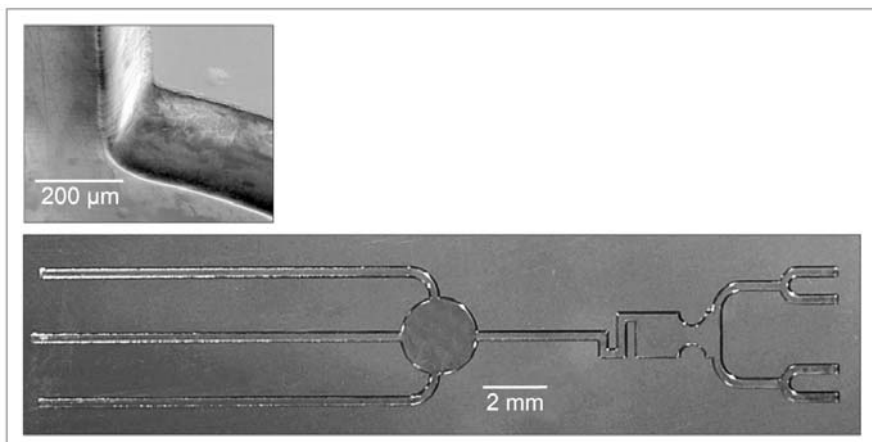


Fig. 11.20. Microfluidic test structure machined in polycarbonate with KrF laser radiation, overview and detail; by courtesy of ILT

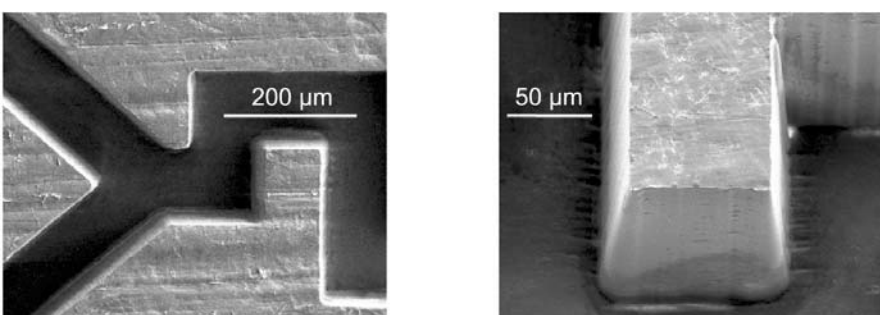


Fig. 11.21. Microfluidic test structure machined in Teflon[®] by fluorine laser radiation, overview and detail; by courtesy of ILT

For the cost effective production of a high volume series, a combination of laser technique and replication technique was proposed [21]. This method has been termed “laser LIGA” from the German acronym LIGA. The acronym is derived from “**L**Ithographie, **G**alvano- und **A**bformung”, i.e. lithography, electroplating and molding and means a combination of X-ray lithography, electroplating and replication by molding. Originally, synchrotron radiation was employed to irradiate thick film resists ($>100\mu\text{m}$) which were then developed, sputtered with metal and filled with nickel by electrodeposition until a solid metal layer was formed. This master copy – or second generation replica of the master – can be used as mould insert or hot embossing tool for mass replication. Because the X-ray synchrotron sources are expensive and not available everywhere, the lithographic process has been substituted by a laser ablation process. A polymer on a substrate is structured stepwise by laser ablation and is then replicated by the LIGA process (see Fig. 11.22). Compared to the enormous aspect ratios feasible by X-ray lithography of more than 100, the aspect ratio in laser ablation is limited to approximately 10, but the important advantage is the relatively simple, cost effective fabrication.

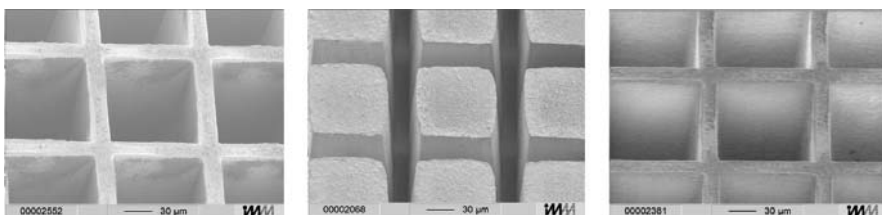


Fig. 11.22. Grid structure of $200\mu\text{m}$ depth and $20\mu\text{m}$ wall width: left: Grating machined in PMMA by ArF excimer laser radiation; middle: Inverse nickel replica; right: Injection-moulded part made from POM; by courtesy of Institut für Mikrotechnik GmbH Mainz IMM

In contrast to lithography, laser processing is able to remove material in locally varying depths by controlling the pulse number per site. This opens the path from planar processing to really three-dimensional structures. This technique is sketched in Fig. 11.23. The laser beam is formed by a rectangular, nc-driven mask. This geometry is projected onto the workpiece where the ablation is performed. By movement of the substrate the geometry is generated pulse by pulse. Machines for such processes are shown in Fig. 11.24. Advanced process modelling allows well adapted beam forming and path calculation to optimise the workpiece quality at a minimal processing time [22]. Implementing the strategies into a powerful software tool allows the automatic nc-data generation. Examples worked out by those and adapted strategies are optical micro components in glass and a ceramic platform for the installation of a micro system, Fig. 11.25.

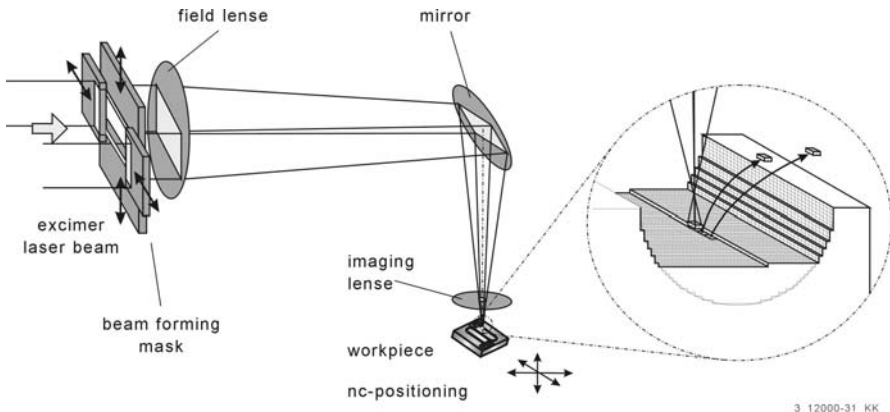


Fig. 11.23. Principle of flexible excimer laser micro-structuring [22]

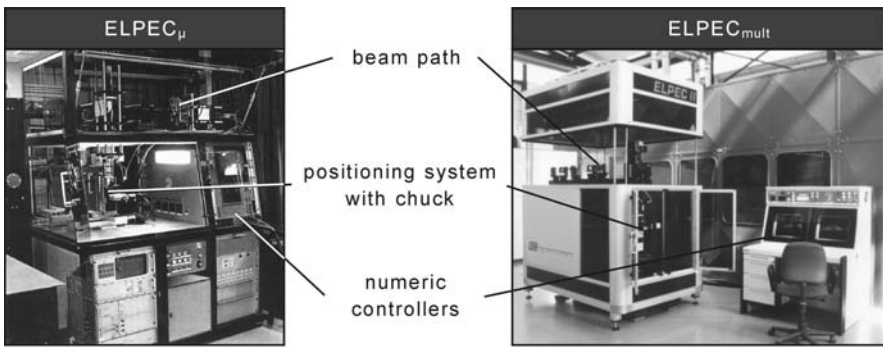


Fig. 11.24. Machines for flexible excimer laser micro-structuring

New approaches are pursued to speed up the small-lot fabrication of functional prototypes. As the next step following direct machining of each single prototype by excimer ablation, the replication via photomolding using mold inserts made from polymers are discussed [23, 24]. Preferentially, photo-curable resins as methylmethacrylate (MMA) are employed and since the light-induced reaction does not require high temperatures or thermal cycling, it is well suited to the service temperature of many polymers. The master consists for example of materials like PSU, PEEK or PI in which the inverse or negative structure is machined by excimer laser ablation. Then a thin metal layer of typically less than 100 nm thickness is deposited onto the polymer mold forming an intermediate layer for the two polymer parts. Otherwise the parts will be destroyed when de-molded. Compared to laser LIGA, the galvano-forming process step is substituted by a simple sputter process, on the other hand, the lifetime (cycles) of polymer mold inserts is

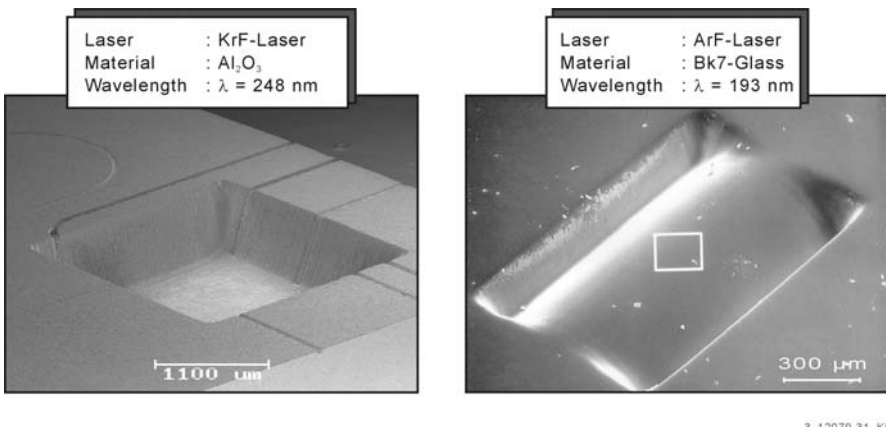


Fig. 11.25. Excimer-laser-machined components with 3D-surfaces

limited yet. In the described experiments (Figs. 11.26, 11.27) [24] it turned out that PI is a very well suited material for the master and, as mentioned before, PI can be patterned very precisely by excimer laser radiation.

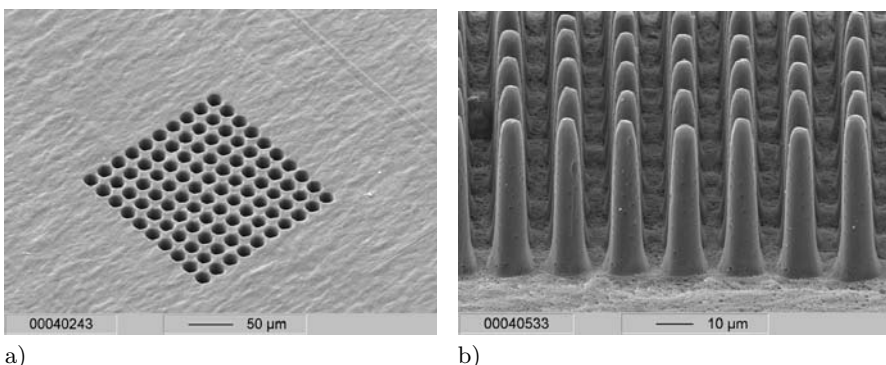


Fig. 11.26. a) Mold insert machined into PI and molded part made of PMMA [24]; by courtesy of IMF

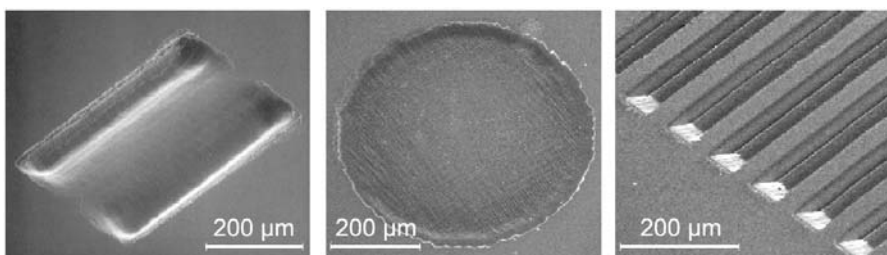


Fig. 11.27. a) High-aspect ratio structure of $100 \mu\text{m}$ height and $10 \mu\text{m}$ width made by photomolding of MMA from PI master [24]; by courtesy of IMF

11.2.5 Indirect Ablation

J. Ihlemann

There are several methods of laser machining where the laser radiation is not directly coupled into the material to be ablated, but indirectly by means of an auxiliary absorber material. This is particularly of interest if the material is transparent at the ablation wavelength. Then the laser light can be delivered to the absorber (instead of directly to the workpiece to be machined), leading to various kinds of indirect ablation:

In the case of “laser-induced backside wet etching” (LIBWE) [25], the backside of the sample to be machined is in contact with an absorbing liquid which may be an alcoholic or aqueous solution of a dye absorbing at the laser wavelength. The energy is coupled into the rear surface of the workpiece by heating this absorber liquid. This method was successfully applied to pattern fused silica (Fig. 11.28) and CaF_2 . The etch rate is rather low compared to direct ablation, but this enables precise depth profiling. Structure resolution down to $1 \mu\text{m}$ has been achieved. The main advantage of this method is that the laser wavelength does not have to be adapted to the material to be machined, but only to the absorbing dye so that the rather convenient wavelength of 308 nm can be used for glass machining.

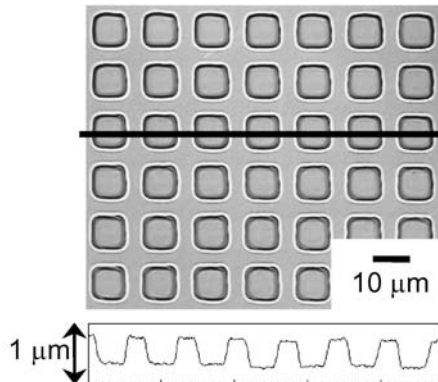


Fig. 11.28. Grating structure fabricated in fused silica by laser-induced backside wet etching [25]

Another method is based on non-permanent but laser-induced indirect absorption. In this process called “laser-induced plasma-assisted ablation” (LIPAA) [26], a metallic sample is positioned behind the transparent workpiece (e.g. fused silica). The laser pulse causes a plasma plume expanding from the metal to the backside of the workpiece, which is then able to absorb light via the deposited metallic layer.

If rear side ablation is possible, which is for example the case for the patterning of thin films on UV-transparent substrates, an absorber film can also be used for laser-induced rear side ablation of these layers. Thus, dielectric layer systems, which do not absorb in the UV because they are designed as highly reflective (HR) interference layer stacks (e.g. $\text{Al}_2\text{O}_3/\text{SiO}_2$), are patterned using an absorbing HfO_2 layer between substrate and HR-system (Fig. 11.29). In this way dielectric masks with high resolution and high damage threshold can be fabricated [27].

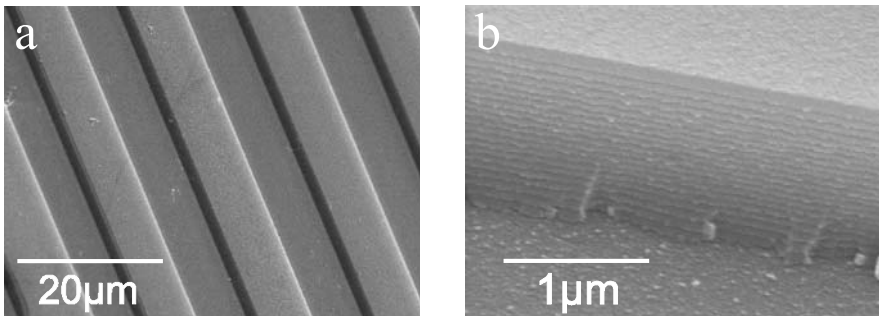


Fig. 11.29. Scanning electron micrograph of a line pattern mask (a) and the detail of the ablation edge (b) made by single-pulse 193 nm-ablation of a highly reflective dielectric layer stack ($\text{Al}_2\text{O}_3/\text{SiO}_2$) with underlying absorber layer [27]

11.2.6 Micro Optics Fabrication

M. Wehner

Another large field of laser microfabrication is that of generating micro optical structures. This is understandable, because the precision or resolution required here matches roughly the ultimate precision or resolution which is possible with standard light-based manufacturing processes. This led to a variety of processes for fabricating optical components like micro lenses, gratings, or complex diffractive structures.

Gratings. The excimer laser based fabrication of optical grating structures has been a subject of study for a long time. This work aimed either at the demonstration of high resolution capability of the ablation process, or at the fabrication of real gratings to be used for example as coupling gratings for planar waveguides. The spatially periodic intensity pattern needed for the generation of a (one dimensional) periodic surface structure with a periodicity of the order of the wavelength of light can be achieved by the interference of two beams. Several optical arrangements are possible: The interfering beams may be generated by a partially reflecting beam splitter (*reflective splitting*) or by a (transmission-) grating (*diffractive splitting*). The beams may interfere in the near field of the splitting element (e.g. using a phase mask with suppressed zeroth order similar to the configuration for writing fiber Bragg gratings) or may be recombined at some distance (using simple beam superposition or imaging). The coherence properties of the applied laser field may, in some cases, be crucial for the development of the periodic patterns.

Such grating designs are used in several micro-optic applications such as grating demultiplexers for telecommunication components, light couplers for planar optical waveguides, Bragg reflectors, and alignment grooves for liquid crystals [28]. Sub-micron periodic structures, which are required for ultraviolet, visible and near-infrared spectral applications, have been structured by

UV-laser ablation with nanosecond (ns) duration pulses on polymer [29] and borosilicate glass [30] surfaces. For the fabrication of gratings on metals or crystalline optical materials, femtosecond excimer lasers (see chapters 14, 15) and for the treatment of weakly absorbing materials like fused silica, F₂-lasers were applied (see chapter 13).

Diffractive optical elements (DOEs). Diffractive optical elements (DOEs) make use of the diffraction at small phase structures. They open a wide range of new beam shaping applications [31]. Specifically, diffractive phase elements (DPEs) enable the generation of complex irradiation patterns without substantial optical system energy losses. In many cases, a computer-generated two-dimensional phase function is transferred into an optically effective phase controlling element by fabricating a surface relief on a transparent substrate.

These elements can be applied for beam homogenization or fiber coupling, for correction of lens systems or for the generation of arbitrary irradiation patterns like ring structures or spot arrays. In laser materials processing, they offer efficient mask illumination or even provide for direct maskless processing. In addition, DOEs enable laser micro machining with ultrashort pulses without vacuum, whereas geometrical imaging leads to air breakdown in the focus at high intensities. DPEs allow for a reduction of optical elements without loss of functionality.

DOEs can be characterized as amplitude or phase elements. Phase elements, often called kinoforms, can have a binary or a multilevel structure. The simplest kinoform to be used at a wavelength λ is a binary surface relief structure on a material of refractive index n with a depth modulation of $d = \lambda/2(n - 1)$. Lateral structure dimensions are of the order of 5λ to some 10λ , depending on the optical configuration and the coherence parameters of the light for which the DOE is designed. For a DOE made of a polymer material, to be used in the visible spectral range, surface structures with a depth of about $0.5\ \mu m$ and lateral dimensions of $5\ \mu m$ are required. These dimensions are easily accessible by excimer laser ablation. Some attempts have been made to fabricate DOEs by laser ablation, either on the basis of pixel-by-pixel irradiation [32, 33] or image-based using chrome masks [34]. Multilevel DOEs could be produced in polymers by excimer laser ablation using a half tone mask [35]. Dielectric masks were used for fabricating DOEs that can be used for UV laser applications, requiring the processing of fused silica or other materials with high UV transmission [36] (Fig. 11.30). The ablative shaping of diamond for IR-DOEs was also demonstrated [37].

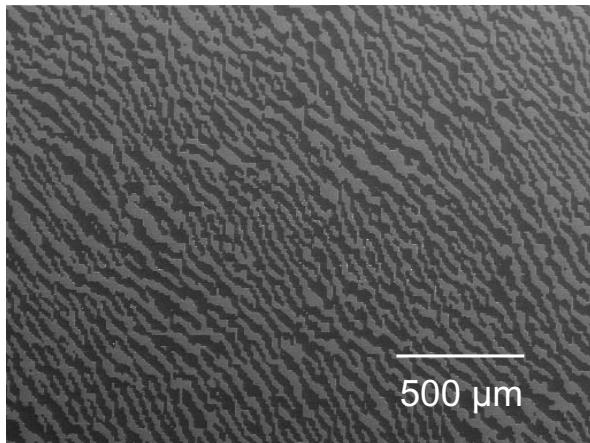


Fig. 11.30. Binary diffractive phase element (scanning electron micrograph) made by single pulse rear side ablation patterning of a 126 nm thick Ta_2O_5 -layer on a fused silica substrate with 248 nm radiation [36]

Lenses. It is very attractive to fabricate micro lenses by laser ablation because if the basic problems of creating a smooth, 3-dimensional surface in an optical material were solved, a great variety of lens shapes should be possible (aspheric etc). The processing of cylindrical lenses is rather straightforward, if a flexible mask technology is applied [38]. In the case of processing glass, the ablation debris is one of the major problems which could be solved by ablating in a vacuum. For the generation of spherical lenses, an approach based on scanning a polymer surface with an excimer beam along well-chosen multiple concentric contours was applied [39]. In this way micro lenses of arbitrary shape could be realized.

11.2.7 MEMS and Nanofabrication

M. Wehner

KrF excimer lasers were applied for the bending of thin metal bands [40]. The influence of the temperature gradient in the metal band and the effect of the ablation plasma generated at high fluences was investigated. Laser fluence and the number of pulses can be tuned to achieve a large range of bending angles from 1° to 180° with high precision.

Beside the standard ablative micro fabrication process, where the final product is sculpted out of a blank substrate, other methods for ablative fabrication have been developed. One of the most promising processes is the laser-induced forward transfer (LIFT): A layer is irradiated with a spatially defined irradiation pattern through a transparent substrate, so that it is detached in the irradiated area and transferred to a second substrate to form a functional pattern. This method was used not only for generating diffractive

optical patterns [41], but also for the laser-assisted assembly of micro motors [42].

The attempt to break the resolution limit of structuring, given roughly by the wavelength of the laser light, was addressed by several methods. Whereas classical sequential near-field processing by light emitted by a fiber tip is mostly applied with non-excimer lasers, excimer lasers can again be used for a parallel process: A densely packed layer of SiO₂ micro spheres is assembled near the sample surface acting as micro lenses to generate an ablation spot array on the sample. In this way hole arrays with hole diameters of 400 nm were produced in polyethylene terephthalate foils [43].

References

1. Lambda Industrial No. 5, June 1989; Publication by Lambda Physik
2. Lambda Industrial No. 8, November 1994; Publication by Lambda Physik
3. F. Bachmann: Chemtronics, UK **4**(3), 142–52 (1989)
4. K. Jasper, P. Berger, H. Hügel: LaserOpto **31**(4), 75–76 (1999)
5. K. Schütze, H. Pösl, G. Lahr: Cell Mol Biol **44**, 735–746 (1998)
6. Lambda Highlights No. 2, December 1986, Publication by Lambda Physik
7. S. Küper, J. Brannon: Appl. Phys. A **57**, 255–259 (1993)
8. R. Lotze, J. Birkel, K. Wissenbach: JOT Journal für Oberflächentechnik (1999/8)
9. M. Wehner, D. Wesner: “Voraussetzungen für wirtschaftliches Bohren von Präzisionslöchern mit UV-Lasern; Teilvorhaben: Bohrungen definierter Geometrie und Randschichtmorphologie”, Research Report Fkz 13 N 6795/0, German Ministry for Education and Science, 1999
10. Lambda Highlights No. 7, October 1987, Publication by Lambda Physik
11. M. Wehner, D.A. Wesner, E. Bremus, A. Gillner, R. Poprawe, R. Zimmer: “Qualification of the laser drilling of catheters”, in *Proc. of the Laser Micro-fabrication Conference ICALOE '99*, Laser Institute of America (2000), pp. 94–103, LIA Vol 88; ISBN: 0-912035-61-7
12. K. Sweeny, N. Sparrow: “Micromachining: An enabling technology in the manufacture of a blood-gas monitor”, Medical Devicelink EMDM (Product Update) May/ June 2001 Laser; <http://www.devicelink.com/emdm/archive/01/05/008.html>
13. E. Bremus-Köpperling, H.C. Lüdtke-Handjery, A. Gillner, H. Höcker, C. Mittermayer, R. Poprawe, H.A. Richter: “Laser microperforation of pdms for the durable fixation of a retina implant”, in *Proc. of the Laser Microfabrication Conference ICALOE '99*, Laser Institute of America (2000), pp. 77–84, LIA Vol. 88, ISBN: 0-912035-61-7
14. M. Wehner, M. Burström: “Excimer laser machining of silicon nitride”, in *4 th International Symposium on Ceramic Materials and Components for Engines* (Elsevier 1992, Göteborg, Sweden, 1991), pp. 813–820, ISBN 1-85166-776-8
15. K.J. Schmatjko, G. Endres, H. Durchholz: “Surface modification of ceramics by excimer laser irradiation”, in *Proceedings Laser in Manufacturing (LIM-5, IFS Publication, Springer, 1988)*

16. P. Pitzius, V. Dworak, U. Hartmann: "Neue Rastersondentechniken auf der Basis von SQUID-Detektoren", Abschlussbericht Universität des Saarlandes, Saarbrücken (DE), Funding Organization: Bundesministerium für Bildung, Wissenschaft, Forschung und Technologie, Bonn (DE), BMBF 13N6562, Apr. 1999. 68 p., available from TIB Hannover: F99B682+a
17. R. Poprawe: "Materialabtragung und Plasmaformation im Strahlungsfeld von UV-Lasern", Dissertation Technische Hochschule Darmstadt D17, Darmstadt 1984
18. M. Wehner: "Werkstoffbearbeitung mit Excimer-Laserstrahlung", Dissertation RWTH Aachen D 82, Aachen 1991, ISBN 3-86073-002-9
19. C. Kulik: "Bearbeitungsstrategien für die lasergestützte 3d-Mikrobearbeitung mittels Excimerlaserstrahlung", Dissertation Universität Hannover, VDI Verlag, Düsseldorf 2002
20. P. Simon, J. Ihlemann: Applied Surface Science **109/110** (43), 1997
21. J. Arnold, U. Dasbach, W. Ehrfeld, K. Hesch, H. Lowe: Applied Surface Science **86**, 251–8 (1995)
22. H.K. Tonshoff, F. Von-Alvensleben, A. Ostendorf, C. Kulik: "Advanced strategies for three-dimensional micro-structuring with excimer lasers", in *Proceedings of International Congress on the Applications of Lasers and Electro-Optics 16–19 Nov. 1998. – In: Proceedings of the Laser Materials Processing Conference ICALEO'98*, Laser Institute of America, Orlando, FL, USA (1998), Vol. 2 of Ix+xxxv+477, pp. E72–80
23. T. Shimizu, J. Murakoshi, T. Sano, R. Maeda, S. Sugiyama: Microsystem Technologies **5**, 90–92 (1998)
24. W. Pfleging, T. Hanemann, M. Torge, W. Bernauer: Proceedings of the Institution of Mechanical Engineers, Part C **217**(C1), 53–63 (2003)
25. J. Wang, H. Niino, A. Yabe: Appl. Phys. A **68**, 111 (1999)
26. J. Zhang, K. Sugioka, K. Midorikawa: Optics Letters **23**, 1486 (1998)
27. J. Ihlemann, K. Rubahn, R. Thielsch: "Laser ablation patterning of dielectric layer stacks for 193 nm mask fabrication", in *Proc. SPIE* Vol. 4426 (2002), p. 437
28. M. Behdani, S. Keshmiri, S. Soria, M. Bader, J. Ihlemann, G. Marowsky, T. Rasing: Applied Physics Letters **82**, 2553 (2003)
29. K. Ilcisin, R. Fedosejevs: Appl. Opt. **26**, 396 (1987)
30. S. Pissadakis, L. Reekie, M. Hempstead, M. Zervas, J. Wilkinson: Appl. Phys. A **69**, 739 (1999)
31. J. Turunen, F. Wyrowski (Eds.): *Diffractive Optics for Industrial and Commercial Applications* (Akademie Verlag, Berlin, 1997)
32. M.T. Duignan, G.P. Behrman: Appl. Opt. **36**, 4666 (1997)
33. N. Vainos, S. Mailis, S. Pissadakis, L. Boutsikaris, P. Parmiter, P. Dainty, T. Hall: Appl. Opt. **35**, 6304 (1996)
34. X. Wang, J. Leger, R. Rediker: Appl. Opt. **36**, 4660 (1997)
35. F. Quentel, J. Fieret, A. Holmes, S. Paineau: "Multilevel diffractive optical element manufacture by excimer laser ablation and halftone mask", in *Proc. SPIE* Vol. 4274 (2001), p. 421
36. J. Ihlemann, D. Schäfer: Applied Surface Science **197–198**, 856 (2002)
37. V. Kononenko, V. Konov, S. Pimenov, A. Prokhorov, V. Pavelyev, V. Soifer, B. Lüdge, M. Duparré: "Laser shaping of diamond for ir diffractive optical elements", in *Proc. SPIE* Vol. 4426 (2002), p. 128

38. J. Ihlemann, B. Wolff-Rottke: Applied Surface Science **106**, 282 (1996)
39. K. Naessens, P.V. Daele, R. Baets: "Excimer laser ablation based microlens fabrication for optical fiber coupling purposes", in *Proc. SPIE* Vol. 4941 (2003), p. 133
40. M. Geiger, F. Meyer-Pittroff: "Laser beam bending of metallic foils", in *Proc. SPIE* Vol. 4426 (2002), p. 187
41. I. Zergioti, S. Mailis, N. Vainos, A. Ikiades, C. Grigoropoulos, C. Fotakis: Appl. Surf. Sci. **82**, 138–139 (1999)
42. A. Holmes: "Laser fabrication ans assembly processes for mems", in *Proc. SPIE* Vol. 4274 (2001), p. 297
43. R. Denk, K. Piglmayer, D. Bäuerle: Appl. Phys. A **74**, 825 (2002)

11.3 Via Drilling

M. Hessling, J. Ihlemann

11.3.1 Introduction

Six years after the first commercial excimer lasers had found their way into research laboratories, in 1982 Srinivasan and co-workers reported their discovery of the laser ablation phenomenon [1]. Organic polymers were etched by pulsed ultraviolet (UV) radiation of an ArF excimer laser with a wavelength of 193 nm .

This discovery led to further activities in academic and industrial research laboratories. Important advances in laser ablation technology took place during the years 1984 and 1985 when researchers at IBM [2, 3] demonstrated that laser ablation of polymers could also be performed with excimer lasers at longer wavelengths: 248 nm (KrF), 308 nm (XeCl) and 351 nm (XeF). This meant simplification of the laser beam propagation and shaping and played a key role in the transfer of the excimer laser from the research laboratory to the manufacturing environment.

The KrF excimer laser was the first excimer laser used in an industrial application. Siemens AG put pulsed 248 nm radiation in their production line for drilling vias with diameters of $80\mu\text{m}$ in polyimide dielectric layers of printed circuit boards [4].

11.3.2 Basics

There are several advantages in the use of excimer lasers for hole drilling. The laser beam profile has nearly a rectangular flat top shape and can easily be optimized by use of a beam homogenizer. The low coherence enables homogenisation by superposition of beam sections without interference problems. In this way, the beam can be adjusted to illuminate a mask defining a hole pattern to be generated. This enables parallel processing of many holes and provides high process speed. Refractive or diffractive arrangements can be used to illuminate only “active” mask areas providing high efficiency. Further advantages are given by the potential of UV-radiation to ablate nearly any material (Figs. 11.31, 11.32). Hence it is possible to achieve rather congruent ablation of different components of composite materials, e.g. fiber reinforced plastics.

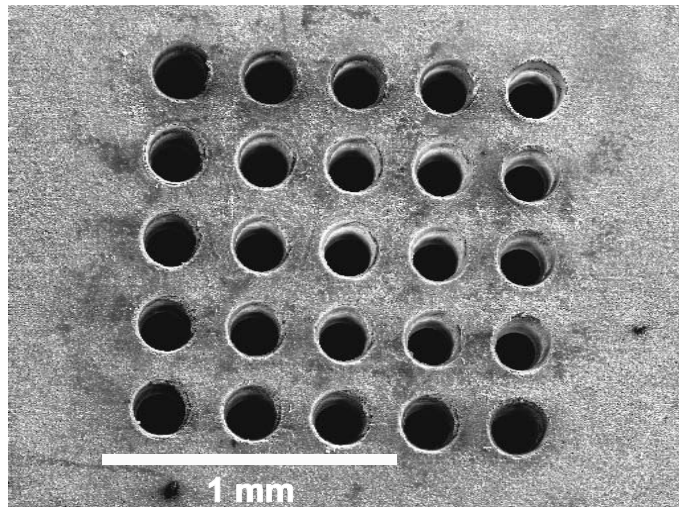


Fig. 11.31. Array of excimer-laser-drilled holes in Al_2O_3 ceramic

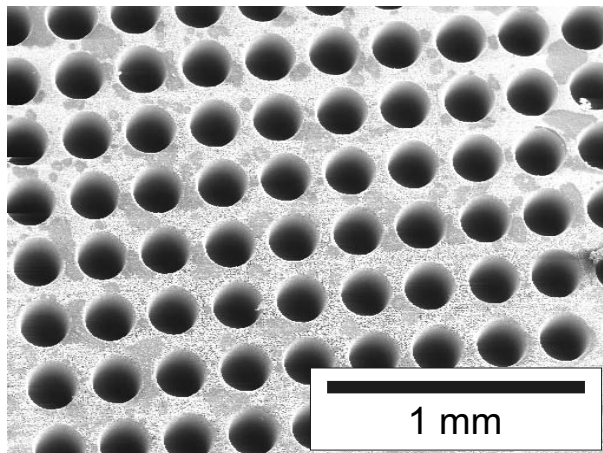


Fig. 11.32. Array of excimer laser-drilled holes in polyether-sulfone

Even glass material with low UV-absorptivity like fused silica can be drilled with excimer lasers [5]. For these materials, a so called “incubation effect” is observed. The first laser pulses create surface defects, which then lead to more effective absorption of successive pulses. Thus deep holes with high aspect ratio can be produced (Fig. 11.33).

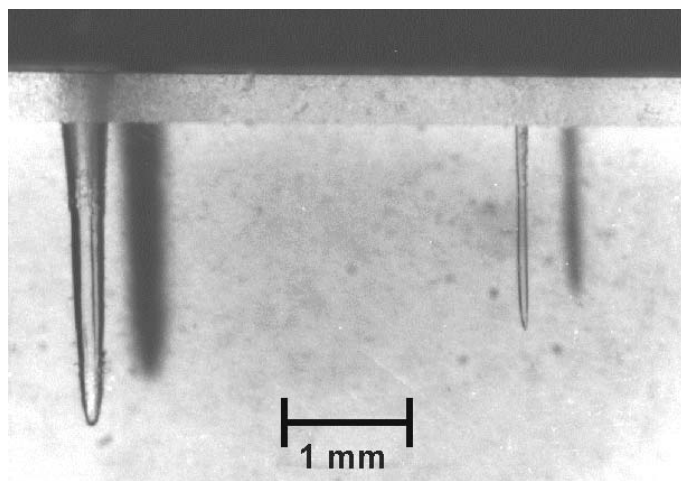


Fig. 11.33. Excimer laser (308 nm) drilled holes in fused silica

These are the main advantages of the use of excimer lasers as compared to IR lasers for hole drilling:

- i The absorptivity of most materials is higher in the UV compared to the IR range. This leads to an improved coupling of the laser energy into the material and therefore to an improved quality of ablation features.
- ii The short wavelength enables high optical resolution so that even holes of a few micrometer diameter can be drilled with high precision.
- iii The pulse duration in the nanosecond range enables “cold ablation” of many materials. There is no time for the energy to diffuse out of the irradiated area into the neighboring material so that the thermal load of the material around a hole is low. In the case of IR-lasers operating with microsecond-pulses, the thermal influence is rather large.

The detailed mechanism of the ablation process – whether bonds are broken directly due to high photon energies in the UV, or decomposition is induced by a photothermal mechanism – does not seem to have that decisive influence on the precision of the ablation structures as was postulated in the early years of ablation.

Several observations were made concerning the dependence of the ablation results on the beam or pulse properties. The ablation rate depends on the laser fluence. Above a certain threshold, which depends on wavelength and material, the ablation rate increases with increasing fluence and levels off more or less steeply in the high fluence range. But other observations have been made which are not as plausible. They were made mainly in the ablation of polymers but are also to some extent applicable to other materials.

- i The ablation rate depends on the pulse duration, even in the nanosecond range. For example, the ablation rate of polyimide at 248 nm laser wavelength and a fluence of 10 J/cm^2 is $0.7\text{ }\mu\text{m/pulse}$ at 20 ns pulse duration and $2.0\text{ }\mu\text{m/pulse}$ at 230 ns pulse duration ($200\text{ }\mu\text{m}$ spot diameter).
- ii The ablation rate depends on the laser spot size on the sample (at constant fluence). Whereas it is rather constant for large spot diameters, it increases significantly below a spot diameter of about $200\text{ }\mu\text{m}$. Again for polyimide at 248 nm at 10 J/cm^2 and 20 ns pulse duration, the ablation rate is $0.7\text{ }\mu\text{m/pulse}$ at $200\text{ }\mu\text{m}$ and $1.1\text{ }\mu\text{m/pulse}$ at $30\text{ }\mu\text{m}$ diameter. Both effects (influence of pulse duration and spot size) are caused by the dynamic attenuation of the expanding ablation plume [6].
- iii At high fluence, the entrance diameter of a drilled hole is not equivalent to the diameter of the irradiation spot. For polyethylene-terephthalate (PET) at 248 nm and 10 J/cm^2 and an irradiation diameter of $200\text{ }\mu\text{m}$, a hole of $200\text{ }\mu\text{m}$ depth will have an entrance diameter of about $230\text{ }\mu\text{m}$. This “hole widening” develops during the plasma plume interaction of successive pulses with the wall [7].
- iv The wall angle of drilled holes depends on the fluence (and on the numerical aperture of the optical system). At high fluence, steep holes are created; with decreasing fluence, the wall steepness diminishes. This effect can be compensated by choosing a beam path of appropriate numerical aperture [8].
- v The laser via drilling process is often accompanied by unwanted processes like redeposition of splashes or soot (debris) around the holes, especially if longer wavelengths, e.g. 308 nm are used. To avoid these effects and to improve the ablation structures, special functional polymers were developed which combine specific application-defined properties for optimized laser ablation performance [9]. Figure 11.34 shows a hole produced without debris at 308 nm in an azopolymer.

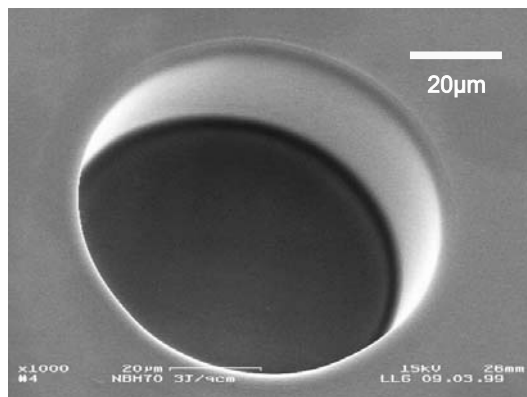


Fig. 11.34. Debris-free via hole in azophosphonate polymer made at 308 nm

For the production of micrometer or sub-micrometer holes in metallic or semiconducting materials, short pulse (femtosecond) excimer lasers are used. The thermal conductivity of these materials is very large, so that during a normal pulse of 20 ns the absorbed energy is spreading over some micrometers to inhibit the formation of precise structures. Laser systems with pulse durations of 100 fs – 500 fs with pulse energies of some 10 mJ at 248 nm are available. Using these femtosecond pulses very small holes can be produced (Fig. 11.35) [10]. For more details on the application of *fs*-pulses see chapters 14 and 15.

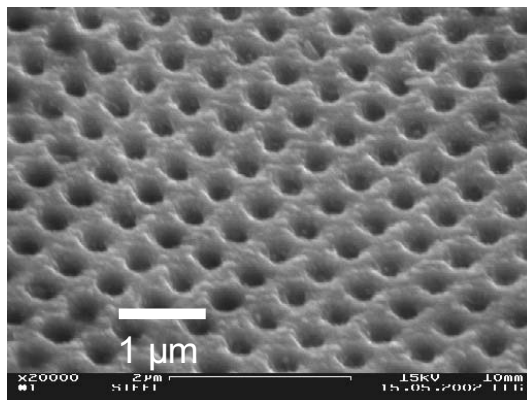


Fig. 11.35. Femtosecond excimer laser (248 nm) drilled sub- μ m hole pattern in stainless steel

11.3.3 Applications

Vias in microelectronics. Via hole drilling was one of the very first industrial application of excimer lasers. Bachmann and co-workers at Siemens AG in 1990 used the pulsed 248 nm radiation of KrF excimer lasers for the production of highly integrated multilayer printed circuit boards (PCBs) for Siemens computers [4]. These printed circuit boards consisted of several dielectric layers of polyimide ($10 - 50 \mu\text{m}$) with a fine layer of structured copper between the polyimide layers (Fig. 11.36). A conducting connection between the different copper layers was produced by first drilling vias followed by chemical deposition of copper at the via walls. The ablation of the polyimide layer was achieved after several laser pulses. The ablation process stopped automatically when the underlying copper was uncovered due to the higher necessary laser fluence for the ablation of copper, which is one order of magnitude above the ablation threshold of polyimide.



Fig. 11.36. Cross-section through a completed multilayer printed circuit board for the Siemens 7500H90 computer produced with a KrF excimer laser [4]

Today, more than ten years later, lasers are common for the drilling of small vias in PCBs. However, for holes with diameters of about $100 \mu\text{m}$ and above, CO₂ lasers are generally used. CO₂ lasers offer high laser power, high material removal rate and high repetition rate for a lower price than excimer lasers. They are suitable for the ablation of organic dielectrics and due to their wavelength of about $10 \mu\text{m}$, they are not able to ablate copper and therefore the ablation process stops at the underlying copper layer. A cross section of a via with a diameter of $100 \mu\text{m}$ that was drilled with a CO₂ laser in a $80 \mu\text{m}$ -thick fiber-reinforced resin layer of a PCB is shown in Fig. 11.37.

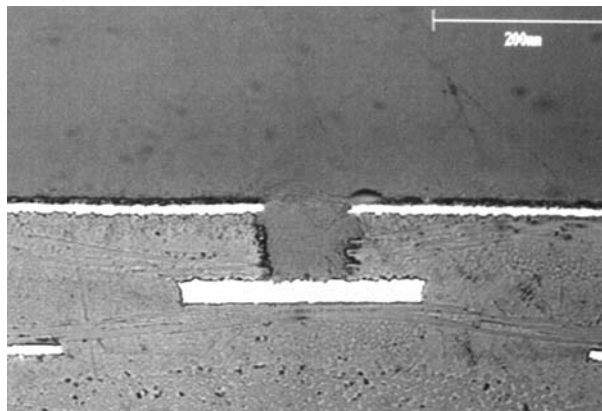


Fig. 11.37. Cross-section of a via with a diameter of $100\mu m$ that was drilled with a CO_2 laser in a $80\mu m$ -thick fiber-reinforced resin layer (Prepreg 1080). The upper copper layer was removed by the 351 nm radiation of the third harmonic of a Nd:YLF laser; by courtesy of FUBA Printed Circuits GmbH, Gittelde, Germany

Due to its long wavelength (approx. $10\mu m$) and to the “thermal” ablation process that produces much debris and a destructive heat affected zone around the via, the CO_2 laser is not able to drill much smaller vias.

Charrier et. al. [11] investigated in drilling $100\mu m$ microvias, and even through-holes, in a multi-layer microwave antenna substrate with CO_2 and KrF lasers. Though the CO_2 laser had the higher drill velocity, it was decided to employ the excimer laser due to the observed better hole cleanliness and wall quality (Fig. 11.38).

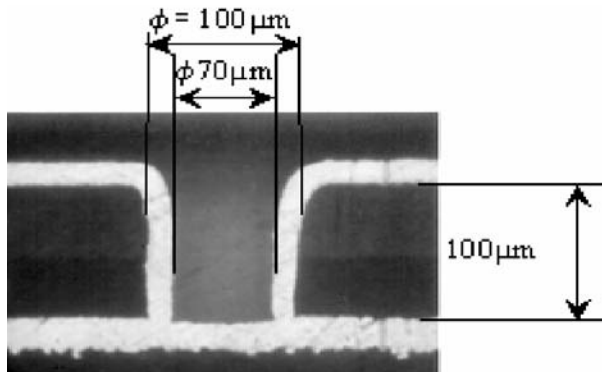


Fig. 11.38. Cross-section of an excimer laser-drilled $100\mu m$ microvia after chemical deposition of copper [11]

The excimer lasers with their more than 30 times shorter wavelengths ($157 - 351\text{ nm}$) and their “cold” ablation process should be suited better for the drilling of small diameter holes ($< 100\text{ }\mu\text{m}$) in PCBs than most longer-wavelength lasers.

This is backed by Manirambona’s [12] presentation of cross sections of excimer-laser-drilled $50\text{ }\mu\text{m}$ microvias (Fig. 11.39) and his claim that his system is even able to produce vias with diameters of only $5 - 10\text{ }\mu\text{m}$ in printed circuit boards.

Also vias with diameters of only a few micrometers in polyimide have already been reported [13, 14].

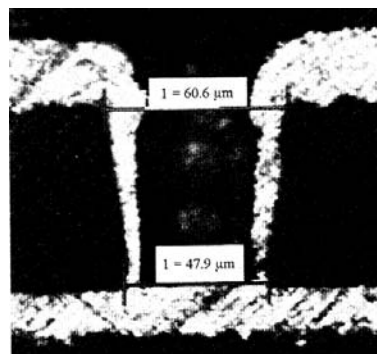


Fig. 11.39. Cross-section of an excimer laser-drilled $50\text{ }\mu\text{m}$ microvia in RCC after copper deposition [12]

Hole quality and the potential of machining of smaller hole diameters are the main reasons why excimer lasers, or other UV lasers, will play the key role in future PCB production as the layout densities increase and tiny vias are consequently required.

Excimer lasers are already first choice in other micro electronic applications with small structure sizes like ball grid arrays (BGAs), multichip modules (MCMs) and surface mount technology (SMTs). All of these applications benefit from the excimer laser’s high spatial resolution, its ability to ablate metals and nonmetals and its high reliability.

BGAs, for example, have become more and more popular over the last ten years because of the decreasing size of integrated circuits (ICs), the increase of their circuit density and their need for more and more external connections [15, 16, 17]. There are physical limits on how closely the leads for external connections to ICs can be placed before solder yield becomes a problem. One of them is the so-called “208-pin limit”. Once the number of necessary external connections exceeds this number, packages like BGAs have to be used.

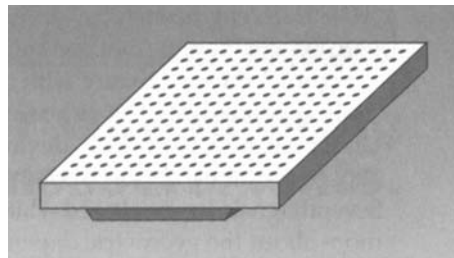


Fig. 11.40. Fully assembled BGA package pre-loaded with solder balls for a direct leadless connection to a printed circuit board; by courtesy of T.Lizotte [15]

Here the connections are made through an array of small solder balls deposited on the surface of the device (Fig. 11.40). To make the connections within the chip, excimer lasers are used to drill holes with diameters down to $25\ \mu m$ through the different chip covering layers. This package can be mounted, e.g. on a PC board, with a minimum total footprint by melting the solder balls with an infrared heater to create very strong joints. In 1996, the most densely packed product manufactured with an excimer laser was a 1000-connection BGA on a $25 \times 25\ mm^2$ substrate [15].

A technology that is similar to the BGA method is IBM's C4 technology (controlled collapse chip connection) used for attaching semiconductor chips to microelectronic packages (Fig. 11.41). The chip is covered with a polyimide layer ("passivation layer"). An excimer laser drills an array of vias

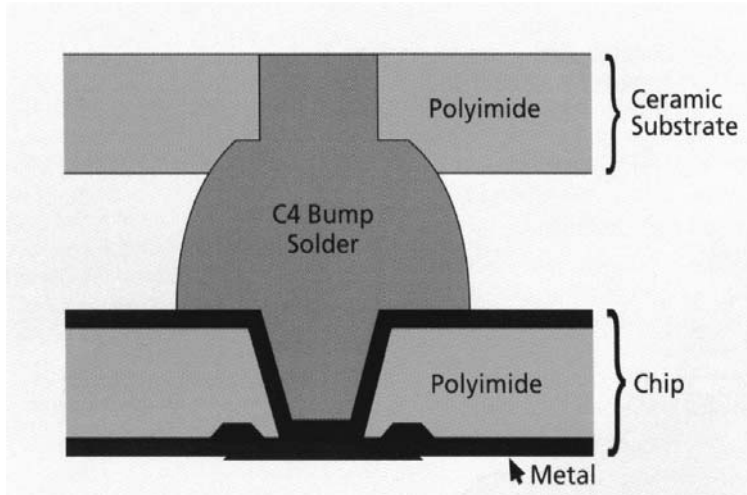


Fig. 11.41. Cross-section of an individual C4 connection; by courtesy of E.Wolbold [14]

with diameters of only $10\ \mu m$ (Fig. 11.39) through the passivation layer, and the conducting connections between chip and microelectronic package are realized with solder bumps similar to BGAs, but here the solder bumps are partially inside the vias [18, 4]. The use of vias in the passivation layer provides a strong mechanical connection between solder balls and chip beside a good electric connection (Fig. 11.42).

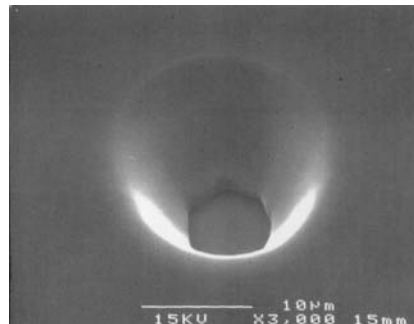


Fig. 11.42. REM picture of an excimer-laser-drilled via in polyimide with shallow wall angle; by courtesy of R.S. Patel [13]

Microvias and Microholes for Biomedical Applications. There is a wide range of applications of excimer-laser-drilled holes besides vias in microelectronics. One of them, the ablation of vias for inkjet-printer head nozzles, is discussed in chapter 9.2.

Another field is medical applications. ArF excimer lasers have been used for microfenestration of hydrophilic contact lenses with $50\ \mu m$ holes to improve their oxygen permeability [19].

The same author [20] reports the drilling of $700\ \mu m$ holes in the PVC walls of bilumen catheters with KrF lasers (Fig. 11.43). These catheters are used for the detection of the oxygen content in the blood of prematurely born babies. The most important components of these catheters are the arterial partial pressure O₂ and CO₂ (PaO₂ and PaCO₂) sensors that consists of a spiral of up to five rectangular holes (Fig. 11.44), which are drilled simultaneously through an optical fiber with the $193\ nm$ radiation of an ArF excimer laser and a spatial multiplexer. These holes are filled with reagents whose transmission properties depend on the blood's O₂ and CO₂ partial pressures.

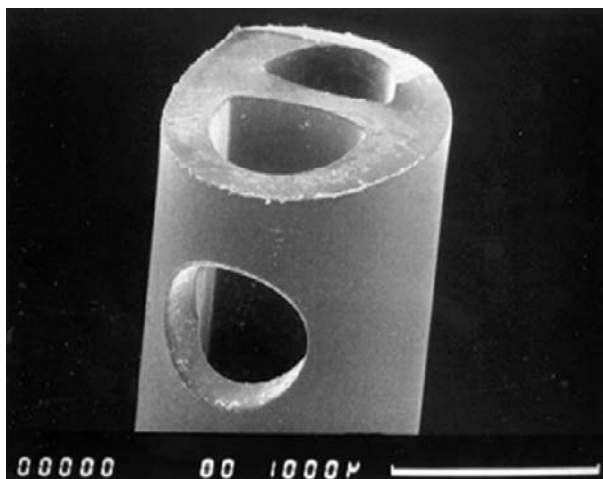


Fig. 11.43. $700\mu m$ excimer laser-drilled hole in a PVC bilumen sleeving tube [20]

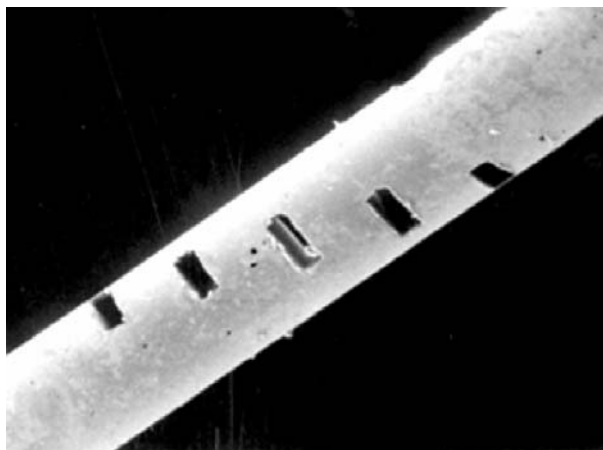


Fig. 11.44. $20 \times 50\mu m^2$ through-holes in a $100\mu m$ acrylic optical fiber [20]

Excimer laser hole drilling was even employed for fertility treatment. Holes through the outer ovum layer (zona pellucida) of artificially fertilized ovas allow easier rooting in the uterus. After first experiments with mouse oocytes in 1991 (Fig. 11.45), the “first excimer laser babies” were born in Israel in 1997 [21].

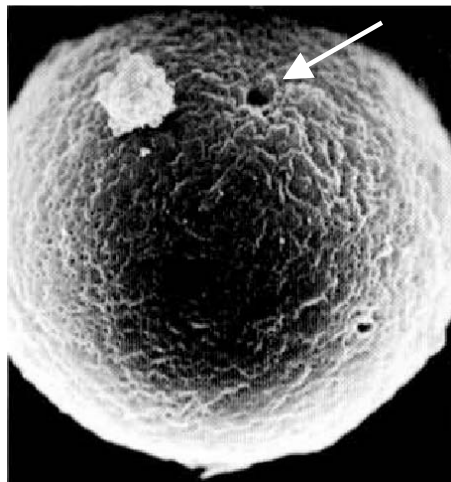


Fig. 11.45. Mouse oocyte with $3 \mu\text{m}$ excimer-laser-drilled hole [22]

Nowadays the excimer laser is more often used for contraception than for fertilization. Precise holes with diameters of typically $10 \mu\text{m}$ are drilled in latex condoms to calibrate condom leak-testing equipment [23].

Further application are the drilling of micro- and nanotiter plates and the machining of high transmittivity meshes and membranes. Thin film particles and bacterial filters having mesh sizes down to $0.5 \mu\text{m}$ can be fabricated with excimer lasers.

It is believed that with sub- μm nozzles in an inhaler, medication forced through this tiny holes would be so small that it is absorbed directly in the lung's blood vessels [24]. This medication would be hundreds of times faster than classical medication like tablets or syringe shots, which might be interesting not only in the case of biological warfare.

Other Applications. Surface treatments for other industrial purposes are also reported.

Examples in the aerospace industry are manufacturing of porous panels for hybrid laminar flow systems or drilling of carbon fiber composites for acoustic damping panels [25]. Williams and co-workers drilled holes with diameters of $40 - 60 \mu\text{m}$ in 1 mm -thick titanium for the production of porous panels. They performed multiple hole drilling but not with the usual mask technology that uses only a small part of the laser energy but with diffractive optical elements and beam utilisation factors of 80%. In 1.6 mm -thick aluminium, they drilled 6.6 million holes at a rate of more than 200 holes per minute. The same group even drilled arrays of larger holes with diameters up to the millimeter range like hexagonal holes in titanium.

Another impressive application of excimer laser hole drilling was presented by the Nederlands Centrum voor Laser Research (NCLR). In a joint-venture

with a US jet-engine company, they developed a drilling system that generates an array of equal intensity laser beams out of one original XeCl excimer laser beam by employing either a lens array or a hologram [26]. By this means they are able to drill more than a hundred holes simultaneously (Fig. 11.46).

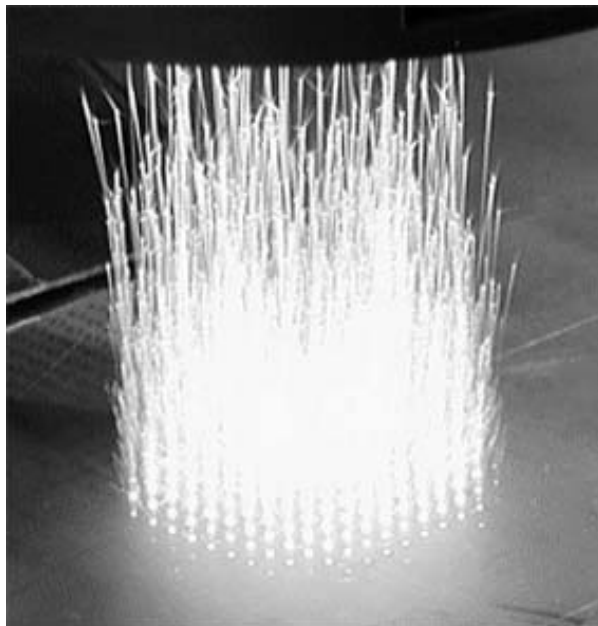


Fig. 11.46. Parallel hole drilling with a XeCl excimer laser in a titanium plate [26]

References

1. R. Srinivasan, V. Mayne-Banton: Appl. Phys. Letter **41**(6), 576–578 (1982)
2. R. Srinivasan, B. Braren: Sci. **22**, 2036–2043 (1984)
3. J. Brannon, J. Lankard, et al.: J. Appl. Phys. **58**(5), 2036–2043 (1985)
4. F. Bachmann: Appl. Surface Science **46**, 254–263 (1990)
5. J. Ihlemann, B. Wolff, P. Simon: Appl. Phys. A **54**, 363 (1992)
6. H. Schmidt, J. Ihlemann, B. Wolff-Rottke, K. Luther, J. Troe: Journal of Applied Physics **83**, 5458 (1998)
7. B. Wolff-Rottke, H. Schmidt, A. Scholl, J. Ihlemann: “Micro machining with excimer lasers: Photoablation and plasma sputtering”, in *Proceedings SPIE* Vol. 1810 (1992), p. 650
8. B. Burghardt, H.J. Kahler, D. Basting: “High resolution excimer laser based micromachining”, in *Proc. ECLAT Laser Treatment of Materials*, ed. by B. Mordike (1992), p. 609
9. M. Nobis, C. Scherer, O. Nuyken, F. Beinhorn, J. Ihlemann: Macromol. Mater. Eng. **275**, 1 (2000)

10. J. Békési, J.H. Klein-Wiele, D. Schäfer, J. Ihlemann, P. Simon: "Surface texturing of metals with sub-micron precision using a short pulse uv laser", in *Proc. SPIE* Vol. 4830 (2003), p. 497
11. M. Charrier, D. Everett, J. Fieret, T. Karrer, S. Rau, J.L. Valard: "Manufacture of a conformal, multi-layer RF antenna substrate using mask imaging technology and a 6-axis robot", in *SPIE* Vol. 4274 (2001), p. 393
12. B. Manirambona, J.D. Baets, A. Vervaet: Applied Surface Science pp. 171–176 (2003)
13. R. Patel, T. Redmond, C. Tessler, D. Tudry, D. Pulaski: Laser Focus World **1**, 71–75 (1996)
14. G. Wolbold, C. Tessler, J. Tudry: Lambda Physik Industrial Report No. 10 pp. 1–6 (5/1997)
15. T. Lizotte, O. Ohar, T. O'Keefe, C. Kelly: Solid State Technology pp. 120–128 (9/1996)
16. D. Zankowsky: Laser Focus World pp. 135–139 (12/1998)
17. L. Burgess, F. Pauri: Circuit World **25**(2), 31–34 (1999)
18. C. Tessler, D. Tudry: "Projection laser ablation – an alternative method of patterning semiconductor polyimide passivation layers", in *Proceedings of the 12th International Congress (Laser'95), Key Technology Laser: Challenge for the Factory 2000* Munich (Germany) (1995), pp. 61–68
19. M. Gower, P. Rumsby, D. Thomas: "Novel applications for fabricating biomedical and sensor products", in *SPIE* Vol. 1835 Excimer Lasers (1992), pp. 133–142
20. M. Gower: "Excimer laser micromachining: A 15 year perspective", in *SPIE* Vol. 3618 (1999), pp. 251–261
21. J. Siege: "New laser technique improves fertilization chances", in *Jerusalem Post, 10. July* (1997)
22. D. Palanker, S. Ohad, A. Lewis, J. Shenkar, S. Penchs, N. Laufer: Lasers in Surgery & Medicine **11**, 580 (1991)
23. B. Gu, R. Hunter, D. Wall, M. Frechette: Medical Device & Diagnostic Industry Magazine (1998). Cover Story November
24. B. Leighton, S. Holes: The (Nashua) Telegraph (online) (July 28 2002)
25. S. Williams, P. Marsden, N. Roberts, J. Sidhu, M. Venables: "Excimer laser beam shaping and material processing using diffractive optics", in *SPIE conference on High-Power Laser Ablation, Santa Fe, New Mexico, April 1998*, *SPIE* Vol. 3343 (1998), pp. 205–211
26. M. Hatcher: Opto & Laser Europe **Issue 94**, 12 (2002)

12 Micro-Processing of Borosilicate Glass and Polymers

B. Keiper, T. Petsch, H. Exner

12.1 Borosilicate Glass

Presently, there is a growing demand from the industry for micro-processing of materials. In particular, for applications in the fields of microsystems technology, biotechnology and medical technology it is necessary to produce structures with dimensions down to the micrometer scale. This refers especially to materials that cannot or not in a sufficient quality be processed by conventional methods used in silicon technology.

The excimer laser mask projection technique is a powerful tool for the generation of the required micro structures in a variety of materials. Due to its anodic bondability to silicon, Pyrex glass (7740 borosilicate Pyrex® glass, Corning Inc.) is an interesting material for many applications in the field of microsystems technology. The possibility of microstructuring of Pyrex glass using laser technologies will enlarge the number of potential applications considerably. Micro holes in the glass represent the precondition for the generation of electrical through-connections. Such through-connections are beneficial for the minimization of the area of microsystems by transferring electrical ports to the backside of the system. Therefore more systems can be placed on a single wafer stack. The alternatively used ultra-sonic drilling technology is not suitable for this application due to the limitation to relatively large minimum hole diameters normally of over $200 \mu\text{m}$.

Small channel structures in glasses are needed for micro fluidic applications (i.e. Lab-on-Chip). Via small holes in the glass liquids can be supplied into the fluidic structures. We investigated the structuring of Pyrex glass to acquire the knowledge for the realisation of the required devices. The experiments were carried out in the framework of cooperative research projects of 3D-Micromac AG, Chemnitz and Laserinstitut Mittelsachsen e.V., Mittweida.

Hence $500 \mu\text{m}$ -thick Pyrex glass wafers were drilled and micro structured (see also references [1, 2]) using the subsequently explained excimer laser micro processing equipment (see Fig. 12.1) at the Laserinstitut Mittelsachsen e.V. An ArF-excimer laser (ExciStar S-500, TUILASER AG) was connected

to an optical assembly (LightBench, ATL Lasertechnik GmbH). The processing parameters used are condensed in Table 12.1. The oxygen content of the air absorbs the laser radiation at 193 nm wavelengths, resulting in a loss of laser energy of about 10 percent per meter length of the optical path (20 percent in our set-up) and in the formation of ozone. To prevent the ozone we air-sealed the optical assembly and connected one side to an argon gas supply and the other side to an exhaust exit.

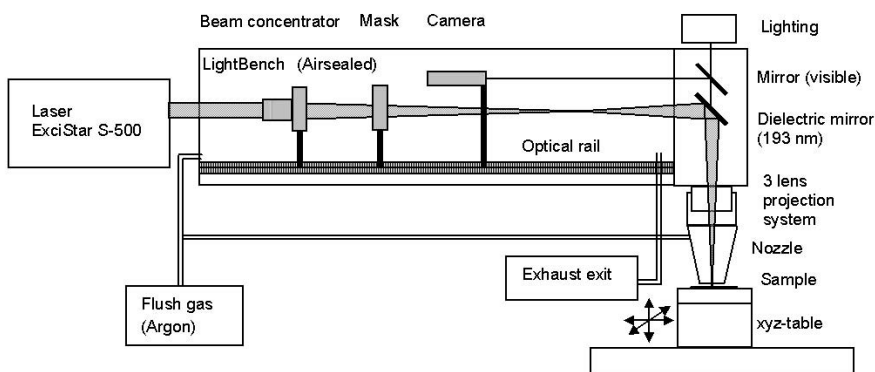


Fig. 12.1. Experimental set-up for excimer laser micro processing

Table 12.1. Processing parameters

Excimer laser					
Wavelength [nm]	Pulse duration [ns]	Repetition rate [Hz]	Pulse energy [mJ]	Laser fluence [J/cm^2]	Reduction scale with 3 lens
193	10	1 to 500	Up to 8	0.3 to 25	1:10

The use of the beam concentrator consisting of two lenses allows us to increase the laser fluence from 40 to 250 mJ/cm^2 at the surface of the mask and therefore to 25 J/cm^2 at the sample surface at a reduction scale of $1:10$. A camera system enables the adjustment of the sample surface to the projection plane and the observation of the sample surface during the laser processing. The sample is moved by a xyz-table ($150 \times 150 \times 11\text{ mm}^3$, Feinmess Dresden GmbH) with contouring control (A.C.S. Electronics Ltd.). A “Position Event Generator” ensures the precise trigger of the laser pulse with respect to the actual position of the x- and y-axis. The resolution of the system is $0.1\text{ }\mu\text{m}$.

We used circular and square masks in our experiments. The size of the processed area at the surface of the samples was varied between 30 and $200\text{ }\mu\text{m}$. The following reported values for the size of conical holes and channels are the values at the surfaces of the samples. In order to generate channels and other deep structures at the surface of our samples, too, we have applied a scanning contour mask technique with variable overlap of the laser pulses.

After processing of Pyrex glass we can observe a lot of debris around the processed area. Therefore it is necessary to clean the samples with a standard process using buffered hydrofluoric acid. The roughness values R_a at the bottom of the generated structures were measured with a Dektak 3030 profilometer.

12.1.1 Drilling of Holes in Pyrex Glass

Investigations of the ablation rates of Pyrex glass in dependence on the laser fluence and on the total ablation depth (the number of pulses) were carried out at different repetition rates. The first laser pulses of a pulse trail did not lead to a distinct ablation of material. They caused only a laser-induced change of the properties of the sample surface, e.g. the ablation of impurities or water as well as an increasing roughness and absorption. After initialisation of the ablation process the ablation rate increased to 140 nm per pulse (ten pulses, 10 J/cm^2 fluence and 500 Hz repetition rate). Between 50 and 100 laser pulses the ablation rate decreased to 50 nm per pulse. This behaviour - the trend of the change of the ablation rate in dependence on the total ablation depth - was the same at repetition rates from 50 to 500 Hz . Increasing laser fluences between 7 and 13 J/cm^2 led to higher ablation rates but not to a change in the dependence of ablation rate on the total ablation depth. Those ablation rates at the beginning of the drilling process were generally smaller than the mean ablation rate for drilling through the $500\mu\text{m}$ thick wafer.

For drilling we used a special vacuum chuck with a hollow space below the inner part of the wafer. The projection plane was adjusted to the surface of the wafer and was kept in this position throughout the whole drilling process. The moment the hole is drilled through was determined by the UV-laser-induced fluorescence observed on a white sheet of paper placed beneath the wafer. We calculated the average ablation rate for different laser fluences, repetition rates and diameters.

The results are shown in Fig. 12.2 exemplary for holes with 30 and $50\mu\text{m}$ diameters and 100 Hz repetition rate. The first points of the curve characterize the minimum fluence that is required for drilling through the whole wafer. Below that fluence the drilling process stopped before drilling through. This behaviour is due to the conical shape of the holes. The slope of the walls and thus the maximum thickness that can be drilled through depends on the laser fluence. Consequently smaller hole diameters require larger laser fluences: 4 J/cm^2 for $50\mu\text{m}$ diameter and 7 J/cm^2 for $30\mu\text{m}$ (100 Hz repetition rate).

The steep walls ($< 2.3^\circ$) reflect probably a large part of the radiation down to the ground of the hole so that the laser fluence can increase with growing total bore depth with a decreasing ground area, resulting in larger average ablation rates compared to the ablation rates during the first hundred laser pulses.

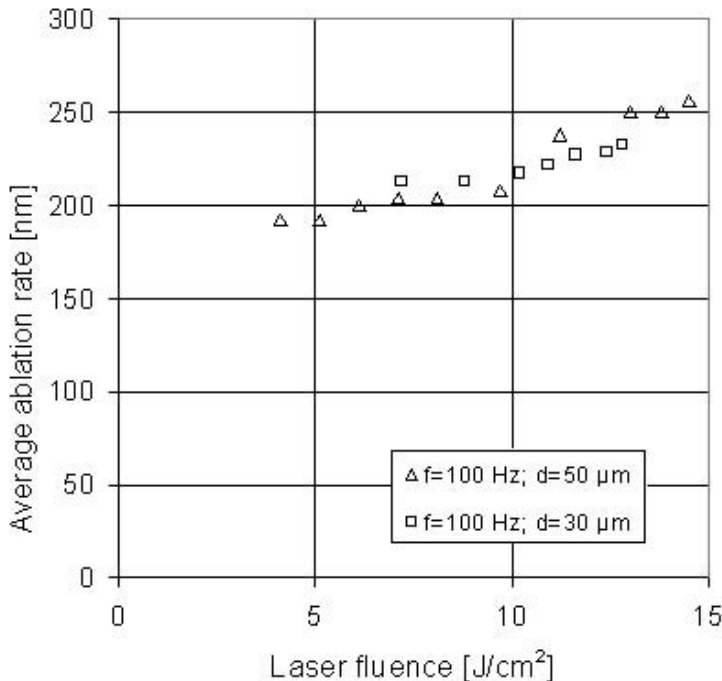


Fig. 12.2. Average ablation rate (ablation per pulse) in dependence on laser fluence (50 and 30 μm hole diameters, 500 μm thickness of Pyrex glass and 100 Hz repetition rate)

The influence of the laser fluence on the average ablation rate is relatively small: The threefold increase of laser fluence results only in the 1.4 fold increase in ablation depth (see Fig. 12.3). We assume that the excess of energy is partly consumed by the evaporation of the larger volume that is ejected from the bore due to the decreasing conicity of the hole. The ejected material probably absorbs another part of that energy and produces stronger laser plasma. At repetition rates between 50 and 500 Hz we can observe a similar behaviour. Thus the ablation rate is nearly independent on the hole diameter (30...100 μm).

During the drilling experiments with both diameters we can observe differences in the ablation process at different laser fluences: At a laser fluence just above the minimum for drilling through, the observed fluorescence light becomes visible only after drilling through the wafer. When we used higher laser fluences, we observed some violet fluorescence light already at nearly half the drilling time. However, only when the hole is drilled through, the fluorescence area becomes clearly defined and the observed fluorescence became more intensive allowing us to determine exactly the drilling time. This behaviour indicates that some laser light obviously shines through micro cracks

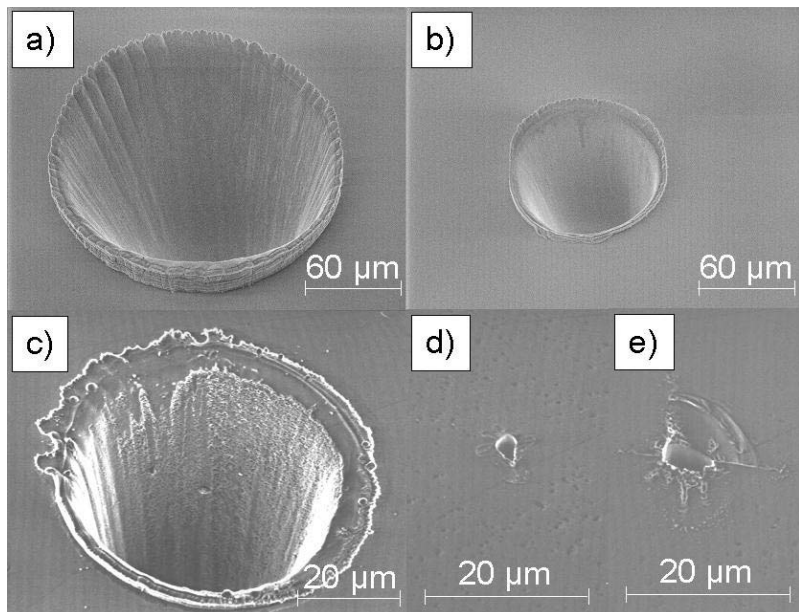


Fig. 12.3. SEM micrographs of typical excimer-laser-drilled holes with diameter of a) $200 \mu\text{m}$, b) $100 \mu\text{m}$, c) $50 \mu\text{m}$ front side view; 500 Hz repetition rate; a, b, e) 5 J/cm^2 , c, d) $4, 4 \text{ J/cm}^2$; d, e) view from rear side

in the glass already after half the drilling time. The crack formation should be due to the high pressure at the ground of the hole caused by the expansion of the strong laser plasma. Another reason for the cracks might be the thermally induced mechanical stress in the glass, but since the behaviour is nearly independent of the repetition rate this mechanism is not probable.

The influence of the repetition rate on the mean ablation rate is not significant. The mean ablation rates vary between 200 and 250 nm per pulse, resulting in about 5 s drilling time for $500 \mu\text{m}$ thickness of the wafer and 500 Hz laser pulse repetition rate.

The results of Scanning Electron Microscopy (SEM) investigations agree with the above explained relationships: The repetition rate has only a minor influence on the quality of the holes at the rear side of the wafer, whereas increasing laser fluence leads to an increasing crack formation and break-off of material at the bottom of the wafer. Best results were obtained with low laser fluences where no crack formation and only little break-off of material but also a decreasing hole diameter at the rear side of the wafer was observed. The reason for this behaviour should be the force that is caused by the high pressure of the expanding laser-induced particle plasma. That force increases with growing diameter of the bottom of the hole. That means we can minimize

or prevent the damage inside the glass when the hole diameter at the rear side of the wafer is small.

The appearance of the front side of the holes shows only little dependence on the laser fluence. On the front side rim of the hole a small (about $20\ \mu m$ wide) ridge can be detected. With holes of the same diameter larger ridges can be detected with increasing laser fluence. Additionally under optimized parameters we observed an increase of the ridge with increasing hole diameter. The height of the ridge can vary from $1\ \mu m$ at low fluences and $50\ \mu m$ diameter to about $20\ \mu m$ at $200\ \mu m$ diameter. These ridges have to be taken into account during the design of the microsystem; otherwise the wafers must be polished after laser processing. Some examples of Scanning Electron Microscopy (SEM) micrographs of holes with different diameters drilled with $500\ Hz$ repetition rate are shown in Fig. 12.3 (see also reference [1]).

The holes show a conical shape and have a relatively small diameter at the rear side of the wafer provided the optimized parameters are used. The slope of the walls varies between 3.5° and 1.6° (100 and $30\ \mu m$ diameter, respectively).

Up to now it seems not possible to avoid the break-off of material in the moment of drilling through completely merely by optimizing the laser parameters. In our experiments we have also tested a number of other possibilities to avoid such break-off: The wafer was coated with a photo resist or with a $1.5\ \mu m$ -thick physically enhanced CVD- SiO_2 -film in order to support the wafer during drilling through. However, those films did not distinctly improve the quality of the holes.

In another experiment we put a second Pyrex glass wafer beneath the drilled wafer, but also without any positive result. Only after putting an alcohol film between the pressed wafers we did observe fewer breaks-off of material. This might be caused by the generation of a counteracting force at the rear side of the wafer and/or by the cooling effect of the alcohol.

Summarizing those experiments: We were able to minimize cracks and break-off at the rear side of the wafer but we could not prevent it completely. Therefore we solved the problem in another way: we drilled the glass from both sides of the wafer. Using this method we were able to prevent cracks and break-off or to remove it during drilling from the rear side. Additionally, it is possible to enlarge the minimum diameter inside the hole. The optical micrograph in Fig. 12.4 shows a cross-section of such a hole.

12.1.2 Generation of Channels in Borosilicate Glass

We investigated the dependence of the properties of micro channels in Pyrex® glass on the laser processing parameters. The channels were produced using a square or circular mask, at a laser pulse repetition rate of $500\ Hz$ and a constant velocity of the movement of the sample. With the velocity of the sample and the pulse repetition rate the distance between two pulses was adjusted. In our experiments we varied the pulse distance from 1.5 to $3\ \mu m$,

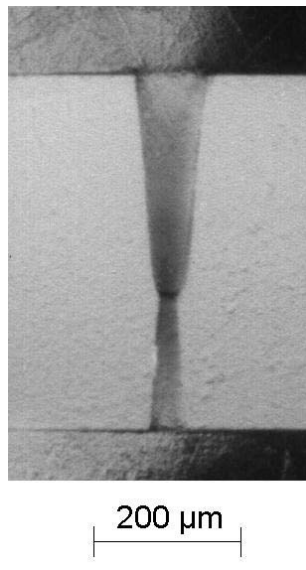


Fig. 12.4. Cross-section preparation of a hole in $500 \mu\text{m}$ -thick Pyrex glass. Drilled with $100 \mu\text{m}$ diameter from the front side and $50 \mu\text{m}$ diameter from the rear side of the wafer.

the laser fluence from 2.5 to 5.5 J/cm^2 and the size of the reproduction from 50 to $100 \mu\text{m}$. We observed a strong dependence of the surface quality on the laser fluence and on the pulse distance. The roughness of the bottom of the channels was very small ($R_a = 35 \dots 150 \text{ nm}$) but from the SEM-pictures we can see a distinct difference in the surface properties: Using low laser fluences (4.8 J/cm^2 and below) and high pulse distances ($3 \mu\text{m}$) the surface is very smooth, only with a certain waviness due to the pulse distance (see Fig. 12.5, left). With decreasing pulse distance and increasing laser fluence we can observe, inside the smooth channel, a number of isles with a micro roughness. At high laser fluences (5.5 J/cm^2 and above) the whole channel show this micro roughness (see Fig. 12.5, right). We assume that changes in the glass surface caused by high laser fluences and incubation effects (at increasing numbers of pulses at a certain position) led to an enlarged reactivity of the material with the cleaning mixture resulting in a surface with the observed characteristic micro roughness. This behaviour can be used to adapt the surface properties to different requirements (i.e. adsorption properties, friction coefficient and wetting behaviour). The values of the roughness R_a are displayed in Fig. 12.6 for the different laser fluences and pulse distances. The parameter ranges for smooth surfaces, surfaces containing isles with micro roughness and micro rough surfaces are marked, too, in this diagram. The ablation rates vary between 150 nm/pulse (at low laser fluences) and 250 nm/pulse . The ablated depth after single processing of the sample

is about $5 \mu\text{m}$ ($3 \mu\text{m}$ pulse distance and 3 J/cm^2). Repeated processing until the desired depth is reached can produce deeper channels. To generate larger cavities we processed a number of parallel lines with the same line spacing like the pulse distance.

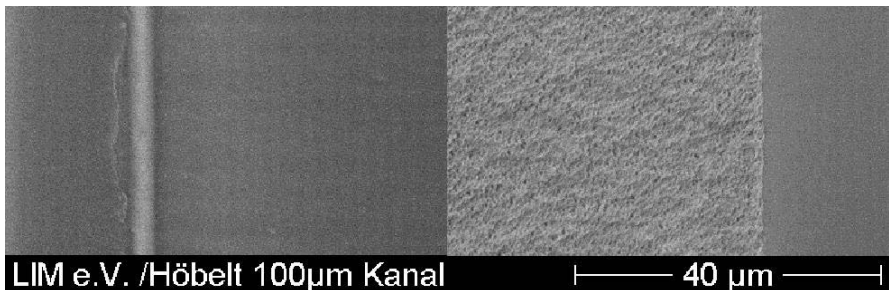


Fig. 12.5. SEM-view of laser-generated channels in Pyrex[®] glass (cut-out). Fluence: 4.8 J/cm^2 , pulse distance: $3 \mu\text{m}$, $R_a = 50 \text{ nm}$ (left). Fluence: 5.5 J/cm^2 , pulse distance: $1.5 \mu\text{m}$, $R_a = 150 \text{ nm}$ (right).

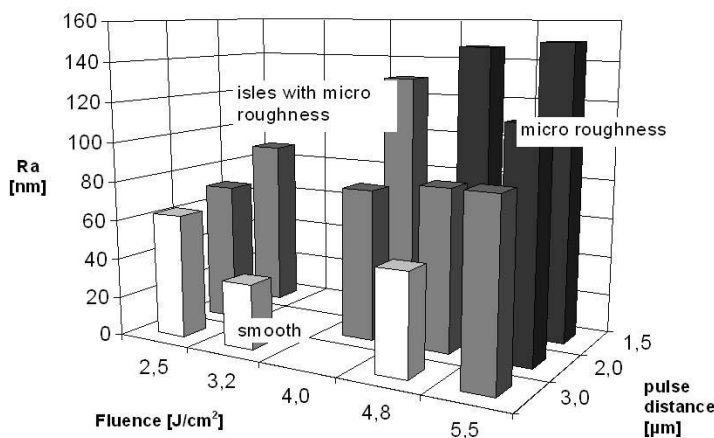


Fig. 12.6. Roughness R_a of the bottom of $100 \mu\text{m}$ wide channels in dependence on the laser fluence and the pulse distance. All channels are one time processed.

In order to produce precise structures with homogeneous depth we used a special motion controller with a “Position Event Generator” permitting a precise position-controlled trigger of every laser pulse. To realize constant processing conditions, the acceleration of the motion system starts about $100 \mu\text{m}$ ahead of the beginning of the channel, thus the triggering of the laser starts not until the desired velocity is reached. The deceleration starts in the same way after the end of the channel.

In Fig. 12.7 we show an example of a special structure in Pyrex® glass, applicable in micro fluidics, diagnostics, analytics and kinetics. The fluidic structure represents a cavity with three channels to supply, respectively, to drain liquids. The structure was generated using 4 J/cm^2 laser fluence, a $500 \mu\text{m}$ square mask ($50 \mu\text{m}$ at the sample surface) and $2 \mu\text{m}$ pulse and line distance. The length and width of the cavity is $350 \mu\text{m}$ at the glass surface and $250 \mu\text{m}$ at the ground of the cavity. This difference is due to the two-dimensional overlap of the laser pulses. The cavity and the channels have a depth of $55 \mu\text{m}$. The cavity is single processed and the channels have to be processed 25 times to get the same depth. The roughness of the base of the cavity is $R_a = 0.6 \mu\text{m}$. The high roughness value compared to the results of the single processed channels is partly due to the larger depth of the structure, but the chief cause is probably the use of laser parameters sub-optimal for achievement of a smooth surface.

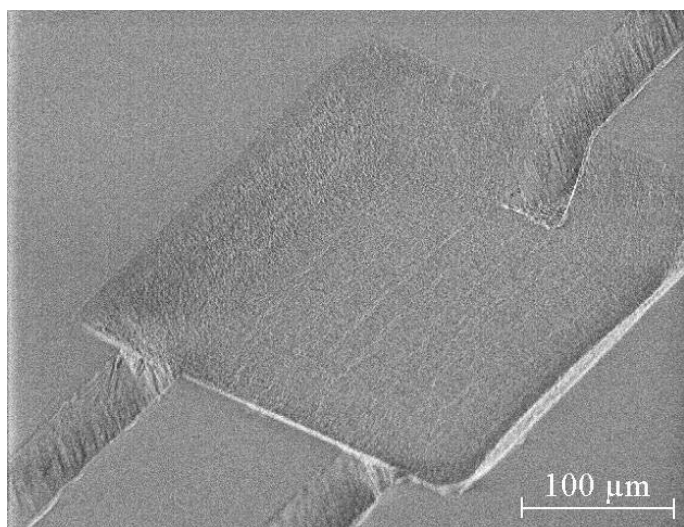


Fig. 12.7. SEM-view of a laser-generated cavity ($350 \times 350 \times 55 \mu\text{m}^3$) with channels ($50 \mu\text{m}$ width, $55 \mu\text{m}$ depth) in Pyrex® glass

By diagonal movement of the sample relative to the square mask lines with a V-shaped profile were generated. Using circular masks channels with semi-elliptically shaped profiles were generated.

Sloping walls at the beginning and the end of the channels and cavities due to the pulse overlap have to be taken into account in the design of fluidic devices or microsystems. Those sloping walls can be avoided by successive clearing and closing of the mask at the beginning and the end of each channel. This can be implemented by the use of a motorized slit mask.

This structure was also generated in Borofloat® glass. These channels exhibit higher roughness values at the bottom of the channels compared to Pyrex® glass. Depending on processing parameters more or less break-off of material inside or around the channel was observed.

In order to find the reason for the differences in the quality of the channels in similar glasses we have determined the absorption properties of the glasses. The transmission of 200 μm -thick Pyrex® glass and 500 μm -thick Borofloat® glass were measured at 193 nm wavelength and used to calculate the absorption coefficients and the skin depths (decay of the intensity to the $1/e$ -fold value) (see Table 12.2). The absorption coefficients of both glasses are high enough for ablation at relatively low fluences, but the high skin depth may be a reason of cracks inside the material. The better quality of channels in Pyrex® glass can be explained by the higher absorption coefficient.

Table 12.2. Absorption properties of borosilicate glasses at 193 nm wavelength

	Absorption coefficient α	Skin depth
Pyrex® glass	258 / cm	39 μm
Borofloat® glass	64...105 / cm	95...157 μm

Since the absorption coefficient increases with growing temperature the crack formation decreases with growing mean temperature during laser processing. We find this behaviour during drilling with high repetition rates, where no differences between the glasses were observed.

Additionally, we investigated the influence of different working gases (Ar, N₂, and He) on the quality of the channels in Borofloat® glass. The size of the reproduction was 100 μm , the repetition rate 500 Hz and the laser fluence 3 J/cm². The pulse distance was varied from 0.5 to 8 μm . Most of the generated channels are characterized by a lot of break-out of material around them (up to 50 μm in size). The lowest quality was achieved using He as working gas. The quality becomes successively better applying N₂ and Ar as working gas. Utilizing Ar between 0.5 and 1 μm pulse distance only small pieces of glass were broken out, and from 2 to 8 μm pulse distance no break-out was observed. In the mentioned sequence of changing from He to Ar the thermal conductivity and heat capacity of the gases decrease (see Table 12.3). Therefore we assume that the observed difference in the surface quality of the processing is caused by the different cooling effect, that means a quenching effect of the gases to the sample surface.

Table 12.3. Thermal properties of working gases at 20°C , 101.3 kPa

Gas	Thermal conductivity [Wm ⁻¹ K ⁻¹]	Heat capacity c_p [kJkg ⁻¹ K ⁻¹]
He	0.143	5.24
N ₂	0.024	1.04
Ar	0.0177	0.5

The dependence of the roughness of the bottom of the channels on the pulse distance is comparable to the above explained results with Pyrex® glass.

Some experiments were carried out using a $10\text{ }\mu\text{m}$ reproduction size and Ar as working gas. In accordance with the results of our drilling investigations, increasing laser fluences are required in order to process a decreasing area. For generation of $10\text{ }\mu\text{m}$ -wide channels we need a fluence of 5 J/cm^2 . Compared to 100 and $50\text{ }\mu\text{m}$ -wide channels observed at $10\text{ }\mu\text{m}$ over a larger range of pulse distances a lot of relatively large pieces of glass (around $10\text{ }\mu\text{m}$) broke out around the channels even if Ar was used as working gas. Only at high pulse distances ($1.9\text{ }\mu\text{m}$ and more) and low pulse overlap no break-out was noted but the channel depth is than nearly zero. At small pulse distances (0.05 to $0.1\text{ }\mu\text{m}$) only small pieces of glass (around $1\text{ }\mu\text{m}$) were broken out. Accordingly, higher thermally induced stresses, due to larger laser fluences at smaller areas, affect the increase of broken-out material.

12.1.3 Summary

Holes with diameters from 30 to $200\text{ }\mu\text{m}$ were created by excimer laser mask projection technique in Pyrex® glass ($500\text{ }\mu\text{m}$ thickness). Smaller diameters of holes require higher laser fluences to create clearance holes. The holes are conically shaped with slopes of the walls between 3.5° and 1.6° . By drilling from both sides of the wafer-holes with the best quality without break-off of material can be made. Moreover, this method offers the possibility to enlarge the minimum diameter inside the conical hole, too.

Smooth channels in Pyrex® glass (50 to $100\text{ }\mu\text{m}$ wide) were also generated. By varying the processing parameters we modified the surface properties of the channels. Increasing pulse distances and decreasing thermal conductivities of the processing gases affect decreasing roughness values of the processed surfaces. Additionally, a higher absorption coefficient reduces the roughness, too.

12.2 Polymers

For microstructuring of polymers we used the experimental set-up explained in the previous chapter. Additionally a SCANLAB scanner with a 56 mm scan lens was included. That scanner achieved the movement of the laser beam. A mask with a square aperture was projected onto the sample surface with a 14-fold size reduction. The processing parameters are listed in Table 12.4.

In PMMA samples channel structures were produced with a square aperture of $1 \times 1\text{ mm}^2$. The depth of channels was varied by using a different number of repetitions of the processing with the optimized parameters (see also reference [2]). The mask projection condition was kept at the sample surface during the whole process.

Table 12.4. Processing parameters

Excimer laser					
Wavelength [nm]	Pulse duration [ns]	Repetition rate [Hz]	Pulse energy [mJ]	Laser fluence [J/cm ²]	Reduction scale with scanner
193	10	1 to 500	Up to 8	0.3 to 2	1:14

Three-dimensional structures were generated using a smaller mask with a square aperture of $0.3 \times 0.3\text{ mm}^2$ ($22.5\text{ }\mu\text{m}$ at the sample surface). The structures were designed utilizing the 3D design software “SolidWorks” and saved to STL-format. To convert the STL-files into a scanner-compatible program a special software program was developed. The conversion includes the slice of the structure into layers with the same thickness. This value compares to the ablation depth after single processing of an area. The layers have to be successively processed to create the desired structure. The mask projection condition was updated after processing of each layer in order to realize the best possible qualities of the surfaces of the structures.

12.2.1 Generation of Channels in PMMA Using Scanner

The scanner is not perfectly suitable for mask projection due to different lengths between mask and sample surface in dependence on the processing position, particularly at large angles of deflection, and the projection requirements are not equally fulfilled for the whole cross-section of the beam. But at relatively small angles of deflection and using laser beams with small diameters and low divergences, the occurring errors can be neglected. The corresponding scan field was determined to be maximally $10 \times 10\text{ mm}^2$. The maximum scan field allowed by the scanner geometry is $20 \times 20\text{ mm}^2$. Another problem is the small bandwidth of dielectric mirrors for 193 nm wavelengths, resulting in an angle-dependent reflectance. We have determined a maximum scan field of $8 \times 8\text{ mm}^2$ where the variation of the laser fluence is smaller than 5%.

The performed tests with regard to the repetition accuracy of the applied scanner system showed the positioning errors to be smaller than the measurement uncertainty of the used microscope of $2\ \mu m$.

For the generation of microstructures in PMMA the projection of the $1\ mm$ square mask was scanned across the sample surface. This polymer is well machinable with excimer laser wavelengths of $193\ nm$. In order to achieve low roughness values at the bottom and at the walls of the structure we used a high pulse overlap of 97% (pulse distance: $1.75\ \mu m$). The channels have a width of $70\ \mu m$. The ablation rate at a laser fluence of $0.4\ J/cm^2$ was about $200\ nm$ per pulse. Channels with depths from 10 to $120\ \mu m$ were generated at a 2- to 8-fold repetition of the process. Remaining bridges between channels have a width between 5 and $20\ \mu m$.

At the bottom of the $30\dots50\ \mu m$ deep structures we measured a roughness R_a from 0.5 to $0.6\ \mu m$.

In cross-section preparations of different channels a deviation of the walls of the channels is noticeable. The tilt decreases with the growing number of repetitions and amounts to an angle between 19 and 7° at 2 to 8 repetitions, respectively.

The SEM-view of a complex spiral structure is shown in Fig. 12.8. The structure was generated using $360\ mJ/cm^2$ laser fluence and $300\ Hz$ pulse repetition rate. A 6-fold repetition of the process was necessary to obtain a depth of $80\ \mu m$. The remaining bridges between the channels exhibit a $10\ \mu m$ width.

Some experiments were carried out with $100\ \mu m$ channel width, where lowest roughness R_a of about $100\ nm$ was achieved using pulse distances of about $2\ \mu m$ compared to $1.75\ \mu m$ for a channel width of $70\ \mu m$. Those results indicate that the parameters have to be optimised not only for different materials but also for different sizes of the mask.

Consequently, we have shown that highly resolved channel structures in PMMA could be reproducibly generated via mask projection by the combination of excimer laser with scanner.

12.2.2 Generation of Three Dimensional Structures in PMMA Using Scanner

Preliminary investigations were carried out in order to optimize the pulse distance regarding smallest roughness of the three dimensional processed sample surfaces. Best results were obtained using $4.5\ \mu m$ pulse distance. A three-dimensional test structure was created using $650\ mJ/cm^2$ laser fluence and $4.5\ \mu m$ pulse distance.

The corresponding layer thickness was determined to $8.5\ \mu m$. Therefore the structure was sliced to 18 layers in order to produce a total structure depth of $153\ \mu m$. The scan direction of the laser beam was rotated 90° after processing of every single layer in order to reduce the roughness of the surface of the structure.

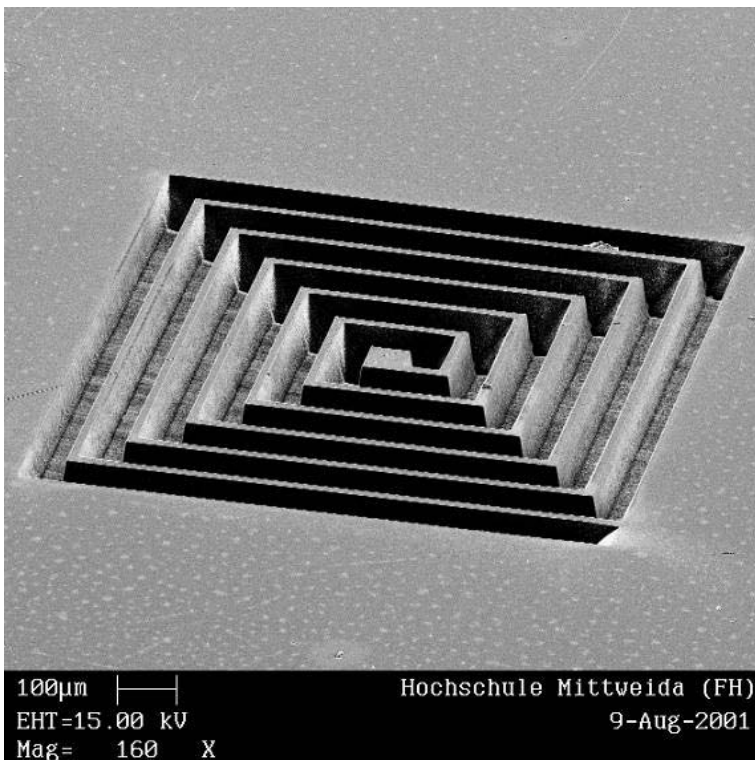


Fig. 12.8. SEM-view of a spiral structure in PMMA. The sample was micro structured using excimer laser radiation in association with a scanner. Parameters: 360 mJ/cm^2 laser fluence, 300 Hz pulse repetition rate, $1.75\text{ }\mu\text{m}$ pulse distance, 6 repetitions, $10\text{ }\mu\text{m}$ width of the bridges, $80\text{ }\mu\text{m}$ depth.

We measured a depth of the structure of $135\text{ }\mu\text{m}$, somewhat smaller than expected. The roughness R_a of the bottom of the structure was relatively large ($2\text{ }\mu\text{m}$). The SEM-views in Fig. 12.9 show a cut-off of the test structure, a small bridge indicating the high precision of the technique. The surface of the base shows an unwanted wave structure probably due to a disadvantageous pulse overlap at different processing directions. The layer thickness of $8.5\text{ }\mu\text{m}$ was found to be too large to produce precise three-dimensional structures. Especially a pyramid and a hemisphere show therefore rough, cascaded surfaces of those walls which feature angles of about 45° to the normal plane.

Some debris can be seen in detailed views of several surfaces. At relatively high laser fluences of 650 mJ/cm^2 , apparently not the whole ablated volume was transformed into gaseous form, as observed at lower fluences.

Further investigations were done using a lower fluence (200 mJ/cm^2) i.e. smaller layer thickness ($2.5\text{ }\mu\text{m}$) to achieve a better resolution of the sur-

faces of structures. The pulse distance was optimized again applying the new processing parameters. Best results were obtained with $5\ \mu m$ pulse distance.

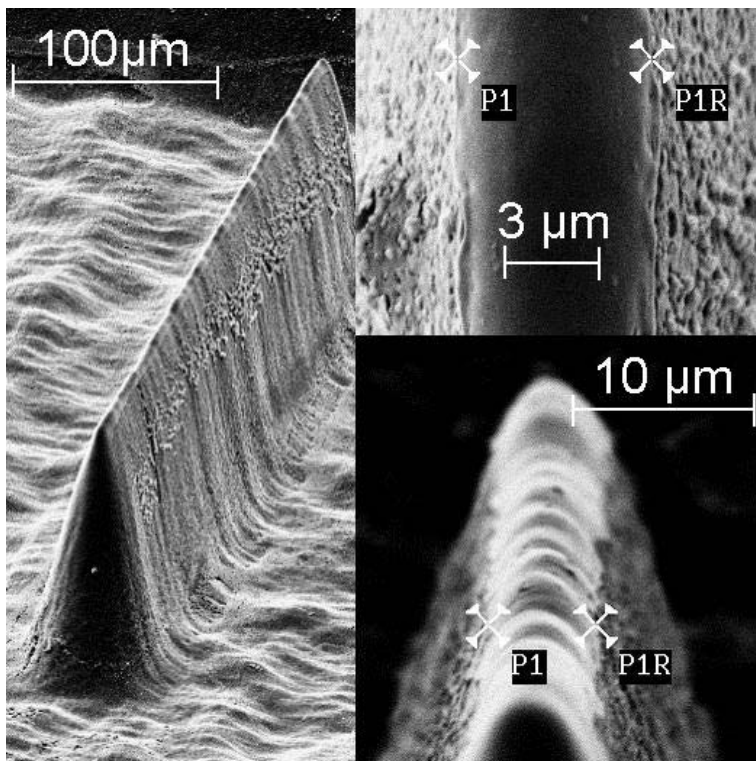


Fig. 12.9. SEM-views of a small bridge (cut-off of a test structure) in PMMA. The sample was micro structured using excimer laser radiation and scanner. Parameters: $650\ mJ/cm^2$ laser fluence, $300\ Hz$ pulse repetition rate, $4.5\ \mu m$ pulse distance, 18 layers, $150\ \mu m$ depth.

The roughness R_a of the bottom of structures was remarkably reduced to values between 0.2 and $0.4\ \mu m$. Some structures like cone, pyramid and hemisphere were generated with a good resolution. The SEM-view of the hemisphere (see Fig. 12.10) should clarify the results exemplary. Detailed views of surfaces of the different structures did not show any debris indicating the complete transformation of the ablated species into gaseous form at the above mentioned parameters. Some waviness remained at the structured surface but was much lower than in the above explained experiments. Maybe a fine tuning of the pulse distance is still possible.

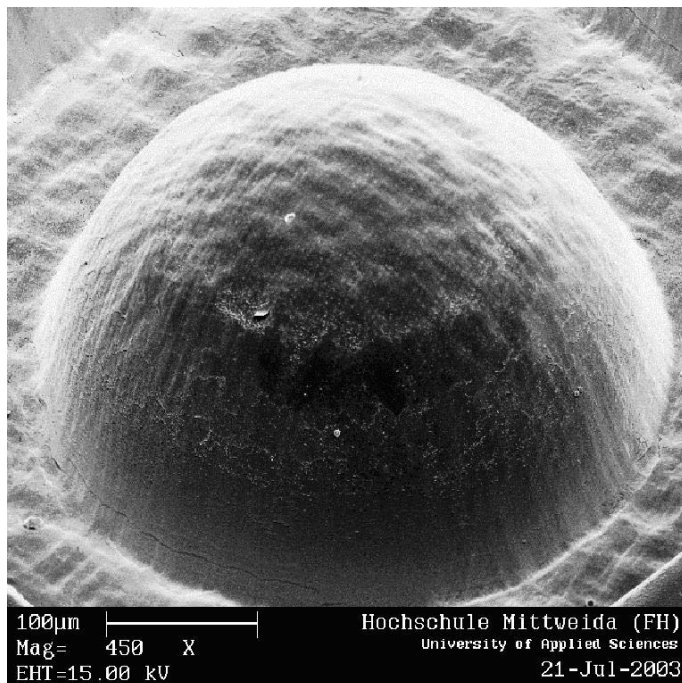


Fig. 12.10. SEM-view of a hemisphere in PMMA. Parameters: 200 mJ/cm^2 laser fluence, 300 Hz pulse repetition rate, $5\text{ }\mu\text{m}$ pulse distance, 81 layers, $225\text{ }\mu\text{m}$ depth, $R_a \approx 0.28\text{ }\mu\text{m}$.

The above explained results document the good applicability of the excimer laser mask projection technique via scanner for generation of highly resolved three-dimensional structures in PMMA. The fundamental requirement for the solution of that task is a coherent software concept for the conversion of CAD-data (STL files) to the required machine language. By means of a fruitful cooperation between user - Laserinstitut Mittelsachsen e.V. Mittweida, machine manufacturer – 3D-MICROMAC AG, Chemnitz, and the software developer – IVS Solutions AG Chemnitz the problem was solved effectively.

12.2.3 Microstructuring of Polymer Tubes

The placement of many small openings in nylon tubular bodies is an interesting challenge useful for a variety of applications. Depending on the form and size of the openings different applications are imaginable: stents, filter cartridges, modules for dosage and so on. We investigated the generation of perforated nylon tubular bodies with excimer laser mask projection technique. Experiments were carried out in the clean room laser application laboratory of 3D-Micromac.

The radiation of an Excistar M 100 (TUI-Laser AG) with 193 nm wavelength, 150 mJ pulse energy and 100 Hz repetition rate was used to illuminate a hexagonally mask with 2.88 mm height. Using a five-lens projection objective ($f = 50\text{ mm}$) we projected the structure of the mask to the sample surface with a reduction scale of 1:8. The sample was assembled to a $\text{xyz}\varphi$ -positioning system ($200\text{ mm} \times 200\text{ mm} \times 300\text{ mm}$). The tubes have a diameter of 6 mm and a material thickness of $150\text{ }\mu\text{m}$.

Best results were obtained using a laser fluence of 2 J/cm^2 at the sample surface. At that fluence we needed 200 pulses to create a clearance hole. Those parameters represent a compromise between product quality and machining speed. That means we can observe an unacceptable increase of melting zones at the rims of the openings if higher laser fluences are applied. Upon completion of each opening the sample was moved to the position of the next opening applying the x - and φ -axis. An example for a micro structured nylon tubular body is given in SEM micrographs (see Fig. 12.11). Those micrographs document the good quality of the laser-generated honeycomb structure, which was made without use of an expensive laser beam homogenizer. Remaining bridges between the hexagons feature a width of $30\text{ }\mu\text{m}$.

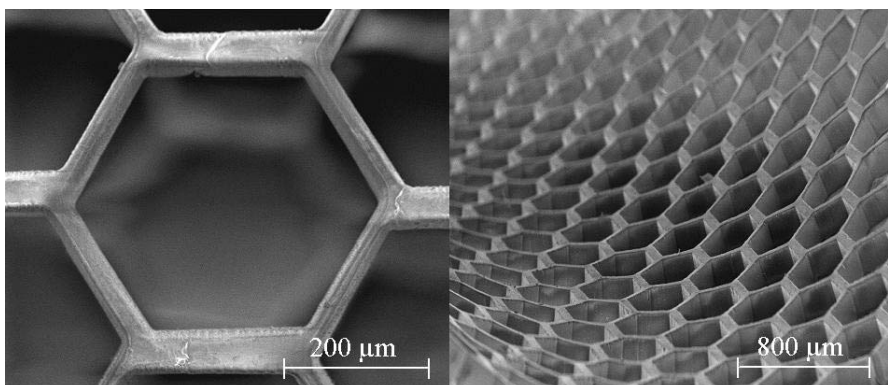


Fig. 12.11. SEM micrographs of a honeycomb structure in a nylon tubular body: height of hexagon $360\text{ }\mu\text{m}$, width of bridges $30\text{ }\mu\text{m}$

12.2.4 Writing of Mixer Structures in PMMA

Mixer structures are applicable to stir several liquids in fluidic systems. Such systems are of growing interest in the fields of medical technology, biotechnology and chemical technology. For instance, micro reaction systems are useful for the economic synthesis of small amounts of expensive chemicals.

Investigations for the generation of such mixer structures were realized at the laser micro processing laboratory of the Laserinstitut Mittelsachsen e.V. We wrote the required structures in PMMA using a KrF excimer laser

LPX 305i (Lambda Physik AG). The laser beam was homogenized with crossed micro cylinder lens arrays. The square mask aperture was projected to the sample surface applying a 1:8 reduction scale. The ablation rate of PMMA increases from $0.85 \mu\text{m}/\text{pulse}$ at a fluence of 1 J/cm^2 to $3.5 \mu\text{m}/\text{pulse}$ at 3 J/cm^2 .

In order to create the requested structures, the sample was moved during laser processing with constant velocity over a distance that is in accordance with the reproduction length of $600 \mu\text{m}$. Thus a triangular form of the cross-section of the cavity in machining direction was created (see Fig. 12.12). The parameters were selected in order to produce the demanded depth of the structure ($350 \mu\text{m}$ in the presented example). Such a structure can be made using a laser fluence of 1.5 J/cm^2 ($2 \mu\text{m}/\text{pulse}$ ablation rate) at 10 Hz laser pulse repetition rate and $35 \mu\text{m/s}$ feed speed of the sample. After creation of such a single element the sample was moved by the length of the projection in x- or rather in y-direction, the laser being switched off. Those process steps were repeated until the desired structure was completed. The real mixer structure arises from the offset of the neighbouring rows of cavities by one reproduction length.

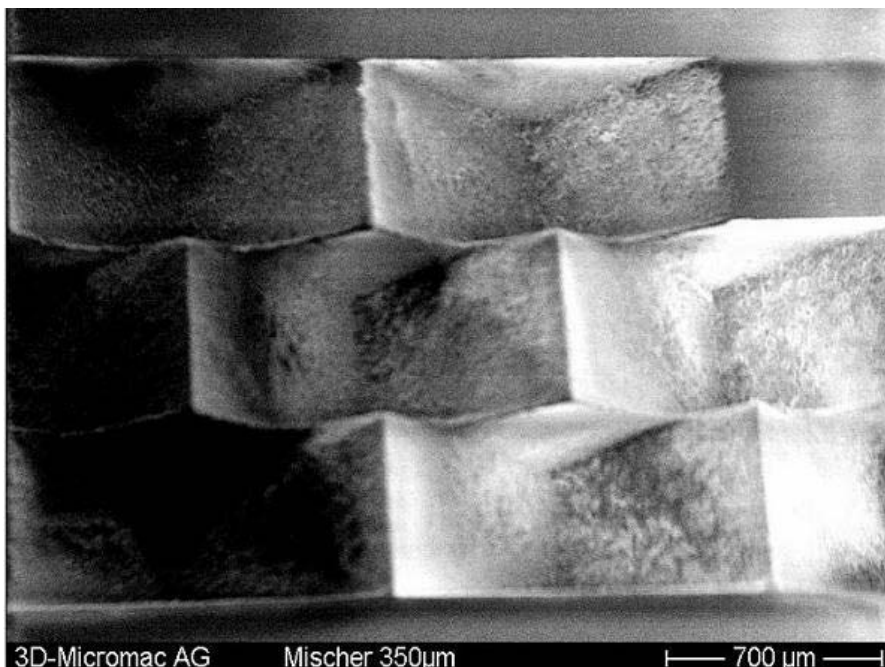


Fig. 12.12. SEM micrograph of a mixer structure in PMMA. Size of a single element $1200 \mu\text{m} \times 600 \mu\text{m} \times 350 \mu\text{m}$.

12.2.5 Acknowledgement

The investigations on microstructuring of borosilicate glass and polymers were partly supported with EFFRE-means of the EU and of the Freistaat Sachsen (Project-no.: 4355/679) and with means of the BMBF (Innoregio InnoSachs, FKZ 03i1702).

For their cooperation we thank Robby Ebert, Udo Löschner (Laserinstitut Mittelsachsen e.V., Mittweida), Jens Hänel and Sven Albert (3D-Micromac AG, Chemnitz). We thank Iris Höbelt from the Center of Microtechnologies (ZfM) at Chemnitz University of Technology for SEM views and Andreas Eysert and Enrico Gehrke from the University of Applied Sciences Mittweida for cross-section preparations and SEM views.

References

1. B. Keiper, H. Exner, U. Löschner, T. Kunze: J. Laser Applications **12**(5), 189–193 (2000)
2. B. Keiper, R. Ebert, R. Böhme, H. Exner: Proceedings of SPIE **5116**, 20–27 (2003)

13 F₂-Laser Microfabrication for Photonics and Biophotonics

Peter R. Herman

13.1 Introduction

The F₂ laser defines the short-wavelength forefront of commercial laser systems. As such, the 157-*nm* lasing wavelength is highly attractive for defining features to $\sim 100\text{ nm}$ in size during laser processing [1], and extensions to sub-100 nm processing were under development for the next generation semiconductor lithography exposure tool [2, 3]. The F₂ laser further provides a high photon energy of 7.9 eV that drives strong interactions with nearly all materials, opening a broad base of laser applications to wideband-gap materials such as transparent glasses like fused silica or robust polymers like Teflon. The F₂-laser light can smoothly microsculpt optical surfaces with precise $\sim 10\text{-nm}$ depth control without generating the microcracks normally produced by longer-wavelength lasers [4, 5, 6, 7]. The strong interactions can be further tailored to more gentle internal modification of glasses to imprint buried refractive index structures like volume gratings or optical waveguides [5, 6, 8]. Such processes merit a broad range of new applications such as custom fabrication of micro-optic components, diffractive optical elements, microfluidic channels for laboratory on a chip (LOAC), planar or bulk 3-D optical circuits, and repair and phase trimming of optical functions. Microfabrication also extends to weakly absorbing inorganics or polymers like polyethylene, PMMA, and PTFE [4, 9, 10, 11, 12, 13, 14, 15, 16] for potential biomedical, electronic, and MEMs applications, and to sapphire [17] and semiconductor materials [18].

Commercial exploitation of F₂-laser processing applications has been hampered in the past by the need for robust vacuum-ultraviolet (VUV) optics that can withstand the hard 157-*nm* photons and by special requirements for optical beam systems that flush out ambient air, a strong absorber of 157-*nm* light. A large research effort to meet F₂-laser lithographic requirements set in the International Technology Roadmap for Semiconductors by Sematech [2] has expedited the development of 157-*nm* optics and related nanofabrication technology [19]. Although 193-*nm* immersion lithography has recently superseded F₂-laser lithography, high quality CaF₂ and dielectric coatings now rou-

tinely provide > 98% transmittance per optic at 157 nm and new gas flushing systems offer high transmittance over several meters of optical path length.

To this end, the University of Toronto group [20, 21] has co-developed with MicroLas Lasersystems and Laser-Laboratorium Göttingen a high-resolution optical processing system for high-fluence machining and refractive index structuring of optical glasses. Such systems are proving to be robust laser technology, providing the convincing metrics to unlock the first generation of microfabrication applications for the F₂ laser. This chapter is primarily devoted to the research study undertaken with this system in Toronto. The chapter begins by describing the optical tooling system and its micromachining performance. Section 13.3 is devoted to micromachining of optical glasses, and describes the process precision and control of surface morphology. Section 13.4 presents several micromachining examples, including microvias, microchannels, mask fabrication, gratings, and diffractive optical elements. Section 13.5 examines the photosensitivity responses for imprinting refractive index structures inside various glasses. The latter two sections examine prospects for F₂-laser microfabrication of photonic components in the telecommunication and general optics manufacturing fields. The final section looks at special opportunities for fabricating laboratory-on-a-chip devices, including new means for integrating photonic functions with microfluidics. The objective of this chapter is to demonstrate that optical tools are well developed for F₂-laser material processing, and application opportunities are waiting for exploitation.

13.2 Vacuum-Ultraviolet Optical Tools

The F₂ laser is today a reliable source providing high-power output at the short-wavelength forefront of commercial laser systems. However, a wide base of industrial applications has not emerged due to the need for efficient and reliable 157-nm optical delivery systems as well as the requirement for gas flow systems to overcome absorption by air. The main focus of this section is to describe the performance of two configurations of 157-nm optical delivery systems that were designed to meet, in part, these needs. A special opportunity for high-resolution micromachining of optical glasses was emphasized in the system design, presenting a formidable challenge in delivering high on-target fluences that exceed by several factors the 1-J/cm² ablation threshold of fused silica. The delicate VUV beam homogenizing and focusing system optics must deliver high fluence without succumbing to damage after hundreds of millions of laser pulses.

13.2.1 High-Fluence F₂-Laser Optical Tool

The F₂-laser processing system consists of a commercial laser (Lambda Physik, LPF 220i), a MicroLas Lasersystems 157-nm optical system, and a

high-resolution micromachining station [20, 21]. The laser provides $> 25\text{ mJ}$ single-pulse energy with $\sim 15\text{ ns}$ pulse duration (FWHM) and 1–200 Hz repetition rate. The spectrum is naturally narrow at $< 5\text{ pm}$ and the transverse coherence length is on the scale of $100\text{ }\mu\text{m}$ which is sufficient for interferometric applications including phase mask writing of fiber Bragg gratings. The horizontal and vertical beam divergence is $\sim 3\text{ mrad}$ and $\sim 1\text{ mrad}$, respectively. A recirculating chiller (Thermo NESLAB) heated the laser coolant water to $\sim 35^\circ\text{C}$ for boosting the laser pulse energy and improving the pulse-to-pulse energy stability $\pm 4\%$.

A photograph of the F_2 -laser microfabrication system is shown in Fig. 13.1. Details of the optical system are provided in Ref. [20, 21] and only a summary is provided here. The optical delivery system was assembled inside a 2.5-m long airtight aluminum enclosure. Dielectric-coated CaF_2 optical mounts were mounted on a single base-rail to facilitate changes between medium and high-resolution beam imaging configurations. The high-resolution configuration is shown schematically in Fig. 13.2 and employs beam-shaping optics, a mask, and a $25\times$ Schwarzschild objective lens with 0.4 NA . The F_2 -laser beam is first expanded vertically by two prisms, and then homogenized by four sets of 9×9 cylindrical lens arrays, to produce a uniform ($< \pm 5\%$) illumination field of $6\text{ mm} \times 6\text{ mm}$ with 24 mJ/cm^2 fluence at the mask plane. The prism expanders serve to create a central hole in the energy profile that eliminates obscuration by the Schwarzschilds objective for normal incident light. This objective provided a uniform fluence of up to 9 J/cm^2 (with attenuator removed) across the complete target image plane of $250\text{ }\mu\text{m} \times 250\text{ }\mu\text{m}$, sufficient to ablate silica-based glasses and other wide-bandgap materials. The fluence could be finely adjusted over a 10–70% range with an angle-tuned dielectric-coated attenuator. The theoretical diffraction-limited resolution was $\sim 250\text{ nm}$, and is discussed further in Section 13.2.2.

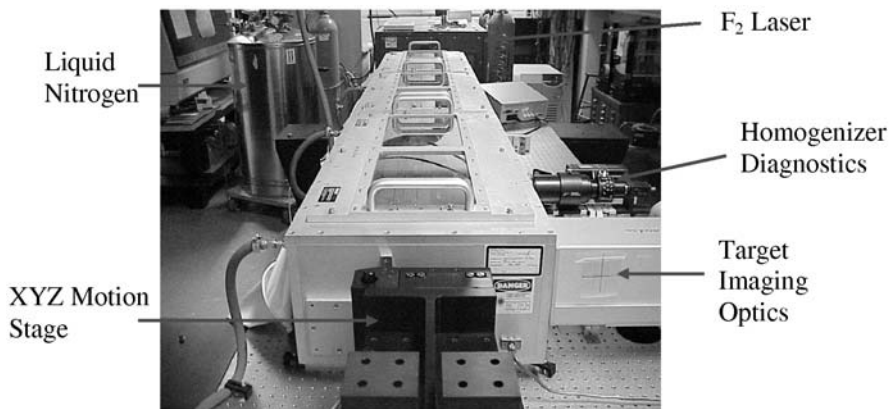


Fig. 13.1. Photograph of the F_2 laser (background) and the 157-nm optical delivery system (foreground) for high-resolution and high-fluence microfabrication

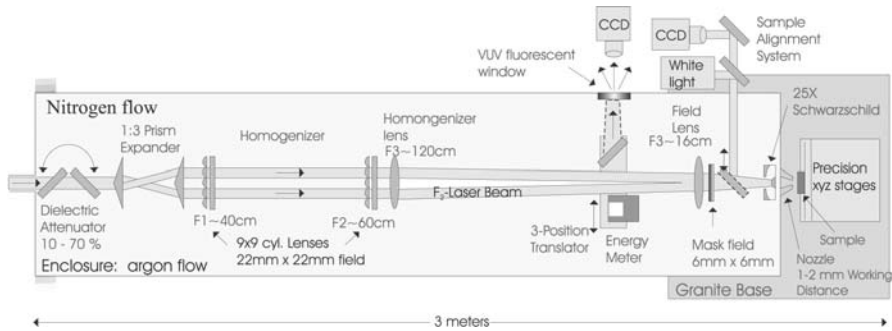


Fig. 13.2. High-resolution Schwarzschild lens configuration of the F₂-laser optical processing system [20]

The lower resolution configuration is shown in Fig. 13.3 and comprised of a CaF₂ doublet lens that provided lower on-target fluence of $\sim 1 \text{ J/cm}^2$ over a larger $800 \mu\text{m} \times 800 \mu\text{m}$ field. This fluence is sufficient for micromachining or imprinting refractive-index structures into many glass types, as well as machining most other material types (i.e. polymers). The beam is not homogenized in this arrangement. A 3:1 cylindrical lens telescope compresses the long-axis of the laser beam to an $\sim 8 \text{ mm} \times 8 \text{ mm}$ field size at the mask plane. The doublet lens offers spherical aberration correction and a 10× demagnification ratio to provide $< 5 \mu\text{m}$ resolution across the full field at the target plane. This arrangement also shares with the Schwarzschild configuration the dielectric mirror attenuator, energy meter, nozzle, sample alignment optics and precision stages. The Schwarzschild and doublet lens systems could be readily interchanged on the rail system without the need for careful re-alignment. A summary of the operating specifications of each system is shown in Table 13.1.

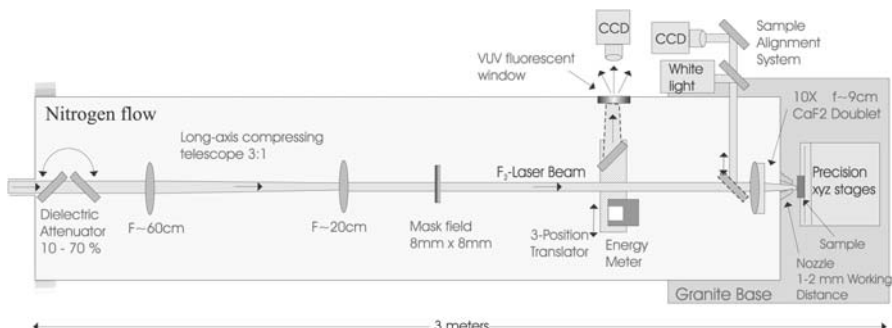


Fig. 13.3. Medium-resolution CaF₂-doublet configuration of the F₂-laser optical processing system [20]

Table 13.1. Comparison of high- and medium-resolution configurations of the 157-nm optical system [20]

	High-Resolution Schwarzschild Optics	Medium-Resolution CaF_2 Doublet Optics
Mask Field Size	6 mm x 6 mm	8 mm x 8 mm
Uniformity	Homogenized \pm 5%	Non-uniform raw laser beam
Demagnification	25 \times	10 \times
NA	0.4	\sim 0.1
Target Field Size	0.24 mm x 0.24 mm	0.8 mm x 0.8 mm
Resolution (glass machining)	0.8 μm full field (0.25 μm theoretical)	\sim 5 μm full field
Peak on-Target Fluence	9 J/cm ²	1.5 J/cm ²

The 157-nm optical system of Fig. 13.2 combines several beam diagnostics. A 157-nm mirror can be moved by a mechanical link to redirect the laser beam to a VUV fluorescent plate positioned in a plane equivalent to the mask plane to monitor the beam homogeneity, facilitate alignment of the homogenizing optics, and note degradation of optical components. A second CCD camera images the sample surface through the Schwarzschild lens, which was coated for both 157-nm and visible light. Laser machining patterns were computer controlled with LabView or Visual Basic software that moved the target sample on 3-axis linear stages (Newport TSPI100 with MM4006 controller) having 50-nm resolution and 100-nm repeatability. The patterning mask was mounted on a 2-axis motion stage that was synchronized with target stages to extend the sample work area beyond the 250 $\mu\text{m} \times$ 250 μm projection field of the Schwarzschild lens.

Absorption of 157-nm light by ambient air was treated by flushing the full optical beam path with high-purity N₂ gas collected from a liquid-nitrogen dewar. The 157-nm attenuation across the full 3-m beam path was < 30% when the O₂ and H₂O levels were reduced to less than 4 ppm and 3.5 ppm, respectively, as monitored with a gas sensor (Cambridge Sensotec, Rapidox 2000). The large chamber volume (Fig. 13.1) necessitated a long flushing time of 1.5 hours to reach this level of transmission. Much faster flushing times would be available by replacing the chamber with small diameter beam tubes as demonstrated by Gower and coworkers [15]. High purity gases and a sealed chamber are required to overcome 157-nm losses of 1%/meter/ppm of O₂ [22]. Figures 13.2 and 13.3 show a gas-flow nozzle positioned between the sample and the Schwarzschild lens for the purpose of directing a transparent stream of nitrogen gas to the working sample. In this way, all samples could be processed outside of the chamber in the ambient air, facilitating the exchange and simple re-alignment of new samples without the need to open or re-flush the optical chamber. The optical system, diagnostics, and

precision motor drives floated on an optical table for isolating acoustic noise. This combination of features enabled micromachining to the nano-scale.

The anti-reflection-coated CaF₂ optics provided at least 96% transmittance (two surfaces) at 157 nm, and showed little degradation over three years of constant use, equivalent to a total of ~ 200 million laser pulses. Fluence values were typically below 15 mJ/cm² per pulse on each optic. The Schwarzschild lens (Fig. 13.2) also received similar fluence exposure, but degraded from $\sim 65\%$ transmittance (after radiation burn in) to $\sim 40\%$ transmittance in this same period. This loss appears to be due to the accumulation of significant quantities of ablation debris visible on the mirror surfaces. The doublet lens was not tested for long exposure but is expected to offer considerably longer lifetime than the Schwarzschild lens for similar fluence level.

13.2.2 Optical Resolution

Laser lithography is at the forefront of high-resolution laser processing, having demonstrated 40-nm ridges on 100-nm pitch in resists exposed by F₂-laser interferometry [19]. Direct laser ablation of polymethylmethacrylate (PMMA) can generate a similar pitch of 110 nm [1] for a larger single-pulse fluence ($> 15 \text{ mJ/cm}^2$) exposure, but aspect ratio (< 1) is much less than 3:1, values typically seen in processed resist. Chemical amplifiers in resists and low thermal conduction of polymers serve well to yield such small features in comparison to direct ablation. Fine pitch processing is also more challenging in glass than polymers because of a ~ 10 -fold larger thermal diffusion coefficient ($0.009 \text{ cm}^2/\text{s}$) that yields a ~ 200 -nm diffusion scale length for the 15-ns pulse duration. Simple optical projection systems such as a Schwarzschild lens further reduce the resolution as noted by the 200–400 nm ablation features produced in various polymers by Gower and coworkers with a 36 \times Schwarzschild lens [15]. Smaller features are available with better quality optical systems and the use of phase-shift elements in the mask. This section presents the resolution limits for F₂-laser ablation of silica-based glasses with the 25 \times Schwarzschild optical system of Fig. 13.2.

The micromachining resolution was assessed from the surface relief patterns excised in soda-lime glass (Corning 2947) with a chrome-coated CaF₂ transmission mask and the 25 \times Schwarzschild lens [21]. The chrome mask comprised of three parallel open rectangular bars (vertical and horizontal) having various line-and-space periods (lines per millimeter). The modulation transfer function for optical systems is normally obtained from the expression [23]:

$$Mod = \frac{I_{max} - I_{min}}{I_{max} + I_{min}} \quad (13.1)$$

where I_{max} and I_{min} refer to the maximum and minimum light intensity projected on the sample surface by the mask and lens system. For an overall

micromachining response, time-integrated intensity values were inferred from the maximum and minimum ablation depths patterned in the glass by the projected F₂-laser light. The *Mod* also includes thermal transport effects that further wash out the modulation features. The laser ablation rate, D , per pulse is related to the laser fluence, F , by

$$D = \frac{1}{\alpha_{eff}} \ln \left(\frac{F}{F_{th}} \right) \quad (13.2)$$

where α_{eff} is the effective absorption coefficient ($\sim 170,000 \text{ cm}^{-1}$) and F_{th} is the ablation threshold fluence ($\sim 1 \text{ J/cm}^2$) as presented in Fig. 13.4 for fused silica [4, 5]. The time-integrated intensity values (i.e. F) were therefore obtained from the simple scaling relationship, $I \propto \exp(\alpha_{eff}D)$, to provide values for *Mod* in Eq. 13.1.

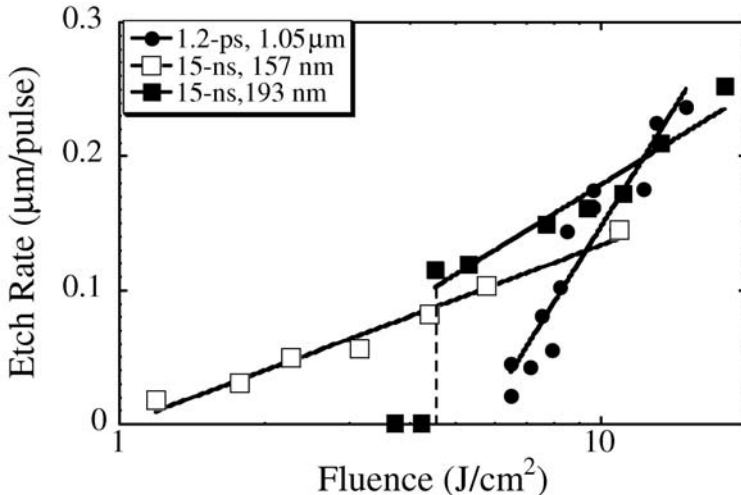


Fig. 13.4. Ablation etch rates for fused silica (Corning 7940) comparing 157-nm F₂-laser and 193-nm ArF-laser pulses of 15–20 ns duration with 1.2-ps 1.054-μm laser pulses. The solid lines are represented by $D = (1/\alpha_{eff}) \ln(F/F_{th})$ [5].

The modulated ablation depths, D_{max} and D_{min} , were obtained by atomic force microscopy (AFM), and the resulting modulation transfer function is plotted as shown in Fig. 13.5. The resolution for F₂-laser glass ablation is $\sim 1 \mu\text{m}$ (line and space), beyond which finer etch features such as $\sim 300 \text{ nm}$ can only be formed with a small ~ 0.2 aspect ratio. The 1-μm resolution does not meet the theoretical 250-nm diffraction limit for the 25× Schwarzschild lens, possibly owing to imperfect surface figure and alignment of the Schwarzschild mirrors. However, thermal transport as discussed above, the dynamics

of surface melt and the ablation plume also play a significant factor. Approximately two-fold smaller features can be generated in polymer materials with the same lens because of the lower thermal diffusivity, the volatile ablation species, and the absence of melt-phase dynamics in polymers relative to glasses.

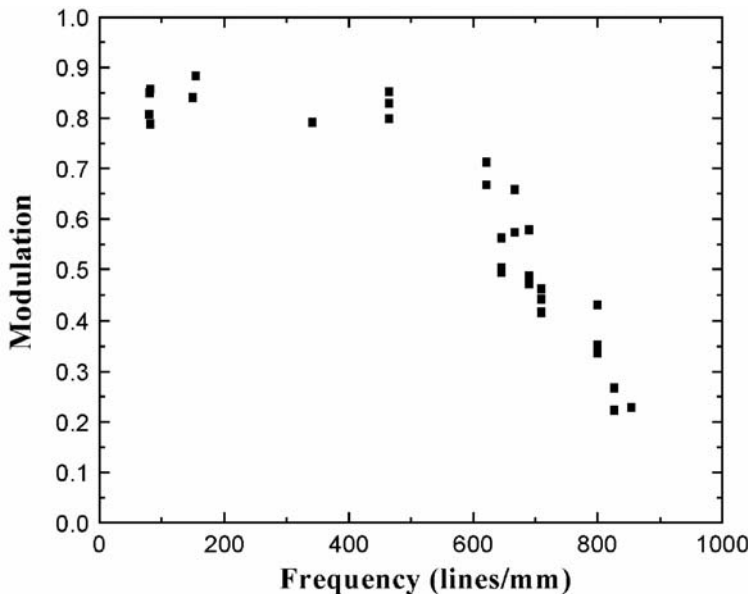


Fig. 13.5. The Modulation Transfer Function as a function of the spatial frequency for 157-nm micromachining of soda-lime glass with a 25 \times and 0.4 *NA* Schwarzschild lens. More than two-fold higher resolution is available in polymer ablation with the same projection optics [21].

13.3 Micromachining of Silica Glasses

Transparent glass materials serve in the backbone of many of today's rapidly expanding photonics application areas, including optical communications, displays, electronics, sensor technologies, biomedical devices, and laboratory-on-a-chip. F₂-laser processing is especially attractive here for the precise incisions possible without generating microcracks. This section presents etching rates and the limits of surface morphology, heat-affected zone, and ablation debris on precise F₂-laser processing of various glasses, highlighting several key advantages over other laser types.

13.3.1 Ablation Rates and Surface Morphology

The absorption of 157-nm radiation in fused silica is highly sensitive to impurities, defects, OH content, stresses, and even hydrogen gas soaking, leading to varied laser interactions from one glass to another. Dopants such as GeO₂ are commonly used to define the optical guiding region in fibers or planar optical chips by increasing the refractive index. The addition of germanium lowers the bandgap to strongly increase the 157-nm absorption. The germanium also creates copious defect centers (i.e. Ge-O deficiency centers) that underlie strong photosensitivity responses for imprinting Bragg gratings inside optical fibers with $\sim 240\text{-nm}$ light [24, 25].

For pure UV-grade fused silica, weak absorption of $\alpha = 10\text{ cm}^{-1}$ gives rise to a large 1-J/cm^2 ablation threshold for 157-nm light as noted in Fig. 13.4. The inverse slope yields a large ‘effective’ absorption coefficient (following Eq. 13.2 of $\alpha_{eff} = 170,000\text{ cm}^{-1}$ – representing a 17,000 fold increase over the small-signal loss that attests to the importance of transient defect formation and recovery during high-fluence 157-nm interactions. For contrast, a modest 8% doping level of GeO₂ decreases the ablation threshold by 70% to 0.38 J/cm^2 and nearly doubles α_{eff} to $320,000\text{ cm}^{-1}$ [4].

In both cases, fused silica and germanosilica etch rates follow a logarithmic fluence dependence to exceptionally shallow etch rates of only 10–20 nm per pulse near the ablation threshold. Further, there is no strong evidence of incubation effects, noted when etching does not occur with the first laser pulse or when etch depth does not extend linearly with the number of laser pulses. F₂-laser processing therefore offers excellent control and reproducibility for precise profiling of fused silica and related glass surfaces without a significant dependence on the exposure history. Weak incubation effects manifest only after very long ($\sim 100,000$ pulses) exposures near or below the 1-J/cm^2 ablation threshold, but not to levels of significant importance to the micromachining precision.

Fused silica is highly transparent at slightly longer wavelength such as 193 nm from the ArF laser. Two-photon interactions [26, 27] are noted here to underlie refractive-index changes and glass compaction at low fluence, while numerous pulses are required at higher fluence to ‘incubate’ the sample before ablation can proceed. Fig. 13.4 shows the fused silica etch rates for 193-nm ablation. The ablation threshold of $\sim 4.5\text{ J/cm}^2$ is a demarcation between fluence zones where ablation will not develop even after 100’s of laser exposures and where ablation cannot proceed until after dozens or hundred’s of incubation pulses are applied. Just above this threshold, surface swelling ($\sim 57\text{-nm}$ in 20 pulses) is noted before the development of a steady-state etching rate of $\sim 120\text{ nm/pulse}$. Surface morphology is less smooth than for 157-nm ablation, and surface cracks will form on occasion, particularly for deep etching. The prompt onset of deep excision ($> 100\text{ nm}$) at the ablation threshold is a signature of the 2-photon interactions underlying absorption at this wavelength. Only when larger fluences ($\sim 10\text{ J/cm}^2$) are applied, does

prompt ablation occur (on the first pulse), improving surface morphology through more predictable etch rates. The 200-nm etch rate at such high fluence is 10-fold larger than the minimum features producible by F₂-laser ablation, while the 193-nm incubation processes diminish the micromachining control for ArF lasers for photonics device fabrication.

The disadvantages of weakly interacting 193-nm light are more pronounced in composite materials like silica-on-silicon optical circuits (PIRI SMPWL; 8-μm germanosilicate on 20-μm fused silica on silicon). High transparency in upper glass layers lead to gross mechanical ejection and fracturing of the glass by strong laser heating at the underlying silicon-glass interface. In contrast, F₂-laser ablation provides smooth and precise excisions in the top germanosilicate guiding layer without underlying damage, key features in the successful writing of optical rib waveguides with modest losses of ∼3 dB/cm [28].

Ultrafast lasers offer another approach to coupling laser energy into glasses by strong nonlinear absorption that provides precise etch depths of ∼10–20 nm on par with the F₂ laser. A ‘gentle’ ablation-processing window exists in the 5.5 to 45 J/cm² fluence range for 1.2 ps ablation of fused silica [5, 29]. Etch rates in this window follow a logarithmic fluence dependence as shown in Fig. 13.4, and are in general agreement with other ultrafast laser studies [30, 31]. Although incubation effects are not strongly evident over a small number of laser pulses, surface roughness exceeded 10% (rms) of the etch depth, which is >10-fold rougher than the tens of nanometer roughness noted in Fig. 13.6 for F₂ laser ablation. Overall, incubation effects, swelling, shock-induced microcracking, and shearing and flaking of surrounding surfaces were generally far more evident with the ultrafast laser than with F₂-laser machining. The F₂ laser provided the best surface morphology and control over etch depth, and the lowest threshold fluence for ablation amongst the lasers tested.

The surface morphology of F₂ laser-ablated fused silica has been assessed [32] by atomic force microscopy (AFM) over a large range of exposure conditions, yielding the surface roughness (rms) data plotted in Fig. 13.6. A short-range periodic ($\Lambda \sim 5 \mu\text{m}$) structuring of ∼6-nm amplitude was noted on all surfaces. On longer scale, surface roughness was ∼15 nm rms over a ∼60 μm × 60 μm inspection area and may be due to inhomogeneity in the laser beam. (The homogenization optics of Fig. 13.2 were not available when Fig. 13.6 was produced.) What is especially noteworthy is the near independence of the roughness on the laser fluence or the number of laser pulses applied, yielding nearly identical surface morphology independent of whether deep and shallow excisions were made. This is consistent with a view presented in the next section of each laser pulse removing ‘damaged’ surfaces by ablation, and leaving behind thin melt layers that evolve towards new nearly identical surfaces at the end of the laser ablation cycle. Overall, the surface roughness (< 20 nm) only represents 1 to 0.1% of the hole depths tested here, and constitutes an exceptional smoothness that is only a fraction of an

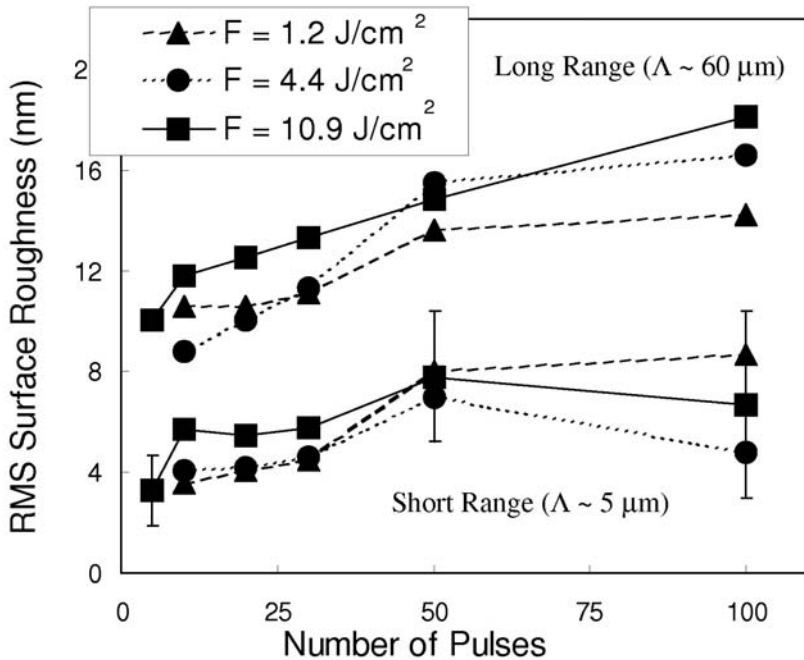


Fig. 13.6. Surface roughness (rms) of 157-nm ablated fused silica (Corning 7940) as a function of pulse number. AFM revealed both long- and short-range surface roughness, which showed little dependence on either the laser fluence or the number of laser pulses applied. The short-range roughness is approximately periodic with $\Lambda \sim 5 \mu\text{m}$ [5].

optical wavelength as required for shaping optical components. The surface roughness generated by F_2 -laser ablation is similar in other glass types. Near the edges of ablation channels or other projected features, the surface roughness becomes significantly larger as near-field diffraction and ablation effects redistribute the laser fluence profile and induce deeper surface undulations.

13.3.2 Heat-Affected Zone

Laser micromachining like most surface treatment processes leads to near-surface modification of macroscopic properties and generation of residual stresses [33] around patterned structures. For low-fluence irradiation of optical glass, this manifests in volume densification, modification of the refractive index, changes in the absorption spectrum, stresses, and birefringence effects that permanently modify the optical properties of the material [34]. At higher laser exposures, laser-generated microcracks will form, producing strong localized tensile-stress fields [35, 36]. Glass microcracking is more common with

weakly interacting lasers but can be avoided with F₂-laser micromachining [4, 5, 14] to offer precise etch control with smooth morphology over a wide processing window. Nevertheless, physical distortion has been noted especially in thin glass samples that we attribute to residual tensile stresses formed during the cooling phase that follows the laser ablation heating cycle [32].

To assess [32] the F₂-laser micromachining distortion, fused silica cover slips (Corning 7940, UV grade) of 160- μm thickness were cut into 0.25- mm by 10- mm rectangles with a diamond scribe, immersed in HF acid (50%) for 90 s to relieve scribing stress, and then radiated (Fig. 13.7(a)) at fluences of 1.9–4.7 J/cm^2 at scanning speeds of 94 or 220 $\mu\text{m}/\text{s}$ to remove the top 0.15 to 1.0 μm surface layer. All samples distorted into a curved shape as noted in Fig. 13.7(b). All samples were concave on the laser-irradiated side and yielded nearly identical deflection of $195 \pm 15 \text{ nm}$ (across a 4.7- mm length) irrespective of the irradiation conditions or ablation depth. This invariant radius suggests the formation of a fixed thickness of laser-affected material, comprising of a thin tensile stress layer along the laser-radiated surface. Each additional laser ablation pulse must therefore remove and re-generate an equal thickness of tensile material in the laser-affected zone. This process is consistent with Eq. 13.2, where an increase in fluence will increase the ablation depth to position D , which defines the interface for the new surface that receives fluence value, F_{th} . In this way, the heat-affected zone will be invariant with the laser irradiation condition.

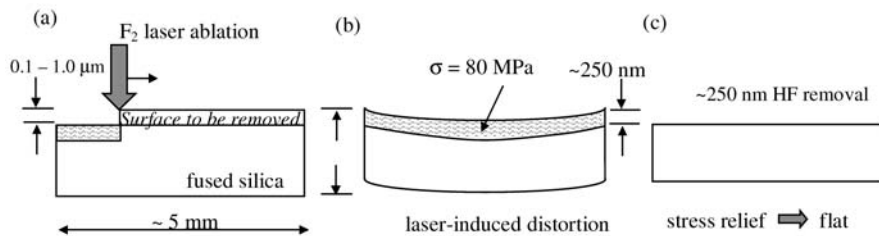


Fig. 13.7. Sequence of laser ablation by scanning (a), sample distortion due to formation of a thin tensile stress layer (b), and HF acid etching (c) to assess a $\sim 250\text{-nm}$ thickness for the laser-induced stress layer – the heat affected zone [32].

The thickness of the heat-affected layer was evaluated [32] by noting the increase in bending radius as samples were chemically thinned by immersion in hydrofluoric acid (50%) for short 10 s intervals. The radius of curvature doubled when only a 100-nm thick surface layer was removed, and all laser-irradiated samples became flat (Fig. 13.7(c)) after removal of $\sim 275 \mu\text{m}$. The thickness of the stress layers are consistent with the 200-nm thermal diffusion scale length introduced in Section 13.2.2, which exceed, as expected, the

59-nm optical penetration depth inferred from the $170,000\text{ cm}^{-1}$ effective-absorption coefficient for fused silica (Fig. 13.4).

An estimate of the tensile stress, σ , in this laser-affected zone can be found from $\sigma = Ed^2/6rt$ [37], where the radius of curvature, r , will arise from a uniform stress layer of thickness, t , formed over a non-stressed substrate of thickness d . If we assume the laser-induced stress profile is uniform across a $t = 275\text{-nm}$ thickness on the $d = 160\text{-}\mu\text{m}$ thick samples studied above, then a Young Modulus value of $E = 72\text{ GPa}$ [38] yields an average residual stress of 80 MPa in this 275 nm thick layer. Such large tensile stress exceeds the 50 MPa tensile strength of bulk-fused silica [38, 39], suggesting that F₂-laser treatment of fused silica strengthens the near-surface layer ($200\text{--}300\text{ nm}$) of fused silica. This effect appears contrary to observations of a 2 to 4-fold lower damage threshold for 325-nm light in thermally treated fused silica and BK-7 glass, relative to untreated samples [40]. On the other hand, cleaved fused silica generally offers higher laser damage threshold [41].

The apparent strengthening of glass surfaces by F₂-laser ablation is a novel advantage and may explain the wide F₂-laser-processing window available for crack-free machining of fused silica and related glasses. Nevertheless, the sample distortion and deflection on $\sim 200\text{ nm}$ -size scale is a disadvantage for cases of high-resolution glass micromachining, particularly in thin or small glass structures such as fibers, micro-optics, and cantilevers [32]. However, such laser-induced distortion is an opportunity for controlling nano-scale bending and alignment of optical fibers for photonics packaging or glass cantilevers for MEMs applications.

13.3.3 Ablation Debris

The plume dynamics in laser ablation of silica glasses generates non-volatile products, leading to debris accumulation directly on and over nearby ablated surfaces. Submicron glass particulates will collect and partially sinter on surfaces to form coatings of 10 nm thickness in an $\sim 10\text{ }\mu\text{m}$ wide perimeter region around small structures ($< 5\text{ }\mu\text{m}$ dimensions), and growing thicker and broader with the volume of material removed by the laser. Recast comprising of a $\sim 100\text{-nm}$ rim of ejected silica melt will also normally define the upper perimeter of ablated trenches or holes, and can grow to micron thicknesses for very deep holes tens of microns deep.

Several approaches to managing the debris are available. A significant reduction ($> 60\%$) of the amount of fine particle soot is possible in a low pressure or vacuum ambient, but this requires placing samples in a vacuum chamber, eliminating the advantages of the optical configurations used in Fig. 13.2 and Fig. 13.3. Because such debris is only loosely bonded to surfaces, a chemical etch is very effective in $> 95\%$ removal. A simple procedure involves 45 minutes of ultrasonic cleaning in ethanol followed by 5 minutes in methanol. Acid solutions and KOH are also very effective, but recipes change dramatically with the type of glass and the tolerance for removing thin surface

layers in differently sized glass microstructures. Figure 13.8 shows channels formed by a projected $20\text{ }\mu\text{m} \times 130\text{ }\mu\text{m}$ F₂-laser beam in fused silica as seen immediately after ablation (Fig. 13.8(a)), after rinsing with water and acetone (Fig. 13.8(b)), and after ultrasonic cleaning in 1.7 molar concentration KOH solution for 30 minutes (Fig. 13.8(c)). Soot is no longer evident after cleaning at the resolution provided by the optical microscope.

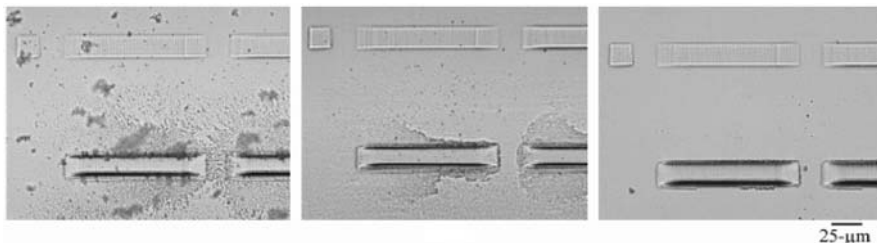


Fig. 13.8. Optical images of ablation debris deposited around two channels excised by the F₂ laser (a), after rinsing in water and acetone (b), and following ultrasonic cleaning in KOH solution (c). The top and bottom channels were formed with 10 and 110 laser pulses, respectively, of $\sim 3\text{--}4\text{ J/cm}^2$.

Melt recast cannot be effectively removed by these methods. However, a second scan with the F₂ laser at a lower fluence can remove the recast layer under judicious operator control in shaping the perimeter towards a desirable contour. Such procedures are required for leak-tight sealing in glass biochip applications (Section 13.6).

13.4 Micro-Optics Fabrication

The F₂ laser offers the controlled fabrication of glass microstructures with smooth and crack-free profiles at $\lambda/10$ surface precision and sub-micron lateral resolution. Attractive application directions for micro-optics fabrication include:

- shaping lens surfaces
- diffractive, binary, kinoform optics
- micro-lens arrays
- optical circuits: waveguides, grating couplers, splitters, multiplexers
- fiber lenses, taps, tapers
- optical mask patterning: chrome, dielectric, phase mask
- acousto-optic devices
- microwave-circuits
- lab-on-a-chip: hole arrays, microfluidic channels, micro-optics integration
- mounting structures for photonics assembly and packaging
- stress-induced micro-bending, forming, and alignment.

Such applications serve widespread interest in biomedical, biophotonics, display, and optics fields [42, 43, 44, 20]. Several micro-optic fabrication directions are presented in this section, while refractive index writing and biochip applications are discussed in Sections 13.5 and 13.6, respectively.

13.4.1 Microchannels and Holes

The F_2 laser can excise rectangular and V-shaped microgrooves of 2–40 μm width by both static projection and scanning spot techniques [21, 45]. Fig. 13.9 shows various channels formed in glass microscope slides (Corning 2947) at 5–9 J/cm^2 fluence using free-standing metal foils as projection masks. All channels were crack free. The rectangular channels (Fig. 13.9a,b) were formed in static projection at the maximum available on-target fluence of $\sim 9 \text{ J}/\text{cm}^2$ per pulse, using 100 or 200 laser pulses at a pulse repetition rate of 5–10 Hz . These channels have vertical walls and flat bottoms, yielding an aspect ratio of up to 3:1 for the 8- μm channel. In contrast, the 10 μm wide V-channel in Fig. 13.9(c) yielded 25° walls by using a reduced fluence of $\sim 3 \text{ J}/\text{cm}^2$ and a smaller 100-pulses exposure. The observed wall angle, γ , coarsely follows the empirical relation, [46]

$$\gamma = \sin^{-1}(F_{th}/F) \quad (13.3)$$

for a F_{th} value of $1.0 \text{ J}/\text{cm}^2$ for fused silica. The combination of high and variable fluence, large numerical optic ($NA = 0.4$), and micropositioning tools offers wide latitude in fabricating custom microstructure shapes with controllable surface morphology. Thermal diffusion and other effects described in Section 13.3 play a significant role at smaller feature size, preventing the formation of high-aspect ratio channels. Fig. 13.9d shows the AFM profile of a 1.5 μm wide V-channel formed with a scanning $\sim 1\text{-}\mu\text{m}$ beam spot, $\sim 7\text{-}\text{J}/\text{cm}^2$ fluence, and 100 Hz repetition rate. Vertical walls and high aspect-ratio channels could not be generated to 1 μm feature size, but might be available at fluences greater than the current maximum of $9 \text{ J}/\text{cm}^2$ according to Eq. 13.3.

Microholes are readily formed in static projection, yielding optically smooth near-vertical walls and flat bottoms as seen in Fig. 13.10. The hole diameters are $\sim 15 \mu\text{m}$ and applied for isolating single cells in a standard 96-hole microarray. The glass slides were chemically cleaned after laser ablation to remove soot, although some evidence of $\sim 250\text{-nm}$ particles are seen surrounding the hole in Fig. 13.10b. Fig. 13.10b also shows evidence of a small $\sim 250\text{-nm}$ recast layer at the top perimeter of the hole. Biochip applications are discussed further in Section 13.6.

The optical configuration of Fig. 13.2 is not well suited to forming high-aspect through-holes. The maximum fluence dose is only 9-times larger than the $1\text{-}\text{J}/\text{cm}^2$ ablation threshold of fused silica. Only tapered structures are possible at this fluence as predicted by Eq. 13.3. Significant laser energy is

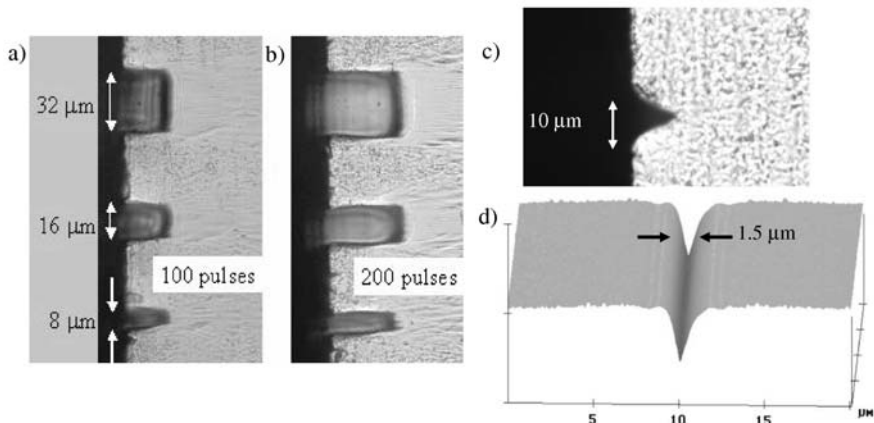


Fig. 13.9. Optical microscope end-views of microscope glass slides (Corning 2947) in which steep-walled rectangular (a, b) and V-grooved (c) microchannels were excised by F₂-laser ablation. The V-groove in (c) has 25° wall angles. An AFM image (d) of a 1.5 mm wide by 1.5 mm deep V-channel. See text for further details [45].

also lost through the slightly transparent walls, which is especially significant for the 0.4 NA Schwarzschild lens. An optical design delivering higher fluence and smaller NA would greatly extend the processing range to excise deep and high-aspect ratio holes in glass.

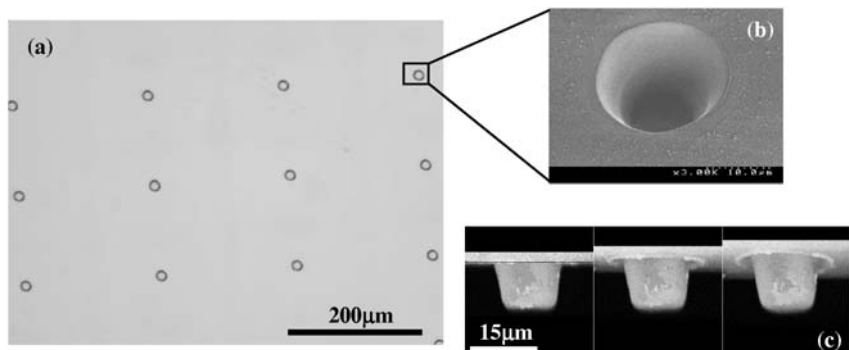


Fig. 13.10. Optical photograph of a cell array (200 μm centers) drilled with an F₂-laser (a); SEM micrograph close-up of a typical hole in the array (b); and montage of pictures of a typical hole in the array using 3-D scanning confocal microscopy (c) [45].

13.4.2 Fiber and Rib Waveguides

The formation of optical-quality vertical walls is attractive in glass cutting applications such as cleaving optical fibers and dicing planar lightwave circuits. A standard single-mode optical communication fiber (Corning SMF-28) was *cleaved* with single-pulse fluence of 9 J/cm^2 over a 2-min. exposure at 10 Hz [21]. A $750\text{-}\mu\text{m}$ wide slit served as a projection mask to provide a $30\text{ }\mu\text{m} \times 180\text{ }\mu\text{m}$ cutting beam on the $125\text{-}\mu\text{m}$ diameter glass fiber. The polymer jacket was stripped and the glass fiber cleaned with methanol prior to laser cutting. Fig. 13.11(a) illustrates the side view microscope image of the cut fiber. An AFM surface scan near the $9\text{-}\mu\text{m}$ fiber core indicated a modest 50-nm roughness (rms), representing a $\lambda/30$ surface figure with respect to the $1.5\text{-}\mu\text{m}$ telecommunication wavelength. This surface roughness originates with defects along the edge of the projection mask and can therefore be improved by use of a higher quality mask. The fiber facet yielded very little light loss suggesting that laser cleaving may also do away with the time-consuming polishing step normally required after mechanical cleaving. A rapid fiber cleaving time of several seconds is available at 100 Hz repetition rate.

The laser cleave method can be extended to cutting spherically curved lens shapes for focusing or light coupling applications. The lensed fiber tip shown in Fig. 13.11(b) was formed by projecting a curved mask pattern using the beam configuration of Fig. 13.2 while simultaneously rotating the fiber in the beam. The curvature of the cut fiber was demagnified $25\times$ from that defined by the mask and yielded a 30-nm rms surface roughness.

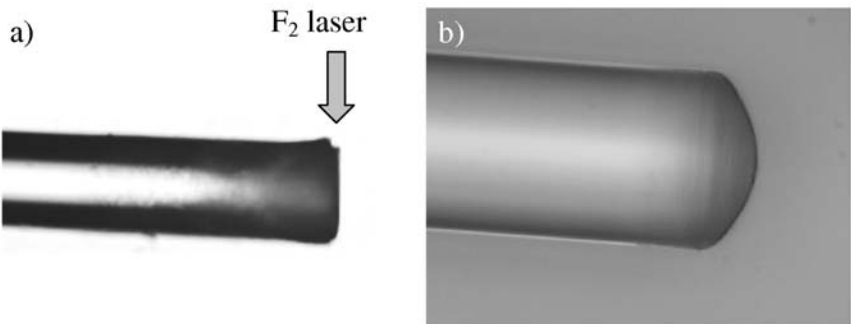


Fig. 13.11. Side view of a standard single-mode telecommunication fiber (Corning SMF-28) (a) after cleaving by F₂-laser ablation. The diameter of the fiber is $125\text{ }\mu\text{m}$ and the roughness of the fiber facet is 50 nm rms. Optical microscope side-view (b) of a $200\text{-}\mu\text{m}$ diameter multi-mode optical fiber shaped into a focusing lens by F₂-laser projection ablation. The surface roughness is 30 nm rms [21, 47].

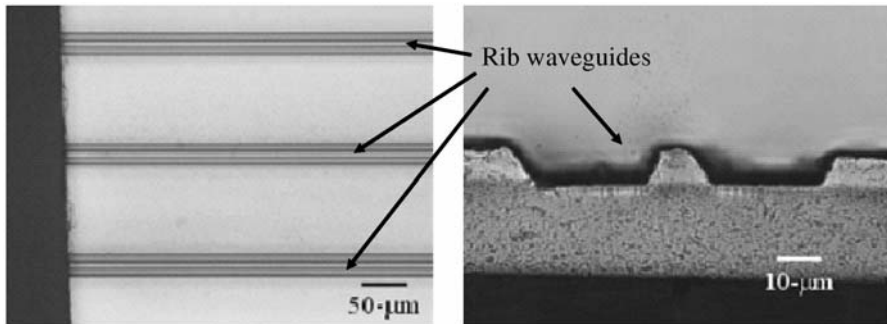


Fig. 13.12. Single-mode rib waveguide in top view (left) and end view (right) formed by F₂-laser ablation of parallel trenches in a planar optical waveguide (PIRI SMPWL). Laser parameters were a fluence of 3 J/cm², 10 Hz rate, and 20 μm/s scan speed [28].

Figure 13.12 shows the results of F₂-laser machining of a planar optical waveguide (PIRI SMPWL) to form a single-mode rib waveguide [28]. The Schwarzschild optical system of Fig. 13.2 was used. The end profile shown in Fig. 13.12(b) comprises of 8 μm thick GeO₂-doped silica grown on 20 μm of silica glass over a silicon wafer. Two parallel trenches were excised leaving behind a smooth waveguide of 8 μm width and 8 μm depth that could guide both visible and infrared light. Ablation soot was cleaned by KOH solution in an ultrasonic bath which dramatically reduced the surface roughness from ~60 nm rms to < 20 nm rms as measured by an AFM. Waveguide losses are very sensitive to surface debris and undulations due to the large refractive index difference ($\Delta n = 0.46$) at the air-to-glass top surface. Losses were below our instrumentation limit of 3 dB/cm.

13.4.3 Mask Fabrication

Laser fabrication promises a flexible and rapid means for custom fabrication of mask designs to very fine feature size, doing away with the multi-step lithographic and etching steps in conventional mask fabrication. Ultrafast lasers are applied commercially in photomask repair of feature sizes of ~100 nm [48]. This section examines prospects for F₂-laser mask patterning of chrome-coated fused silica and CaF₂ [49], as well as dielectric-coated substrates [50], reporting on processing windows for controlling features to submicron dimensions. The patterning of phase shift masks in fused silica is also discussed in the next section on gratings.

F₂-laser ablation of a multi-layer dielectric stack [50] is shown in Fig. 13.13. Because of the high transparency of CaF₂ to 157-nm radiation, an unconventional approach of second surface ablation could be applied with the advantage of removing the whole stack in a single pulse. The multi-layered mirror

consisted of 48 alternating $\lambda/4$ layers of SiO_2 and Al_2O_3 for high fluence 193-nm applications. The left figure shows the untouched dielectric coating next to the 157-nm irradiated surface. The 157-nm laser light selectively couples into the Al_2O_3 dielectric layers without damage to the underlying CaF_2 substrate and SiO_2 buffer layer. These ideal conditions are only available in a narrow processing window of ~ 320 to 400 mJ/cm^2 fluence. The right figure shows the rectangular profile of 193-nm laser light created by the laser-patterned mask. The 193-nm light is only transmitted through the 157-nm laser-processed surface. A 70% total transmission is estimated for the laser processed surface of which 10% is due to Fresnel losses. Remaining losses are attributed to roughness at the laser-processed surface and absorption in the substrate. This example shows that F₂-laser structuring offers flexible means for creating high-damage-resistant transmission masks for 193-nm applications.

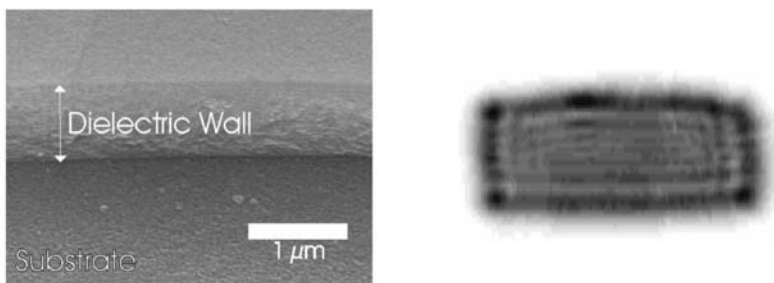


Fig. 13.13. SEM micrographs of a 193-nm high-reflectivity mirror (left) following ablation with a single 157-nm laser pulse at 380 mJ/cm^2 . Clean removal of the whole dielectric stack (except the SiO_2 adhesion layer) is noted in the laser-irradiated region (bottom) without damage to adjacent surfaces. The right figure is a linear gray scale profile in far field of a 193-nm beam demonstrating transmission only through the laser-processed area ($82 \mu\text{m} \times 168 \mu\text{m}$) of the dielectric mirror [50].

A key challenge in laser patterning of chrome-coated optics is to avoid laser damage to the fused silica or CaF_2 substrate while completely removing the thin chrome layer. The ablation properties for fused silica, presented in Section 13.3.1, define an upper exposure limit of $\sim 1 \text{ J/cm}^2$ per pulse to avoid etching of a fused silica substrate. Due to the larger 12-eV bandgap, CaF_2 has a larger ablation threshold of $F_{th} = 1.7 \text{ J/cm}^2$. However, unlike fused silica, CaF_2 yields a coarse tiling structure under ablation that follows the crystalline planes. These must be avoided to prevent light scattering losses or undesirable phase shifts [49]. Such surface tiling has also been observed in

CaF₂ by Gogoll et al. [51] with 248-nm irradiation and Ashkenasi et al. [52] with ultrafast laser irradiation.

CaF₂ (Coherent, 36-1790-000 2" dia × 4 mm thick) and fused silica (ESCO Products, 1" dia × 160-μm thick) blanks were coated with a ~110 nm thick chrome film by Accucoat Inc. The 157-nm transmittance of the blank substrates were ~82% for the CaF₂ window and ~63% for the fused silica cover slip. Absorption losses are minimal in the CaF₂ and ~10 cm⁻¹ for the fused silica.

An atomic force microscope (AFM) image of Cr-coated CaF₂ is shown in Fig. 13.14(a) after a single 157-nm pulse at 6 J/cm² and ultrasonic cleaning. While the chrome was effectively removed in the exposed area, surface roughness and tiling structure are clearly evident in CaF₂ for this overexposed sample. A significant improvement is noted in Fig. 13.14(b) for low-fluence exposure below the 1.7 J/cm² ablation threshold. Because helium buffer gas was used in the F₂ laser during this experiment, red wavelength light at ~0.6 J/cm² was generated in combination with 0.6 J/cm² of 157-nm light. This modest-fluence dual-exposure was sufficient to remove the chrome layer, although there remains evidence of the tiling structure even in the case of a single laser pulse as shown in Fig. 13.14(b). The high opacity of the chrome layer effectively lowers the laser damage threshold for the CaF₂ substrate, narrowing the processing window for defining high-quality photomask features. At lower single-pulse fluence exposure, a metallic hue is observed, indicating incompletely removed chrome. However, this could be cleaned by a second laser pulse. Visible colour changes were noted with each laser pulse suggesting the generation and redistribution of metallic debris.

Even with the tiling effect in the laser-treated surfaces, surface roughness was only ~70 nm rms and ~12 nm rms over an ~200-μm² observation area for the 6-J/cm² and 1.2-J/cm² exposures in Fig. 13.14(a) and 13.14(b), respectively. This compares with a native ~5-nm roughness (rms) of the CaF₂ blank over a similar area. The 12-nm surface roughness appears to represent good optical quality of < λ/10 for 157-nm light, which is sufficient for several optical applications. However, small micron-sized droplets of chrome are present in the processed area, which together with the tiling, increase the absorption and scattering loss of the surface. Further comparison of Fig.s 13.14(a) and (b) reveal a cleaner and better defined chrome edge with little chrome debris in the high fluence (6 J/cm²) exposure case. For low fluence of ~0.6 J/cm², small cracks in the Cr layer were observed radiating out from the ablation perimeter. Such cracks become open fissures in the Cr layer during ultrasonic cleaning, thereby reducing the effective masking resolution to ~2 μm. Therefore, fluence optimization for photomask fabrication favours higher fluence for high contrast and high resolution at the expense of higher substrate surface damage and scattering loss.

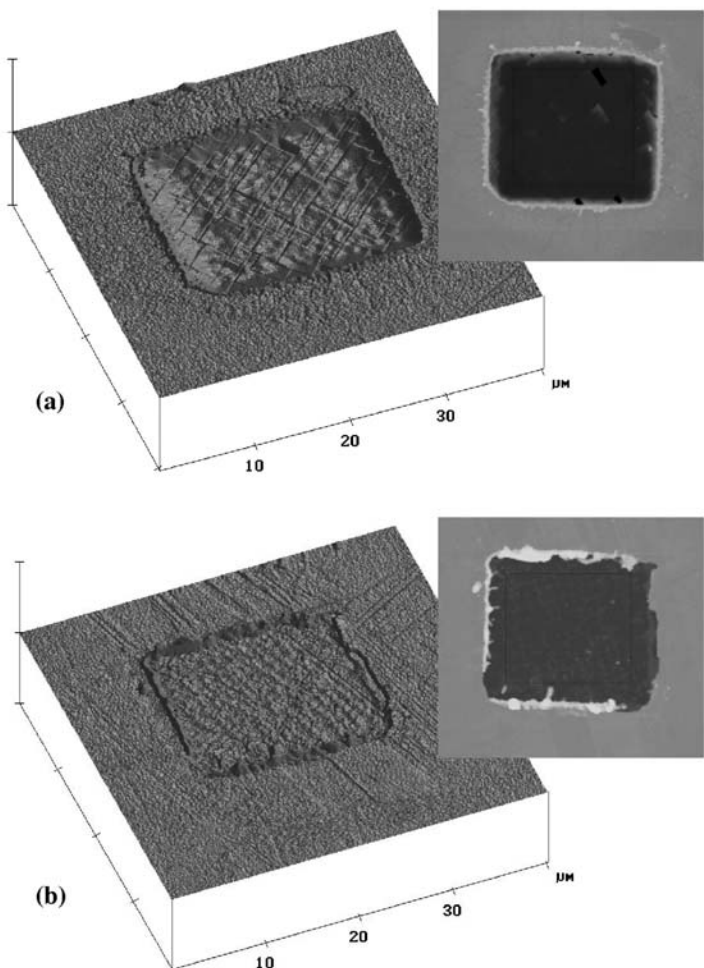


Fig. 13.14. AFM image of Cr-on-CaF₂ ablated with a single (a) 157-nm pulse at 6 J/cm^2 , and (b) a combined red and 157-nm pulse of $F = 1.2\text{ J/cm}^2$, after ultrasonic cleaning. The tiling effect in CaF₂ is present in both cases, but the surface flaking and overall roughness is much improved in (b) than at 6 J/cm^2 in (a) [49].

Similar challenges were faced in F₂ laser ablation of the Cr-coated silica. Chrome could not be completely removed without etching into the underlying silica substrate [49]. For fluences near the $\sim 1 \text{ J/cm}^2$ ablation threshold of fused silica, incomplete chrome removal was accompanied by micron-sized chrome droplets scattered onto neighbouring surfaces.

In spite of these challenges, a logo was laser-patterned into Cr-on-CaF₂ and Cr-on-SiO₂ substrates as shown in Fig. 13.15. Chrome debris is evident in the 20- μm pixels that make up the checkerboard design in Fig. 13.15(b) and 13.15(c). Both mask types were tested in the F₂-laser processing system at fluences of up to 30 mJ/cm². Without full optimization of laser parameters, the best quality masks offered only low transmittance of 20–25%, yielding loss estimates of 70–75% for the Cr-on-CaF₂ mask and 60–68% for the Cr-on-SiO₂ mask after accounting for bulk and Fresnel losses. These large losses arise from scattering and absorption by the micron-sized chrome droplets and surface roughness, especially for the tiled CaF₂ substrate.

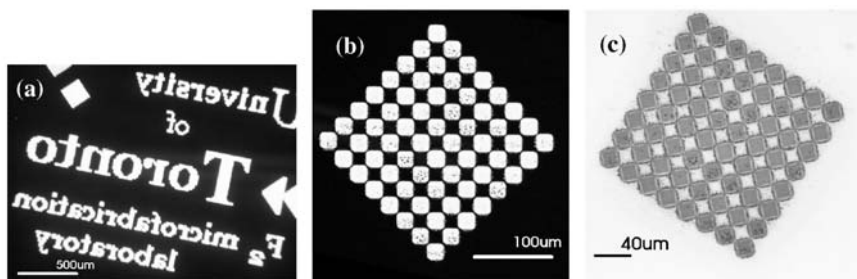


Fig. 13.15. Microscope image in backlighting of a laser-patterned Cr-on-CaF₂ mask (a) and an enlargement (b) of the diamond structure in the uppermost left corner of the same logo. Front lighting microscope image (c) of the same diamond structures in Cr-on-SiO₂ substrate [49].

Even with such large losses, the projection system of Fig. 13.2 delivered 1.0 J/cm² fluence on-target (together with a 0.4 J/cm² red component) to faithfully reproduce the mask features by laser ablation as seen in Fig. 13.16 for a soda lime microscope slide. An enlarged AFM view of the uppermost diamond figure, showing the full detail of the checkerboard pattern is shown in Fig. 13.16(b). The micron-sized chrome droplets in the photomask were too small after 25 \times demagnification to affect the glass patterning. The inset shows a $\sim 130 \text{ nm}$ depth modulation with a peak-to-peak separation of 1.6 μm horizontally and 1.1 μm diagonally, corresponding to sub-micron pixel features of smaller than $\sim 800 \text{ nm}$.

Further optimization of F₂-laser ablation is required to reduce laser damage and the concomitant surface scattering losses in the Cr-coated substrates and improve the VUV transmittance above the present value of $\sim 25\%$. The precision of F₂ laser ablation also promises means to add phase-shift features that enhance the optical resolution of the photomask.

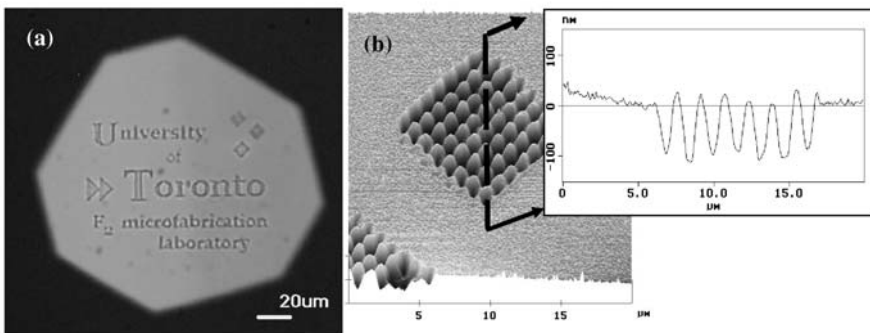


Fig. 13.16. Microscope image (a) in top lighting of a logo ablated in soda-lime glass with one laser pulse patterned by the Cr-on-fused silica mask of Fig. 13.15(c). Higher magnification AFM profile (b) of the diamond-shaped logo in the top right of (a) and a surface line profile inset [49].

13.4.4 Gratings

Laser fabrication is a promising and flexible approach for excising custom grating designs for several micro-optic applications such as grating demultiplexers for telecommunication components [53], phase-masks for writing fiber Bragg gratings, light couplers for planar optical waveguides, mode-selective coupling into fiber facets, 1×2 or $1 \times N$ beam splitters and combiners, micro-interferometric phasemask illuminators, alignment grooves for liquid crystal displays, and grating-spectrometer on a biochip. Sub-micron gratings are desirable for visible and UV light applications, and have been structured by UV-laser ablation with nanosecond pulses on polymer [1, 54, 55, 56, 57] and borosilicate glass [58] surfaces. Ultrafast lasers have also been applied to pattern sub-micron grating structures on metals and optical materials [59, 60], but such lasers generate relatively poor surface morphology, including debris and molten splatter, as noted [61] for fused silica (SiO₂). Gratings in the range of $10 \mu m$ to $\sim 1 \mu m$ period were also fabricated in fused silica with 248-nm KrF-laser radiation by *laser-induced backside-wet etching* (LIBWE) [62, 63] and *laser-induced plasma-assisted ablation* (LIPAA) [64]. The F₂-laser ablation is attractive as a direct patterning method, with the advantages of high resolution as described in Sections 13.2 and 13.3 for UV-grade glasses such as fused silica.

Various optical means for patterning gratings with F₂-laser light include mask projection, direct write, phase mask, and interferometry. Mask projection is attractive here to take advantage of the uniformity of the homogeneous beam and the moderately large field size ($250\text{ }\mu\text{m} \times 250\text{ }\mu\text{m}$) of the $25\times$ Schwarzschild lens for the configuration in Fig. 13.2. Cr-coated CaF₂ masks were produced by laser patterning with 193-nm [65] or 157-nm (Section 13.4.3) ablation, or provided by commercial vendors, to offer $\Lambda = 20$ to $250\text{ }\mu\text{m}$ periods that yielded 0.8 to $10\text{ }\mu\text{m}$ periodic patterns on target. Free-standing aluminum foils were also laser cut to form high transmission masks with $> 75\text{ }\mu\text{m}$ period ($> 3\text{ }\mu\text{m}$ period on target).

Figure 13.17 (a) and (c) show a large $\Lambda = 10\text{-}\mu\text{m}$ period grating formed at 3.2 J/cm^2 fluence and 100 Hz repetition rate [66]. A near-rectangular profile is evident in the AFM image of Fig. 13.17(c). The 630-nm etch depth was designed to eliminate the zeroth order in the far-field diffraction pattern for 633-nm laser light as seen in Fig. 13.17(e). The measured diffraction efficiencies are 3% for 0^{th} order and $2 \times 32\%$ for the two 1^{st} order spots. Gratings were also etched groove-by-groove ($\sim 1\text{-}\mu\text{m} \times 250\text{-}\mu\text{m}$ channels on target) to produce the $\Lambda = 2\text{-}\mu\text{m}$ grating pattern shown in Figs. 13.17 (b) and (d). A 4.2-J/cm^2 fluence at 10 Hz yielded sinusoidal profiles as seen in Fig. 13.17(d) – the rectangular beam profile washed out here due to the thermal effects described in Section 13.3. The crest-to-trough modulation depth is $1.3\text{ }\mu\text{m}$ (Fig. 13.17 (d)), which is close to a maximum value obtainable for $1\text{-}\mu\text{m}$ line-and-space trenches. The 633-nm diffraction pattern produced by the $2\text{-}\mu\text{m}$ period grating is shown in Fig. 13.17(e). Because of under-etching, the diffraction efficiencies were 11% for first order and $2 \times 21\%$ for the 1^{st} orders.

Fabrication of finer gratings is challenging in glasses [65] as seen in the AFM image of Fig. 13.18. The sinusoidal profile for this 830-nm period grating could only be etched to 250-nm modulation depth, yielding a 0.6 aspect ratio. This profile required excess exposure of 60 laser pulses at 3.0-J/cm^2 fluence. The differential etch rate (trough to crest) was only $\sim 4\text{ nm}$ per pulse or $\sim 10\%$ of the expected etch rate for this fluence (Fig. 13.4). The grating efficiency was only 8% for 1^{st} order at 633 nm wavelength, but would be much higher for UV light. Finer features of $\sim 250\text{ nm}$ were also replicated on fused silica from the small defects present on projection mask. However, laser conditions could not be found for the present configuration to generate large aspect ratio (~ 1) and produce strong grating structures in glasses at sub-micron periods [65].

F₂-laser grating microfabrication is broadly extensible to other geometries attractive in photonics integration. Fig. 13.19 shows a surface-relief diffraction grating etched onto the end facet of a multi-mode optical fiber having a $50\text{-}\mu\text{m}$ core diameter of pure fused silica [67]. A Cr-coated ($\sim 90\text{ nm}$) CaF₂ grating mask (Sine Patterns) of $50\text{ }\mu\text{m}$ period produced the $2\text{-}\mu\text{m}$ grating period. A uniformly deep $1.3\text{-}\mu\text{m}$ modulation depth was excised with 36 pulses at 4 J/cm^2 fluence and 100 Hz repetition rate. The 1^{st} order diffraction ef-

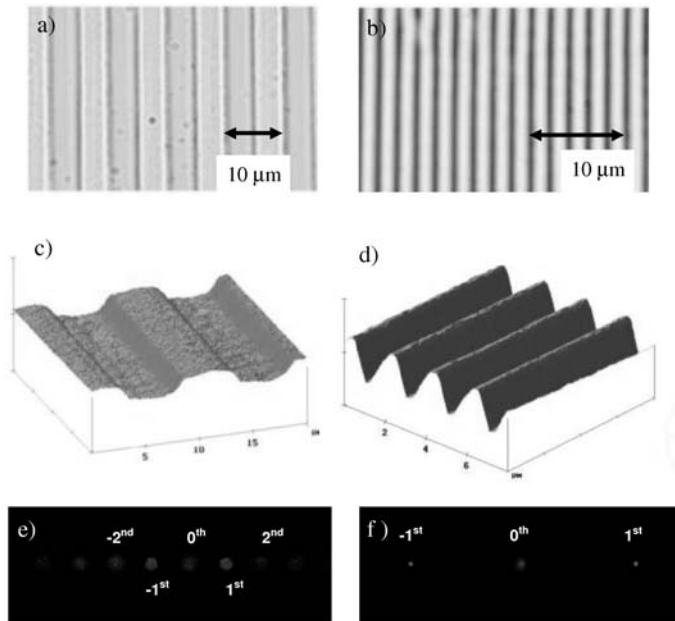


Fig. 13.17. Surface relief gratings etched on fused silica by large-area projection (a, c) and single-line projection (b, d) as observed by optical microscopy (a, b) and AFM (c, d). Grating periods are $10\ \mu\text{m}$ for the left column and $2\ \mu\text{m}$ for the right column. The 633-nm laser diffraction patterns are shown in (e) and (f) for the $10\text{-}\mu\text{m}$ and $2\ \mu\text{m}$ period gratings, respectively [66].

ficiency for 635 nm wavelength emerging from the fiber core was 50% and can be further improved by blazing the grooves and optimizing the grating modulation depth to null the 0^{th} order intensity. Such gratings are attractive for compact end pumping of fiber amplifiers and biomedical fiber applications [67].

Overall, the F_2 laser offers precise and clean ablation to generate micron and submicron gratings on fused silica. Modulation depths of several hundred nanometers are controllable by variation of pulse number and fluence. The F_2 -laser precision is also attractive for blazing, chirping, and apodizing the grating relief for tailoring spectral responses in custom grating applications.

13.4.5 Diffractive Optical Elements

Diffractive optical elements (DOE) are pervasive in many optical systems for enhancing the resolution and efficiency of refractive optics while also reducing the system size [68]. A DOE is any optical element that takes advantage of diffraction through modulation of the phase front, the field amplitude, or a combination of the two. DOEs manipulate the direction and shape of a light beam, and include the gratings and phase masks in the previous section as

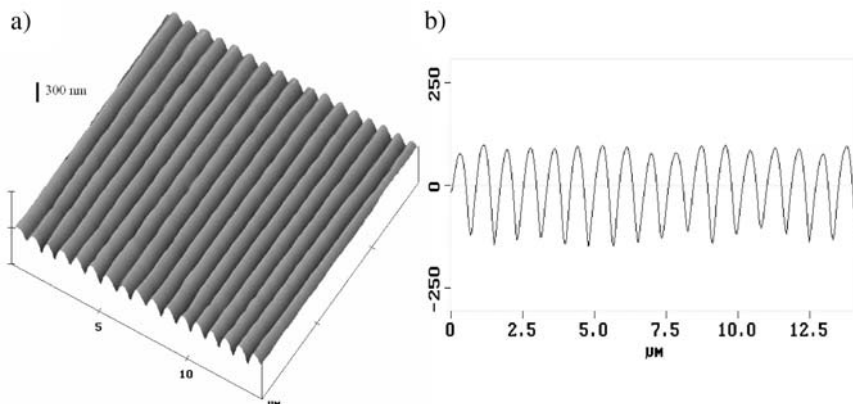


Fig. 13.18. AFM surface plot (a) and cross-sectional profile (b) of a submicron surface relief grating formed on fused silica by large-area mask projection and F₂-laser ablation. Exposure was 60 laser pulses at $3.0\text{ J}/\text{cm}^2$ fluence [65].

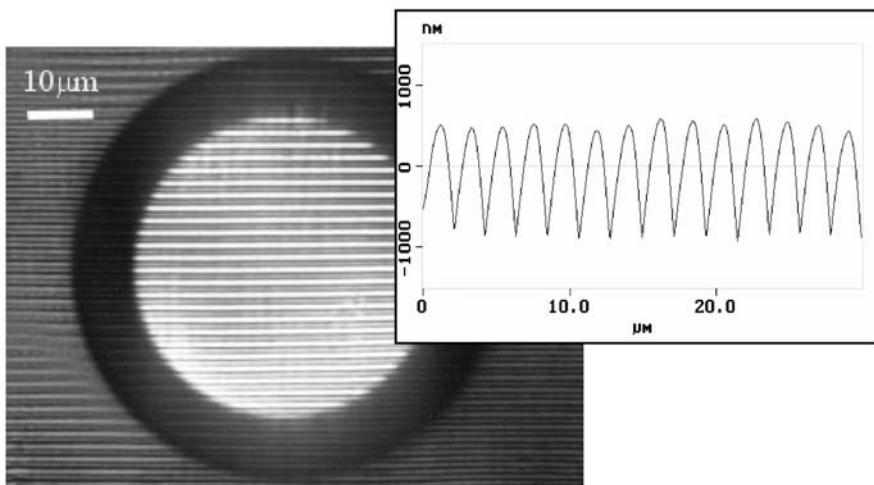


Fig. 13.19. Optical image and AFM cross-section profile (inset) of a 2- μm period diffraction grating fabricated on the end facet of a multimode optical fiber by F₂-laser projection ablation [67].

examples of one-dimensional binary DOEs. Multi-level DOEs are attractive in fully using all the incident light power while arbitrarily patterning light shapes in lateral and longitudinal propagation directions. Kinoforms are another class of DOEs introduced in 1969 by Lesem *et al.* [69] as a type of computer-generated hologram. Kinoforms combine refractive surfaces with phase modulation for correcting aberrations in lens systems. Other DOE

applications include optical communication components, fiber couplers [70], free-space optical interconnects [71], wavelength division multiplexers, scanners, architecture, fingerprint sensors, beam shaping, beam homogenization [72], and applications art, information processing, and the computer industry. Phase-shift masks are also key in lithographic exposure tools for defining the critical $\sim 90\text{-}nm$ gate dimensions in today's semiconductor transistor circuits.

DOEs can only be effective when surface excisions are defined to sub-wavelength precision. Micromolding offers such precision for high-volume and low-cost batch production of polymer-based DOEs. Fabrication in high-transparency glasses such as fused silica is usually met through expensive multi-step manufacturing processes such as lithographic patterning and etching [68, 73]. However, such methods are not flexible for rapid prototyping and custom fabrication. Laser micromachining is therefore an attractive approach in custom DOE fabrication that has been examined in fused silica with various lasers [74]. Both $193\text{-}nm$ and $248\text{-}nm$ excimer lasers have demonstrated some capability for DOE fabrication [75], but are constrained by weak light absorption and incubation processes to overly large and difficult-to-control excision depths ($> 100\text{ nm}$). A short wavelength extension to the $157\text{-}nm$ F_2 laser affords significant advantages as noted in Section 13.3 – tens of nanometer depth control without the disadvantages of microcracking and surface roughness associated with longer wavelength or ultrafast laser systems [5]. The F_2 laser has demonstrated the highest precision reported to date amongst various classes of lasers to directly fabricate DOEs [76, 77, 78]. Other indirect laser approaches to glass etching such as laser-induced back-side wet etching [62, 79] also provide small etch depths that have been recently extended to DOE fabrication [80].

This section describes the design and testing [78] of a 16-level 128×128 -pixel DOE fabricated in fused silica with the F_2 -laser fabrication system described in Fig. 13.2. The goal was to create a smiley face pattern as shown in Fig. 13.20(a) by passing a uniform HeNe laser beam through a suitably pattered DOE.

Amongst several approaches to computer-based design of diffractive optical elements [73], the Iterative Fourier Transform Algorithm (IFTA) [81] is most commonly used. In IFTA, one applies random phases to the electric field in the desired far-field distribution (i.e. Fig. 13.20(a)) and then propagates the distribution back to the DOE plane using an inverse discrete Fourier transformation. The amplitude is made to conform to a plane wave, while the phase is not altered. This ‘DOE’ field distribution is then translated back to the far-field signal plane using a discrete Fourier transformation where phase freedom is applied to begin the next iteration. After a sufficient number of iterations, the difference between the simulated and the desired far-field amplitude will become acceptable and a quasi-continuous phase function will be obtained at the DOE plane. This phase function is then ‘quantized’ into spatial elements at a specified number of discrete levels (N) to approximate

the desired phase function and complete the design. For the present case of $N = 16$ levels, phase steps of $2\pi/16$ are defined by etching the glass surface in incremental steps of $\Delta d = \lambda/16(n - 1)$ depth. For a $\lambda = 633\text{-nm}$ HeNe-laser application in a fused silica ($n = 1.457$), one obtains $\Delta d = 87\text{ nm}$ for the step increment.

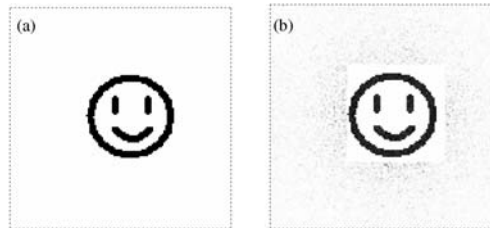


Fig. 13.20. Desired design of far-field light pattern (a) to be generated in 1st order by a diffractive optical element and the simulated far-field pattern (b) for a 16-level DOE design [78]

The simulated far-field pattern for a 16-level 128×128 pixel element design is shown in Fig. 13.20(b). There were no modeling constraints in the IFTA to specifically reduce the scattered light seen outside the square area tangential to the smiley face. Light scattering is therefore expected in the present design, but can be reduced with other modeling criteria. Scattering can also be reduced by using more than 16 etch levels and by increasing the number of pixel elements above 128×128 .

The DOE fabrication was automated by Visual Basic software to control both laser triggering and target sample positioning via GPIB IEEE-488 and DAQ cards (National Instrument). The pixels were etched one at a time in a raster scan with the sample moving site to site by three-axis motion stages (Newport TSPI100 with MM4006 controller). An amplitude mask defined a uniform $200\text{ }\mu\text{m} \times 200\text{ }\mu\text{m}$ beam that was projected by the $25\times$ demagnifying Schwarzschild lens to excise $8\text{ }\mu\text{m} \times 8\text{ }\mu\text{m}$ area pixels on the fused silica sample. The translation stage velocity was 0.3 mm/s and the laser repetition rate was 28 Hz . The low repetition rate ensured accurate positioning of the motion stages at each pixel element to $< 500\text{ nm}$ precision.

The etch depths as defined by the IFTA design were converted into laser exposure data with the results of Fig. 13.4. The approximate fluence at the target plane was 8 J/cm^2 , predicting $\sim 120\text{-nm}$ excisions per pulse for a design wavelength of 880 nm . Full exposure of the 128×128 DOE surface required ~ 90 minutes, but could be reduced with only modest effort since less than 0.1% of the laser beam area was used here. The average laser fluence was stable throughout the long exposure, with pulse-to-pulse laser fluctuations

of $\sim 4.5\%$ (rms) that ensured reproducible etch depths across the full DOE surface.

Laser ablation at atmospheric pressure generates ablation debris comprising of fine submicron particles collecting over the DOE and surrounding surfaces as seen in the AFM section of the laser-generated DOE in Fig. 13.21(a) [78]. Such debris masks the precise underlying features formed by the laser and also generates significant light scattering. The DOEs were submerged in a beaker of ethanol and placed in an ultrasonic cleaner for approximately 45 minutes, followed by 5 minutes of ultrasonic cleaning in methanol, to dislodge the debris. A much-improved DOE surface is shown in Fig. 13.21(b) for the same sample. Each pixel is approximately $7\text{ }\mu\text{m} \times 7\text{ }\mu\text{m}$ in area and there is clear distinction between the different pixel levels. Also, box-shaped troughs and projections are now visible as expected, and seen in closer view in the inset in Fig. 13.21(b).

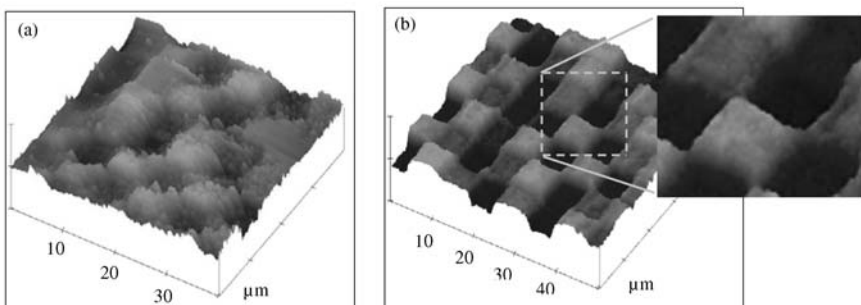


Fig. 13.21. AFM images of laser-fabricated DOE showing significant ablation debris in (a). Ultrasonic cleaning effectively removes this debris as seen in (b) and in the enlargement over several pixels in the inset [78]

Fig. 13.22 shows the observed etched depth (by AFM) for several pixels at each designated DOE level. The etched depths follow a linear line as expected, yielding level separations of $\sim 138\text{ nm}$ – the resulting single-pulse etch depth [78]. The linear dependence is an important advantage in ensuring accurate construction of the DOE to the full design depth. Pixel-to-pixel depth variance within a single level, N , was also much less than the 138-nm level spacing in this sample. This precision originates with the reproducibility of the F₂-laser ablation process in fused silica. The 4.5% (rms) pulse-to-pulse laser energy fluctuations contributes only $\sim 3\text{ nm}$ depth deviation according to the etch rate dependence in Fig. 13.4. The observed depth fluctuations of 10's of nanometers (in Fig. 13.22) are significantly large due to the melt and debris formation dynamics of laser ablation. Based on these findings, it can be concluded that the F₂-laser process can indeed fabricate 16-level DOEs

with distinguishable etch depths, and that further extensions to smoothly varying DOE structures are highly promising [78].

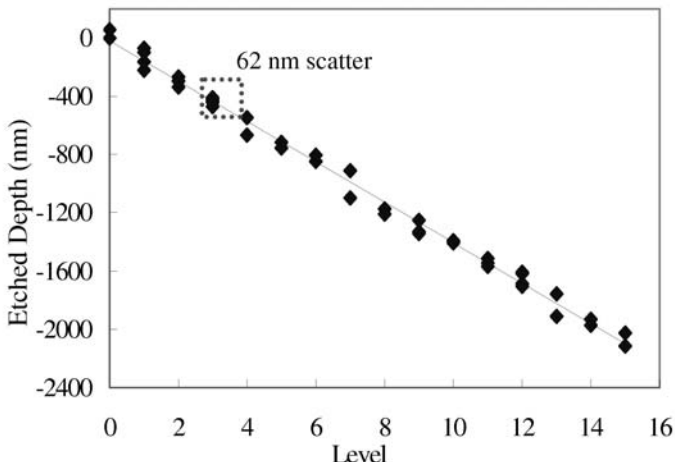


Fig. 13.22. Etch depth of several pixels produced at each design level of the DOE, demonstrating reproducibility of etch depth within each level [78]

An assessment of the mean surface roughness of pixels was obtained by examining AFM surface profiles in the central 55–65% area of individual pixels. Without ultrasonic solvent cleaning, the sample in Fig. 13.21(a) yielded a mean surface roughness of $\sim 150\text{ nm}$, which exceeded the level spacing of the DOE. For the cleaned surface in Fig. 13.21(b), Fig. 13.23 plots the mean roughness averaged over several pixels as a function of the pixel level. The cleaning step yielded a four-fold improvement in the mean surface roughness to 38 nm , with maximum and minimum values of 55 nm and 17 nm , respectively. There was no clear correlation between the mean roughness and the etch depth, suggesting that deep pixels will not scatter any more light or diminish the DOE performance relative to the shallow pixels.

Far-field intensity patterns were generated by illuminating the DOE surface of the sample in Fig. 13.21(b) with spatially filtered HeNe-laser light (632.8 nm , 1 mW). A 40-cm focal length lens focused the light through a square aperture that was aligned and matched in size to the $896\text{ }\mu\text{m} \times 896\text{ }\mu\text{m}$ size of the DOE aperture without over or under filling. The far-field intensity pattern was recorded with a CCD camera and is shown in Fig. 13.24 for the DOE sample of Fig. 13.21(b). A precise replication of the expected smiley face in Fig. 13.20(b) is clearly seen in 1^{st} and 2^{nd} orders. Scattered light is also seen to surround the smiley face as also predicted in Fig. 13.20(b). However, the amount of scattered light is larger than expected owing to surface roughness and imperfections in the pixel shapes as discussed further below.

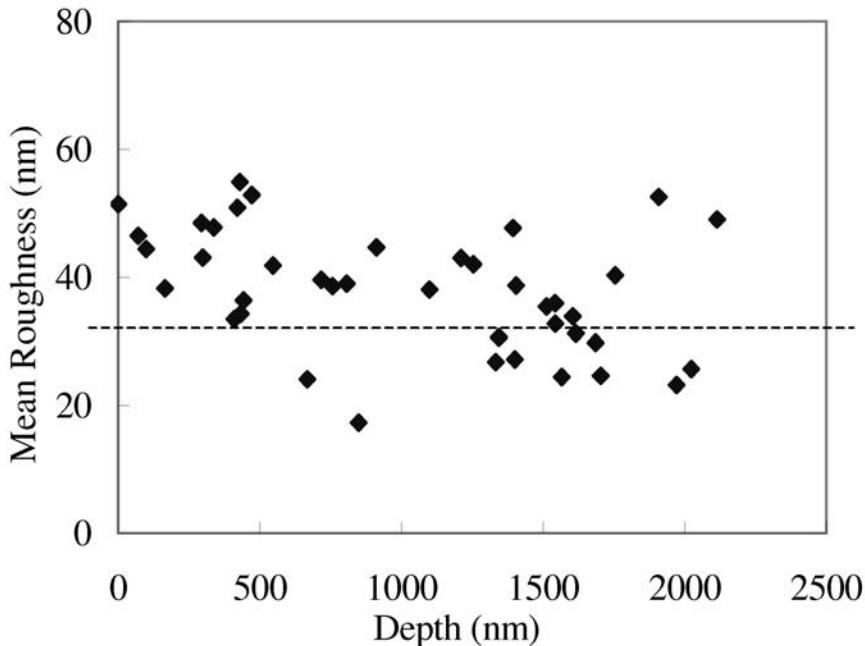


Fig. 13.23. Mean surface roughness of the DOE pixels in Fig. 13.21(b) with respect to the etch depth of the pixel [78]

In addition, the orthogonal DOE grid of $7\mu m \times 7\mu m$ pixels also generated a two-dimensional grating pattern. Table 13.2 shows the percentage of the total incoming laser power diffracted to the central 0^{th} and adjacent 1^{st} order spots arising from this grating effect. The 22.6% 0^{th} -order light arises from the mismatch of the $\Delta d = 138\text{-}nm$ level-to-level spacing and the ideal 86-nm spacing required for the present 633-nm probe light. A lower on-target laser fluence to produce smaller etch depth (or the use of 880-nm probe light) will reduce this 0^{th} -order diffraction as well as the higher order spots, although limited by the sloped-wall pixel defects that also contribute to this grating pattern. A significant amount of the light was also scattered backwards towards the source. These losses together with 8% Fresnel loss at the two surfaces greatly diminished the 1^{st} -order efficiency of the smiley face to 21.9% (Table 13.2) when summed over all the four quadrants in Fig. 13.24.

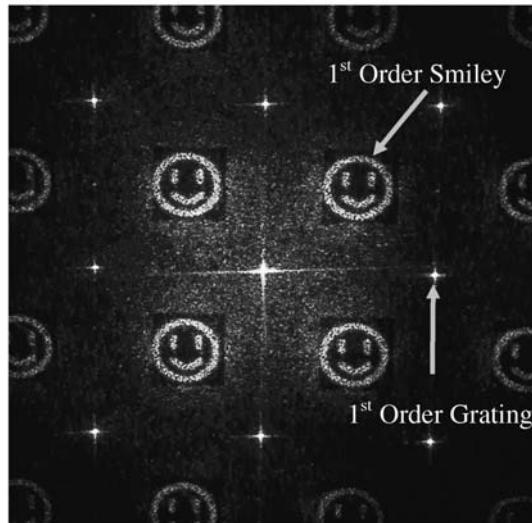


Fig. 13.24. Far-field intensity pattern of 633-nm light generated by the DOE shown in Fig. 13.21(b) [78]

Table 13.2. Percent of total incoming laser power in 0th and 1st order

Order	Percent of total incoming power
0 th	22.6%
1 st (Smiley)	21.9%
1 st (Grating Spot)	4.5%

The steepness of the DOE pixel walls as seen in the inset in Fig. 13.21(b) was typically in the range of 10° to 20° from normal. However, interfaces between the very shallow and deep pixels were less steep, and occasionally as large as 40° from normal. Such defects wash out the required phase delay. A larger pixel size would serve to steepen the walls and decrease the relative area of these wall defects, but at a trade-off against the relative amount of light diffracted to higher orders. Alternatively, an extension to shorter wavelength DOE applications will offer an improvement in the wall steepness by reducing the required pixel etch depth.

Several directions are available to improve the DOE performance and place more of the diffracted light into the first diffraction order. The computational design can be improved to reduce the scattered light as predicted in Fig. 13.20(b). Adding blazing to the design can further re-direct all 1st-order light to only one quadrant. An example of the required terracing of pixel levels is shown in the microscope image of Fig. 13.25. A 4-level DOE was

fabricated in fused silica by F₂-laser ablation to create a single 1st-order pattern from a uniform 193-nm ArF-laser beam [77]. Further improvements in debris management, sample cleaning, and laser stability are showing promise to greatly improve the precision of DOE fabrication and reduce the amount of scattered light. Such improvements will be investigated further to demonstrate that custom designs of efficient DOEs can be practically generated in fused silica and related glasses. In this way, laser microfabrication promises to open new applications for DOEs in high-quality optical materials.

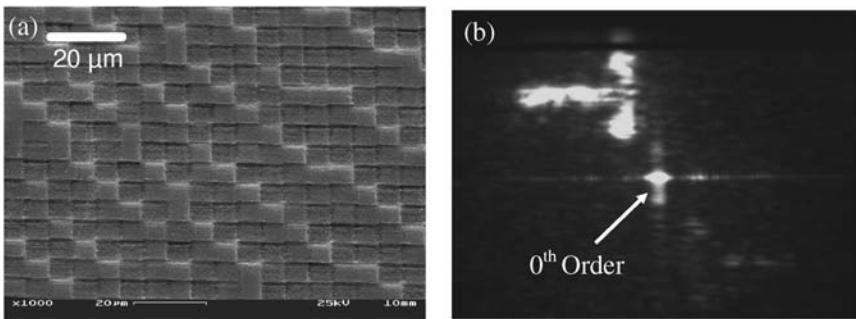


Fig. 13.25. Scanning electron micrograph (a) of a four-level DPE fabricated in fused silica by F₂-laser ablation. The terracing of levels yields a single 1st-order pattern shaped as the rotated T in (b) for 193-nm laser probe light [77].

13.5 Controlling Refractive Index

When transparent glasses are irradiated at laser fluences below the ablation threshold, photochemical processes take place that permanently alter the refractive index of the medium. These ‘radiation-damage’ processes underlie such photosensitivity response and relate also to the incubation effects described in Section 13.3.1. Long-term laser exposure of 10² to 10⁴ pulses are typically required to yield appreciable refractive index change in the range of $\Delta n = 10^{-4}$ to 10^{-2} [25]. Such refractive index change serves several commercial directions for shaping useful photonic components such as the Bragg gratings inside the core of optical telecommunication fibers and optical fiber sensors.

Ultraviolet lasers such as the 248-nm KrF or the 244-nm frequency-doubled argon-ion are commonly employed because such UV wavelength accesses a defect channel provided by weak germanium-doping of the guiding core of standard telecommunication fiber (SMF 28; 3% GeO₂ doping). However, photosensitivity enhancement techniques such as hydrogen loading [30], high-germanium concentration [31], and ion implantation [32] remain

necessary here to generate a useful refractive index change in such optical waveguides.

One approach to improving the photosensitivity response of such germanosilicate glasses is to extend laser sources to shorter wavelength where new defect channels in glass may be accessed. In the case of the 157-nm F₂ laser, weakly doped germanosilicate glasses become opaque and provide strong photosensitivity mechanisms in the near surface region without the need for enhancement techniques. Even pure fused silica glasses become photosensitive to 157-nm light to offer new means for creating micro-photonic components internally in the bulk glass. This section summarizes the 157-nm photosensitivity responses of germanosilicate and fused silica glasses, and describes examples of fabricating Bragg gratings in fibers, trimming waveguide birefringence in a planar optical circuit, and writing of buried optical waveguides in bulk fused silica glass.

13.5.1 F₂-Laser Photosensitivity: Silica Glasses

Theories of the mechanism behind photosensitivity response [25] fall principally into two camps: the color centre model assumes that defect precursors within the glass network respond to sub-bandgap light and form new color centers, changing the refractive index of the material through the Kramers-Kronig relationship; the second theory [27, 82] emphasizes material compaction through radiation damage. In both cases, subtle laser interactions lead to useful and controllable amounts of refractive index change.

The F₂ laser was directly applied [5, 83, 84] to various grades of fused silica through a proximity amplitude mask of 140 μm period to form volume phase gratings. Stylus profilometry revealed the formation of a surface relief grating, with 10 to 300 nm deep surface compaction occurring above the laser irradiated volume. Fig. 13.26 shows a side view of a 2 mm thick polished window (Corning 7940; 1200 ppm OH) after exposure to 180,000 pulses at $\sim 84 \text{ mJ/cm}^2$ fluence. A refractive index contrast is clearly visible. This volume phase grating is $\sim 700 \mu\text{m}$ deep, matching approximately the penetration depth associated with the 157-nm absorption coefficient of $\alpha_{157} \sim 10 \text{ cm}^{-1}$. Changes in glass absorption at 157 nm and in the near infrared were also noted [83] with increasing laser exposure. These observations suggest that the color center and densification models are coupled for F₂-laser irradiated silica glasses.

The surface-relief modulation depth, dh (*peak to trough*) induced in fused silica blanks is plotted as compaction-to-thickness ratio (dh/h) versus total (accumulated over N shots) laser dose, NF , in Fig. 13.27(a). Sample thickness varied from $h = 0.16$ to 1.0 mm. Additional samples were also soaked in H₂ gas ($\sim 100 \text{ bar}$, $\sim 10 \text{ days}$) prior to radiation to investigate photosensitivity enhancement in fused silica. Here, dh/h increased from $\sim 100 \text{ ppm}$ to $\sim 270 \text{ ppm}$ in at an exposure of $NF = \sim 37 \text{ kJ/cm}^2$, attesting to a useful > 2 -fold enhancement. A nonlinear relationship between dh/h and NF is

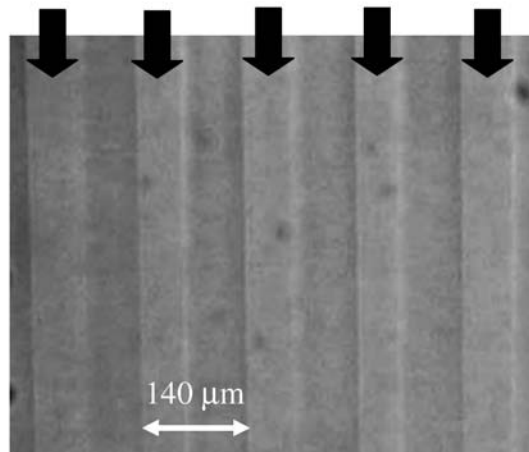


Fig. 13.26. Optical microscopy side view of a 140- μm period refractive index grating formed with a 157-nm dose of $NF = 15.6 \text{ kJ}/\text{cm}^2$ (180,000 pulses $\times 84 \text{ mJ}/\text{cm}^2$ fluence). Arrows indicate illumination positions of F₂ laser patterned by a multi-slit mask. The phase contrast is clearly visible and penetrates $\sim 700 \mu\text{m}$ deep into the 2.0 mm thick SiO₂ glass [83].

evident that coarsely follows a universal material densification response of $dh/h \sim (NF)^{0.82}$ and $dh/h \sim (NF)^{1.18}$ for samples without and with H₂-loading, respectively. The linear fluence responses are strong evidence of a single photon mechanism underlying the 157-nm glass densification.

Kitamura et al. [85] established a simple relationship, $\Delta n/n = 0.4504 dh/h$, to estimate refractive-index change resulting from compaction. For our exposure of $NF = \sim 37 \text{ kJ}/\text{cm}^2$ in H₂-loaded silica (Fig. 13.27(a)), we obtain Δn of $\sim 1.8 \times 10^{-4}$ from a compaction ratio of dh/h of 270 ppm, predicting a modestly strong refractive index change for fused silica.

To characterize F₂-laser-induced refractive index changes, wet-fused silica (OH: 1200 ppm; $\alpha_{157} = 26 \text{ cm}^{-1}$) cover slips of thickness $d = 0.16 \text{ mm}$ were stacked together and radiated through a 140- μm period grating mask [83]. The resulting surface and bulk structural changes induce opposing optical effects in the laser-exposed volume: 1) the surface relief grating reduces the physical path length, and 2) the increased density increases the refractive index, giving rise to advancing and retarding phase delays, respectively. Corrections for the surface grating were therefore applied to the diffraction efficiency measurements. First-order diffraction efficiency of 0.1 to 1.5% was observed with a HeNe laser for samples exposed to $N = 60,000$ to 360,000 laser pulses at single-pulse fluence values varied from $F = 10$ to $90 \text{ mJ}/\text{cm}^2$. A numerical model of exponential index profile, $\Delta n e^{\alpha d}$, yielded an effective absorption coefficient of $\alpha = 26 \text{ cm}^{-1}$. The near-surface index changes, Δn , are plotted in Fig. 13.27(b) as a function of NF . The clustering of the data

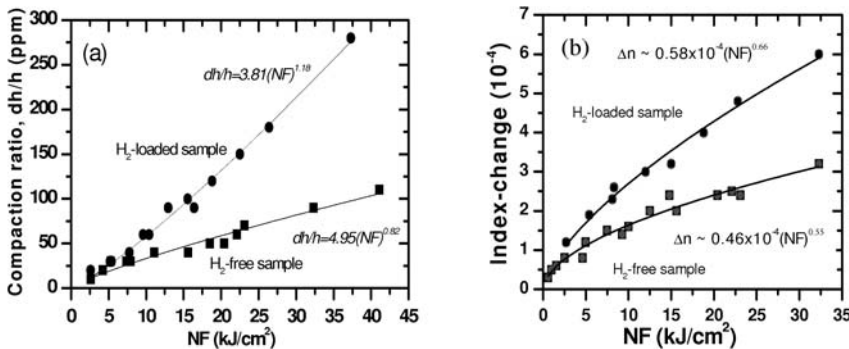


Fig. 13.27. Compaction ratio (a) as a function of F₂-laser dose, NF , observed in SiO₂ without and with H₂-gas photosensitivity enhancement. The peak refractive index change induced in the bulk glass by the 157-nm radiation is shown in (b) [83].

about a single line shows that index changes are controlled by accumulated fluence, NF . This simple response offers advantages in concentrating finite laser energy to increase fluence and processing speed, or reducing fluence for larger area exposure at slower rates of refractive index change.

The 157-nm refractive index data follow a universal material compaction response of $\sim \Delta n(NF)^{0.6}$, a single-photon response commensurate with the densification data of Fig. 13.27(a). Overall, 157-nm laser-induced compaction and refractive index changes in fused silica are approximately three orders of magnitude faster than reported for 193- or 248-nm lasers [26, 27]. Allen et al. [27] observed a nonlinear compaction response of $\sim (NF^2)^{0.53}$ for 193-nm laser irradiation of fused silica, providing evidence for a weaker two-photon process. The linear fluence dependence at 157 nm points to a single-photon process associated with bandgap or near bandedge states such as oxygen deficiency centers. The mechanism may involve Si-O bond scission and the formation of the Si-Si wrong bond as noted in related VUV Raman laser studies of fused silica by Sugioka and coworkers [86].

F₂-laser irradiation of fused silica provides an absolute index changes of $\sim 5 \times 10^{-4}$ in an $\sim 400 \mu\text{m}$ thick surface layer to provide useful phase changes for a wide range of applications in shaping and trimming optical components made with pure silica.

Germanium doping of fused silica is widely applied to increase the refractive index of fused silica and define the waveguide core of optical fibers and planar lightwave circuits. Such doping also lowers the bandgap from ~ 9.1 eV of fused silica to values comparable with the 7.9-eV photon energy of the F₂ laser. This provides strong absorption in thin layers on scale lengths commensurate with the $\sim 10\text{-}\mu\text{m}$ size of the guiding core. The F₂ laser is therefore

attractive for fabricating photonic components and circuits inside germanosilicate fiber and planar waveguides [87, 88, 89, 90, 91, 92, 93, 94, 95].

Standard telecommunication fibers (SMF 28) and silica-based cladless planar waveguides (PIRI SMPWL) were exposed to 157-nm radiation. The planar waveguide consisted of $8\ \mu m$ thick GeO₂-doped (3%) core layer grown over $20\ \mu m$ of fused silica, all on a silicon substrate. Germanosilicate glasses are much more photosensitive ($> 10\times$) than the fused silica cladding, dominating the contribution of measured refractive-index change.

Figure 13.28 shows the peak refractive-index change observed in planar waveguides as a function of accumulated laser fluence [87]. The single-pulse fluence was $\sim 7.5\ mJ/cm^2$. Effective index values from three guiding modes were determined from prism-coupling angle changes using HeNe-laser probe light. These values were applied to a simple step-profile model of refractive index [93], with bulk index change and penetration depth as the only adjustable parameters. The inferred penetration depth decreased from $\sim 8\ \mu m$ at low fluence to $\sim 4\ \mu m$ for above $10\ kJ/cm^2$ total exposure, a dynamic response that develops asymmetric refractive index profiles useful in birefringence trimming of the waveguide.

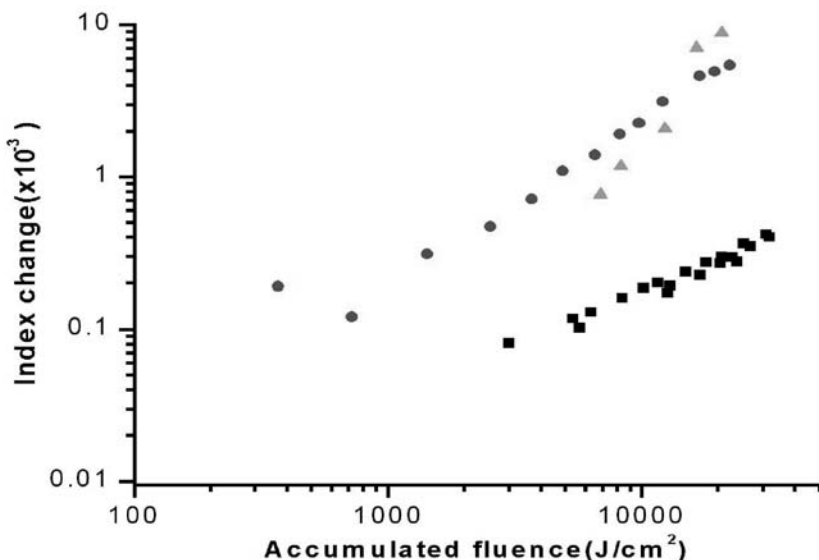


Fig. 13.28. Comparison of deep-UV F₂-laser and ultrafast-laser-induced refractive index changes for $\sim 633\text{-}nm$ probe light in fused silica and germanosilicate glasses: ● F₂ laser in GeO₂ doped (3%) silica, ■ F₂ laser in UV-grade fused silica, △ ultrafast laser in fused silica [87].

An unsaturated peak index change of 0.005 is obtained with only 22- kJ/cm^2 fluence. Hydrogen loading of the planar waveguide (105 bar for 10 days) provided a 3-fold faster response rate [6], a modest improvement in comparison with order-of-magnitude enhancements seen with longer wavelength exposure [96]. Figure 13.28 also includes the fused silica data of Fig. 13.27. Because of stronger absorption, the germanosilicate waveguide responds more than 10-fold faster than for the case of pure fused silica. Further, this index change is strong and rapid compared with longer-wavelength exposure of similar germanosilicate waveguides (3% GeO₂) without H₂-loading techniques. For example, responses are an order of magnitude faster than with 193-nm radiation, and follow a single-photon response in comparison with inferred two-photon responses [97]. Figure 13.28 also shows that F₂-laser photosensitivity responses in germanosilicate glass is similar to that induced by ultrafast lasers in fused silica glasses [87].

13.5.2 F₂-Laser Photosensitivity: Optical Fiber

A rapid 157-nm photosensitivity response was also found [88, 89, 92, 94, 95, 98] for standard telecommunication fiber (Corning SMF-28), permitting the formation of strong long-period gratings and fiber Bragg gratings.

The transmission spectrum of long-period fiber grating with 304- μm period is shown in Fig. 13.29 for the case of a H₂-loaded fiber (at 100 bar for 10 days). A ~ 20 -dB loss peak is noted at the 1.58- μm telecommunication band. This response developed with 2,700 pulses at ~ 1.8 - mJ/cm^2 fluence – or with only 4.75- J/cm^2 total fluence. In contrast, a > 300-fold larger total fluence is required from 248-nm KrF lasers to develop a loss peak of the same strength [88, 89]. F₂-laser radiation clearly drives strong photosensitivity responses in germanosilicate glasses.

A comprehensive characterization of F₂-laser photosensitivity responses had been undertaken [94] for both hydrogen-free and hydrogen-loaded standard fibers (SMF-28) by means of trimming FBGs. Results showed that a modest F₂-laser exposure of 1–10 kJ/cm^2 offers a large $> 1 \times 10^{-3}$ index change in standard fibers, while 2-fold larger index changes and 15-fold faster responses were found with hydrogen soaking. Because of strong interactions, only weak single-pulse fluence of < 10 mJ/cm^2 was applied to avoid fiber damage that prematurely saturates the refractive index change. Although this exposure is $\sim 50\times$ less than the fluences typically applied with UV excimer lasers, strong and rapid photosensitivity responses more than compensated for the low damage threshold. Further, the 10^{-3} refractive index change is large without the need for hydrogen enhancement, offering additional benefits of improved stability of fiber Bragg gratings and other devices formed in SMF-28 fiber [89, 94].

The F₂-laser-modified index profiles of SMF-28 fiber were studied by a combination of selective chemical etching and AFM in conjunction with microreflectivity, and revealed the creation of highly anisotropic changes

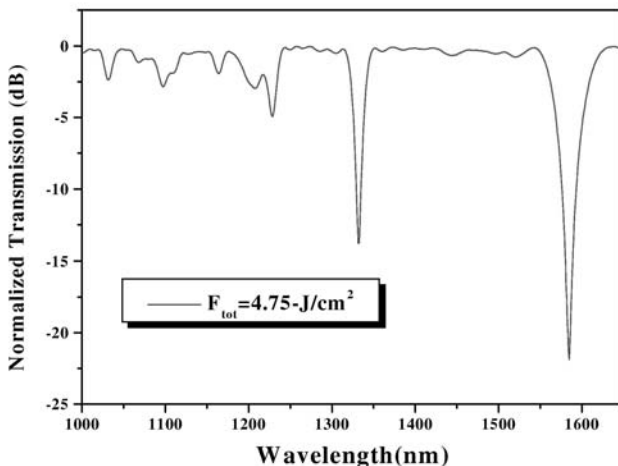


Fig. 13.29. Transmission spectrum of a long-period grating ($\Lambda = 304 \mu\text{m}$) formed in hydrogen-loaded SMF-28 fiber with the 157-nm F_2 laser [89]

only for cases where hydrogen soaking was applied [94]. A modest exposure of 1.3 kJ/cm^2 with single-pulse fluence of 5 mJ/cm^2 yielded the narrow crescent-shaped etch zone toward the laser radiation side of the fiber core after 12 minutes in a HF bath as shown in Fig. 13.30. The etch profile correlates linearly with the refractive index profile. Highly asymmetric refractive index profiles such as shown in Fig. 13.30 were only noted for hydrogen-soaked fiber. Given an accelerated etch rate ~ 1.5 times above that for the core plateau, a peak index change of $(1.5 \times 0.005 =) 0.0075$ was inferred for inside the 900-nm wide laser-modification zone. An index change of $\sim 1.2 \times 10^{-2}$ was observed in a 700-nm wide crescent at slightly higher dose of 2.2-kJ/cm^2 , possibly representing the largest index change ever induced in a standard fiber. The peak index change, Δn , is well represented by a power law relationship of $\Delta n = 4 \times 10^{-5} (NF)^{0.74}$, that supports a one-photon photosensitivity mechanism. As index change rises, the $1/e$ penetration depth gradually falls from $1.4 \mu\text{m}$ to $\sim 0.7 \mu\text{m}$ for the maximum $2,200 \text{ J/cm}^2$ exposure tested here. Similar trends were also seen in planar germanosilicate waveguides [93]. Combination of F_2 -laser irradiation and hydrogen loading drove strongly anisotropy refractive index profiles in germanosilicate waveguides, causing strong waveguide birefringence of up to 5×10^{-5} . While such large birefringence is not normally desirable for writing filters for telecommunication applications, such large birefringence is attractive for writing polarization mode converters or trimming polarization in fiber devices and systems.

Table 13.3 compares the 157-nm F_2 -laser photosensitivity responses (effective index changes) of hydrogen-free and hydrogen-soaked standard fibers [94] to that provided by the more common 248-nm KrF [94] and 193-nm

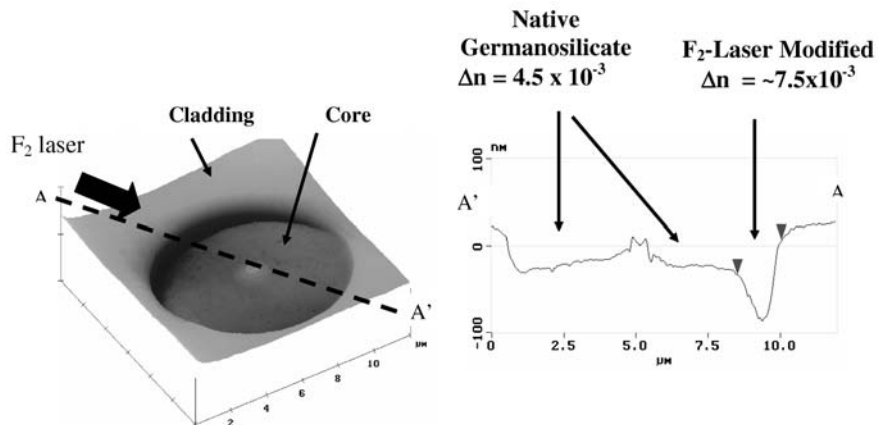


Fig. 13.30. AFM topology (left) and cross-sectional view (right) of a 157-nm-irradiated hydrogen-loaded SMF-28 fiber after 12 min of HF etching. The F₂-laser-induced refractive index change is represented by the one-tenth crescent-moon-shaped trench, formed within the 8-μm diameter fiber core. The shallow penetration (<1 μm) attests to the strong 157-nm absorption in hydrogen-soaked fiber; uniform index changes were inferred in untreated SMF-28 fiber [94].

ArF lasers [99]. In hydrogen-free fiber, the 193-nm and 157-nm photosensitivity response rates are approximately two-orders of magnitude stronger than with the 248-nm KrF laser. A two-photon process was inferred [97] for the 193-nm photosensitivity response, which is approximately 4-fold weaker than the single-photon response underlying the 157-nm photosensitivity. Table 13.1 also illustrates the significant enhancement effect of hydrogen loading [96] in 248-nm photosensitivity, which is dramatically reduced to a 15× enhancement (Δn normalized to laser exposure) for the 157-nm case under identical hydrogen loading condition (105 atmosphere, 10 days, 20°C): Comparisons are Δn normalized against the total laser exposure. Nevertheless, the hydrogen-enhanced 157-nm responses are more than 30-fold faster than the comparable 248-nm hydrogen-enhanced response, and further offers new means for birefringence trimming applications in optical fibers.

Table 13.3. Comparison of photosensitivity responses with various UV lasers [94]

Radiation source	H ₂ -free standard fiber			H ₂ -loaded standard fiber		
	Δn	Pulse fluence (mJ/cm ²)	Total fluence (kJ/cm ²)	Δn	Pulse fluence (mJ/cm ²)	Total fluence (kJ/cm ²)
248-nm	2.0×10 ⁻⁵	400	45	0.82×10 ⁻³	750	27
193-nm	1.1×10 ⁻³	650	58	-	-	-
157-nm	1.1×10 ⁻³	5.2	14	2.2×10 ⁻³	5.0	0.97

13.5.3 Trimming Planar Lightwave Circuits

In this section, we extend the basic 157-*nm* photosensitivity study towards the practical demonstration of phase error and birefringence trimming applications in planar lightwave circuits [93]. Planar lightwave circuits (PLC) are intrinsically birefringent because of stresses built up during the glass coating processes, and are therefore ideal candidates for developing laser birefringence trimming processes. The F₂ laser is targeted here because of the strong interactions noted above in germanosilicate glasses, and the asymmetric index profiles seen in Fig. 13.30 that underlie large changes in waveguide birefringence.

The PLC samples selected for the 157-*nm* trimming studies were Mach-Zehnder (MZ) type, frequency-domain modulators (FDM) having directional couplers and 100-*GHz* free spectral range (FSR) [93]. A 8 μm × 8 μm germanium-boron-phosphor co-doped core was grown and patterned on a custom quartz substrate and embedded in 40 μm thick cladding glass to provide a ~0.3% refractive-index contrast (GeO₂ concentration of ~3%). This fully cladded waveguide has optical features similar to those commonly employed by industry on silicon substrates, while the custom quartz substrate overcomes the 157-*nm* absorption problem in the cladding glass by accessing the waveguide core through the quartz substrate. A 5-mm section of only one interferometer arm was masked off and radiated with the F₂-laser light at 100 Hz and single-pulse fluence of ~5 mJ/cm². Interferometer transmission spectra (Ando AQ6315E) were recorded during irradiation, using linearly polarized light from an Er-doped ASE broadband-light source (Thorlabs ASE FL7002) and polarization maintaining fibers. Hydrogen loading was not applied to the planar waveguide samples.

TE-mode transmission spectra are shown in Fig. 13.31 both before and after 157-*nm* laser trimming with a 1.1 kJ/cm² accumulated fluence [93]. The fringe shift, Δλ, moves towards shorter wavelength, representing an increase in the effective refractive index, Δn, of 1.2 × 10⁻⁴. At an accumulated fluence of ~50 kJ/cm², the FDM spectrum shifted by more than six-times the FSR, corresponding to a 1.7 × 10⁻³ effective index change. (Index values are smaller than reported in Fig. 13.28 due to 157-*nm* absorption in the quartz

substrate.) Such laser trimming offers very precise tuning of the FDM spectral response for locking to the telecommunication grid. Traditional manufacturing processes cannot easily fabricate FDM and other interferometric devices such as arrayed waveguide gratings to the necessary tolerances.

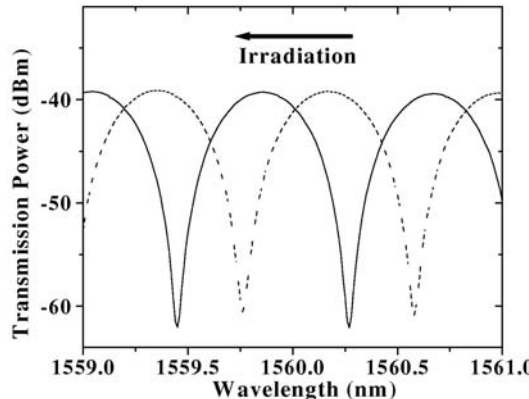


Fig. 13.31. Transmission spectra of a frequency domain modulator before (dashed line) and after (solid line) F₂-laser trimming with a 1.1- kJ/cm^2 dose. Arrow indicates direction of wavelength shift with laser exposure [93].

The FDM photosensitivity responses are 25 to 75% faster for the TE mode (Δn_{TE}) than that for the TM mode as shown by the waveguide birefringence, $\Delta n_{TM} - \Delta n_{TE}$, and relative birefringence, $(\Delta n_{TE} - \Delta n_{TM})/\Delta n_{TM}$, plotted as a function of the accumulated fluence in Fig. 13.32. The absolute birefringence (left scale) increases with the laser dosage, reaching a possibly saturated maximum value of 0.5×10^{-3} . The relative birefringence (right scale) rises quickly, and peaks at 75% before decreasing with further exposure above $\sim 25\text{ kJ}/cm^2$. A non-uniform index change profile such as seen in Fig. 13.30 together with a shallow 157-nm penetration depth is responsible for such large birefringence.

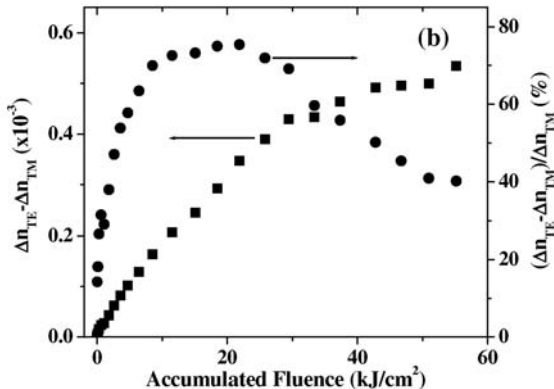


Fig. 13.32. The absolute (left scale) and relative (right scale) birefringence in a germanosilicate frequency domain modulator plotted as a function of the 157-nm laser dosage [93]

The large VUV-laser-induced birefringence is attractive for compensating the native waveguide birefringence in as-manufactured FDMs as illustrated in Fig. 13.33. The as-manufactured FDM has a $\sim 0.1\text{-nm}$ fringe shift between the TE and TM modes (Fig. 13.33(a)), which can be completely tuned away with a modest 1.1 kJ/cm^2 laser dose as shown in Fig. 13.33(b). In a worst-case-scenario for the present FDM, a TE- and TM-mode fringe mismatch of 0.4 nm ($\Delta\lambda_{FSR}$), corresponding to a 0.2×10^{-3} birefringence, can be compensated by applying a modest 10 kJ/cm^2 laser dose.

The most striking feature of F_2 -laser photosensitivity is the gross birefringence of $\sim 0.5 \times 10^{-3}$ induced by a moderate dose of 157-nm radiation (Fig. 13.32). To our best knowledge, this is the largest UV-laser-induced birefringence reported for germanosilicate waveguides to date and presents a practical opportunity for laser birefringence control in both fibers and PLCs. The relative 157-nm birefringence of 40–75% (Fig. 13.32) exceeds reports of ~5–20% birefringence induced by longer wavelength lasers [91, 100, 101, 102]. Further, hydrogen loading is required in several of these cases to drive a large birefringence. Recently, a thermally induced CO_2 -laser process was shown to provide birefringence trimming, however, physical waveguide damage increased the losses by up to 1 dB [33, 34].

Overall, the F_2 laser provides strong birefringence and large index changes without the need for H_2 loading and without increasing the waveguide loss. The resulting index profiles are more stable than processes involving H_2 loading, as noted in a 157-nm laser fiber grating study [89]. Lastly, such highly confined index change ($\sim 1\text{ }\mu\text{m}$ depth) affords wide opportunity in both phase and birefringence tuning of novel polarization-sensitive photonics components in post-laser trimming applications.

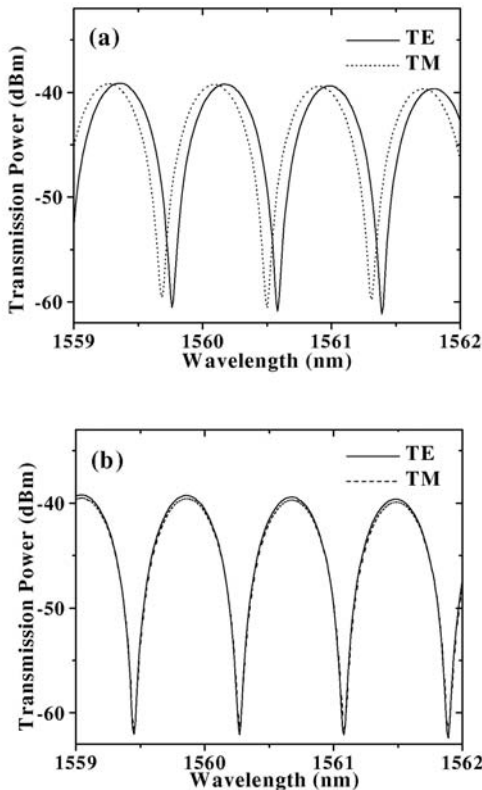


Fig. 13.33. Transmission spectra for excited TE and TM modes in a frequency domain modulator before (a) and after (b) F₂-laser trimming. Waveguide birefringence is compensated in (b) [93].

13.5.4 Writing Buried Optical Waveguides

Ultrafast lasers have been widely studied in modifying refractive index [103] and forming buried waveguides [104, 105, 106] by driving highly nonlinear interactions in transparent materials. This direct laser writing approach focuses a beam inside the bulk material for generating localized refractive index change in a small focal volume of 100 to 1000 μm^3 . Translation of the sample as depicted in the side writing approach in Fig. 13.34(a) permits the carving out of basic three-dimensional (3-D) microoptic components such as cylindrical optical waveguides [103, 107, 108], couplers [109] and 3-D optical memory storage [110, 111].

Long-pulse ultraviolet (UV) lasers have also been applied to the formation of buried waveguides [26, 112], but limited to 2-D patterning within photo-sensitive glass layers. The short-wavelength F₂ laser has a key advantage over other UV laser sources in this regard, by driving efficient one-photon photo-

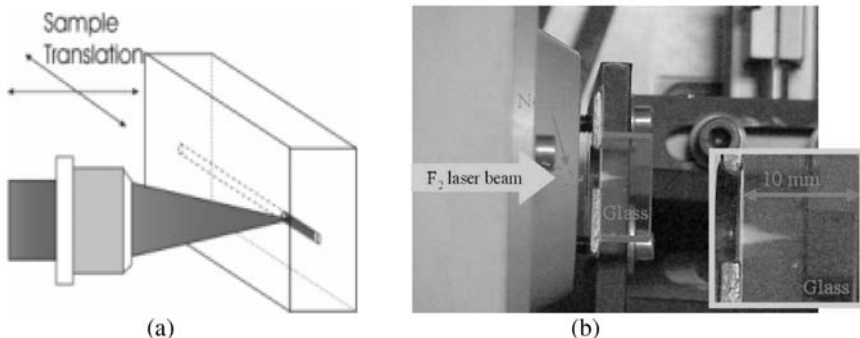


Fig. 13.34. Large numerical aperture (NA) optics in (a) confines laser light into small focal volumes inside glasses where linear absorption in the case of deep-ultraviolet light and non-linear absorption in the case of ultrashort-duration light induce refractive index changes. Sample translation leads to formation of buried cylindrical waveguides. Photograph (b) shows F_2 -laser-induced red fluorescence from a fused silica sample under 0.4 NA illumination. Inset shows a magnified view of the irradiated glass sample. Waveguides were generated at the conical apex, typically at depths less than 1 mm to avoid significant beam attenuation [87].

sensitivity responses in bulk fused silica glasses that access the near band-edge defect states [4, 20, 83]. We recently demonstrated [8, 87, 113] that high numerical aperture optics ($NA = 0.4$) such as depicted in Fig. 13.2 are sufficient to concentrate F_2 -laser photosensitivity responses within a tight focal volume inside fused silica without the need for ultrafast nonlinear interaction physics. In this way, 3-D patterning of buried refractive index structures becomes available for writing waveguides and optical circuit components.

Figure 13.34(b) shows a side-view photograph of a polished fused silica optic in the imaging plane of the F_2 -laser optical-processing tool. The 0.4 NA Schwarzschild optic projects a uniform spot of $\sim 6\text{ }\mu\text{m}$ diameter and $\sim 6\text{ }\mu\text{m}$ depth-of-focus internally into the glass to excite red fluorescence in a conical shape that follows the beam path to an apex several millimeters into the sample. The strongest refractive index changes appear at the apex of the cone, enabling the formation of buried waveguides such as shown in Fig. 13.35 by simple translation of the glass sample [8, 87, 113]. Such structuring is limited to volumes within one optical penetration depth of the surface – 1 mm for the case of fused silica – a range more than ample for extending UV laser processing to 3-D fabrication of optical circuits.

Buried optical waveguides were formed in fused silica at high fluence of 5 to 9 J/cm^2 . This exposure significantly exceeds the 1-J/cm^2 ablation threshold, but no internal damage was evident as seen in the optical images of waveguides in Fig. 13.35. Single-mode waveguides of 5 mm and 10 mm length and 6 to $8\text{ }\mu\text{m}$ diameter were fabricated by side writing (Fig. 13.34) at 50 – $400\mu\text{m}$ depths below the glass surface using scan rates of several microns per second.

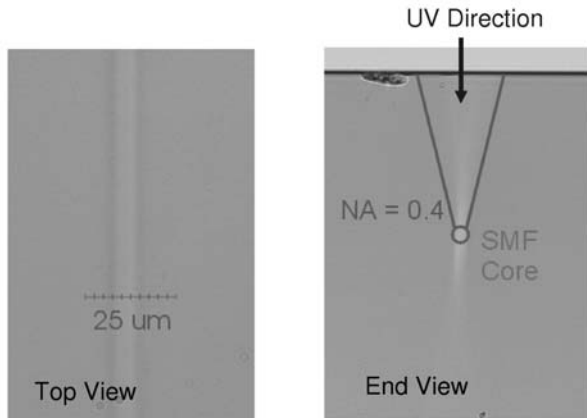


Fig. 13.35. Optical microscope images in top view (left) and side view (right) showing refractive index contrasts of cylindrical waveguides written inside fused silica glass with a deep-ultraviolet F₂ laser [87]

Total fluence exposures of 10 to 40 kJ/cm^2 provided single or multimode waveguides.

The refractive index profile apparent in the end view of Fig. 13.35 shows the concentration of refractive index change below the glass surface. Symmetric single-mode waveguides were observed at this position as noted by the symmetric near-field intensity profile of 635-nm probe light shown in Fig. 13.36 (inset). This waveguide was formed with $\sim 10 kJ/cm^2$ total fluence. There appears some leakage of light to the left of the waveguide core, which is the incoming F₂-laser radiation direction in which a modest increase in refractive index is anticipated. The transverse mode profiles of three different waveguides are also plotted in Fig. 13.36 and show a near Gaussian profile as expected in weakly guiding waveguides. Increased exposure clearly provides stronger guiding, associated with a larger increase in the refractive index. Near-field refractometry showed a large 5×10^{-3} refractive index change at the largest exposures tested. This refractive index modification is 10-fold larger than the values plotted in Fig. 13.28 (solid squares) for F₂-laser irradiated fused silica and compares well with the large refraction changes generated by ultrafast lasers (triangles in Fig. 13.28). The apparent 10-fold photosensitivity enhancement for F₂-laser-formed waveguides may originate with enhanced absorption as a result of transient absorption species created only when high single-pulse fluence is applied. The waveguides were formed at single-pulse fluence of $\sim 5 J/cm^2$ compared with only $\sim 0.1 J/cm^2$ fluence per pulse for the 157-nm fused silica data in Fig. 13.28.

The F₂-laser-formed waveguides were characterized with visible (635 nm) and infrared (1550 nm) laser sources as well as broadband (800–1600 nm) light [8, 87, 113]. No absorption features were noted within these spectral re-

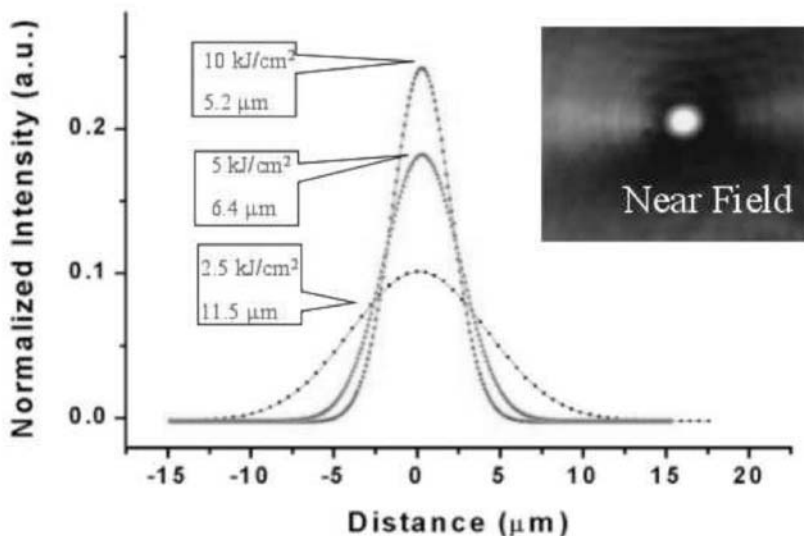


Fig. 13.36. Near-field intensity profile (inset, top-right) and Gaussian line profile (graph) of F_2 -laser-formed buried waveguides in fused silica as probed with 635-nm light. Boxes indicate the total fluence dose and beam width (FWHM) for three waveguides [87].

gions. Transmission losses were large, although less than $3\text{-dB}/\text{cm}$ measurement limit of the present instrumentation. Some form of radiation damage may be generated by the high single-pulse fluence ($5\text{--}9 \text{ J}/\text{cm}^2$). However, low fluence exposure (tens of J/cm^2) of SMF-28 fiber did not induce a waveguide loss suggesting that other processing parameters may generate low-loss waveguides in fused silica.

A method of sweeping a linear hole-array mask pattern at small offset angle offered control of waveguide cross-section by matching depth of focus with widened beam waist. In this way, cylindrically symmetric mode profiles were obtained as shown in the inset in Fig. 13.36(a) [113]. Without this modification, elliptically shaped refractive index profiles will result as shown in the end view in Fig. 13.35. Controlling the waveguide symmetry by this method also alters the waveguide birefringence which can be as large as $\sim 1 \times 10^{-5}$. Such beam shaping methods therefore serve to manage the waveguide birefringence and will become important in controlling polarization and optical polarization-mode dispersion losses in planar and 3-D optical circuits.

In summary, the F_2 laser offers new means for shaping buried waveguide structures and other 3-D micro-optics structures in fused silica glasses. Large NA optical lenses are sufficient for ultraviolet lasers to concentrate single-photon interactions within a small focal volume without the need for ultrafast nonlinear interactions. More broadly, F_2 -laser radiation can drive useful

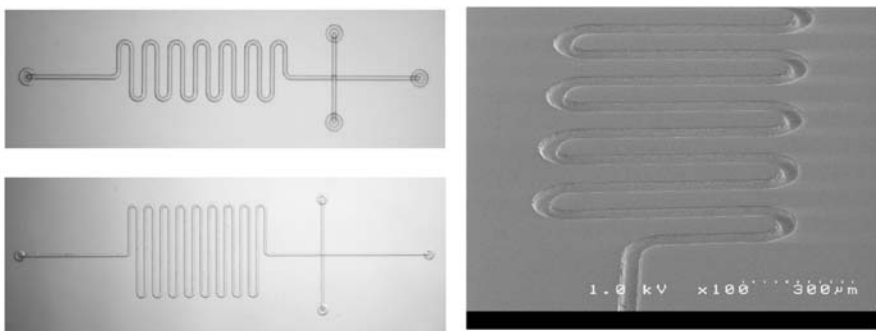


Fig. 13.37. Optical top-view (left) and SEM view (right) of various serpentine microfluidic channels formed on soda-lime glass by F₂-laser ablation. The channel profile is semi-circular with 50 μm width and 10 to 40 μm depth [114].

amounts of refractive index change in silica and germanosilicate materials that offers excellent prospects for shaping novel 3-D photonic components for a range of applications.

13.6 Biophotonics on a Chip

We have seen in this chapter the special merits of F₂-laser processing for precise surface or internal structuring of optical glass that enabled the fabrication of micro-optical components, buried optical waveguides, micro-channels, and thin metal film masks. These are the basic building blocks on which to create a highly functional biophotonic laboratory on a chip or micro-total analysis systems (μ -TAS). Glasses are the optimal biochip substrate, offering high transparency, low fluorescence, and biologically benign surfaces. The strong glass interactions and flexible delivery of F₂-laser light facilitate novel designs and rapid prototyping of highly functional biological chips.

This section describes the fabrication of basic biochip functions on glass or polymer substrates. Optically smooth micro-hole arrays for self-loading of cells were fabricated for three-dimensional multi-photon confocal microscopy [45]. Microfluidic channels were laser patterned on a planar chip for electrophoretic separation of cellular content [45, 114, 115, 116, 117]. Laser processing flexibility was exploited to develop a custom microchannel injector for low-dispersion cell lysing, making possible the high-resolution electrophoretic separation of cellular content on a planar chip [115, 117]. Laser processing also enabled interconnection of buried optical circuits with microfluidic channels that opens new optical means for probing, sensing and trapping of single cells on a chip [114]. Dielectrophoretic single-cell traps are also presented by laser patterning of metallic films on the glass chip [114].

The intersection of microfluidic channels and optical circuits in combination with electrophoretic separators and dielectrophoretic traps collectively

provide powerful single-cell manipulation and biophotonics diagnostics on a compact integrated biochip. The laser processes support monolithic integration and device miniaturization for large-scale three-dimensional fabrication of novel biological and photonic functions. Such devices will enable cell-by-cell analysis in large-scale population studies at the frontiers of proteomics research, and eventually scale towards applications that unlock a molecular-level understanding of cellular functions. Flexible laser processes promise to support a broad base of biological and sensor applications from large-scale population studies of cells to intracellular processes.

Section 13.4.1 described how laser fluence can be used to control microchannel profiles in the range of $1\text{--}50\,\mu\text{m}$ width. Channels such as shown in Fig. 13.9(a) and (b) indicate 1:1 aspect ratio channels with near-vertical wall are available to dimensions smaller than that of a typical cell, namely, $10\,\mu\text{m}$. The channels were formed at $5\,\text{Hz}$, single-pulse fluence of $9\,\text{J/cm}^2$, and 100 and 200 pulses, respectively. By lowering the fluence below $9\,\text{J/cm}^2$, steep walls gave way to semi-circular or V-shaped channels. Fig. 13.37 shows various serpentine channels produced in soda-lime glass with a circular mask and computer-controlled motion stages. Various widths ($10\text{--}40\,\mu\text{m}$) and depths ($10\text{--}50\,\mu\text{m}$) are available for semi-circular channel profiles ideally suited to cell transportation. Ultrasonic cleaning was effective in removing thin layers ($\ll 1\,\mu\text{m}$) of ablation debris to aid top-surface sealing of the channels and to reduce light scattering inside micro-optic devices. Other approaches for debris management were described in Section 13.3.

Microfluidic channels for electrophoretic analysis of cellular material were ablated into glass- and PMMA-based lab-on-a-chip devices [115, 116, 117]. Fig. 13.38 illustrates how the F_2 laser added new functions to customize a commercial biochip (Micronit Microfluidics, the Netherlands) for a new application. Here, $11\,\mu\text{m}$ wide microchannels were excised in parallel to enable parallel single-cell electrophoresis with independent fluorescence characterization of the cellular analytes. A cover slip was sealed onto the chip. Acute myeloid leukemia (AML) suspension cells, labeled with fluorescein derivative, were selected from a reservoir and manipulated by optical trapping into the entrance of a laser-formed microchannel as shown in Fig. 13.38(b). In this design, the microchannel was slightly smaller than the cell to prevent the cell from entering prior to lysing. However, cellular content was dispersed over a large volume that prevented high-resolution electrophoretic separation on the chip. Injector channels were then custom designed as shown in Fig. 13.39(a) to minimize cross contamination between adjacent microchannels and to prevent dilution of analyte volume ($500\,\text{fL}$) during cellular lysis. Fig. 13.39(b) shows an acute myeloid leukemia cell in the injector prior to lysing. The injector provided much improved resolution during on-chip electrophoretic separation [115, 116].

Micro-vias of cellular ($10\,\mu\text{m}$) and smaller dimensions are highly desired in many cell or gene chip applications. Fig. 13.10 shows a microscope ph-

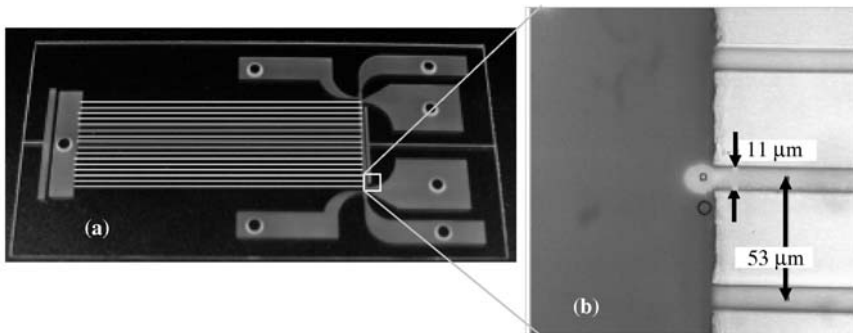


Fig. 13.38. A commercial microfluidic biochip (Micronit Microfluidics, Netherlands) of $9\text{ cm} \times 4.5\text{ cm}$ size after custom modification by F₂-laser ablation to form parallel electrophoretic channels. The channels are identified by the white horizontal lines in (a). In (b), a fluorescein-labeled cell has been positioned at the entrance of one of the laser-formed channels with optical tweezers (b) [45, 115, 117].

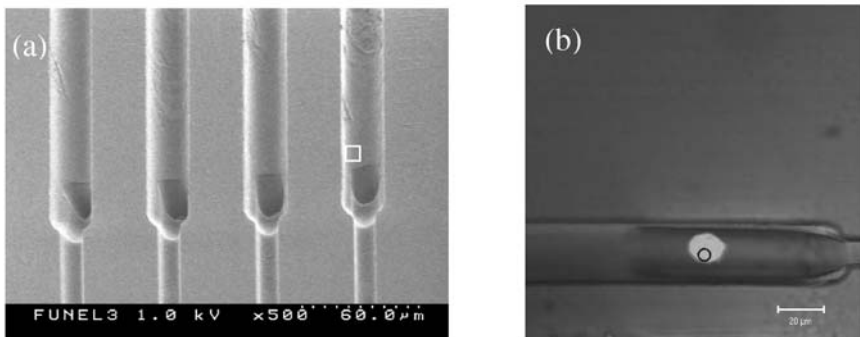


Fig. 13.39. F₂-laser-ablated injector channels (a) for high resolution and parallel electrophoretic separation of single cell content. A fluorescein-labeled cell (b) is shown after manipulation into the injector volume by optical tweezers (open circle indicates laser focal position) and prior to lysing. The injector and electrophoretic channels are $20\text{ }\mu\text{m}$ and $10\text{ }\mu\text{m}$ wide, respectively [114, 115].

tograph of a 96-hole cell-chip array formed by F₂-laser ablation on $200\text{-}\mu\text{m}$ centers [45]. Each hole was formed with 100 laser pulses at 10 Hz (10 second exposure), using $\sim 6\text{ J/cm}^2$ fluence. A closer view is shown in the SEM photograph in Fig 13.10(b), which reveals a slightly tapered hole with diameter of $\sim 17\text{ }\mu\text{m}$ at the top and $\sim 12\text{ }\mu\text{m}$ at the bottom – well matched to self-loading of single cells. A 3-D profile of the hole in Fig. 13.10(c), obtained by confocal-microscope scanning under oil immersion, reveals a flat hole bottom. The walls are sufficiently smooth for optical imaging of cellular content. With appropriate masking and 100-Hz operation, dozens of holes may be ex-

cised per second. Fig. 13.10(b) also reveals accumulation of ablation debris. No cleaning methods were used in the present case but may be applied as described in Section 13.3.

From the laser patterning of chrome-coated masks in Section 13.4.3 were offered recipes for patterning metal electrodes on a glass chip. Such electrodes offer means for cell manipulation and sorting by the dielectrophoretic force. Fig. 13.40 shows castellated electrodes formed on a chrome-coated soda-lime glass slide by F₂-laser ablation. This device aligned and levitated (right figure) 15- μm polystyrene microspheres above the electrodes when AC biased at 10 V and 10 kHz. In another dielectrophoretic device, 3- μm yeast cells were trapped at the intersection of two crossing microfluidic channels [45, 114].

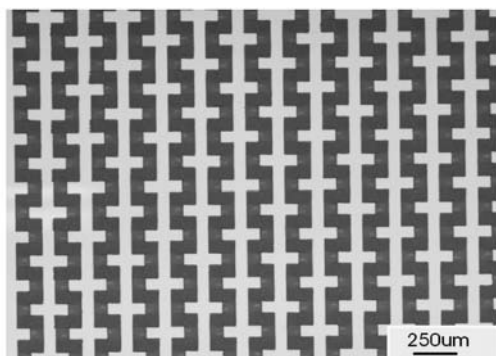


Fig. 13.40. Castellated electrodes formed by F₂-laser ablation of chrome-coated soda lime glass. AC voltage biasing provides dielectrophoretic levitation of cell-sized structures [114].

Ultrafast lasers are attractive for forming optical waveguides [103, 105, 106] and other refractive structures inside transparent glasses, yielding refractive index changes as high as 0.01 in fused silica. Section 13.5.4 also describes the formation of buried optical waveguides with F₂-laser radiation, yielding single-mode waveguides with $\Delta n = 5 \times 10^{-3}$ [8]. The F₂ laser offers a single process step for interlacing 3-D buried optical circuits with microfluidic channels to enable on-chip spectroscopy analysis and other biophotonic functions. Fig. 13.41 shows two buried optical waveguides intercepting an open microfluidic channel [114]. The waveguides were formed 50–100 μm below the surface. An access channel of 120 μm width by 60 μm depth was formed by the laser just above the waveguides. A 20 μm wide microfluidic channel was then excised in the bottom of this trench to intercept the buried waveguide at 90° angle. The waveguides were found to transmit both infrared and visible light through the channel, were acted as a weak Fabry-Perot resonator due to the glass-channel refractive index contrast. Such waveguides will be useful

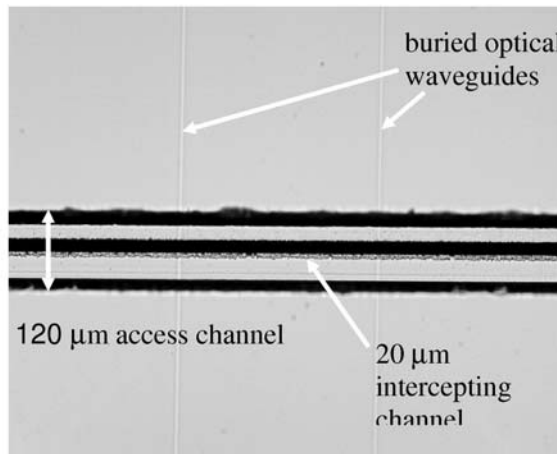


Fig. 13.41. Laser-fabricated biophotonic chip with buried optical waveguides intercepting an open microfluidic channel on a fused silica substrate [114]

in the next generation of biochips for probing and manipulating cells and cellular content.

In summary, F₂-laser microprocessing offers precise and flexible means for sculpting novel biophotonic functions into biochips to create 3-D networks of microfluidic channels and interlacing optical circuits. Such miniaturization and scaling to 3-D will enable the customization of powerful biochips and rapid prototyping of new chip designs, promising to advance the forefronts of cytometry and proteomics research.

References

1. P.R. Herman, K. Beckley, R.A. Potyrailo: "VUV holographic gratings etched by a single F₂ laser pulse", in *OSA: Conference on Lasers and Electro-Optics*, Anaheim, Ca. (1994), paper CFI2
2. <http://www.sematech.org>
3. S. Switkes, T.M. Bloomstein, M. Rothschild: *Appl. Phys. Lett.* **77**, 3149 (2000)
4. P.R. Herman, K. Beckley, B. Jackson, K. Kurosawa, D. Moore, T. Yamanishi, J. Yang: *Proc. SPIE* **2992**, 86–95 (1997)
5. P.R. Herman, R.S. Marjoribanks, A. Oettl, K. Chen, I. Konovalov, S. Ness: *Appl. Surf. Sci.* **577**, 154–155 (2000)
6. P.R. Herman, K.P. Chen, P. Corkum, A. Naumov, J.Z. S. Ng: *Proc. SPIE* **4088**, 345–350 (2000)
7. J. Fair, E. Mayer, M. Scaggs, D. Basting: *Lambda Highlights* **56**, 7 (2000)

8. M. Wei, K.P. Chen, D. Coric, P.R. Herman, J. Li: "F₂-laser microfabrication of buried waveguide structures in transparent glasses", in *Photon Processing in Microelectronics and Photonics*, (Proc. SPIE **4637**, Photonics West, 2002), pp. 251–257
9. P.E. Dyer, J. Sidhu: JOSA B **3**, 792 (1986)
10. M. Lapczyna, M. Stuke: Appl. Phys. A **66**, 473 (1998)
11. M. Lapczyna, M. Stuke: Mat. Res. Symp. Proc. **526**, 143 (1998)
12. M. Fiebig, M. Kauf, J. Fair, H. Endert, M. Rahe, D. Basting: Appl. Phys. A **69**, 305 (1999)
13. P.R. Herman, B. Chen, D.J. Moore: MRS Proc. **285**, 163 (1993)
14. P.R. Herman, B. Chen, D.J. Moore, M. Canaga-Retnam: MRS Proc. **236**, 53 (1992)
15. P. Gruenewald, J. Cashmore, J. Fieret, M. Gower: Proc. SPIE **4274**, 158 (2001)
16. D. Basting (Ed.): *Excimer Laser Technology: laser sources, optics, systems and applications* (Lambda Physik, Göttingen, 2001)
17. A. Yick, J. Li, P. Herman: "F₂-Laser micropatterning of chrome-coated CaF₂ for vacuum-ultraviolet masks", in *Laser Applications in Microelectronic and Optoelectronic Manufacturing* Vol. VIII (Proc. SPIE **4977**, Photonics West, San Jose, CA, 2003), pp. 400–410
18. A. Ostendorf, T. Bauer, T. Temme, T. Wagner: Proc. SPIE **4274**, 116 (2001)
19. A.K. Bates, M. Rothschild, T.M. Bloomstein, T.H. Fedynyshyn, R.R. Kunz, V. Liberma, M. Switkes: IBM J. Res. & Dev. **45**(5), 605 (2001)
20. P.R. Herman, K.P. Chen, M. Wei, J. Zhang, J. Ihlemann, D. Schäfer, G. Marowsky, P. Oesterlin, B. Burghardt: Proc. SPIE **4274**, 149 (2001)
21. J. Li, P.R. Herman, M. Wei, K.P. Chen, J. Ihlemann, G. Marowsky, P. Oesterlin, B. Burghardt: Proc. SPIE **4637**, 228–234 (2002). Photonics West
22. H. Okabe: *Photochemistry of Small Molecules* (John Wiley and Sons, New York, 1978)
23. W.J. Smith: *Modern optical engineering: the design of optical systems*, 2nd edn. (McGraw-Hill, New York, 1990)
24. K.O. Hill, Y. Fujii, D.C. Johnson, B.S. Kawasaki: Appl. Phys. Lett. **32**, 647 (1978)
25. R. Kashyap: *Fiber Bragg Gratings* (Academic Press, New York, 1999)
26. M. Rothschild, D.J. Ehrlich, D.C. Shaver: Appl. Phys. Lett. **55**, 1276 (1989)
27. D.C. Allan, C. Smith, N.F. Borrelli, T.P.S. III: Opt. Lett. **21**, 960 (1996)
28. P.R. Herman, J. Yang, K. Kurosawa, T. Yamanishi: Proc. SPIE. **2991**, 170–174 (1997)
29. P.R. Herman, A. Oettl, K. Chen, R.S. Marjoribanks: Proc. SPIE **3616**, 148 (1999)
30. D. Du, X. Liu, G. Korn, J. Squier, G. Mourou: Appl. Phys. Lett. **64**, 3071 (1994)
31. B.C. Stuart, M.D. Feit, S. Herman, A.M. Rubenchick, B.W. Shore, M.D. Perry: J. Opt. Soc. Am B **13**, 459 (1996)
32. I.A. Konovalov, P.R. Herman: "Ablation-induced stresses in fused silica by 157-nm F₂-laser irradiation", in *Laser-Solid Interactions for Materials Processing*, Vol. **617** (MRS Proc., San Francisco, CA, 2000)
33. F. Guignard, M.L. Autric, V. Baudinaud: Proc. SPIE **3343**, 534 (1998)
34. N.F. Borrelli, C. Smith, D.C. Allan, T.P. Seward: J. Opt. Soc. Am. **B14**, 1606 (1997)

35. E.R. Cochran, C. Ai: *Appl. Optics* **31**, 6702 (1992)
36. F. Dahmani, A.W. Schmid, J.C. Lambropoulos, S. Burns: *Appl. Optics* **37**, 7772 (1998)
37. R.W.H. (ed. G Hassand, R.E. Thun): *Physics of Thin Films*, 3rd edn. (Academic Press Inc., New York, 1996)
38. W.C. Oliver, G.M. Pharr: *J. Mater. Res.* **7**, 1564 (1992)
39. F. Dahmani, J.C. Lambropoulos, A.W. Schmid, S. Papernov, S.J. Burns: *J. Mater. Res.* **14**, 597 (1999)
40. O.M. Efimov, L. Glebov, S. Papernov, A.W. Schmid: *Proc. SPIE* **3578**, 564 (1999)
41. S. Papernov, D. Zaksas, J.F. Anzellotti, D.J. Smith, A.W. Schmid, D.R. Collier, F.A. Carbone: *Proc. SPIE* **3244**, 434 (1998)
42. A.T. Woolley, R.A. Mathies: *Natl. Acad. Sci.* **91**, 11348 (1994)
43. C. Backhouse, M. Caamano, F. Oaks, E. Nordman, A. Carrillo, B. Johnson, S. Bay: *Electrophoresis* **21**, 150 (2000)
44. G.C. Bjorklund: *Proc. SPIE* **4290**, 94 (2001)
45. P.R. Herman, A. Yick, J. Li, N.R. Munce, L. Lilge, E. Jervis, S. Krylov: “F₂-laser micromachining of microfluidic channels and vias for biophotonic chip applications”, in *Conf. on Lasers and Electro-Optics Tech. Digest paper CFL5*, Baltimore, Md. (OSA, Wash DC, 2003) (2003)
46. D. Basting (Ed.): *Excimer Laser Technology: laser sources, optics, systems and applications* (Lambda Physik, Göttingen, 2001)
47. T. Fricke-Begemann, J. Ihlemann, G. Marowsky, J. Li, P.R. Herman: *Proc. SPIE* **5578**, 589 (2004)
48. A. Wagner, R. Haight, P. Longo: *IBM Res. Report RC* **22562**, 1–12 (2002)
49. A. Yick, J. Li, P.R. Herman: *Proc. SPIE* **4977**, 400–410 (2003)
50. D. Schäfer, J. Ihlemann, G. Marowsky, P. Herman: *App. Phys. A* **72**, 377 (2001)
51. S. Gogoll, E. Stenzel, H. Johansen, M. Reichling, E. Matthias: *Methods Phys. Res. B* **116**, 279–283 (1996)
52. D. Ashkenasi, H. Varel, A. Rosenfeld, F. Noack, E. Campbell: *Appl. Phys. A* **63**, 103–107 (1996)
53. J. Nitta, Y. Handa, T. Numai: (2001), U.S. Patent No. 6,334,014
54. K. Ilcisin, R. Fedosejevs: *Appl. Opt.* **26**, 396 (1987)
55. H. Phillips, D. Callahan, R. Sauerbrey, G. Szabo, Z. Bor: *Appl. Phys. A* **54**, 158 (1992)
56. P. Dyer, R. Farley, R. Giedl, D. Karnakis: *Appl. Surf. Sci.* **96–98**, 537 (1996)
57. F. Weisbuch, S. Lazare, F. Goodall, D. Débarre: *Appl. Phys. A* **69**, 413 (1999)
58. S. Pissadakis, L. Reekie, M. Hempstead, M. Zervas, J. Wilkinson: *Appl. Phys. A* **69**, 739 (1999)
59. P. Simon, J. Ihlemann: *Appl. Surf. Sci.* **110**, 43 (1997)
60. F. Beinhorn, J. Ihlemann, P. Simon, G. Marowsky, B. Maisenhölder, J. Edlinger, D. Neuschäfer, D. Anselmetti: *Appl. Surf. Sci.* **138–139**, 107 (1999)
61. K. Kawamura, N. Sarukura, M. Hirano, H. Hosono: *Appl. Phys. Lett.* **78**, 1038 (2001)
62. J. Wang, H. Niino, A. Yabe: *Appl. Phys. A* **68**, 111 (1999)
63. K. Zimmer, R. Böhme, A. Braun, B. Rauschenbach, F. Bigl: *Appl. Phys. A* **74**, 453 (2002)

64. K.M. K. Sugioka: RIKEN Review **32**, 36 (2001)
65. J. Ihlemann, S. Müller, S. Puschmann, D. Schäfer, M. Wei, J. Li, P.R. Herman: Appl. Phys. A **76**, 751 (2003)
66. S. Leung: (2003), "Baasc thesis, laser micro-fabrication of diffractive optical elements", Ph.D. thesis, U. of Toronto
67. J. Li, P. Herman: "Vacuum-ultraviolet laser nano-milling of surface-relief gratings on optical fiber ends", in *CLEO*, ed. by P.C. Tech. Digest, (OSA, Wash DC) Baltimore, Md. (2003)
68. D.C. O'Shea, T.J. Suleski, A.D. Kathman, D.W. Prather: SPIE Tutorial Texts **TT62** (2004)
69. L. Lesem, P. Hirsch, J.A. Jordan, Jr.: IBM J. Res. Dev. **13**, 150–155 (1969)
70. A. Schilling, H. Herzig, L. Stauffer, U. Vokinger, M. Rossi: App. Optics **40**, 5252–5259 (2001)
71. J. Turunen, A. Vasara, J. Westerholm: Opt. Eng. **28**, 1162–1167 (1989)
72. F. Nikolajeff, S. Hard, B. Curtis: App. Optics **36**, 8481–8489 (1997)
73. F.W. J. Turunen (Ed.): *Diffractive Optics for Industrial and Commercial Applications* (Akademie Verlag, Berlin, 1997)
74. C. Buerhop, B. Blumenthal, R. Weissmann, N. Lutz, S. Biermann: App. Surf. Sci. **46**, 430–434 (1990)
75. D. Schäfer, J. Ihlemann, K. Mann, G. Marowsky: App. Phys. A **69**, 319–322 (1999)
76. A. Nejadmalayeri, A. Yick, J. Li, P. Herman: "Kinoform optics: direct fabrication by F₂ laser ablation", in *CLEO*, ed. by P.C. Tech. Digest, (OSA, Wash DC) Baltimore, Md. (2003)
77. M. Schulz-Ruhtenberg, J. Ihlemann, G. Marowsky, A. Nejadmalayeri, M. Ng, J. Li, P. Herman: "Fabrication of diffractive phase elements by F₂-laser ablation of fused silica", in *Proc. 4th Int. Conf. on Laser Precision Microfabrication*, Munich DE (2003)
78. M.L. Ng, P. Herman, A. Nejadmalayeri, J. Li: to appear in *Laser Applications in Microelectronic and Optoelectronic Manufacturing IX*, Proc. SPIE **5339** (2004)
79. X. Ding, Y. Kawaguchi, H. Niino, A. Yabe: App. Physics A **75**, 641–645 (2002)
80. G. Kopitkovas, T. Lippert, C. David, A. Wokaun, J. Gobrecht: Microelectronic Engineering **67–68**, 438–444 (2003)
81. F. Wyrowski: J. Opt. Soc. Am. A **7**, 961–969 (1990)
82. N. Borreli, C. Smith, D.C. Allan, T.S. III: Opt. Lett. **24**, 1401 (1999)
83. J. Zhang, P. Herman, C. Lauer, K. Chen, M. Wei: Laser Appl. in Microelectronic and Optoelectronic Manuf. V , Proc. SPIE **4274**, 125–132 (2001)
84. P. Herman, K. Chen, P. Corkum, A. Naumov, S. Ng, J. Zhang: RIKEN Review **32**, 31–35 (2001)
85. N. Kitamura, Y. Toguchi, S. Funo, H. Yamashita, M. Kinoshita: J. Non-crystal. Solid **159**, 241–245 (1993)
86. J. Zhang, K. Sugioka, S. Wasa, H. Tashiro, K. Toyoda: IEEE J. Selected Topics in QE **3** 1 (1997)
87. P. Herman, M. Wei, D. Coric, J. Li, A. Nejad-Malayeri, P. Corkum, R. Bhardwaj, D. Rayner: "Writing buried optical waveguides: Contrasts in ultrafast and ultraviolet lasers", in *Proc. International Congress on Applications of Lasers and Electro-Optics (ICALEO)*, Scottsdale AZ (2002)

88. K. Chen, P. Herman, R. Tam, J. Zhang: Electronics Lett. **36**, 2000–2001 (2000)
89. K. Chen, P. Herman, J. Zhang, R. Tam: Opt. Lett. **26**, 771–773 (2001)
90. K. Chen, P. Herman: Electronics Lett. **38**, 24–26 (2002)
91. K. Chen, P. Herman: IEEE Photonic Tech. Lett. **14**, 71–73 (2002)
92. K. Chen, P. Herman, R. Tam: IEEE Photonics Tech. Lett. **14**, 170–172 (2002)
93. K. Chen, P. Herman, R. Taylor: IEEE J. Lightwave Tech. **21**, 140–148 (2003)
94. K. Chen, P. Herman, R. Taylor, C. Hnatovsky: IEEE J. Lightwave Tech. **21**, 1969–1977 (2003)
95. K. Chen, P. Herman: J. Lightwave Tech. **21**, 1958–1968 (2003)
96. P. Lemaire, R. Atkins, V. Mizrahi, W. Reed: Electron. Lett. **29**, 1191 (1993)
97. J. Albert, B. Malo, K. Hill, F. Bilodeau, D. Johnson, S. Thériault: App. Phys. Lett. **67**, 3529 (1995)
98. P. Herman, K. Beckley, S. Ness: “157-nm photosensitivity in germanosilicate and fused-silica glasses”, in *Conf. on Lasers and Electro-Optics*, OSA (1998), tech. Dig. 6, pp 513
99. B. Malo, J. Albert, K.O. Hill, F. Bilodeau, D.C. Johnson, S. Thériault: Electron. Lett. **31**, 879–880 (1995)
100. J. Albert, F. Bilodeau, K.O. Hill, D. Johnson, S.J. Mihailov, Y. Hibino, M.A. (ed: Turan Erdogen, E.J. Friebel, R. Kashyap): *Birefringence control for ultraviolet-induced index change in planar lightwave circuits*, Vol. 33 of OSA Trends in Optics and Photonics: Bragg Gratings, Photosensitivity, and Poling in Glass Waveguides (Optical Society of America, Washington, DC, 2000)
101. J. Canning, M. Åslund, A. Ankiewicz, M. Dainese, H. Fernando, J. Sahu, L. Wosinski: Appl. Opt. **39**, 4296–4299 (2000)
102. J. Albert, F. Bilodeau, D.C. Johnson, K.O. Hill, S.J. Mihailov, D. Stryckman, T. Kitagawa, Y. Hibino: Electron. Lett. **34**, 485–486 (1998)
103. K. Davis, K. Miura, N.S. and K. Hirao: Opt. Lett. **21**, 1729–1731 (1996)
104. K. Miura, J. Qiu, H. Inouye, T. Mitsuyu, K. Hirao: Appl. Phys. Lett. **23**, 3329–3331 (1997)
105. D. Coric, P. Herman, K. Chen, M. Wei, P. Corkum, R. Bhardwaj, D. Rayner: Proc. SPIE **4638**, 77–84 (2002)
106. A. Streletsov, N. Borrelli: J. Opt. Soc. Am. B **19**, 2496–2504 (2002)
107. D. Coric, P. Herman, R. Bhardwaj, P. Corkum, D. Rayner: Opt. Fiber Comm. Conf., (OSA) (2002)
108. K. Minoshima, A. Kowalevicz, I. Hartl, E. Ippen, J. Fujimoto: Opt. Lett. **26**, 1516–1517 (2001)
109. A. Streletsov, N. Borrelli: Opt. Lett. **26**, 42–44 (2001)
110. E. Glezer, M. Milosavljevic, L. Huang, R. Finlay, T. Her, J. Callan, E. Mazur: Opt. Lett. **21**, 2023–2025 (1996)
111. D. Schaffer, A. Brodeur, J. Garcia, E. Mazur: Opt. Lett. **26**, 93–95 (2001)
112. M. Svalgaard, C. Poulsen, A. Bjarklev, O. Poulsen: Electron. Lett. **30**, 1401–1403 (1994)
113. C. Valdivia, X. Wei, D. Coric, P. Herman: “F₂ laser-induced visible- and infrared-confining buried waveguides in fused silica”, in *OSA Conf. on Lasers and Electro-Optics Tech. Digest (OSA, Wash DC)*, Baltimore, Md. (2003), paper CW14
114. P. Herman, A. Yick, J. Li, C. Valdivia, N. Munce, L. Lilge: “Advanced laser processing for integrated biophotonics on a chip”, in *OSA Conf. on Lasers and Electrophysics (CLEO)*, San Francisco, CA (2004), paper CFK

115. N.R. Munce: (2004), "MSc thesis, enabling technologies for parallel single cell electrophoresis in a microchip platform", U. of Toronto
116. N.R. Munce, J. Li, P. Herman, L. Lilge: Micromachining and Microfabrication: Microfluidics, BioMEMS, and Medical Microsystems, Proc. SPIE **4982**(28–36) (2003)
117. N. Munce, J. Li, P. Herman, L. Lilge: Analytical Chem. **76**, 4983–4989 (2004)

14 Nano-Structuring with Femtosecond Excimer Laser Pulses*

J.-H. Klein-Wiele, J. Bekesi, J. Ihlemann, P. Simon

14.1 Introduction

Nano-scale fabrication of materials is one of the biggest challenges for next-generation devices in science and technology. There is a general trend to reduce the size of opto-mechanical components, and there is a growing need for components with feature sizes below one micron. Also, the fabrication of 2- and 3-dimensional structures, specifically the creation of photonic crystals has attracted tremendous interest in recent years. Such a technical challenge calls for the development of fast, low-cost, and flexible fabrication technologies. Laser direct processing via ablation offers exactly these properties, thus representing a great potential for numerous new applications.

It has been shown in a number of studies that short-pulse lasers, generating pico- or femtosecond pulses, provide a much better precision of the ablation process. The reason for the observed improvement is mainly due to two effects. In case of solids with high heat conductivity, the lateral spreading of the absorbed energy outward from the irradiated zone within the laser pulse duration sets a limit for the achievable spatial resolution. A short pulse duration reduces the so-called heat-affected zone (HAZ) [1], thus resulting in sharp boundaries of the fabricated structures.

Besides a dramatic reduction of the HAZ, sub-picosecond pulses offer further potentials. Sub-picosecond lasers can be new tools for the micro-machining of transparent materials [2]. Ultrashort pulses possess high peak powers while carrying only moderate energies. At such high power levels, multi-photon absorption becomes dominant and ensures the concentration of the irradiated energy in a thin surface layer necessary for precise machining. In this way, high quality structuring of materials like fused silica, fluoride crystals, diamond, sapphire, or Teflon® have become possible.

Following the general worldwide trend of miniaturization, many groups tried to fabricate sub-micron features on a variety of materials. However, using the radiation of a Ti:Sapphire laser system, which is the most commonly

* The cover picture of this book resembles a structure as discussed in detail in [10] of this article

used short-pulse laser nowadays (with an emission wavelength centred around 800 nm), special methods have to be used to obtain structures in the sub-wavelength range.

The first publication on fabrication of sub-micron features on metals with a Ti:Sapphire laser was that of Pronko et al. [3], unfortunately with features of very poor quality. Later, similar results have also been achieved by Korte et al. [4]. The reason for the poor reproducibility and edge quality of these features is the requirement to keep the size below the wavelength (800 nm). In this case, for metals and semiconductors, the only possibility is to adjust the laser power in such a way that only the central part of the focal distribution exceeds the ablation threshold of the sample. This is a very critical adjustment, resulting in very limited ablation rates, and responding very sensibly to intensity fluctuations. It is also evident that any variation of the pulse intensity is converted into a change of the feature size.

This problem can be entirely solved by using ultraviolet radiation. Since the optical resolution scales with the wavelength, a system running at 248 nm (at the KrF excimer wavelength) provides more than three times better spatial resolution compared with a Ti:Sapphire laser. This means that feature sizes below 500 nm can easily be created without special control of the peak fluence of the pulse relative to the threshold fluence of the material. In this way, reproducible, clean and sharp structures can be fabricated on the sub-micron scale on virtually all materials, even on metals and semiconductor surfaces.

14.2 The Laser System

In the UV part of the electromagnetic spectrum, the only high-gain media to date are the excimers. Because of their molecular properties, excimers cannot generate short optical pulses, but can only amplify them. Consequently, UV excimer modules can be used as amplifiers in dual-wavelength systems, where the short pulses are first generated in the long-wavelength region, and then converted into the UV through frequency up-conversion. Such a dual-wavelength system has a front end that can, for example, be a Ti:Sapphire laser system. After frequency tripling, the pulses are sent through a specially designed KrF amplifier. Our current laser arrangement (Fig. 14.1) uses a commercial Ti:Sapphire front end system (Spectra Physics) delivering $500\text{ }\mu\text{J}$

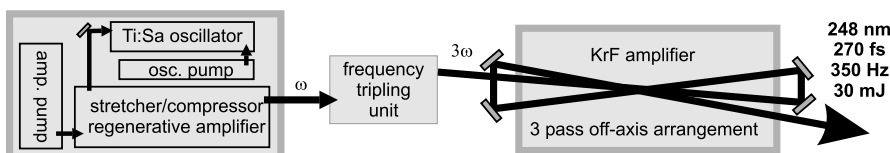


Fig. 14.1. Layout of the UV femtosecond laser system

pulses of 150 fs duration at a wavelength of 745 nm . After frequency conversion in a compact arrangement, seed pulses are obtained for the KrF amplifier module, which is the key component of the system. This module is a modified version of a Lambda Physik laser, e.g. of the type "NovaLine". In this case, the pulse is amplified in a three-pass amplification scheme to an energy of 30 mJ at repetition rates exceeding 350 Hz , resulting in an average power of $\sim 10\text{ W}$ at 248 nm [5].

14.3 Mask Projection

In industrial applications of laser micro-fabrication, beside the spatial resolution limit the processing speed is a further fundamental issue. There are two well known optical schemes for laser processing: focus scanning and mask imaging. Focus scanning offers the capability of creating arbitrary structures, thus providing a greater flexibility in fabricating a diversity of structures. However, the processing speed is strongly limited in case of large sample areas (sequential processing). In contrast, mask projection (Fig. 14.2) allows the treatment of an extended sample area at the same time (parallel processing). Fortunately, the available single-pulse energy of excimer amplifier modules is well suited for the parallel illumination of extended sample areas.

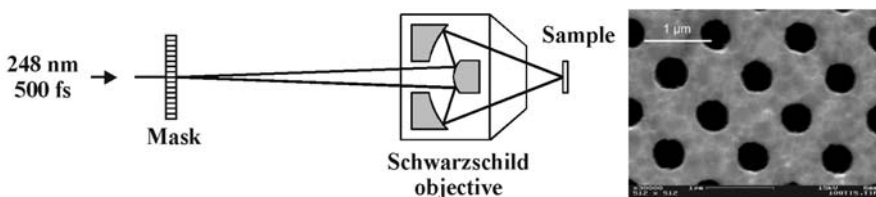


Fig. 14.2. Mask projection layout for parallel irradiation of extended sample areas. Fabrication of a matrix of sub-micron holes in a titanium foil, using mask projection.

14.4 Interference Techniques

Interference techniques are especially suited for the fabrication of periodic nano-structures. In such schemes the incoming laser beam is split into partial beams which are then recombined on the sample surface. In case of temporal and spatial overlap of the beams, the resulting interference pattern is converted into the desired surface texture. In this way gratings with periods of $\sim 400\text{ nm}$ have been fabricated on metals, semiconductors, and optical materials like LiNbO_3 or Ta_2O_5 [6, 7, 8].

More advanced methods based on the interference of multiple beams can be the key to the fabrication of complex 2- and 3-dimensional structures,

specifically for the creation of photonic crystals. According to this approach, the intensity distribution caused by the interference of multiple laser beams is transferred into a modulation of the optical properties of the sample. The period and shape of the pattern can be controlled by the intersecting angles, the polarization and the phase differences of the interfering beams [9]. In order to provide an easy way to change the phase relationship between partial beams of multiple beam interference schemes, we recently proposed a new arrangement [10].

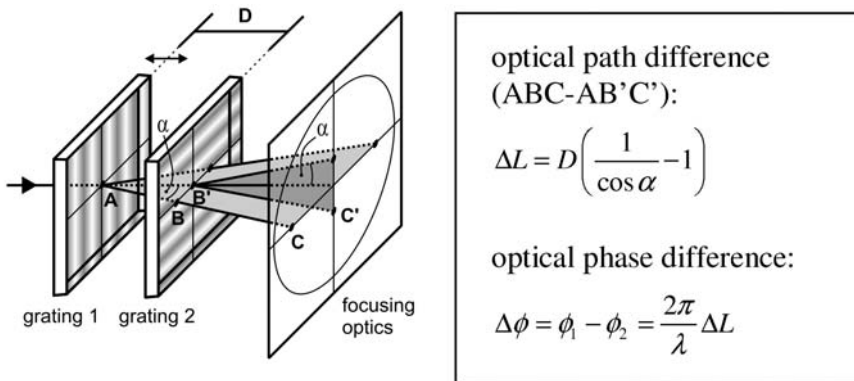


Fig. 14.3. Experimental setup for phase-controlled four-beam interference

This scheme, in its simplest version, uses two transmission gratings whose grooves are perpendicular to each other (see Fig. 14.3). Let us regard the beams that are diffracted into the $\pm 1^{st}$ orders by the first grating and propagate directly through the second grating (path ABC), as well as the 0^{th} order beam travelling straight through the first grating and splitting into $\pm 1^{st}$ order beams at the second grating (path AB'C'). All other diffracted beams can be blocked in front of the focusing optics. It can be shown that simple translation of the first grating changes the optical phases of the two beam pairs relative to each other (Fig. 14.3). A subsequent focusing optics is used to provide spatial and temporal overlap of the four beams on the target. Variation of the phase difference results in a variety of textures in the target plane, as indicated in Fig. 14.4.

Here the calculated interference patterns were folded with a threshold-like ablation function to predict the resulting ablated structures. These are in excellent agreement with the fabricated patterns measured via scanning electron microscopy (SEM). Thus we can conclude that complex nano-structures can be designed and precisely reproduced in practice by applying this technology.

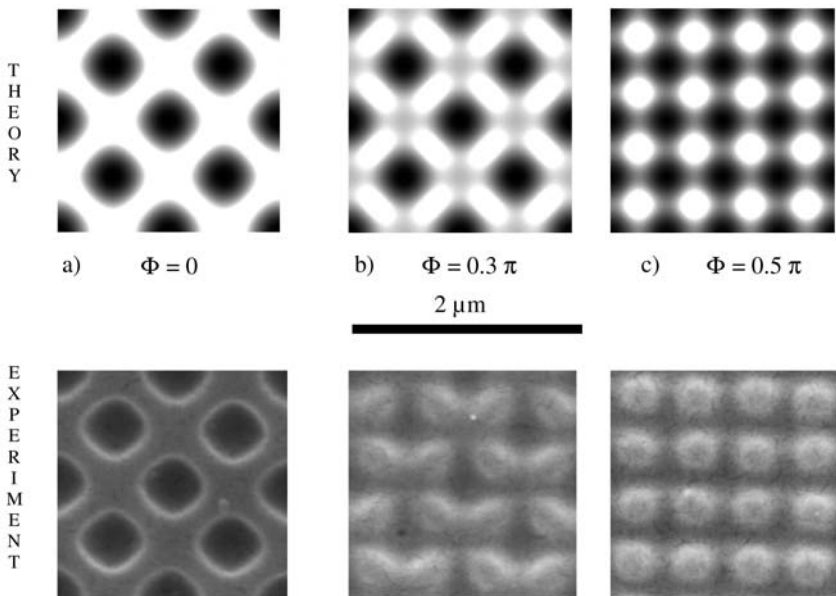


Fig. 14.4. Comparison between theory and experiment for the ablation of sub-micron two-dimensional surface patterns on polyimide, PI, through four-beam interference. The phase delay between two beam pairs is a) $\Phi = 0$, b) $\Phi = 0.3\pi$, c) $\Phi = 0.5\pi$.

References

1. E. Matthias, M. Reichling, J. Siegel, O.W. Käding, S. Petzoldt, H. Skurk, P. Bizenberger, E. Neske: *Appl. Phys. A* **58**, 129–136 (1994)
2. K. Kawamura, T. Ogawa, N. Sarukura, M. Hirano, H. Hosono: *Appl. Phys. B* **71**, 119–121 (2000)
3. P.P. Pronko, S.K. Dutta, J. Squier, J.V. Rudd, D. Du, G. Mourou: *Opt. Commun.* **114**, 106–110 (1995)
4. F. Korte, S. Adams, A. Egbert, C. Fallnich, A. Ostendorf, S. Nolte, M. Will, J.P. Ruske, B.N. Chichkov, A. Tünnermann: *Optics Express* **7**(2), 41–49 (2000)
5. J. Bekesi, S. Szatmari, P. Simon, G. Marowsky: *Applied Physics B-Lasers and Optics* **75**, 521–524 (2002)
6. P. Simon, J. Ihlemann: *Appl. Phys. A* **63**, 505–508 (1996)
7. K. Chen, J. Ihlemann, P. Simon, I. Baumann, W. Sohler: *Appl. Phys. A* **65**, 517–518 (1997)
8. F. Beinhorn, J. Ihlemann, P. Simon, G. Marowsky, B. Maisenhölder, J. Edlinger, D. Neuschäfer, D. Anselmetti: *Applied Surface Science* **138–139**, 107–110 (1999)
9. M. Campbell, D.N. Sharp, M.T. Harrison, R.G. Denning, A.J. Turberfield: *Nature* **404**, 53–56 (2000)
10. J.H. Klein-Wiele, P. Simon: *Applied Physics Letters* **83**, 4707–4709 (2003)

15 Physical Aspects of Ultra-Fast UV Laser Transfer

D. G. Papazoglou, I. Zergioti, C. Fotakis

Abstract. Precise patterns with high density and sub- μm spatial resolution are fabricated by Laser-induced Forward Transfer (LIFT). By using ultra-fast UV laser pulses, the thermal effects are minimal, the material transfer is highly directional and there is practically no damage to the transferred material. This is a non-contact, rapid and simple method applicable to a wide variety of target materials.

The physical aspects of the ultrafast UV laser transfer process are discussed while time-resolved stroboscopic Schlieren imaging is used to visualize and study the effect of ultra-short (0.5 ps) and short (15 ns) pulses on the laser transfer process. In contrast to the ns laser, the directionality of the ejected material is very high in case of the sub- ps laser process. The shock wave propagation is expected to be the main mechanism for material removal in the sub- ps laser transfer process.

The use of sub- ps UV laser pulses ensures that, through linear and non-linear absorption regimes, a very thin layer of the target material absorbs the laser pulse energy initiating a thermo-elastic shock-assisted process that expels the remaining target material, which retains its functionality for further use in micro-printing applications.

15.1 Introduction to the Laser Transfer Process

In the Laser-induced Forward Transfer Process (LIFT), a thin layer of material preliminary deposited on a transparent substrate is removed from the substrate surface by a single laser pulse irradiating the film (target) through the substrate (Fig. 15.1). A lift-off process takes place and the ejected material impacts with high velocity on the receiver substrate parallel and in close proximity to the target film [1, 2, 3, 4]. In the last decade, LIFT has been successfully applied by several groups for the selective micro-deposition of metals [5, 6, 7], oxides [8, 9], diamonds [10], and biomaterials [11].

A typical micro-printing workstation is presented in Fig. 15.1. The pulsed laser beam is delivered on the target substrate via a modified microscope system. The laser beam after expansion illuminates a variable-width rectangular aperture. An objective lens images the mask onto the target-substrate interface. The receiver substrate is parallel and in close proximity to the target

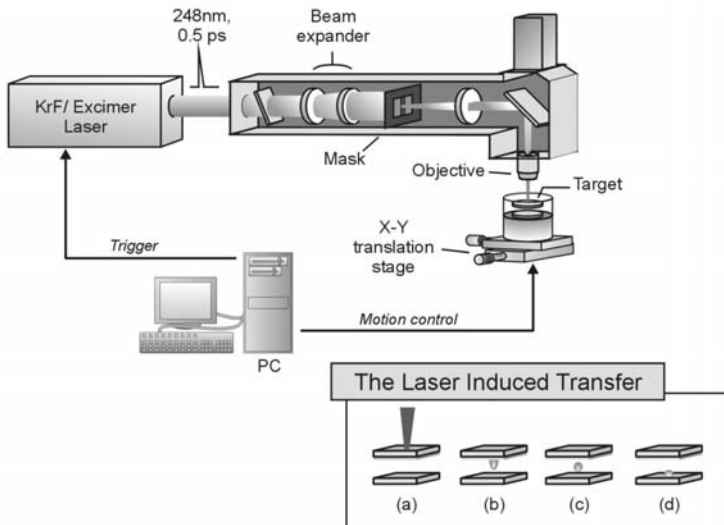


Fig. 15.1. Micro-printing/micro-machining workstation. Inset:(a) The pulsed laser beam is focused onto the interface between the target material and the substrate, (b) a violent lift-off process takes place, (c) the ejected material impacts on the receiver substrate, (d) the target material is deposited on the receiver substrate.

substrate. The whole process takes place in vacuum ($\sim 0.1 \text{ Torr}$). Complex structures are constructed in a pixel-by-pixel repetitive process.

During the LIFT process the pressure build-up due to the absorption of laser radiation in the target layer near the film-substrate interface unloads the target material through a thermo-elastic shock wave, causing its expansion in the direction of propagation of the incident laser beam. The laser energy is absorbed in the target skin layer and is then transported by heat conduction to the cold parts of the target. The material expansion starts when the absorbed laser energy, which initially is confined in the electron component, is transferred to the lattice (ions).

The optimization of the LIFT process depends on the laser parameters, i.e. pulse shape, duration, fluence, and the specific optical, thermo-physical and mechanical properties of the materials used. The dynamics of the laser transfer technique using time-resolved optical microscopy has been studied by Lee et al. [12, 13], who used a pulsed Nd:YAG laser ($1.064 \mu\text{m}$, 250 ns) for the transfer and observed the plume using a 25-ps probe pulse of a Nd:YAG-pumped dye laser which propagated nearly perpendicularly to the 250-ns pump laser pulse. They measured velocities of the metallic lift-off film up to 0.75 Mach under atmospheric conditions. More recently, Young et al. [14] investigated the dynamics of a similar technique, "Matrix Assisted Pulsed Laser Evaporation Direct Write", using a frequency-tripled Nd:YAG transfer laser

(355 nm , 150 ns) with ultra fast microscopy, and measured the plume velocity $\sim 0.2\text{ km/sec}$. Bullock et al. [15] studied the laser-induced back ablation of aluminum thin films with picosecond laser pulses (Ti:sapphire, 1053 nm , $2\text{-}3.6\text{ ps}$) under vacuum conditions, using a shadowgraphic and interferometric system. Nakata et al. [16] investigated the LIFT process (dye laser 440 nm , 9 ns) of metal films by applying the two-dimensional laser-induced fluorescence method with a fast imaging technique and a long-working-distance microscope. They measured the dynamic behaviour of gold atoms and emissive particles in vacuum and in air and found velocities of atoms up to 2 km/sec .

15.2 Visualization of the Laser Materials Transfer

15.2.1 Time Resolved Schlieren Imaging Method

A very effective method for visualizing the dynamics of the laser transfer process for time delays in the ns range is the use of stroboscopic Schlieren imaging. The experimental configuration is depicted in Fig. 15.2. The target is a thin film deposited on 1-mm thick fused silica substrate. A variety of materials such as metals (Cr), oxides (InO_x) and biological molecules (DNA) are examined. The pump laser, a hybrid distributed-feedback dye laser/KrF laser delivering 0.5 ps pulses of $10\text{ mJ}/\text{pulse}$ at 248 nm wavelength, irradiates the target and selectively ablates a $\sim 250 \times 250\text{ }\mu\text{m}^2$ rectangular spot of film. The laser fluence on the target surface varies from 100 to 400 mJ/cm^2 .

A second XeCl excimer laser, delivering 30-ns pulses at 308 nm , is used as the probe for obtaining the Schlieren stroboscopic images of the ejected material and the associated shock wave under atmospheric pressure, at delay times ranging from 50 ns up to $10\text{ }\mu\text{s}$. The pulse energy of the probe laser is kept well below $4\text{ }\mu\text{J}$. The collimated probe beam, after propagating through the ejected material and the shock wave in air, is focused by a short-focal-length lens. The unperturbed part of the probe beam was partially filtered out by a knife edge positioned on the back focal plane of the lens. By transforming the refractive index changes to intensity variations, this method is capable of monitoring the density or pressure perturbations of the medium surrounding the sample. Atoms or low-density particles are not directly detected by this method. A second lens is used to image the plume onto the CCD detector and a frame grabber is used to capture the image from the CCD camera. A pulsed delay generator triggers in turn the pump and the probe laser.

15.2.2 Dynamics of the sub-*ps*- and *ns*-Process – A Comparative Study

We consider two limiting cases of short, sub-*ps*, and long, *ns*-range laser pulses. The short sub-*ps* pulse duration, t_p , is less than all relaxation times, namely, the electron-to-ion (lattice) energy exchange time t_{ei} and the electron

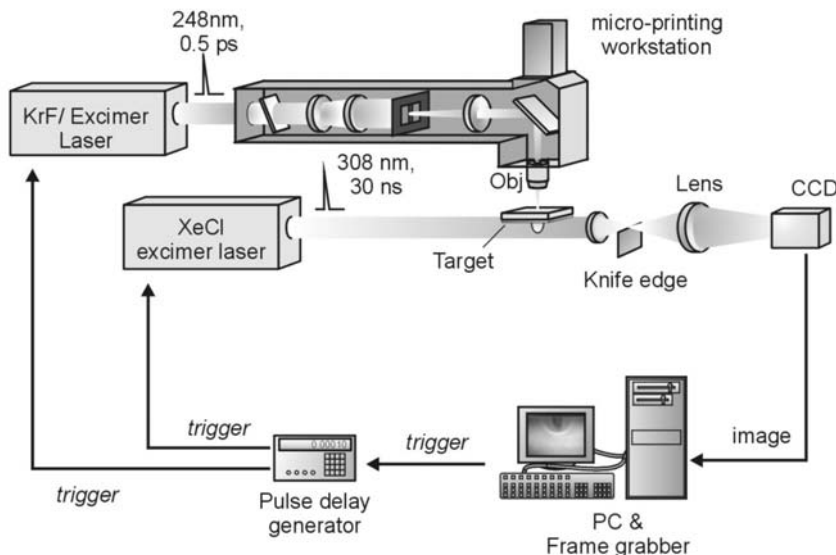


Fig. 15.2. Stroboscopic Schlieren imaging setup

heat conduction time, t_{heat} : $t_p < \{t_{ei}, t_{heat}\}$. On the other hand, the long pulse duration is much longer than all relaxation times, $t_p \gg \{t_{ei}, t_{heat}\}$. Due to these diverse conditions, the unloading of the target material proceeds in different ways.

Figure 15.3 displays a comparative study of the dynamics of the sub-*ps*- and *ns*-process through a series of stroboscopic Schlieren images of the plume ejection at various delay times. The target material is Cr and the film thickness is 40 nm. The laser fluence is $\sim 330 \text{ mJ/cm}^2$. In Fig. 15.3a the shock wave formation and transition from a plane shape to a spherical one, in the case of sub-*ps* process, are clearly seen. The dark area behind the shock wave front is the ablated material. The ablated material is ejected in a cylinder-like shape with minimum divergence ($\sim 3^\circ$). It is clear that the material effectively stops after $\sim 1 \mu\text{s}$ at a distance of $\sim 400 \mu\text{m}$ while the shock wave transforms to an acoustic wave and continues its propagation. On the other hand, in the case of the *ns*-process (15 ns irradiating pulse), visualized in Fig. 15.3b, the formation of a shock wave of spherical shape is clearly seen. The dark area behind the shock or sound wave is the ablated material. The ablated material is not ejected in a cylinder-like shape but rather in a highly divergent hemispherical one ($\sim 30^\circ$). The material effectively stops after $\sim 1 \mu\text{s}$ at a distance of $\sim 400 \mu\text{m}$ while the shock wave transforms to an acoustic wave and continues its propagation. Young et al. [14] have observed conically

shaped ejected plumes using a 150 ns Nd:YAG transfer laser. Furthermore, the ejected material velocity as measured by the stroboscopic Schlieren images in Fig. 15.3 indicates that sub- μs laser pulses produce plumes whose velocity ($400 \pm 10\text{ m/sec}$ at 150 ns after irradiation) is faster than that reported [14, 16] to be produced by nanosecond laser pulses.

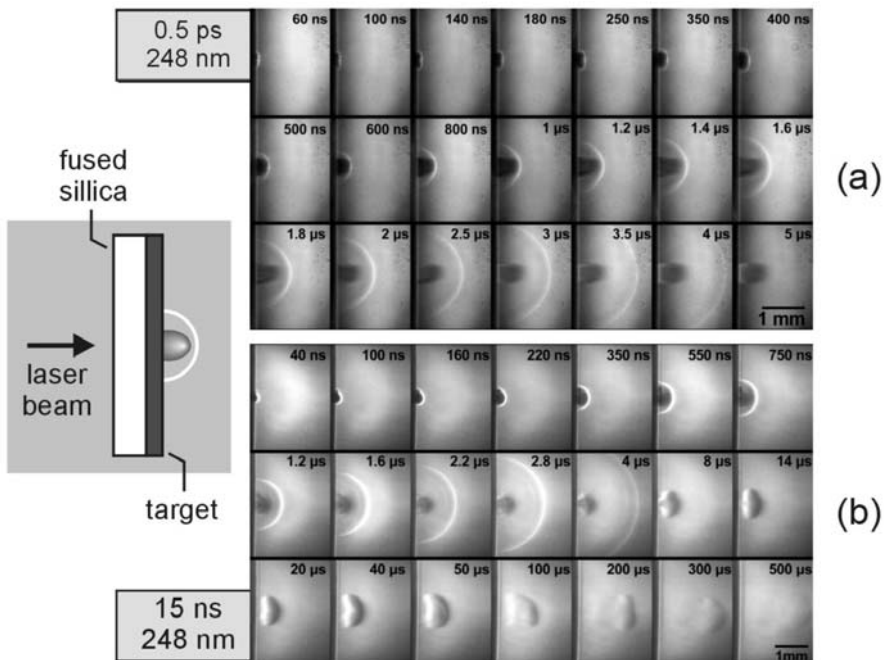


Fig. 15.3. Stroboscopic Schlieren images for Cr 40-nm target, (a) 0.5 ps , 248 nm , fluence $330\text{ mJ}/\text{cm}^2$ LIFT, (b) 15 ns , 248 nm fluence $330\text{ mJ}/\text{cm}^2$ LIFT

The effect of the material confinement is studied in the case of sub- μs laser transfer of InO_x . The InO_x target film thickness is 200 nm . The film is irradiated by 248 nm , $0.5\text{-}\mu\text{s}$ laser pulses. Figure 15.4 depicts a comparison between the forward and backward irradiation process. By keeping all the experimental conditions the same and simply reversing the target substrate, the process proceeds in qualitatively distinct ways. In the case of forward irradiation (Fig. 15.4a) the shock wave formation and transition from a plane shape to a spherical one are clearly seen. The ablated material is ejected in a cylinder shape with minimum divergence, a behavior similar to that of laser transfer of Cr and of biomaterials [11]. On the other hand, in the case of backward irradiation (Fig. 15.4b), the images clearly show the blast wave and the ejected material propagation that follow a shape closer to a hemispherical rather than a plane wave. Forward [14] and backward [17, 18]

laser removal of thin films bonded to substrate has been studied in detail. In case of the backward configuration, Hare et al. [18] have reported that picosecond time scale ablation involves solid-state shock waves, which are not produced by longer ablation pulses. Because the film is heated faster than the characteristic hydrodynamic volume relaxation time t_h , a several *kbar* pressure jump is induced which is released by propagation of a shock rarefaction wave toward the surface. As a result, and upon reflection from the substrate interface, a tensile force is exerted on the thin film, causing it to break away from the substrate. Schoen et al. [19] also studied the shocks resulting from picosecond irradiation of confined foils. In our case, the shocked InO_x emerges as small particles rather than an intact plate as often observed [12, 13] for shock-induced ejection. Particle formation may be partly due to vaporization and/or due to stress wave amplitude being large enough to result in the fragmentation of the material. Another explanation may be the instability and non-uniformity of the laser beam, which deforms and cracks the thin films into small pieces.

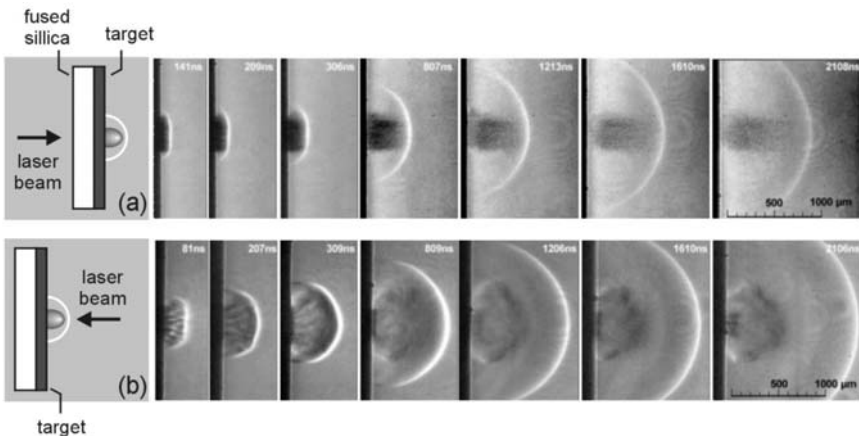


Fig. 15.4. Stroboscopic Schlieren images for InO_x 200 nm target, 0.5 ps, 248 nm laser pulse 420 mJ/cm^2 , (a) forward irradiation, (b) backward irradiation

A theoretical interpretation of the laser material transfer should be able to provide an answer to the basic qualitative result of the visualization studies. The laser transfer process follows the same dynamics in the case of sub-*ps* UV irradiating pulses irrespective of the target material [11, 20, 21]. In the case of the sub-*ps* lift, the pulse duration, t_p , is less than all relaxation times, namely, the electron-to-ion (lattice) energy exchange time t_{ei} and the electron heat conduction time, t_{heat} : $t_p < \{t_{ei}, t_{heat}\}$.

As the material is ejected from the target substrate, it generates a shock wave in air. Figure 15.5 depicts the displacement of the shock wave front

in air versus the time delay (+) after the laser irradiation (0.5 ps , 248 nm , 330 mJ/cm^2) for a Cr thin film (40 nm) LIFT as visualized and measured by stroboscopic Schlieren images. The solid and dotted curves represent fitting of the experimental data by t^x propagation laws. The shock front in air initially propagates as a plane shock wave in proportion to $t^{2/3}$ and at about 300 ns is gradually transformed into a sound wave ($\sim t$). This transformation is an indication that the ejected material has practically stopped.

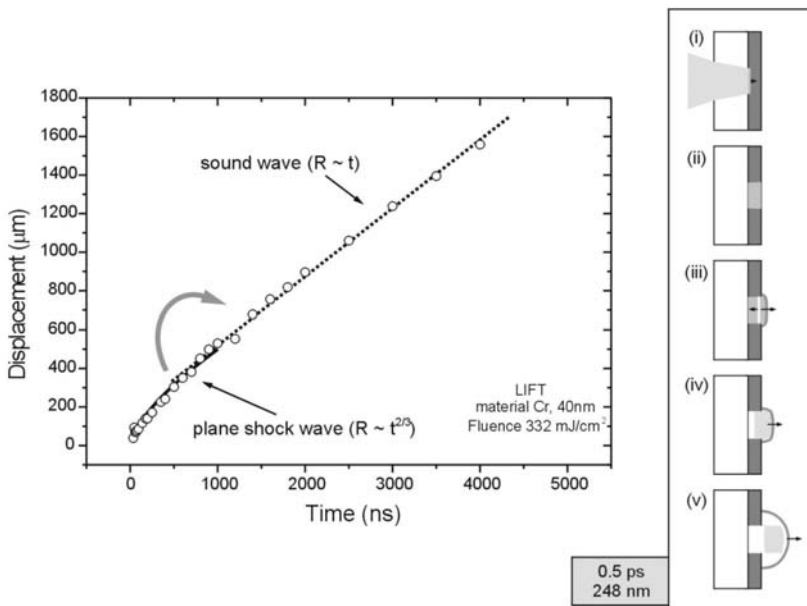


Fig. 15.5. Displacement of the shock wave front in air (o) versus the time delay after the laser irradiation (0.5 ps , 248 nm , 330 mJ/cm^2) for Cr thin film (40 nm) LIFT. The solid and dotted curves represent fitting of the experimental data by t^x propagation laws - (solid line) plane shock wave $R \propto t^{2/3}$, (dotted line) sound wave $R \propto t$. Inset: represents schematically the various steps of the sub-ps LIFT process: (i) the laser pulse is absorbed in the skin depth ($\sim 20\text{ nm}$), (ii–iii) a strong shock wave and a rarefaction wave propagate in opposite directions ($\sim 40\text{ ps}$), (iv–v) the whole material is removed and propagates in air. The associated shock wave in air propagates as a plane shock wave ($R \propto t^{2/3}$) and at about 300 ns is gradually transformed into a sound wave ($R \propto t$).

The inset in Fig. 15.5 schematically depicts the main steps of the sub-ps LIFT process. The laser energy is absorbed in the skin depth, which for Cr is in the order of 20 nm , by considering only linear absorption. Since for a sub-ps, 248-nm UV pulse there is also a considerable increase of the absorption coefficient through non-linear absorption effects (multiphoton ionization,

avalanche ionization etc.), the skin depth is greatly reduced compared to the linear absorption regime, especially in the case of materials such as InO_x and biomaterials. Thus one can safely assume that in the case of sub-*ps* UV laser pulses, the laser energy is absorbed in a very thin layer (in the order of a few tens of nanometers) of the target material for a wide variety of materials. In this thin layer high pressure is induced and a thermo-elastic shock wave propagates towards the target material-air interface. After reaching the interface, a shock wave propagates in air while a rarefaction wave propagates in the opposite direction. The target material is completely removed when the rarefaction wave reaches the target-quartz substrate interface (20–40 *ps*). During the initial states of material ejection, the shock wave in air propagates as a strong plane shock wave due to the fact that the focal spot size is considerably larger than the target film thickness ($d_{focal} \approx 250 \mu\text{m} \gg d_{thick} \approx 40 \text{ nm}$) and the high pressures involved. The ejected material practically stops after the irradiating pulse and the associated shock wave in air is transformed to a sound wave.

On the other hand, in the case of *ns* laser transfer, the pulse duration, t_p , is much longer than all relaxation times. Figure 15.6 depicts the displacement of the shock wave front in air (o) versus the time delay after the laser irradiation (15 *ns*, 248 nm, 330 mJ/cm²) for Cr thin film (40 nm) LIFT. The solid and dotted curves represent fitting of the experimental data by t^x propagation laws, as measured by stroboscopic Schlieren images. In this case the shock front in air initially propagates as a spherical shock wave in proportion to $t^{2/5}$ and is gradually transformed into a sound wave at about 200 *ns*.

The inset in Fig. 15.6 schematically depicts the main steps of the *ns* LIFT process. Although the laser energy is absorbed within the skin depth ($\sim 20 \text{ nm}$ for Cr), which for long 15-*ns* laser pulses is mainly attributed to linear absorption, for this long pulse duration the thermal diffusion ($L_{th} \sim 660 \text{ nm}$) length is comparable to the target material thickness and considerably larger than the skin depth. Therefore, the laser energy is diffused over the whole material thickness gradually increasing the temperature of the thin target film ($< 15 \text{ ns}$). Melting and evaporation may occur, resulting in gas phase effects, which account for the almost hemispherical shape of the ejected material. The associated shock wave in air propagates as a spherical shock wave ($R \propto t^{2/5}$) and at about 200 *ns* is gradually transformed into a sound wave ($R \propto t$).

15.2.3 Conclusions

The shock wave propagation is expected to be the main mechanism for the material removal in the sub-*ps* laser transfer process. The use of sub-*ps* UV laser pulses ensures that through linear and non-linear absorption regimes, a very thin layer of the target material absorbs the laser pulse energy and is removed by a thermo-elastic shock-assisted process. These results show that the laser transfer of confined foils can be successfully applied to a wide

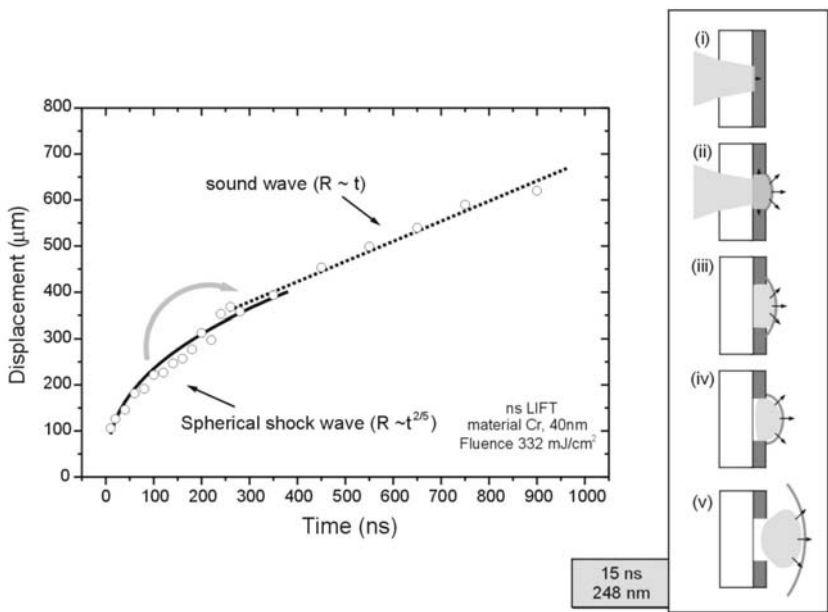


Fig. 15.6. Displacement of the shock wave front in air (o) versus the time delay after the laser irradiation (15 ns, 248 nm, 330 mJ/cm²) for Cr thin film (40 nm) LIFT. The solid and dotted curves represent fitting of the experimental data by t^x propagation laws – (solid line) spherical shock wave $R \propto t^{2/5}$, (dotted line) sound wave $R \propto t$. Inset: represents schematically the various phases of material removal during the ns LIFT process. (i–ii) The laser pulse is firstly absorbed in the skin depth ($\sim 20 \text{ nm}$) while the whole material volume is continuously heated by heat diffusion ($< 15 \text{ ns}$), (iii)–(iv) the whole material is removed and propagates in air. The associated shock wave in air propagates as a spherical shock wave ($R \propto t^{2/5}$) and at about 200 ns it is gradually transformed into a sound wave ($R \propto t$).

range of materials for the fabrication of complex patterns with high spatial resolution in a one-step process.

Acknowledgments

The described work has been carried out through projects within the “Ultra-violet Laser Facility” (ULF), which operates at FORTH, with support from the EU Directorate Research Programme “Access to Large Installation” at the Foundation for Research and Technology-Hellas. Useful discussions with E. Rode and A. Gamaly are gratefully acknowledged.

References

1. J. Bohandy, B.F. Kim, F.J. Adrian, A.N. Jette: *J. Appl. Phys.* **63**, 1158–1162 (1988)
2. Z. Toth, T. Szörenyi, A.L. Toth: *Appl. Surf. Science* **69**, 317 (1993)
3. I. Zergioti, S. Mailis, N.A. Vainos, P. Papakostantinou, C. Kalpouzos, C.P. Grigoropoulos, C. Fotakis: *Applied Phys. A* **66**, 579 (1998)
4. M. Pimenov, G.A. Shafeev, A.A. Smolin, V.I. Konov, B.K. Bodolaga: *Appl. Surf. Sci.* **86**, 208–212 (1995)
5. Z. Toth, T. Szörenyi, A.L. Toth: *Appl. Surf. Sci.* **69**, 317 (1993)
6. I. Zergioti, S. Mailis, N.A. Vainos, P. Papakonstantinou, C. Kalpouzos, C.P. Grigoropoulos, C. Fotakis: *Appl. Phys. A: Mater. Sci. Process* **66**, 579 (1998)
7. H. Esrom, J.Y. Zhang, U. Kogelschatz, A. Pedraza: *Appl. Surf. Sci.* **86**, 202 (1995)
8. E. Fogarassy, C. Fuchs, F. Kerherve, S. Hauchecorne, J. Perriere: *J. Appl. Phys.* **66**(1), 457 (1989)
9. G. Koundourakis, C. Rockstuhl, D. Papazoglou, A. Klini, I. Zergioti, N.A. Vainos, C. Fotakis: *Appl. Phys. Lett.* **78**(7), 868 (2001)
10. S.M. Pimenov, G. Shafeev, A. Smolin, V. Konov, B. Vodolaga: *Appl. Surf. Sci.* **86**, 208 (1995)
11. A. Karaiskou, I. Zergioti, C. Fotakis, M. Kapsetaki, D. Kafetzopoulos: *Appl. Surf. Sci.* **208–209**, 245 (2003)
12. I.Y.S. Lee, W.A. Tolbert, D.D. Dlott, M.M. Doxtader, D.M. Foley, D.R. Arnold, E.W. Ellis: *J. Imaging Sci. and Technology* **36**(2), 180 (1992)
13. W.A. Tolbert, I.S. Lee, M. Doxtader, E.W. Ellis, D. Dlott: *J. of Imaging Sc. And Techn.* **37**(4), 411 (1993)
14. D. Young, R. Auyeung, A. Pique, D. Chrisey, D. Dlott: *Appl. Phys. Lett.* **78**(21), 3169 (2001)
15. A.B. Bullock, P. Bolton: *J. Appl. Phys.* **85**(1), 460 (1999)
16. Y. Nakata, T. Okada: *Appl. Phys. A* **69**, 275 (1999)
17. S.G. Koulikov, D.D. Dlott: *Journal of Photochem. and Photobiol. A: Chem.* **145**, 183 (2001)
18. D.E. Hare, J. Franken, D.D. Dlott: *J. Appl. Phys.* **77**, 5950 (1995)
19. P.E. Schoen, A.J. Campillo: *Appl. Phys. Lett.* **45**, 1049 (1984)
20. D. Papazoglou, A. Karaiskou, I. Zergioti, C. Fotakis: *Appl. Phys. Lett.* **81**, 1594 (2002)
21. I. Zergioti, D.G. Papazoglou, A. Karaiskou, C. Fotakis, E. Gamaly, A. Rode: *Appl. Surf. Sci.* **208–209**, 177 (2003)

16 Material Modification

16.1 Microlithography

M. Wehner

16.1.1 The Patterning Process

Optical projection lithography is a key technology for producing microelectronic circuits or chips. The fabrication of transistors and logic gates consists of many processing steps to obtain the required sequence of functional layers. The fundamental processing steps comprise thermal oxidation, masking, etching, and doping. For each type of chip a predefined sequence is repeated several times until the last “front end” layer is completed. Individual devices and circuits are then interconnected by structured metal layers, which are separated by dielectric layers for insulation. After patterning of all metal layers, a final dielectric layer is deposited for passivation. The top layer protects the circuit from contamination such as particles and products from the ambient atmosphere. Later, openings are etched into that layer to allow access to the interconnects by electrical probes and wire bonds.

Chips are manufactured using planar process technology which means that the whole area of the chip is processed simultaneously. The masks applied in every single processing step define the pattern and protect the shielded areas from processing. Therefore, at each processing step a lithographic process is needed. The principal steps to form a structured layer are depicted in Fig. 16.1. Typically about 9–30 layers are used to fabricate a chip, and consequently, the alignment of the subsequent layers and the dimensional stability of the layout have to be very precise. The increasing number of elements and the trend of ever shrinking feature sizes in chip technology pose new challenges to optical lithography. Integrated circuits (ICs) like dynamic random access memory (DRAM) chips and microprocessors for PCs are manufactured based on latest process technologies. In 1965 Gordon Moore made the observation that the number of transistors on a chip doubles every couple of years and predicted that this exponential growth will continue [1]. This has been acknowledged as “Moore’s law”, and until now, the forecast has become true with a reduced steepness of the curve arising in the 1970’s.

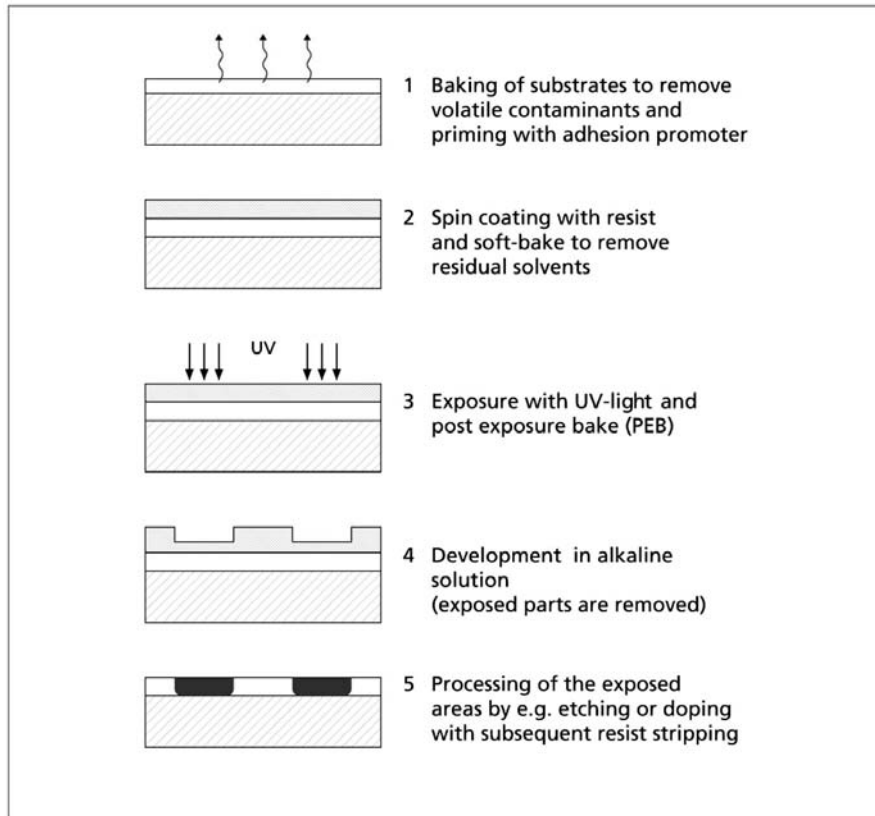


Fig. 16.1. Overview of a typical lithographic patterning process

16.1.2 Optical Resolution

The resolution of the patterning process is principally restricted by the wavelength of the light and the numerical aperture of the optics. The smallest feature or line width, LW , is determined by the wavelength, and the numerical aperture, NA , of the imaging optics:

$$LW = k_1 \lambda / NA \quad (16.1)$$

Another critical parameter is the depth of focus DoF , which describes the maximum allowable variation of the photoresist surface relief:

$$DoF = k_2 \lambda / NA^2 \quad (16.2)$$

The parameters k_1 and k_2 depend on the processing conditions, typical values are $k_1 \sim 0.5$ and $k_2 \sim 2.5$ [2]. With the g-line (436 nm) or the i-line (365 nm) of mercury lamps resolutions of $0.5\text{ }\mu\text{m}$ and $0.4\text{ }\mu\text{m}$, respectively,

were attained. Manufacturing of 64 MB DRAMs or 256 MB DRAMs, for instance, requires higher resolution which could only be obtained by using a shorter wavelength. The region below $0.35 \mu m$ wavelength of the electromagnetic spectrum is called deep ultraviolet (DUV). Feature sizes of $0.25 \mu m$ and $0.18 \mu m$ are achieved today by KrF exposure tools. Since 1998, 0.63 NA 248 nm 4:1 step-and-scan-systems have been in production at $180 nm$ achieving DoF $1.5 \mu m$. In 1999, first-generation 193 nm production systems were installed on production lines [3]. A prototype very-high-numerical-aperture (VHNA) system reveals a resolution of better than $130 nm$ (half pitch*) and DoF $0.4 \mu m$ [4] at 193 nm . Laboratory results of $110 nm$ lines with a pitch of $270 nm$ are shown in Fig. 16.2. When, for instance, the NA of the imaging optics is increased to improve resolution, the DoF gets smaller with the second power. This can pose problems when the surface relief of the resist resulting from underlying structures exceeds the DoF . Since the image contrast depends on DoF compared to resist thickness and surface topology of the chip, an additional planarization process may be required. If the DoF is sufficiently large ($>0.5 \mu m$), costly planarization processes become obsolete. Therefore, the demand for smaller feature size has led to an ever shrinking wavelength of the exposure tool.

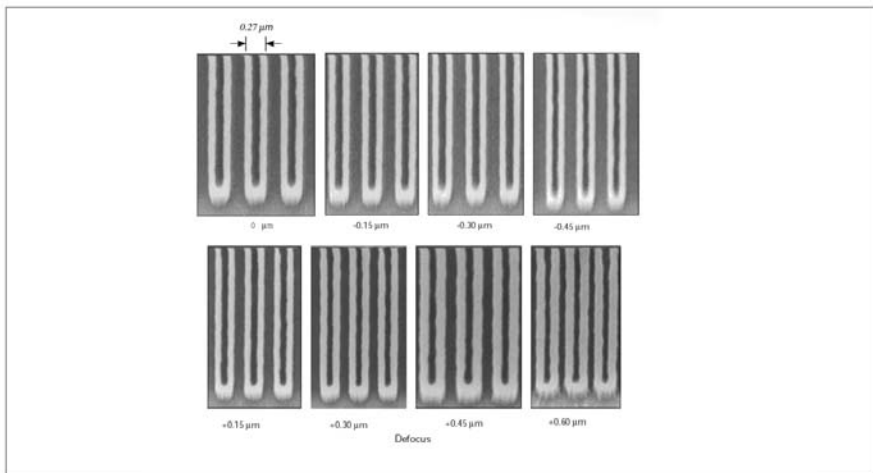


Fig. 16.2. SEM micrograph of $110 nm$ lines on $270 nm$ pitch, the feature size varies slightly with defocus (ArF laser and phase shift mask, NA 0.5, DoF $1 \mu m$) [2]

* Pitch: separation of two lines

16.1.3 Optical Materials

Using shorter wavelength also has an impact on related process technologies. Because the absorption properties and photo-chemistry of resists are highly sensitive to the applied wavelength, development of new resists is required to meet the demands in respect to optical penetration depth, photosensitivity, intrinsic resolution and various processing issues [2]. Further, mask (reticle) making has to be adapted. Sophisticated optical techniques like optical proximity correction (OPC) require a feature size at the reticle of about 250 nm , and phase shift masks (PSM) may demand new solutions and materials for mask making below 248 nm wavelength. PSMs offer enhanced edge definition due to destructive interference occurring at the edges of an imaged structure. The steeper rise of the intensity distribution then results in a better resolution of resist features. On the other hand, binary masks consisting of opaque and open features enable greater depth of focus (*DoF*) and process latitude. Manufacturers of exposure tools claim that binary mask techniques for 193 nm will result in a production-worthy process window with less than 300 nm pitch [5].

The trend towards shorter wavelengths has a strong impact on optical materials because refractive optical elements are used in the illumination system of the mask, for the mask itself and in the imaging lens. When going deeper into the UV, usable materials are becoming rare. The choice of optical materials is restricted to fused silica and crystalline CaF_2 , since other UV-transparent materials like MgF_2 and LiF are not acceptable because of their inherent birefringence or high susceptibility to humidity. The absorbed radiation heats up the optical elements at the center and heat dissipates by heat conduction in the lens to the optic mounts. Then the resulting temperature distribution is governed by the absorption coefficient and the heat conductivity of the material. These temperature gradients can induce changes in the refractive index or stress birefringence in the material which lead to distortion of image quality. Depending on the purity of the material, slowly growing transmission losses can be induced through the formation of “color centers” (development of absorption centers in the bulk) or compaction which result in a change of the optical path length by changing the refractive index. The latter are dose effects which grow continuously when under irradiation. To keep the optical elements within their specifications, these cumulative effects have to be restricted.

Table 16.1. Comparison of fused silica and CaF₂ for lithographic applications [6, 7]

Parameter	Fused Silica	CaF ₂
Absorption coefficient [cm ⁻¹]	< 0.004	< 0.002
dn/dT [ppm/K]	22	8
Thermal conductivity [W/K cm]	1.4	9.7
Expansion coefficient [ppm/K]	0.52	19
OPD/dT [ppm/K]	14	12
Bulk scatter coefficient [cm ⁻¹]	0.0008	< 0.0001
Color center formation	observed	observed
Compaction	increasing with dose	not observed
Stress birefringence	low	low
Homogeneity	good	good
Availability	good	not sufficient
Precision machining	practice	special procedures required

The pros and cons of silica and CaF₂ are summarized in Table 16.1. CaF₂ shows comparatively good properties regarding the absorption coefficient, scattering losses, the refractive index change with temperature (dn/dT) and high thermal conductivity. Despite that the expansion coefficient seems to be improperly high, the resulting optical path difference (OPD) is smaller than in the case of fused silica for a given temperature variation. Due to the low absorption coefficient and the high heat conductivity, the power loading capability of CaF₂ will be higher than for fused silica. Further efforts are needed to provide independent supply with high-purity crystalline material of about 200 mm size, and existing shaping and polishing techniques have to be refined to meet the ultimate issues of optical lithography.

Depending on the various functions of optical elements, the requirements may differ. In the illumination system the energy density (fluence) of the radiation is relatively high near the laser output. Here optical elements of high fluence capability are indispensable, requirements on homogeneity or surface quality may be of less importance. In contrast, the imaging optics has to assure highest optical quality, but at a comparatively lower fluence level. For application at 248 nm fused silica is used throughout, whereas at 193 nm both silica and CaF₂ are in competition. But for 157 nm, it is no doubt that only CaF₂ will be applicable. Supply of high purity material in the required quality, volume and size is one prerequisite to implement 157 nm lithography.

16.1.4 Technology Roadmap

International organizations and associations contribute in the yearly update of the International Technology Roadmap for Semiconductors (ITRS) [8]. This roadmap is published by SEMATECH (*SEmiconductor MAnufacturing TECHnology*), which is an initiative of 13 semiconductor manufacturing companies from seven countries and has a decisive influence on the development of semiconductor manufacturing technology. From the 2001 update (Fig. 16.3), it is evident that approximately every 3 years the next “node” will be approached. The term “node” here describes the feature size which is required to produce Dynamic Random Access Memory (DRAM) chips, where the resolution is measured as half pitch.

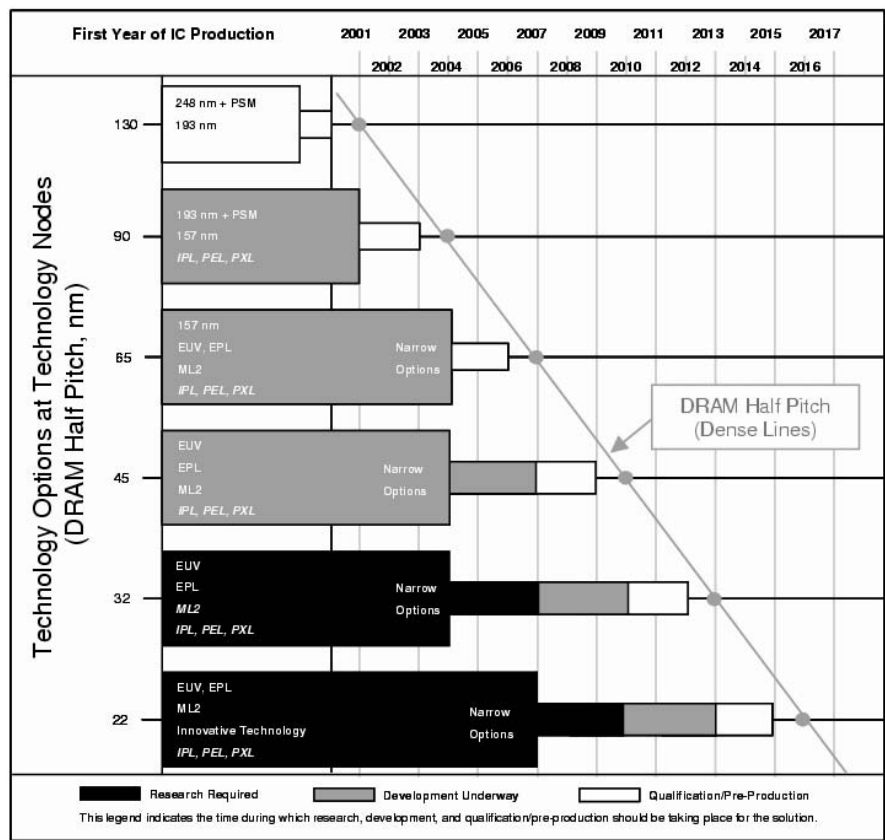


Fig. 16.3. ITRS roadmap 2001 [8] for lithography exposure tool potential solutions
 PSM: Phase shift mask, EPL: Electron projection lithography, XRL: 1x proximity X-ray lithography, IPL: Ion projection lithography, EUV: Extreme ultraviolet, EBDW: Electron beam direct write

The potential of optical technology is now highly speculative, because unexpected advances have been achieved before enabling the 130 nm node. Experts from the semiconductor industry anticipate that excimer laser lithography will be the mainstream approach until the year 2010 [8]. Now 248 nm lithography has been extended by phase shift mask techniques to the 130 nm node and 193 nm lithography will be a concurring process to 157 nm to reach the 90 nm node. So far, features of 65 nm were expected as the ultimate goal by optical methods using 157 nm radiation. But, as an indication of the unexploited potential of 193 nm technology, printing of 50 nm resist lines by a test tool has been demonstrated [9]. 157 nm lithography is considered to fill the “lithography gap” as a migration from 193 nm technology if issues on mask making, resist technology and ultrahigh purity optical materials (CaF_2) are successfully addressed. And probably, optical lithography could be extended to reach a half pitch of about 30 nm , delaying the need to switch to new methods.

Next generation lithography (NGL) methods such as extreme ultraviolet (EUV) [10], or scattering with angular limitation projection electron-beam lithography (SCALPEL) [11] are being discussed for the 65 nm node and beyond. Solutions for the 65 nm node envisaged in year 2007 – or possibly earlier – are not clear. NGL methods will require strong research efforts and are far from becoming available.

Improved integrated platforms (that means lithographic tools consisting of parts handling, resist coating, alignment and exposure) for handling and supporting 90 nm and 65 nm geometries have to be developed. As the feature size shrinks, the accuracy of all alignment steps, such as overlay, focus control and stage accuracy have to be improved, too. Further, as a consequence from the wavelength shift, the whole optical path must be purged with pure nitrogen, because oxygen and water vapor strongly absorb the 157 nm radiation. Typically, a contamination level of 1 ppm has to be assured. A key component of the 157 nm exposure tool will be the imaging optics. Due to the relatively wide 2 pm bandwidth of fluorine lasers, a catadioptric lens design is required to meet the demands. A feasibility study to design such a lens and to provide CaF_2 material of sufficient optical quality was successfully conducted by SVG Lithography Inc., Wilton, Connecticut, and Schott Glaswerke, Germany [7].

Mask-making is one of the big concerns for 157 nm lithography. High transmittance is achieved by using CaF_2 or MgF_2 , but the inherent birefringence of MgF_2 precludes its use for precision optical elements. The thermal expansion coefficient of CaF_2 is relatively large compared to silica (19 ppm/K vs. 0.52 ppm/K see Table 16.1). During mask writing, energy from the electron beam is absorbed causing the substrate to expand and thereby distort accuracy. More research is required to possibly avoid these writing errors or to elaborate compensation schemes, because the reticle is a critical element where a dimensional stability of better than 10 nm is essential. Alternatively, work is being done to modify silica where structural OH groups absorb the

UV light. Therefore modified fused silica has been developed with low OH content and doped with fluorine to allow for operation at 157 nm . Minimizing the content of OH groups or doping with fluorine leads to substantially reduced absorption of UV light. Reticles with transmission of 70% – 80% have been fabricated [12] where the reduced thermal expansion during mask writing and exposure minimizes distortion effects. A particular problem arises by the fact that for 157 nm , up to now, no appropriate pellicle material is available. A pellicle serves as a thin membrane to protect the mask from contamination by particulates. This membrane is placed near the mask but outside of the conjugate image plane, corresponding to the depth of focus. Here high transmission and a thickness of less than $1\text{ }\mu\text{m}$ is essential, otherwise the performance of the optical system will be disturbed. There are three approaches to solve that problem: Development of new organic material without degradation by the 157 nm radiation, or insertion of inorganic material of considerably higher thickness with the need to re-design the optical system, or using masks without pellicles where ultra clean handling will be required. These options are pursued concurrently [13].

Furthermore, work is required to develop resists suitable for 157 nm lithography. For first trials, resists for 193 nm are applicable, when the resist thickness will be limited to 50 – 80 nm thickness, which will be an affordable way of initial tool testing. For production systems, thicker layers are required because thin resists are prone to more defects. Alternatively, a technique called top surface imaging (TSI) could be applied, which is also discussed for use in 193 nm lithography [2]. Here a thin polymer layer is cross-linked by the UV radiation. Then the resist is exposed to an organosilicon compound which diffuses into the unexposed areas of the resist forming an etch resistant layer. In a subsequent plasma etching step, only the cross-linked resist is etched away leaving a negative image of the mask pattern. This technique could overcome the difficulties to develop semi-transparent DUV resist.

Small field mini-scanners were installed at different sites for process development [12, 14]. First, the silicon chip manufacturers consortium – International SEMATECH, Austin, Texas – announced in December 1999 their order of an Exitech 157 nm fluorine laser microstepper tool. SEMATECH were funding a 157 nm program in 2000 targeted at the 90 nm node and to extend the photolithography to resolutions below 90 nm . For the manufacturing requirements of 4 Gbit memory and 1 GHz processor chips around the year 2006, this node requires photolithography on wafers of critical features having sizes ranging between 65 nm – 90 nm . With a $1.5\text{ mm} \times 1.5\text{ mm}$ image field size, the Exitech tool will be used primarily to carry out high-resolution exposures at 157 nm for resist development programs of International SEMATECH, its member companies and resist manufacturers. Scheduled to begin exposure work in the first quarter of 2000, the tool incorporates a 6 W 157 nm Lambda Physik NovaLine F630 F₂ laser and a 0.6 NA 157 nm imaging objective manufactured by Tropel Corp. [15].

Pressing forward, International Sematech has agreed in a joint effort with Europe's Interuniversity Micro Electronics Center (IMEC) to install the first 157 nm full-field scanner [16]. The concept consists of a catadioptric lens of 0.75 NA (ASML Micrascan VII) in conjunction with a hard pellicle made from inorganic material of non-negligible thickness which has to be considered in the optical design. The tool will be used to study requirements on mask making and pellicles, to characterize 157 nm resists when irradiated by high NA lenses and to establish monitoring procedures to ensure stable operation of the tool. Industry expects the 157 nm tool coming to market in 2007 to be ready for the 45 nm node [17], preliminarily early production tests of 65 nm node devices are scheduled for 2004 [18]. The development of 0.9 NA lenses or 1.4 NA immersion lenses could possibly expand 193 nm technology to the 65 nm or 45 nm nodes [18], which is a concept concurrent to the 157 nm pursuit concept and an example of before unexpected improvements. In principle, the same approach will be applicable to 157 nm technology, continuing optical lithography to previously unthought achievements and delaying the need to switch to extreme ultraviolet (EUV) or electron beam technology further.

Microlithography poses the most demanding requirements on excimer laser technology. Specifications result from the technical requirements regarding resolution and depth of focus, primarily small band width and high line width stability, as well as from the economical issues where high power and reliable operation define throughput. The need for an ever increasing output power has led to the development of dual-chamber master oscillator/power amplifier (MOPA) laser systems [19, 20] delivering 40 W of optical power compared to single chamber oscillators capable of 20 W output power. Further, pulse stretching is considered to narrow the spectral bandwidth by increasing the number of roundtrips in the cavity, and as an extra benefit the detrimental effects of long-term exposure of optical elements will be reduced by decreasing the peak irradiance [20]. Optical pulse stretcher modules [19] or alternatively, specific pulse-power techniques [21, 22] are employed for a two-fold stretching of the pulse length from typically 20 ns FWHM to about 40 ns . Table 16.2 summarizes the state of the art regarding ArF excimer lasers for lithography in year 2003, which is the scheduled time for implementation of 193 nm technology into production.

Table 16.2. Lithographic requirements and related laser performance of ArF lasers scheduled for production in 2003, data compiled from [23, 19, 22, 24, 25, 26]

lithographic requirement	laser parameter	performance data
resolution, depth of focus	wavelength	193 nm
	spectral bandwidth	0.25 – 0.35 pm FWHM
	spectral purity	0.75 – 1 pm (95%)
focus stability, critical dimension	wavelength stability	< +/- 0.025 pm
	energy dose stability	< +/- 0.3 %
throughput	power	20 – 40 W
	repetition rate	4000 Hz
	pulse energy	5 - 10 mJ
	maintenance intervals	5 billion pulses
cost of ownership	up-time	> 99 %

References

1. <http://www.intel.com/research/silicon/mooreslaw.htm> and related downloads from that site
2. M. Rothschild: "Photolithography at wavelengths below 200 nm", Proc. SPIE Vol. **3274** (1998)
3. P. Burggraaf: "Optical Lithography to 2000 and beyond", Solid State Technology February 1999, p. 31–41
4. Press release SVG DEC 14, 1999, see <http://www.svg.com/press/1999/99-29pr.html>
5. Press release SVG July 13, 1999, see <http://www.svg.com/press/1999/99-17pr.html>
6. V. Liberman, M. Rothschild, J.H.C. Sedlacek, R.S. Uttaro, A. Grenville, A.K. Bates, C. van Peski: "Excimer laser-induced degradation of fused silica and calcium fluoride for 193nm lithographic applications", Optics Letters **24**, No. 1, January, 1999, p. 58–60
7. J.A. McClay, A.S.L. McIntyre: "157nm optical lithography: The accomplishments and the challenges", Solid State Technology June 1999, p. 57–68
8. SEMATECH-Roadmap, see http://www.itrs.net/1999_SIA_Roadmap/Home.htm
9. <http://www.intel.com/research/silicon/mooreslaw.htm> or download ftp://download.intel.com/research/silicon/Gordon_Moore_ISSCC_021003.pdf
10. J.P.H. Benshop, A.J.J. Dijsseldonk, W.M. Kaiser, D.C. Ockwell: "Euclides: European EUV lithography milestones", Solid State Technology, September 1999, p. 43–52
11. L. Harriott, W. Waskiewicz, A. Novembre, J.A. Liddle: "Favored SCALPEL's continued progress", Solid State Technology on June 20, 2000, p. 73–84, see also: <http://sst.pennnet.com/home/search.cfm>
12. C. Smith, L.A. Moore: "Fused silica for 157nm transmittance", Proc. SPIE-Int. Soc. Opt. Eng. (USA), USA: SPIE-Int. Soc. Opt. Eng. **3676**, pt.1–2, 1999 p.834–41
13. A.K. Bates, M. Rothschild, T.M. Bloomstein, T.H. Fedynyshyn, R.R. Kunz, V. Liberman, M. Switkes: "Review of technology for 157nm lithography", IBM

- Journal of Research and Development, USA: IBM **45**, no.5, Sept. 2001 p.605–14, see
<http://www.research.ibm.com/journal/rd/455/bates.pdf>
- 14. P. Burggraaf: “2000 begins with a revised industry roadmap”, Solid State Technology January 2000, pp. 31
 - 15. Press release SEMATECH 21 December 1999, see
<http://www.sematech.org/public/news/releases/157nmtool.htm>
 - 16. <http://www.imec.be/wwwinter/business/157nm.pdf>
 - 17. <http://www.eetimes.com/story/OEG20030313S0070>
 - 18. <http://www.eetimes.com/story/OEG20021016S0040>
 - 19. <http://www.cymer.com>
 - 20. H. Watanabe, N. Kitatuchi, K. Kakizaki, A. Tada, J. Sakuma, T. Ariga, K. Hotta: “Long pulse duration of F₂ laser for 157nm lithography”, Proc. SPIE **4346**, pt.1–2, 2001 p.1074–9
 - 21. K. Kakizaki, T. Matsunaga, Y. Sasaki, T. Inoue, S. Tanaka, A. Tada, H. Taniguchi, M. Arai, T. Igarashi: “Ultra-high-repetition-rate ArF excimer laser with long pulse duration for 193nm lithography”, Proc. SPIE **4346**, pt.1–2, 2001 p.1210–18
 - 22. T. Saito, T. Masunaga, K. Mitsuhashi, K. Terashima, T. Ohta, A. Tada, T. Ishihara, M. Yoshino, H. Tsushima, T. Enami, H. Tomaru, T. Igarashi: “Ultra-narrow bandwidth 4-khz ArF excimer laser for 193nm lithography”, Proc. SPIE **4346**, pt.1–2, 2001 p.1229–37
 - 23. U. Stamm, R. Paetzsel, I. Bragin, V. Berger, J. Kleinschmidt, R. Osmanov, T. Schroeder, K. Vogler, W. Zschocke, D. Basting: “High Repetition Rate Excimer Lasers for DUV Lithography”, SPIE-Microlithography 1999
 - 24. <http://www.lambdaphysik.com>
 - 25. R. Paetzsel, H.S. Albrecht, P. Lokai, W. Zschocke, T. Schmidt, I. Bragin, T. Schroeder, C. Reusch, S. Spratte: “Excimer Lasers for Super-High NA 193 nm Lithography”, SPIE Microlithography 2003, to be published
 - 26. <http://www.gigaphoton.com>

16.2 TFT Annealing

M. Fiebig

Flat panel displays are used for computers, workstations, information displays and other ‘multimedia’ devices. They are replacing bulky CRTs but also opening up new applications.

TFT (thin film transistors) flat panel displays are rapidly increasing their share in the display market. Polycrystalline-silicon TFT technology is opening the door to highly reliable, high-resolution, high performance and large size active matrix liquid crystal displays (AMLCD). For the formation of polycrystalline silicon, excimer laser annealing at 308 nm has proved to be superior to all other techniques as far as quality, reliability and economy is concerned.

In liquid-crystal displays, the individual picture cells (pixels) are formed by transmissive polarization-switchable liquid crystals (LCs) which are illuminated with polarized light from the rear (see Fig. 16.4).

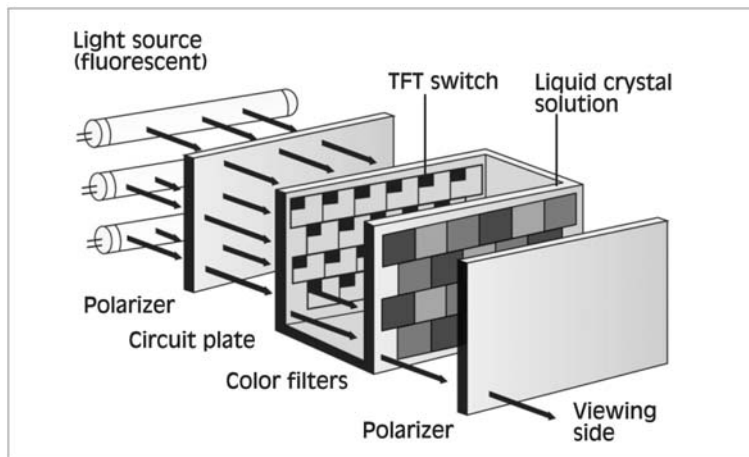


Fig. 16.4. Flat panel TFT-switched LCD

Thus, depending on the picture or graph to be displayed, the individual LCs stop light or allow its transmission, as controlled by the crystals orientation. The switching of crystal orientation is controlled by thin-film transistors arranged as a matrix on the display’s surface. In order to minimize light attenuation by the elements of these circuits they must be small. On the other hand, they must meet the specifications of a standard transistor such as sufficient field-effect mobility and low leakage current. Silicon was the material of choice for LCD technology. Silicon thin films can be easily made by chemical

vapor deposition on a transmissive substrate. The Si layer formed in this way is amorphous (α -Si).

However, the current trend towards higher resolution, higher brightness and larger size displays strikes against the technical limitations of amorphous silicon. The development of low-temperature polysilicon (LTPS) technology has drawn the attention of many display manufacturers because it has several potentially significant advantages compared to amorphous or high-temperature polysilicon technology:

- A much higher carrier mobility.
- Decreased pixel charging times which makes the display faster.
- The process is CMOS compatible.
- Integration of the driver circuitry on the display panel itself is possible. This avoids thousands of TAB (tape automated bonding) -bonded interconnects and reduces the manufacturing costs.
- The screen pitch is no longer limited by interconnection pitch.

Finding the way to transform amorphous silicon into polycrystalline form – in a quality suitable for subsequent transistor generation – became a major task for researchers. In principle, amorphous silicon heated to just above the melting point crystallizes spontaneously upon cooling; apparently this is a straightforward procedure. These days excimer laser annealing has proved to be superior to all other techniques such as furnace, lamp, and argon ion laser annealing. With excimer laser annealing, a glass substrate is coated, e.g. by chemical vapor deposition, with a thin film of amorphous silicon. The coated substrate is placed into a vacuum or inert-gas-ventable chamber. A shaped and homogenized beam of a high-power excimer laser is coupled into the vacuum chamber and scanned over the surface of the silicon layer (Fig. 16.5).

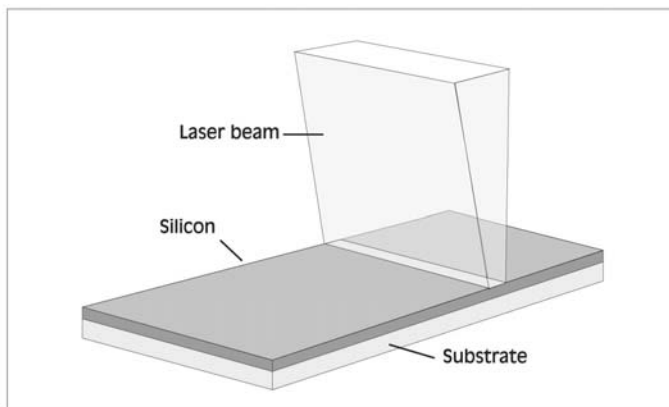


Fig. 16.5. Scanning process for excimer laser annealing

Efficient heating can be achieved by applying excimer laser radiation of sufficient fluence (energy/area). Due to the strong absorption of ultraviolet light, the absorption is limited to a thin layer of about 10 nm , and during the short pulse duration no significant transfer of thermal energy to the substrate occurs. This leaves the substrate nearly unaffected by heat so that inexpensive glass substrates can be used – an almost ideal situation for cost-effective production. However, it quickly became apparent that the transformation process must be controlled extremely carefully in order to achieve polycrystals of sufficient quality and size distribution. Considerable research efforts became necessary to find such conditions. We will briefly trace the recent development.

The first attempts about 15 years ago led to polycrystals of less than 100 nm grain size (see references in [1]) – too low for the making of suitable transistors as they showed insufficient electron mobility. Subsequently, investigations were directed to carefully optimizing the processing conditions so as to produce improved polycrystalline Si films. Extensive effort was undertaken to characterize the dependence of electrical parameters on crystal grain size.

Today, most major problems have been solved due to the efforts of many academic and industrial work groups, so that mass production was able to begin in October 1996.

16.2.1 Electron Mobility Increases with Grain Size

Several research groups at universities and industrial companies modeled the melt-phase duration of a thin α -Si layer (100 nm) on glass after an excimer-laser pulse, looking at the dependence on depth for different substrate temperatures. They found that the solidification velocity could be decreased by a factor of three, in comparison to room temperature, when the substrate was heated to 400°C [2] (this temperature represents a typical upper limit that glass substrates can tolerate without being damaged).

Experimentally, it was found that the average grain size of polycrystals could be increased up to 300 nm with the substrate kept at 400°C and field-effect mobility increased by a factor of two up to $230\text{ cm}^2/\text{Vs}$, being uniform to $\pm 10\%$ within the effective laser irradiation area. Since it was protected by a thin SiO_2 buffer layer, no thermal damage occurred to the substrate. This result was very promising for the realization of high-performance transistors using inexpensive glass substrates. These properties could be further improved by thinning the α -Si layer to 50 nm , then a 500 nm grain size was achieved. Furthermore, by applying multiple-shot irradiation, substantial grain growth was induced, which yielded grain sizes well above $3\text{ }\mu\text{m}$ (Fig. 16.6) [1].

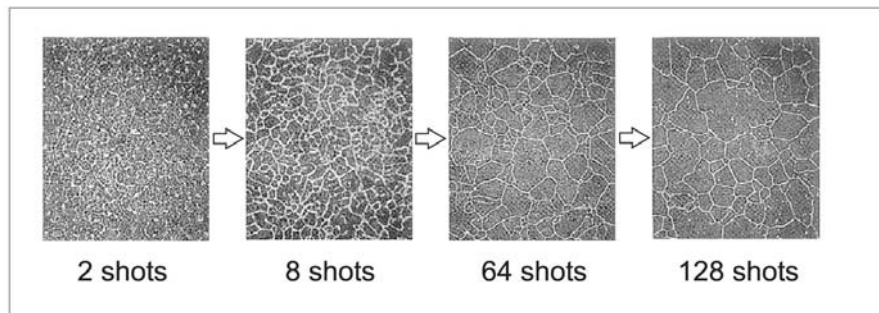


Fig. 16.6. SEM images of Secco-etched poly-Si films recrystallized using various numbers of shots to induce grain growth [1]

A ‘super lateral growth’ regime of crystallization was found (almost at the same time) by Im and coworkers at Columbia University [3] under near-melt-through conditions; on the basis of these findings, these authors set up a new model to explain the super-lateral growth phenomenon and succeeded in the realization of largely monocrystalline areas.

Because the spot of a typical excimer laser is only a few square centimeters, the whole area of a panel must be covered in a stepwise fashion. Therefore, problems at edges and overlapping regions had to be investigated. Kuriyama and coworkers found (summarized in [4]) 50 nm layers also to show the best performance in the overlap region of two successive laser pulses; the uniformity of the field-effect mobility being within $\pm 8\%$, which is considered an acceptable reproducibility for the fabrication of circuits.

Ultimately, the authors succeeded in generating a top-gate thin-film transistor structure. Figure 16.7 [4] shows the drain current versus gate voltage characteristics.

The electrical data were recently further improved and several prototypes of active-matrix liquid-crystal displays have been demonstrated by different groups (see references in [4]).

16.2.2 Layer Stratification, Near and Complete Melt-Through

Im et al. [3] showed that under near melt-through conditions of an α -Si layer, a sudden increase in grain size occurs, termed the ‘super-lateral growth (SLG) mechanism’, which is followed by a reduction in grain size on complete melt-through. Obviously, there exists a strong relation between polycrystal grain size and local and timely development of the melt phase. Stan D. Brotherton and coworkers at Philips Research Laboratories in Redhill, UK, investigated this in detail by scanning the excimer laser beam across the sample, varying thicknesses of the Si layer and the laser fluence, and providing doping and transistor architecture [5].

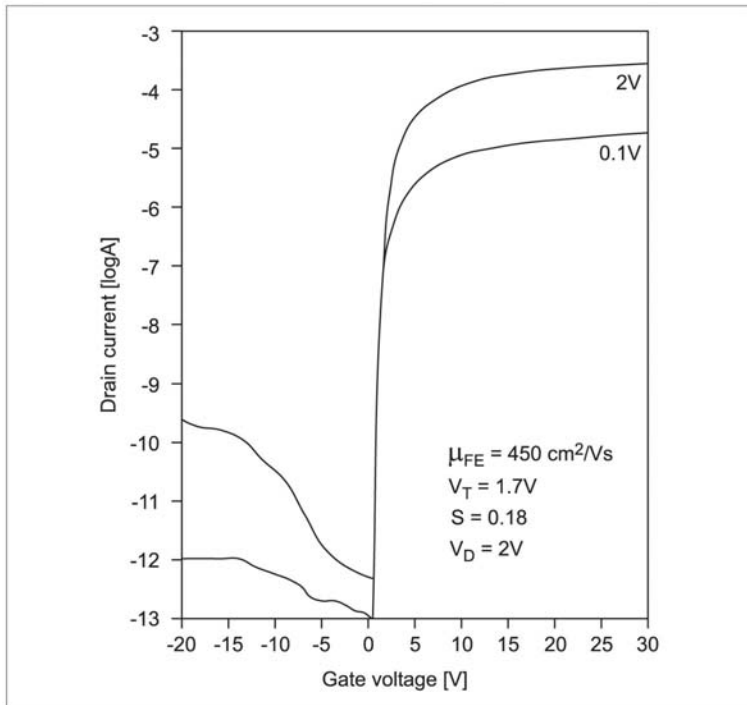


Fig. 16.7. Drain current versus gate voltage characteristics of a poly-Si TFT [4]

In the meantime, Im and coworkers succeeded in an improved excimer-laser-based recrystallization process called sequential lateral solidification (SLS) [6, 7]. This process can be accomplished using a precisely focused line beam, obtained by shaping the excimer laser beam by an appropriate optics. In the line focus, complete melting is induced. The film is then translated over a distance shorter than the single-pulse-induced lateral growth distance and then subjected to the next laser shot so that a directionally solidified microstructure is obtained, consisting of Si grains with almost unidirectional boundaries. The spacing of the grain boundaries in the crystallized films was found to depend on film thickness [8]. In order to optimize the SLS process precise demagnifying mask imaging has been used, the mask geometry being subject of experimental studies. SLS technology has been licensed non-exclusively to various manufacturers for further exploration. The technique could become the basis also for the generation of cost-effective integrated circuits on glass or even polymers instead of the build-up on silicon wafers.

16.2.3 Excimer-Laser Based Annealing System

The key components of the annealing system are the annealing controller system with integrated excimer laser and line beam optics, and masks, respectively. As an example, some data are reported here on a laser exposure system provided by an excimer laser manufacturer (Lambda Physik) and an optics manufacturer (MicroLas).

Laser and Line Beam Optics for the Mass Production Using SLG Standard line beam excimer laser annealing (ELA) has been transferred to industrial production in the mid 90s. For the SLG (super lateral growth, see preceeding section) process best results have been obtained if the film is almost completely melted, with a few grains remaining at the glass interface [9]. The line beam optics converts the raw excimer beam profile into a stable and homogeneous rectangular illumination field with high aspect ratio. It consists of a telescope, a long-axis and a short-axis homogenizer forming an intermediate image at a selected slit position, and a demagnifying ($5\times$) cylinder optics. The illumination field typically is up to 370 mm long and 0.4 mm wide. The applied energy density is around $350 - 400\text{ mJ/cm}^2$, the process window is limited to a range of $20 - 30\text{ mJ/cm}^2$. The line beam is scanned in $20\text{ }\mu\text{m}$ steps (thus the overlay being 95%) across the substrate. In this way, homogenous poly-Si films with $100 - 150\text{ cm}^2/\text{Vs}$ electron mobility have been produced.

The most important application-specific performance data are:

- High optics efficiency of 55% into line beam.
- Homogeneous long axis, standard deviation smaller or equal to 1.2% for up to 465 mm .
- Stable beam profile performance.
- Optics lifetime of 10 bn pulses.

The excimer laser is of industrial type, delivering 1 J at 300 Hz , 300 W average power. Both excimer laser and line beam optics are integrated into fully automated annealing systems. These annealing systems consist of a substrate handling and annealing chamber, cassette loading and unloading chambers, fully automated steppers, handling robots and a main system controller (Japan Steel Works (JSW)).

Longer lines to scan larger areas were obtained by combining the beams of two excimer lasers [9].

High Resolution Mask Imaging Using SLS The SLS process requires that crystals grow in the full melt in a controlled manner, proceeding from the solid edges. This can be obtained if a high resolution exposure pattern melts lines narrower than twice the crystal growth length, realizable by spaces and lines typically 2 and $3\text{ }\mu\text{m}$ wide, respectively. Following the first exposure, the substrate is shifted by $2.5\text{ }\mu\text{m}$ with a precision within $0.1\text{ }\mu\text{m}$. High-resolution UV optics and diffraction-limited imaging are required. The field for a 15-inch display can be crystallized with less than 3000 laser pulses; in comparison, the

line-beam method requires about 15.000 pulses. Moreover, the SLS methods enables an electron mobility up to $200 - 300 \text{ cm}^2/\text{Vs}$ [10]. “Intelligent” mask designs are under investigation. In addition, longer laser pulses are favorable for the generation of longer grains.

16.2.4 Outlook

The remarkable progress in display technology over the last few years requires a continuous improvement and highly sophisticated development of the total annealing setup. Moreover, new display technologies like field emission displays (FED) or organic light emitting diodes (OLED) are becoming additional devices for flat panel displays. Many companies and institutes are investigating these technologies with the help of excimer laser technology (see [11]) and also solid-state lasers (e.g. [12]), and are already marketing products obtained by SLS technology e.g. [13]. The field is in rapid progress.

References

1. H. Kuriyama, et al.: Jpn. J. Appl. Physics **32**(12B), 6190–5 (1993)
2. H. Kuriyama, et al.: Jpn. J. Appl. Physics **30**(12B), 3700–3 (1991)
3. J.S. Im, H.J. Kim, M.O. Thompson: Appl. Phys. Lett. **63**, 1969 (1993)
4. H. Kuriyama: Paper given at ESSDERC '96, Bologna, 8–11 September 1996
5. S.D. Brotherton, et al.: in *Proceedings of the AMLCD 96 Conference* Kobe, Japan (1996)
6. R. Sposili, J. Im: Appl. Phys. A **67**, 273–276 (1998)
7. M. Crowder, et al.: IEEE Electron Device Letters **19**(8) (1998)
8. M. Crowder, et al.: in *Mat. Res. Soc. Symp. Proc.* Vol. 621 (2000), pp. Q9.6.1–6
9. H.J. Kahlert, et al.: in *SPIE* Vol. 5004 (2003), pp. 20–27
10. H.J. Kahlert: Rev. of Laser Engin. **31**(1), 40–45 (2003)
11. in *SPIE* Vol. 5004 (2003)
12. Y. Helen, et al.: Thin Solid Films **383**, 143–146 (2001)
13. Samsung 21.3-inch TFT-LCD (May 2003)

16.3 Fiber Bragg Gratings

K. Körber, C. Kulik

16.3.1 Introduction to Fiber Bragg Gratings (FBGs)

Due to their high reliability, low transmission loss and a high signal-to-noise ratio, optical fibers have been strongly connected with information, telecommunication, and sensor networks since the 1960s. Further developments in the technology of fiber networks was slowed down because of the reliance on bulk optics for conditioning and controlling the guided beam. Bulk optics for selective diffraction, refraction or filtering and the appropriate fiber coupling units usually require high quality optics with stringent tolerances in their optical properties and alignment, leading to the demand for fiber-integrated functional optical units. With the rise of photosensitive materials, which allow the controlled alteration of their optical properties by external irradiation, selected segments of a fiber can be modified, giving the fiber the functionality of an integrated optical component in the irradiated area. One of the most widespread in-fiber components are fiber Bragg gratings (FBGs) [1].

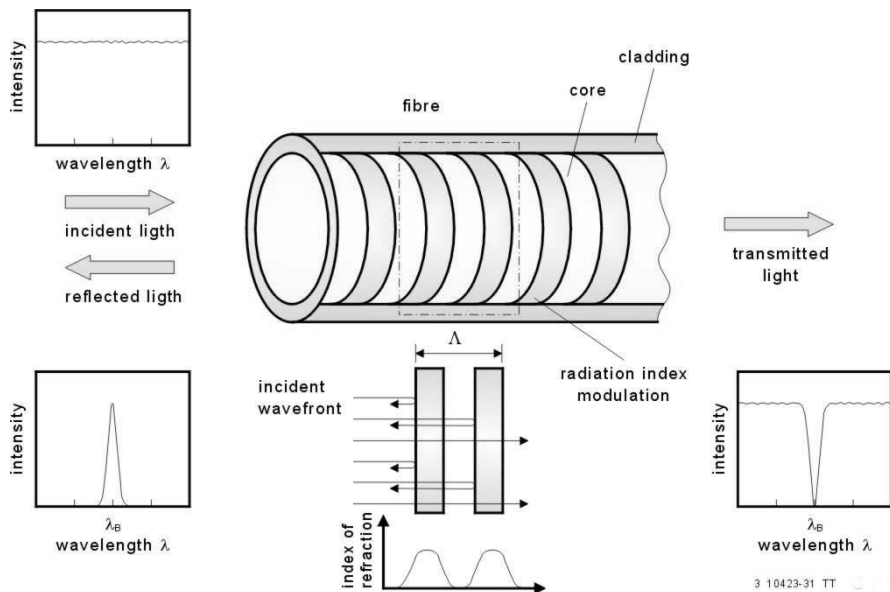


Fig. 16.8. Principle of fiber Bragg gratings

In its simplest form, a FBG consists of a periodic modulation of the refractive index in the core of a single-mode optical fiber. Its functionality can

be derived directly from Maxwell's equations. If an electromagnetic wave approaches an interface to a region of different refraction indexes, the field vector is, due to the condition of continuity, split up into a reflected and a transmitted component. When a wavefront approaches a region of continuously changing refraction index n , which is given in a real FBG, this process changes into continuous reflection and transmission, leading to an overall integration of the transmitted or reflected electromagnetic field vector. This integration results in an effective refraction index n_{eff} for one modulation. With the periodic modulation, this effect leads to a superposition of the reflected vector of each index modulation.

If the periodicity of the modulation Λ (= grating spacing shown in Fig. 16.8) meets the requirements of the Bragg condition for the design wavelength λ_B :

$$\lambda_B = \Lambda n_{eff}/N \quad (N = 1, 2, 3, \dots) \quad (16.3)$$

constructive interference occurs and the light with the design wavelength λ_B will be reflected. In this equation N is the order of the reflection.

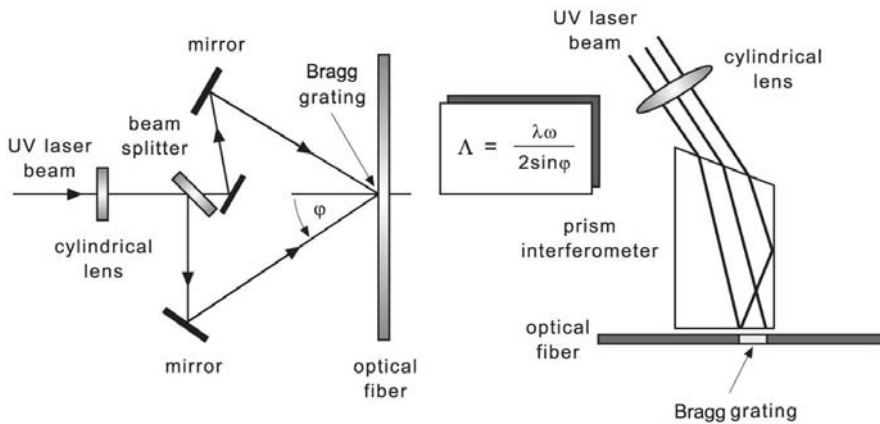
Besides the above mentioned common Bragg reflector, additional designs are feasible, expanding the optical properties of the fibers. By changing the inscribed patterns and/or in combination with additional FBGs, a broad range of optical characteristics can be achieved. A band pass can be realized with two FBGs either configured as a Michelson or Fabry-Perot type interferometer. Selective cladding guiding of a certain wavelength is the result of angular inscribed gratings, and dispersion compensation is one application for chirped Bragg gratings with a continuously varying period [1].

16.3.2 Manufacturing of Fiber Bragg Gratings

The manufacturing of FBG is based on the photosensitivity of some fiber core materials. This characteristic material property in optical fibers results in a permanent change of the refractive index when irradiated under certain conditions. The wavelengths and intensities where this effect occurs depend on the material properties of the fiber core. Although there are few core materials which show photosensitivity at several UV wavelengths, the emphasis here is on germanium-doped fiber cores sensitive to wavelengths between 240 nm and 260 nm. In order to inscribe the periodicity of the index modulation into the core, several internal and external techniques have been developed. Although the external techniques like the phase mask method, interferometric method, and point-by-point method require sub-micron resolution and stability, these techniques have successfully replaced the internal inscribing method [1].

Interferometric Method In the interferometric method, the incoming UV laser beam is split up into two or more beams and recombined at a certain angle to form an interferometric pattern inside the photosensitive fiber [2], inducing a permanent refractive index modulation. In Fig. 16.9 two principles for

generation of interference patterns are shown; the amplitude splitting and the wavefront splitting method.



3 10424-31 TT Source: A. Othonos, K. Kalli

Fig. 16.9. Interferometric method of writing FBGs [1]

In the amplitude splitting technique (left), a beam splitter is used to divide the UV laser beam. The reflected and the continuous beam are guided with an equal number of reflections, thus eliminating the different lateral orientation to the fiber core, generating an interference pattern which depends on the angle of the intersecting UV beams. With

$$\Lambda = \lambda_W / 2 \sin \phi \quad (16.4)$$

where λ_W is the inscribing UV wavelength and ϕ is the half angle of the intersection of the UV beams (Fig. 16.9), the Bragg wavelength λ_B can be directly expressed by λ_W .

$$w \cdot \lambda_W = n_{eff} \lambda_W / \sin \phi \quad (16.5)$$

The cylindrical lens is used to form the interference pattern to a line along the fiber core.

In the wavefront splitting method, a laser beam is guided to the edge of a UV-grade, fused silica interferometric prism, thereby generating two wavefronts which interfere on the bottom of the prism after one wavefront has been reflected by the prism's rear plane.

The advantages of the interferometric method are the flexible adjustment of the Bragg wavelength, by adjusting the intersection angle of the UV light, and that high-quality narrow-band filters can be made very precise for the desired wavelength. FBGs are written with this technique during the fiber

draw process which eliminates the need of stripping the coating of the fiber resulting in mechanically stronger components.

Despite these advantages, this method is not widespread. This is due to the requirements of a very stable optical setup and difficult adjustment. The high temporal coherence that is needed cannot be achieved with standard excimer lasers.

Phase Mask Method The phase mask method is based on the diffraction of UV light by a mask placed in close proximity to the fiber (Fig. 16.10). The mask is designed to suppress the zero-order diffracted beam to a few percent and to maximize the plus and minus one order. Each of them carries typically 35% of the transmitted power. When light of two orders of opposite sign cross, an interference pattern is produced. The period of this pattern is the first half of the phase mask pattern and not a function of the inscribing wavelength. The interference fringes lose contrast at a distance from the mask that is in the region of the spatial coherence length of the UV light.

A cylindrical lens is usually used to focus the fringe pattern along the fiber core.

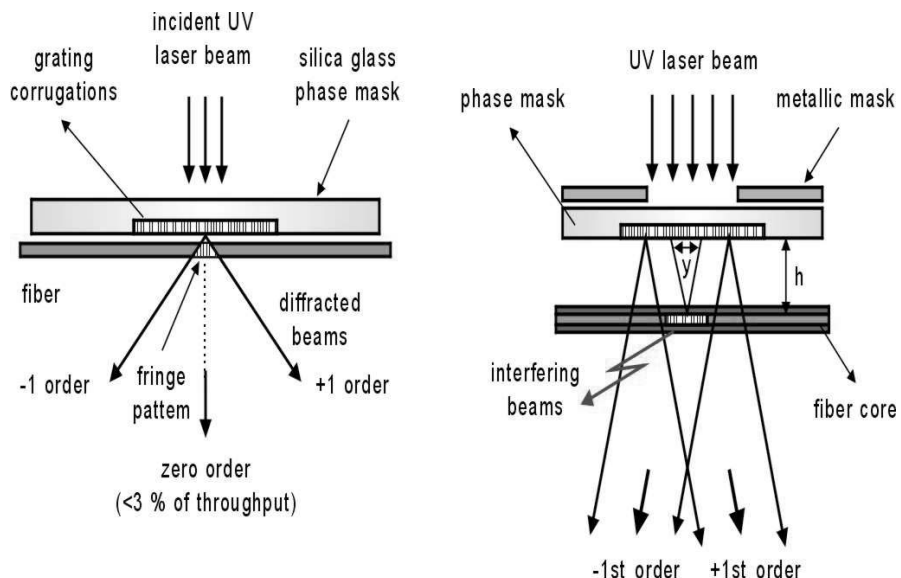


Fig. 16.10. Phase mask method of writing FBGs [1]

3 10425-31 TT Source: A. Othonus, K. Kall

The advantages of this method are the independence of the grating from the alignment, the period is just determined by the mask; the low requirement of temporal coherence and the feasibility of chirped gratings by using special

masks. However, the dependency on the mask reduces the flexibility of this inscribing technique. The spatial coherence must be higher than 1 mm to ensure a mask distance that avoids any damage of the fiber.

Use of Excimer Lasers for FBG Inscribing Currently two types of UV sources are used for inscribing FBGs, frequency-doubled argon ion lasers and excimer lasers. The argon ion laser with frequency conversion emits between 244 nm and 514 nm , while the excimer laser is mainly used at 248 nm (KrF) or, for some special core materials, at 193 nm (ArF). The fabrication of FBGs places, depending on the inscribing method, several requirements on the scribing light source. Table 16.3 gives an overview of the laser source requirements for different FBG inscribing methods.

Table 16.3. Requirements for FBG inscribing

Inscribing Method	Spatial Coherence	Temporal Coherence	Pulse to Pulse Stability	Pointing Stability	Homogenous Beam Profile
<i>Interferometric</i>					
- Amplitude Splitting	high (~1 mm)	high (~10 mm)	high	high	yes
- Wavefront Splitting	high	high	high	moderate	high
<i>Phase Mask Method</i>	high (~1 mm)	moderate	high	high	yes

Although argon ion lasers can meet the requirements regarding spatial and temporal coherence without any problems, they have to compete with excimer lasers which can supersede these systems due to their reliability, proven track record in high-duty-cycle industrial applications and competitive cost of ownership. Industrial excimer lasers offer near ‘black-box’ packaging, competitive costs of ownership, and multi billion shot tube lifetimes, providing them with excellent conditions for writing FBGs. The major obstacle in meeting the requirements for FBG inscribing is low spatial and temporal coherence. While standard excimer lasers have only limited spatial coherence, Lambda Physik has developed spherical unstable resonators, which are the basic source of spatially coherent UV radiation. Unstable resonators magnify the laser beam intra-cavity, reducing the divergence of the output beam and increasing the spatial coherence. The temporal coherence length can be increased using a diffraction grating and prism beam expander to narrow the spectral bandwidth of the emission. A system with improved spatial coher-

ence is the Lambda Physik L1-FBG, designed to meet the requirements of inscribing FBGs.

16.3.3 Applications for Fiber Bragg Gratings

With the variety of design possibilities and combination of FBGs, the field of applications is also broadly spread, e.g. in telecommunications as passive (filter, band pass) or active (fiber lasers) components or in sensor networks.

Basic band-pass filters are considered one of the most fundamental devices in multi-wavelength optical networks and in most communication systems where wavelength demultiplexing is required. There are several techniques for fabricating these band-pass filters using Bragg gratings. A simple interferometric band-pass e.g. can be realized by placing two identical gratings in two ports of a fiber coupler (Fig. 16.11). The multi-wavelength signal incident at port one is divided into two equal power portions by the 3 dB coupler, which are incident on the respective gratings where only the light at λ_B is reflected. The reflected light is incident on the coupler with a phase difference of π between them, which results in the direction the signal into port 2.

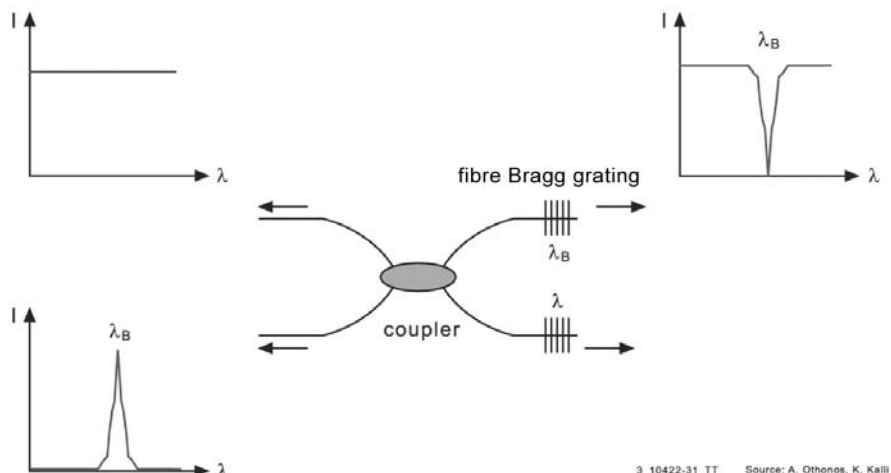
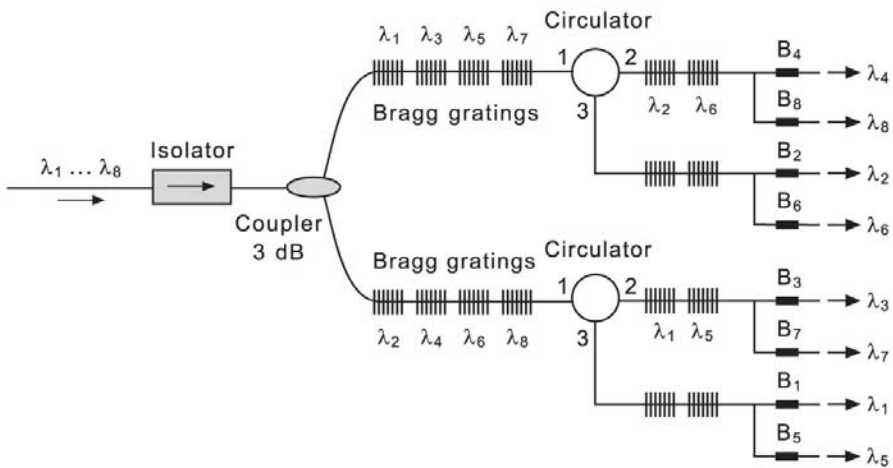


Fig. 16.11. Band-pass FBG [1]

In order to fulfil the requirements of higher transmission rates in future communication networks, wavelength division multiplexing will extend the standard frequency modulated transmission (Fig. 16.12).



3 10470-21 TT source: Othonos Kalli

Fig. 16.12. Hybrid dense wavelength division multiplexing [1]

FBGs also offer a broad potential in sensor networks, suitable for measuring static and dynamic fields, such as temperature, strain and pressure. The principle advantage is that the measured information is wavelength-encoded (e.g. changing Bragg wavelength under strain due to elongation and therefore different Bragg conditions), thereby making the sensor self-referencing and immune to unstable light levels or external distortion.

One of the first uses of FBGs in civil engineering has been the Beddington Trail Bridge, Canada. Here 16 sensors have been applied to steel-reinforced bars and carbon fiber composite tendons in order to monitor the long-term structure of the bridge. At the 12.9 km iced-water-spanning Confederation Bridge (Fig. 16.13 a), Canada, the long-term effects of wind, ice, and traffic loads are monitored by fiber optic grating strain sensors, which are mounted at various locations in flanges of concrete box girders and at other critical points. Besides long-term strain monitoring, dynamic traffic monitoring is possible for traffic observation and smart traffic management purposes. With the setup and monitored signal in Fig. 16.13 c and d the load of the tractor and the trailer can be clearly depicted at Taylor Bridge, Canada.

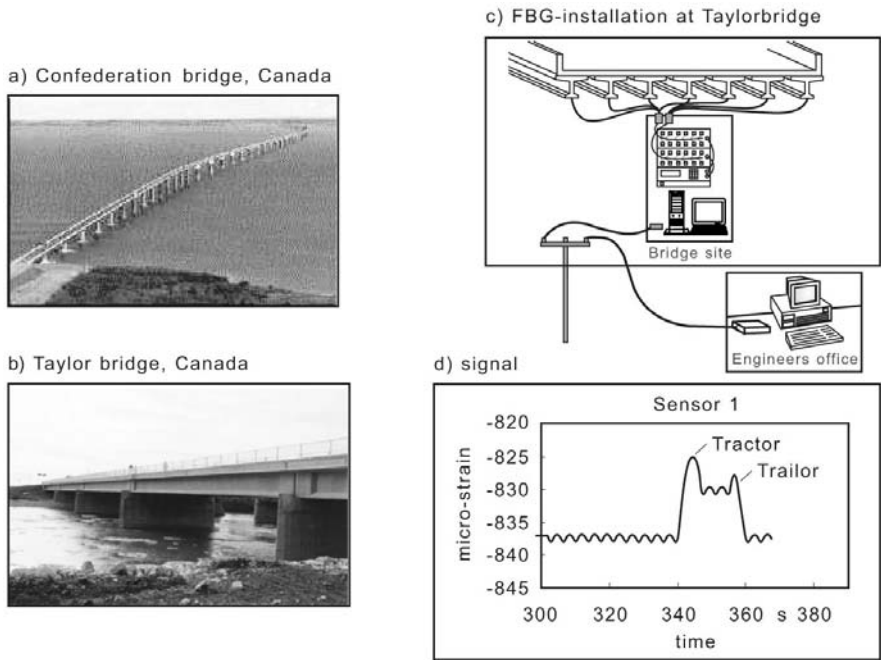


Fig. 16.13. FBG in civil engineering

In the aerospace industry, potential applications for FBGs are temperature, pressure, and strain measurement. The focus here is on new aerospace materials, particularly reinforced carbon fiber composites. Besides the excellent mechanical properties and low weight, the fiber and the composite have similar structures, thus enabling the formation of embedded sensor systems, in literature referred to as “smart skin”, or, in case of using the sensor signal to drive an actuator, as “smart structure”.

References

1. A. Othonos, K. Kalli: *Fiber Bragg Gratings: Fundamentals and Applications in Telecommunications and Sensing* (Boston: Artech House, ISBN 0-89006-344-3, 1999)
2. G. Meltz, W. Morey, W.H. Glenn: Optical Letters **14**, 823–825 (1989)

16.4 Marking

M. Wehner

Nearly all products in everyday life are labeled by identification codes and lot numbers. Expiry dates on food packages, batch identification of food and consumer products and inscriptions on automotive parts and electronic devices are typical markings. In many cases, laser marking is even used for the decoration of products, e.g. imprinting logos and providing functional information. Usually, Nd:YAG lasers emitting at $1.06\ \mu m$ wavelength are employed for laser engraving of metals or ceramics, but marking of plastics can also be performed by laser-induced foaming which generally results in light marks on dark surfaces. Further, frequency-doubled Nd:YAG lasers at $532\ nm$ are mainly affecting pigments by photo-thermal bleaching, leading to light marks without engraving. High irradiance at both wavelengths results in removal of material which is often accomplished with carbonization of the polymer and thus darkening of light resins.

Excimer lasers find their application when least modification of a surface layer is desired, e. g. the extension of the heat affected zones has to be minimized and the formation of microcracks has to be strictly avoided. This can be achieved when photochemical reactions or ablation of thin layers are used to perform marking. In Table 16.4 examples of various markings printed with excimer lasers are listed. Practically all materials can be marked in high quality by engraving (ablation) or discoloration (photochemical process). Figure 16.14 shows a product for home use, which is decorated by the typical excimer laser marking process, resulting in grey marks on white material.

Table 16.4. Overview of excimer laser marking applications

Product	Purpose	Variety of Markings
Aircraft cables	Identification label	medium - high
Medical devices	Product identification, Functional information	medium
Consumer products (white goods)	Logo, Product identification, Functional information	low - medium
Eye glasses	Logo, Product identification	low
Electronic devices	Parts identification, Functional information	medium



Fig. 16.14. Marking of products for home use, example electrical tooth brushes (with kind permission of Braun)

Table 16.5. Typical parameters for marking of different materials; by courtesy of ILT

Material	Process	Excimer	Fluence [J/cm ²]	Single Shot Area [mm ²] ¹⁾
Filled polymers	Photochemical reduction of TiO ₂	XeCl XeF	0.5	30
	Degradation of pigments	XeCl, XeF	0.5	30
Metals	Melting, recrystallization	KrF	1	15
Glass	Ablation	ArF	2 – 10	1.5 – 7.5
Ceramics	Chemical changes, surface morphology	KrF, XeCl	1 – 2	7.5
	Ablation	KrF, XeCl	2 – 10	1.5 – 7.5

¹⁾ calculated for 300 mJ pulse energy and 50% transmission losses

The advantages of laser marking compared to hot stamping (Fig. 16.15), tampon printing or ink jet printing can be summarized as follows:

- marking of nearly any material by engraving or color change
- no additional or extrinsic materials
- contact-less marking
- durable, indelible marks

In addition to the common features of laser marking, application of excimer lasers provides extra technical advantages:

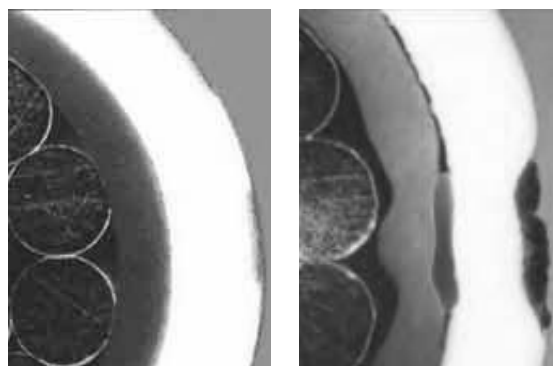


Fig. 16.15. Comparison of heat-affected zone when marking with excimer laser (left) or hot stamping technique (right)

- engraving of delicate or transparent materials with minimal thermal stress
- microscopic marks of high precision (“hidden” marking)
- simultaneous printing by mask projection (flash-on-the-fly)
- photochemical marking of filled polymers

Depending on the size of the field to be marked, either mask printing or mask scanning can be applied. Small fields are marked with a single shot technique, where the whole pattern is transferred simultaneously (flash-on-the-fly). Due to the short interaction time of typically 30 ns , the motion of a product freezes and it can be marked with excellent edge definition while being transferred on a feeding system. The laser pulse is triggered just when the sample is in the right position. A set of several different signs, e.g. characters, can be printed sequentially when a fast mask change dispenser is used. Alternatively, scan marking is employed when the size of the pattern exceeds the maximum single shot area (cf. Table 16.5). Here, the beam is scanned across the mask while the sample is stationary and marking is achieved by multiple pulsing. A synchronized motion between a moving product and a moving mask, similar to the technique described in Fig. 16.16, can also be applied for simple integration into an existing parts feeding system. Here the product can be marked without interference with the transportation sequence.

Many polymer materials are pigmented to reveal a special coloration or they are filled with ceramic particles to improve the wear resistance. Irradiating with fluences below the ablation threshold of the polymer can introduce structural or chemical changes in a near-surface layer which results in bleaching of dark pigments or darkening of light pigments. Examples of some materials and the resulting color changes are given in Table 16.6. Excimer laser marking of polymers results in a dark (grey or brown) mark on a light

substrate. The darkening of white material is related to the photochemical reduction of TiO_2 which is used as a filler. During laser irradiation, oxygen deficient TiO_2 is generated, which induces coloration by increased absorption in the infrared region near $1.1 \mu\text{m}$ overlapping in the visible [1].

Table 16.6. Marking of pigmented polymers by excimer laser radiation [2]

Trade Name	Generic Material	Original Color	Color Change
Hostaform®	POM	red	white
		yellow	gray
		ivory	black
		white	black
Hostacom®	PP reinforced	white	black
Celanex®	PBT	white	black

Excimer laser marking has been employed for identification codes on aircraft cables (see Fig. 16.16), where very strict regulations exist. For safety reasons each cable has to be marked in regular intervals along its length with identity codes. Cables wrapped with non-sticking fluoropolymers like PTFE tape or covered with FEP or PTFE emulsion cannot be marked by ink jet systems but are susceptible to laser marking. In these polymers, titanium dioxide is added which is one of the most commonly used pigments in the world and an usual additive for many polymers to whiten the insulation and for protective purposes. Studies on different pigmented cables revealed that contrast is optimized with a content of 4% TiO_2 by weight and the integrity and electrical characteristics of cables were maintained after excimer laser marking.

Compared to the previously used hot stamping technique, excimer laser marking is regarded as much less aggressive and less potentially damaging. The typical marking depth is of about $10 - 20 \mu\text{m}$ [3] and the inner parts of the cables remain untouched. In case of hot stamping, the high heat input and pressure leads to deformation and shrinking of the outer tubing as well as of the inner cover (see Fig. 16.15). Now, excimer laser marking complies with SAE 50881 as a proven and allowable marking technique for non-sticking PTFE cables. Laser radiation of 248 nm , 308 nm and 351 nm wavelength is well suited for marking of TiO_2 filled materials, whereby the highest contrast is realized using 308 nm radiation. Marking can be performed with fluences above 100 mJ/cm^2 , with high contrast marks being achieved in the range

from 0.5 J/cm^2 to 1 J/cm^2 . Further, the contrast of a mark can be increased by applying several pulses, depending on the polymer and the concentration of TiO_2 particles. Commercially available cable marking systems equipped with XeCl excimer lasers allow for a wire marking speed of up to 60 m/min . [4]. A high-speed mask changer is used for printing different alpha-numeric characters which can be marked on cable down to 0.85 mm diameter, bar codes are feasible on cable down to 0.60 mm diameter. Fig. 16.16 shows different types of cables marked with 308 nm radiation. Even colored cables can be printed with a high contrast.

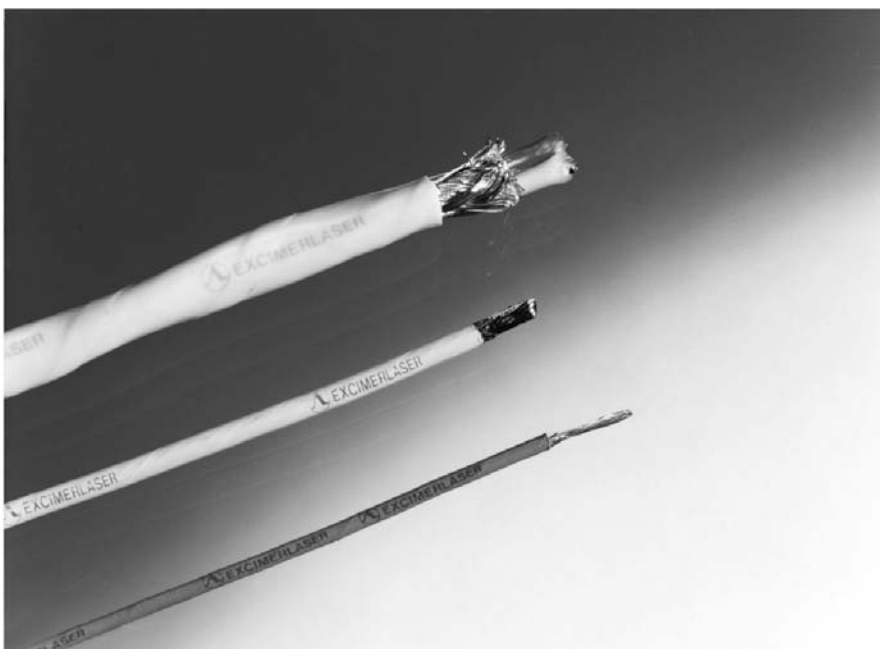


Fig. 16.16. Marking of Teflon[®]-coated wires with 308 nm radiation

Medical products like catheters have to be marked with identification labels and, for certain applications, with distance marks to give control over the insertion length. If the tubings are made from TiO_2 filled polymers, these marks can be easily applied with an excimer laser (see Fig. 16.17). Compared

to tampon or ink-jet printing, the durability of laser marking without the need for any additional material results in higher product quality. Recently, the marking of single pills is discussed. Since upcoming regulations for identification of each pill by labeling are expected, techniques for marking capsules or tablets without destroying the protective cover are required. Here the photochemical reduction of TiO_2 is also applicable, since many covers contain TiO_2 as a whitener. Even marking of packaged pharmaceuticals has been demonstrated. Long wavelength UV-light is able to penetrate the thin polymer film of the blister package and thus influencing the TiO_2 particles in the capsules [5, 6].



Fig. 16.17. Length marks near the distal end of catheters; by courtesy of ILT

Marking of small electronic components like surface mounted devices (SMDs) can be performed with XeF or XeCl lasers at fluences between 1 J/cm^2 to 2 J/cm^2 . Through irradiation with fluences equivalent to the ablation threshold, morphological and/or chemical changes are induced by the transient heating of a thin layer. If the material consists of a mixture from different oxides, modifications of the oxidation states and grain size could result in coloration or topological changes of the surface, similar to the reduction of titanium oxide mentioned before. This technique has been proven for the marking of small capacitors for surface mounting (see Fig. 16.18) where engraving would risk altering the electrical characteristics or would make the device susceptible to corrosion.



Fig. 16.18. Marking of surface mounted devices (SMDs) [7]

Laser ablation marking is accomplished by high fluences which leads to melting and evaporation of a thin surface layer. In many cases, a single pulse results in a clearly visible mark. When metals are irradiated, the surface of the molten metal layer is deformed through the action of the vapor pressure and freezes through rapid solidification in an irregular pattern. This leads to increased surface roughness of the irradiated area which induces light scattering and, in that way, a visible mark is printed. The depth of the marks can be very small since a melting depth of about $1\ \mu\text{m}$ is obtained for a $30\ \text{ns}$ pulse.

Marking of spectacles is performed with ArF laser radiation through ablation of a thin coating layer at typical fluence of $6\ \text{J}/\text{cm}^2$. Clean ablation with good edge definition is a feature of this type of marking. Micro-cracks can be definitely avoided and the fracture strength of products preserved. Due to the very small ablation depth, light impinging normally onto the surface is not affected, but under grazing incidence the mark becomes visible (cf. Fig. 16.19). That has the advantage that the user's vision is not perturbed. For improving the visibility of such markings, it is sometimes necessary to impose a superstructure consisting of edges and flanks to provide a sufficient degree of light scattering. The example in Fig. 16.20 shows characters consisting of many small spots marked in glass. Here a mesh was included in the mask to divide large open areas into many small imprints.

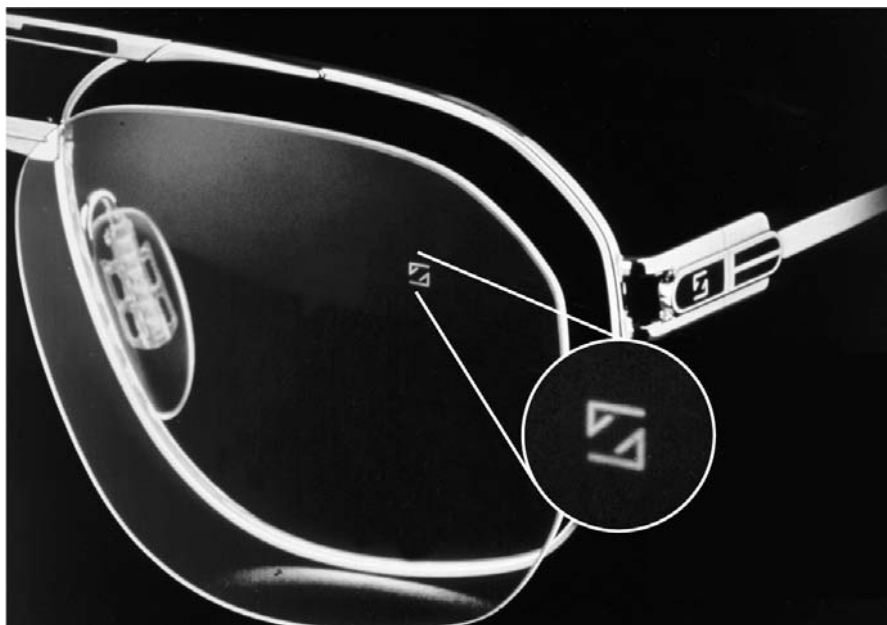


Fig. 16.19. Logo-labeled eye glass, visible only under grazing incidence; by courtesy of Carl Zeiss [7]

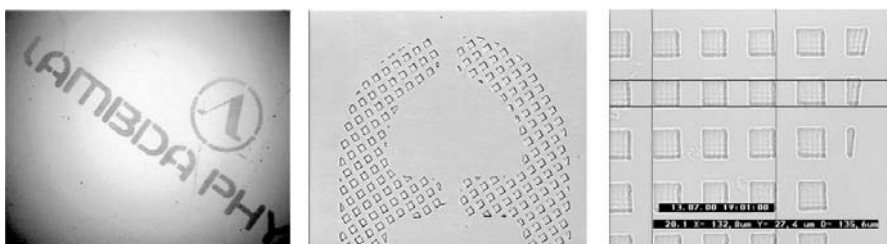


Fig. 16.20. Improving visibility of glass markings by raster screen printing; by courtesy of MicroLas [7]

Sometimes “hidden” identification marks are desired to identify the origin of high value products or to distinguish them from fakes. These markings should not affect the visual appearance of the product. The mark itself has to ensure high protection against faking up and therefore should be applied by a special technique not available anywhere. The detection of identification codes may also require a special technique to read out, e. g. microscopic marks only appearing under particular illumination.

Recently marking of diamonds has been investigated to certify quality and origin since the quality of artificial diamonds has been improved dramatically and thus the differentiation between synthetic diamonds, treated diamonds and diamond simulants needs high expertise. Despite the fact that a high quality synthetic or treated diamond will have the same “practical value”, the imaginary value of such an emotional object as diamond jewellery will be affected. Further, the term “conflict diamonds” [8] has been brought into public awareness since diamonds coming from suspicious sources had entered the market. Civil warfare has been financed by exploitation of diamonds and people were pressed to work under conditions normally not accepted. Similarly, child labor is not the appropriate background to enjoy luxury goods.

The precise ablation of diamond materials by excimer laser radiation can be used to imprint “invisible” marks along the girdle of a polished diamond. The typical character size is between $30\text{ }\mu\text{m}$ and $150\text{ }\mu\text{m}$ and the engraving depth from sub-micron to about $10\text{ }\mu\text{m}$ depth, typically $1 - 2\text{ }\mu\text{m}$. Thermal stress has to be minimized to avoid initiation or enlargement of cracks, and because of the high absorption of the UV radiation, the thickness of heat-affected layers and therefore the total heat input is minimal. The visibility depends on the engraving depth and the process parameters used. The laser energy is a main parameter influencing the darkness of marks: At low energy, the marks are mostly transparent, and for higher energy, the marks are getting darker, which is attributed to the formation of carbon deposits. The pulse number per site as well as the spatial overlap are parameters controlling the engraving depth and the definition of lines, allowing for clearly visible marks (see Fig. 16.21), when viewed by a magnification lens, or very shallow pits only visible under controlled illumination.

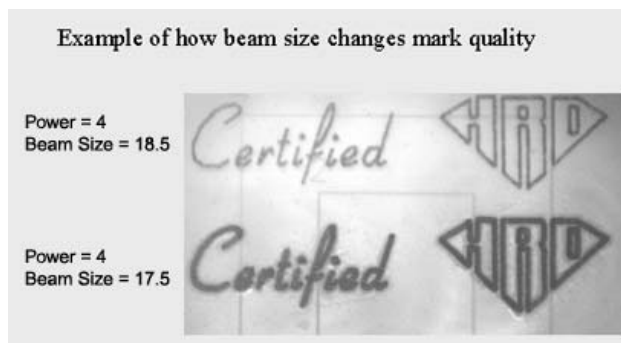


Fig. 16.21. Certification of diamonds by excimer laser scribing; by courtesy of PhotoScribe Technologies Inc. [9]

In the last few years, frequency-tripled Nd:YAG lasers have become available which emit up to 10 W power in the UV. Thus vector marking by solid-state UV-lasers of 355 nm wavelength can also take advantage of the TiO₂-process. These scribing systems use beam deflection by scanning mirrors and are very flexible because all patterns are generated under software control. Therefore the decision to use either an excimer laser or an UV solid-state lasers depends on the application and special requirements. Mask projection or one-shot-marking by excimer lasers allows for high throughput on moving parts, but printing of many different patterns would require a complex and fast mask changer. Recently, the development of compact high-repetition-rate excimer lasers [10, 11] of 1 kHz repetition rate provides high photon energy for scribing applications.

The marking depth, in which the material is influenced by the laser radiation, correlates with the optical and thermal properties of the materials. When considering dielectric materials, highest precision can be obtained using excimer lasers because heat conduction plays a minor role and the absorption coefficient rises strongly going to deep UV. Therefore a superficial marking in a depth ranging from sub-micron (ablation marking of eye glasses or diamonds) to about 10 µm to 20 µm (photochemical marking of pigmented polymers) becomes feasible.

References

1. S.W. Williams, P.C. Morgan: "Excimer laser printing of aircraft cables", Lasers Materials Processing, Proc. of the 7th International congress on Applications of Lasers and Electrooptics ICALEO '88, Santa Clara, CA, USA, p. 148–156
2. Product information from TICONA, document pages 73–74, see
<http://www.ticonaeu.com/downl/hostaform/brochure/Product-broch-Hostaform.pdf>
3. <http://www.spectrum-technologies.co.uk/technology/marketing.htm>
4. http://www.spectrum-technologies.co.uk/products/capris/c100_ts.htm
5. Pharmaceutical & Medical Packaging News, November 2002, see
PMPN online, Nov 2002; <http://www.devcelink.com/pmpn/archive/02/11/009.html>
6. Technical information Tri-star technologies, see
http://www.tri-star-technologies.com/m1001_pharm.htm
7. Lambda Industrial Report No. 8, November 1994, Publication by Lambda Physik
8. <http://www.debeersgroup.com/hotTopics/edrebelfunding.asp>
9. <http://www.photoscribetechnology.com>
10. <http://www.potomac-laser.com> <http://www.tuilaser.com>
11. L. Herbst, I. Klaft, T. Wenzel, U. Rebhan: "High-repetition rate excimer laser for micromachining", Photonics West 2003, to be published, see
http://www.lambdaphysik.com/pdf/pdf_208.pdf

16.5 Activation and Metallization of Dielectrics

K. Körber

The combination of high flexible beam shaping and guiding techniques with the short wavelength and thus high optical resolution of excimer laser radiation make these laser sources an extremely versatile tool for the generation of highly complex electronic circuits. Especially the generation of metallic layers on dielectric material can be realized with either laser-induced or laser-activated processes.

Characteristic for laser-induced techniques is that the laser energy is used for the initiation of a chemical and/or physical reaction by which a metal is deposited out of the gaseous, liquid or solid state. The latter is also known as *laser CVD* and can be used to form metallic layers on a large variety of materials like silicon, polyimide, glasses or alumina ceramics as long as the gaseous metal compound is transparent for the laser wavelength [1]. KrF or XeF radiation can also be utilized to decompose liquid palladium (Pd) – acetate into metallic Pd germs which can be electroless plated in a following process step [2, 3, 4]. An attractive alternative is the so-called *MAPLE-DW process*, where MAPLE-DW stands for “matrix-assisted pulsed laser evaporation – direct write”. With this method the solid metal compound is transferred by the excimer laser pulse from a carrier plate to the substrate surface. Chrisey et al. used this technique to form metallic structures on polyimide, glasses and ceramics [5].

Laser activation of surfaces is in general characterized by an increased sensitivity of the irradiated areas. This property is based on a variety of effects like a changed topography, material composition and/or atomic structure. In different experiments the activation could be demonstrated using materials like e. g. SiC, Al₂O₃, AlN or polymers [6, 7, 8].

A very apparent activation process can be seen using aluminium nitride (AlN) as the substrate material. Due to the thermal decomposition of AlN, the ceramic is decomposed into aluminium, which forms a surface layer after re-solidification, and gaseous nitrogen. The metallic Al constituent, which forms about 10% of the layer volume when using excimer lasers, imparts electrical conductivity to the activated surface [9]. The formation of the laser-activated surface layer on AlN can be seen in Fig. 16.22 with an increasing number of pulses.

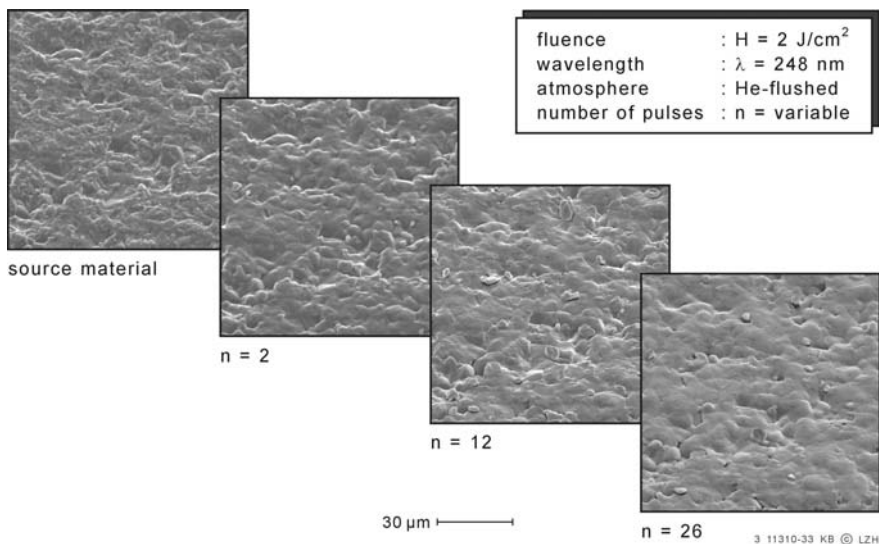


Fig. 16.22. Generation of laser-activated surface layer on AlN

In order to reduce the electrical resistance of the generated surface layer, electroless plating processes can be applied. By adapting the deposition parameters of commercial bath systems it is possible to generate bondable $\text{Cu} - \text{Ni} - \text{Au}$ layers on AlN [9]. Figure 16.23 shows an example of a bonded IC on a laser-activated and metallized AlN substrate.

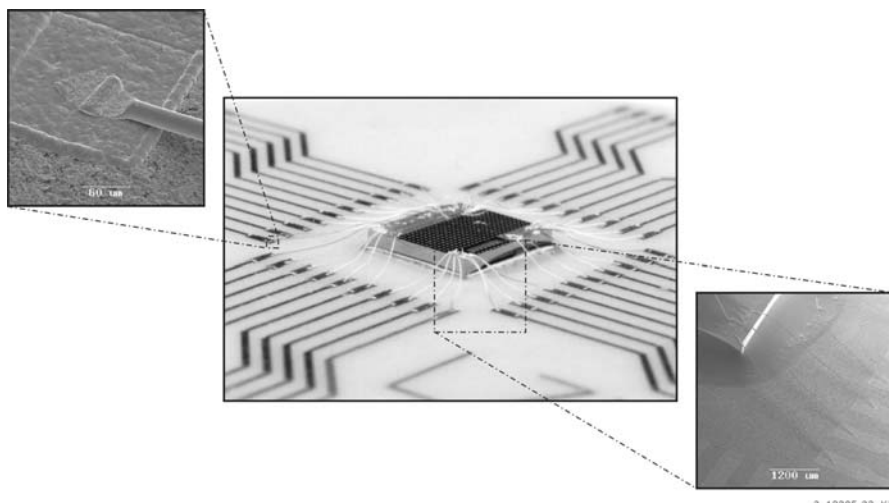


Fig. 16.23. Bonded IC on laser-activated and metallized AlN substrate

Applications of the laser-activation of AlN can be seen in the area of high-power electronics and high-frequency engineering, where *AlN* is an often used substrate material with increasing importance. A special potential for this process is in the area of prototyping and small batch production, since activation can be complemented by material processing, e. g. for the generation of vias.

References

1. H.S. Cole, Y.S. Liu, J.W. Rose, et al.: *Appl. Phys. Lett.* **53**(21), 2111–2113 (1988)
2. A. Bauer, J. Ganz, K. Hesse, et al.: *Applied Surface Science* **46**, 113–120 (1990)
3. O. Dupuis, J.P. Soumillion, et al.: *Applied Surface Science* **62**, 269–276 (1992)
4. J. Ganz, E. Köhler: *Metall* **45**(1), 18–23 (1991)
5. B. Chrisey, A. Pique, J. Fitz-Gerald, et al.: *Applied Surface Science* **154–155**, 593–600 (2000)
6. S. Beil: “Photochemische Funktionalisierung von Polymeroberflächen zur ortsselektiven Metallisierung”, Aachen: Shaker, 2000. ISBN 3-8265-7268-8, Aachen, RWTH, Fakultät für Maschinenwesen, Dissertation (2000)
7. K.J. Schmatjko: *Industrie Anzeiger* **111**(99), 39–43 (1989)
8. G.A. Shafeev, L. Bellard, J.M. Themlin, et al.: *Surface and Coatings Technology* **80**(1–2), 224–228 (1996)
9. K. Körber: “Lokale Metallisierung von *AlN*-Keramik mittels Laserstrahlung”, Düsseldorf: VDI-Verlag, 2002. ISBN 3-18-361802-8, Hannover, University, Fachbereich Maschinenbau, Dissertation, (2002)

17 Excimer-Laser Assisted Deposition of Carbon and Boron Nitride-Based High-Temperature Superconducting Films

G. Reiße, S. Weißmantel

17.1 Introduction

In the past two decades, excimer laser ablation has been an extensively explored technique for the deposition of thin films. In particular, the discovery of high-temperature supraconductors and the desire to produce thin films from those ceramic multicomponent materials led in the late eighties to strongly enhanced efforts to understand the mechanisms involved and, moreover, to the application of the method to other materials [1, 2]. While in the beginning the interest in the deposition method was centred on its unique capability to preserve largely the stoichiometry of the target in the films, other unique characteristics of ablation, namely the development of a laser plasma with high degrees of ionization, the high kinetic energies of the ablated species and the two-dimensional film growth became more and more important. By deliberately using them, the method proved to be suited for the preparation of thin films of nearly all materials that are of interest for industrial applications and for which solid or even liquid targets with good absorption at the excimer laser wavelengths are available. The method was used also for the preparation of thin carbon [3, 4, 5, 6, 7, 8] and boron nitride [9, 10, 11] films, and it was shown that metastable superhard phases of those materials can be deposited at parameters superior to other methods. In this chapter, the deposition of such superhard coatings by using excimer laser ablation and the modification of their properties by excimer laser irradiation of growing and as-deposited films is presented and discussed.

Due to their outstanding mechanical properties, superhard tetrahedral amorphous carbon (ta-C) and cubic boron nitride (c-BN) films are most interesting for use as wear resistant and, in combination with their optical, electrical and other properties, as multifunctional coatings. Both carbon and boron nitride may have a variety of different bonding configurations. The most important ones for the preparation of thin films are the two-dimensional sp^2 bonds that are characteristic for graphite and hexagonal boron nitride (h-BN) and the three-dimensional sp^3 bonds characteristic for diamond and cubic boron nitride. Besides the crystalline graphite and diamond there exist amorphous carbon phases with nearly any ratio of sp^2 to sp^3 bonds, the

properties of those phases varying from graphite-like (a-C) to diamond-like (ta-C) with that ratio decreasing. In addition, a lot of hydrogen (up to 40%) may be present in carbon films deposited with methods using hydrocarbons as precursor (termed accordingly a-C:H and ta-C:H). Which bonding configuration prevails depends on the deposition conditions, namely on the kinetic energy of the film-forming species and the substrate temperature during deposition. In hydrogen-free carbon films high sp^3 fractions of up to 85% can be obtained at kinetic energies above 30 eV if the substrate temperature during deposition does not exceed 90° C.

Boron nitride with perfect stoichiometry exists only in crystalline form, which is due to the ionic part of bonding. In general, the hexagonal phase forms easily during film preparation, whereas the nucleation and growth of the cubic phase requires very special conditions. C-BN nucleation was so far observed to occur exclusively with sufficient energy supply to the growing films and on top of a specially oriented h-BN layer, which forms prior to nucleation at the same conditions as nucleation. Moreover, a minimum substrate temperature of some 160° C is necessary. In the majority of deposition methods, the boron species (atoms) are produced by evaporating or sputtering a target, having thus too low kinetic energies, and the necessary energy supply is usually realized by an ion bombardment using argon/nitrogen ion beams or plasmas with substrate bias. It has been found that the minimum ion energy is some 60 eV and the ion-to-atom (I/A) ratio at the substrate must exceed 1 depending, however, on ion energy itself. Even though the further c-BN growth after completed nucleation requires a somewhat reduced I/A ratio it is still so high that the growth rates are limited to some 10 nm/min. The only way to reduce the I/A ratio is to deliver both the boron and nitrogen components with sufficiently high kinetic energy.

The particular significance of excimer laser ablation for the deposition of ta-C and c-BN films lies in the generation of species with high kinetic energies from a solid target. As will be shown in the following sections it provides a source of atoms and ions suited for the preparation of superhard coatings from those materials.

17.2 Characteristics of Excimer Laser Ablation

The processes involved in excimer laser ablation from a solid target are described in detail in [1] and comprise absorption by electrons, fast heating up by electron-phonon interaction, flash evaporation, formation of a plasma and expansion of the cloud of ablated species. They are determined by the high-intensity nanosecond laser pulses resulting in the input of a large amount of energy in a very short time and depend particularly on the laser energy fluence. The high temperatures at which flash evaporation occurs as well as the plasma formation lead to high kinetic energies of the ablated atoms and ions.

Even at moderate fluences of a few J/cm^2 those energies are significantly higher than those obtained by thermal evaporation and ion sputtering.

For example, the mean kinetic energy of the atoms and ions ablated from a hexagonal boron nitride and a graphite target is shown in Fig. 17.1 as a function of laser energy fluence. It can be seen that the threshold energies of some 30 eV and some 60 eV, at which tetrahedral amorphous carbon (ta-C) and cubic boron nitride (c-BN), respectively, are well-known to form, are easily reached. This implies that those phases may form without additional ion bombardment, which is necessary with other methods.

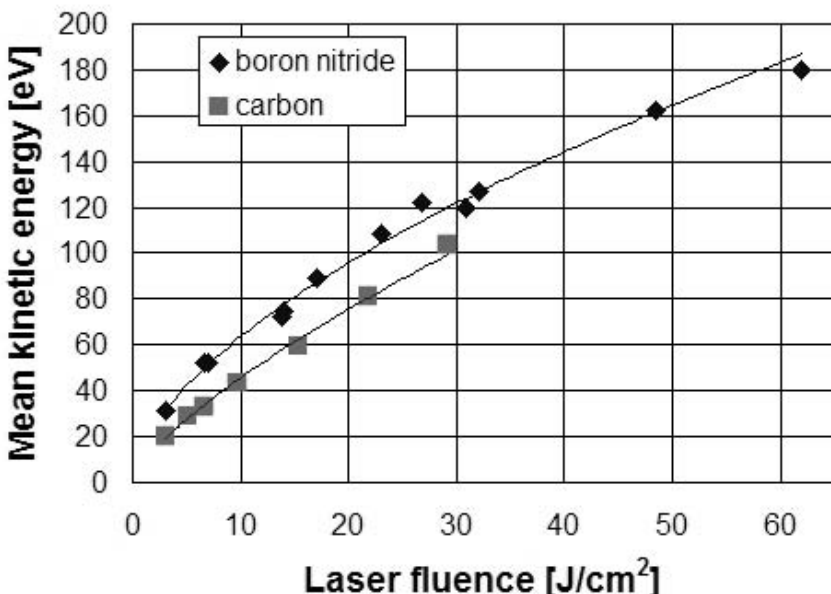


Fig. 17.1. Mean kinetic energy of atoms and ions ablated from boron nitride and carbon as a function of laser fluence (248 nm wavelength)

For a correct interpretation of the experimental results it must, however, be taken into consideration that the ablated ions were found to have considerably higher kinetic energies than the atoms and show, moreover, a shifted Maxwellian energy distribution. This phenomenon is thought to be due to the acceleration of the ions by the electrons. As the electrons and ions get the same energy in the plasma generation process, the electrons have a much higher velocity. When escaping the target surface the ions are accelerated and the electrons decelerated to the same velocity by electrostatic interaction. A shifted Maxwellian energy distribution was measured by [12] on carbon ions ablated from a graphite target at a fluence of $13 J/cm^2$. Thereby, the mean

kinetic energy was 130 eV and, hence, considerably higher than measured by us on all ablated species, which was some 50 eV at that fluence. In order to illustrate the particular energy distribution, the calculated one is shown in Fig. 17.2. The percentage of ablated ions increases also with increasing laser energy fluence. For BN we measured a percentage of 55% at a fluence of 30 J/cm^2 .

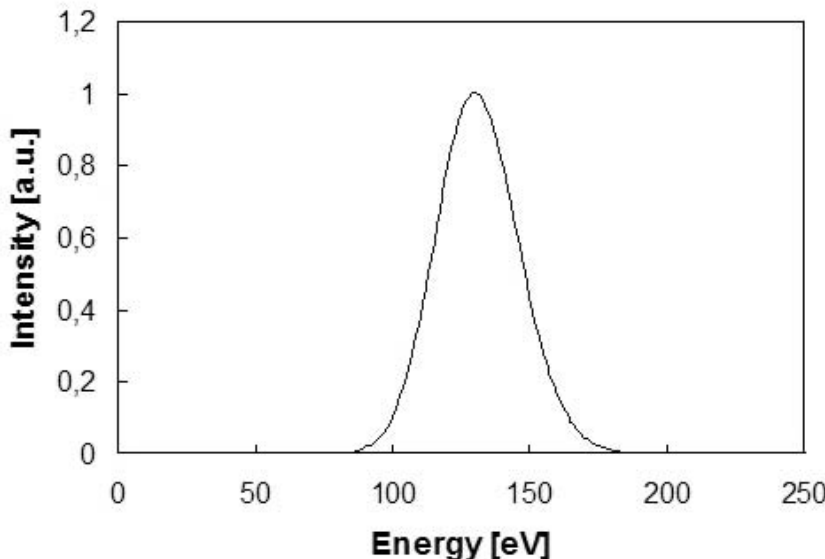


Fig. 17.2. Shifted Maxwellian energy distribution of ablated ions with a mean kinetic energy of 130 eV

In order to achieve proper growth rates a sufficient particle flux from the target is needed, that is sufficient particles have to be ablated per laser pulse. As can be seen in Fig. 17.3 for hexagonal boron nitride, the ablation depth per pulse is a characteristic function of the laser energy fluence. Up to 25 J/cm^2 the logarithmic dependence, shown more clearly for boron nitride in the inserted graph, is due to the logarithmic dependence of the depth at which the laser energy fluence decreases down to the ablation threshold. At higher fluences the dependence becomes exponential resulting in a drastic increase of the ablation depth above 60 J/cm^2 , a not fully understood phenomenon which is sometimes attributed to the onset of phase explosion [13, 14]. The behaviour would be useful for the further increase of the deposition rates of hard coatings if the high fluences required could be obtained with sufficiently large cross-sections of the laser beam on the target, that is if lasers with sufficiently high pulse energy would be available.

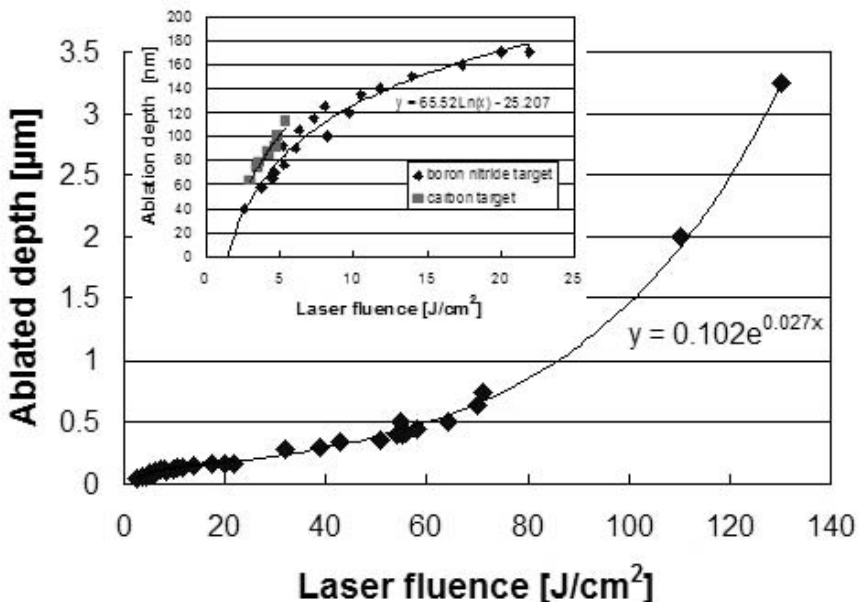


Fig. 17.3. Ablation depth per laser pulse as a function of laser fluence (boron nitride target, 248 nm wavelength)

A further characteristic of excimer laser ablation, which is important particularly for the preparation of c-BN films from boron nitride targets, is the well-known fact that the stoichiometry of multicomponent targets is largely preserved in the films. Though in the case of boron nitride some nitrogen deficiency occurs, a relatively weak additional nitrogen supply by ion bombardment is necessary for a good stoichiometry.

For some applications the two-dimensional layer-by-layer film growth which is typical for excimer laser deposition is of advantage. This growth mode is attributed to the short high-intensity particle pulses arriving at the substrate, and combined with the fact that several pulses are needed to form a monolayer it can be used for the preparation of dense ultrathin films with precisely adjustable thicknesses in the range of a few nm. Such films are presently demanded of the industry for use as wear-resistant coatings on hard disks or in X-ray optics.

The greatest problem with excimer laser ablation is the incorporation of so-called particulates or droplets, particles of several hundred up to several micron diameter, into the films. Their abundance depends generally on the material and the manufacturing process of the target and the laser energy fluence. At the fluences used for the deposition of ta-C and c-BN films from graphite and h-BN targets the particulates are relatively small with average

diameters of several 100 nm. Especially the preparation of thick c-BN films in the μm range is prevented at present by the accumulation of too many particulates consisting of h-BN in the films. Some measures for particulate reduction will be shown in the next section.

17.3 Deposition Techniques

Quite a number of various deposition techniques using excimer laser ablation as particle source have been developed over the years. Those developments were aimed at a greater flexibility in modifying the properties of growing or as-deposited films, the coating of large areas and the reduction of particulates. The techniques employed for the preparation of hard coatings range from simple ablation in vacuum or reactive gases to ion-beam- [10, 11, 15] and plasma- [16, 17] assisted ablation. In Fig. 17.4 the experimental set-up used for the deposition of ta-C and c-BN films by simple and ion-beam-assisted excimer laser ablation is shown for example. Additionally, a laser beam can also be directed onto the sample surface providing a further possibility for film modification. As will be shown in the next section, this proved to be essential for the stress relaxation in ta-C films. The set-up shown in the figure is designed such that the same excimer laser beam used for ablation can swiftly be redirected to the sample via a flip mirror allowing the quick alternation of deposition and modification of sublayers.

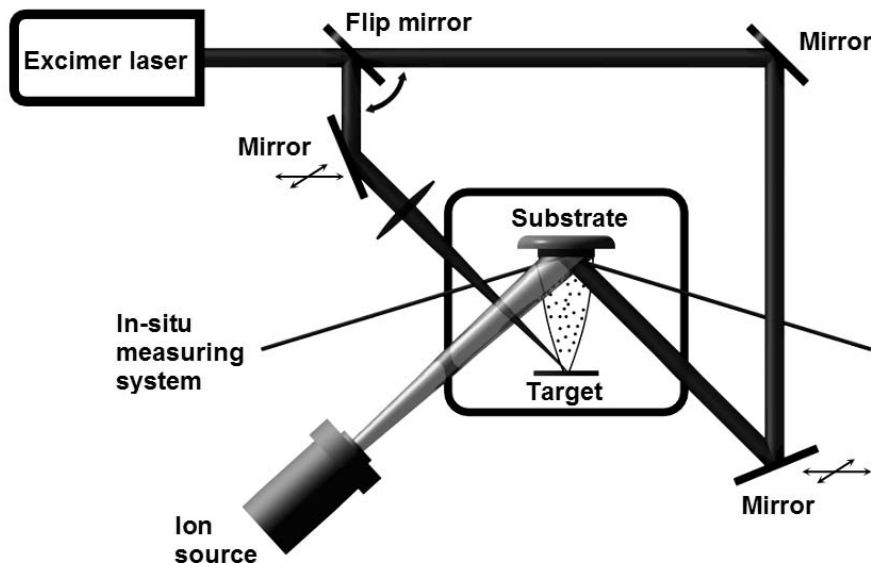


Fig. 17.4. Experimental set-up used for successive pulsed laser deposition and annealing of ta-C films and for ion-assisted pulsed laser deposition of c-BN films

Much attention has been given to the reduction of particulates, as those are a real problem with excimer laser ablation. Several techniques were shown to effectively reduce or even eliminate the particulates in the films. Amongst them are the crossed-beam laser ablation technique [18], the magnetic-field-assisted ablation [19, 20, 21] and the elimination of particulates by using a second laser beam parallel to the target surface. Moreover, mechanical velocity filters were used [1, 22], but their implementation in industrial equipment seems to be problematic.

17.4 Deposition and Properties of Tetrahedral Amorphous Carbon (ta-C) Films

Hydrogen-free amorphous carbon films prepared by excimer laser ablation from graphite targets may have a content of diamond-like (sp^3) bonds in the range of 0 to 85% and are correspondingly soft (a-C) to superhard (ta-C). Thereby, that content is determined exclusively by the laser energy fluence at the target provided the substrate temperature does not exceed $90^\circ C$ during deposition. Key parameter is the kinetic energy of the film-forming species. In own experiments, the sp^3 content determined by means of electron-energy-loss spectroscopy (EELS) increased from 20% at $3.3\text{ J}/cm^2$ to some 75% at $6.7\text{ J}/cm^2$ (see Fig. 17.5). The maximum values of some 85% are obtained at fluences in the range of $10\text{--}20\text{ J}/cm^2$ and mean kinetic energies in the range of $40\text{--}80\text{ eV}$ (see Fig. 17.1), respectively. The sp^3 content decreases slightly at still higher fluences. Substrate temperatures of more than $90^\circ C$ result, independently of the laser energy fluence, also in decreasing sp^3 content, and already at $150^\circ C$ the films are nearly completely sp^2 bonded [23].

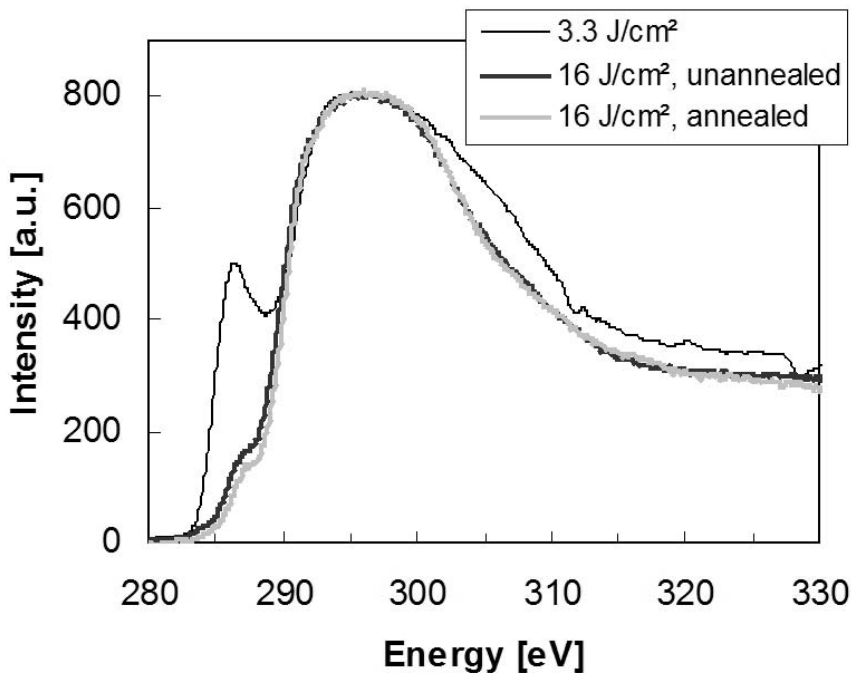


Fig. 17.5. Electron-energy-loss spectra of various pulsed-laser-deposited carbon films

As can be seen in Fig. 17.6, the variation of the optical band gap of the films with laser energy fluence correlates directly with the sp^3 content. According to Robertson [24] the relatively low maximum values (compared to the high maximum sp^3 content) is related to a relatively high degree of clustering of sp^2 bonds in the films. Though that clustering influences strongly the optical properties of the films, its influence on the mechanical properties is much less pronounced. Hardness values as high as 95 GPa have accordingly been measured by nanoindentation on ta-C films of 100 nm thickness, which is only slightly less than the hardness of crystalline diamond (being some 100 GPa).

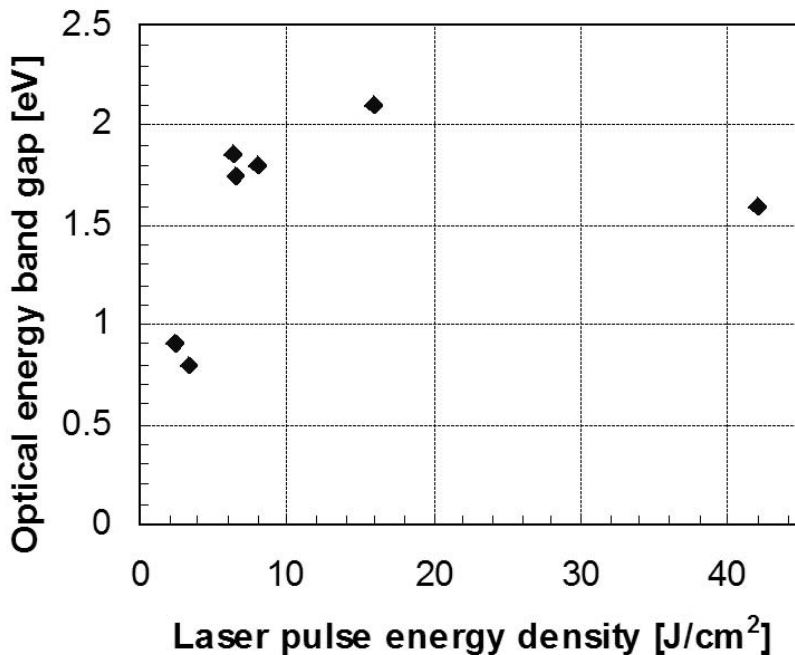


Fig. 17.6. Optical energy band gap of pulsed-laser-deposited carbon films as a function of target laser energy fluence. The values have been determined according to the method of Tauc, which is applicable to amorphous semiconductors.

It is that hardness combined with a low surface roughness of the amorphous films that makes them such exceptionally interesting for use as wear-resistant coatings on tools. For this, however, several micron thick films with good adhesion to the substrates are needed. Since as-deposited ta-C films possess high internal compressive stresses in the range of $8\text{--}12\text{ GPa}$, their preparation was limited until recently to a thickness of $200\text{--}400\text{ nm}$. For the preparation of thicker films measures must be taken to avoid or reduce those stresses.

Several years ago, Friedmann et. al. have found [5] that the stress in ta-C films can be removed by thermal annealing. A complete stress relaxation requires a minimum annealing temperature of 873 K and a minimum annealing time of several minutes. The sp^3 content and with it the diamond-like properties of the ta-C films are maintained during that process, so that they were able to measure hardness values of up to 80 GPa on such films. Problems of that method are that it is necessary to successively deposit and anneal sublayers of a few hundred nm thickness, where the samples must cool down

after annealing prior to the subsequent deposition of the next sublayer, and that temperature sensitive substrates such as plastics cannot be coated.

Recently, a novel method for the stress relaxation in ta-C films has been developed by us [25]. Using this method excimer laser pulses are used to anneal the ta-C films either during, using a second laser, or alternately to the deposition process. The advantages of using excimer lasers are their short high-intensity pulses, which allow the use of large laser beam cross-sections of 2 cm^2 on the sample surface, and the good absorption of the ta-C films at short wavelengths (absorption coefficient at 248 nm : $1.8 \times 10^5\text{ cm}^{-1}$). Moreover, due to the use of nanosecond pulses the temperature increases only in a thin surface layer of a few hundred nm, so that also films on temperature sensitive substrates can be annealed (if necessary with using a thermal barrier layer).

In annealing experiments performed with as-deposited ta-C films using 248 nm wavelength it was found that stress relaxation occurs very rapidly. After only 200 pulses (of 30 ns duration) the stresses in the films do not decrease any more, that is the residual stress is reached. Thereby, the residual stress decreases with increasing laser energy fluence. For example, the residual stress in 150 nm thick ta-C films was found to decrease from 3 GPa at 110 mJ/cm^2 down to 1 GPa at 165 mJ/cm^2 . Completely stress-free films were obtained at 180 mJ/cm^2 .

As mentioned above, the preparation of thick ta-C films requires the successive deposition and annealing of sublayers, which can nicely be done with excimer laser ablation and annealing. In Fig. 17.7 the variation of total stress with film thickness measured during the preparation of a $1\mu\text{m}$ thick ta-C film on Si is shown for example, where 8 sublayers of some 150 nm thickness have successively been deposited and annealed. The annealing fluence was kept constant at 150 mJ/cm^2 . The total residual stress in the whole film is only 0.3 GPa and made up completely from that in the first sublayer, for which the annealing fluence should have been 180 mJ/cm^2 . The behaviour is in agreement with the results of temperature calculations, from which follows that the maximum temperature per pulse increases with film thickness up to a thickness of 300 nm and remains constant for thicker films. From the variation of the reflectivity with film thickness it can be concluded that the film is not influenced by the pulsed laser annealing process with respect to its optical properties.

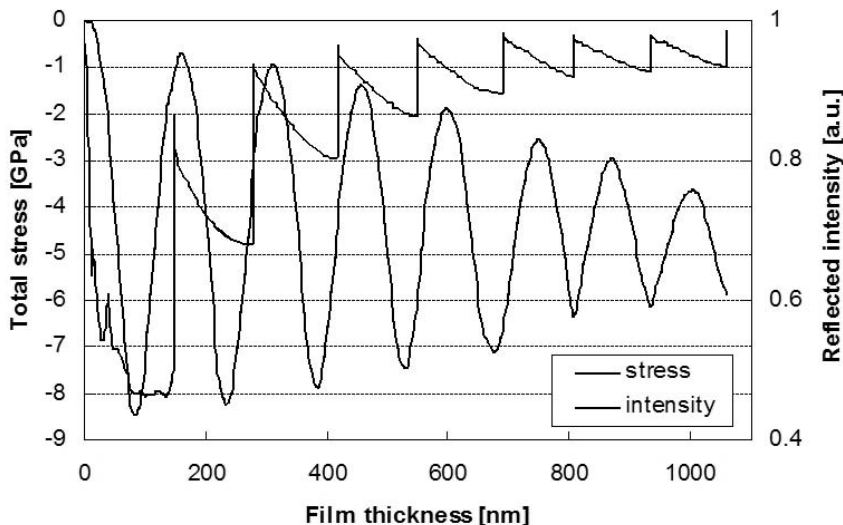


Fig. 17.7. Development of stress and reflected intensity normalized to the uncoated substrate during the preparation of a $1\ \mu m$ thick ta-C film on a $400\ \mu m$ Si-substrate by successive deposition and annealing (target laser energy fluence $12\ J/cm^2$, substrate laser energy fluence $150\ mJ/cm^2$)

Temperature calculations show that the maximum temperature per pulse in the film must be $1050\ K$ if complete stress relaxation is to occur. It should be kept in mind, however, that the temperature exceeds $873\ K$, the temperature needed for conventional thermal annealing, only for some $30\ ns$, that is the relaxation process during pulsed laser annealing takes place within several $10\ \mu s$, much faster than in conventional annealing. The results suggest that the process is determined mainly by thermal processes and that the high heating and cooling rates in the order of $10^{10}\ K/s$ result in an acceleration of the atomic site interchanging and reordering processes, which are necessary for stress relaxation.

Several μm thick adherent ta-C films on Si, WC hard metal and steel substrates were prepared by using the method. The preparation of a $2\ \mu m$ thick film on $20\ cm^2$ substrate area requires about 1 hour in our experimental set-up (see Fig. 17.4), where the excimer laser from Lambda Physik LPX 305 was operated at $248\ nm$ with $1\ J$ pulse energy and $50\ Hz$ pulse repetition rate. Thereby, it is important that we can go immediately from deposition to annealing and vice versa by reguiding the laser beam via a flip mirror from the target to the substrate and vice versa. For this it is important that the mean temperature during annealing does not exceed $90^\circ C$ at the maximum repetition rates, the substrate temperature during deposition at which increasing graphitization occurs.

The mechanical properties of thick excimer-laser-deposited ta-C films are shown in Table 17.1. Extraordinarily high values of hardness and Young's modulus have been measured on several $2\ \mu\text{m}$ thick films prepared on WC-hard-metal substrates. Thereby, the hardness even appears to be somewhat too low compared to the Young's modulus. This is probably attributable to the presence of particulates with sizes of several $100\ \text{nm}$ in the films, an assumption that is supported by a relatively large scattering of the 10 values measured on different spots of the same sample, from which the mean hardness denoted in the table was derived. The highest values of those single measurements, measured probably in a particulate-free film region, were as high as 85 to 95 GPa. The stress-free superhard ta-C films show good adherence to Si and WC hard metal substrates. The high values of the critical loads, at which film damage occurred during the scratch test, is of great significance for industrial applications.

Table 17.1. Properties of pulsed-laser-deposited DLC and c-BN films

	DLC	c-BN
Film thickness	$2\ \mu\text{m}$	$0.5\ \mu\text{m}$
Structure	amorphous	nanocrystalline
sp^3 -content	80 – 85 %	95 %
Band gap energy	1.8 – 2.2 eV	6.4 eV
Density	$3.2 - 3.3\ \text{g}/\text{cm}^3$	$3.1 - 3.4\ \text{g}/\text{cm}^3$
Film stress after annealing	$\rightarrow 0\ \text{GPa}$	4 – 6 GPa
Vickers microhardness	60 – 65 GPa	40 – 45 GPa
Young's modulus	880 – 920 GPa	430 – 590 GPa
Adhesion on WC (critical load with scratch test)	50 – 55 N	35 – 50 N
Friction coefficient	0.08 – 0.14	0.10 – 0.12

17.5 Deposition and Properties of Cubic Boron Nitride (c-BN) Films

Excimer laser deposition has widely been used for the preparation of c-BN films where mostly boron nitride targets were employed. The high kinetic energies of the ablated species are of great significance also for the preparation of c-BN films, even though an additional nitrogen or nitrogen / argon ion bombardment of the growing films is still needed for c-BN nucleation and growth at high growth rates. It depends on the laser energy fluence whether excimer laser deposition is of advantage compared to other methods. At fluences up to some $15\ \text{J}/\text{cm}^2$ and mean kinetic energies up to 80 eV, respectively, the

parameters and in particular the ion-to-atom (I/A) ratio needed for the deposition of c-BN don't differ much from those of other methods. This has been shown by various groups worldwide. With the excimer laser deposition method the I/A ratio is, however, the ratio of ions from the additional ion beam or plasma to ablated atoms and ions arriving at the substrate. That means a great part of the energy and momentum needed for c-BN nucleation and growth must still be supplied to the growing films by the additional ion bombardment. At higher laser energy fluences this energy and momentum comes increasingly from the ablated atoms and ions themselves. In addition, the momentum and energy transfer into the growing films from the pulses of ablated species is more effective than the momentum and energy transfer from the continuous ion beam bombardment [15]. In consequence the supply of energy and momentum to the growing films by additional ion bombardment and with it the I/A ratio can be reduced. This phenomenon can alternatively be used for the increase of the growth rate of c-BN by increasing the flux of ablated particles without reducing the additional ion bombardment. In this way growth rates up to 100 nm/min have been achieved at a laser energy fluence of 30 J/cm^2 , being an order of magnitude higher than at low fluence or with other methods. Those growth rates are limited so far by the laser parameters used (1 J pulse energy at 248, nm wavelength, 50 Hz pulse repetition rate). The further increase of the growth rate requires either higher laser pulse energies or higher laser pulse repetition rates.

At fluences above 60 J/cm^2 corresponding to mean kinetic energies above 180 eV , it is even possible to grow c-BN without any additional ion bombardment, but only at growth rates up to 10 nm/min , as at higher growth rates the nitrogen supply from the background gas (10^{-1} Pa nitrogen) is not sufficient to ensure stoichiometric film composition. High growth rates can only be achieved with additional nitrogen ion bombardment.

A special feature of ion-assisted excimer laser deposition is that the ablated species arrive at the substrate in pulses of several microseconds duration and that the contribution of the ions from the continuous ion beam or plasma is negligible during those pulses. Consequently, the main action of the ion beam occurs in the pauses between the particle pulses.

Apparently, it is important for the deposition of c-BN films at high growth rate to supply both components, nitrogen and boron, with high energies to the growing film surface. The minimum values of total momentum and energy transfer per deposited film atom into the growing film needed for c-BN nucleation were found to be about $200\sqrt{\text{eVamu}}$ and 630 eV , respectively. The minimum values during c-BN growth were found to be roughly by a factor of $1/3$ lower.

The layered structure of typical c-BN films deposited at high laser energy fluences and growth rates is shown in Fig. 17.8. Prior to c-BN nucleation an h-BN layer is always deposited by excimer laser ablation without additional ion bombardment. This layer exhibits a relatively high hardness of

some 20 GPa due to a strong cross-linking between the hexagonal planes. It was found to adhere strongly to Si and WC hard metal and to be suited to improve the adhesion of c-BN. Ion bombardment is switched on using appropriate parameters after deposition of that layer and c-BN begins to nucleate. The actual c-BN layer is nearly phase pure. No contrast from h-BN can be seen in it in the left dark field image and there is no h-BN reflection in the upper diffraction pattern. The diffraction pattern is quite similar to those of films deposited at low fluence showing that the c-BN crystallites are strongly <110> oriented perpendicular to the substrate surface and randomly oriented about the substrate normal [26].

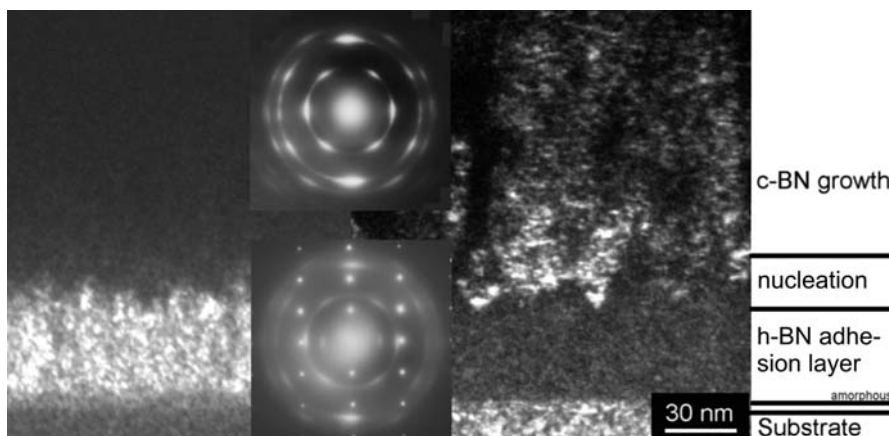


Fig. 17.8. Cross-sectional TEM investigation of c-BN films deposited on h-BN adhesion layers: Selected-area diffraction patterns from the upper and lower part of the cross-section and dark-field micrographs formed with a part of the (002) h-BN reflection (left hand-side image) and with a {111} c-BN reflection (right hand-side image).

The mechanical parameters of the c-BN films are shown in Table 17.1. The films are also superhard, and by using the above mentioned excimer-laser-ablated h-BN interlayers it is possible to improve the adhesion such that 0.5 μm thick films show good adhesion to silicon and WC-hard-metal. A general problem of the preparation of c-BN coatings for industrial applications is the high stress of as-deposited films (see Fig. 17.9). This stress is related to the high kinetic energies of the film-forming species and the strong ion bombardment. Recently it was shown that thermal annealing of c-BN films results in stress relaxation. Though the minimum residual stress was 4 GPa [15], the annealed c-BN films prepared on h-BN adhesion layers might be suited for applications. Most applications require, however, films of greater thickness than the 0.5 μm achieved so far with excimer laser deposition. The thickness limitation of those layers is attributed to the incorporation of particulates.

As their number is getting too high at greater thickness the preparation of thicker films requires the elimination of those particulates.

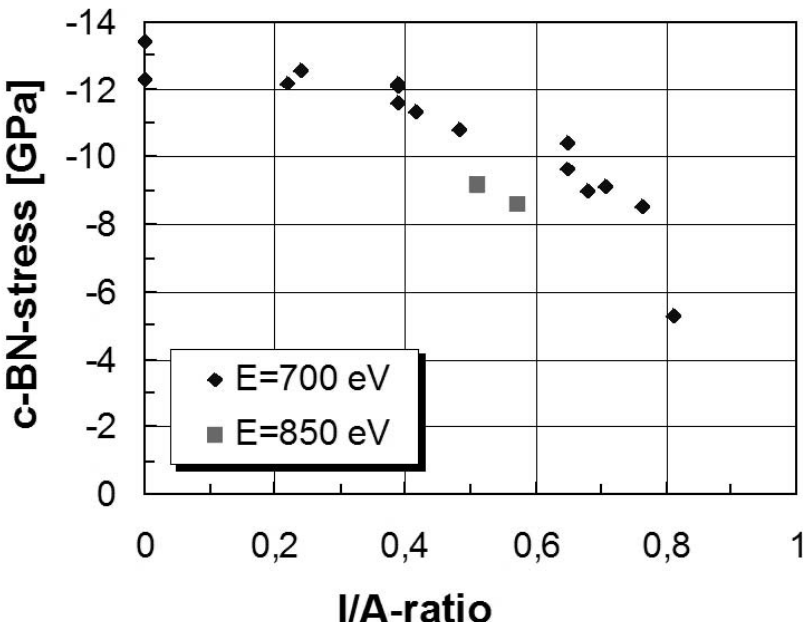


Fig. 17.9. Film stress of c-BN films as a function of the I/A ratio during c-BN growth (E: energy of bombarding ions from the ion source)

17.6 Summary and Outlook

In the past years it has been shown that excimer laser deposition is a well-suited method for the preparation of hard ta-C and c-BN coatings. Thereby, the special characteristics of the ablation process and of the ablated species, respectively, lead to special film-forming conditions and consequently to special film properties. The high sp^3 content associated with the high hardness of ta-C films and the deposition of superhard nearly phase-pure c-BN films at high growth rates are of particular significance.

Excimer laser irradiation of as-deposited ta-C films was found to be suitable for a complete removal of stresses in the films. In combination with the excimer laser ablation technique it provides a tool for the deposition of μm -thick superhard ta-C coatings. The same method should also be suited for stress relaxation in c-BN films, provided a wavelength is used at which c-BN shows good absorption, for example the F_2 -laser wavelength of 157 nm .

Further work must be directed towards enlarging of the substrate areas that can be deposited uniformly, the coating of 3D work-pieces and tools with the superhard materials and the reduction of particulates by a method suited for the implementation in industrial equipment.

References

1. D.B. Chrisey, G.K. Hubler (Eds.): *Pulsed Laser Deposition of Thin Films* (John Wiley & Sons Inc., 1994)
2. D. Bäuerle, R. Rössler, J. Pedarnig, S.H. Yun, R. Dinu, N. Arnold: Appl. Phys. A [Suppl.] **69**, 45 (1999)
3. T. Sato, S. Furuno, S. Iguchi, M. Hanabura: Jap. J. Appl. Phys. **26**(9), L1487–L1488 (1987)
4. D.L. Pappas, K.L. Saenger, J.J. Cuomo, R.W. Dreyfus: Jap. J. Appl. Phys. **72**(9), 3966 (1992)
5. T.A. Friedmann, J.P. Sullivan, J.A. Knapp, D.R. Tallant, D.M. Follstaedt, D.L. Medlin, P.B. Mirkarimi: Appl. Phys. Lett. **71**(26), 3820 (1997)
6. K.Y. et.al.: Appl. Phys. A **66**(115) (1998)
7. G. Reiße, B. Keiper, S. Weißmantel, U. Falke: Appl. Surf. Sci. **127–129**, 500 (1998)
8. M. Bonelli, A.C. Ferrari, A. Fioravanti, A.L. Bassi, A. Miotello, P.M. Ossi: Eur. Phys. J. B **25**, 269 (2002)
9. G.L. Doll, J.A. Sell, A. Wims, C.A.T. II, R. Clarke: Phys. Rev. B **43**, 6816 (1991)
10. D.L. Medlin, T.A. Friedmann, P.B. Mirkarimi, P. Rez, M. J.Mills, K.F.M. Carthy: Jap. J. Appl. Phys. **76**(1), 295 (1994)
11. S. Weißmantel, G. Reiße, B. Keiper, A. Weber, U. Falke, M. Röder: Appl. Surf. Sci. **127–129**, 444–450 (1998)
12. G. et.al.: Diam. and Rel. Mater. **3**, 598 (1994)
13. N.M. Bulgakova, A.V. Bulgakov: Appl. Phys. A **73**(2), 199 (2001)
14. A. Miotello, R. Kelly: Appl. Phys. A **69**(1), 67 (1999)
15. S. Weißmantel, G. Reiße: Diam. Relat. Mater. **10**(11), 1973 (2001)
16. J. Krishnaswamy, A. Rengan, J. Narayan, K. Vedam, C.J.M. Hargue: Appl. Phys. Lett. **54**, 2455 (1989)
17. E. Cappelli, S. Orlando, G. Mattei, S. Zoffoli, P. Ascarelli: Appl. Surf. Sci. **197–198**(452) (2002)
18. A. Tselev, A. Gorbunov, W. Pompe: Rev.Sci.Instrum. **72**, 2665 (2001)
19. H. Minami, D. Manage, Y.Y. Tsui, R. Fedosejevs, M. Malac, R. Egerton: Appl. Phys. A **73**(5), 531 (2001)
20. G. Radhakrishnan, P.M. Adams: Appl. Phys. A [Suppl.] **69**, 33 (1999)
21. S. Weißmantel, D. Rost, G. Reiße: Appl. Surf. Sci. **197–198**, 494 (2002)
22. T. Yoshitake, G. Shiraishi, K. Nagayama: Appl. Surf. Sci. **197–198**, 379 (2002)
23. Y. Lifshitz: Diam. Relat. Mater. **5**, 388 (1996)
24. J. Robertson: Adv. Phys. **35**, 317 (1968)
25. G. Reiße, D. Rost, S. Weißmantel: (25.04.2003), "Patent: Verfahren und Vorrichtungen zur Spannungsreduzierung in dünnen Schichten", Aktenzeichen 103 19 206.9
26. G. Reiße, S. Weißmantel: Appl. Physics A **69**, 749 (1999)

18 Combustion Analysis

V. Beushausen

Excimer lasers are excellent tools not only for micro-machining and material processing, but also for measurement applications. The unique combination of high-brightness laser emission in the UV spectral range and wavelength tuning makes these laser systems extremely suitable for monitoring of different molecules, like H₂, O₂, CO₂, CO, NO, OH, CH, and a variety of hydrocarbons. These molecules are major or minor components of the atmosphere as well as important constituents of high pressure/high temperature technical combustion systems and facilities. The spatial and temporal distribution of these species can be detected, even in complex chemical and physical environments, owing to the short pulse duration and high pulse energy of excimer laser light.

Excimer lasers are therefore well suited for spectroscopic analysis of technically applied combustion processes and their optimization in car engines and powerplants. The main objectives in this context are the improvement of fuel consumption and the reduction of pollutant emissions from these technical systems. A detailed understanding of the complex non-stationary and multiply interwoven processes inside the combustion chambers like fuel atomization, vaporization, mixture formation, combustion and pollutant formation is required. Chemical reaction kinetics and the gas dynamical phenomena demand the knowledge of physical properties, like density- and temperature gradients, size, distribution and temperature of fuel droplets, distribution of liquid and already vaporized fuel, etc.

The information can be obtained by using excimer lasers in connection with different diagnostic techniques, including Mie-, Rayleigh- and Raman-scattering, laser-induced fluorescence and its various derivatives [1, 2, 3, 4]. By combining these techniques with efficient detection equipment like intensified CCD cameras or spatially resolving optical multichannel analyzers, sensitive and powerful measurement systems can be built, which are comparatively simple because most of the above mentioned techniques use the same basic experimental set-up with only minor changes.

In the following, some techniques are briefly described.

18.1 Scattering Methods

Mie scattering is an elastic scattering process which takes place at the wavelength of the incident radiation if the dimensions of the particles are close to or larger than the optical wavelength. The scattered light is concentrated in the forward direction, with a much smaller backward intensity. The cross-section is usually very large (in the order of $10^{-26} - 10^{-8} \text{ cm}^2/\text{sr}$) so that high sensitivity can be achieved for the detection of droplets and aerosols.

Rayleigh scattering arises from light which is elastically scattered from molecules or small particles. It occurs in both forward and backward direction with cross-sections in the range of $10^{-26} \text{ cm}^2/\text{sr}$. The wavelengths of the incident and the scattered light appear closely together, and care has to be taken to avoid interference from other scattering processes.

The scattered intensity from a multicomponent gaseous mixture depends on the number density of molecules, the mole fraction and the scattering cross-section of the different species. Therefore, applying the ideal gas law, these methods can be used for temperature measurements if the pressure and the effective scattering cross-section are known. This has been demonstrated by Miles et al., who determined the temperature in turbulent air flows using an ArF excimer laser [5].

Rotational or vibrational Raman scattering usually describes a non-resonant inelastic interaction of light with molecules. The energy shift between the excitation and the emission wavelengths, the Raman shift, depends on the rotational and vibrational energies of the molecules. Therefore, the Raman emission spectrum can be used to determine the specific constituents of a gaseous mixture. However, the Raman scattering cross-section and therefore the Raman signal is very weak (cross-sections of only $10^{-29} \text{ cm}^2/\text{sr}$ are typical) and therefore powerful laser systems have to be employed. Just as Mie and Rayleigh scattering, the scattered light intensity scales with the fourth power of the frequency. Therefore the use of UV lasers can dramatically enhance the Raman signal strength. With an excimer laser wavelength of 193 nm , this scaling leads to a 60-fold increase in the scattering cross-section with respect to that obtained with a frequency-doubled Nd:YAG laser at 532 nm .

Due to the nature of the scattering phenomenon, which is instantaneous and therefore avoids influences of quenching effects, the described scattering techniques provide real quantitative information on the relevant measurands. This is in contrast to the fluorescence measurement techniques which strongly suffer from fluorescence quenching by intermolecular collisions and where the extraction of quantitative data is very difficult.

In practice, a combination of the described light scattering techniques is frequently used. An impressive application of both Mie and spontaneous Raman scattering for spatially resolved characterization of fuel sprays was performed by Müller and co-workers [6, 7]. Their method offers the simultaneous quantitative mapping of liquid and vapor fuel distributions as well as

droplet temperature and droplet diameter inside fuel sprays. The measurement was carried out on pulsed methanol and ethanol sprays generated by an automotive gasoline direct-injection valve, operating in ambient air at a backing pressure of 50 bar and a pulse duration of 1.5 ms. In Fig. 18.1, a snapshot of the investigated spray is shown, visualized by Mie-scattered light of a XeCl-excimer-laser (308 nm).

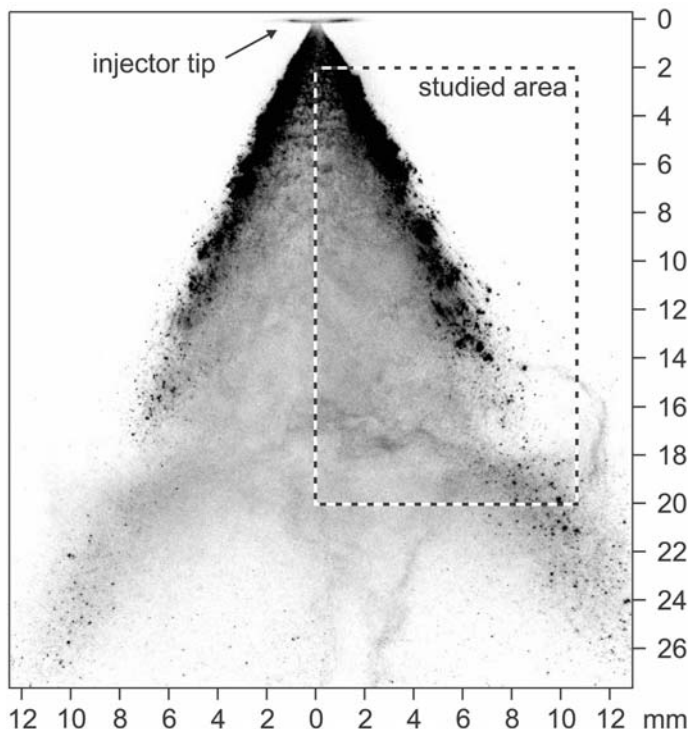


Fig. 18.1. Mie scattering snapshot of the investigated pulsed hollow cone spray (by courtesy of Müller, T. [7])

Raman scattering is induced by a KrF excimer laser (Lambda Physik EMG 160 MSC), operating at 248 nm, pulse length 20 ns, and pulse energy up to 250 mJ. The laser beam is focused by a spherical lens, forming a 1-d probe volume perpendicular to the vertical spray axis, as shown in Fig. 18.2 (a). The emission spectrum is measured by using a spatially resolving optical multichannel analyzer (SROMA). The results are presented in Fig. 18.2 (b).

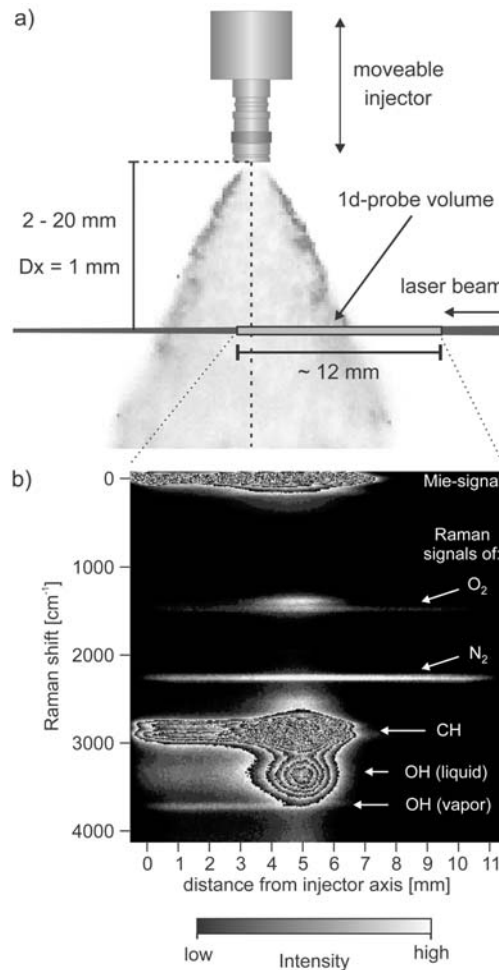


Fig. 18.2. Experimental set-up and spatially resolved Raman spectrum (by courtesy of Müller, T. [7])

The signal intensities are coded in a grey scale, depicted at the bottom of the figure. Besides the Mie signal at 0 cm^{-1} , vibrational Raman lines of O₂, N₂, CH and OH appear. Due to hydrogen bonding in the liquid phase, the OH-stretch Raman line is spectrally shifted in the liquid compared to the vapour phase. This effect enables a separate measurement of liquid and already vaporized alkanol with one-dimensional spatial resolution. Additionally the spectral peak position of the liquid phase OH Raman line is strongly temperature dependent due to temperature sensitive intermolecular binding forces. This effect can be utilized for the measurement of the droplets' temperature.

The determination of the droplet diameter is based on the different dependency of Raman and Mie scattered light intensity on droplet size. Mie scattered light originates from the droplet surface and the intensity scales with the second power of the droplet radius. The Raman scattering occurs from the droplet volume, and the intensity of this signal scales with the third power of the radius. Therefore the droplet radius can be calculated by dividing the Raman intensity by the Mie intensity.

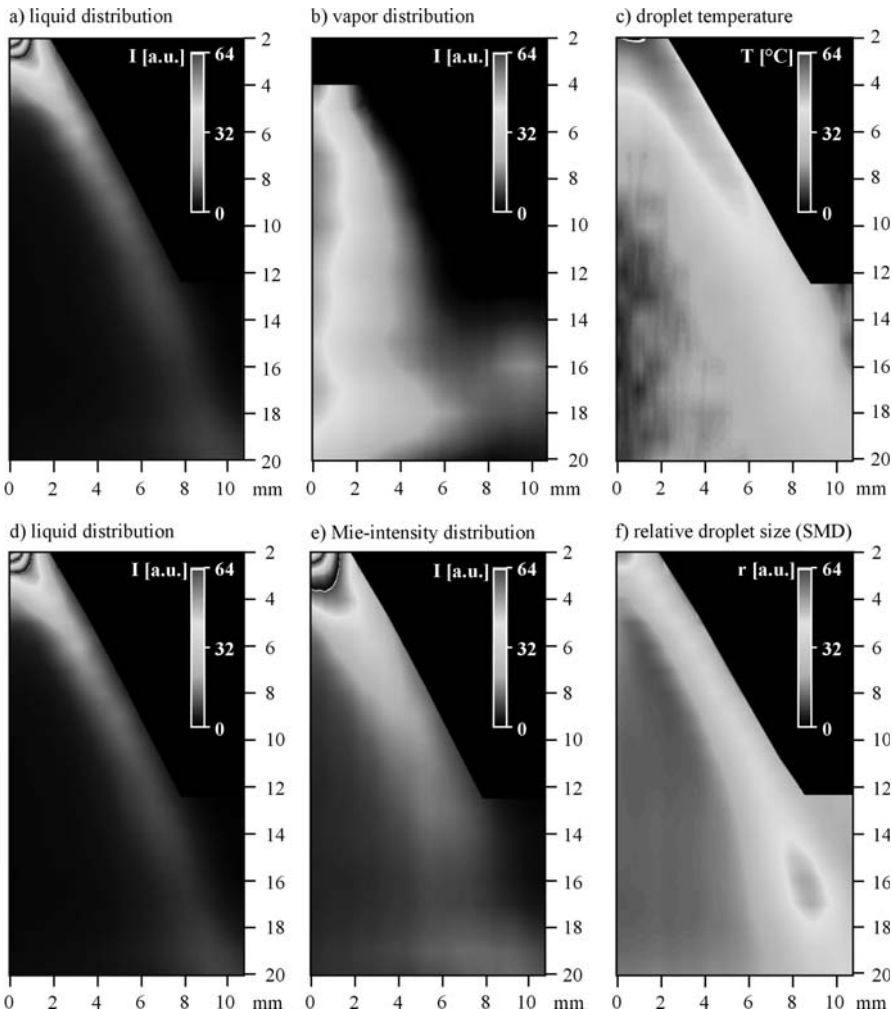


Fig. 18.3. 2d distributions of liquid (a,d), vapor concentrations (b), droplet temperature (c), Mie-scattering intensity (e), droplet size (f) (by courtesy of Müller, T. [7])

Combining several 1d-measurements from different locations inside the spray, a nearly complete 2d-characterization can be performed. This is illustrated in Fig. 18.3 (a-f), where the resulting distributions of liquid, vapor, temperature, droplet size etc. are shown.

In a combined Rayleigh- and Raman-scattering experiment, Grünefeld et al. applied these measurement techniques for the detection of the mean temperature field, the distribution of H₂, O₂, H₂O and N₂ in a jet engine burner. The laser source was a tunable KrF excimer laser operating at 248 nm with a pulse energy of 200 mJ [8].

18.2 Fluorescence Methods

Another widely used technique in combustion analysis is laser-induced fluorescence (LIF). Here, the laser wavelength is either tuned to a molecular or atomic transition or a casual coincidence of an absorption line with the output of a fixed-frequency laser being utilized. The spontaneous emission from the excited state to all low-lying energy levels connected by allowed transitions is measured. In principle, the intensity of each fluorescence line is proportional to the transition probability, which in turn depends only on the molecular constants. Therefore, the spectrum of this emission as well as the decay time allows a very simple identification of the molecules. Furthermore, in contrast to an absorption measurement, all spectral information can be obtained with single shot measurements, assuming that powerful and narrow-bandwidth light sources like excimer lasers are available. Such work was performed by Böckle et al., allowing single-pulse formaldehyde imaging in a turbulent flame to visualize the flame front positions [9]. The authors used a tunable XeF excimer laser (Lambda Physik EMG 150 TMSC) emitting at 353 nm for excitation of the CH₂O molecules. The experimental set-up of the TECFLAM swirl burner is shown in Fig. 18.4. The burner is operated with a thermal load of approximately 150 kW natural gas. Swirl is provided to the air flow by a moveable block swirl generator, and rapid mixing of the gas and air takes place within the combustion chamber. The imaged field of 82 × 25 mm² is located 25 – 40 mm above the burner exit.

Figure 18.5 shows the distribution of CH₂O in the swirl flame. Large formaldehyde LIF signals are found in extended areas, indicating low-temperature combustion processes in preheated zones of the mixed gases.

These results are significantly different with respect to laminar or weak turbulent flames and give further insight into the combustion with a highly turbulent technical swirl burner.

Under high pressure conditions in technical combustion environments, the fluorescence efficiency of the involved transitions is influenced by numerous collisional processes, like quenching, energy transfer to other excited states, interfering emissions, etc.. Therefore, quantitative measurements with laser-induced fluorescence require a calibration of the whole detection system in

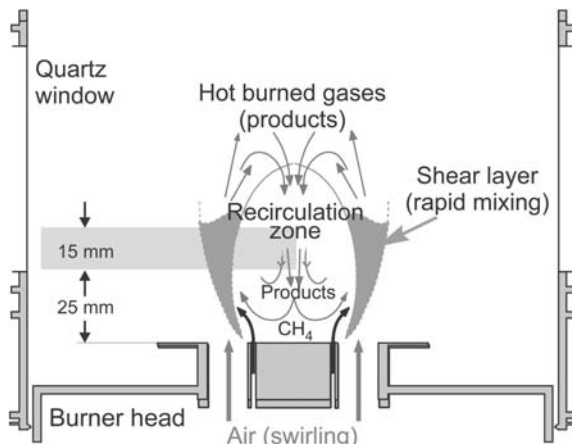


Fig. 18.4. Set-up of the 150 kW TECFLAM standard swirl burner (by courtesy of Schulz, C. [9])

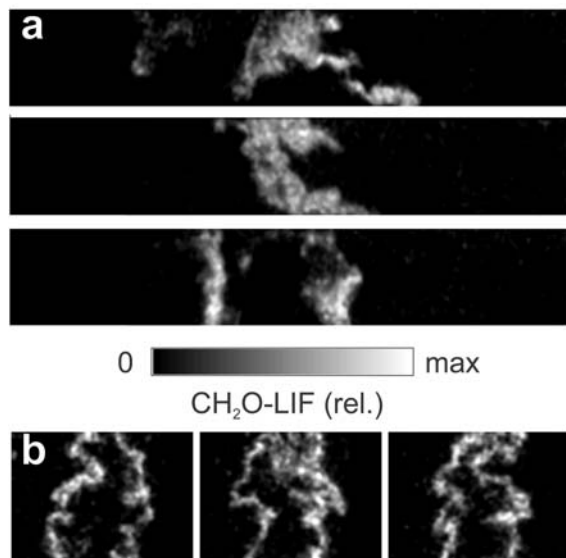


Fig. 18.5. Single-shot measurements of CH_2O LIF in the TECFLAM burner (by courtesy of Schulz, C. [9])

order to account for its unknown response. M. Knapp described such a measurement system for the detection of NO in the combustion chamber of an engine [10]. LIF was performed with a tunable narrowband KrF excimer laser (Lambda Physik, LPX 150), operating around 248 nm. NO concentrations and 1-d spatially resolved NO profiles were measured for different engine operating conditions and different fuels (isooctane, regular gasoline).

A further fluorescence technique, excimer-laser-induced fragmentation fluorescence (ELIF), is based on the photodissociation of molecular compounds by using for example 193 nm ArF excimer laser radiation. On fragmentation, electronically excited atoms are formed, and the fluorescence emitted from those atoms can be measured. This technique is a suitable optical on-line diagnostic method for detecting gas-phase alkali species released from coal combustion in powerplants. The major issue here is the removal of alkali metals, like NaCl and KCl, because even at very low alkali concentrations down to the *ppb* range, the deposition of these vapours can lead to severe damage of reactor parts and downstream equipment. Especially in combined plants, where an additional expansion turbine is included behind the combustion chamber, appropriate filtration and getter systems have to be installed, and the alkali concentrations have to be measured prior to the turbine entrance. The in-situ measurement of low concentrations with high time resolution requires ultrahigh sensitivity. On the other hand, for coals with high alkali and chlorine content and for high combustion temperatures (1300 – 1500°C), the concentrations of alkalis in the flue gas may reach ppm levels. Thus a dynamic range of several orders of magnitude is also needed.

A sophisticated ELIF-based system for the detection of Na and K atoms in large flue gas ducts has been developed by Gottwald and Monkhouse [11]. The authors designed a single-port arrangement, shown in Fig. 18.6, where laser access and fluorescence detection were achieved through the same window.

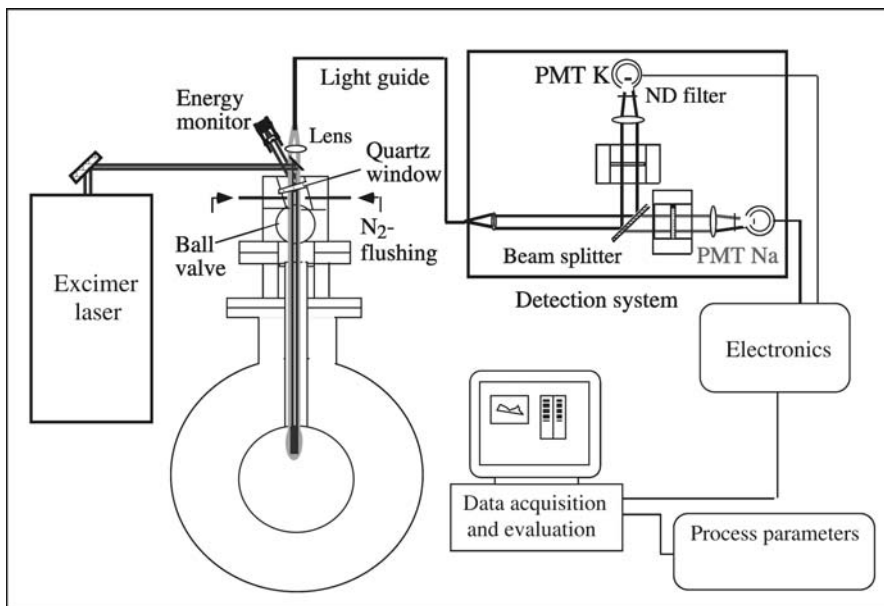


Fig. 18.6. Single-port set-up for ELIF measurements (by courtesy of Monkhouse, P. [11])

An ArF excimer laser operating at 193 nm illuminated a small section of the flow gas to generate an ELIF signal which was detected via an optical fiber. The fiber transmitted the fluorescence light to the detectors which were kept with the rest of the detection optics and electronics in a separate unit. Optical filters were placed in front of the photomultipliers for spectral discrimination against background emission from the gas pipe walls or glowing particles.

An alkali concentration history obtained over several hours using the described set-up is depicted in Fig. 18.7. Measurements were performed in the flue gas of the 10 MW pressurized circulating fluidized bed (PCFB) pilot plant of Foster Wheeler Energy (FWE) Oy/Karhula, Finland, behind the hot gas filter at a total pressure of 10 bar using a hard coal as fuel [12]. Alkali profiles are shown together with the reactor temperature. As can be seen, the amounts of alkali released follows the reactor temperature quite well. The sensitivity achieved was at sub- ppb level for both alkali species.

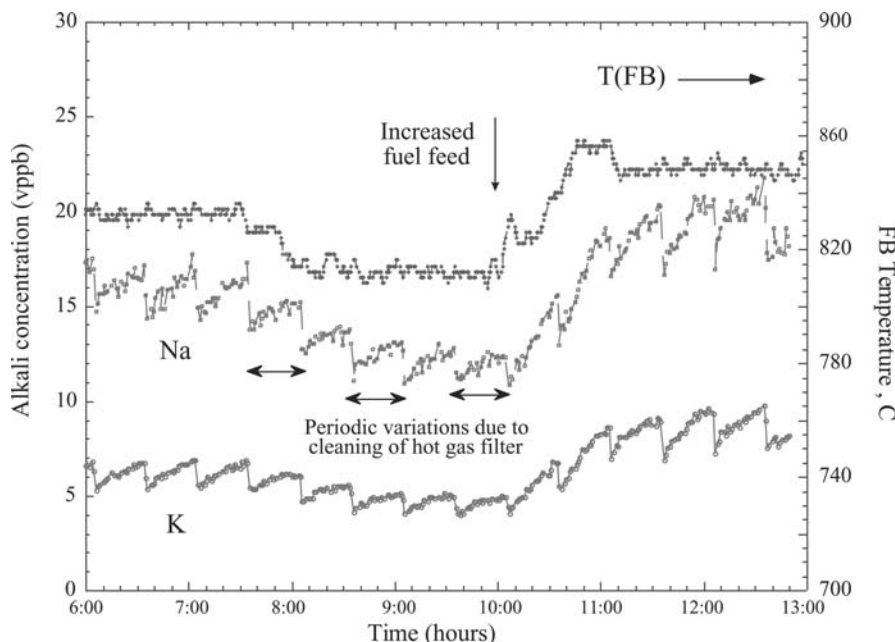


Fig. 18.7. Alkali concentration profile in PCFB flue gas (by courtesy of Monkhouse, P. [12])

There are a number of further LIF-based techniques, like laser-induced tracer fluorescence, laser-induced exciplex fluorescence, etc., which can be applied for the detection of molecules and the visualization of vapors and liquids [13, 14, 15].

References

1. E.W. Rothe, P. Andresen: *Appl. Optics* **36**, 3971–4033 (1997)
2. M. Knapp, A. Luczak, V. Beushausen, W. Hentschel, P. Manz, P. Andresen: “Polarization separated spatially resolved single laser shot multispecies analysis in the combustion chamber of a realistic SI engine with a tunable KrF excimer laser”, in *Twenty-Sixth Symposium on Combustion* (1996), pp. 2589–2596
3. C. Schulz, V. Sick, J. Heinze, W. Stricker: *Appl. Optics* **36**, 3227–3232 (1997)
4. C. F. Hildebrand, E. Schulz, Wagner, V. Sick: *Appl. Optics* **38**, 1452–1458 (1999)
5. R.B. Miles, W. Lempert: *Appl. Phys. B* **51**, 1–5 (1990)
6. T. Müller, G. Grünefeld, V. Beushausen: *Appl. Phys. B* **70**, 155–158 (2000)
7. T. Müller, V. Beushausen, W. Hentschel: “1D spontaneous Raman scattering for comprehensive 2D spray characterization”, in *Eighth International Conference on Liquid Atomization and Spray Systems, Pasadena, CA, USA July* (2000)
8. G. Grünefeld, V. Beushausen, A. Brockhinke, P. Andresen: *AIAA Journal* **35**, 500–508 (1997)
9. S. Böckle, J. Kazenwadel, T. Kunzelmann, D.I. Shin, C. Schulz: *Appl. Phys. B* **70**, 733–735 (2000)
10. M. Knapp: (1997), “UV laser spectroscopy applied to in-cylinder phenomena of spark-ignition engines”, Ph.D. thesis, University of Bielefeld, Cuvillier Verlag, 1997.- ISBN 3-89588-825-7
11. U. Gottwald, P. Monkhouse: *Appl. Phys. B* **69**, 151–154 (1999)
12. V. Ebert, C. Schulz, H.R. Volpp, J. Wolfrum, P. Monkhouse: *Israel J. Chemistry* **38**, 1–3 (1999)
13. M. Knapp, V. Beushausen, W. Hentschel, P. Manz, G. Grünefeld, P. Andresen: *SAE Technical Paper Series* **970827**, 69–85 (1997)
14. M. Knapp, A. Luczak, V. Beushausen, W. Hentschel, P. Andresen: *SAE Technical Paper Series* **961122**, 1–7 (1996)
15. C. Kornmesser, T. Müller, V. Beushausen, W. Hentschel, P. Andresen: “Spectroscopic investigation of mixture formation in a DI-gasoline engine using two different exciplex tracers and model fuels”, in *ILASS Americas, 14th Annual Conference on Liquid Atomization and Spray Systems, Dearborn, MI, May*, (2001)

19 Medical Applications of Excimer Lasers

H. Lubatschowski

Excimer laser radiation, especially at the wavelength of 193 nm , is well suitable for processing biological tissue. Its absorption length is below $0.25\text{ }\mu\text{m}$ and due to the short interaction time of only several nanoseconds, the collateral thermal damage of ArF-laser-ablated tissue is limited to less than 100 nm with a uniformly appearing surface [1, 2]. Micro surgical interventions like refractive surgery of the eye take advantage of this high quality standard. However, due to the poor transmission of 193 nm radiation through optical fibers, endoscopic operations inside the human body are impossible today.

248 nm radiation of KrF lasers shows better transmission, but this wavelength is banned for medical application due to its high mutagenic risk [3, 4]. At 308 nm the mutagenic risk is negligible and fiber transmission is satisfactory. Though the absorbance has decreased by more than one order of magnitude at 308 nm , surgical interventions which allow a thermal damage of some $10\text{ }\mu\text{m}$ are possible applications. The main clinical application for 308 nm radiation is laser angioplasty where occluded vessels are opened by means of photoablation via an optical fiber. Another promising attempt of 308 nm photoablation is an ophthalmological application: The reduction of the intra-ocular pressure on glaucoma surgery.

19.1 Refractive Laser Surgery

Refractive laser surgery, in terms of reshaping the surface of the human cornea with an UV excimer laser has been proposed in 1983 by S. Trokel and R. Srinivasan [5]. In the early nineties first clinically controlled studies were performed [6, 7, 8, 9] and today it is almost a routine surgical procedure, shared into three different methods: PRK, PTK and LASIK.

19.1.1 Photo Refractive Keratectomy (PRK)

The principle of the so-called photo-refractive keratectomy (PRK) is shown in Fig. 19.1. For myopic eyes, where the refractive power of the cornea and

the lens is too strong in relation to the length of the eyeball, the corneal surface will be flattened by ablation of corneal tissue in the center, in order to reduce its refractive power. On the other hand, at the cornea of a hyperopic eye where the refractive power is too low, the surface will be steepened by removing most of the tissue at the edge of the cornea.

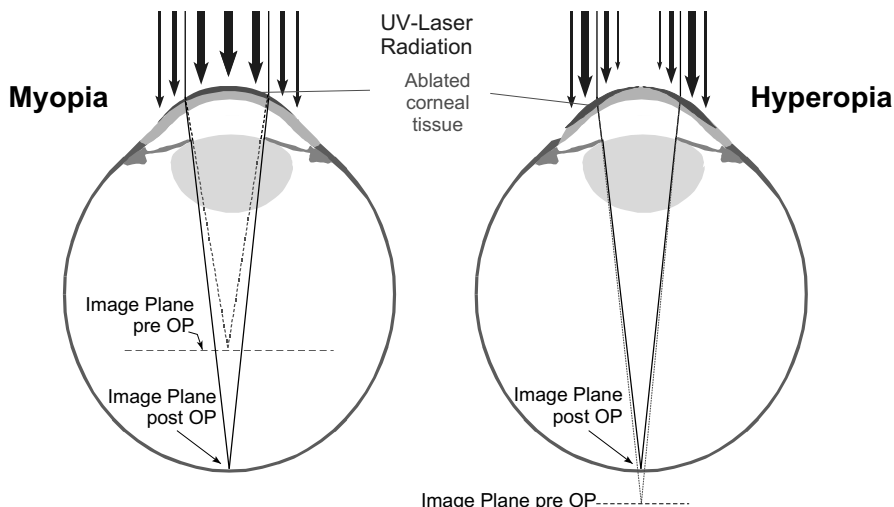


Fig. 19.1. Principle of photo-refractive keratectomy (PRK). On myopic eyes (left), where the refractive power of the cornea and the lens is too strong in relation to the length of the eyeball, the corneal surface will be flattened by ablation of corneal tissue in the center, in order to reduce its refractive power. On the other hand, the cornea of a hyperopic eye (right), where the refractive power is too low, the surface will be steepened by removing most of the tissue at the edge of the cornea.

By shaping the corneal surface to a certain degree on different axes, refractive errors like astigmatism can be corrected. According to the amount of the refractive error, some $10 \mu\text{m}$ as much as $100 \mu\text{m}$ of the superficial layer of the cornea will be removed. At a typical laser fluence of $120 - 180 \text{ mJ/cm}^2$ approximately $0.5 \mu\text{m}$ of corneal tissue will be removed at each laser pulse.

Before the laser treatment starts, a $70 \mu\text{m}$ thick superficial cell layer, the so-called epithelium of the cornea (Fig. 19.2) is removed mechanically. The epithelium is a thin multi layer of cells with a rapid turnover. The cell layers heal up within 24 to 48 hours after removal, in contrast to the underlying corneal stroma, which shows almost no regression after ablation.

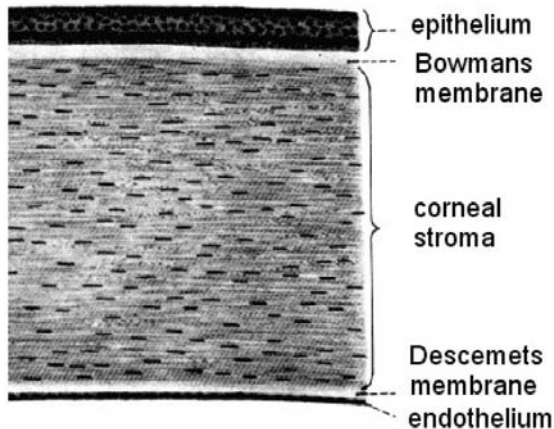


Fig. 19.2. Cross-section of the human cornea. The thickness of the cornea is about $500\ \mu\text{m}$. Before the laser treatment starts, the epithelium is removed mechanically.

The postoperative recovery of the epithelium in combination with the tear film has a smoothing effect. Thus little irregularities in the sub-micrometer scale which will occur during laser processing of the tissue will cause no problems for the visual acuity of the patient's eye.

19.1.2 Photo Therapeutic Keratectomy (PTK)

Besides changing the refraction of the eye, irregularities like corneal scars, injury or a variety of corneal infections can be smoothed down in a certain degree. This procedure is called photo therapeutic keratectomy (PTK) [10].

By applying a protective solution of methylcellulose, similar to artificial tears, the protruding tissue of the corneal irregularities are exposed to the excimer irradiation and ablated. Through controlled applications of a methylcellulose solution, the surgeon can smooth the corneal irregularities, while protecting the adjacent smooth normal corneal tissue.

The first step of the PTK procedure involves the removal of the epithelium. Then, the methylcellulose solution is applied and the excimer laser is used to ablate the exposed corneal tissue (Fig. 19.3). Typically some degree of hyperopia is induced by this process because usually more tissue is removed from the center than from the periphery of the cornea.

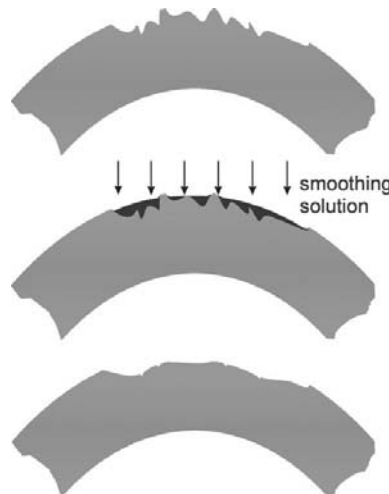


Fig. 19.3. Principle of photo therapeutic keratectomy (PTK). An irregular corneal surface can be smoothed, using an ArF excimer laser. A smoothing agent with similar ablation properties like the corneal tissue (dilute methylcellulose) fills the crevices. This shields the valleys and improves the smoothing process.

19.1.3 Laser In-situ Keratomileusis (LASIK)

At low and medium myopia (up to -6 dpts), PRK stands for a save and established procedure. At higher corrections of the refractive error, however, complications like scar formation and regression occur. This is in the first place caused by a stronger induction of wound healing, induced by the removal of a higher amount of tissue [11]. These difficulties can be avoided by a procedure which was proposed by Pallikaris in the early 90ies [12, 13]. At the so-called ‘laser in-situ keratomileusis’ (LASIK), not the superficial layer of the corneal stroma but the inner part of the cornea will be processed with the ArF excimer laser (Fig. 19.4). For this, a layer with a thickness of approximately $160 \mu\text{m}$ is separated partially by a knife, the so-called micro keratome, and opened. Afterwards corneal tissue will be ablated by the laser, as far as it is necessary to correct the refractive error. Finally, the top lamella will be replaced. This flap joins with the new surface and fits without any joint due to adhesion forces. By means of LASIK, myopic corrections well over -6 dpts can be performed and also hyperopia and astigmatism of more than 4 dpts can be corrected.

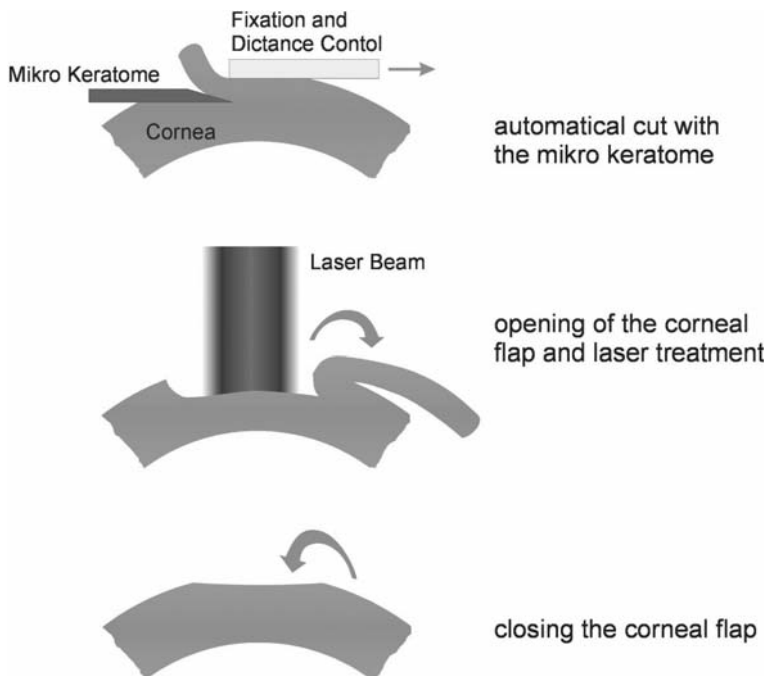


Fig. 19.4. Principle course of laser in-situ keratomileusis (LASIK). A layer with a thickness of approximately $160 \mu\text{m}$ is separated partially using a knife and opened. Afterwards corneal tissue is ablated by applying laser radiation, as far as it is necessary to correct the refractive error. Finally, the top lamella is replaced. This flap joins with the new surface and fits without any joint due to adhesion forces.

19.1.4 Customized Ablation

In the first generation of ArF excimer laser systems a so-called large-area ablation mode was used to shape the corneal surface. In this mode, the excimer laser beam had a flat-top intensity profile, with a diameter corresponding to the treatment zone of the patients eye, which was up to 9 mm.

For myopic treatment, an aperture with increasing diameter was used to flatten the corneal curvature. For hyperopic and astigmatic treatment appropriate diaphragms were implemented into the beam path [14, 15]. In accordance with the principle of beam shaping, which generates only spherical or axial symmetrical ablation profiles, only spherical or regular astigmatic corrections on the eye could be performed. Besides, the so-called central island phenomenon [16, 17, 18, 19] was a typical problem which appeared on myopic treatment. Here, a small central rise in the ground of the ablated corneal stroma remains, leading to a considerable disturbance in the visual acuity of the treated eyes. The corneal central island phenomenon is likely caused by plume dynamics of the expelled ablation products [20, 21].

With increasing reliability and accuracy of the video keratographic systems, which generate a map of the radius of curvature of the patient's eye, the demand for a more flexible delivery system for the corneal shaping laser systems arose. Figure 19.5 shows a typical corneal topography of a patient's eye where the asymmetry in the radius of curvature of the corneal surface is demonstrated.



Fig. 19.5. Corneal topography of a patient's right and left eye. The color code represents the radius of curvature of the corneal surface which indicates the local refractive power. The asymmetry in the radius of curvature of the corneal surface is typical for refractive errors of the eye.

As a consequence, so-called 'flying spot' scanning systems were introduced for clinical application. Here a beam of smaller diameter of less than 2 mm is scanned across the corneal surface. Due to the smaller beam diameter and the flexibility gained by that scanning procedure a variety of irregularities on the corneal surface can be corrected. Figure 19.6 shows the principal setup of such a scanning system, where, as an example, a spiral pattern is used to flatten the radius of curvature of the corneal surface.

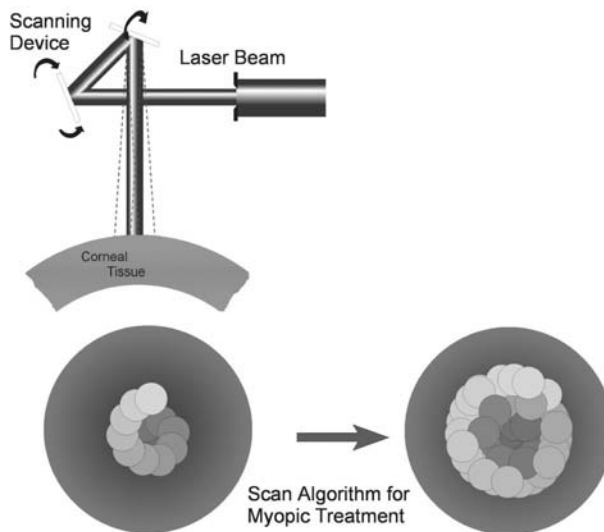


Fig. 19.6. Principal setup of a scanning system, where a spiral pattern is used to flatten the radius of curvature of the cornea

Recent investigations were done to improve the visual acuity of the whole eye by designing the ablation pattern to correct both the spherocylindrical refractive error as well as individual optical aberrations. This so-called customized ablation is based on measurements of the corneal topography [22, 23, 24] or the wavefront deviations when the light passes the cornea and lens by means of an aberrometer [25, 26, 27]. Wavefront optical aberrations usually are induced by the cornea and the lens at the periphery, where their natural shape deviates from the ideal shape.

19.2 Glaucoma Surgery

The front part of the eye contains a fluid called ‘aqueous humor.’ This fluid normally drains away through a sponge-like structure inside the eye, called the trabecular meshwork. If the meshwork becomes impermeable for any reason, the fluid cannot escape and pressure will build up inside the eye, pressing on the optic nerve. As a result the sight of the eye is permanently lost. This disease is called ‘glaucoma’.

One way to relieve the dangerously high pressure in an eye with glaucoma is to open the meshwork by means of photoablation (Fig. 19.7). This is called a trabeculotomy. For this, 308 nm radiation of the XeCl excimer laser is best suited, because the trabecular tissue is ablated without significant thermal damage. The edges of the openings are very smooth, thus only minimal wound healing reactions are induced and the openings will not close again (Fig. 19.8).

Only a few openings (6 – 8) are necessary to reduce the resistance of the outflow and consequently decrease the intra-ocular pressure.

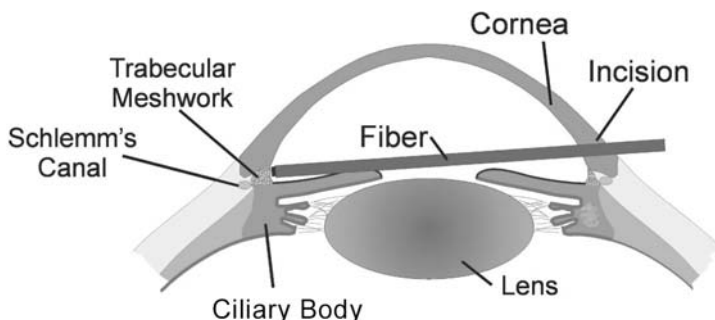


Fig. 19.7. Principle of laser trabeculotomy. 6 – 8 openings of the trabecular mesh-work are necessary to reduce the resistance of the outflow of the aqueous humor to Schlemm's Canal. The openings are created by 308 nm radiation which is delivered through an optical fiber.

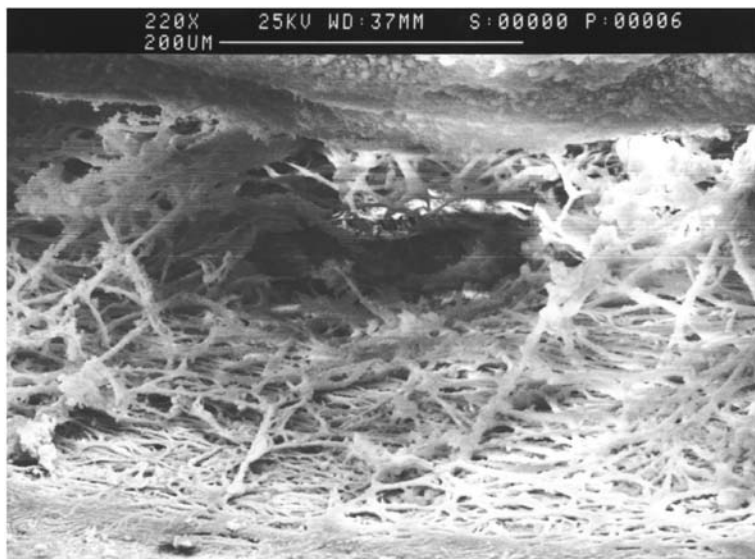


Fig. 19.8. SEM micrograph of a XeCl-laser-induced opening of the trabecular meshwork

19.3 Laser Angioplasty

Angioplasty is a method used to open arteries blocked by plaques. Plaque is a build-up of cholesterol and other fatty molecules inside an artery. Over time, plaques can slow or even stop the flow of the blood. Thus, the normal flow of blood must be retained by cleaning or bypassing the blockage.

Methods for removing plaque from an artery include artery bypass surgery, mechanical removal surgery, balloon angioplasty (Fig. 19.9) and laser angioplasty. Balloon angioplasty is the most frequently applied interventional technique for treatment of coronary artery disease. The method used depends on the location of the plaque, size of the plaque and the number of plaques.

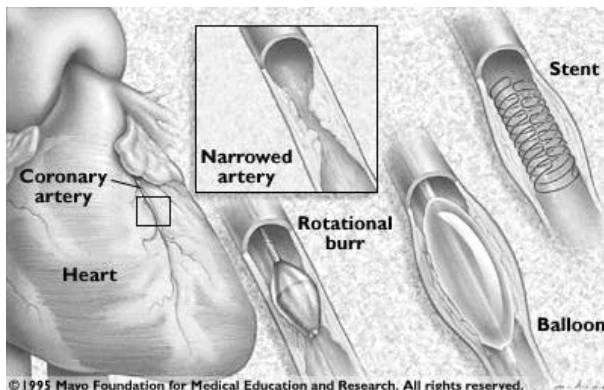


Fig. 19.9. Customary methods for removing plaque from an artery

Excimer laser angioplasty was developed in the early 1980s in an effort to solve two of the limitations of balloon angioplasty, recanalization and restenosis. Laser angioplasty offers the potential for moving a thin tube (a fiberoptic catheter) through the artery to vaporize all plaques along the arterial wall [28, 29, 30]. 308 nm XeCl excimer laser angioplasty today is the laser technique of choice for clinical application. However, even though thermal damage has been sufficiently reduced with this laser, the procedure is still used only in minority of cases as a stand-alone operation due to high-pressure waves and bubble formation caused by excimer laser radiation. Typically, it is used in combination with balloon angioplasty. When a plaque has totally blocked an artery, the laser can drill a hole in the plaque, so the balloon angioplasty can be successfully performed. Therefore, laser angioplasty has become a safe and a cheap alternative for expensive bypass open-heart surgery.

19.4 XeCl Excimer Laser Treatment of Psoriasis

Psoriasis is a persistent skin disease. The skin becomes inflamed, producing red, thickened areas with silvery scales, most often on the scalp, elbows, knees, and lower back. Extremely, severe psoriasis covers large areas of the body. In the United States four to five million people suffer from psoriasis. Approximately 150,000 new cases occur each year.

UV-B photo therapy is a well-established form of treating psoriasis that generally requires up to 30 treatments to produce clearing. The 308 nm excimer laser offers a new, effective approach to treat localized psoriasis [31]. With an appropriate scanning device only the psoriasis plaques are treated and high initial UV-B doses can be applied. Compared with standard UV-B photo therapy fewer treatments with the excimer laser are necessary.

An other important advantage of photo therapy over other therapies is that after clearing of the plaques, the lesions may remain clear without further therapy for a long period [32, 33, 34, 35].

Up to now, 308 nm excimer laser treatment appears to offer relapse-free periods for localized psoriasis that are comparable or better than that offered by standard topical therapy treatment. However, further data are needed to determine how the excimer laser remission rate may be maximized in order to provide patients good long-term control of their disease.

References

1. J. Marshall, S. Trokel, S. Rothery, H. Schubert: Ophthalmology **92**, 749–758 (1985)
2. M.G. Kerr-Muir, S.L. Trokel, J. Marshall, S. Rothery: Am. J. Ophthalmol. **103**, 448–453 (1987)
3. H. Green, J. Boll, J.A. Parrish, I.E. Kochevar, A.R. Oseroff: Cancer Res. **47**, 410–413 (1987)
4. C. Jones, E. Huberman, M. Cunningham, M. Peak: Radiat. Res. **110**, 244–254 (1987)
5. S.L. Trokel, R. Srinivasan, B. Braren: Am. J. Ophthalmol. **96**, 710–715 (1983)
6. M.B. McDonald, J.M. Frantz, S.D. Klyce, R.W. Beuerman, R. Varnell, C.R. Munnerlyn, T.N. Lapham, B. Salmeron, H.E. Kaufman: Arch. Ophthalmol. **108**, 799–808 (1990)
7. T. Seiler: Ophthalmologe **92**(4), 379–384 (1995)
8. T. Seiler, P.J. McDonnell: Surv. Ophthalmol. **40**(2), 89–118 (1995)
9. W. Verdon, M. Bullimore, R.K. Maloney: Archives of Ophthalmology **114**(12), 1465–1472 (1996)
10. W. Forster, U. Atzler, I. Ratkay, H. Busse: Graefes Arch. Clin. Exp. Ophthalmol. **235**(5), 296–305 (1997)
11. C.P. Lohmann, E. Hoffmann, U. Reischl: Ophthalmologe **95**(2), 80–87 (1998)
12. I.G. Pallikaris, M.E. Papatzanaki, E.Z. Stathi, O. Frenschock, A. Georgiadis: Lasers Surg. Med. **10**(5), 463–468 (1990)
13. I.G. Pallikaris, D.S. Siganos: J. Refract. Corneal Surg. **10**(5), 498–510 (1994)

14. E. Schröder, M.U. Dardenne, T. Neuhann, A. Tenner: Am. J. Ophthalmol. **103**(3), 472–473 (1987)
15. T.N. Clapham, J. D'Arcy, L. Bechtel, H. Glockler, C.R. Munnerlyn, P.J. McDonnel, J. Garbus: “Analysis of an adjustable slit design for correcting astigmatism”, in *Proc. SPIE* **1423** (1991), pp. 2–7
16. A. Castillo, F. Romero, J.A. Martin-Valverde, D. Diaz-Valle, N. Toledano, O. Sayagues: Journal of Refractive Surgery **12**(6), 715–720 (1996)
17. N.F. Krueger R. R. Saedy, P.J. McDonnell: Archives of Ophthalmology **114**(4), 377–381 (1996)
18. E.E. Manche, R.K. Maloney, R.J. Smith: Journal of Cataract and Refractive Surgery **24**(4), 464–470 (1998)
19. G. Lafond, L. Solomon: Journal of Cataract and Refractive Surgery **25**(2), 188–196 (1999)
20. J. Noack, R. Tönnies, K. Hohla, R. Birngruber, A. Vogel: “Central-Islands in excimer-PRK: The influence of ps-time-scale ablation dynamics”, in *Gordon Research Conference on “Lasers in Medicine and Biology”*, Meriden, NH, USA (1996)
21. C. Dörbecker, H. Lubatschowski, S. Lohmann, C. Ruff, O. Kermani, W. Ertmer: “Influence of the ablation plume on the removal process during ArF-excimer laser photoablation”, in *Proc. SPIE* **2632** (1996), pp. 2–9
22. D.T. Lin: Ophthalmology **101**(8), 1432–1439 (1994)
23. S.J. Coopender, S.D. Klyce, M.B. McDonald, M.W. Doubrava, C.K. Kim, A.L. Tan, S. Srivannaboon: Journal of Cataract and Refractive Surgery **25**(5), 674–684 (1999)
24. D. Dausch, E. Schroeder, S. Dausch: Journal of Refractive Surgery **16**(1), 13–22 (2000)
25. J. Schwiegerling, R.W. Snyder: Journal of Cataract and Refractive Surgery **26**(2), 214–221 (2000)
26. S. MacRae, J. Schwiegerling, R.W. Snyder: Journal of Refractive Surgery **15**(2 Suppl.), 246–248 (1999)
27. M. Mrochen, M. Kaemmerer, T. Seiler: Journal of Refractive Surgery **16**(2), 116–121 (2000)
28. K. Haase, K. Karsch: Z Kardiol **85**(Suppl. 1), 81–86 (1996)
29. T. Leeuwen, E. Jansen, A. Welch, C. Borst: Lasers Surg. Med. **18**(4), 381–390 (1996)
30. T. Leeuwen, E. Velema, G. Pasterkamp, M. Post, C. Borst: Lasers Surg. Med. **23**(3), 128–140 (1998)
31. P. Asawanonda, R.R. Anderson, Y. Chang, C.R. Taylor: Arch. Dermatol. **136** (2000)
32. S.A. Muller, H.O. Perry: “The Goeckerman treatment in psoriasis: six decades of experience at the Mayo Clinic”, Cutis, 265–268 (1987)
33. J.G. Kreuger, J.T. Wolfe, R.T. Nabeya, V.P. Vallat, P. Gilleaudau, N.S. Heftler, L.M. Austin, A.B. Gottlieb: J. Exp. Med. **182**, 2057–2068 (1995)
34. T.R. Coven, I.B. Walters, I. Cardinale, J.G. Kreuger: Photodermatol. Photoimmunol. Photomed. **15**, 22–27 (1999)
35. J. Koo, M. Lebwohl: J. Am. Acad. Dermatol. **41**, 51–59 (1999)

20 High-Intensity Applications of Excimer Lasers

Alex B. Borisov, Jack Davis, Keith Boyer, and Charles K. Rhodes

20.1 Introduction

A key high-intensity application of excimer lasers has been the study of nonlinear interactions at ultraviolet wavelengths in atoms, molecules, and plasmas. A principal outcome of this research has been the demonstration of saturated amplification in the multikilovolt ($\sim 4230\text{--}4570\text{ eV}$) X-ray regime that arises from the ability to produce and controllably combine two new highly ordered forms of excited matter, hollow atoms and stable electronically hollow plasma channels. Over an intensity range spanning $\sim 10^{14}\text{--}10^{20}\text{ W/cm}^2$, this article reviews the main experimental and theoretical advances made over the past two decades in relation to the realization of this new X-ray source whose peak brightness is sufficient for the implementation of a new high-resolution technology for biological micro-imaging.

20.2 Précis of Experimental Findings

20.2.1 Anomalous Nonlinear Coupling to Atoms at 193 nm

The evaluation of the nonlinear coupling of intense coherent radiation to atoms is a central issue that has undergone extensive experimental and theoretical examination. The principal findings of the initial studies [1] with atoms (X) of collision-free multiphoton processes of the form

$$n\gamma + X \rightarrow X^{q^+} + qe^- \quad (20.1)$$

with 193 nm radiation were (1) an unexpectedly large rate for high-order amplitudes ($n \gg 1$) and (2) a coupling strength that was dramatically enhanced at higher Z values. These features of the data are illustrated in Fig. 20.1. In particular, the magnitude of the total energy which could be communicated to the atomic systems, especially for high-Z materials, was viewed as entirely anomalous. In the case of uranium, the total energy transfer observed in the ionization channel was $\sim 633\text{ eV}$ for the production of U^{10^+} from the neutral

atom, a value equivalent to 99 quanta. The magnitude of this energy transfer represented by far the highest value reported for a collision-free nonlinear process at that time. We note further that the removal of only the tenth electron from uranium, which requires $\sim 133\text{ eV}$ if viewed as an independent sequential process ($U^{9+} \rightarrow U^{10+} + e^-$), is also quite strong, since it requires a minimum of 21 quanta.

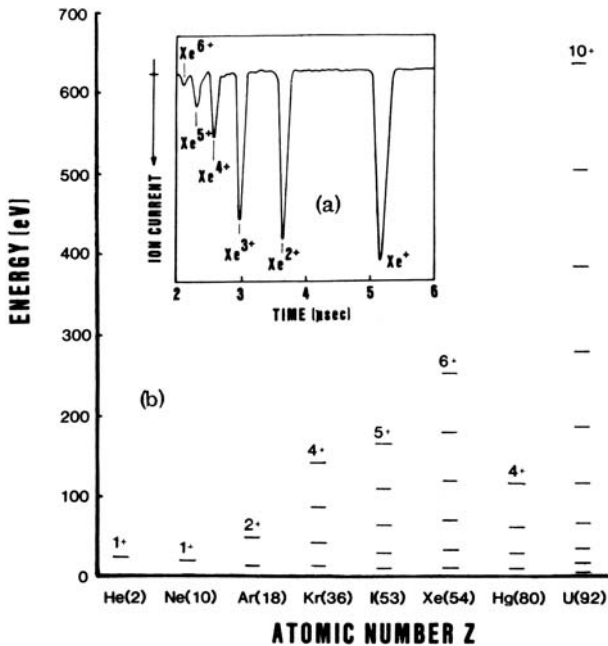


Fig. 20.1. Data concerning the multiple ionization of atoms under 193 nm irradiation at $\sim 10^{14}\text{ W/cm}^2$. (a) Inset: typical time-of-flight ion current signal for xenon. (b) Plot of total ionization energies of the observed charge states as a function of atomic number (Z). Figure taken from Ref. [1].

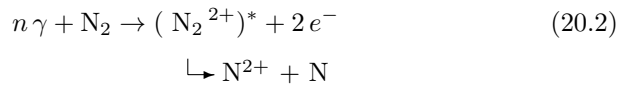
The coupling strength implied by both the high transition rates and the large size of the energy transfer observed at the relatively low intensity of $\sim 10^{14}\text{ W/cm}^2$ used in this study very substantially surpassed the magnitude characteristic of conventional theoretical treatments of multi-quantum ionization [1]. Basically, these results indicated (a) that some important consideration was being overlooked in the evaluation of the coupling strength and (b) that energy transfers in the kilovolt region could probably be reached in an appropriate system. The leading theoretical hypothesis [2, 3] stimulated by these findings involved an ordered driven motion of weakly bound electrons as the physical basis of the enhanced coupling.

The work on multiphoton ionization also led to two key predictions [4], both of which have been realized. They are (a) "that stimulated, emission in the X-ray range can be produced by direct, highly nonlinear coupling of

ultraviolet radiation to atoms" and (β) "that the coherence of the radiative environment can act to introduce a measure of control on the energy transfer that will enable considerable selectivity on the energy flow to be achieved."

20.2.2 Direct Multiquantum Inner-Orbital Excitation of N₂ at 248 nm

Historically, examinations of molecular structure and interactions have been valuable sources of information on electromagnetic interactions that have complemented corresponding studies of atoms. In the case of nonlinear processes, work on ion production [5] at 248 nm with N₂ had indicated the strong presence of the charge asymmetric dissociative channel



arising as a consequence of the multiphoton ionization. Since other experiments [6] examining soft X-ray produced fragmentation of N₂ showed that process (2) corresponds to the production of a two-hole state having an excitation energy of $\sim 70\text{ eV}$, the obvious implication was that the laser excitation produced a similar configuration of molecular excitation. The states [7, 8] implicated in the X-ray studies [6] of N₂, which has the ground-state configuration $(1\sigma_g)^2(1\sigma_u)^2(2\sigma_g)^2(2\sigma_u)^2(1\pi_u)^4(3\sigma_g)^2$, were the ${}^1\Sigma_g(2\sigma_g^{-1}, 3\sigma_g^{-1})$, ${}^1\Sigma_u(2\sigma_g^{-1}, 2\sigma_u^{-1})$ and ${}^1\Pi_u(2\sigma_g^{-1}, 1\pi_u^{-1})$ levels, all involving a $2\sigma_g$ hole. We note that the $2\sigma_g$ orbital has a binding energy of 37.7 eV , a value considerably higher than the $2\sigma_u$, $1\pi_u$, and $3\sigma_g$ orbitals. Therefore, the N₂²⁺ states having a $2\sigma_g$ vacancy and correlating to the N²⁺+N asymptote have an energy substantially above the lowest manifold of states [9] in N₂²⁺ that are associated with the symmetric N⁺+N⁺ limit.

Spectral observations of fluorescence in the 7–79 nm range were made [10] to gain additional information on the mechanism of excitation leading to the N²⁺+N channel and, by implication, the production of the $2\sigma_g$ hole. The spectral resolution of the spectrometer-detector system used was less than 0.1 nm full width at half maximum (FWHM). Typical target gas densities, produced with a pulsed valve, ranged from $10^{18} - 6 \times 10^{19}\text{ cm}^{-3}$. The source used for excitation was a subpicosecond ($\sim 600\text{ fs}$) KrF* (248 nm) system. The peak intensities produced by the focusing lens used in these experiments was estimated to be in the $10^{16} - 10^{17}\text{ W/cm}^2$ range, a value which corresponds to a field strength on the order of one atomic unit (e/a_0^2).

The chief result of these measurements was the identification of the anomalous 55.8 nm feature that is shown in Fig. 20.2. The spectrum in this range has several salient characteristics; the 55.8 nm line has (i) a characteristic frequency that does not match *any* known transition arising from an atomic [11], molecular [8], or ionic [11] species; (ii) an anomalously large

linewidth ($\sim 0.3 \text{ nm}$ FWHM); and (iii) an integrated intensity comparable to the strongest lines observed throughout the entire spectral region (7–79 nm) studied. The anomaly associated with the 55.8 nm transition was underlined by the fact that N₂ has undergone extensive spectroscopic study with many modalities of excitation for approximately a century, an experimental history that makes the discovery of a strong and previously unobserved transition extremely unusual. Consequently, these results pointed to the existence of a new mechanism that enabled the direct multiphoton excitation of inner-shell electrons in molecules.

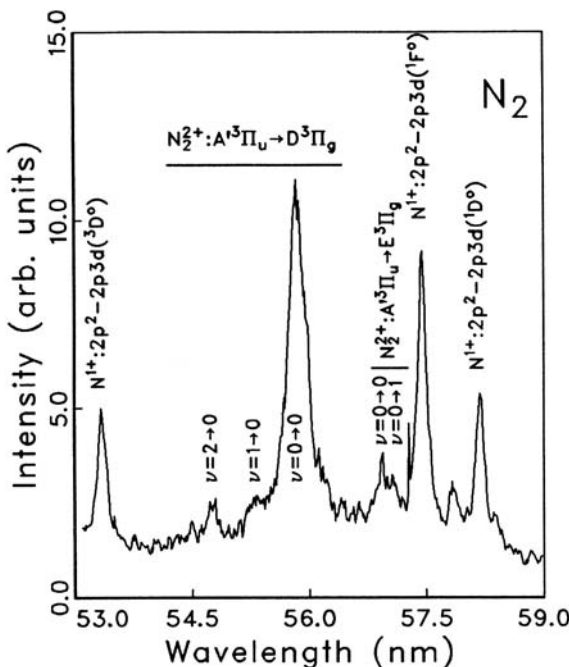


Fig. 20.2. The spectrum observed in N₂ in the 56 nm region produced with intense subpicosecond ($\sim 600 \text{ fs}$) 248 nm irradiation. Two groups of molecular features are identified, including the main transition at 55.8 nm attributed to N₂²⁺, as well as several atomic lines. The density of N₂ used was $\sim 10^{19} \text{ cm}^{-3}$. Figure taken from Ref. [10].

The key to the understanding of the spectrum shown in Fig. 20.2 is the presence of a 2 σ_g hole. The outcome of the spectral analysis of the fluorescence [10], which was based on a concordance of spectroscopic evidence, gave the potential energy diagram shown in Fig. 20.3. Since the original clues for the presence of the 2 σ_g hole were provided by the Auger work [6], we present an interpretation of the spectrum that commences with those results. The Auger process starts with the removal of a 1 σ_g electron, an orbital that is highly lo-

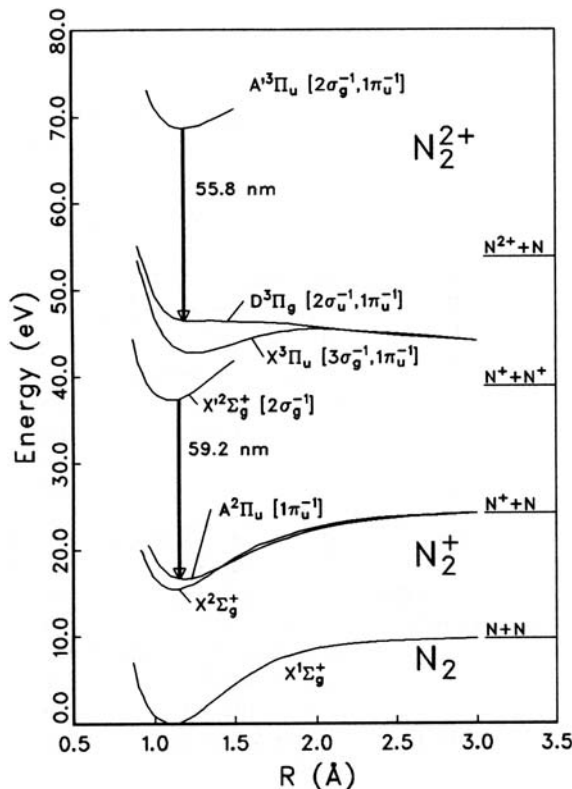
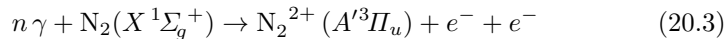


Fig. 20.3. Potential energy curves for N_2 for selected states of interest. Two observed transitions [10] involving a $2\sigma_g$ hole are indicated. In order to construct those curves, data were taken from a variety of sources (Refs. [7, 8, 9]) as well as the authors' own estimates. Dissociation limits are given for reference. Figure taken from Ref. [10].

calized. Since the Auger effect arises from a direct coulombic electron-electron interaction, it is reasonable to assume, at least for some channels, that the second electron ejected in the Auger process is similarly localized, leading to an asymmetric charge distribution. Thus, we can make a connection of the Auger amplitude with the multiphoton process through the association of the excited states with the charge asymmetric asymptote ($\text{N}_2^+ + \text{N}$). The common feature is the $2\sigma_g$ vacancy in the final state of the two interactions. The Auger process has some specificity in that singlet states are generally more likely to be populated than triplets, a property that can be related to the exchange interaction. The multiphoton process, however, is not affected by this property of the electronic wave functions and can efficiently populate both singlet and triplet upper states, leading to ion fragments characteristic of Auger events *and* radiation connected to the quasibound triplet states. In this case [10], it was found that the triplet levels were the important ones.

The conclusion of this work on N₂ had a profound influence on the direction of future work and the eventual ability to produce amplification in the X-ray region. Basically, an entirely new band of radiation at 55.8 nm had been observed from transitions involving *inner orbitals* in N₂²⁺ produced by a *direct* multiphoton process involving N₂ in a reaction of the form



The asymmetry of the excited (N₂²⁺)^{*} state showed that the mechanism had a strong charge-transfer character. Moreover, this observation was clear evidence that deeply bound electrons, in this case 2σ_g, can be directly excited by strong-field processes *without* extensive loss of the more weakly bound outer valence electrons. The retention of the outer electrons conferred on the excited state the ability to emit a *prompt* quantum to fill the 2σ_g hole. With the inauguration of a new molecular state of N₂ designated as A'³Π_u, the transition giving rise to the 55.8 nm emission was identified as A'³Π_u → D³Π_g in which the lower level is sufficiently flat that only a single vibrational state (v' = 0) is supported. The upper A'³Π_u state has a *double-hole* (2σ_g⁻¹, 1π_u⁻¹) configuration, a vibrational quantum of 1900 ± 100 cm⁻¹, an estimated radiative lifetime of ∼100 ps, and an equilibrium internuclear separation of ∼1.2 Å. Finally, the picture that emerged concerning the nature of the levels involved in the 55.8 nm emission indicated that (a) the binding characteristics of the two levels, specifically, the attraction in the upper state and the repulsion in the lower state, and (b) the presence of a large transition moment are both direct consequences of the charge-transfer character of the transition. This situation is exactly analogous [12] to the rare-gas-halogen excimers such as KrF*.

20.2.3 Hollow Atoms and the Cluster Concept

The work described above on the N₂ system (1) conclusively demonstrated that inner-shell electrons could be ejected while a substantial number of outer electrons remained bound and (2) revealed that molecules are highly appropriate systems for this mode of multiphoton interaction as a consequence of the charge-transfer mechanism. These results led quickly to a new general molecular concept. Specifically, they suggested the possibility of *designing* a new class of molecular materials *optimized* for the efficient production and amplification of X-rays [13]. This idea was immediately tested with Xe clusters [14] with the outcome that the copious production of Xe hollow atom states [15, 16, 17] emitting both Xe(M) and Xe(L) radiation in the kilovolt spectral region [14] was observed. These data confirmed that the selective excitation of the inner-shell states initially observed in N₂ could be scaled into the multikilovolt spectral region. A good example [14, 17] is given by the characteristic Xe(L) 3d → 2p hollow atom emission profile centered at

$\lambda \sim 2.8 \text{ \AA}$ shown in Fig. 20.4. “Hollow atoms” are atoms (ions) that intrinsically possess an “inverted” electronic configuration consisting of deeply bound inner-shell vacancies, perhaps multiple, with the simultaneous retention of several electrons in relatively weakly bound outer orbitals [15, 16, 17]. Accordingly, these states are optimally suited for the prompt emission and amplification of X-rays.

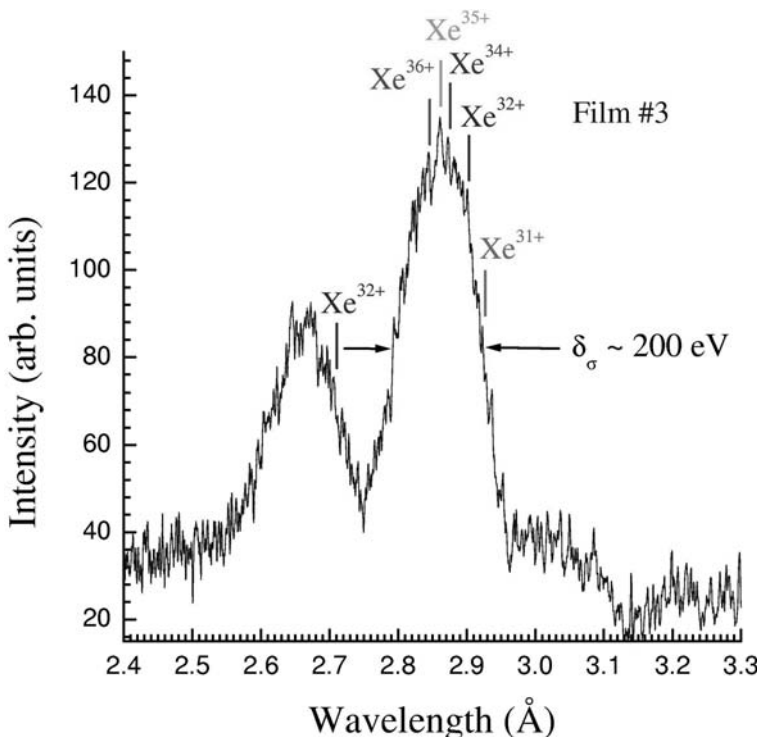


Fig. 20.4. Characteristic spontaneous emission profile of the $\text{Xe}(\text{L})$ $3d-2p$ hollow atom spectrum (film #3) produced from Xe clusters with intense ($\sim 10^{19} \text{ W/cm}^2$) femtosecond 248 nm excitation. The splitting between the major and minor lobes arises from the spin-orbit interaction of the $2p$ vacancy. The full width of the main feature is $\delta_{\sigma} \sim 200 \text{ eV}$. The positions of selected charge state transition arrays (Xe^{31+} , Xe^{32+} , Xe^{34+} , Xe^{35+} , and Xe^{36+}) are indicated. The spectral resolution of these film data is $\sim 4 \text{ eV}$. Figure taken from Ref. [18].

An important outcome of these studies on Xe clusters was preservation of the basic initial conclusion [2] that ordered electronic motions were necessary to explain the anomalously high energy transfer rate and the inner-shell selectivity [19, 20].

20.2.4 Multikilovolt X-ray Amplification with Clusters in Self-Trapped Plasma Channels

Given the results observed with N₂ and the Xe clusters, a new way to amplify X-rays became possible. However, the implementation of this possibility required an additional ingredient, namely, a method to control spatially the excited material. Fundamentally, in order to achieve significant amplification in the multikilovolt spectral region, the ability to produce high power compression ($\sim 10^{19}\text{--}10^{20}\text{ W/cm}^3$) controllably in *appropriately configured material* is the difficult and key requirement.

The solution to this fundamental power compression issue and its spatial organization was found in the alliance of two phenomena. They are (a) the direct multiphoton excitation of hollow atoms from clusters with ultraviolet radiation, described in Section 20.2.3 above, and (b) a nonlinear mode of stable confined propagation in plasmas resulting from a relativistic/charge-displacement mechanism of self-channeling [21, 22]. Basically, with this combination [23], the concept for amplification is founded on the proper matching [18] of the cluster excitation with the channeling process and the characteristics of the confined electromagnetic propagation. Consequently, the amplification proceeds through the *creation of an excited and highly ordered state* that is comprised of four mutually coupled components; namely, atomic (ionic) matter, plasma electrons, and two coherent radiative fields. The high stability of the plasma channel [22, 24] and its ability to guide [18] both the ultraviolet (248 nm) and X-ray (2.8 Å) waves are essential features of this complex excited state. Since this dynamical mechanism enables the energy transfer (1) to be confined to a small fraction of the available phase space and (2) to occur through a radiation-dominated interaction, both (α) the potential for high efficiency and (β) the ability to control the spectrum of effective X-ray amplification are conferred on the system. It is this combination of factors that leads to the high amplifications observed [18, 25].

A spectrum typical of the X-ray beam axially amplified in the narrow plasma channel and recorded on film with a von Hámɒ spectrograph is illustrated in Fig. 20.5. In this case, the strongly enhanced lines observed correspond to the Xe³⁰⁺, Xe³¹⁺, and Xe³²⁺ charge state arrays of the major lobe shown in Fig. 20.4. This observation, along with additional spectra showing comparable results on several other transition arrays in the $\lambda \sim 2.71\text{--}2.93\text{ \AA}$ region, indicate that the hollow-atom states are strongly inverted and that the amplification can be tuned across a substantial fraction of the spectral profile illustrated in Fig. 20.4. An estimate of the peak spectral brightness achieved in the initial experiments [18] gave a value of $\sim 10^{31}\text{--}10^{32}\text{ photons} \cdot s^{-1} \cdot mm^{-2} \cdot mr^{-2} (0.1\% \text{ bandwidth})^{-1}$, a range approaching that required for single-molecule imaging in living biological material [26, 27, 28].

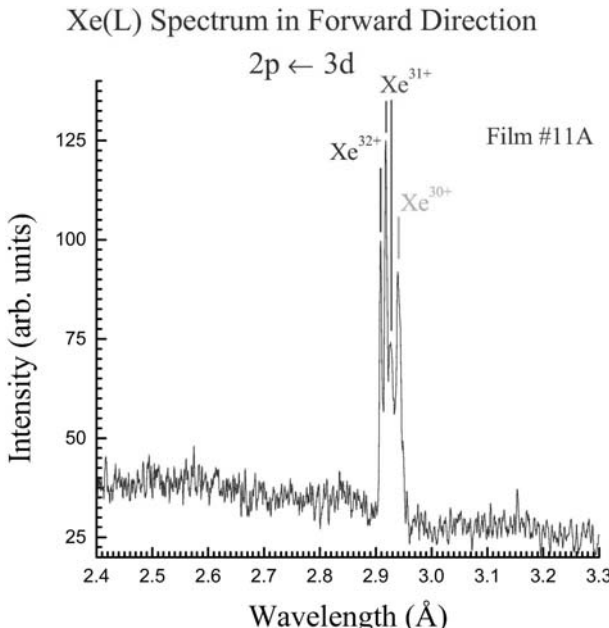


Fig. 20.5. Axially amplified lines corresponding to the Xe^{30+} , Xe^{31+} , and Xe^{32+} $3d \rightarrow 2p$ transition arrays observed (film #11A) with a von Hámós spectrograph equipped with Kodak RAR 2492 film. The emission originates from a self-trapped plasma channel generated by the intense ($10^{19} - 10^{20} \text{ W/cm}^2$) femtosecond 248 nm pulses that provide the excitation of the Xe(L) hollow atom states from the xenon clusters. Figure taken from Ref. [25].

20.3 Conclusions

The organized study of high-intensity interactions with ultraviolet excimer lasers on atoms, molecules, and plasmas over the last 20 years culminated in the ability to produce new forms of matter that are both highly excited and highly ordered [29]. A leading consequence is the capacity to achieve saturated X-ray amplification in the multikilovolt regime to peak brightness figures sufficient for the implementation of new modalities of micro-imaging. Basically, the amplification proceeds through the creation of a highly ordered excited state [18, 25] that is comprised of four mutually coupled components; namely, atomic (ionic) matter, plasma electrons, and two coherent radiative fields, specifically, the ultraviolet and X-ray waves. The chief consequence is energy flow conducted through a radiation dominated interaction that is confined to a small phase space volume.

Acknowledgements

Support for this research was partially provided under contracts with the Army Research Office (DAAG55-97-1-0310) and the Department of Energy at the Sandia National Laboratories. Sandia is a multiprogram laboratory operated by the Sandia Corporation, a Lockheed Martin Company, for the United States Department of Energy under contract no. DE-AC04-94AL85000. Correspondences should be addressed to C.K.R. (e-mail: rhodes@uic.edu).

References

1. T.S. Luk, H. Pummer, K. Boyer, M. Shahidi, H. Egger, C.K. Rhodes: Phys. Rev. Lett. **51**, 110 (1983)
2. K. Boyer, C.K. Rhodes: Phys. Rev. Lett. **54**, 1490 (1985)
3. A. Szöke, C.K. Rhodes: Phys. Rev. Lett. **56**, 720 (1986)
4. C.K. Rhodes: Science **229**, 1345 (1985)
5. K. Boyer, T.S. Luk, J.C. Solem, C.K. Rhodes: Phys. Rev. A **39**, 1186 (1989)
6. W. Eberhardt, E.W. Plummer, I.-W. Lyo, R. Carr, W.K. Ford: Phys. Rev. Lett. **58**, 207 (1987)
7. H. Ågren: J. Chem. Phys. **75**, 1267 (1981)
8. A. Lofthus, P.H. Krupenie: J. Phys. Chem. Ref. Data **6**, 113 (1977)
9. R.W. Wetmore, R.K. Boyd: J. Phys. Chem. **90**, 5540 (1986)
10. G. Gibson, T.S. Luk, A. McPherson, K. Boyer, C.K. Rhodes: Phys. Rev. A **40**, 2378 (1989)
11. R.L. Kelly: J. Phys. Chem. Ref. Data **16**, (Suppl. No. 1) (1987)
12. C.K. Rhodes (Ed.): *Excimer Lasers*, 2nd edn. (Springer-Verlag, Berlin/Heidelberg, 1984)
13. A. McPherson, T.S. Luk, B.D. Thompson, K. Boyer, C.K. Rhodes: Appl. Phys. B **57**, 337 (1993)
14. A. McPherson, B.D. Thompson, A.B. Borisov, K. Boyer, C.K. Rhodes: Nature **370**, 631 (1994)
15. H. Winter, F. Aumayr: J. Phys. B **32**, R39 (1999)
16. N. Vaeck, J.E. Hansen, P. Palmeri, P. Quinet, N. Zitane, M. Godefroid, S. Fritzsche, N. Klystra: Physica Scripta **T95**, 68 (2001)
17. M.W. Clark, D. Schneider, D. DeWitt, J.W. McDonald, R. Bruch, U.I. Safranova, I.Y. Tolstikhina, R. Schuch: Phys. Rev. A **47**, 3983 (1993)
18. A.B. Borisov, X. Song, F. Frigeni, Y. Koshman, Y. Dai, K. Boyer, C.K. Rhodes: J. Phys. B **36**, 3433 (2003)
19. K. Boyer, C.K. Rhodes: J. Phys. B **27**, L633 (1994)
20. W.A. Schroeder, T.R. Nelson, A.B. Borisov, J. Longworth, K. Boyer, C.K. Rhodes: J. Phys. B **34**, 297 (2001)
21. A.B. Borisov, A.V. Borovskiy, V.V. Korobkin, A.M. Prokhorov, O.B. Shiryaev, X.M. Shi, T.S. Luk, A. McPherson, J.C. Solem, K. Boyer, C.K. Rhodes: Phys. Rev. Lett. **68**, 2309 (1992)
22. A.B. Borisov, J.W. Longworth, K. Boyer, C.K. Rhodes: Proc. Natl. Acad. Sci. USA **95**, 7854 (1998)

23. A.B. Borisov, A. McPherson, B.D. Thompson, K. Boyer, C.K. Rhodes: *J. Phys. B* **28**, 2143 (1995)
24. A.B. Borisov, S. Cameron, Y. Dai, J. Davis, T. Nelson, W.A. Schroeder, J.W. Longworth, K. Boyer, C.K. Rhodes: *J. Phys. B* **32**, 3511 (1999)
25. A.B. Borisov, X. Song, Y. Koshman, Y. Dai, K. Boyer, C.K. Rhodes: *J. Phys. B* **36**, L285 (2003)
26. J.C. Solem, G.C. Baldwin: *Science* **218**, 229 (1982)
27. K. Boyer, J.C. Solem, J.W. Longworth, A.B. Borisov, C.K. Rhodes: *Nature Medicine* **2**, 939 (1996)
28. R. Netze, R. Wouts, D. van der Spoel, E. Weckert, J. Hajdu: *Nature* **406**, 752 (2000)
29. G. Marowsky, C.K. Rhodes: *Neue Zürcher Zeitung* **254**, 42 (1995)

21 High-Repetition-Rate Applications of Excimer Lasers

R. F. Delmdahl, L. Herbst, B. Nikolaus

21.1 Introduction

A decade of steady improvements as to reliability and simplicity of operation as well as components longevity has changed the excimer laser from an essentially scientific light source to a true mass production tool. Despite the widespread industrial use of CO₂- and solid-state-lasers, excimer lasers are still the most powerful lasers at shortest commercially available wavelengths below 351 nm down to 157 nm. Apart from specific high-end excimer lasers designed for microlithographic chip production at up to 4 kHz repetition rate [1], common excimer-laser-based processing systems work in various fields of application at several hundred millijoules of energy with only moderate repetition rates of up to 300 Hz. Nonetheless, upcoming technologies demand for significantly higher repetition rates between 500 Hz and several kilohertz. In parallel, for these applications low to moderate pulse energies in the order of 10 mJ are sufficient or even at the process limit.

One of the main requirements resulting in the demand for a combination of high repetition rate with low pulse energy is the better dose energy stability which is achievable during the illumination of a substrate. From a statistical viewpoint, it is of advantage to apply the total amount of energy within a series of numerous pulses with lower energy rather than having the entire energy amount provided by one single pulse of high energy. While the high repetition rate basically saves processing time, the moderate pulse energy can be extracted from much more compact laser tubes and dimensions. Accordingly, compact, high repetition rate excimer lasers with moderate pulse energies represent both enabling and affordable tools for efficient mask and wafer inspection systems in chip manufacturing or rapid data accumulation in optical materials and coatings testing. Recently, material processing approaches based on spatial light modulation or excimer laser scanning have shown the capability to leverage the combined effects of high repetition rate and moderate energy together with the well known advantages of the record-short wavelengths of excimer lasers [2, 3].

21.2 Technological Advances

21.2.1 Solid-State Pulsed High-Voltage Switch

One of the very important technological aspects of an excimer laser is the layout of its electrical discharge circuit involving capacitors for energy storage and transfer, preionization arrangement as well as a high-voltage switching module. Conventional high-pulse-energy excimer lasers incorporate thyratrons in their electrical circuits capable of high-voltage switching at up to 32 kV within several nanoseconds. With regard to an enhancement of the lifetime of stressed electrical components, the introduction of the magnetic switch control (MSC) technology 20 years ago eliminated detrimental current reversal in the pulsed power circuit. By now, thousands of excimer lasers have been installed with MSC technology achieving typical thyratron lifetimes of a billion pulses range. Thyratron-based pulsed excimer lasers doubtlessly offer advantages for mostly scientific low-to-moderate repetition rate applications. Especially the relatively small time delay between electrical trigger signal and emitted light pulse associated with very low temporal jittering of only about 2 ns (1σ) facilitates multi-laser synchronized experimental setups, as of relevance, e. g. in pump-probe laser spectroscopic investigations [4]. However, for applications of 500 Hz and above and increasing duty cycle operation, even an MSC-protected thyratron represents the limiting factor for system lifetime. At 2 kHz repetition rate, for example, costly thyratron replacement would have to be performed every four weeks. The key to solve this lifetime issue was the advent of a technological change from classical thyratron to solid-state high-voltage switching. A solid-state switch module (Fig. 21.1) essentially consists of magnetic isolation (A), low voltage semiconductor

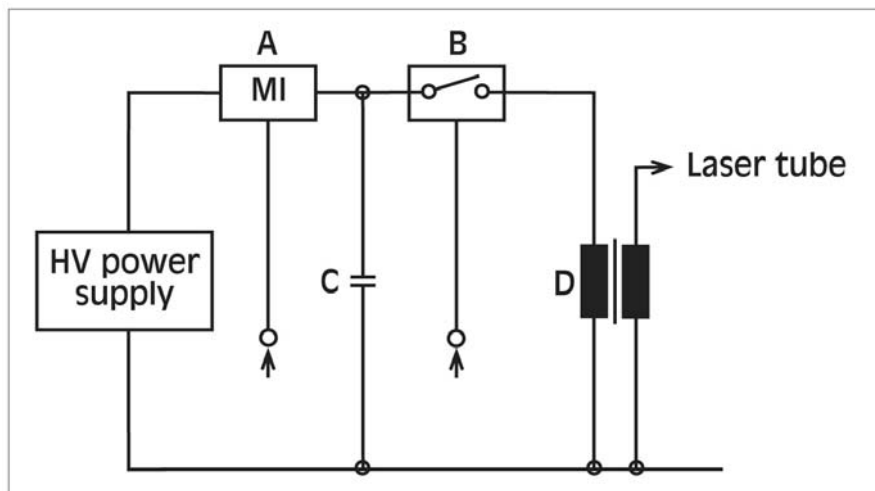


Fig. 21.1. Principal layout of a solid-state pulsed power circuit

tor switching (B), and storage capacity (C) with pulse transformation stage (D) to achieve pulsed high voltage discharge together with maintenance-free electrical components.

The lifetime of the NovaPowerSwitch, which has been introduced by Lambda Physik in 1997 [5], and its successor solid-state pulsed power modules used in today's advanced high-repetition-rate excimer lasers is practically unlimited even when being operated under 24/7 maximum duty cycle conditions.

21.2.2 Performance Characteristics

When used for industrial production economic considerations require the excimer laser performance parameters to be matched to a great extent with the demands of tight process windows. Equally important is the cost of ownership of an excimer laser, since this largely influences the profitability of a specific application. Correspondingly, the end user carefully compares the overall expenditures for installation, operation, safety regulations and maintenance of an excimer laser system with the productivity of the excimer-laser-based production tool. This implies that for industrial high-repetition rate applications an excimer laser not only needs to fulfill specific performance requirements but also has to exhibit long-term stable performance characteristics, in order to allow a high level of productivity to be realized.

In light of the abovementioned, the compact solid-state switch driven excimer laser NOVATEX from Lambda Physik represents a benchmark system of a new generation of advanced high repetition rate – moderate pulse energy excimer lasers. The most relevant performance parameters will be summarized in the following.

Based on Lambda Physik NovaTube metal/ceramic technology, elaborate design of both gas flow dynamics and discharge geometry led to a laser tube designed to deliver optimum energy stability at repetition rates as high as 2 kHz . The energy stability of 0.5% (1σ) observed in a typical 50 million pulses run at 2 kHz repetition rate and a stabilized energy of 16 mJ at 248 nm (Fig. 21.2) is the key to a reproducibility as is required in high-speed material processing tasks.

In many systems the transfer of a well-defined energy dose to the surface of the sample is more conveniently achieved when the excimer laser is operated in burst mode, i.e. when it repeatedly emits a predefined number of pulses at a stabilized preset energy. During the pause between two bursts the workpiece or the laser beam can be scanned as is usually done in step-and-repeat processes [6]. Hence, the laser must meet the energy stability requirements also in the burst operation mode. Conventional excimer lasers show the leading train of pulses at the beginning of any burst to deviate considerably from the preset energy (Fig. 21.3, upper data). The reason is simply that the energy control needs time, i.e. pulses for sensing and adjusting before the energy value is attained. For sensitive applications this so-called overshoot behavior,

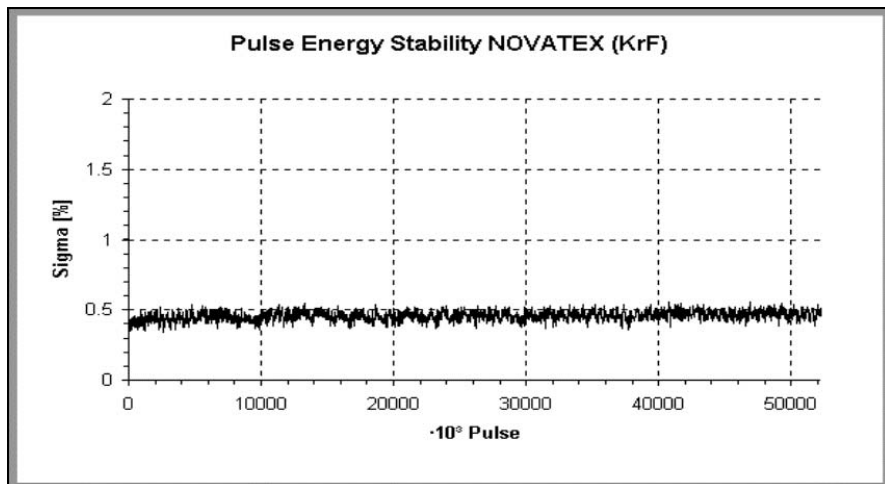


Fig. 21.2. NOVATEX long-term run over gas lifetime at 16 mJ stabilized energy operation at a wavelength of 248 nm and 2 kHz repetition rate

which is typical for excimer lasers in burst operation, is unacceptable since it is detrimental to dose energy stability, and therefore to the final process quality. In order to prevent overshooting at the beginning of every burst of pulses, the POWERLOK technology was developed which allows to reliably stabilize also the leading train of pulses of a burst, and to thereby completely suppress any initial energy deviation (Fig. 21.3, lower data). The POWERLOK software technology is based on a self-learning algorithm which is able to keep the laser performance constant even under changing duty cycle conditions. Dose energy stability and thus processing reproducibility is, as a matter of fact, guaranteed also for processes where burst mode operation is mandatory.

Reproducible high-speed exposure requires a laser beam which is spatially stable. As a consequence, the NOVATEX laser employs purgeable external resonator optics which are decoupled from the discharge chamber yielding optimum beam pointing stability and extended lifetime of optics.

On account of this mechanically stable resonator design a typical beam pointing stability of less than $20 \mu\text{rad}$ (1σ) is obtained (Fig. 21.4). The beam pointing describes the angular movement of the beam determined from the far-field focus position change over time.

While stable performance of the excimer laser is a prerequisite for high-quality processing with good reproducibility, both investment cost and running costs are crucial for enabling excimer-laser-based techniques to further penetrate and maintain profitable niche markets.

Consequently, to reduce the operation cost all components of the NOVATEX high-repetition rate excimer laser have been developed with highest possible lifetimes and longest system up-time in view. Marathon testing over

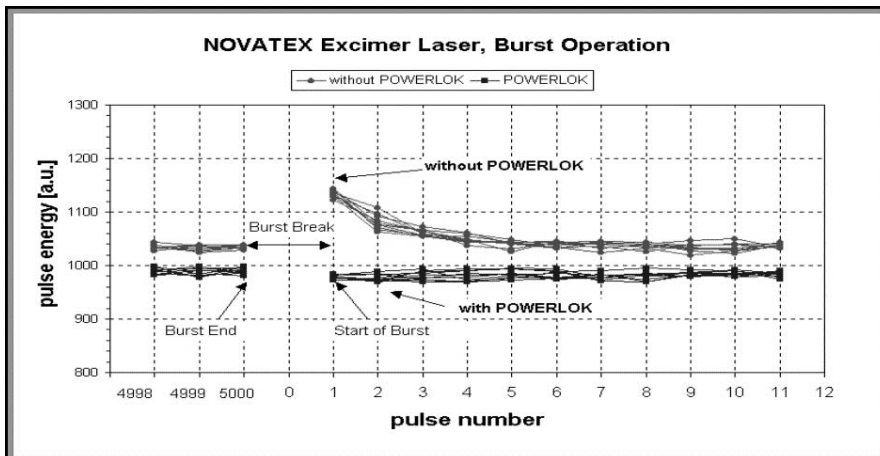


Fig. 21.3. Superposition of 5 bursts of 5000 pulses with 500 msec pause between each burst. Upper data are obtained without and lower data with additional POWERLOK compensation. Only the last and the first pulses of two bursts are shown.

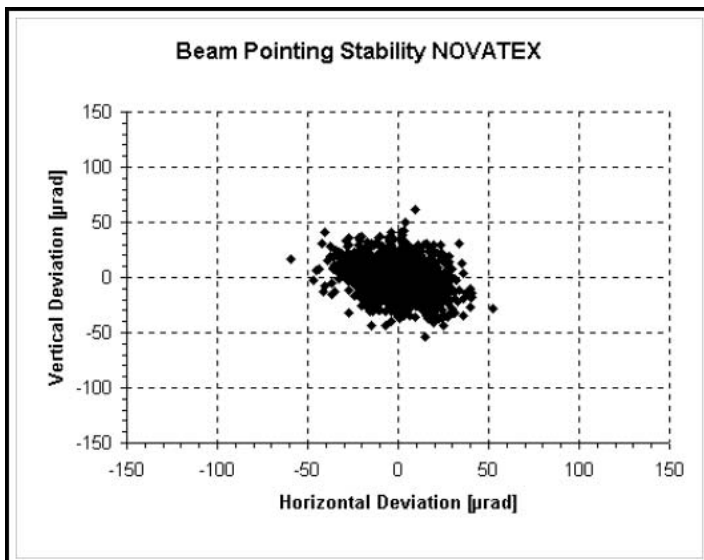


Fig. 21.4. Typical far-field beam pointing stability measurement of NOVATEX stable resonator design

several billion laser pulses has been conducted manifesting the exceptional reliability of the NOVATEX which is of particular value for industrial material processing purposes at high speed and maximum duty cycle. The laser tube of this high repetition-rate laser has a lifetime of more than 4 billion

pulses, with the tube windows lasting up to 1 billion pulses and the externally mounted resonator optics more than 2 billion pulses. Maintenance routines such as components and optics exchange are largely facilitated by a modular design concept or even performed automatically by the laser itself as is the case for partial and total gas fill routines.

Some examples of high-repetition-rate excimer laser applications requiring only moderate pulse energy as provided by the NOVATEX will be pictured in the subsequent chapter.

21.3 High-Repetition-Rate Applications

21.3.1 Flexible Mask Patterning

In today's industrial mass manufacturing the majority of excimer laser systems used at a high level of production maturity make use of the classical mask projection technique [7]. This method is ideally suited to excimer lasers due to their spatially extended rectangular beam profile of some $2 \times 1\text{ cm}^2$ allowing to cover a relatively large substrate area, and thus parallel, repeated structuring is well established. Perhaps, next to microlithographic chip fabrication, most prominent are the areas of aircraft cable marking and as well ink-jet printer nozzle drilling where excimer lasers working at high pulse energy of up to 400 mJ pulse energy and repetition rates of 200 to 300 Hz are capable to drill some 100 holes within a second.

Although conventional mask projection enables parallel processing, and therefore is fast by nature, its drawback is lack of flexibility. This means, that changing a pattern is always connected to a cumbersome mechanical exchange of a mask.

With the advent of compact high-repetition-rate excimer lasers featuring stable performance and low cost of ownership, alternative manufacturing approaches, based on existing but hitherto cost-prohibitive technologies, which enable less time consuming and more flexible patterning, become economical for a variety of industries such as packaging or marking industry.

Reflective masks on the basis of spatial light modulation consisting of well-known micro mirror device technology (Fig. 21.5) are apt to leverage the synergetic effects of a parallel process speed and a virtually unlimited manifold of patterns.

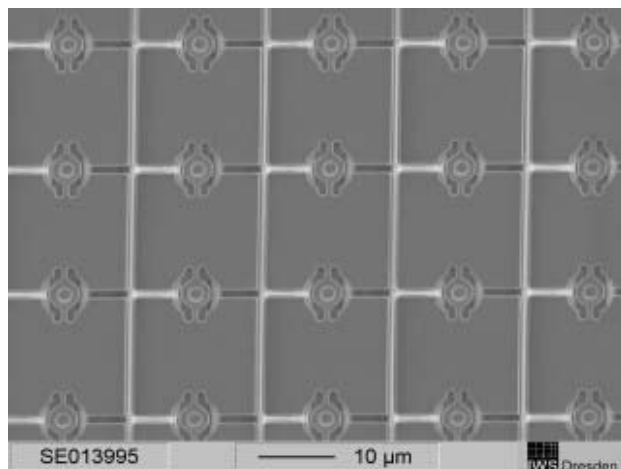


Fig. 21.5. SEM picture of a 25 mm^2 sized micro mirror device. Selective deflection of the individual $16\text{ }\mu\text{m}^2$ sized micro mirrors hinged to torsion bars is achieved via exertion of an electrostatic force. Courtesy of Fraunhofer IWS, Dresden, Germany

A desired projection pattern on the sample is obtained in a typical set-up by illuminating the entire field of micro mirrors with a homogenized and appropriately shaped excimer laser beam. The light reflected by the mirror array acting as spatial light modulator (SLM) then passes a flat-field lens, a Fourier aperture and a reduction lens before selectively exposing the substrate (Fig. 21.6). The inherently low coherence of excimer laser light prevents unwanted interference patterns to be generated upon passing the optical components.

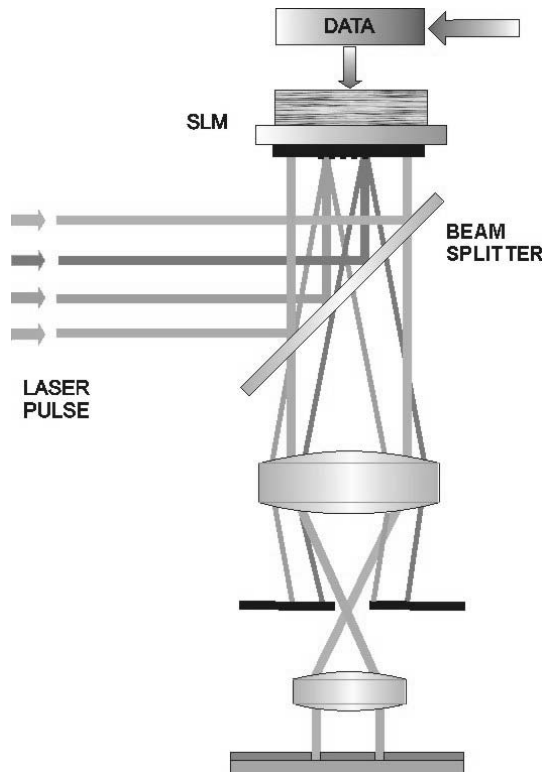


Fig. 21.6. Schematic view of spatial light modulation (SLM) principle for flexible mask illumination of a sample. Source: Micronic Laser Systems, Täby, Sweden

By applying a low voltage to selected mirrors, the electrostatic force causes the micro-mirrors to be slightly deflected out of the plane. This causes a diffraction-induced phase shift of the reflected laser beam which is subsequently transformed into the programmed intensity modulation of the excimer light on the sample. By varying the time of deflection voltage signal also gray-scale control is achieved.

Spatial light modulation on the basis of micro mirror arrays provides the flexibility needed for instance for bar code marking in industrial packaging (Fig. 21.7) but also for variable cable and electronic components marking to name but a few.

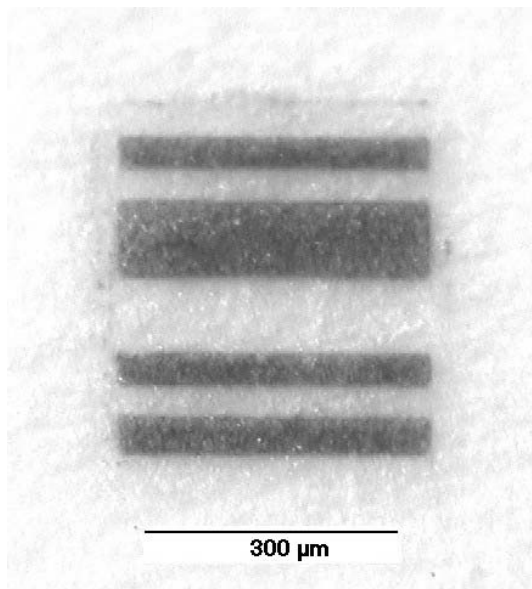


Fig. 21.7. Bar code on paper obtained by color change from a single-pulse exposure using the Lambda Physik OPTexPro at a wavelength of 308 nm . The energy density applied on the paper surface was 600 mJ/cm^2 . Courtesy of Fraunhofer IWS, Dresden, Germany

Depending on the illuminated material and the applied fluence at the surface of the sample also flexible ablative fabrication of elaborate three dimensional structures is possible (Fig. 21.8) which are required for biomedical lab-on chip technologies and various other microsystems used as sensors or actuators in today's advanced automotive, telecommunication and semiconductor industries.

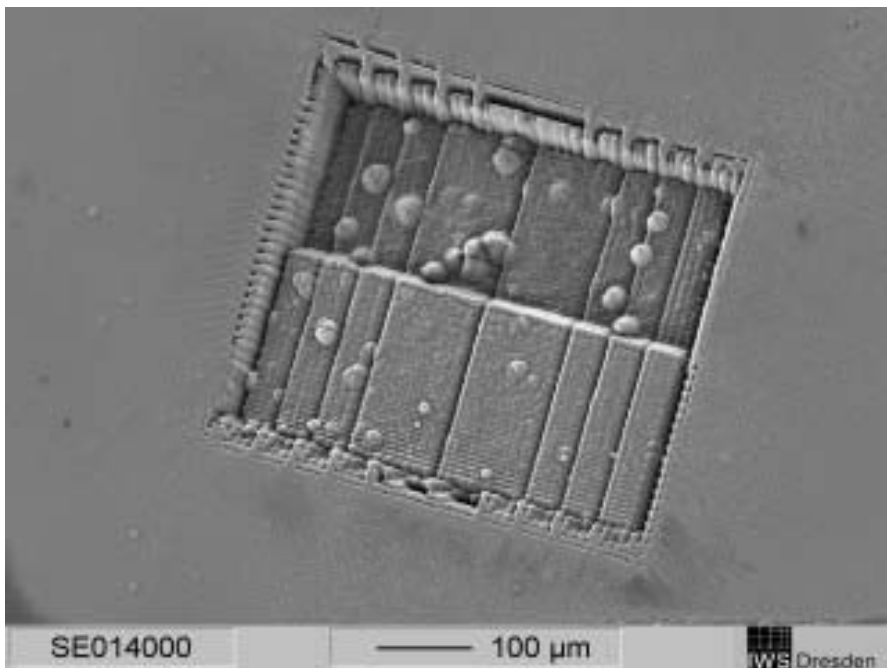


Fig. 21.8. Three-dimensional structure ablated in polyimide (Kapton®) using the Lambda Physik OPTexPro at a wavelength of 308 nm. An ablation depth of 50 μm was achieved with 100 pulses at 0.5 μm ablation rate. Courtesy of Fraunhofer IWS, Dresden, Germany

Since the high mirror deflection reload capability of such flexible systems easily supports fast 1 to 2 kHz excimer laser pulse repetition rates [8], this means in case of, for instance, single pulse marking tasks 1000 to 2000 different predefined mask patterns per second can be flexibly transferred to a substrate, hence, exceeding conventional mask projection marking speed by a factor of 10.

21.3.2 Long-Term Testing of Optical Material and Coatings

Demand for testing of optical component's transmission behavior and also of coatings resistance [9] is driven by advanced microlithography wafer steppers and scanners requiring both reliable spectral and intensity output stability for precise chip manufacturing. The typical energy density of 20 mJ/cm² experienced by the excimer laser tube windows combined with the static and dynamic stress sets high requirements for the quality of the window materials. Long-term testing of optical material such as lenses and windows is, thus, essential for quality assurance and as well to foster further material improvements. Since resist exposure in advanced high-throughput wafer

stepper/scanners occurs with excimer laser repetition rates of two to four kilohertz, a meaningful optics material testing requires accumulation of hundreds of millions of pulses (Fig. 21.9).

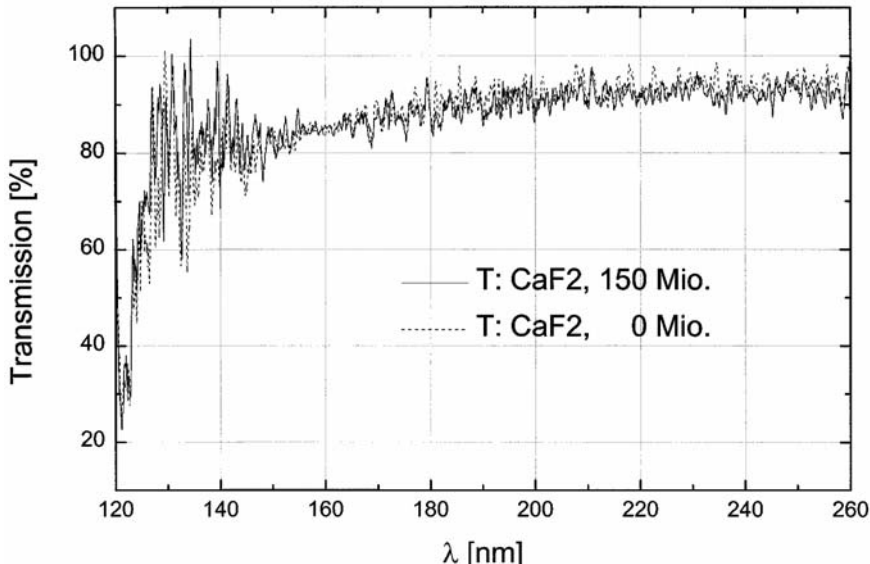


Fig. 21.9. Transmission spectrum of calcium fluoride (CaF₂) excimer laser windows before (dotted line) and after (solid line) pulsed excimer laser irradiation at a wavelength of 157 nm and an energy density of 10 mJ/cm². No material degradation is observable after 150 million excimer laser pulses accumulated.

Against this background, compact, high-repetition rate excimer lasers such as the OPTexPro or NOVATEX (see section 21.3.2), connected to appropriate test chambers (Fig. 21.10) allow effective evaluation of long-term physical properties of optical materials under well-defined conditions and with low cost of investment and operation.

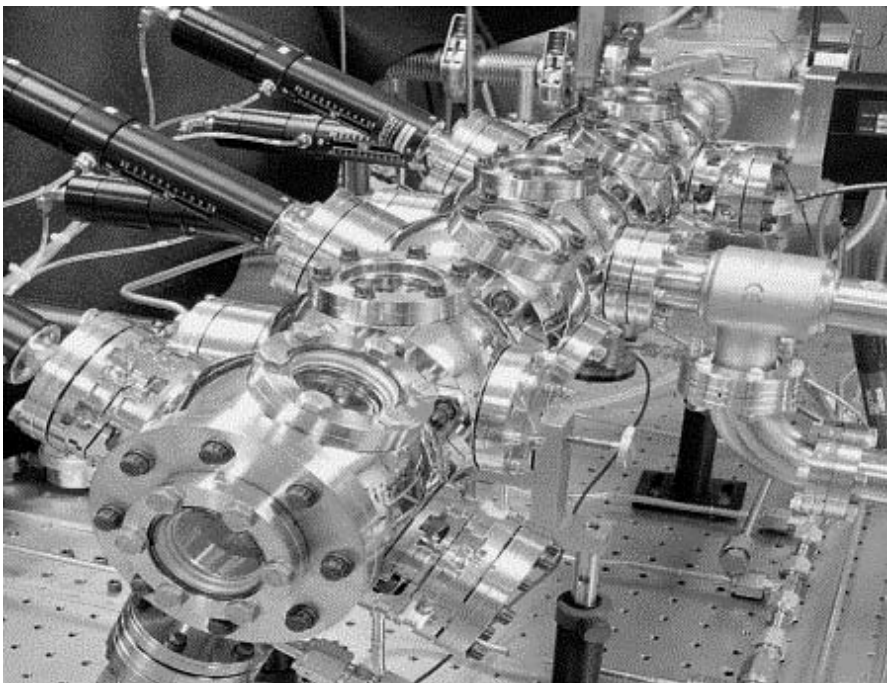


Fig. 21.10. Ultraclean test chambers for marathon irradiation testing of CaF_2 optical material. Courtesy of MIT-Lincoln Laboratory, Cambridge, USA

21.3.3 Advanced Medical Excimer Laser Systems

Refractive eye surgery based on small scanning spot ArF excimer lasers has been undergone steady progress in the past years mainly fueled by sophisticated measurement techniques (see also chapter 19.1). With the introduction of precise, individual mapping of the patient eye's refractive power utilizing wavefront analysis among other methods to be performed prior to excimer laser treatment of the cornea, ever finer ablation patterns are to be sculpted by the scanned laser spot. While decreasing the spot diameter will allow scanned ablation at a more refined scale, this is connected to relatively higher total numbers of pulses needed to ablate a given total volume of the cornea. This aspect is still prohibitive to a market introduction of refractive surgery systems based on solid-state femtosecond lasers at a wavelength of 1035 nm . These systems work with a focal beam diameter of only a few microns, and correspondingly, must provide customized ablation at repetition rates of several hundred kilohertz to achieve treatment times comparable to excimer laser systems [10]. Hence, avoiding prolonged treatment times posing a critical drawback to a refractive surgery system, the market requires higher repetition rate excimer lasers to be employed. As a consequence, customized excimer laser refractive eye surgery, currently performed by excimer laser

systems working at up to 250 Hz, will benefit from compact 500 to 1000 Hz excimer lasers enabling both shorter treatment time and increasingly precise customized ablation at smaller spot diameters. In the near future, refractive surgery systems based on excimer lasers of up to 500 Hz and maybe even 1 kHz repetition rate can be expected. Since thermal effects in the cornea pose a natural limit to the employed repetition rate, further reduction of treatment time might then be tackled by parallel, multi-laser beam scanning approaches.

The development of small excimer lasers with relatively small pulse energies but with the capability of reaching high repetition rates, coupled to acceptable gas lifetimes and good beam quality, has opened opportunities for much more efficient excimer laser systems in flexible manufacturing and refractive eye surgery. In the future, this will lead production engineers and system integrators to increasingly consider using high-repetition-rate, compact excimer lasers due to the reduced capital investment and smaller footprint.

References

1. W. Zschocke, H.S. Albrecht, T. Schröder, I. Bragin, M. Sprenger, F. Seddighi, C. Reusch, A. Cortona, K. Schmidt, R. Pätzelt, K. Vogler: "High repetition rate excimer lasers for 193 nm lithography", in *Proc SPIE Microlithography*, Santa Clara, CA (March 2002)
2. B. Burghardt, H.J. Kahlert, D. Basting: "High resolution excimer laser based micromachining", in *Laser Treatment of Materials, Proc. of ECLAT*, ed. by B.L. Mordike (1992), pp. 609–613
3. R. Delmdahl: Laser Focus World pp. 53–58 (July 2002)
4. D.H. Parker, R. Delmdahl, B.L.G. Bakker, H.P. Loock: J. Chin. Chem. Soc. **48**(3), 327–332 (2001)
5. R. Pätzelt, U. Stamm, I. Bragin, F. Voß, B. Nikolaus, H. Endert, D. Basting: Proc. SPIE **2992**(01), 2 (1997)
6. G. Spiecker, R. Delmdahl: Laser Magazin **6**, 10–13 (2002)
7. H. Endert, M. Kauf, R. Pätzelt: Laser Opto **31**(4), 46–53 (1999)
8. T. Kuntze, M. Panzner, U. Klotzbach, E. Beyer: "New excimer laser marking method using micro mirror devices", in *Proc. 4th International Symposium on Laser Precision Microfabrication*, Munich (2003)
9. D. Ristau: Business Briefing: Global Photonics Applications and Technology pp. 1–6 (2002)
10. H. Lubatschowski, A. Heisterkamp, F. Will, A.I. Singh, J. Serbin, A. Ostendorf, O. Kermani, R. Hermann, H. Welling, W. Ertmer: RIKEN Review No. 50: Focused on Laser Precision Microfabrication (LPM 2002) **50**, 113–118 (2003)

22 New Frontiers: Extreme-Ultraviolet (EUV) Technology at 13.5 nm

Uwe Stamm

22.1 Prospects of EUV Lithography Drive the Development of High-Power EUV Sources

Is there any technology available when structures finer than those currently made by excimer laser radiation are needed? Experts from semiconductor industry have asked this question since the early nineties of the last century. From their perspective excimer-laser-based lithography is projected to generate structures down to the 32 nm node (critical dimension, 45 nm half-pitch). However, even excimer lasers operating at the shortest wavelengths at 193 nm or 157 nm, combined with immersion lithography, will likely not allow further shrinking of the structure size. The essential limit is given by diffraction.

In optical lithography the “critical dimension” (CD) and “depth of focus” (DOF) are the two determining parameters for the limits of resolution obtainable by a technology. Both depend on the wavelength λ of the light used for exposure of a photo-sensitive resist on the silicon wafer, and are given according to Ernst Abbe by

$$CD = \frac{k_1 * \lambda}{NA} \quad (22.1)$$

and

$$DOF = \frac{k_2 * \lambda}{NA^2} \quad (22.2)$$

with k_1 and k_2 being system- and process-specific constants and NA the numerical aperture of the optics. The process parameters k_1 and k_2 describe how close the imaging properties are at the theoretical limit. To generate finer structures with optical lithography one has therefore the possibility to:

- (a) reduce the k-factor,
- (b) increase the numerical aperture,
- (c) reduce the wavelength of the illuminating light,

(see also chapter 6 “Excimer Lasers for Microlithography” in this book).

In semiconductor lithography industry all three ways have been followed since many years. Numerical apertures reach values of 0.85, and k-factors are down to below 0.35. Here we discuss the possibility to reach new frontiers in wavelength reduction - leaving excimer laser technology completely towards the extreme ultraviolet (EUV) technology.

Extreme ultraviolet (EUV, sometimes called also XUV) is defined as the spectral range between soft X-rays and ultraviolet radiation, between 1 nm and 100 nm wavelength. It is the extreme ultraviolet range around 13.5 nm (today typically named EUV) that is of practical importance because, at present, only for this wavelength range efficient optical elements can be made. The short wavelength of EUV radiation offers tremendous potential for semiconductor lithography. Figure 22.1 summarizes the historical development of optical lithography and tries an outlook into the next decade. The wavelengths used in lithography are plotted together with the minimum feature sizes of the integrated circuits. Approximately in the mid-nineties of the last century the minimum feature size became smaller than the wavelength used for imaging. Leaving excimer laser technology towards the extreme ultraviolet (EUV) technology, in about 2009 the wavelengths will be shorter than the structures to be printed, which offers large potential for manufacturing multiple technology nodes, i.e. computer chips for several generations of critical dimensions with EUV lithography.

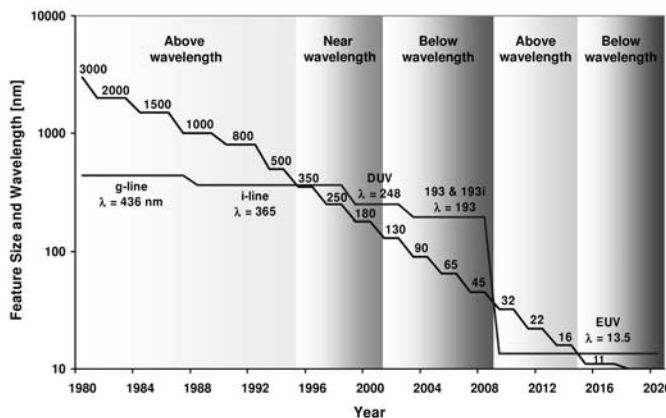


Fig. 22.1. Development of optical lithography over almost four decades: Wavelengths used for imaging and minimum feature size (critical dimension) printed. EUV lithography is projected to start in high-volume manufacturing in 2009. Then the wavelength will be again smaller than the structures to be made, offering potential for use at multiple nodes. Data are partially from David Tennenhouse, Intel, on Nanotech 2004, Boston, MA, USA.

Technologically it seems to be reasonable to start the manufacturing of chips with extreme ultraviolet light at the 32 nm node. This is the consensus of the experts from industry and universities working in EUV: EUV LLC, USA demonstrated the feasibility of EUV lithography at the “Engineering Test Stand” [1]; all components of the new technology were successfully tested. The British company Exitech Ltd. has developed EUV microsteppers [2] that have been installed at Intel and International SEMATECH. They are being used as technology pathfinders for EUV lithography by the semiconductor chip industry. The capital lithography equipment manufacturers ASML (Netherlands), Canon and Nikon (both Japan) are developing full-field EUV exposure tools that are scheduled for introduction in 2006.

22.2 Challenges of EUV Lithography

The jump from the 193 nm excimer laser wavelength to the more than 14 times shorter EUV wavelength of 13.5 nm will be surely a quantum leap with respect to the potential in resolution. On the other hand, it means a tremendous technical challenge as the requirements onto all elements of an EUV lithography exposure tool are significantly higher than for conventional optical lithography tools.

The first technical challenge comes with the generation of structures with critical dimensions of 32 nm and below which puts extraordinary requirements onto the opto-mechanical layout as well as metrology and active feedback loops in the EUV exposure tool. During exposure, mask and wafer (in an EUV scanner mask and wafer are scanned synchronously according to the 4x demagnification between mask and wafer) have to be positioned with few nanometer accuracy at stage velocities between 0.5 m/s to 2 m/s . For comparison, imagine a high-speed ICE train traveling at 200 km/h : to achieve a similar relative accuracy the positioning of the train along the track must be better than $0.1\text{ }\mu\text{m}$!

The second challenge of EUV technology comes from absorption: all materials including gases absorb at 13.5 nm . The absorption depth of EUV radiation in air at normal pressure is below 1 mm . Consequently the optical beam must be guided under vacuum conditions. The entire EUV exposure tool means a big high-vacuum installation.

The third challenge of EUV lithography arises from the design of the optics. Because of the lack of EUV transmitting materials lenses as used in excimer laser lithography are no longer applicable. Instead mirrors must be applied – either grazing-incidence metal-coated mirrors or near-normal-incidence multilayer-coated mirrors. Grazing-incidence collector optics consists of multiple tube-like mirrors, so-called elliptical or Wolter telescopes. These telescopes – a spin-off from satellite-based X-ray astronomy – transfer the EUV radiation from the EUV source into a first focal plane in larger

distance from the source. Multilayer mirrors consist of large aspherical substrates coated with few nanometer thick layers made alternately of molybdenum and silicon. The number of layer systems may reach 60 or more. To better understand the requirements onto surface accuracy of the mirrors a comparison is illustrative: Multilayer mirrors have a diameter of several 10 cm. The Federal Republic of Germany has a north-south dimension of about 1000 km. The requirements onto surface accuracy of multilayer mirrors for EUV would mean that the biggest mount in Germany has a height of less than 0.5 cm.

The fourth challenge is the manufacturing and handling of the EUV mask (also called reticle). Similar to the imaging optics also the mask cannot be used in transmission as in conventional optical lithography. EUV masks are reflective elements. This increases demands for surface figure substantially to levels as for the mirrors in the imaging system. And because of the small structure, the number of defects or particles on the mask with dimensions of 50 nm and larger must be zero. More specifically, handling of the mask in the EUV exposure tool as well as storage and transport have to be optimized to prevent particle contamination.

The biggest technical challenge for EUV lithography is the realization of an appropriate EUV light source. The losses for EUV light in the optical beam path of the exposure tool are substantial. One multilayer mirror used in the imaging beam path reflects only between 65% and 70% of radiation in a spectral range $\Delta\lambda/\lambda$ of about 3% around 13.5 nm. The EUV sources emit in a rather broad spectral range as shown in Fig. 22.2 for an EUV source with xenon as operating medium. The implementation of about 12 multilayer mirrors in the EUV exposure tool results in a usable spectral range from the EUV source emission of 0.27 nm. Only about 0.5% of the source power fed into the EUV scanner reaches the wafer plane because of the limited reflectivity of the mirrors. Taking into account additional geometrical losses in the beam path, experts expect only about 200 mW EUV power in the

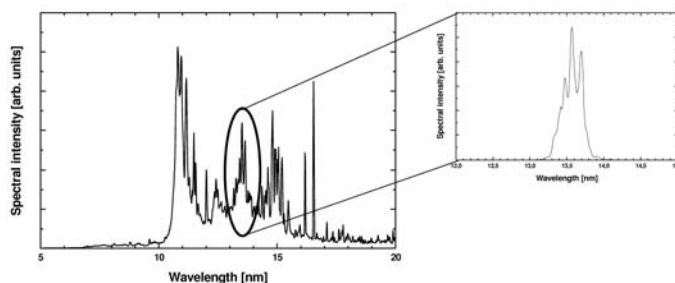


Fig. 22.2. Typical emission spectrum of a GDPP (gas-discharge-produced plasma) EUV source with xenon target. Left part: Spectrum as directly emitted from the source. Right part: Spectrum after reflection at two 13.5 nm multi-layer mirrors. Only this portion of the radiation can be used in EUV lithography.

wafer plane from a source that emits about 500 W [2]. Furthermore, because of the expected high cost of an EUV exposure tool, a throughput of 100–120 300 mm-wafers/hour is required to reach acceptable manufacturing costs. The combination of necessary throughput and inevitable losses requires the power of the EUV source for high-volume manufacturing amount to 115 W [3, 4, 5]. This power is needed in the focal plane of a first source collector optics (see Fig. 22.3) which also has only a limited transmission.

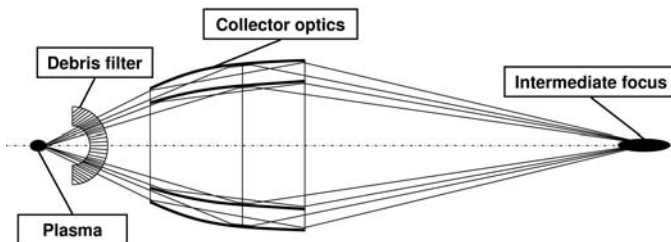


Fig. 22.3. Components and optical beam path of a source collector module. The EUV emission volume is imaged by source collector optics into a focal plane (intermediate focus) that is the input plane of the EUV scanner illumination optics. Between plasma and intermediate focus plane means to suppress debris are installed to protect the collector optics. Residual gas absorption in the beam path also introduces additional losses.

No wonder that the EUV source power and lifetime have been regarded the most critical issues the industry will face in developing EUV lithography. The list of the top 6 critical issues of EUVL has been updated at the 2nd International Symposium on EUV Lithography in Antwerp, Belgium in October 2003 and the 3rd International Symposium on EUV Lithography in Miyazaki, Japan in November 2004 [6]. While in 2003 source power and lifetime including condenser optics lifetime were still on top of the critical issues, significant progress achieved with respect to the available source power has shifted source power to the lower ranks. The top-3 critical issues for commercial introduction of EUV lithography in 2009 are according to the ranking by the EUVL experts in 2004:

- (1) availability of defect free masks,
- (2) lifetime of source components and source collector,
- (3) resist resolution, sensitivity and line edge roughness.

As other remaining critical issues have been identified:

- (4) reticle protection during storage, handling and use,
- (5) source power,
- (6) projection and illuminator optics quality and lifetime.

In addition to technical risks, economic factors are playing an increasing role: The price of an EUV scanner could be more than 40 million US dollars, while end users expect pricing to be in the 20 million to 30 million dollar range. This is a conflict that must be solved before EUVL becomes integrated into chip production.

22.3 Basic Technology and Requirements for EUV Sources

According to the list of critical technical issues, the development of EUV sources with sufficient power and lifetime has been a top priority in EUVL development. XTREME technologies – the EUV joint venture between Lambda Physik and JENOPTIK Laser, Optics and Systems – operating in Jena and Göttingen, both Germany, is committed to solve the problems in development and manufacturing of EUV sources for lithography.

At XTREME technologies, the most promising approach for EUV lithography sources – the excitation of a very hot plasma – is employed to generate extreme ultraviolet radiation. This is a well-known method that has been used in research laboratories for many years. The spectral emission properties of the plasma are known from Planck's formula of black body radiation. The temperature T of the plasma determines the maximum emission wavelength λ_{max} of the plasma:

$$\lambda_{max} = 2898 \mu m \text{ Kelvin}/T \quad (22.3)$$

or

$$\lambda_{max} = 250 nm \text{ eV}/T. \quad (22.4)$$

For the emission maximum to be positioned at 13.5 nm the temperature of the plasma must be about 220 000 K. This plasma temperature can be reached both by excitation through a pulsed electrical discharge or through pulsed laser radiation. In comparison to excimer laser radiation, the plasma emission is incoherent and more or less homogeneous in all directions (4π steradian solid angle).

At XTREME technologies EUV sources based on the two most promising plasma technologies – gas-discharge-produced plasma (GDPP) and laser-produced plasma (LPP) – are currently under development. While GDPP sources are simpler and more compact than LPP sources, the latter have basic physical advantages regarding lifetime and power handling. However, the LPP sources are expected to be much more costly – therefore the “lithography community” is hopeful that GDPP sources can fulfill the production lithography requirements. Today it is not yet decided which source will prevail for high-volume manufacturing of computer chips with EUV lithography.

Lithography exposure tool manufacturers have agreed on joint top-level specifications of the EUV source performance for high-volume manufacturing (HVM) using EUV lithography. The specifications for various EUV source parameters are summarized in Table 22.1 [3, 4, 5].

Table 22.1. Requirements for EUV source parameters to be installed in EUV lithography high-volume manufacturing tools. The specifications are meant in a plane of the intermediate focus behind the first source collector optics that belongs to the EUV source. The collector optics module separates the plasma generator from the illumination optics (condenser).

Source Parameter	Requirement
Central wavelength	13.5 nm
EUV power (in-band) in intermediate focus	115 W
Repetition frequency	≥ 7000 Hz ... $\geq 10,000$ Hz
Integrated energy stability (3σ , over 50 pulses)	< 0.3 %
Maximum solid angle input to illuminator	0.03 – 0.2 sr
Etendue (area \times solid angle)	$\sim 1.0 – 3.3 \text{ mm}^2\text{sr}$
Condenser optics lifetime	30,000 hours

The listed specifications of the EUV source parameters are meant in a focal plane behind a first source collector optics (i.e. at intermediate focus). How tremendous these power requirements are becomes clear when the losses in the beam path from the plasma to the intermediate focus are considered (see Fig. 22.3). First of all, the power problem results from the requirement that the allowed EUV emission volume must measure about 1 mm in diameter or smaller because of the etendue limit of the optical system. EUV light emitted from larger volumes cannot be transmitted through the optical system of the EUV exposure tool. The optical system of the exposure tool determines which fraction of the EUV volume in the intermediate focus can be used. In ideal case the “etendue transmission factor” is 1. In case of larger plasma size as observed generally in GDPP sources the etendue transmission may decrease to 70% or less. In this case only a part of the power available in intermediate focus can be transported through the optical system of the EUV exposure tool. In Table 22.2 estimates of the necessary EUV power emitted into 2π solid angle for both GDPP and LPP sources are made, based on the 115 W EUV power specification in the intermediate focus for high-volume manufacturing (HVM) sources.

Additional geometrical losses occur because of the practical limits of collection angles of typical collector optics that can collect only a fraction of the angular homogeneous EUV emission from the plasma. For GDPP sources

Table 22.2. EUV power emitted into 2π solid angle necessary for HVM GDPP and LPP sources to achieve 115 W power at the entrance of the illuminator optics system of the EUV exposure tool.

Required power @ intermediate focus (13.5 nm, 2% bandwidth) for high-volume manufacturing with EUV lithography: 115 W		
	GDPP source	LPP source
Etendue factor / transmission	1.0 – 0.5	1.0
Transmission of debris mitigation in collector module	0.8	0.9
Transmission of gas in collector module	0.85	0.85
Required power from the source in collection angle:	169 – 338 W	150 W
Geometrical collector efficiency with respect to 2π sr	0.5	0.8
Angular averaged collector reflectivity	0.55	0.55
Required power from the source emitted into 2π sr	615 – 1230 W	340 W

the practical limit in maximum collection angle may be at π sr (solid angle). LPP collectors may capture up to 5 sr. Further losses occur because of the limited reflectivity of the collector optics of < 70%, the gas absorption over the optical path length (about 10%), and transmission loss in the debris filter system (about 80–90% transmission may be practicable) which is needed to protect the collector optics. Taking these effects into account the required power from the EUV source into 2π sr is between 340 W for LPP sources and 615 W to 1230 W for GDPP sources, dependent on the etendue transmission factor. Also under discussion, an additional spectral filter may be necessary in the beam path which could increase the power requirement by another factor of 2 in the worst case. Compared to 193 nm excimer laser lithography where 20 W to 40 W power out of the laser are sufficient this requirement for EUV sources is extremely high.

22.4 Gas-Discharge-Produced and Laser-Produced Plasma EUV Sources

22.4.1 Gas-Discharge-Produced Plasma EUV Sources

A well known and the most efficient method of plasma generation is that by an electrical gas discharge, for example as spark or flash. Unfortunately, to generate EUV radiation the densities and temperatures of conventional gas discharges as those used in discharge lamps or excimer lasers are not high enough. However a “cold” and “low-density” plasma can be compressed by

magnetic fields to a hot, high-density plasma with maximum intensity at an emission wavelength of 13.5 nm . The effect that can be used is that of self-compression of a cylindrical plasma by the azimuthal magnetic field of the axial discharge current. This effect is called “pinch effect”, the compressed plasma is called pinch plasma.

The discoverer, Willard H. Bennet, described the pinch effect as magnetic self-focusing in a plasma with electrical current flow. The plasma temperature can be estimated from the balance between pressure of the magnetic field P_{mag} and thermal pressure of the plasma P_{plasma} [7]:

$$P_{mag} = P_{plasma} \Rightarrow \frac{B^2}{2\mu_0} = (\langle Z \rangle + 1) \cdot n_i \cdot kT \quad (22.5)$$

$$\Rightarrow kT = \frac{\mu_0 \cdot I^2}{8 \cdot \pi \cdot (\langle Z \rangle + 1) \cdot N_i}, \quad (22.6)$$

with B as magnetic field of the discharge current I , μ_0 as magnetic field constant, n_i as ion density, $\langle Z \rangle$ as average degree of ionization, kT as plasma temperature, N_i as line density, $N_i = n_i \pi r^2$, and $B = \mu_0 I / 2\pi r$.

From the relation above and the requirements for EUV sources for lithography (plasma diameter about 1 mm , almost spherical) the current I necessary to generate a plasma temperature of kT of 20 eV can be estimated to about 20 kA for gases as xenon. The magnetic field amounts to about 20 Tesla and compresses the plasma cylinder to about 2000 bar pressure. The total energy in magnetic field, plasma and external circuit can be estimated to $5\text{--}10\text{ J}$. A stable plasma cylinder would possess a resistance of $50\text{ m}\Omega$. The plasma is heated with some 10^7 W due to its ohmic resistance. Because of the heating of the plasma the current decreases significantly after several hundred nanoseconds. The discharge can be operated only in a pulsed regime.

XTREME technologies is working on a highly efficient pinch plasma EUV source – the preionized Z-pinch [8] (see Fig. 22.4). The plasma generator consists of two cylindrical electrodes that are properly shaped to achieve the desired plasma size and emission angle. A cylindrical insulator separates anode and cathode. The design of the Z-pinch source supports an accessible emission solid angle for collection of above 1.8 sr , i.e. $\pm 45^\circ$. Xenon gas is used as an EUV emitter, continuously flowing through the discharge region. The key for the high emission stability of the Z-pinch source is a highly efficient surface-discharge pre-ionization device included in the Z-pinch source. After preionization of the xenon gas a pulsed high-current discharge is ignited close to the insulator walls and immediately compressed to a hot high-density plasma column. In the Z-pinch design the length and diameter of the EUV emitting volume can be varied by the separation between anode and cathode as well as by their shapes. This is necessary to match the specific illuminator optics design. The possibility of scaling the emission volume from 0.8 mm

length and 0.25 mm diameter to above 2 mm length and 1.3 mm diameter has been demonstrated.

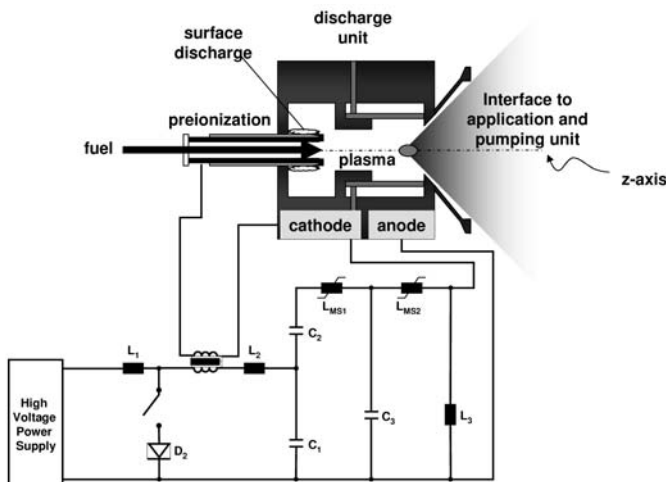


Fig. 22.4. Schematics of a GDPP Z-pinch EUV source. The EUV emitting plasma is generated in low pressure xenon between cathode and anode of the Z-pinch source. Preionization of the xenon gas stabilizes the EUV emission. A pulsed-power circuit drives the discharge with about 5 J input energy to the plasma.

22.4.2 Laser-Produced Plasma EUV Sources

The other possibility to generate EUV radiation is the excitation of the plasma by focusing laser radiation. In this approach a nanosecond pulsed laser beam is focused onto a target. At intensities I_L above $I = (10^{10} - 10^{11}) W/cm^2$ the target atoms are ionized. The electrical field of the laser pulse accelerates the free electrons in the plasma. The mean kinetic energy E_{osc} of the oscillating electrons is

$$E_{osc} = (1/4) \frac{e^2 E_0^2}{(m_e \omega^2)}, \quad (22.7)$$

with $E_0^2 = 2I_L / (c \epsilon_0)$ being the square of the electric field strength, e the elementary charge, ϵ_0 the dielectric constant, m_e the mass of the electron and ω the frequency of light. The leading edge of the laser pulse generates a plasma which interacts during expansion with the following part of the incident laser pulse. Light can be absorbed by the plasma until the critical density $n_{crit} = \omega^2 m_e \epsilon_0 / e^2$ is reached. At the critical density the frequency of the light is equal to the plasma frequency. At higher densities the refractive

index of the plasma is imaginary and the light is reflected. The critical density for a laser wavelength of $\lambda = 1064\text{ nm}$ is about $n_{crit} = 10^{21}\text{ cm}^{-3}$, hence only about one thousandth of the density of solid-state targets.

The hot electron gas heats the plasma by collisions with the plasma ions to a plasma equilibrium temperature T_L . For a laser wavelength $\lambda = 1064\text{ nm}$ and targets with low or medium degree of ionization the plasma temperature is about $T_L = 220\,000\text{ K}$ or 20 eV at a laser intensity I_L of several 10^{13} W/cm^2 . These laser intensities can be easily reached with pulsed high-beam-quality lasers.

In laser-produced plasma EUV sources at XTREME technologies a nanosecond pulsed Nd:YAG laser beam is directed and focused onto a target of liquid xenon. A laboratory installation is shown in Fig. 22.5. The laser emits at 1064 nm and operates up to $10\,000\text{ Hz}$ repetition rate. With these EUV sources plasma diameters of below 0.3 mm have been demonstrated, which is well matched to the etendue of projected EUVL optical projection systems.



Fig. 22.5. LPP laboratory EUV source at XTREME technologies. The 500 W diode-pumped solid-state laser (left side) excites the target in the vacuum interaction chamber (right side).

22.4.3 How to Characterize EUV Sources

Both GDPP and LPP EUV sources emit the EUV radiation from a small plasma volume with spherical to ellipsoidal shape and dimensions in the order of 1 mm . EUV light is emitted into all directions more or less homogeneously, i.e. into the full solid angle of $4\pi\text{ sr}$. Obscurations by electrodes or target

nozzles and holders make the accessible angle in practice typically smaller than $2\pi \text{ sr}$.

In order to characterize the parameters and specifications of EUV sources also the necessary metrology tools had to be developed. Currently metrology is available to measure energy, average power, energy and power stability, spectral distribution, spatial plasma shape, angular distribution of the emission as well as the temporal shape of the EUV pulse. There are three devices that allow measuring these characteristics: in-band energy meter, spectrometer and pinhole camera [9].

The in-band energy meter (also often called multi-layer tool) employs an EUV sensitive photodiode as detector and can measure energy, average power, and energy and power stability. It is also used to measure the angular distribution of the EUV emission. In front of the photodiode a Zr filter and an arrangement of two plane multilayer mirrors reflecting at 13.5 nm are mounted. The detectable solid angle is defined by two apertures included in the tool and their distance to the plasma. The energy meter is cross-calibrated at synchrotron facilities or plasma-based EUV sources. With knowledge of the source emission spectrum around 13.5 nm and the detected solid angle the EUV in-band energy of single pulses of the source can be determined. Subsequently with the corresponding data acquisition hardware and software also average power and energy and power stability can be determined.

As mentioned above the knowledge of the EUV spectral distribution of the emission is essential for an accurate measurement of in-band power. In addition, the spectral distribution of the EUV radiation is of importance for the design of the whole optical system of the EUV exposure tool. JENOPTIK Mikrotechnik GmbH has developed the EUV spectrograph "E-Spec". It consists basically of a piezo-driven entrance slit (shutter), a 1200 line / mm spherical aberration-corrected flat-field grating and a thinned backside-illuminated CCD. The flat-field range of the grating is between 5 nm and 40 nm. In practice, the detectable spectral range is smaller (standard 5–20 nm) due to limitations of the size of the CCD array. For the precise measurement of the absolute emission power of an EUV source the spectrometer is calibrated at the Radiometry Laboratory of the Physikalisch-Technische Bundesanstalt (PTB) with respect to wavelength and sensitivity. The calibration yields a wavelength accuracy of $\lambda/\Delta\lambda > 800$ (relative to the PTB standard) and a resolving power of $\lambda/\Delta\lambda \approx 600$. The sensitivity of the spectrometer can be determined with an accuracy of $\pm 10\%$, mainly limited by fluctuation of the shutter opening time and CCD inhomogeneity. Due to the absolute calibration for wavelength and sensitivity the spectrometer can also be used as power monitor at any wavelength of the covered spectral range.

The dimension and shape of the EUV source plasma are very important parameters, which have to be matched to the design of EUV optical system to optimize efficiency. The EUV plasma shape is measured by an EUV pinhole camera which uses a CCD sensor coated with an EUV-VIS quan-

tum converter, and a zirconium filter which is integrated in the pinhole. The magnification of the camera can be adjusted by changing the distance of the pinhole to the source and the CCD. The camera can be operated to an image readout up to 50 Hz to measure the stability of the plasma position, dimension and shape and is therefore much faster than back-illuminated slow-scan cameras. Figure 22.6 gives an example of the EUV image of the plasma of a GDPP EUV source measured on-axis of the emission. The FWHM diameter of the emission is $< 500 \mu m$. The single pulse emission (left part) as well as the average over 200 pulses of the emission (right part) is shown, documenting the excellent stability of the plasma.

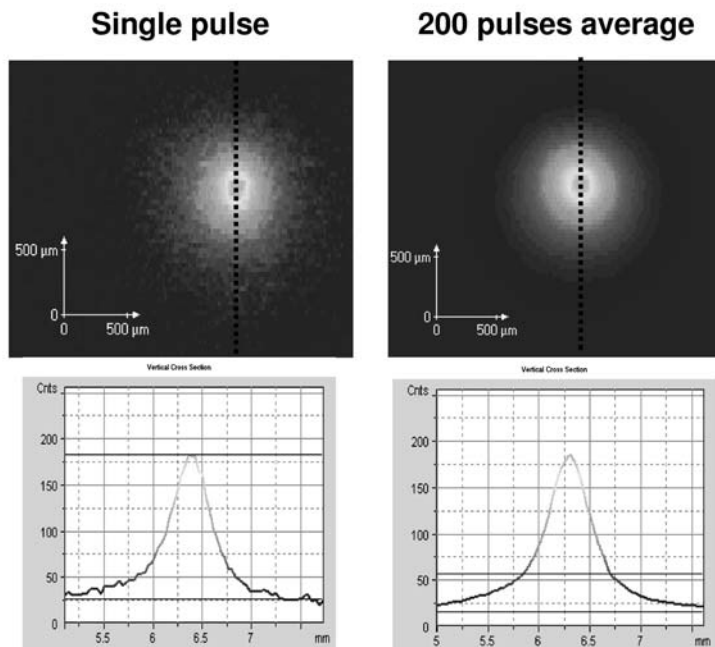


Fig. 22.6. EUV spatial emission from a Z-pinch GDPP EUV source measured on-axis of the emission by an EUV pinhole camera. The FWHM diameter of the emission is $< 500 \mu m$. The single pulse emission (left part) as well as the average over 200 pulses of the emission (right part) is shown documenting the excellent stability of the plasma.

During the development process of EUV sources for lithography at XTREME technologies, metrology equipment as described above was used in order to characterize the EUV source output. In the following paragraph we give an overview of the state of the art of both GDPP and LPP EUV sources so far achieved.

22.5 GDPP and LPP EUV Sources – State of the Art

22.5.1 GDPP EUV Source XTS 13–35 for Integration into EUV Microstepper

The GDPP EUV source development program at XTREME has led to completion of first commercial gas-discharge-produced plasma EUV source prototypes of the type XTS 13–35; in XTS 13–35, 13 stands for the wavelength of 13.5 nm , 35 for the power of 35 W into 2π steradian emitted from the source. These EUV sources have been integrated into the EUV microstepper MS 13 developed at EXITECH Ltd., Oxford, UK [2]. A photograph of the microstepper is shown in Fig. 22.7. The MS 13 is the first commercial EUV exposure tool in the world. The first two EUV microsteppers MS 13 operate at Intel as well at International SEMATECH, both US. The microsteppers are being used as pathfinders for process development to prepare pre-production tools and production process development.

The GDPP source XTS 13–35 uses non-contaminating xenon gas as fuel and is highly efficient: The conversion efficiency of electrical energy stored in the first capacitor C_0 to EUV energy amounts to 0.55%. This includes losses in the pulsed-power circuit as well as reflected energy at the plasma. The intrinsic conversion efficiency, i.e. the ratio of EUV energy to electrical energy fed into the plasma, is significantly higher and amounts to 1.2%.

The main performance parameter of the source is an output power of 35 W EUV in-band radiation (2% bandwidth) into a solid angle of $2\pi\text{ sr}$. The nominal repetition rate is 1000 Hz and the pulse-to-pulse stability is $3\sigma < 20\%$. Assuming a collector optics module with 10% total efficiency, this leads to 3.5 W EUV in-band power in the intermediate focus.

The XTS source is equipped with a debris mitigation system, which was developed at XTREME technologies and extends the optics lifetime to more than 100 Mio. pulses until the reflectivity drops below 90% of the initial value. The collector optics was designed and manufactured by Carl Zeiss, Oberkochen, Germany. First results obtained with the EUV microstepper at Intel were reported in November 2004 [6] demonstrating the generation of 50 nm structures. All components were working still in specifications after 25 million pulses of exposure. The microstepper will be used as technology pathfinder for EUV process development in semiconductor industry as at International SEMATECH, USA.

22.5.2 High-Power Gas-Discharge-Produced Plasma EUV Sources at XTREME Technologies

Porous-Metal Cooling Technology

One of the main challenges in achieving the high power levels required for high-volume manufacturing using EUV lithography with GDPP sources is the thermal management of the electrode discharge region. Using the conventional cooling design of the EUV source XTS 13–35 with cooling fins and water flow a maximum power of 5 kW can be dissipated from the discharge region. Above this power level the electrodes begin to melt.

To achieve significantly better heat dissipation from the discharge region a cooling technology has been developed called porous-metal cooling. In porous-metal cooling the electrodes consist mainly of porous metal that is similar to a sponge and has a very large surface. Water flow is forced by high pressure through the porous metal and high heat exchange from the surface to the water is obtained. With a first version of this setup a cooling power of about 15 kW was achieved in October 2003. Improvements of the geometry led to an increased cooling power of up to 18 kW in February 2004.

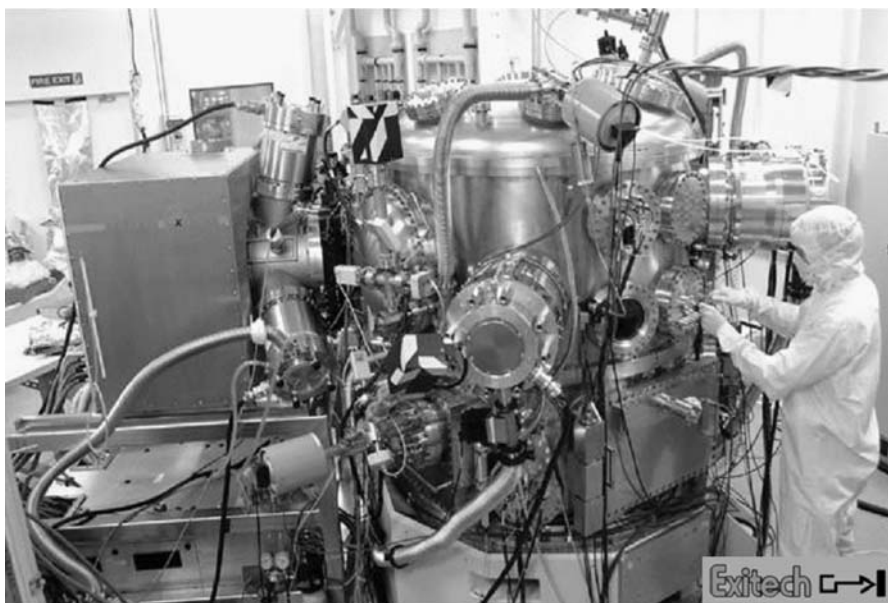


Fig. 22.7. Photograph of one of the first commercial gas-discharge-produced plasma EUV source prototypes of the type XTS 13–35 (in XTS 13–35 13 stands for the wavelength of 13.5 nm , 35 for the power of 35 W into $2\pi\text{ sr}$ emitted from the source). These EUV sources are currently under integration into the microstepper MS 13 at EXITECH, Oxford, UK.

Using the porous-metal cooling technology the GDPP EUV sources can be operated continuously up to a repetition rate of 4500 Hz. The electrical input energy per pulse is kept constant by adaptation of the power supply circuits, and also the conversion efficiency is preserved at the same value as at low repetition rates. The output power curve shows a linear dependence on the repetition rate. 200 W output power into $2\pi \text{ sr}$ are achieved with this high-power GDPP sources (see Fig. 22.8). The electrical power dissipated in the plasma amounts to 20 kW, the conversion efficiency into EUV radiation is 1%.

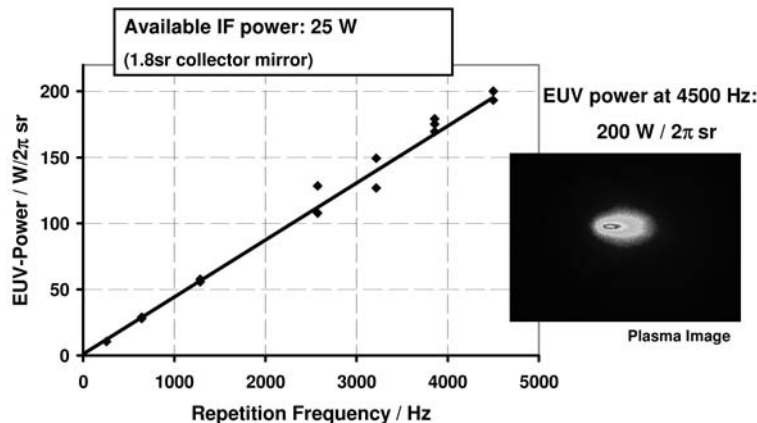


Fig. 22.8. EUV output power as a function of the repetition rate of the discharge for a porous-metal-cooled GDPP EUV source. A maximum power of 200 W in $2\pi \text{ sr}$ can be generated. The linear dependence indicates a constant conversion efficiency for all repetition rates.

The in-band EUV power of 250 W into $2\pi \text{ sr}$ solid angle corresponds to an available power in the intermediate focus of 25 W calculated for a multi-shell Wolter-type collector with 1.8 sr source collection angle and taking into account the practical losses by geometric obscuration by the debris mitigation filter as well as gas absorption in the source collector vacuum chamber (see Fig. 22.3).

The available intermediate focus power achieved in the laboratory with xenon-fueled GDPP sources needs less than 5 times improvement to reach the 115 W required for high-volume manufacturing of chips using EUV lithography. How much of this power can be used in the EUV exposure tool depends on the optical design of the system. The etendue or geometrical flux or phase

space volume of an optical system with the field area A and the numerical aperture given by the solid angle is defined as:

$$E = \int_A \int_{\Omega} dA \cos \alpha \, d\Omega \quad (22.8)$$

The etendue is invariant for the system. For typical values of the EUV scanner etendue of $3.3 \text{ mm}^2 \text{ sr}$ and typical plasma sizes of the GDPP source approximately 70–80% of the available IF power can be used in the scanner. Work is ongoing to reduce plasma sizes so that 90% of the available IF power can be used.

Alternative Target Materials Tin or Lithium

In order to further increase the EUV output power, possibilities of further improvement of heat removal, i.e. cooling as well as improvements of conversion efficiency are under investigation. While still improvements of the conversion efficiency of xenon seem possible (at 200 W output as described above the conversion efficiency is already 1.0%) the implementation of higher efficient emitters at 13.5 nm can provide advantages as compared to xenon. Tin and lithium are potential candidates the emission spectrum of which has been shown to better match to the EUV reflectivity band of the exposure tool mirrors around 13.5 nm [10].

Tin-vapor-based GDPP EUV sources have been built at XTREME technologies. At the same electrical input energy the conversion efficiency for Sn was measured approximately double that of xenon. Emission spectra from tin and xenon under the same excitation conditions are shown in Fig. 22.9. The intensity of the 13.5 nm emission peak for tin is two times higher than that of xenon. Absolute conversion efficiencies into the 13.5 nm band vary from 1.7% to 2.9% depending on the method of tin vapor generation by either electron beam or laser beam evaporation.

The tin-based EUV sources use the same porous-metal cooling technology as the xenon sources described above. It can be operated continuously at 4.5 kHz repetition frequency and emits an in-band EUV power of 400 W into $2\pi \text{ sr}$ with reasonable energy stability. With an 1.8 sr collector mirror and a source collector chamber designed in the same way as for the xenon source the available IF power amounts to 50 W for the tin source. Table 22.3 shows the direct comparison of the experimentally achieved performance of the xenon-fueled and tin-fueled discharge-produced plasma EUV sources.

For the available intermediate focus power still an improvement by a factor of 2.3 is needed to meet HVM power requirements. This should be no “show stopper” and be possible by further improvement of thermal management and conversion efficiency. A large step may also come from collector mirror design. If it is possible to further reduce the size of the EUV emitting plasma size, further development in the field of collector optics will allow

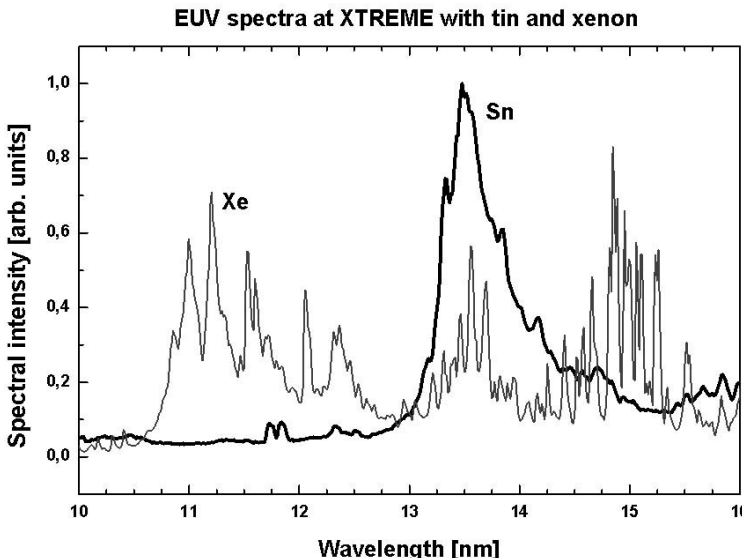


Fig. 22.9. Emission spectra from a GDPP source working with tin in comparison to the xenon spectrum under the same excitation conditions. The intensity at the 13.5 nm band emission for tin is approximately two times higher than that of xenon. In conclusion the conversion efficiency of tin is approximately twice compared with the conversion efficiency of xenon.

Table 22.3. Comparison of the EUV power of Xe and Sn discharge sources

Fuel	xenon	tin
	status 11/2004	status 11/2004
Heat removal from discharge (kW)	20	20
Conversion efficiency (%)	1.0	2.0
EUV power (W/2π sr)	200	400
Transmission of debris mitigation	0.8	0.8
Collection solid angle (sr / 2π sr)	0.3	0.3
Average reflectivity of collector	0.63	0.63
Gas transmission in collector module	0.85	0.85
Available IF power (W)	25.7	51.4
Etendue acceptance factor	0.5-1.0	0.5-1.0
Usable IF power (W)	12.8-25.7	25.7-51.4

a maximum collection angle larger than the 1.8 sr (90° full opening angle) realized today. Depending on the EUV source size the collectable solid angle of πsr seems to be realistic. Taking into account the lower reflectivity at

larger incidence angles the collection efficiency is expected to improve, due to the larger collection angle, by a factor of approximately 1.5. With these values without any additional improvement of the heat extraction from the discharge region the estimated power for Sn EUV sources can reach already 75 W in the intermediate focus.

The data presented above and the discussion show that it will be possible to achieve the power necessary for high-volume manufacturing with EUV lithography by using Sn as the emitter material in GDPP EUV Source. Also lithium has been reported to show 2% conversion efficiency in GDPP sources.

However the risks in the technology are still high. Firstly, source collector mirrors have to be developed which withstand the high total radiation power load of about 10 kW from EUV to IR onto the collector including the necessary cooling capability. Secondly the risks of highly efficient but condensing fuels instead of xenon are still high taking into account the requirements connected with collector optics lifetime and source component lifetime.

Several 100 g of condensing material throughput per day have to be supplied and handled in an EUV source at distances of only 10 cm to 20 cm from the collector optics. Fuel supply, handling and optics protection against contamination are some of the most important development task to be solved in the next future.

22.5.3 Laser-Produced Plasma EUV Sources at XTREME technologies

The other approach for EUV sources that reduces the problem of thermal management significantly is that of laser-produced plasma. LPP sources employ a quasi mass-limited target [10] that is injected in a vacuum chamber where it is excited by a pulsed laser-beam [11, 12]. These sources are investigated at XTREME technologies GmbH since 2001, in parallel with gas-discharge-produced plasma (GDPP) sources. The laser-produced plasma can be generated at a large stand-off distance of several centimeters from any surrounding hardware, which is an inherent advantage when dealing with the heat-load per unit-area associated with the requirements of high-volume manufacturing.

At XTREME technologies xenon targets have been used exclusively in the LPP sources in the past because this particular target material provides an excellent compromise of high efficiency and low debris ejection. To comply with the large stand-off distance requirement, the injection system was specifically designed to provide a spatially very stable target. The plasma is typically generated at a distance of 5 cm or more from the nozzle orifice which is the closest hardware surrounding the actual EUV source.

To drive LPP EUV sources pulsed high-power lasers based on side-pumped rod lasers have been developed. Earlier results have been reported

for LPP EUV sources at XTREME technologies which used a high-power laser, which delivered up to 500 W at almost diffraction limited beam quality ($M^2=2$) in short ns pulses [11]. A photograph of a laboratory installation of such a LPP EUV source is shown in Fig. 22.5. These sources emit 2 W EUV in-band output power into $2\pi\text{ sr}$ solid angle. One of the most crucial tasks in this source development has been to achieve the maximal conversion efficiency (CE) of laser energy into the desired EUV band centered at 13.5 nm within a 2% bandwidth. Considering LPP as an approach for high-volume manufacturing using EUV lithography, high CE values are required

- (a) to minimize the heat that is dissipated in the source and must be removed by cooling, and
- (b) to minimize the necessary drive power of the laser system.

By continuous improvements of the target systems and by adapting the laser pulses to optimize the plasma conditions for the emission of in-band EUV radiation a maximal conversion efficiency from laser light into EUV radiation of 1% (assuming isotropic emission) in a $2\pi\text{ sr}$ solid angle has been achieved. Due to the high spatial stability of the targets the conversion efficiency under typical operation conditions of the LPP EUV sources is reaching almost the maximum average conversion efficiency. Typical values of day-to-day achievable conversion efficiency are at 0.8%. Connected with the directional stability of the target is also the pulse-to-pulse energy stability of the EUV emission. Also with the LPP sources energy stabilities of $3\sigma < 20\%$ are obtained as for the GDPP sources and are thus coming close to high-volume manufacturing requirements.

To further increase the EUV power, recently a high-power laser with average output power in excess of 1.2 kW has been completed as driver of a LPP EUV source. With a beam quality of $M^2 = 10$ the pulse repetition frequency can be adjusted to arbitrary values up to 10 kHz. The laser consists of a Q-switched oscillator, pre-amplifier and two chains of four cw diode-pumped rod amplifiers. Using this laser an EUV in-band power of up to 10 W in $2\pi\text{ sr}$ can be generated. This power corresponds to a power of approximately 3.5 W which can be achieved in the intermediate focus by using a 5 sr collector mirror. The power delivered to the intermediate focus has to be achieved while complying with the etendue restrictions imposed by the optics design of the EUV scanner. The dimensions of the source are well below any etendue limits. Also, the shape of the EUV distribution is quasi Gaussian, which implies that 86% of the energy is emitted from a volume of about 250 μm in diameter. The angular distribution of the EUV emission indicates that the anisotropy is relatively small in a plane perpendicular to the laser axis while it becomes significant in a plane parallel to the laser beam.

In order to collect the EUV radiation emitted from the plasma as efficient as possible, collectors for large solid angles have to be developed. Taking

into account limitations of the collectible plasma size, collectors with 5 sr collection angle seem to be viable approaches. At XTREME technologies first LPP collectors have been developed based on a normal-incidence mirror to project the emitted power of a $\pi\text{ sr}$ solid angle into the intermediate focus. A first set of these mirrors has been integrated into the LPP EUV source. A photograph of one of these mirrors is shown in Fig. 22.10.

The development of LPP EUV sources with output powers necessary for high-volume manufacturing with EUV lithography is considered the biggest challenge for the development of extremely high-power laser drivers. From Table 22.2 an EUV power of 340 W in $2\pi\text{ sr}$ has been estimated to be necessary for high-volume manufacturing. With a conversion efficiency of 1.0% for the xenon LPP source the driver laser(s) must have a power of 32 kW at the target. Alternative target materials as tin or lithium show conversion efficiencies of 3%. These target materials would reduce the necessary laser power to about 10 kW , however with the disadvantage of the more difficult handling of the metal fuels as well as the related contamination potential of the optics. The most powerful commercial solid state laser available today for machining applications have an average power of 6 kW . However, these lasers are cw lasers and not Q-switched pulsed laser systems as demanded for the EUV source application. Carbon dioxide lasers may be an also viable alternative because pulsed lasers with more than 2 kW average power are commercially available. Also excimer lasers seem to be possible, which has however the disadvantage of rather high cost of the UV photons. Estimates about cost of operation of high-power driver lasers give a clear indication that diode-pumped solid-state lasers offer the most cost-efficient technology because of the long lifetimes of the laser diodes of more than 20 000 hours. It will be crucial for the EUV lithography source development based on LPP technology to build highly efficient solid-state lasers with reliable modules of proven design. Corresponding work is going on at XTREME technologies.

22.6 Outlook

Since 2001 considerable progress in terms of power and lifetime has been made in the development of EUV sources based on laser-produced plasmas and gas discharge plasmas at XTREME technologies.

Gas-discharge-produced plasma source have improved the available EUV in-band power by more than 2 orders of magnitude over the last 3 years and are leading the power race towards sources for high-volume manufacturing (HVM) (see Fig. 22.11). The progress has resulted in an EUV power of 400 W at 4.5 kHz repetition rate from a tin-fueled source and 200 W from a xenon-fueled source. This power, obtained in continuous operation, could be achieved due to major cooling improvements and implementation of porous-metal cooling technology. The available intermediate focus power for these sources is calculated to be in the range of 50 W . How much of this power

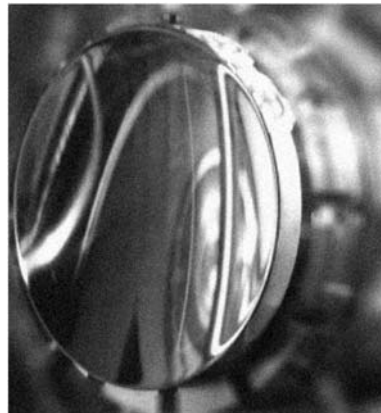


Fig. 22.10. Photograph of a coated 0.35 sr EUV multi-layer collector mirror for a LPP source

can be used in the EUV exposure tool depends on the optics design and therefore and on the etendue specification. The pulse-to-pulse stability of the EUV energy is better than standard deviation $3\sigma < 20\%$ without any active stabilization.

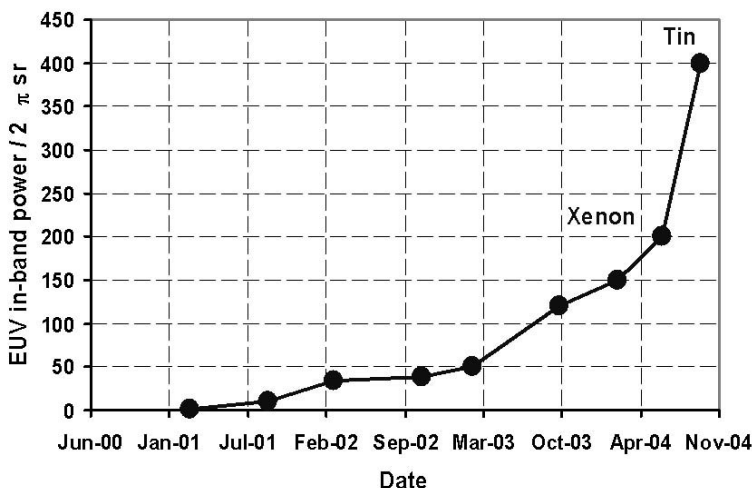


Fig. 22.11. Historical evolution of EUV in-band power emitted into $2\pi \text{ sr}$ solid angle for GDPP EUV sources from the same plasma volume. The available EUV output power could be increased by more than 2 orders of magnitude from April 2001 to November 2004.

Prototypes of commercial gas discharge sources with an EUV power of 35 W in $2\pi \text{ sr}$ have been integrated into EUV microsteppers which are being used as pathfinders for EUVL. The microstepper source XTS 13–35 is equipped with a debris filter which results in an optics lifetime exceeding 100 million discharges at 1000 Hz repetition frequency. The same lifetime was achieved for the components of the discharge system itself.

The LPP laboratory sources achieved an output power of 10 W in $2\pi \text{ sr}$ with a laser driver power of above 1 kW. The LPP sources were reliably operated and employed to investigate components lifetime. The source diameter of about $250\mu\text{m}$ ($1/e^2$) will allow large collection angles of 5 sr while staying well below the etendue limit. The expected intermediate focus power is accordingly 3.5 W.

GDPP and LPP sources still compete for the technology of HVM sources. LPP sources have demonstrated the feasibility of the technology itself. Although currently LPP sources deliver much less power into $2\pi \text{ sr}$ today they offer high efficiency when projecting the power into intermediate focus. In addition they have much more relaxed cooling requirements than GDPP sources which makes forecast about power scaling easier. However LPP sources will be very complex and much less robust than GDPP sources.

Gas-discharge-produced plasma sources are currently more advanced in power than LPP sources. The first industrial installations – the EUV microsteppers – are equipped with GDPP pinch sources and have printed circuits as technology pathfinders starting in 2004. The GDPP development program at XTREME technologies is focused onto the main critical issues in EUV source technology as lifetime of the electrodes and collector optics lifetime. We expect GDPP technology to be able to support lifetimes reasonable for high-volume manufacturing of computer chips with EUV lithography. Once these data will be nearly demonstrated the industry will focus on GDPP EUV source technology because of its robustness and reliability. Only in case the targets will not be met by GDPP the very complex and expensive LPP technology will be used to realize the light sources before high-volume manufacturing in 2009. XTREME technologies' EUV source development program focuses onto a decision on the technology in 2005.

References

1. D.A. Tichenor, W.C. Replogle, S.H. Lee, W.P. Ballard, A.H. Leung, G.D. Kubiak, L.E. Klebanoff, S. Graham, J.E. Goldsmith, K.L. Jefferson, J.B. Wronosky, T.G. Smith, T.A. Johnson, H. Shields, L.C. Hale, H.N. Chapman, J.S. Taylor, D.W. Sweeney, J.A. Folta, G.E. Sommargren, K.A. Goldberg, P.P. Naulleau, D.T. Attwood, E.M. Gullikson: Proceedings of SPIE **4688**, 72–86 (2002)

2. M. Whitfield, A. Brunton, V. Truffert, P. Gruenewald, J. Cashmore, P. Richards, M. Gower: "MS-13 EUV microstepper", in *2nd International Extreme Ultra-Violet Lithography (EUVL) Symposium*, Antwerp, Belgium (Sept. 30–Oct. 02, 2003)
3. V. Banine, R. Moors: Proceedings of SPIE **4343**, 203–214 (2001)
4. R. Gontin: "EUV source requirements", in *SEMATECH International EUV source workshop* Santa Clara, CA, USA (March 3, 2002)
5. Y. Watanabe: "EUV source requirements", in *SEMATECH International EUV source workshop*, Santa Clara, CA, USA (February 22, 2004)
6. EUVL: "EUV source requirements", in *Proceedings of 2nd International Extreme Ultra-Violet Lithography (EUVL) Symposium*, Antwerp, Belgium (30 Sept.–02 Oct. 2003)
7. W.H. Bennett: Phys. Rev. **45**, 890 (1934)
8. V. Borisov, A. Demin, A. Eltzov, A. Ivanov, O. Khristoforov, Y. Kirykhin, A. Vinokhodov, V. Vodchits, V. Mischenko, A. Prokofiev: "A comparison of EUV sources for lithography based on Xe and Sn", in *Proceedings of 2nd International Symposium of Extreme Ultraviolet Lithography*, Antwerp, Belgium (2003)
9. M.C. Schüermann, T. Mißalla, R. Lebert, L. Juschkin, C. Wies, R.M. Klein, F. Scholze, G. Ulm, K. Mann, S. Krantzsch: in *Proceedings of 2nd International Symposium of Extreme Ultraviolet Lithography*, Antwerp, Belgium (2003)
10. M. Richardson, K. Gäbel, F. Jin, W.T. Silfvast: OSA Proc. on Soft X-Ray Projection Lithography **18**, 156–162 (1993)
11. U. Stamm, I. Ahmad, I. Balogh, D. Bolshukhin, F. Flohrer, K. Goebel, S. Goetze, G. Hergenhan, J. Kleinschmidt, D. Kloepfel, P. Koehler, V. Korobotchko, J. Ringling, G. Schriever, C.D. Tran: "High-power EUV lithography sources based on gas-discharges and laser-produced plasmas", in *Proceedings of SPIE's 28th Annual International Symposium on Microlithography*, **5037**, Santa Clara, CA, USA (2003)
12. U. Stamm, I. Ahmad, V.M. Borisov, F. Flohrer, K. Gäbel, S. Götze, A.S. Ivanov, O.B. Khristoforov, D. Klöpfel, P. Köhler, J. Kleinschmidt, V. Korobotchko, J. Ringling, G. Schriever, A.Y. Vinokhodov: Proc. of SPIE **4688**, 122–133 (2002)

List of Abbreviations

a-C	amorphous carbon
AFM	atomic-force microscope/microscopy
AMLCD	active matrix LCD
APD	ablative photodecomposition
AR	antireflective
ASE	amplified spontaneous emission
BGA	ball grid array
BN	boron nitride
c-BN	cubic boron nitride
CCD	charge-coupled device
CE	Conformité Européenne
CEN	European Committee for Standardization
CFC	chlorofluorocarbon
CMOS	complementary metal oxide semiconductor
CVD	chemical vapor deposition
DLC	diamond-like carbon
DNA	deoxyribonucleic acid
DOE	diffractive optical elements
DoF	depth of focus
DPE	diffractive phase elements
DRAM	dynamic random access memory
DUV	248 nm, 193 nm
DUV	deep UV
EBDW	electron beam direct write
EDM	electro discharge machining
EEA	European Economic Area
EELS	electron-energy loss spectroscopy
ELA	excimer laser annealing
ELIF	excimer-laser-induced fluorescence
EMC	electromagnetic compatibility
EMI	electromagnetic interference

EPL	electron projection lithography
EUV	extreme UV
FBG	fiber Bragg grating
FDA	Food and Drug Administration (U.S.A.)
FDM	frequency-domain modulation
FED	field emission displays
FEL	free-electron laser
FEP	fluorinated ethylene propylene
FHG	fourth harmonic generation
FSR	free spectral range
FWHM	full width (at) half maximum
GDPP	gas-discharge-produced plasma
GTO	gate turn-off
HAZ	heat-affected zone
h-BN	hexagonal boron nitride
HR	highly reflective, high-reflective
HVM	high-volume manufacturing
IC	integrated circuit
IFTA	iterative Fourier transform algorithm
IGBT	insulated gate bipolar transistor
IPL	ion projection lithography
ITRS	international technology roadmap for semiconductors
LASIK	laser in-situ keratomileusis
LC	liquid crystal
LCD	liquid crystal display
LCVD	laser-induced CVD
LDE	laser dry etching
LIBS	laser-induced breakdown spectroscopy
LIBWE	laser-induced backside wet etching
LIDT	laser-induced damage threshold
LIF	laser-induced fluorescence
LIFT	laser-induced forward transfer
LIGA	Lithographie, Galvanik, Abformung = lithography, electroplating, molding
LIPAA	laser-induced plasma-assisted ablation
LPP	laser-produced plasma
LSC	laser-supported combustion
LSI	large scale integrated
LTPS	low temperature polysilicon (technology)
LVD	low voltage directive

MALDE	microwave-assisted LDE
MAPLE-DW	matrix-assisted pulsed laser evaporation-direct writing
MCM	multichip modules
MMA	methyl methacrylate
MOPA	master oscillator power amplifier
MZ	Mach-Zehnder (interferometer)
μ -TAS	micro total analysis system
NA	numerical aperture
OLED	organic light-emitting diodes
OPC	optical proximity correction
OPD	optical path difference
PA	polyamide
PaCO ₂	partial arterial pressure CO ₂
PaO ₂	partial arterial pressure O ₂
PC	personal computer
PC	polycarbonate
PCB	printed circuit board
PDMS	polydimethyl-siloxane
PE	Polyethylene
PED	pressure equipment directive
PEEK	poly-ether ether-keton
PES	Polyester
PET	Polyethylene-terephthalate
PFL	pulse forming line
PI	Polyimide
PLC	planar lightwave circuits
PLD	pulsed laser deposition
PMMA	polymethyl-methacrylate
PP	Polypropylene
ppb	parts per billion (10^{-9})
ppm	parts per million (10^{-6})
PRK	photo refractive keratectomy
PSM	phase shift mask
PTFE	Polytetrafluoro-ethylene (DuPont: Teflon [®])
PTK	photo therapeutic keratectomy
PU	Polyurethane
PVC	Polyvinyl-chloride
PVD	pulsed vapor deposition
PSU	polysulfon
R ² P ²	Resonant Regulating Pulsed Power supply

REM	raster electron microscope/microscopy
RIE	reactive ion etching
RGH	rare gas halide
rms	root mean square
RP	retinitis pigmentosa
SCALPEL	scattering with angular limitation projection electron-beam lithography
SCP	surface corona preionization
SEM	scanning electron microscope (=REM)
SEMI	Semiconductor Equipment and Materials Institute
SLG	super lateral growth
SLS	sequential lateral solidification
SMD	surface mounted device
SMPS	switched mode power supply
SMT	surface mount technology
SROMA	spatially resolving optical multichannel analyser
TAB	tape automated bonding
ta-C	tetrahedral amorphous carbon
TE	transverse electric
TFT	thin film transistor
THG	third harmonic generation
TM	transverse magnetic
TSI	top surface imaging
UV	ultraviolet
UV-A	spectral region A of the UV
UV-B	spectral region B of the UV
VHNA	very high numerical aperture
VUV	157 nm – 50 nm
WC	tungsten (wolfram) carbide
XRL	X-ray lithography
XUV	50 nm – 1 nm

Index

- Abbe diffraction limit, 399
ablation, 17, 127, 139, 149f, 155, 162, 179f, 187f, 203, 229f, 336f, 365f
 rear side ablation, 180, 183
ablation debris, 183, 226, 233f, 249, 269, 271
 ablation soot, 238
ablation depths, 2, 142, 150, 155, 203f, 212, 232, 327, 339, 394
ablation of ceramics, 155
ablation of diamond, 329
ablation of glass, 201f, 328
ablation of metals, 151
ablation of polymers, polymer ablation, 20, 167, 187, 189, 212f, 228
ablation of tissue, 361f
ablation plume, 151, 190, 224
ablation photodecomposition, 17
ablative photo decomposition(APD) 139
ablation rate, 151, 172, 189, 203, 213, 218, 227, 229f, 394
 ablation etch rates, 227
ablation threshold, 142, 165, 192, 222, 227, 229, 253, 265, 326
absorbance, 169, 361
absorption, 35, 120f, 149, 152, 210, 229, 256, 285, 298f
absorption by air, 222, 225
absorption coefficient, 150f, 210, 162, 227, 254, 168, 210, 227, 254, 291, 299, 330, 344
absorption depth, 401
absorption depth of EUV radiation, 401
absorption length, 17, 361
absorptivity, 188
activation of dielectrics, 331
active matrix liquid crystal display (AMLCD), 306
aircraft cable, 321, 324, 330
all-solid-state switching, 56
amorphous carbon (a-C), 335f
amplified spontaneous emission (ASE), 100, 261
annealing, 26, 52, 87, 140, 144, 340, 306f, 340f
arc-free discharge, 49
arcing, 49, 52, 54, 75
ArF laser, 76, 82f, 166f, 227f, 253, 260, 297, 304, 327, 361
atomic force microscope (AFM), 227, 230f
attenuator, 122, 128f

bacterial filter, 198
ball grid array (BGA), 194
bar code, 321, 324
batch identification, 321
beam diagnostics, 105, 109, 133f, 225
beam divergence, 110
beam parameter, 107
beam profile, 52, 109, 105f, 112, 131, 133, 135, 187, 244, 311, 317, 390
bilumen catheter, 196
biocompatibility test, 168
biomimetic matrix, 169
biophotonics, 221f
biophotonic chip, 272
 biophotonics on a chip, 268
birefringence, 231, 254, 257, 259f, 267, 298f
black body radiation, 404
bleaching, 321, 323
Boltzmann distribution, 36
boron nitride (c-BN), 335f, 346

- borosilicate glass, 182, 201f
 buried optical waveguide, 254, 264f
 burst mode operation, 99, 387, 388
 C-C transfer, 53
 C4 technology, 195
 capacitive sensor, 162
 car engines, 351
 carbon, 140
 carbon deposits, 329
 carbon fiber, 198, 318, 320
 carbon (ta-C) film, 140, 335f,
 castellated electrodes, 271
 catheter, 167f, 196, 325, 326, 396
 central island phenomenon, 365
 ceramics, 140, 153f, 170f, 321, 331
 channels, 23, 24, 43, 163, 175, 202, 206f,
 221, 231, 234f, 254, 268
 plasma channels, 373
 chemical vapor deposition (CVD), 206
 chrome on quartz, 14
 chrome films, 240
 chrome layer, 239f
 chrome mask, 182, 226, 234, 271
 chrome-coated optics, 239
 chromophores, 149, 150
 cleaning, 121, 141f, 160, 161, 207, 233,
 234, 240, 241, 249f, 269, 359, 369
 cleaning of paintings, 142
 cleaning of rotogravure, 160
 cleaning of the laser gas, 62f
 clearing ratios, 75
 coatings, 119f, 221, 233, 335f, 385, 394
 coatings for X-ray mirrors, 140
 cold ablation, 127, 139, 189, 194
 collector mirror, 415, 418, 420
 collector optics, 401, 403, 405f
 collisional deactivation, 44
 color centers, 254, 298
 color changes, 322, 323, 393
 combustion analysis, , 351f
 command resonant charging, 60
 compaction, 101, 171, 229, 254f, 298
 condom leak-testing, 198
 conflict diamonds, 329
 conformal scanning, 157
 Conformité Européenne (CE), 64, 423
 congruent evaporation, 140, 339 contact
 lenses, 196
 contact mask, 156
 contamination control system, 64
 controlling refractive index, 253f
 conversion efficiency (CE), 14, 62, 412,
 414f
 cooling system, 63
 corpuscular theory, 33
 critical dimension, 98, 304, 399f
 cubic boron nitride (c-BN), 335, 346
 current rise time, 53
 customized ablation, 365
 cylindrical lenses, cylinder optics, 130,
 218, 311
 damage fluence, 120, 121
 damage threshold, 120, 180, 223, 240,
 258
 dc resonant, 58, 59, 60
 debris, 152, 183, 190f, 203, 214f, 233f,
 253, 269, 404, 412, 414f
 debris filter, 403, 406, 421
 debris mitigation, 412, 414
 deep ultraviolet (DUV), 15, 90, 94, 98,
 119, 123, 266, 297, 302, 423
 DUV lithography, 94, 98
 deoxyribonucleic acid (DNA), 159, 287
 depth of focus (DoF), 91, 132f, 163,
 265f, 296f, 302f, 399
 detonation waves, 165
 dielectric mask, 157, 180, 182
 diamond, 232, 242f, 279, 285, 329f, 335,
 341
 dielectrical sensor, 162
 diffractive optical elements (DOE), 116,
 182, 198, 221, 222, 245f, 423
 diffractive phase elements (DPE), 182,
 183
 direct multiphoton excitation, 376, 380
 discharge arcing, 51
 discharge circuit, 48, 52, 53, 386
 discharge cross-section, 49, 85f
 discharge electrodes, 48f, 78, 86
 discharge stability, 49, 76, 82, 83
 discoloration, 321
 double pulse excitation, 57
 drilling, 4, 17, 25, 28, 128, 140, 143f,
 155, 162f, 187f, 201, 203f, 390
 duct oscillations, 77
 dust, 141

- dust filtration, 64
 dust precipitator, 64
 DUV, see deep ultraviolet
- E95%, 95, 96
 electrode burn-off, 50, 64
 electrode erosion, 49
 electrode lifetime, 12, 52
 electrode materials, 51, 52, 64
 electrode profile, 51, 83
 electrode structures, 49
 electromagnetic compatibility (EMC),
 65, 68, 423
 electromagnetic interference, (EMI),
 61, 423
 electron beam, 81f, 300
 electron beam direct write (EBDW),
 300
 electron beam evaporation, 415
 electron beam lithography, 301
 electron densities, 49f, 58, 83
 electroplating, 176
 EMC directive, 65, 423
 EMC standards, 65, 67, 68
 energy dose control, 98f
 engraving, 321f, 329
 erosion, 22, 52f, 64
 erosion rate, 51, 64
 etching, 17, 18, 19, 93, 140, 140f, 156,
 179f, 228f, 238f, 258f, 295, 302
 etendue, 405, 409, 414, 415, 418, 420,
 421
 European Committee for Standardization (CEN), 70
 European directives, 65, 68
 EUV, see extreme ultraviolet
- excimer laser transitions, 41, 42
 excimer lasers for microlithography,
 89f, 303
 excimer lasers for medical applications,
 361f
 exciplexes, 6, 8, 42
 excitation rate, 43
 excited dimer, 8, 42
 extreme ultraviolet (EUV), 91, 121,
 124f, 300, 399f, 424
 EUV lithography, 125, 399f
 EUV sources, 399f
- XUV, 119, 124, 400
 XUV coatings, 124f
 XUV lasers, 126
 EUV mask, 402
 EUV microstepper, 401, 412f
 EUV pinhole camera, 410, 411
 EUV scanner, 401, 402, 403, 404,
 415, 418
 EUV spectograph, 410
- F₂-laser, fluorine laser, 42, 107, 108,
 115, 121, 182, 212f, 301, 349
 F₂-laser photosensitivity, 254, 258, 263,
 265
 feature size, 90, 91, 92f, 135, 235, 238,
 279, 295, 297f, 400
 femtosecond excimer laser, V, 182, 191,
 279f
 fertility treatment, 197
 fiber Bragg grating (FBG), 6, 22, 25,
 140, 143, 144, 181, 223, 243, 258,
 313f
 field emission displays (FED), 312
 flow clearing (ratio), 75, 76
 flow loop, 76, 77f
 fluorine passivation, 52
 flying spot scanning, 366
 free electron laser (FEL), 38, 124
 free spectral range (FSR), 96, 261
 fuel sprays, 352, 353
 fused silica, 94, 101, 129, 132, 152, 156,
 179, 180, 182, 183, 188, 221, 227,
 229f, 279, 287, 298f, 315
- g-line, 92, 296
 gas discharge, 11, 41, 51, 82, 402, 419
 gas filter, 63, 359
 gas lasers, 9, 38, 69
 gas lifetime, 11, 50, 88, 388, 397
 gas purification, 64
 gas-discharge-produced plasma
 (GDPP), 402, 404, 419
 GDPP EUV sources, 406, 414, 420
 germanosilica, 229, 254, 263, 268
 glass marking, 144, 328
 glaucoma surgery, 361, 367
 glow discharge instability, 48, 58, 83
 Gordon Moore, 89, 295

- gratings, 140, 174, 182, 238, 243, 258, 262, 282, 314
- halogen gas loss, 64
- halogen injections, 64
- harpooning reaction, 43
- Hartmann-Shack wavefront sensor, 114
- heat diffusion length, 152
- heat exchanger, 63, 81
- heat-affected layer, 232
- heat-affected zone (HAZ), 17, 140, 168, 193, 228, 231f, 279, 321, 325, 424
- hidden identification marks, 328
- high-resolution mask imaging, 311
- high-average-power excimer lasers, 79
- high-energy lasers, 81
- high-power excimer lasers, 59, 75, 130, 307
- high-repetition-rate, 75, 76, 385
- high-repetition-rate excimer lasers, 14, 75, 50, 56, 173, 390
- high-temperature superconducting films, 335
- high-volume lithography, 14
- high-volume manufacturing (HVM), 43, 400, 421
- hole drilling, 17, 187, 192, 197
- hollow atoms, 373, 377, 379
- hollow plasma channels, 373
- homogenized beams, 112
- homogenizer, 112, 130, 133, 159, 187, 311
- hyperopic eye, 362
- i-line, 26, 92, 296
- identification codes, 144, 321, 328
- imaging optics, 156, 296, 402
- immersion fluid, 91
- immersion lithography, 121, 221, 399
- implant materials, 169
- in-band energy meter, 410
- incubation, 174, 188, 207, 229, 247, 253,
- indirect ablation, 179
- injector channels, 269, 270
- ink jet nozzles, 25, 127, 144, 167, 322, 390
- interference of multiple beams, 281, 282
- intermediate focus, 403, 405, 412, 418
- intermediate focus power, 414, 421
- k-factor, 399, 400,
- kinetic energy, 164, 336, 337, 338, 341, 408
- kinoforms, 182, 246
- KrF laser, 1, 9, 14, 42f, 82f, 84, 97, 99f, 111f, 112, 126, 144, 161, 169, 172, 183, 187, 247, 258, 280, 317, 331, 361, 377
- L-C inversion circuit, 55, 56
- lab-on-(a)-chip, 201, 234, 269, 393
- large-area ablation, 365
- laser activation, 331, 333
- laser angioplasty, 361, 369
- laser beam characterization, 105, 116
- laser cavity, 37, 54
- laser cleaning, 141, 142, 147
- laser chemical vapor deposition (LCVD), 140, 141, 144, 146
- laser dry etching (LDE), 141, 146
- laser engraving, 321
- laser in-situ keratomileusis (LASIK), 19, 143, 144, 361, 364
- laser radiation safety, 65, 70,
- laser resonator, 37, 94, 133,
- laser sputtering, 140
- laser vision correction, 28, 143, 144
- laser-induced backside wet etching (LIBWE), 179, 180, 243, 247
- laser-induced breakdown spectroscopy (LIBS), 142
- laser-induced chemical vapor deposition (LCVD), 140, 141, 144, 146
- laser-induced damage threshold (LIDT), 120
- laser-induced fluorescence (LIF), 29, 203, 287, 351, 356
- laser-induced forward transfer (LIFT), 183, 285
- laser-induced plasma-assisted ablation (LIPAA), 180, 243
- laser-produced plasma (LPP), 406, 409, 412, 417, 421
- laser-produced plasma EUV sources, 408, 417
- LASIK, 19, 143, 144, 361, 364, 424
- leak detectors, 174
- lenses, 94, 132f, 183, 196, 234, 267, 394

- LIGA, 176, 424
 light amplification, 6, 36, 124
 line beam optics, 311
 line narrowing, 94, 97, 103
 liquid-crystal displays, 243, 306, 309, 424
 lithium target material, 415
 lithography, 5, 12, 27, 71, 89, 93, 100, 140, 401
 lithography equipment, 15, 401
 lithography lenses, 163
 logos, 321
 long optical pulses, 57, 88
 long-term testing, 394
 loss processes, 43, 44, 49
 low-voltage directive, 65, 68, 70
 LPP sources, 404, 417, 421
- machinery directive, 65, 69, 70
 magnetic pulse compression, 54, 56
 magnetic self-focusing, 407
 magnetic switch, 12, 55, 57, 402
 marking, 321
 marking depth, 324, 330
 marking of diamonds, 329
 marking of spectacles, 327
 mask fabrication, 10, 156, 185, 222, 238
 mask projection, 11, 128, 134, 156, 172, 201, 211, 216, 244, 281, 323
 mask projector, 157
 mask writing, 26, 223, 301
 matrix-assisted pulsed laser
 evaporation-direct writing (MAPLE-DW), 331, 425
 Max Planck, 11, 12, 33
 metallization of dielectrics, 331
 metals, 122, 151, 155, 174, 243, 280f, 321f, 358
 micro channels, 10, 206, 222, 235, 268, 269 (see also "channels")
 micro-electric mechanical systems (MEMS), 183, 221, 233
 micro fabrication, 144, 149f, 275, 281
 microfluidic channels, 221, 234, 268, 269, 271, 274
 micro fluidics, 209
 microfluidic test structure, 175
 micro gears, 173
 micro-lens arrays, 234
 micro lenses, 115, 181, 183
 microlithography, 26, 56, 89, 91, 92, 95, 98, 102, 127, 143, 144, 295, 303, 394
 micro machining, 155, 286, 351
 micro-machining distortion, 232
 micro-machining workstation, 286
 micro nozzles, 174
 micro-optics fabrication, 181, 234
 micro parts, 174
 micro reaction systems, 217
 micro structuring, 25, 144, 153, 177, 185
 micro vias, 193, 194, 196, 222, 269
 Mie scattering, 352
 minimum feature size, 92, 400
 mixer structures, 218
 Moore's Law, 89, 295
 multi-component ceramics, 140
 multichip modules, 17, 194, 425
 multilayer mirrors, 126, 402, 410
 multilayer printed circuit boards (PCBs), 192, 425
 multilayer-coated mirrors, 401
 multilayer tool, 410
 multipass-illuminator, 158
 myopic eyes, 361, 362
- nano-lithography, 5
 nano-scale fabrication, 279
 nano-structuring, 5
 nano-structuring with femtosecond excimer laser pulses, 279
 nanofabrication, 183, 221
 node, 92f, 121f, 300f, 399f
 nozzle, 25, 77, 127f, 144, 163, 174, 196f, 224, 390, 410, 417
- one-shot-marking, 330
 optical fiber, 6, 186, 196, 229, 233, 237, 244f, 258f, 275, 313, 314, 359, 368
 optical lithography, 89, 91, 119, 126, 295, 299f, 399f
 optical materials, 119, 132, 182, 243, 253, 281, 298f, 385, 395
 optical penetration depth, 150, 152, 153, 155, 233, 265, 298
 optical resolution, 296
 optics protection, 416

- organic light-emitting diode (OLED), 312
- overshoot behavior, 387
- parallel hole drilling, 199
- particle contamination, 152, 402
- particle theory of light, 33
- particulate reduction, 340
- particulates, 233, 302, 339f
- passivation, 52, 64, 195f, 295
- pellicle, 302, 303
- pharmaceuticals, 326
- phase elements, 182, 423
- phase mask method, 314f
- phase shift mask (PSM), 300, 425
- photo refractive keratectomy (PRK), 361, 425
- photo therapeutic keratectomy (PTK), 363, 425
- photonic crystals, 279, 282,
- photosensitive fiber, 314
- photosensitivity response, 253f
- pinch effect, 407
- pinch plasma, 407
- Planck's formula, 404
- plasma cleaning, 64
- plume ejection, 288
- polymer tubes, 216
- polymers, 19, 132, 143, 149f, 177f, 201, 212f, 221f, 310
- population inversion, 34f, 52
- porous-metal cooling, 413, 415
- power supply topologies, 59
- powerplants, 351, 358
- precipitation system, 64
- precise depth profiling, 179
- precision orifice, 173
- preionization, 9, 49f, 85f, 386, 407, 426
- pressure equipment directive, 65, 68
- pressure waves, 76, 369
- profile of the laser beam, 51
- projection lenses, 94, 132, 135
- psoriasis, 370
- pulse compression techniques, 56
- pulse forming line (PFL), 57, 425
- pulse length, 100, 101, 121, 150, 303
- pulsed laser deposition (PLD), 29, 140, 342, 346, 404, 425
- pulser, 52, 57f
- pump energy densities, 52
- pump power densities, 43
- purge systems, 63
- Pyrex, 201
- radiation-damage, 253
- Raman scattering, 352, 353, 355, 356
- Rayleigh scattering, 352, 356
- reaction channels, 43
- rear side ablation patterning, 183
- reduction of particulates, 340, 341, 350
- refractive eye surgery, 357, 396
- refractive index modulation, 314
- refractive laser surgery, 19, 361
- resists, 20, 98, 176, 226, 242, 298,
- resonant charging, 58, 59, 60
- resonant regulating pulsed power, 60
- restoration, 142
- reticle, 298, 301, 302, 401, 402
- retina implant, 169
- safety standards, 64, 65, 68, 71
- screen electrodes, 49, 51
- selective micro-deposition, 285
- SEMI standards, 71, 426
- semiconductor lasers, 22, 38, 39
- semiconductor switches, 56, 61
- sensor networks, 313, 318, 319
- sequential lateral solidification (SLS), 310
- shaping lens surfaces, 234
- shock wave, 64, 76, 151, 285
- silica glasses, 228, 233, 254, 266
- silicon thin films, 306
- silicones, 169
- solid-state lasers, 3, 38, 165, 312, 385
- solid-state switch module, 386
- solid-state switching, 56, 57
- soot, 190, 233
- spark preionization, 49, 50, 86
- spatial light modulator (SLM), 391
- spiker-sustainer circuits, 57, 58
- spinnerets, 173
- spontaneous emission, 35, 36, 44, 100, 356, 379
- SQUID, 140, 171, 185
- stents, 216
- step-and-repeat, 157, 387
- stimulated emission, 6, 34, 36, 43, 374

- stoichiometry of multicomponent targets, 339
strain, 319, 320
streamer and arc formation, 48
stress relaxation, 340, 343, 349
stroboscopic Schlieren images, 285, 288, 289, 290
super-lateral growth (SLG), 309
superhard coatings, 335, 336, 349
support system, 133
surface cleaning, 6, 141
surface corona preionization (SCP), 50
surface mount technology, 194
surface mounted devices (SMDs), 326
surface-discharge pre-ionization, 407
surface-guided discharges, 50
sustainer, 57, 58
switched mode power supply (SMPS), 58, 61, 62
switching technology, 57, 58
technical combustion, 351, 356
technology nodes, 89, 93, 400
technology roadmap, 90, 221, 300
telecommunication components, 181, 243
test leaks, 174
TFT annealing, 140, 143, 306,
Theodore H. Maiman, 6, 35, 39
thermo-elastic shock wave, 286, 292
thick ta-C films, 344, 345
thin film transistors, 26, 306
threshold fluence, 150, 165, 227, 230, 280
through-holes, 159, 174, 193, 197, 235
thyatron tube, 53
thyristor-switched compressor, 56
time resolved Schlieren imaging, 287
tin-vapor-based, 415
trabecular meshwork, 367, 368
trabeculotomy, 367, 368
triatomic gases, 44
trimming planar lightwave circuits, 261
Ultra-fast UV Laser Transfer, 285
UV preionization, 9, 49, 86
UV solid-state lasers, 330
UV-coating, 119
vacuum-ultraviolet optical tools, 222
vector marking, 330
via drilling, 144, 187
voltage regulation, 60
wave theory, 33
wave-particle duality, 33
wavefront analysis, 28, 396
wavefront measurement, 114, 115
waveguides, 165, 237, 238, 264, 265
wavelength control, 95
wear-resistant coatings, 339, 343
Willard H. Bennet, 407
window contamination, 51
wire stripping, 144,
Wolter telescopes, 401
X-ray, 38, 49, 124, 176, 339, 380
X-ray preionization, 13, 87
X-ray source, 86, 373
XeCl laser, 12f, 42f, 82, 85f, 113, 171, 199, 287, 353, 368, 370
XeF, 9f, 42, 144, 187, 322, 331, 356
xenon target, 402, 417
XUV coatings, 124, 126
Z-pinch, 407, 408, 411

Printing and Binding: Strauss GmbH, Mörlenbach